THE UNIVERSITY OF NOTTINGHAM

Centrifuge and analytical modelling of offshore wind turbine monopile foundations

by

John E Elvis

A thesis submitted in partial fulfillment for the degree of Doctor of Philosophy

in the

Faculty of Engineering
Department of Civil Engineering

October 31, 2019

Declaration of Authorship

I hereby declare that, except where the reference is made to the work of others, the contents of this thesis are original and have not been submitted for any other degree at any university. I can confirm that this dissertation is the result of my own work, which I have conducted for four years, and it includes nothing from outside except where it is indicated specifically.
The thesis includes no more than 65,000 words, including references, figures, equations and tables.

Signed: ____

Date: ____

Abstract

Wind energy is an interesting prospect due to its availability and sustainability along the coast and offshore locations. Development of offshore wind farms is projected to increase very rapidly within the next decades, which is expected to efficiently improve the electricity challenges in areas located along the sea. While the offshore wind energy is collected by turbine structures, which are supported by towers and foundations, the challenge remain on the provision of cost-effective foundations to resist the lateral loads from wind, waves and dynamic actions of the wind turbine nacelle-rotor. The popular foundations used are monopiles, having a competitive advantage of stability, ease of installation and low cost of materials compared to other types. The loads acting on monopiles are cyclic in nature, and can be resisted by horizontal earth pressure mobilised in the soil surrounding the pile. The cyclic loads can affect the strength and stiffness of both the soil and pile, leading to accumulated rotation and change of overall stiffness. Studies have been carried out regarding these effects, however there has not been a clear understanding of the response of a stiff pile when subjected to a large number of cycles.

The literature has revealed that the current method (*p*-*y* curves method) for analysing and designing the offshore monopiles is insufficient, tend to overestimate the stiffness of the rigid piles, and leading to interference between resonance and natural frequency of the wind turbines. The method usually regards the soil as a series of non-linear wrinkle spring and derives its base on the empirical relationships developed from full-scale tests on slender piles. The deficiency of the prevailing design approach, therefore, justifies a need for further research to develop a model which will monitor how the monopiles foundations respond to both monotonic and cyclic loading.

This thesis therefore, presents an experimental and theoretical research approach that will improve the understanding of the response of monopile foundations in sands when subjected to both monotonic and cyclic loading. The experimental work involves a comprehensive design and development of a new mechanical loading system in a geotechnical centrifuge, with model tests scaled to represent full-scale wind-turbine monopiles. The test programme is designed to identify the key mechanisms driving pile response, including investigating the monotonic loading behaviour as well as the response of a pile to long term cyclic loads. The methodology

developed and data collected from this thesis will provide a potential contribution to the establishment of a better understanding of monopile responses within the field.

The experiment was carried out by initially, scaling down the prototype monopile using a 1:100 geometric scale. Three monotonic tests were carried out at 100g to identify the responses under monotonic loading, estimate the ultimate capacity and determine the initial (tangent) stiffness of the pile-soil system. One monotonic test was conducted at 30g as a reference to the cyclic test results. The parameters extracted from the monotonic tests are used as the basis for the design of cyclic loading system and analysis of the cyclic test results. Available models from the literature were modified to capture the ground global response of the pile under monotonic loading. The models were employed in a kinematic approach, with soil being modelled as a series of spring elements and the pile as an elastic beam element. The model pile in the centrifuge was not instrumented, hence assumptions were made to match the global response of the monotonic centrifuge tests at the ground surface. With the absence of data along the embedded depth of the pile, the fitting constants were used to estimate the ultimate capacity and the concept of the modulus of subgrade reaction. The model was also used to the published centrifuge test results of the past monopile research.

The methodology developed for cyclic load tests incorporated the effects of cyclic loading on the response of a monopile. The validity of the model is supported by centrifuge tests in which a stiff model pile, installed in cohesionless soil, was subjected to a series of load cycles with load amplitude and frequency. The tests were carried out to investigate the responses of the newly developed model. Due to technical challenges during the model testing, all cyclic tests were achieved at centrifuge acceleration of 30g instead of the 100g for the monotonic tests. Selected tests were used to examine the total cyclic pile-head response to gain an insight into the accumulation of pile-head displacement and change in cyclic secant stiffness. Power and logarithmic functions were used to predict the accumulated displacement and cyclic stiffness variation using the data from the centrifuge, respectively. The key experimental findings of the cyclic tests were then used to develop a theoretical model that captures the unload-reload hysteresis behaviour. The model function, called the modified Romberg Osgood (MR-O), is rigorous yet simple, and is framed where the pile-head cyclic response is modelled as the hysteresis loops for the backbone, unloading and reloading curves. The model was calibrated against the cyclic centrifuge tests and successfully reproduce the main elements of the pile response with high accuracy. However, it does not predict precisely the cyclic accumulation and change in cyclic stiffness as shown in the experiment, thus further justification will still be required. Nevertheless, the newly developed model and suggested methodologies in this thesis can be used as a primary stage for research developers to understand the behaviour of foundations supporting offshore wind turbines, with scientific justification based on the centrifuge model scale tests.

Acknowledgements

The work described in this dissertation was carried out at the University of Nottingham through the entire period, from February 2014 to May 2019. Over this period there have been a people who provided academic assistance and social motivation. First and foremost, I would like to sincerely thank my supervisors, Dr Alec Marshall, Dr Charles Heron, for their assistance, encouragement, and guidance during my time at Nottingham. I also extend my heartfelt gratitude to Dr David Hargreaves for encouraging me to pursue my PhD. My deepest gratitude is also extended to Mr Andrew Dawson as my MSc. Geology lecturer and PhD internal examiner. His advice and motivation have been helpful on my research plan.

Furthermore, the experimental achievement would not have been successful if not the support of the technical staff at the Department of Engineering, University of Nottingham. I appreciate their keen support. In particular, I am grateful to Dr Idinyang Solomon, Jim Meakin and Luke Bedford for their patience in the development of experimental equipment and help to solve some challenges. I am also grateful to all my colleagues in the Nottingham Centre for Geomechanics (NCG), who indirectly supported me in school life, and kindly acknowledge their social encounter.

My utmost acknowledgement to my scholarship providers, the Commonwealth Scholarship Commission and the University of Nottingham for the financial support which enabled me to undertake my PhD studies and live peacefully for the entire period here in the UK. I also acknowledge the support from my current employer, the University of Dar Es Salaam, Tanzania for a nomination in the scholarship award, their patience and moral support. Lastly but with an utmost importance I recognise the contribution of my fiancee, Eng. Patricia Burure and my daughter Pauline for bearing my absence for the entire duration of my studies.

Contents

List of Figures

List of Tables

Abbreviations

MW	**M**ega **W**att
DNV	**D**et **N**orske **V**eritas
MR-O	**M**odified **R**amberg **O**sgood
R-O	**R**amberg **O**sgood
KZ	**K**ondner and **Z**elasko
MKZ	**M**odified **K**ondner and **Z**elasko
OWT	**O**ffshore **W**ind **T**urbine
GW	**G**iga **W**att
EU	**E**uropean **U**nion
UK	**U**nited **K**ingdom
OWTP	**O**ffshore **W**ind **T**urbine **P**ile
SLC	**S**tatic **L**oad **C**ell
LVDT	**L**inear **V**ariable **D**ifferential **T**ransducer
BEF	**B**eam **E**lastic **F**oundation
BWF	**B**eam **W**inkler **F**oundation
ULS	**U**ltimate **L**imit **S**tate
SLS	**S**erviceability **L**imit **S**tate
FLS	**F**atigue **L**imit **S**tate
FEM	**F**inite **E**lement **M**odelling
FEM	**F**inite **D**ifference **M**odelling
GWEC	**G**lobal **W**ind **E**nergy **C**ouncil
EWEA	**E**uropean **W**ind **E**nergy **A**ssociation
API	**A**merican **P**etroleum **I**nstitute
OW	**O**ne **W**ay load direction
TW	**T**wo **W**ay load direction
RPM	**R**evolution **P**er **M**inute
LHS	**L**eft **H**and **S**ide
RHS	**R**ight **H**and **S**ide

CPT	**C**one **P**enetration **T**est
NCG	**N**ottinghan **C**entre of **G**eomechanics
MEMS	**M**icro **E**lectro **M**echanical **S**ensor
DAS	**D**ata **A**cquisation **S**ystem
PLC	**P**rogrammable **L**ogical **C**ontrol

Symbols

Roman symbols

A_n or C_k	cyclic secant stiffness rate	–
A_i or A	DNV modified factor for ultimate soil resistance	–
A_k	KLV modified factor for ultimate soil resistance	–
A_j	Thesis modified factor for ultimate soil resistance	–
C_N	displacement increasing rate	–
C_u	coefficient of uniformity	–
C_α, C_c	cyclic stiffness coefficient	–
C_1, C_2, C_3	empirical parameters	–
D	diameter of pile	m
d_{50}	average grain size	mm
DF	ratio of load amplitude	–
D_{ref}	reference diameter of pile	m
D_r	relative density of soil	%
E_p	Young's modulus of pile	kPa
E_s	Young's modulus of soil	kPa
$E_{s,max}$	maximum Young's modulus of soil	kPa
E_{eq}	equivalent Young's modulus for solid pile	kPa
e_o	soil void ratio	–
$E_{s,ref}$	reference soil modulus	MPa
f(e)	void ratio function	–
f_n	natural frequency	Hz
f_e	excitation frequency	Hz
F_y	Bouc-Wen restoring force	kN
G_s	specific gravity of soil	–
G_b	material constant	–
G_{sec}	secant shear modulus of soil	kPa
G_{max}	maximum shear modulus of soil	kPa

G_{tan}	tangent shear modulus of soil	kPa
G^*	modified shear modulus of soil	kPa
g	gravitational acceleration	m/s^2
h	water depth	m
h_m	model depth	m
h_p	prototype depth	m
H_{max}, F_{max}	maximum cyclic load	kN
H_{min}, F_{min}	minimum cyclic load	kN
H_u	ultimate capacity of pile	kN
H_i or H	lateral load on pile head	kN
$H_{i(R)}$	reloading lateral foce	kN
$H_{i(U)}$	unloading lateral force	kN
H_c	force resistance at last load reverse	kN
H_a	lateral load amplitude	kN
H_{avg}	average lateral load amplitude	kN
H_{AMP}	peak to peak lateral load magnitude	kN
$\hat{H_A}$	dimensionless unloading force	–
H_{cyc}	maximum cyclic load	kN, MN
$H_{u(R)}$	reloading ultimate resistance	kN
$H_{u(U)}$	unloading ultimate resistance	kN
$H_{i(U)}$	unloading force for each deflection	kN
$H_{i(R)}$	reloading force for each deflection	kN
H_A	initial load reversal	kN
H_B	final load reversal	kN
I_p	second moment area of pile	m^2
I_R	relative dilatancy index	–
k_h, k_i or k	coefficient of subgrade modulus	kN/m^3
$k_{h,max}$	maximum coefficient of subgrade modulus	kN/m^3
K_h, K_{py}	initial modulus of local *p-y* response	kN/m^2
K_i, K_t	initial (tangent) stiffness of global H-y response	kN/m
$K_{i,ref}$	reference stiffness	kN/m

K_L	lateral foundation stiffness	kN/m or kN/mm
K_R	rotational foundation stiffness	kNm/rad
K_f	final tangent stiffness	kN/m
$K_{h(U)}$	unloading initial subgrade modulus	kN/m^2
$K_{h(R)}$	reloading initial subgrade modulus	kN/m^2
$K_{t(R)}$	reloading tangent stiffness	kN/m
$K_{t(U)}$	unloading tangent stiffness	kN/m
K_N	cyclic secant stiffness after N cycles	kN/m
K_1	cyclic secant stiffness for the first cycle	kN/m
k_R	pile flexibility factor	–
K_p	passive earth pressure coefficient	–
K_a	active earth pressure coefficient	–
K_o	earth pressure coefficient at rest	–
K_c	earth pressure coefficient due to cohesion	–
K_{br}	net earth pressure coefficient from Meyerhof	–
K_1	unloading stiffness of the first cycle	kN/m
$K_{s,N}$	cyclic load stiffness of the N^{th} cycles	kN/m
K_{mon}	stiffness of the monotonic loading	kN/m
K_R, T_R	pile-soil relative stiffness	–
K_b, K_c	stiffness dimensionless functions	–
L_T	total length of the pile	m
L_p or L	length of the pile from the ground	m
L_e	eccentricity of lateral load	m
L_c	critical length	m
L_{max}	maximum embedded length	m
M_i or M	moment on the pile	kNm
M_t	mass of the tower	tonnes
M_a	mass of nacelle-rotor	tonnes
M_1	applied weight	kg
M_2	dead weight	kg
M_3	auto-balance weight	kg

$\mathrm{M_{max}}$	maximum cyclic moment	kNm
$\mathrm{M_{min}}$	minimum cyclic moment	kNm
$\hat{\mathrm{M}}$	dimensionless moment	–
N	number of cycles	–
$\mathrm{N_s}$	geometric scaling factor	–
$\mathrm{N_{sat}}$	geometric scaling factor for saturated sand	–
$\mathrm{N_q}$	bearing capacity factor	–
$\mathrm{P_z}$, $\mathrm{P_{z(i)}}$, $\mathrm{P_n}$	soil resistance along the depth $\mathrm{Z_i}$	kN/m
$\mathrm{P_u}$	ultimate soil resistance	kN/m
$\mathrm{P_{us}}$	DNV ultimate soil resistance at shallow depth	kN/m
$\mathrm{P_{ud}}$	DNV ultimate soil resistance at deep depth	kN/m
$\mathrm{P_{ref}}$ or $\mathrm{P_a}$, $\mathrm{P_{at}}$	reference or atmospheric pressure	$\mathrm{kN/m^2}$
$\mathrm{P_m}$, $\mathrm{p'}$	mean effective stress	$\mathrm{kN/m^2}$
$\mathrm{P_c}$	soil resistance at last load reverse	kN/m
$\mathrm{P_{i(R)}}$	reloading soil resistance	kN/m
$\mathrm{P_{i(U)}}$	unloading soil resistance	kN/m
$\mathrm{P_{u(R)}}$	reloading ultimate soil resistance	kN/m
$\mathrm{P_{u(U)}}$	unloading ultimate soil resistance	kN/m
$\mathrm{P_B}$	initial reloading soil resistance	kN/m
$\mathrm{R_e}$	effective centrifuge radius	m
R	centrifuge radius	m
s, r	MR-O curve control constants	–
t	asymptotic constant	–
$\mathrm{t_p}$	thickness of the pile	–
$\mathrm{t_a}$, $\mathrm{t_b}$, $\mathrm{t_r}$	degradation factors	–
$\mathrm{T_1}$, $\mathrm{T_2}$, $\mathrm{T_3}$, $\mathrm{T_4}$	tension forces on wires	kN
$\mathrm{T_b}$, $\mathrm{T_c}$	Accumulated displacement dimensionless functions	–
$\mathrm{V_T}$	vertical load applied to the pile	kN
W	Energy stored	J
$\mathrm{y_p}$, $\mathrm{Y_p}$	lateral displacement at the pile head	m
$\mathrm{y_g}$, $\mathrm{Y_g}$	lateral displacement at ground surface	m

$y_{z(i)}$, y_n	lateral displacement at depth Z_i	m
$y_{i(R)}$	reloading lateral displacement at depth Z_i	m
$y_{i(U)}$	unloading lateral displacement at depth Z_i	m
y_c	displacement at last load reverse	m
y_N	displacement after N cycles	m
y_1	displacement after the 1 cycle	m
Y_{min}	minimum displacement	m
Y_{max}	maximum displacement	m
Y_{amp}	peak to peak displacement magnitude	m
Y_a	lateral displacement amplitude	m or mm
Y_{avg}	average lateral displacement amplitude	m or mm
Y_A	unloading displacement	$mormm$
Y_B	reloading displacement	$mormm$
Z	depth below the ground surface	m
Z_r	depth to the rotation point, below the ground surface	m
$Z_{i,ref}$	reference depth	m

Greek symbols

α_p	modulus of subgrade (K_h) constant	–
β_p	stiffness adjustment constant for MR-O and DNV	–
γ	effective unit weight of soil	kN/m^3
$\gamma_{z(i)}$	shear strain at i^{th} point	%
γ_r	reference strain at failure	%
γ_c	shear strain at last load reversal	%
γ_{max}	maximum shear strain	%
γ_d	dry unit weight of soil	kN/m^3
γ_{sat}	saturated unit weight of soil	kN/m^3
ν_s	Poisson's ratio	–
ω	angular frequency	kN/m
ϕ	friction angle	degree
ϕ_{max}	maximum friction angle	degree

ϕ_{cr}	critical friction angle	degree
δ	interface friction angle	degree
ρ	density	$\mathrm{kg/m^3}$
σ_{p}	stress in the prototype	$\mathrm{kN/m^2}$
σ_{m}	stress in the model	$\mathrm{kN/m^2}$
σ_3	mean stress	kPa
σ_{v}	vertical stress	kPa
$\tau_{\mathrm{z(i)}}$	shear stress at a point z	$\mathrm{kN/m^2}$
τ_{f}	shear strength of soil	$\mathrm{kN/m^2}$
τ_{c}	shear stress at last load reversal	$\mathrm{kN/m^2}$
θ_{N}	pile rotation after N cycles	degree
θ_1	pile rotation for the first cycle	degree
θ_{s}	pile rotation from static load	degree
θ_{i} or θ_{p}	pile rotation at a point i	degree
ε_{N}	lateral strain after N cycles	–
ε_1	lateral strain of first cycle	–
ζ_{b}	cyclic load amplitude ratio	–
ζ_{c}	cyclic load characteristics ratio	–
ζ	load control factor	–
ξ_{N}	accumulated displacement control function	–
κ_1	stiffness accumulation/degradation constant	–
κ_2	displacement accumulation constant	–
χ	hysteresis loops load amplitude ratio	–

Chapter 1

INTRODUCTION

1.1 Background on offshore wind energy industry

The use of fossil fuels and its impact on the global climate has brought the need of researchers to seek an alternative clean source of energy. Reducing dependence on fuels is of primary importance for governments and industries worldwide. For instance, the European Union has set the binding agreement to ensure that the power from renewable sources will increases up to 20% of the total energy by 2020 (Commission, 2010). Currently, of all renewable energy sources, wind power has received more attention and has been debated as a potential source for achieving the 2030 European carbon reduction target. Apart from the fact that wind power offers competitive prices on production of renewable energy has also been used as alternative technology in achieving the energy and environmental goals (LeBlanc, 2009). In Europe, the onshore wind contributed more wind energy than offshore wind when comparing the total production (for instance, 4.85 TWh was generated onshore above 3.57 TWh offshore in the UK by end of 2015), however, offshore wind has big potential and a larger number of projects are under construction (Abadie, 2015). The offshore environment is generally characterised by stronger wind conditions than onshore, which permits the installation of larger wind turbines with greater power output (Cuéllar, 2011, Klinkvort et al., 2012).In addition, the abundant open space with less obstruction and turbulence intensity are the drivers for offshore wind farms. Despite the extra cost, the larger and substantial energy production have driven most of the European countries to invest more on offshore locations than onshore sites (Klinkvort et al., 2012, LeBlanc, 2009). Figure 1.1 provides an overview of the annual and cumulative capacity of offshore wind power connected to the grid, illustrating the growth of the sector in recent years (Europe, 2018), with the total capacity of 15,780 MW generated by the end of 2017. This achievement motivated several countries of the European Union to develop ambitious policies to set the targets and development visions for harvesting the renewable energies in the future. Germany and the UK have set the global targets of 20% of electricity production from the renewable sources by 2030

(Byrne and Houlsby, 2003), where in 2017, 3,148 MW of new offshore wind power capacity was connected to the grid which is 13% higher than 2016. As shown in Fig. 1.2(a), the UK remains the EU country with the largest amount of installed offshore wind capacity, representing 43% of all installations, followed by Germany 34% and Denmark with 8%, despite no additional capacity in 2017. The Netherlands (7%) and Belgium (6%) follow the pace (Europe, 2018). Other countries around the globe are planning to follow the Europe footsteps by investing in offshore wind energy development. For instance, Asia (China) and North America (United States) have already taken new initiatives (Westgate and DeJong, 2005).

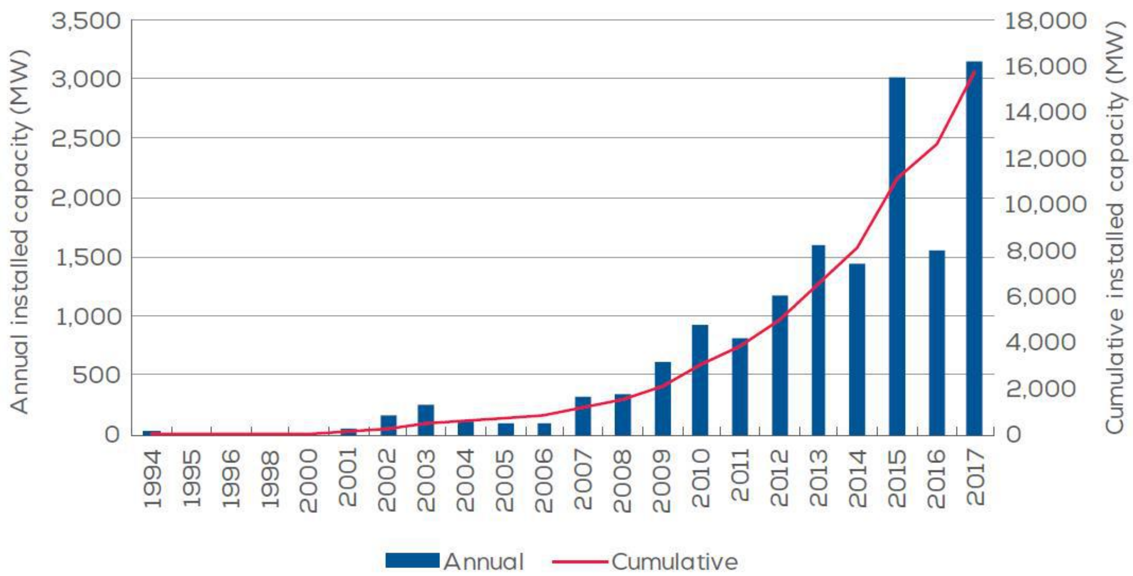

Figure 1.1: European cumulative and annual offshore installed capacity(MW) at the end of year 2017 (Europe, 2018).

Although research indicate a significant improvement on the offshore wind infrastructure and turbine technology, the installation and operation costs can still be a challenge. For example, from 2010 the UK has attracted 47% of the offshore wind turbine investment, worth 35 bn, followed by Germany with 28 bn (37% in investment) (Europe, 2018). A major challenge of the offshore wind industry is to reduce the cost while targeting the installation of larger turbines in deeper water (Europe, 2018). However, this challenge can be tackled by developing an optimised design of the superstructure and foundation (Abadie, 2015), because the foundations accounts for about 25-30% of the total installation cost of the wind turbine project (Byrne and Houlsby, 2003). Apart from the cost involved in the project, the additional challenges may be the geotechnical site conditions, water depth and environmental loads. Therefore, to ensure the sustainability of the wind turbines the foundations must be well designed.

Several types of the foundations have been researched and used, including gravity bases, monopiles, monopod, tripod, jacket and floating structures (Cuéllar, 2011, LeBlanc, 2009, Malhotra, 2010). However, the economic choice of these foundations depend on the water depth, seabed, loading characteristics and cost of materials (Malhotra, 2010). According to statistics provided by EWEA (2013), the most common foundation adopted for a wide range of site conditions are monopiles, which have been used in water depths up to 35 m. For instance, about 74% of all the installed substructures in European offshore wind farms have used monopiles , which is a substantial comparative of other types of foundations (see Fig. 1.2(b)), followed by gravity-based foundations in 16%, jacket foundations in 5%, tri or tetra piles in 3% and tripods only 2%. Therefore, the use of monopile seems likely to dominate compared to other foundation due to the competitive advantages of ease of transportation, cost-effectiveness and ease of installation.

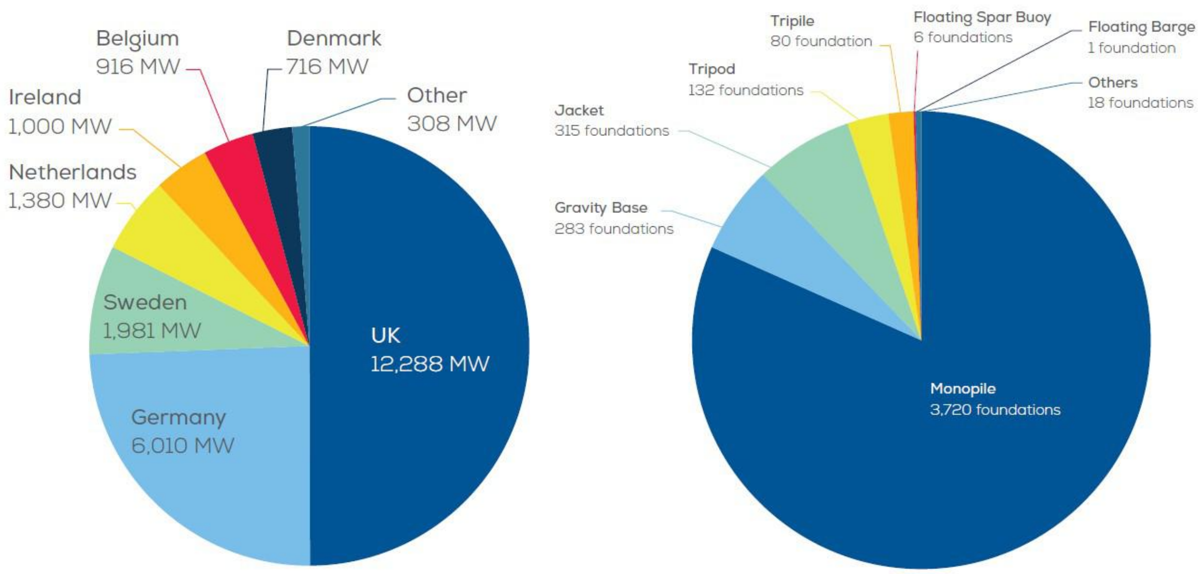

(a) Capacity installed in European countries in 2017

(b) Foundation types end of year 2017

Figure 1.2: Percentage of installed capacity in European countries and common foundation type (Europe, 2018).

Monopiles are designed according to semi-empirical *p*-*y* curves, which were derived from Reese et al. (1974) tests on flexible piles, and specified in the current design codes (API, 2007, DNV, 2014). Although the method has been used over decades, the accuracy of the existing empirical design is till questionable to whether it may suffice the design of monopiles. Previous studies (Abadie, 2015, Kirkwood, 2016, Klinkvort et al., 2012, Lau, 2015, Leblanc et al., 2010) have reported the same argument and suggested that the DNV (2014) code of practice is not sufficient to meet serviceability requirement of monopile foundations. The use of the method has multiple limitations: inappropriate estimation of initial pile-soil stiffness and does not account the effect of cyclic secant stiffness and accumulation displacement. Therefore, the lack of knowledge in these area requires further investigation.

The aim of this thesis is to develop an engineering tools, which can be used in the design of the offshore monopile foundation in cohesionless. The findings will contribute to the science and increase economic feasibility of future offshore wind farms.

1.2 Foundation options for offshore wind turbines

The role of foundations in the offshore environment is to transfer the vertical and horizontal loads from the superstructure to the surrounding soil. While the bearing capacity of the soil and the magnitude of the loads are the primary determinants of the size and depth of the foundation, the choice of the foundation type depends mainly on the depth of water, soil characteristics and economic reasons (Bontempi et al., 2009). Various foundation types have been researched and used in years and can be categorised as either fixed or floating structures in relation to water depth (Bontempi et al., 2009, Byrne and Houlsby, 2006). For instance, in shallow water depth ($\mathrm{h} \leq 30\mathrm{m}$), the foundations used are normaly gravity base, monopiles and single suction caissons, while tripod, jacket and lattice are located at intermediate depths ($30 \leq \mathrm{h} \leq 60$ m). Figure 1.3 shows the range of foundation and support structure concepts for offshore wind turbines. A general discussion of each type of these foundations is presented in the subsequent text.

(a) *Gravity base structure*

In Fig. 1.3, the gravity base foundation is designed to be self-weighted to prevent failure through tilting, uplift and sliding. It is limited to the site where installation in underlying seabed is difficult due to hard rocks (Haigh, 2014, Kaiser and Snyder, 2012, LeBlanc,

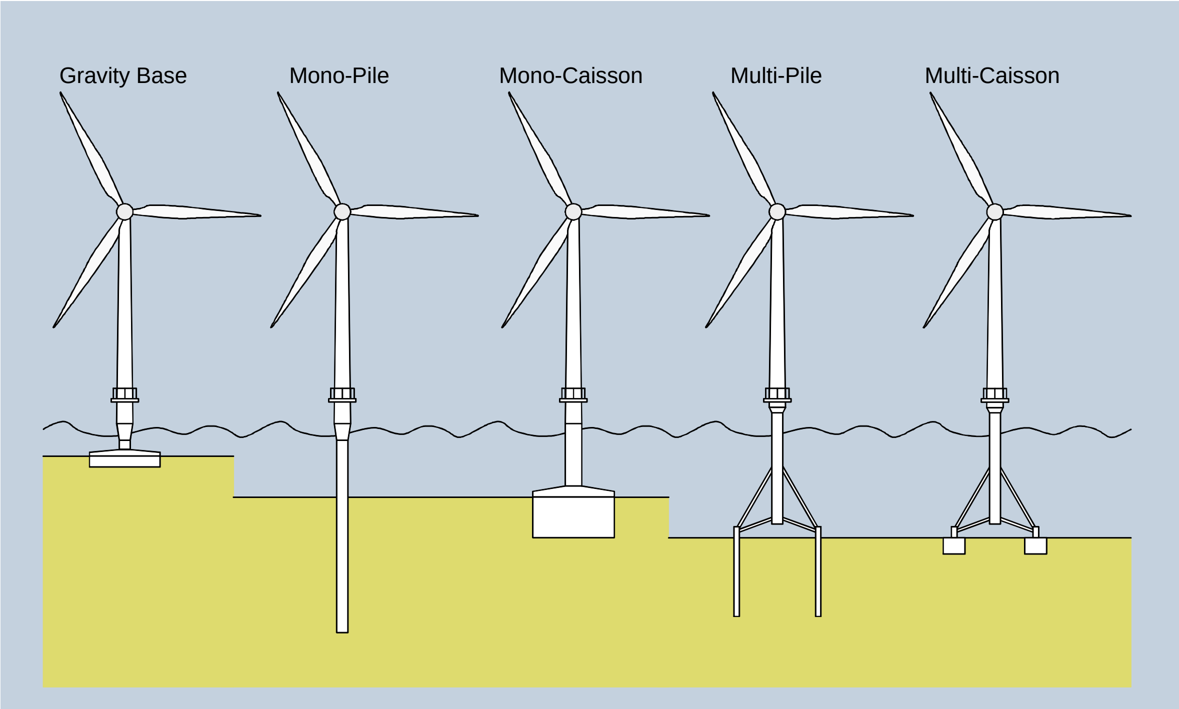

Figure 1.3: Typical offshore foundation types, from Byrne and Houlsby (2006)
.

2009, Malhotra et al., 2009). The structure is more efficiency and cost effective when the environmental loads are relatively low (Malhotra et al., 2009).

(b) *Monopile*

A monopile is a rigid, long steel open ended pile of larger diameter, which is driven into the seabed by using a hydraulic piling hammer or by drilling. The thickness and depth of the pile depends on the design load, soil conditions, water depth, design code and environmental conditions. The typical diameter of the pile ranges from 4-8 m and its wall thickness is between 50 to 150 mm (Kaiser and Snyder, 2012, LeBlanc, 2009, Malhotra et al., 2009). In addition to that, during the installation the pile is always driven 5-6 times its diameter into the seabed and the embedded depth is in the range between 20 to 40 m (Byrne and Houlsby, 2003, Kaiser and Snyder, 2012, Klinkvort et al., 2012). This type of foundation is the focus of this study and more details are provided in Section 1.3.

(c) *Mono-Caissons*

The mono-caisson foundation is a sizeable upturned bucket, made of steel hollow circular tube closed by the lid at the upper end. The suction-caisson may be installed via stage process: the caisson is lowered on a pre-prepared (levelled) seabed where it embeds under its weight. During installation, it penetrates the soil then water is pumped out the caisson interior (create net pressure difference which drives the foundation into the seabed) (Houlsby and Byrne, 2000). They are best in low permeability soils such as normally consolidated clay or fine sand (LeBlanc, 2009). They are not recommended for use in sand with high permeability because the excess pore pressures dissipate rapidly.

(d) *Multipod (Multi-pile and multi-caisson)*

Multipod foundations have a single vertical column above the water level with sub-sea diagonal braces which transfer the turbine weight to three or four legs fixed pile (diameter less or equal to 2 m) or caissons in a triangular arrangement. These foundations defer from monopods as the material cost of each pile is smaller, but construction takes longer, and the design is more complex. They are rarely used for the foundations of offshore wind turbines due to the increased cost of installation and possibly designed for the oil and gas industrial (LeBlanc, 2009).

1.3 OWT components and monopile details

As previously described, monopiles have been proven to be the most popular foundation especially in the offshore wind farming due to their economic advantage and ability to sustain the severe loading conditions (Abdel-Rahman and Achmus, 2005, Achmus et al., 2008, 2009, Arshad and OKelly, 2013, Bontempi et al., 2009, Lau, 2015, LeBlanc, 2009). The wind turbine structure is divided into three parts: the main structure (carrying the main loads), secondary structure (produce and transfer energy) and auxiliary structure (serviceability, maintainability and emergency during design life). However, this study dealt with the main structure including the rotor-nacelle assembly (rotor, nacelle, and blades), support structure (the tower), substructure (include transition piece) and foundation. The schematic drawing and photographs of an offshore wind turbine structure are shown in Fig. 1.4 and 1.5, respectively. All components including a monopile foundation, the substructure, transition piece, tower, rotor blades and nacelle (hub) are detailed in Fig. 1.4(a) and 1.4(b). In Fig. 1.4, support structure and foundation are used to indicate the entire structure below the yaw system. They are made of steel, used to keep the turbine in proper positions and being exposed to environmental forces (waves and sea current). At the seabed level, the substructure connects the transition piece and tower to the foundation. A plate rolled conical section tower is used to carry the nacelle and rotor blades. Transition piece is used to connect the support structure and tower, aiming to correct any vertical misalignment expected during the installation process. A nacelle (a key electromechanical component) including gearbox and generator are used to generate and transmit the electric energy. The rotor blades, made of fibreglass mats impregnated with polyester, are connected to nacelle to receive the wind forces. The power cable is connected to the turbine (nacelle) and inserted in a plastic J tube to carry the cable to the cable trench (Arshad and OKelly, 2013, Malhotra et al., 2009).

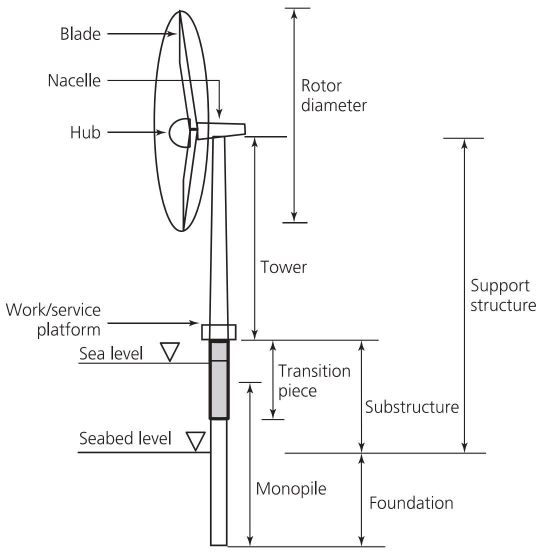

(a) OWT component details

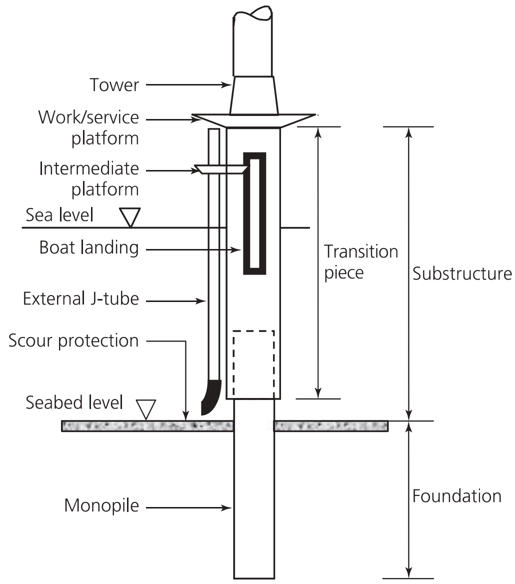

(b) OWT substructure and foundation detail

Figure 1.4: Major components of an OWT system, from Arshad and OKelly (2013).

(a) OWT photograph detail (b) Transition (c) Monopile

Figure 1.5: The OWT photos, from Kallehave et al. (2015).

A 5 MW class wind turbine chosen in this study is supported by a monopile foundation with details presented in Table 1.1 (Lesny and Wiemann, 2006).

Table 1.1: Monopile for 5 MW class wind turbine (Lesny and Wiemann, 2006)

Physical Quantities	**Symbol**	**Value**	**Units**
Load eccentricity	L_e	20	m
Embedded depth	L	30	m
Diameter and thickness of the pile	D, t	6, 0.1	m
Young's modulus	E_p	210	GPa
Area moment of inertia	I_p	8.0675	m^4
Flexural stiffness	E_p I_p	1694	GNm^2

1.4 Offshore wind turbine design loads

1.4.1 Design loads on monopiles

The offshore wind turbines are normally anchored on wide monopiles normally impacted by a number of both lateral, longitudinal and torsional loads and moments. The current design method for piles has been derived from the offshore oil and gas industry. However, there seems to be a potential difference between the loads applied on offshore oil and gas platform to those which may act on the offshore wind turbines. As depicted in Fig. 1.6(b), the vertical loading of oil and gas platform is larger than lateral loading, whereas the offshore wind turbine foundations (see Fig. 1.6(a)) are characterised by relatively small vertical loads, large moments at the seabed and strong cyclic loading (Byrne and Houlsby, 2003, Cuéllar, 2011, LeBlanc, 2009, Malhotra, 2007). Furthermore, the load from oil and gas was designed to achieve an ultimate limit state (ULS) requirement while for the offshore wind turbine the horizontal loads and overturning moments are therefore of more importance (Kirkwood, 2016). The offshore design of monopiles is controlled by serviceability limits in which the pile rotation and pile-head deflection are limited to 0.5 ^{o} and 10%-20% of pile diameter, respectively (Achmus et al., 2009, DNV, 2014, Malhotra, 2007). This study therefore aims at establishing a better understanding on response of the monopiles when subjected to long term cyclic loading including both operational and environmental loads. While the environmental loads are from action of wind and waves the operational loads refer to the dynamic loads due to nacelle-rotor (LeBlanc, 2009, Villalobos, 2006). Most of the operational offshore wind-farms consist of turbines with rated capacity between 2 and 5 MW and would vary according to the water depth and environmental conditions (Byrne and Houlsby, 2015). A typical dimensions and loads on a 5 MW wind turbine is presented in Fig. 1.6(a) (Cuéllar, 2011). This turbine is supported by a monopile of 7.5 m in diameter, driven 30 m into the seabed with a lever arm of 30 m above the seabed (Cuéllar, 2011). From the figure, the maximum horizontal load from wind and wave actions was roughly estimated as 5 to 15 MN. Byrne and Houlsby (2003), LeBlanc (2009), Abadie (2015) and Kirkwood (2016) have employed a typical monopile of 3.5 MW with 3 to 4 m in diameter, 50 mm wall thickness and embedded depth of 20 m. The wind loads applied on the turbine and tower are termed as steady and stochastic aerodynamic forces generated by mean

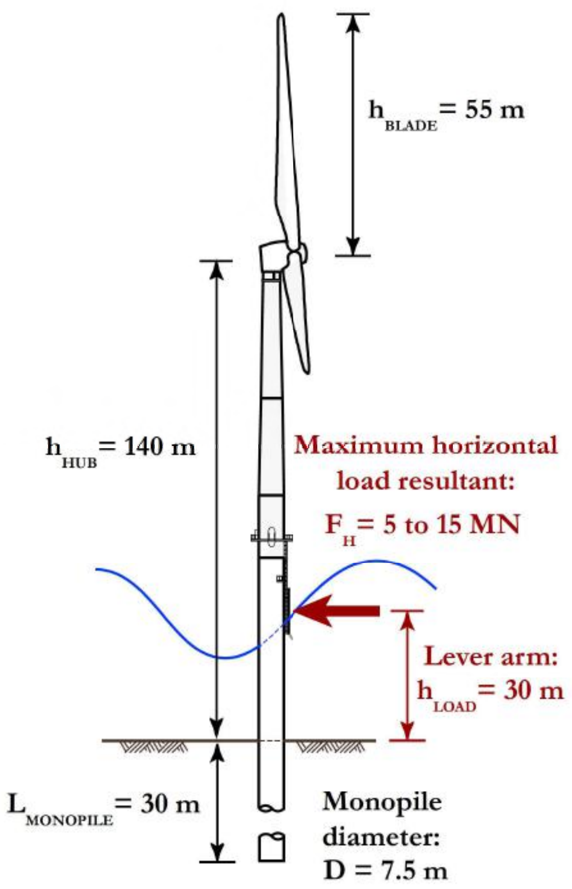

(a) Loads and dimensions for 5 MW class wind turbine, from Cuéllar (2011)

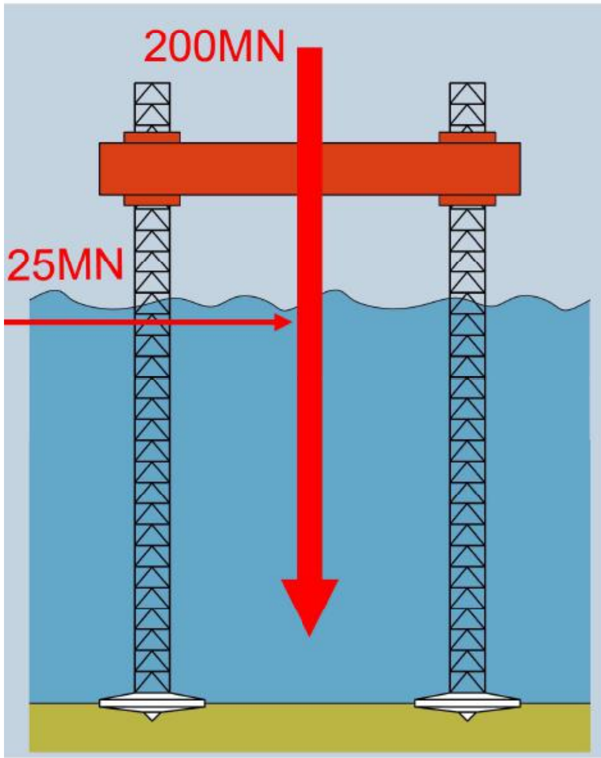

(b) Loads on oil and gas Jack-up Rig, from Byrne and Houlsby (2003)

Figure 1.6: Loads on offshore wind turbine and oil and gas jack-up rig.

wind speed and turbulent wind structures, respectively (Abadie, 2015). The hydrodynamic loads from the waves comprise of drag, inertia and cross-flow forces and depend on the water depth, wave height and period. They both result in a combined shear force and overturning moment at foundation level. The aerodynamic loads are applied at a high level on the turbine hub and typically account for 25% of the horizontal load and 75% of the overturning moment (Byrne and Houlsby, 2003, Kirkwood, 2016). The relevant typical environmental parameters for estimation of resultant offshore lateral load in the North Sea is given in Table 1.2 (Byrne and Houlsby, 2003). The description of load calculation is beyond the scope of this thesis and detailed guidance is available in DNV (2014) code. Table 1.3 provides a breakdown of cyclic lateral load magnitudes for a 2 MW, 3.5 MW and 5 MW offshore wind turbine.

Table 1.2: Environmental conditions in the southern of the North Sea, from Lesny and Wiemann (2005)

Physical Quantities	**Symbol**	**Units**
Wind		
Hub-height 50-year extreme 10min mean wind	50	m/s
Hub-height 50-year extreme 5s gust	60	m/s
Water depth		
Mean water depth	35	m
50-year extreme water depth	41	m
Wave and currents		
50-year maximum wave height	22.3	m
Related wave period	14.5	secs
50-year tidal current surface velocity	1.71	m/s
50-year storm surge current surface velocity	0.43	m/s

Table 1.3: Typical loading on a 2 MW, 3.5 MW and 5 MW, from Byrne and Houlsby (2003), LeBlanc (2009), Lesny and Wiemann (2005)

Load type	**2 MW**	**3.5 MW**	**5 MW**
Vertical load V_T [MN]	5	6	35
Horizontal load H_i [MN]	4.6	4	16
Bending moment M_i [MNm]	95	120	562

The monopiles must fulfil the design criteria to withstand the forces applied on it (Abadie, 2015). In this case, the design must address four load conditions (API, 2007, DNV, 2014): (1) Ultimate Limit State (ULS), which relates to extreme load cases such as the worst-case storm event or a turbine emergency stop (the total collapse or excessive deformation of the foundation); (2) Accidental Limit State (ALS), which accounts for accidental loads such as ship impact on the turbine; (3) Serviceability Limit State (SLS), being a repeated routine loading over the lifetime of the design that could result in excessive deformation or permanent rotation of the tower; (4) Fatigue Limit State (FLS), which relates to repeated loading of small amplitude over a large period that could possibly lead to failure. Although the effect of Accidental Limit State (ALS) is important, it is beyond the scope of this thesis. For the head deflection and rotation of a monopile, the design of monopiles is governed by SLS and FLS. The fatigue limit state (FLS) is sufficient for structure component to resist collapse due to a large number of cycles (commutative damage due to repeated load). This state is good for prediction of foundation and eigenfrequency of entire wind turbine structure. The SLS and FLS design consideration are important to ensure a limited displacement of the infrastructure over time. As noted by Abadie (2015), the maximum pile rotation of the monopile is generally specified by the turbine manufacturer to guarantee good operation of the turbine. Typically, the maximum tolerance for the foundation tilt over its lifetime (including installation tolerance) is 0.5^{o} (Achmus et al., 2009, DNV, 2014, Malhotra, 2010).

1.4.2 Design requirements of monopiles

As noted from Arshad and OKelly (2016), the design of the offshore wind turbines should consider the effects of both aerodynamic and hydrodynamic forces acting from various directions amplitude and frequency. The structural integrity and fatigue lifetime of turbine structure strongly depends on its fundamental natural frequency f_n, and how it is excited by environmental and operational loads (Abadie, 2015). Consequently, under long-term cyclic loading (wind and waves load), the observed increase in cyclic stiffness of the pile-soil system with increasing number of cycles may under certain condition adversely affect the performance of the structure (Arshad and OKelly, 2017). The behaviour of the entire structure will increase the natural frequency, leading to the resonance (the coincide of forcing and natural frequencies) and greater rotation of the monopile. Thus, it is important to consider the natural frequency of the offshore wind turbines to evaluate the dynamic responses. The major sources of forcing frequencies are wind, wave and any out of imbalance of rotating parts of rotor-nacelle system at the hub and blades passing on the tower structure (Bhattacharya and Adhikari, 2011, Haigh, 2013, Malhotra, 2010). The operational excitation of a 3-bladed wind turbine (f_e) consists of the rotational frequency of the rotor (1P) and the blade passing frequency as the blades pass the tower (3P). Offshore wind turbines are commonly designed so that the natural frequency (f_n) is within the *soft-stiff* region, that is to say between the 1P and 3P excitation domains. This is because the *soft-soft* region is close to wave and wind loading frequencies (0.01 and 0.1 Hz, respectively) (see Fig. 1.7) while design in the *stiff-stiff* domain are cost prohibitive (structure considered too rigid and heavy) (Abadie, 2015, Arshad and O'Kelly, 2014). As shown in Fig. 1.7, a typical 5 MW wind turbine has a nacelle-rotor rotational speed between 6-13.2 rpm which experience a rotor frequency (1P) in the range of 0.12-0.22 Hz. For a three-bladed turbine, the blade passing frequency (3P) has excitation frequency of 0.35-0.62 Hz. Both soft-soft and stiff-stiff zones are not suitable for design purpose and more effort is required to ensure that the fundamental natural frequency (f_n) falls within the soft-stiff zone by a margin of 10% from either side (Arshad and OKelly, 2013, Bhattacharya et al., 2013a, Petrini et al., 2010).

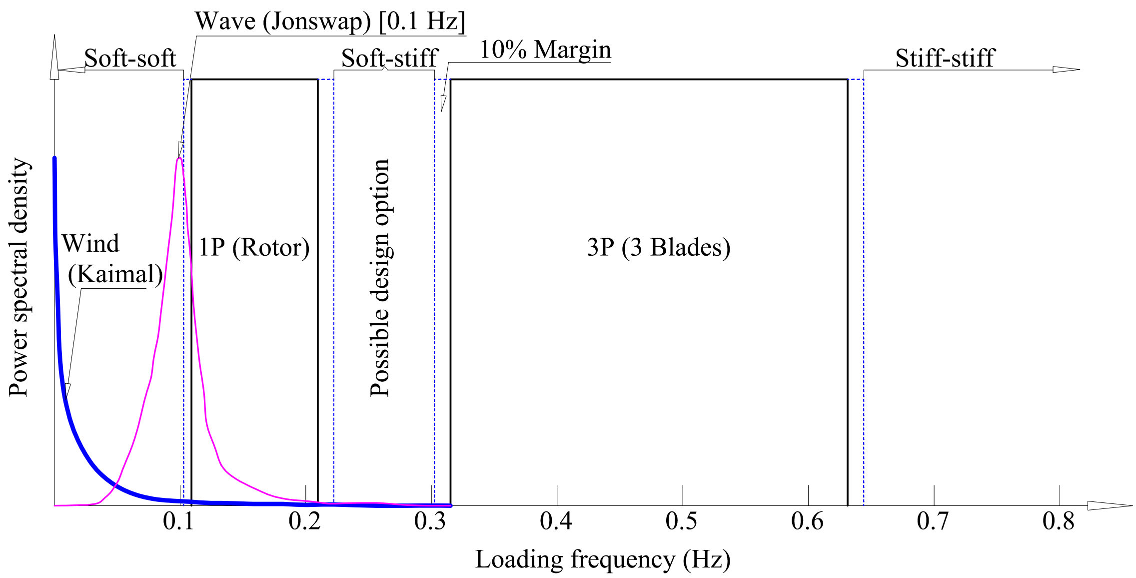

Figure 1.7: Typical loading frequency regions of a 5 MW turbine structure, from Bhattacharya et al. (2013b)

.

As shown in Fig. 1.7, three possible frequency regions in which the natural frequency of the turbine may safely reside without resulting in resonance are discussed below;

1. Soft-Soft design system ($f_n < 1P < 3P$)

   The frequency in soft-soft zone is essential for the design of small turbine with natural frequency limited to 0.1 Hz. The approach of this type is possible for a smaller turbine with output production of less or equal to 2 MW (Augustesen et al., 2009, Haigh, 2014). For the turbines with additional capacity, the mass of blades and nacelle will increase and leading to low fundamental natural frequency. The low natural frequency is not sufficient for soft-soft design and the slender structure would lead to unacceptable rotations and displacement of the pile-head (Byrne and Houlsby, 2003, Haigh, 2014, Kirkwood, 2016).

2. Stiff-Stiff design system ($\mathrm{f_n} > 3\mathrm{P} > 1\mathrm{P}$)
   For this type of structure, the design could be performed by increasing the diameter of the tower while keeping the thickness constant. For instance, a typical 5 MW rated output power of larger tower (D=6 m, t=0.1 m, L=65 m, $\mathrm{M_a} = 350$ tonnes, $\mathrm{M_t} = 650$ tonnes) has the natural frequency ($\mathrm{f_n}$) of 0.97 Hz, which is found in a stiff-stiff frequency range (see Fig. 1.7). The larger the weight of the turbine component leads in high cost of material and construction (Kirkwood, 2016). Therefore, the stiff-stiff structure is not a good choice for offshore wind turbine (Bontempi et al., 2009, Haigh, 2014, Malhotra et al., 2009).

3. Soft-Stiff design system ($1\mathrm{P} < \mathrm{f_n} < 3\mathrm{P}$)
   In the soft-stiff design system, the wind action frequencies could be more dangerous than the waves, but the fatigue effect could still be relevant. The system is susceptible to the changes of foundation stiffness (Bhattacharya et al., 2013b). If the foundation becomes softer under the action of cyclic loading, the natural frequency will drop and leading to more significant oscillation of the tower and foundation. The foundation designed must be able to carry substantial vertical, lateral and moment loads with minimum displacement and maintain the higher stiffness for entire design life of 20 to 25 years (Byrne and Houlsby, 2003, Haigh, 2014). This is the only sensible approach targeting a natural frequency from 0.2 to 0.3 Hz (see Fig. 1.7). DNV (2014) suggested the tolerance of 10% of the natural frequency between 1P and 3P for proper design of wind turbines. To ensure this range of frequency is achieved for designers, it is essential to understand the change in foundation stiffness arising from cyclic lateral loading.

1.5 Research aims and objectives

The work presented in this thesis relates to offshore wind turbine monopiles with the focus on the development of experimental loading device for testing models within a geotechnical centrifuge. The outcomes obtained from this research will improve the available geotechnical centrifuge model testing practices and help resolve challenges arising from 1g laboratory physical model testing. Therefore, the main objective of the project is to model, both experimentally and analytically, the response of wind turbine monopiles, subjected to both monotonic and cyclic loading. This is achieved through the following specific objectives:

1. To design and develop a testing device of a model pile in sand, subjected to both monotonic and cyclic loading, as well as carrying out and interpreting the model pile tests performance when it is embedded in a non-cohesive soil.
2. To identify the monotonic responses and determine the capacity of the pile and its initial stiffness. This is achieved by conducting monotonic pushover tests of the model pile in sand using the centrifuge.
3. To understand clearly the performance of the developed centrifuge model and the model pile-head response in sand, under lateral cyclic loading, particularly in the following aspects;
   (a) Accumulated displacement after several cycles.
   (b) Change in cyclic stiffness as the number of cycles increases.
4. To develop a simplified analytical solution for back analysis of experiment model tests. By knowing the important parameters from the experiment, the analytical solution for a single laterally loaded pile under monotonic and cyclic loading is achieved using the currently available mathematical models.

1.6 Outline of the thesis

This section provides a general outline of the chapters included in this thesis as described below;

1. *Chapter 1: Introduction*

   Outlines the offshore wind energy background, a general outlook of the foundation options, the details of the monopile foundations, a brief overview of the loads, research objectives and outlines of the thesis.

2. *Chapter 2: Literature review*

   Presenting a critical review of the published literature relevant to this study, covering behaviour of soil and pile under lateral monotonic and cyclic loading including the review of the current developed model devices.

3. *Chapter 3: Experimental methodology*

   Provides details of the fundamentals of geotechnical centrifuge testing, the experimental equipment developed for monotonic and cyclic loading, instrumentation and data acquisition systems, testing procedures and programme.

4. *Chapter 4: The monotonic response*

   This chapter presents the monotonic lateral load responses for both experimental and analytical modelling. The response of existing models to predict the lateral response of the monopile are also included and discussed.

5. *Chapter 5: Cyclic experimental results*

   This chapter presents and discusses the results of a series of model tests carried out on a single pile embedded in dry Congleton sand. It includes discussions on the changes in pile head stiffness and displacement that result from cyclic lateral loading of a monopile. The framework is provided that accounts for analysis of collected data from the experiment. The proposed functions are used to predict the response of pile-head displacement and change in stiffness after being subjected to several number lateral load cycles.

6. *Chapter 6: Cyclic theoretical analysis*

   This chapter describes a simple theoretical method for analysis of a single rigid monopile foundation under cyclic loading. Based on the model developed, a procedure of estimating the cyclic load on the pile is suggested. Finally, with available experimental data, the analytical model is validated.

7. *Chapter 7: Conclusions and future work*

   The chapter concludes the findings of the current research, suggests areas of improvement and additional work that will be beneficial for future work.

Chapter 2

LITERATURE REVIEW

2.1 Introduction

This chapter provides a critical review of the previous and recent literature relevant for this study. It aims to review methods being used within the offshore industry, the available research and current development trends. The difference between the existing methods, their limitations as well as other insights are revealed to construct the basis of the model development.

Generally, when lateral monotonic loads are applied to the pile head, the load is transferred directly to the soil. The load transferred creates strains in the soil, which contribute towards the deflection or rotation of the pile. When the soil reaches or exceeds the ultimate soil capacity or maximum shear stress at the soil-pile interface, the pile is expected to fail. Similarly, under cyclic loading the surrounding soil will also experience the effect of cyclic stress and strain, which results in cyclic load-displacement response of the pile head. Therefore, the behaviour of a monopile foundation subjected to both monotonic and cyclic loading will depend on the response of soil and soil-pile interface. Furthermore, when the load is applied on the pile head, rearrangement of soil grains surrounding the pile tend to change the stiffness response of the pile and induce more accumulation of rotation of the tower. The change of pile stiffness will automatically affect the natural frequency of the system. Accordingly, the literature available on the following areas are reviewed.

(a) Monotonic response and design approach of monopiles

(b) Behaviour of soil under cyclic loading

(c) Behaviour of piles under cyclic loading

(d) Existing cyclic loading devices

2.2 Monotonic response and design approach of monopile

2.2.1 Introduction

In this section the basic concept, analysis, and behaviour of laterally loaded piles in soil under monotonic loading are briefly reviewed and discussed. Generally, when the lateral load is applied to the pile head, the load is transferred directly to the soil. The transferred loads can cause a relative deformation of both soil and pile, which creates stresses and strain within the soil (Dodds and Martin, 2006, LeBlanc, 2009). The interaction that occurs between the pile and the soil is the primary topic to be reviewed. The analysis of pile-soil interaction can be classified into two different aspects, namely the deformation response for prediction of the pile head displacement or rotation and estimation of the ultimate resistance for the overall stability of the foundation (Cuéllar, 2011, Klinkvort et al., 2012). Therefore, the behaviour of piles under monotonic loading depends on the following three criteria: soil must not be stressed beyond its ultimate capacity, the pile-head deflection should be in the range of 10-20% of pile diameter and the structural integrity of the system must be assured (Dodds and Martin, 2006). The discussion of these criteria is presented in the following sections.

2.2.2 Failure mechanism, rigidity and ultimate resistance

2.2.2.1 Failure mechanism

The ultimate soil resistance, provided by the soil against the surface of the pile, is an essential parameter in the analysis of the laterally loaded piles (Zhang et al., 2005). It always depends on a complete yielding of the soil along the pile depth or structural failure in the pile material. The two possible failure mechanism, which were assumed to derive the ultimate soil resistance of rigid and flexible piles, are shown in Fig. 2.1. The failure mechanism depends on the pile slenderness (pile length to diameter ratio, $\left(\frac{\mathrm{L}}{\mathrm{D}}\right)$, strength of the soil as well as the yield resistance of the pile section (Broms, 1964, Cuéllar, 2011). As shown in Fig. 2.1(a), a rigid pile mobilises soil resistance along the embedded length excluding the rotation point (Broms, 1964). In contrast, a flexible pile (see Fig. 2.1(b)) will mobilise soil resistance close to the ground surface. As shown in Fig. 2.1, if the similar loads are employed to both rigid and flexible piles the deflection of the pile-head, bending moment and soil resistance, along the pile length, will look different.

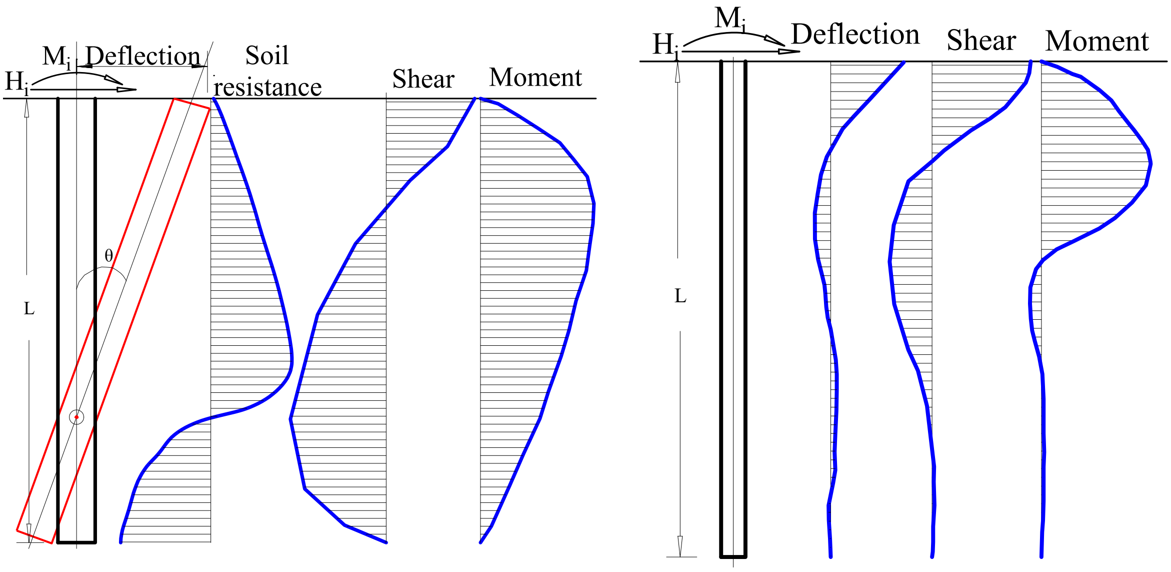

(a) Rigid Pile

(b) Flexible pile

Figure 2.1: Principle behaviour of a rigid and flexible pile, from Cuéllar (2011)

2.2.2.2 Embedded depth and rigidity of the pile

The laterally loaded pile can be classified as rigid or flexible depending on the relative stiffness ratio of the pile-soil system and embedded depth of pile (Briaud et al., 1983, Budhu and Davies, 1987, Carter and Kulhawy, 1992, Dobry et al., 1982, Guo, 2001, Kuo et al., 2011, Poulos and Davis, 1980, Randolph, 1981). According to Arany et al. (2017) and Kuo et al. (2011) the rigidity of pile is depends on the critical embedded pile length, which is based on the following criteria:

1. The pile length is chosen such that the displacement of the pile toe is zero or negative.
2. The pile length is chosen such that the deflection curve has a vertical tangent at the pile toe.
3. The pile length is chosen such that a further increase in pile length has no (or very limited) effect on the displacements (deflection and rotation) at the pile head.

For monopiles, the third rule was seen to be practical and suitable for determining the embedded length of the pile (Arany et al., 2017). Randolph (1981) proposed a critical length based on the ratio of pile length to diameter related to modified shear modulus of soil, G^* (see Eq. 2.3), and equivalent Young's modulus of pile, E_{eq} (see Eq. 2.4). The modified shear modulus, G^*, incorporated the effect of poison's ratio on the deformation of the laterally loaded pile, where G_s is modulus of the soil averaged between the ground surface and the embedded depth of the pile. An equivalent Young's modulus for the solid pile, E_{eq}, is assumed to be of the same flexural stiffness and cross-sectional area as the actual pile. With a known shear modulus, G^*, the pile length embedded into the soil (L_p) is estimated by using Eq. 2.1. However, Eq. 2.1 is frequently used for flexible piles (Arany et al., 2017). Carter and Kulhawy (1992) reported that for the pile to behave more rigidly, Eq. 2.2 should be satisfied with E_{eq} being an effective Young's modulus of the pile, where L_p is embedded length and D_p is the outer diameter of the pile.

$$L_p \leqslant D_p \left(\frac{E_{eq}}{G^*}\right)^{\frac{2}{7}} \tag{2.1}$$

$$L_p \geqslant D_p \left(\frac{E_{eq}}{G^*}\right)^{\frac{2}{7}} \tag{2.2}$$

$$G^* = G_s \left(1 + \frac{3}{4}\nu_s\right) \tag{2.3}$$

$$E_{eq} = \frac{E_p I_p}{\left(\frac{\pi D_p^4}{64}\right)} \tag{2.4}$$

Furthermore, Poulos and Hull (1989) suggested that a pile exhibits rigid or flexible behaviour if the embedded length of the pile (L) satisfies Eq. 2.5 and Eq. 2.6, respectively, where E_p is pile stiffness, E_s is the soil stiffness and I_p is the moment area of inertia.

$$L < 1.48 \left(\frac{E_p I_p}{E_s}\right)^{0.25} \tag{2.5}$$

$$L > 4.44 \left(\frac{E_p I_p}{E_s}\right)^{0.25} \tag{2.6}$$

An example of a typical steel monopile, 5 m in diameter, 60 mm wall thickness and embedded depth (L) of 25 m, is considered to be installed in sand. By using Eq. 2.5, a rigid behaviour is observed when E_s < 7.3 MPa, while flexible behaviour (Eq. 2.6) require E_s > 590 MPa.

Therefore, the length of monopile, L = 25 m, lie closer to the condition required for rigid behaviour (Eq. 2.5), but some bending of the pile will be expected.

2.2.2.3 Ultimate soil resistance for cohesionless soil

The estimation of ultimate lateral load capacity (H_u) of the pile requires two important components: the magnitude of lateral soil resistance (P_u) and distribution of soil resistance (P_i) mobilised along the embedded length of pile (L). Studies have proposed different methods for determining the ultimate lateral resistance of rigid piles in cohesionless soils (Barton, 1982, Broms, 1964, Fleming et al., 1992, Hansen, 1961, Petrasovits and Awad, 1972, Poulos and Davis, 1980, Prasad and Chari, 1999, Reese et al., 1974, Zhang et al., 2005) and they were analysed by approximation and assumptions (Zhang, 2009). Most of these methods have been developed based on the theory of earth pressure and considered a three-dimensional pile-soil interaction. Zhang et al. (2005) reported that an estimate of P_u in the soil can provided different values, leading to a complex choice of the appropriate method to determine the capacity of the pile (H_u). Some other expressions have been proposed from previous studies, most of which use the concept of active and passive lateral earth pressure coefficients to define the ratio of horizontal to vertical stress within the soil (Zhang, 2009).

For the first time, Terzaghi (1955) proposed a method to determine the ultimate soil resistance (P_u) and suggested the maximum capacity less than half the vertical bearing capacity of soil. The yield stress is considered as the maximum average horizontal soil resistance at the pile-soil interface. On the other hand, the ultimate soil resistance (P_u) suggested by Hansen (1961) involves three different sections of failure mechanism such as on the ground surface, at average and deep depth. They are all taken from a test conducted on a rigid square cross section. At deeper depth, the resistance was derived from failure in a horizontal plane; at moderate depth an equilibrium of Rankine passive wedge was used; while on the ground surface, the yield stress is taken as the resultant between the active and passive stress coefficients. A summary review of existing method for prediction of ultimate lateral soil resistance for sandy soil is presented in Table 2.1.

Table 2.1: Ultimate soil resistance, P_u, for cohesionless soil

SN	Expression [FL^{-1}]	Reference
1	$P_u = (qK_q + cK_c)D$	Hansen (1961)
2	$P_u = 3K_p\gamma' ZD$	Broms (1964)
3	$P_u = (3.7K_p - K_a)\gamma' ZD$	Petrasovits and Awad (1972)
4	$P_u = \gamma' ZK_o N_q$	Meyerhof et al. (1981)
5	$P_u = \text{Min}\begin{cases}(C_1 Z + C_2 D)\,\gamma Z \\ C_3 D\gamma Z\end{cases}$	Murchison and O'Neill (1984)
6	$P_u = (10^{(1.3\tan\phi+0.3)})\gamma' ZD$	Prasad and Chari (1999)
7	$P_u = \beta_1 K_p \gamma_d DZ^n$	Tak Kim et al. (2004)
8	$P_u = \left(0.8P_{max} + \tau_{max}\right)D$	Zhang et al. (2005)

where;

$K_p = \tan^2(45 + \frac{\phi'}{2}) \Rightarrow$ Passive earth pressure coefficient

$K_q = e^{\left(\frac{\pi}{2}+\phi'\right)}\cos(\phi')\tan\left(\frac{\pi}{2} + \frac{\phi'}{2}\right) - e^{\left(\frac{-\pi}{2}+\phi'\right)\tan\phi'}\cos\phi'\tan\left(\frac{\pi}{4} - \frac{\phi'}{2}\right)$

$K_c = \left[e^{\left(\frac{\pi}{2}+\phi'\right)\tan(\phi')}\cos(\phi')\tan\left(\frac{\pi}{4} + \frac{\phi'}{2}\right) - 1\right]\cot(\phi') \Rightarrow$ Earth pressure due to cohesion

$N_q = e^{\left(\pi\tan(\phi')\right)}\tan^2(45 + \frac{\phi'}{2}) \Rightarrow$ Bearing capacity factor, $K_o = 1 - \sin(\phi') \Rightarrow$ Earth pressure at rest

$K = (0.7 - 2)K_o \Rightarrow$ Lateral earth pressure coefficient, $\delta \Rightarrow$ interface friction angle, in degree.

$Z \Rightarrow$ Depth from the ground surface, in meter, $D \Rightarrow$ Diameter of the pile, in meter

$\gamma \Rightarrow$ Unit weight of soil, kN/m^3, $\phi' \Rightarrow$ Effective friction angle

$C_1 = 0.115 * 10^{0.0405\phi'}$, $C_2 = 0.571 * 10^{0.022\phi'}$, $C_3 = 0.646 * 10^{0.0555\phi'}$ (API, 1993)

$\beta_1 \Rightarrow$ scaling factor for ultimate soil resistance, $n \Rightarrow$ constant, linear or non-linear constant

A function suggested by Hansen (1961) is shown in Table 2.1, (SN 1). Another method was proposed by Broms (1964) who did not divide the soil into layers to determine the ultimate resistance of soil but argued that at the ground level the soil surface exhibits an upward movement while at increasing depth the soil tends to move horizontally around the pile. This behaviour is only for cohesionless soil, however, for the pile in the cohesive soil the separation on the back of pile is observed. It is observed that in cohesionless soil, the sand tends to flow and fill gap which is termed as a useful behaviour to distinguish between the resistance of soil at the ground surface and that at a depth below the ground. Where Broms (1964) method is empirical and was derived from full-scale tests with function shown in Table 2.1 ((SN 2)). Petrasovits and Awad (1972) and Prasad and Chari (1999) also recommended the empirical method to predict ultimate soil resistance on rigid piles in sand (Shown in Table 2.1 as SN 3 and SN 6, respectively). Petrasovits and Awad (1972) considered both passive (K_p) and active (K_a) earth pressure coefficient and shape factor of 3.7. However, Prasad and Chari (1999) derived the ultimate soil resistance in a different approach. The total ultimate force $(H_u)(kN)$ was obtained by considering $P_u(kN/m)$ distribution along the embedded length (L) of the rigid pile with a depth of rotation point (Z_r) where γ (kN/m^3) is the effective unit weight of soil, ϕ is internal friction angle, D is the diameter of the pile. In this analysis, both sides of shear and passive earth pressure, equilibrium of both forces (see Eq. 2.8), and moment (see Eq. 2.9) are employed and the depth of rotation point is derived as shown in Eq. 2.10. The parameter L_e is a load eccentricity from the ground surface.

$$\mathrm{H_u} = 0.24 * 10^{(1.3\tan\phi+0.3)}\gamma \mathrm{Z_r D}(2.7\mathrm{Z_r} - 1.7\mathrm{L}) \tag{2.7}$$

$$\mathrm{H_u} = \int_0^{\mathrm{L}} 0.8\mathrm{PDdZ} \tag{2.8}$$

$$\mathrm{H_u} * \mathrm{L_e} = \int_0^{\mathrm{L}} 0.8\mathrm{PDZ_i dZ} \tag{2.9}$$

$$\mathrm{Z_r} = \frac{(5.307\mathrm{L}^2 + 7.29\mathrm{L_e^2} + 10.541\mathrm{L} * \mathrm{L_e})^{0.5} - (0.567\mathrm{L} + 2.7\mathrm{L_e})}{2.1996} \tag{2.10}$$

Moreover, Meyerhof et al. (1981) conducted a study and proposed an expression (see Eq. 2.11) to determine the ultimate horizontal force (H_u). The P_u was estimated based on a mobilised passive and active state in front and behind of the pile, respectively. Although the active state was neglected due to its small values. As shown in Eq. 2.11, the modes of failure at shallow and deeper depth is estimated based on the net earth pressure coefficient, K_{br}, which is shown in Fig. 2.2. K_{br} is plotted against the depth to diameter ratio (L/D) of pile and angle of friction for sand, ϕ.

$$\mathrm{H_u} = 0.12\gamma \mathrm{DL^2 K_{br}} \tag{2.11}$$

The plots in Fig. 2.2 are used for estimation of pile capacity (H_u) while the ultimate soil resistance (P_u) of sand is estimated by using Equation (SN 4) in Table 2.1. In Eq.2.11, the

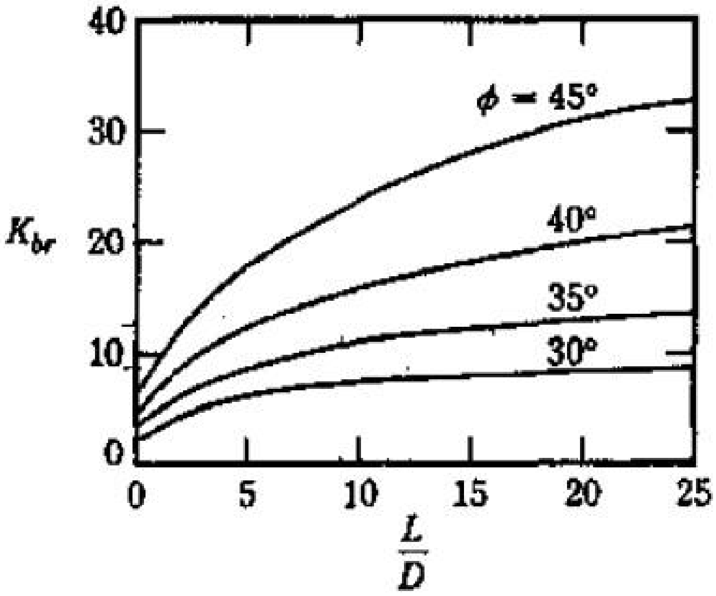

Figure 2.2: Variation of K_{br}, versus shape ratio (L/D), from Meyerhof et al. (1981).

point of rotation (Z_r) is assumed to be at the pile tip.

Zhang et al. (2005) proposed an empirical expression for the ultimate soil resistance (P_u) on a rigid pile (Equation (SN 8) in Table 2.1). As shown in Fig. 2.3, an increase of soil pressure (P_{max}) in front of the pile and side shear stresses (τ_{max}) acting on the side of the pile are considered. A similar approach by Prasad and Chari (1999) was employed and the ultimate load capacity, H_u, was obtained by using Eq. 2.12, where, K_o is lateral earth pressure coefficient at rest, δ is the interface friction angle between the pile and soil.

$$H_u = 0.3(0.8K_p^2 + 1.4K_o\tan\delta)\gamma Z_r D(2.7Z_r - 1.7L) \tag{2.12}$$

Reese et al. (1974) on the other hand, provided a more complex variation of ultimate lateral resistance for cohesionless soil, which include a wedge and plane-strain failure near the ground surface and deep depth, respectively (see Fig. 2.4). From these figures, the values of P_u with depth can be determined from the lesser of the values obtained in Eqs. 2.13 and 2.14 for shallow and deep depth, respectively, where $K_a = \tan^2(45 - \frac{\phi}{2})$ is the active pressure coefficient, K_o is at rest earth pressure coefficient, $\beta = 45 + \phi/2$, α is the shape wedge angle, ϕ is internal friction angle.

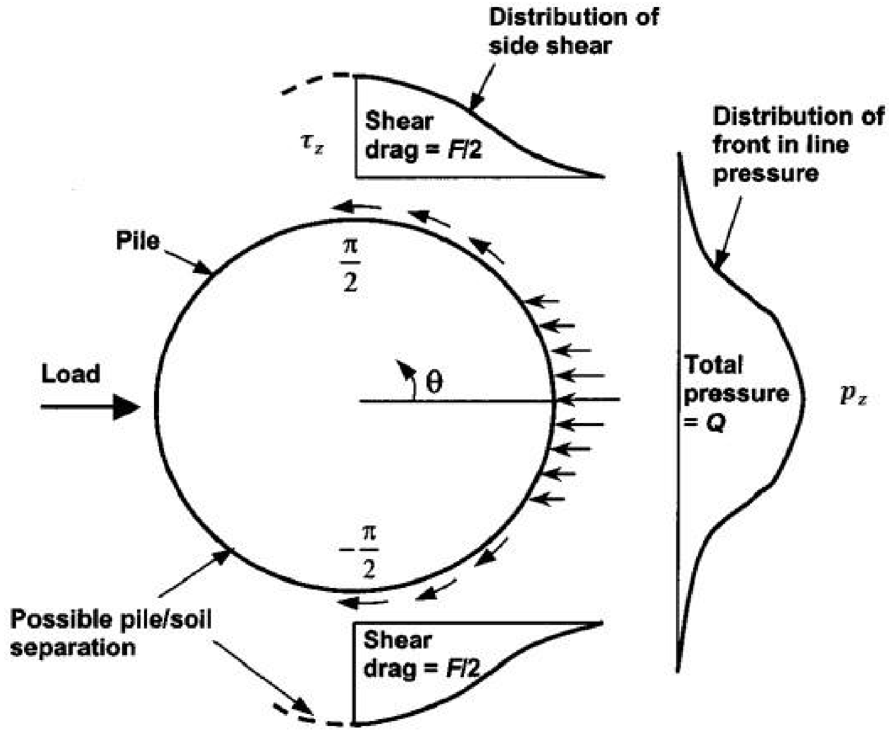

Figure 2.3: Distribution of $\mathrm{P_{max}}$ and τ_{max} around the pile, from Zhang et al. (2005)

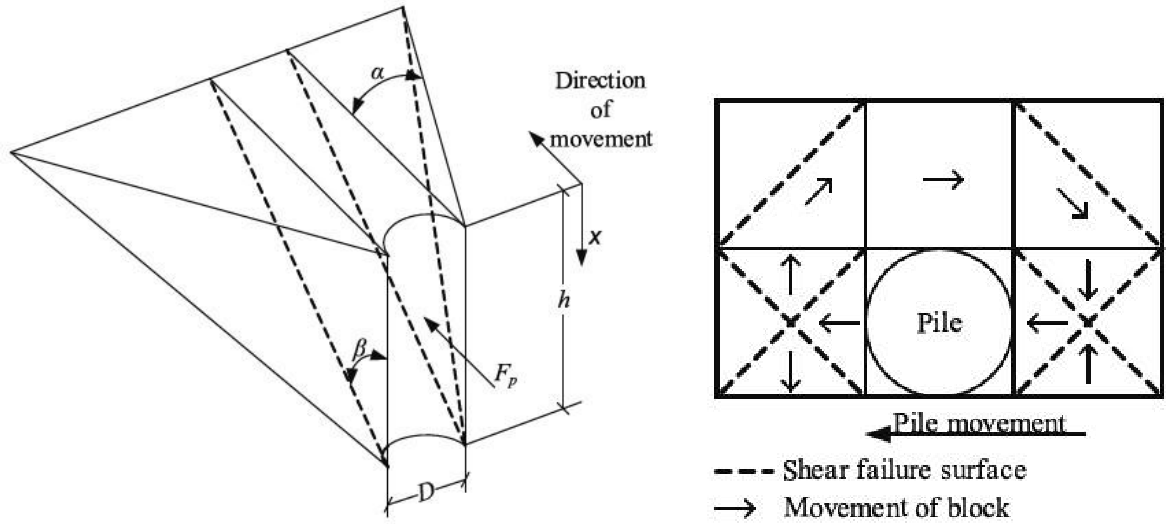

(a) Failure mode for shallow depth (b) Failure mode for deep depth

Figure 2.4: Ultimate resistance at shallow and deep depth, from Reese et al. (1974)

It should be noted that the curves of both equations will intersect at the assumed point A at a depth $\mathrm{Z_A}$. Therefore, above $\mathrm{Z_A}$, Eq. 2.13 can be used to calculate Pu while below $\mathrm{Z_A}$, Eq. 2.14

is used.

$$P_u = \gamma Z\left[D(K_p - K_a) + Z(K_p - K_o)\sqrt{K_p}\tan\alpha + ZK_o\sqrt{K_p}\left(\frac{1}{\mathrm{Cos}\alpha} + 1\right)\tan\phi\sin\beta\right] \quad (2.13)$$

$$P_u = \gamma ZD\left(K_p^3 + K_o K_p^2 \tan\phi - K_a\right) \quad (2.14)$$

Bogard and Matlock (1980) and Murchison and O'Neill (1984) simplified the equations developed by Reese et al. (1974) and grouping the terms to form the factors that varies with ϕ (Zhang et al., 2005). The ultimate soil resistance (P_u) shown in Table 2.1 (SN 5), can be taken as the minimum of Eqs. 2.15 and 2.16. These formulations are the one currently used in the main design standards for offshore wind turbines (API, 2007, DNV, 2014, GL, 2007, ISO, 2007).

$$P_{u,(shallow)} = \gamma Z\left(C_1 Z + C_2 D\right) \quad (2.15)$$

$$P_{u,(deep)} = \gamma ZDC_3 \quad (2.16)$$

According to Cuéllar (2011), the design of monopiles is governed by deformation behaviour rather than ultimate soil resistance, because the main focus is serviceability conditions for the pile rotation. More discussion of deformation behaviour is presented in the following sections.

2.2.3 Methods of pile analysis under monotonic loading

2.2.3.1 Introduction

The analysis of the monotonic response of a pile has advanced from the early idealisation of the beam interacting with a linear elastic embedment to advanced techniques allowing for non-linear behaviour (Cuéllar et al., 2012). Several approaches have been developed that attempted to model the lateral response of piles in sand. As noted by Wesselink et al. (1988) and Tak Kim et al. (2004), the available methods are Winkler or subgrade (Broms, 1964, Carter and Kulhawy, 1992, Choo et al., 2013, Fleming et al., 1992, Hansen, 1961, Matlock, 1970, McClelland and Focht, 1958, Meyer and Reese, 1979, Murchison and O'Neill, 1984, Prasad and Chari, 1999, Reese et al., 1974, Zhang, 2009, Zhang et al., 2005, Zhu et al., 2015), elastic continuum (Banerjee and Davies, 1978, Budhu and Davies, 1988, Han et al., 2015, Kuhlemeyer, 1979, Poulos, 1971, Poulos and Davis, 1980, Randolph, 1981) and finite element (Abdel-Rahman and Achmus, 2005, Ahmed and Hawlader, 2016, Brown and Shie, 1991, Desai and Zaman, 2013, Guo and Ghee, 2006, Kampitsis et al., 2015, Lesny and Wiemann, 2006). These methods are summarised in Table 2.2, including a brief discussion on advantages and disadvantages of each method.

Table 2.2: Current design methods for laterally loaded piles (Tak Kim et al., 2004).

Method	**Description**
Winkler model (BEF/BWF)	• Independent elastic soil springs and K_h is constant • Limited to uniform structural size and impossible to apply practically • By means of FDM, difficult to introduce general boundary conditions at pile top and tip. • Cannot provide a non-linear response
p-y curve method	• Based on Winkler foundation model • Soil springs represented by nonlinear soil response • Widely used in the design due to simplicity • Uncoupled springs (no continuity of soil)
Elastic continuum method	• Models soil as a continuum, use Mindlins equation • Homogeneous, and linearly increasing soil modulus • complex to use in layered soil
Finite element method	• Anisotropic and considered non-linear soil • Considered soil-pile interaction in 3-D • Complex constitutive equations modelling

2.2.3.2 Winkler model (Beam on Elastic Foundation)

The early approach proposed by Winkler (1867), popularly known as *Beam on Elastic Foundation* (BEF) or *Beam on Winkler Foundation* (BWF), treated the embedding soil as a series of independent discrete springs distributed along the length of the pile (L) (see Fig. 2.5). The method assumed that the pile deflection (y_n) at any point of the soil spring in contact with pile is linearly related to the contact pressure ($p_n = P_{z(i)}$) at any given point of the pile and independent of contact stress of other points. The soil pressure (p_n) (in terms of FL^{-2}) is usually defined in terms of constant subgrade reaction (k_h) and pile deflection ($y_n = y_{z(i)}$) ($P_n = k_h y_n$), where the unit of k_h is F/L^3. The distributed springs represent a horizontal modulus of subgrade reaction, K_h, which depend on soil type, depth and size of foundation (Cuéllar, 2011, Qin, 2010) and always is constant along the depth. The behaviour of such pile can be estimated by using a fourth-order differential equation shown in Eq. 2.17, where, y_n is the pile deflection at specific point from 1 to n along the embedded depth, E_p is Young's modulus of pile, and I_p is the moment area of inertia of the pile. As shown in Eq. 2.18, the soil resistance, $P_{z(i)}$ (in terms of FL^{-1}) is the function of contact pressure and pile diameter, D.

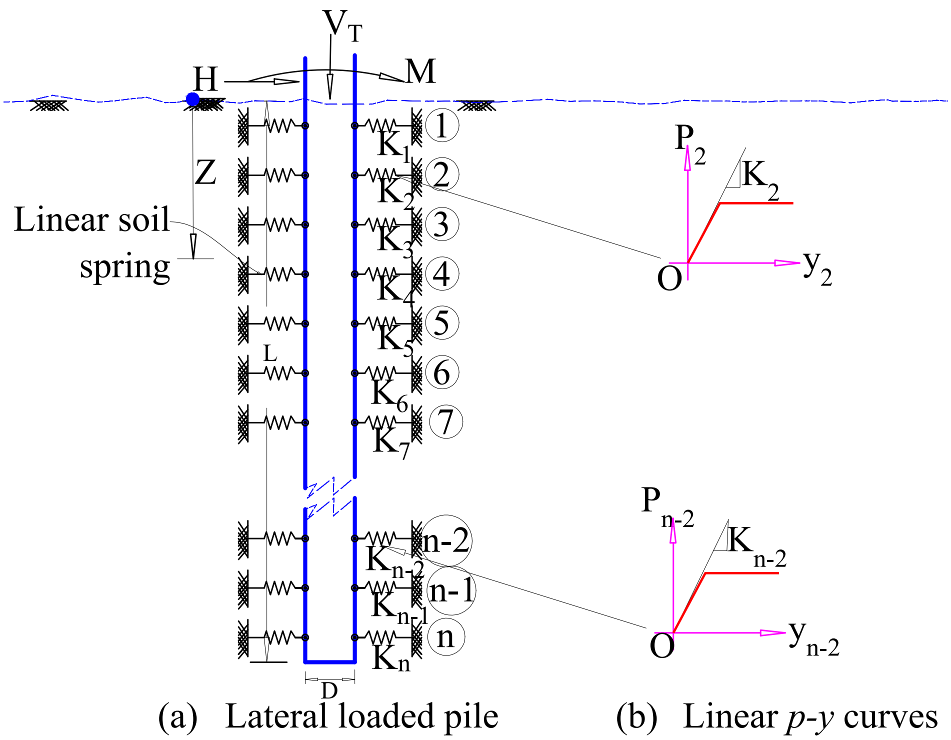

Figure 2.5: Spring distribution for Beam on Winkler Foundation (BWF)

$$E_pI_p\frac{d^4y}{dz^4} + K_hy_n = 0 \tag{2.17}$$

$$P_n = P_{z(i)} = p_nD = k_hy_nD \tag{2.18}$$

A closed form solution suggested by Hetényi (1946) has been used in this method to solve Eq. 2.17, considering a constant K_h along the depth. Reese and Matlock (1956) developed a similar solution using Eq. 2.17 with an assumption that parameter K_h increases linearly with depth, while Matlock and Reese (1960) proposed a different approach with power distribution of K_h with depth. Furthermore, Vesic (1961) conducted a rigorous analysis of beam sitting on elastic, isotropic half-space medium and obtained an analytical solution to determine deflection, slope, moment, shear force and soil pressure.

Numerical solutions using FDM and FEM have also been proposed to solve Eq. 2.17 (Desai and Zaman, 2013, Gleser, 1953, Matlock and Reese, 1960, Reese and Matlock, 1956). These solutions require a repeated application of elastic theory with the values of the modulus of subgrade reaction (K_h) adjusted until the values of soil pressure (P_n) and deflection (y_n) are obtained in the solution (Welch and Reese, 1972). The parameter K_h is important in obtaining the solution of the laterally loaded pile, therefore, the details are discussed in Section 2.2.3.3.

2.2.3.3 Modulus of subgrade reaction

The modulus of horizontal subgrade reaction in the analysis of a single pile, under lateral loading, can play a significant role for the *p-y* curves. A nonlinear *p-y* curves (discussed in the next section) requires an initial (or maximum) modulus of horizontal subgrade reaction at the start of the load application. Therefore, in this section, the historical background of K_h parameter is reviewed. As noted from Qin (2010), several methods are available for determining the modulus of subgrade reaction and some of them are listed in Table 2.3. The modulus of subgrade reaction can be measured directly from a full-scale instrumented pile, where the soil resistance and pile deflection are recorded. Experimentally, K_h has been investigated by researchers (Bowles et al., 1996, Poulos and Davis, 1980, Reese and Van Impe, 2010, Terzaghi, 1955). Nonetheless, the K_h values, along the embedded depth, can be estimated by using the empirical or analytical expression, which employing other properties of cohesionless soil such as Young's modulus, shear strength and relative density.

Table 2.3: General expression for estimating modulus of subgrade reaction

Empirical Expression	Reference
$\mathrm{K_h} = \frac{1.23\mathrm{E_s}}{\mathrm{C}\left(1-\mathrm{v_s^2}\right)}\left[\frac{\mathrm{E_s D^4}}{\mathrm{C}\left(1-\mathrm{v_s^2}\right)\mathrm{E_p I_p}}\right]^{0.11}$	Biot (1937)
$\mathrm{K_h} = \frac{22.24\mathrm{E_s}\left(1-\mathrm{v_s}\right)}{\left(1-\mathrm{v_s}\right)\left(3-4\mathrm{v_s}\right)\left[2\ln\left(\frac{2\mathrm{L}}{\mathrm{D}}\right)-0.443\right]}$	Glick (1948)
$\mathrm{K_h} = \frac{0.65\mathrm{E_s}}{\left(1-\mathrm{v_s^2}\right)}\left[\frac{\mathrm{E_s D^4}}{\mathrm{E_p I_p}}\right]^{\frac{1}{12}}$	Vesic (1961)
$\mathrm{K_h} = \frac{16\pi \mathrm{G_s}\left(1-\mathrm{v_s}\right)}{\left(3-4\mathrm{v_s}\right)\ln\left[\frac{2\mathrm{R}}{\mathrm{D}}\right]^2-\left[\frac{2}{\left(3-4\mathrm{v_s}\right)}\right]}$	Baguelin et al. (1977)
$\mathrm{K_h} = \frac{1.0\mathrm{E_s D}}{\left(1-\mathrm{v_s^2}\right)\mathrm{D_{ref}}}\left[\frac{\mathrm{E_s D^4}}{\mathrm{E_p I_p}}\right]^{\frac{1}{12}}, \Rightarrow \mathrm{D_{ref}} = 1\ \mathrm{m}$	Carter (1984)
$\mathrm{K_h} = \frac{3\pi \mathrm{G_s}}{2}\left[2\gamma_\mathrm{b}\frac{\mathrm{K_1}(\gamma_\mathrm{b})}{\mathrm{K_o}(\gamma_\mathrm{b})}-\gamma_\mathrm{b}^2\left(\left(\frac{\mathrm{K_1}(\gamma_\mathrm{b})}{\mathrm{K_o}(\gamma_\mathrm{b})}\right)^2-1\right)\right]$ $\Rightarrow \gamma_\mathrm{b} = \mathrm{k_1}\left(\frac{\mathrm{E_p}}{\mathrm{G^*}}\right)^{\mathrm{k_2}}\left(\frac{\mathrm{L}}{\mathrm{r_o}}\right)^{\mathrm{k_3}}$	Guo (2008)
$\mathrm{K_h} = \frac{\mathrm{qE_s D}}{\left(1-\mathrm{v_s^2}\right)\mathrm{D_{ref}}}\left[\frac{\mathrm{E_s D^4}}{\mathrm{E_p I_p}}\right]^{\mathrm{j}}, \Rightarrow \mathrm{D_{ref}} = 1\ \mathrm{m}$	Desai and Zaman (2013)

C= Coefficient vary from 1 for uniform pressure distribution to 1.13, uniform deflection
R= Radius of the outer rigid boundary of elastic soil zone
D= Diameter of the pile, L= Embedded depth of the pile
$K_\mathrm{i}(\gamma_\mathrm{b})$ =modified Besel function of second kind of $\mathrm{i^{th}}$ order, q, j= Adjustment constant parameters
$\mathrm{k_1}, \mathrm{k_2}, \mathrm{k_3}$ =Coefficient for estimating non-dimension parameter, γ_b

The concept of beams on the elastic foundation was initially proposed by Biot (1937), who studied the bending of an infinite beam under concentrated load resting on an elastic three-dimensional foundation. His work was extended by Vesic (1961) and a newly developed expression was adopted in a number of studies. The empirical expression was capable to evaluate the distribution of pile deflection, bending moment, shear forces and soil pressure along the depth of the pile. Furthermore, Bowles et al. (1996) suggested that for the soil to be in contact from both sides of the shaft, the Vesic (1961) expression must be doubled to determine the response of the pile. However, the soil cannot have contact all around the pile when the pile is subjected to lateral loading, but the friction developed on both sides of the pile can increase the overall soil resistance (Ashford and Juirnarongrit, 2003, Zhang et al., 2005). Moreover, Carter (1984), Ling (1988) and Ashford and Juirnarongrit (2003) examined the available data from lateral load testing and modified the Vesic (1961) expression to account for the effect of pile diameter. For instance, Carter (1984) and Ling (1988) have found the closest agreement in predicting the pile deflection by using a constant factor of 1.0. However, Desai and Zaman (2013) introduced the parameter q and j in the expression of Carter (1984) instead of using the constant value 1.0 and $\frac{1}{12}$, respectively. These parameters can then be adjusted until the required response is achieved.

The modified expression proposed by Carter (1984) and Desai and Zaman (2013) are preferred in this study for the analysis of monopile in a cohesionless soil as it includes the adjustment parameters and diameter of the pile (D).

2.2.3.4 The p-y method

For deformation analysis, the p-y curve method adopted from the Winkler model, is the most widely used in practice due to its mathematical simplicity and ease of implementation of soil nonlinearity, soil layering and other parameters (Wesselink et al., 1988). In this method, the soil surrounding a pile is replaced by a series of uncoupled nonlinear springs attached along the embedded length of the pile (L) at discrete locations (see Fig. 2.6). The springs can be represented by a relationship between the soil resistances ($\mathrm{P_{z(i)}}$) arising from the non-uniform stress field surrounding the pile and lateral pile deflection ($\mathrm{y_{z(i)}}$), widely known as p-y curves. A major limitation of this method is its inability to capture the continuity of the soil medium. However, the method can accommodate the experimental results and account for soil separation from the pile and sliding at the pile-soil interface (Gerolymos et al., 2009). Most available p-y curve soil models and their features are summarised in Table 2.4.

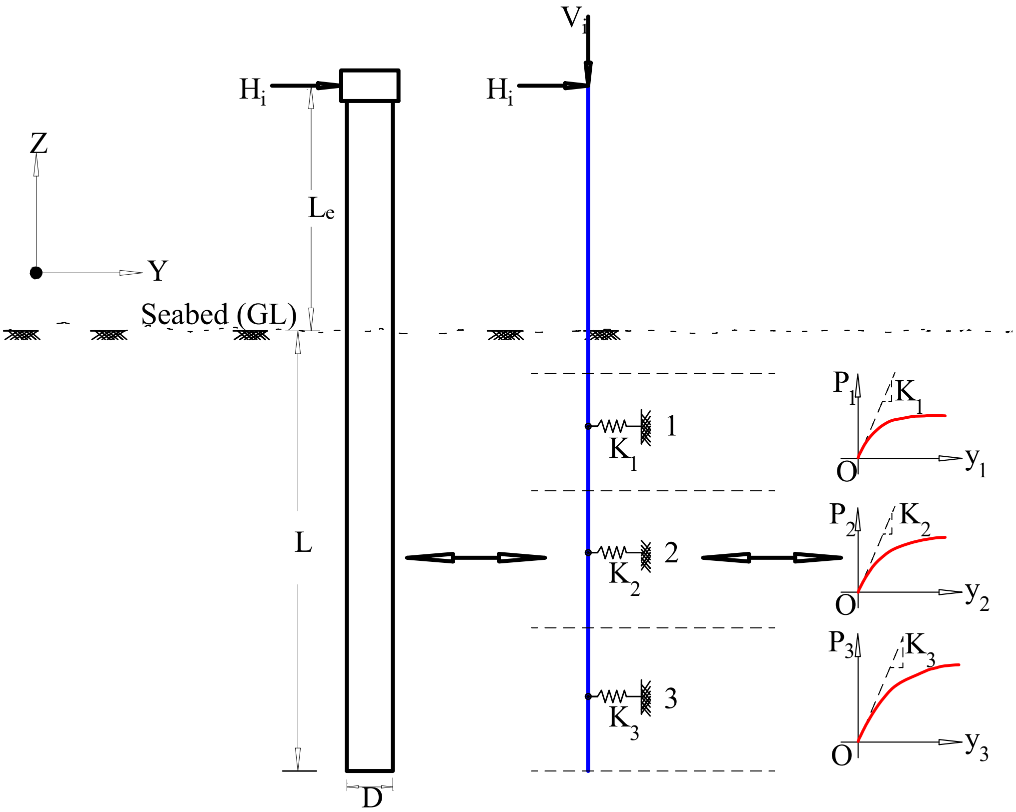

Figure 2.6: Spring distribution for beam on winkler foundation (BWF)

In the past, investigations of the soil-pile interaction using full scale tests on instrumented pile have been carried out to derive the *p-y* curves. Hetényi (1946) developed a concept of representing the ground with a series of elastic springs so that the compression (or extension) of the spring is directly proportional to the applied load. Reese and Matlock (1956) as well McClelland and Focht (1958) and Matlock (1970) experimented and demonstrated that the soil resistance at a given point on the pile is independent of pile deflections at points above and below, supporting the underlying assumption that spring is uncoupled in the *p-y* approach (Brødbæk et al., 2009, Doherty and Gavin, 2012, LeBlanc, 2009). Furthermore, with field experiments carried out on Mustang Island in Texas, Reese et al. (1974) and Cox et al. (1974) developed a semi-empirical non-linear *p-y* approach, in which degradation factors obtained empirically were used to predict cyclic p-y relationship based upon degraded static p-y curves. The tests were carried out on the two an open steel tube of diameter ($\mathrm{D} = 0.61\mathrm{m}$) and wall thickness ($\mathrm{t} = 0.0095\mathrm{m}$), driven to a penetration depth ($\mathrm{L_e} = 21\mathrm{m}$) in saturated sand. From the results, the integration and differentiation of bending moment profile as shown in Eq. 2.19 and 2.20,

Table 2.4: A summary of available soil model p-y curves (Tak Kim et al., 2004)

Reference	Expression	Remark
Ramberg and Osgood (1943)	$\mathrm{P_{z(i)}} = \dfrac{\mathrm{K_h y_{z(i)}}}{\left(1+\left(\dfrac{\mathrm{K_h y_{z(i)}}}{\mathrm{P_u}}\right)^{\mathrm{r}}\right)^{\frac{1}{\mathrm{s}}}}$	Derived from stress - strain relationship of soil in triaxial compression tests
Kondner (1963)	$\mathrm{P_{z(i)}} = \dfrac{\mathrm{K_h y_{z(i)}}}{1+\dfrac{\mathrm{K_h}}{\mathrm{P_u}}\mathrm{y_{z(i)}}}$	Derived from stressstrain relationship of soil in triaxial compression tests
Klinkvort and Hededal (2014)	$\mathrm{P_{z(i)}} = \dfrac{\mathrm{y_{z(i)}}}{\dfrac{1}{\mathrm{k_h Z}}+\dfrac{\mathrm{y_{z(i)}}}{\mathrm{AP_u}}}$	Derived from the results of centrifuge tests for monopile
Scott (1980)	$\mathrm{P_{z(i)}} = \dfrac{\sigma'_{\mathrm{m}}\mathrm{D}}{\dfrac{1}{\pi}\left(\dfrac{1}{\sin^2\phi}+\dfrac{1}{(3-4\mathrm{D})}\right)^{0.5}}$	Derived from the results of centrifuge tests. $\sigma'_{\mathrm{m}} = \frac{1}{3}\left(\sigma'_1+\sigma'_2+\sigma'_3\right)$
Murchison and O'Neill (1984)	$\mathrm{P_{z(i)}} = \mathrm{AP_u tanh}\left[\left(\dfrac{\mathrm{k_h Z}}{\mathrm{AP_u}}\right)\mathrm{y_{z(i)}}\right]$	Derived from back analyses of full-scale instrumented pile load test on sand
Wesselink et al. (1988)	$\mathrm{P_{z(i)}} = \mathrm{RD}\left(\dfrac{\mathrm{Z}}{\mathrm{Z_o}}\right)^{\mathrm{w}}\left(\dfrac{\mathrm{y_{z(i)}}}{\mathrm{D}}\right)^{\mathrm{m}}$	Derived from the results of full-scale tests in calcareous sand. Where, $\mathrm{Z_o}$ =1 m, R=650 kPa, w=0.7, m=0.6

respectively have been used to develop the experimental *p-y* curves, considering soil-pile failure modes at the shallow and deep soil. The typical plots of semi-empirical *p-y* curves for a rigid pile in sand, from Zhu et al. (2015) and Klinkvort (2013), are shown in Fig. 2.7.

$$\mathrm{y_{z(i)}} = \int\int \frac{\mathrm{M(Z)}}{\mathrm{EI}}\mathrm{dZ} \tag{2.19}$$

$$P_{z(i)} = \frac{d^2}{dZ^2}\left(M(Z)\right) \tag{2.20}$$

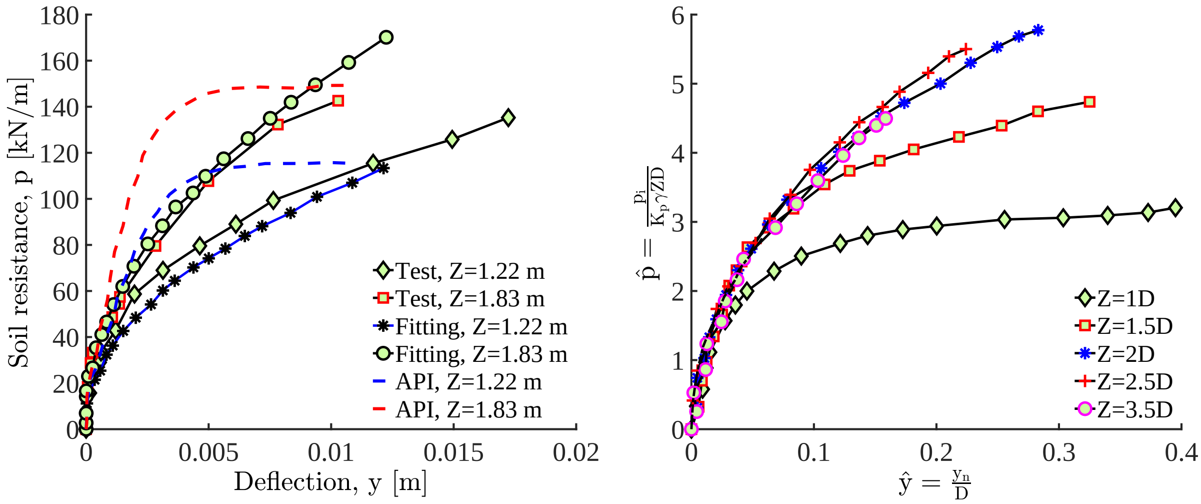

(a) *p-y* curves, from Zhu et al. (2015) (b) *p-y* curves, from Klinkvort (2013)

Figure 2.7: Typical p-y curves from the published studies

Several studies (Bogard and Matlock, 1980, Matlock, 1970, McClelland and Focht, 1958, Reese and Matlock, 1956, Reese and Van Impe, 2010, Scott, 1980, Welch and Reese, 1972) on *p-y* curves have been conducted on both sand and clay, following similar assumptions proposed by Reese et al. (1974). Murchison and O'Neill (1984) was conducted a study to compare different *p-y* curves derived from full-scale test of pile in sand. A compiled data set obtained has led to incorporate the model into API (2007) and DNV (2014) design code, which represent the current state of the art for the design of oil and gas industries and offshore structures, respectively. The *p-y* curves from Reese et al. (1974) and Murchison and O'Neill (1984) were combined to formulate a tangent hyperbolic model (see Eq. 2.21). The model function is currently used for offshore wind turbine monopiles and has been incorporated into current design code (DNV, 2014). A hyperbolic tangent formula is used to describe the relationship between soil resistance and pile deflection instead of piecewise formulation proposed by Reese et al. (1974).

$$P_{z(i)} = AP_u \tanh\left(\frac{k_h Z}{AP_u} y_{z(i)}\right) \tag{2.21}$$

The ultimate soil resistance (P_u), approximated by using Eq. 2.22, can be taken as the minimum of P_{us} and P_{ud} as shown in Eq. 2.23, 2.24, respectively, where γ is the unit weight of soil, D is diameter of pile, C_1, C_2, and C_3 (shown in Fig. 2.8(a)) are the dimensionless parameters.

$$P_u = \min\left(P_{us}, P_{ud}\right) \tag{2.22}$$

$$P_{us} = \left(C_1 Z + C_2 D\right)\gamma Z \tag{2.23}$$

$$P_{ud} = C_3 \gamma Z \tag{2.24}$$

where;

$A = \left(3 - 0.8\frac{Z}{D}\right) \geqslant 0.9$	For static Loading	[–]
$A = 0.9$	For cyclic loading	[–]
C_1, C_2, C_3	Empirical factors depend on ϕ (Fig.2.8(a))	[–]

The pile-soil stiffness K_{py} can be obtained by differentiating Eq. 2.21 and obtain Eq. 2.25

$$\frac{d}{dZ}\left[AP_u \tanh\left(\frac{k_h Z}{AP_u} y\right)\right] = AP_u \frac{\frac{k_h Z}{AP_u}}{\cosh^2 \frac{k_h Z y_{z(i)}}{AP_u}} \tag{2.25}$$

From Eq. 2.25, the initial stiffness at displacement of $y = 0$ is given as shown in Eq. 2.26, where k_h represents the constant initial modulus of subgrade reaction and can be obtained in Fig. 2.8(b), which depends on relative density D_r or friction angles ϕ.

$$K_{py} = k_h Z \tag{2.26}$$

The experiment implementation of the *p-y* curves requires a numerical procedure to solve a fourth order differential equation and integration for beam bending moment profile. According to Euler-Bernoulli beam theory, the governing fourth order differential equation for determination of pile deflection is shown in Eq. 2.27. More details for this equation have been explained by Brødbæk et al. (2009) and Sørensen (2012).

$$E_p I_p \frac{d^4 y_{z(i)}}{dZ^4} - H \frac{d^2 y_{z(i)}}{dZ^2} - K_{py} y_{z(i)} = 0\,, Z \in [0 : L] \tag{2.27}$$

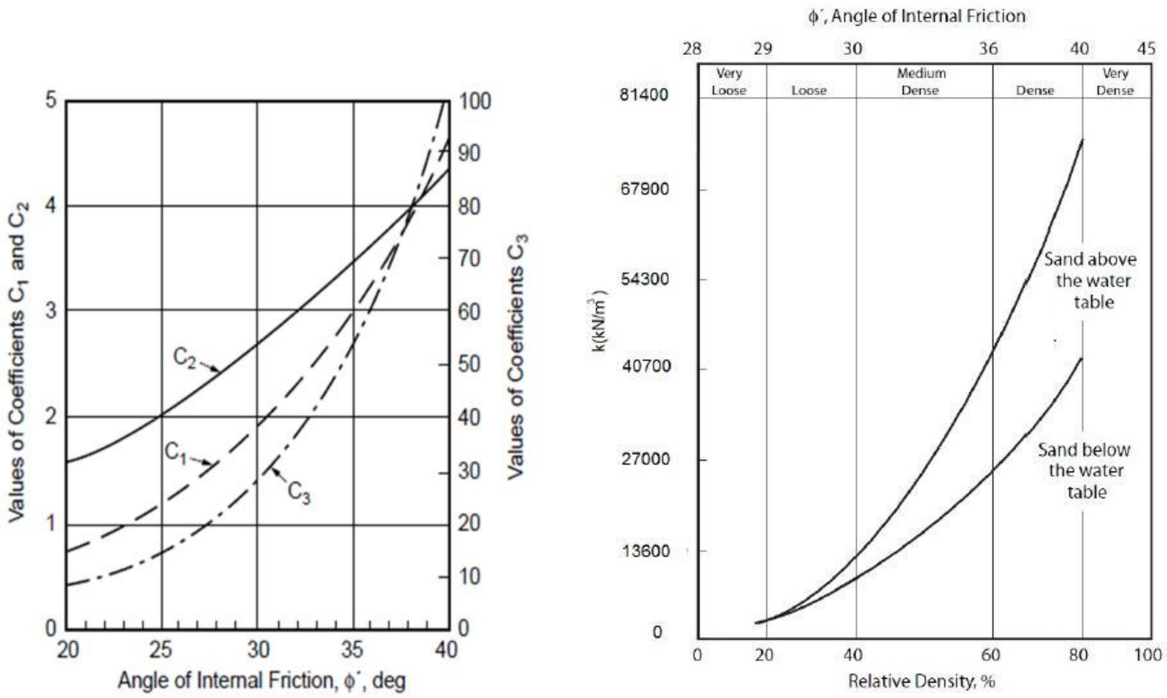

(a) Coefficients, C_1, C_2, C_3 (b) Initial modulus of sub-grade reaction, k_h

Figure 2.8: Coefficients for construction of p-y curves in sand, from Reese et al. (1974) and DNV (2014)

2.2.3.5 Limitations of *p-y* curve method

The diameter of piles used in oil and gas sectors typically ranges from $1.8 - 2.7$ m (Lombardi et al., 2013) with $60 - 100$ m length. However, when compared to an offshore wind turbine, it observed to be different with maximum embedding length, L_{max}, of approximately $30 - 40$m with pile diameter of 4-8 m (Sørensen, 2012). The use of the *p-y* curve method stipulated in the DNV (2014) design standard seems to contain some limitations (Fan and Long, 2005, Klinkvort et al., 2012, Lombardi et al., 2013) such as:

1. Failure mechanism.

   - The p-y curve method was developed from the field experiment conducted on slender piles. However, it is currently used in the design of the offshore monopiles.
   - The method did not consider the failure mode on monopile, in which the formation of a passive soil wedge is considered above and below the point of rotation.

2. Diameter effect on initial stiffness.

   Terzaghi (1955) was the first to estimate the effect of pile diameter based on the initial modulus of subgrade reaction, K_h, on flexible piles, while Pender (1993) investigated the influence of pile diameter into modulus of subgrade reaction. However, there seems to be no clear correlation between the pile diameter and modulus of subgrade reaction. A FE analysis conducted by Ashford and Juirnarongrit (2003), for flexible piles of 0.15-1.07 m in diameter, showed that the pile diameter has insignificant effect on the pile response and modulus of subgrade reaction, instead an increase of pile diameter appeared to decrease the pile head displacement and the maximum moment. A numerical approach was also followed by Fan and Long (2005) to investigate the influence of pile diameter (0.3, 0.61 and 1.2 m), by using a constitutive model proposed by Desai et al. (1991), however, no significant correlation was observed between the pile diameter and initial stiffness. Nevertheless, Lesny and Wiemann (2006) and Sørensen et al. (2009) have concluded differently, showing that the variation of pile diameter has affected the initial stiffness of the pile-soil interaction, which brings a contradiction regarding the effect of increasing the size of foundation, especially on monopile. Further investigation is required.

3. Number of cycles and pile rigidity.

   - Calibration of the widely used API model against the response of small size diameter piles (length to diameter ratio of 30 to 50) were subjected to low numbers of cycles (maximum 200 cycles) suited for offshore fixed platform applications, while, the length to diameter ratio of monopiles is of the order of 5 to 6 and 10^7 to 10^8 cycles of lateral loading expected over a lifetime of 20 to 25 years.

4. Effect of Loading.

   - The ratio of horizontal load, H_i, to a vertical weight, V_T, is very high in offshore wind turbines when compared with oil and gas structures. Therefore, the monopiles experience disproportionately high moment loading in comparison to oil and gas platform piles. This extreme loading condition was not considered during the calibration of the API (2007) and DNV (2014) *p-y* curves.

2.2.3.6 Elastic Continuum Approach

The method infrequently leads to analytical solutions which are usually materialised through boundary element, finite element or finite difference type numerical formulations (Poulos and Davis, 1980). Poulos and Davis (1980) carried the analysis of laterally loaded pile using this method in an elastic homogeneous isotropic media, a method in which the soil mass surrounding the pile was treated as an elastic continuum and the pile as a strip, which applied pressure on the continuum soil. An integral boundary technique and Mindlin (1936) equation was employed to the horizontal pile deflection.
In the method developed by Poulos and Davis (1980), the soil was assumed elastic and homogeneous with constant modulus, $\mathrm{E_s}$, and poison's ratio, $\mathrm{v_s}$, and the pile were split into elements with flexural stiffness, $\mathrm{E_pI_p}$. From this method, the expressions for pile flexibility factor, $\mathrm{k_R}$, pile-head displacement, $\mathrm{Y_p}$ and pile rotation, θ_p are shown in Eq. 2.28, 2.29, and 2.30, respectively, where, $\mathrm{I_{YH}}$, $\mathrm{I_{\theta H}}$ are displacement and rotation influence factors for loads only and $\mathrm{I_{YM}}$, $\mathrm{I_{\theta M}}$ are displacement and rotation influence factors for moment only.

$$\mathrm{k_R} = \frac{\mathrm{E_pI_p}}{\mathrm{E_sL^4}} \tag{2.28}$$

$$\mathrm{Y_p} = \mathrm{I_{YH}}\frac{\mathrm{H}}{\mathrm{E_sL}} + \mathrm{I_{YM}}\frac{\mathrm{M}}{\mathrm{E_sL^2}} \tag{2.29}$$

$$\theta_\mathrm{p} = \mathrm{I_{\theta H}}\frac{\mathrm{H}}{\mathrm{E_sL^2}} + \mathrm{I_{\theta M}}\frac{\mathrm{M}}{\mathrm{E_sL^3}} \tag{2.30}$$

Several studies (Baguelin et al., 1977, Banerjee and Davies, 1978, Guo, 2001, Poulos, 1988, Randolph, 1981, Sun, 1994) have been reported to extend the method whereby the soil modulus was assumed to increase linearly with depth. Poulos (1988) modified the method by including a certain consideration of non-linear behaviour and introducing yielding factors and variation of elastic modulus (Cuéllar, 2011). A similar approach was also used by Banerjee and Davies (1978). Furthermore, the solution to include a linear variation of soil modulus was taken into account by Budhu and Davies (1988) after modifying the work from Banerjee and Davies (1978), aiming to develop a nonlinear analysis of loaded pile in cohesionless soil, where the soil was assumed to be elastic-plastic material (Qin, 2010). However, with all modifications, the method is sufficiently applied if the modulus of soil is accurately determined. The method is not preferable and rarely used in the design of piles (Sørensen, 2012). It is only valid for small strains and useful to estimate the initial modulus of soil.

2.2.3.7 Numerical Approach

A numerical approach has been an area of active research over the past decades due to an increase of interest to predict the material behaviour in practical engineering situations, change of computer capabilities, and a growing interaction between computational mechanics, applied mathematics and different engineering fields (Pérez Foguet, 2000). The method is divided into finite element (FE) and finite difference (FD), widely used to solve 3-Dimensional problems related to geotechnical engineering (Carter and Kulhawy, 1992). Some developments have been made towards understanding the behaviour of laterally loaded piles in three dimensions with assumptions of linear elastic and non-linear elastic-perfectly plastic soil continuum (Budhu and Davies, 1987, 1988, Poulos, 1971, 1988, Poulos and Davis, 1980). Recently, studies have begun to use a computer package software for most continuum-based methods for analysis of numerical modelling. These methods have taken into account a three-dimensional interaction, elastic and non-linear soils through the elastic constants (Young's modulus and Poissons ratio) and appropriate constitutive relationship (Gerolymos et al., 2009). With the rapid development of both computer and geotechnical software, 3D nonlinear analyses have been carried with the soil behaviour being described by advanced constitutive models on the theory of plasticity and hypo-plasticity, such as von Mises, Drucker-Prager, Mohr-Coulomb, and boundary surface plasticity models (Abdel-Rahman and Achmus, 2005, Achmus et al., 2008, 2009, Bourgeois et al., 2010, Fan and Long, 2005, Gerolymos et al., 2009, Heidari et al., 2014, Lesny and Wiemann, 2006, Mardfekri et al., 2013). Augustesen et al. (2009) carried a 3-D FD analysis to investigate the behaviour of sand soil-monopile interaction under monotonic loading and the results were compared with Winkler model approach. Furthermore, a FE study from Abdel-Rahman and Achmus (2005), Achmus et al. (2009), Fan and Long (2005), Lesny and Wiemann (2006) were employed to investigate the behaviour of monopile foundation under monotonic and cyclic loading taking into account the interaction between pile and soil. However, the response of soil around the pile seems to be less understood and unclear about the constitutive models used for the analysis. From these studies a comparison was made through a parametric study with a varying diameter size, embedding depth and magnitude of loading. This research however, does not focus on the numerical modelling, thus further details can be found in the literature summarised in Table 2.5, which summarises the of work carried out in the past to improve the understanding behaviour of monopiles when subjected to lateral loading. It gives a quick review on some of the previous research carried out on numerical modelling. From the table, D represents the diameter of pile (m), t thickness of pile (m), L the embedded depth (m), $\mathrm{L_e}$ is load eccentricity (m), $\mathrm{H_i}$ is horizontal force (MN), V is vertical loading (MN), ϕ internal angle of friction $(^{\mathrm{o}})$, γ is the unit weight of soil $(\mathrm{kN/m^3})$.

Table 2.5: A summary review of numerical modelling for monopile foundation

Author	**Model Pile**			**Loads**		**Soil property**	
	D	L	$\mathrm{L_e}$	$\mathrm{H_i}$	$\mathrm{V_T}$	ϕ	γ
Kellezi and Hansen (2003)	4	22	10.9	2.5	10.6	21-44	20
Fan and Long (2005)	0.61	21	0.3	0.28	–	39	19
Lesny and Wiemann (2005)	1-6	11-39	–	6,16	35	20-40	23
Achmus et al. (2008)	7.5	20-40	15	0.5-15	–	38	21
Achmus et al. (2009)	7.5	20,40	20	4-16	10	35	21
Augustesen et al. (2009)	4	22	21	4.6	5.0	38	20
Bourgeois et al. (2010)	0.72	12	1.6	0.72	–	–	–
Peng et al. (2010)	4	40	–		–	35	16.5
Saue et al. (2011)	4.7	20	0	4.2	–	39,45	–
Ghee and Guo (2011)	5	70	50	2.84	–	38	16.3
Achmus et al. (2011)	0.61-7.5	5-37	–	0.05-23	–	28-43	20
Hamre et al. (2011)	5.7	35	1	9.5	–	20-35	17-20
Achmus et al. (2012)	4,7.5	15, 20	–	–	–	38	21
Haiderali et al. (2014)	3.8	20	30	–	6.5	23	18

2.2.4 Deformation response under monotonic loading

A number of studies (API, 1993, Budhu and Davies, 1987, Dyson and Randolph, 2001, Guo, 2008, Murchison and O'Neill, 1984, Novello, 1999, Randolph, 1981, Reese et al., 1974, Reese and Van Impe, 2010, Wesselink et al., 1988, Xue et al., 2016, Yan and Byrne, 1992) investigated the response of piles subjected to monotonic loading. Most of these studies employed the ultimate soil resistance $(\mathrm{P_u})$ and modulus of subgrade reaction $(\mathrm{K_h})$ to construct the p-y curves, while others such as (Dyson and Randolph, 2001, Wesselink et al., 1988, Yan and Byrne, 1992), only rely on cone resistance, $\mathrm{q_c}$. Yan and Byrne (1992) experimented the piles installed in sand and subjected to monotonic loads, where a parabolic p-y curve was proposed and observed to provide an excellent prediction of the experimental results and the field test data. A similar centrifuge approach by Georgiadis et al. (1992) was used to developed new hyperbolic *p-y* curve relationship, results of which were compared with several numerical analyses. The developed p-y curves provided a satisfactory result. Furthermore, Dyson and Randolph (2001) carried out a similar approach on a centrifuge for the piles embedded in the calcareous sand and subjected to monotonic lateral loading. The features, such as rate of loading and pile head restraint, were explored. The parabolic p-y curves employed in the analysis and the developed responses have shown to provide an excellent match with experiment. This approach has been highly supported by by other studies (Guo, 2008, 2014, Klinkvort and Hededal, 2014, Zhang, 2009, Zhu et al., 2015) who analyses the global load-deflection response of rigid piles.

For rigid pile conditions, the pile tends to rotate as a rigid body and its displacement is assumed to vary linearly with depth. Hence, the studies related to rigid piles, employed the p-y curves soil model in a nonlinear kinematic technique to determine the load-displacement responses. For instance, Guo (2008) performed an analysis on laterally loaded rigid piles in sand with soil resistance along the pile mobilised at different load levels. In a closed form solution, the coefficient of subgrade modulus, $\mathrm{k_h}$, was assumed constant or linearly varying with depth. The solution was obtained from back-calculation of measured responses of rigid piles in cohesionless soils. Zhang (2009) also developed a method for nonlinear analysis of rigid piles in cohesionless soil with the assumption that both the ultimate soil resistance and constant modulus of subgrade reaction vary linearly with depth. The centrifuge test in sand and three-dimensional finite element results were compared with a proposed model. Although the application of this method has proved to agree with experimental results, it was limited to the effect of load eccentricity and pile diameter. Furthermore, Zhu et al. (2015) conducted a 1 g physical modelling to establish a new *p-y* curves using a coefficient of subgrade reaction, $\mathrm{k_h}$, that is correlated to the local pile displacement. The new *p-y* curves and analytical solutions captured well the measured *p-y* curves and the load-displacement relationship of the monopiles in cohesionless soils. Barton et al. (1983) carried out a centrifuge testing on the model pile, driven in a sandy soil and subjected to monotonic lateral loading and compared the results with curves recommended by Reese et al. (1974), where the initial stiffness of the *p-y* curves varied as the square root of depth rather than linear variation, and the ultimate resistance was seen to be underestimated near the ground and overestimated at depth by the Reese et al. (1974) *p-y* curves. Further modification of the *p-y* curves recommended by Reese et al. (1974) has shown to agree with experimental behaviour. According to DNV (2014), the initial stiffness of the *p-y* curves in a uniform sandy soil is assumed to vary linearly with depth irrespective of other properties (see Eq. 2.31). A similar argument was also recommended on flexible piles by other studies (Ashford and Juirnarongrit, 2003, Reese et al., 1974, Terzaghi, 1955, Vesic, 1961).

$$\mathrm{K_h} = \frac{\mathrm{dP}}{\mathrm{dy}}\bigg|_{\mathrm{y}=0} = \mathrm{AP_u}\frac{\left(\frac{\mathrm{k_h Z}}{\mathrm{AP_u}}\right)}{\cosh^2\left(\frac{\mathrm{k_h Z}}{\mathrm{AP_u}}\mathrm{y_{z(i)}}\right)}\bigg|_{\mathrm{y}=0} = \mathrm{k_i Z} \tag{2.31}$$

A monotonic analysis and response of monopile in sandy soil were reported by Lesny and Wiemann (2006) and compared with p-y curves from API (1993). The results indicated that at great depth, the initial stiffness of the *p-y* curves is overestimated, which lead to development of a new power law (see Eq. 2.32) to predict the response of the data. In Fig. 2.9, the reference stiffness, $\mathrm{K_{i,ref}}$, and depth, $\mathrm{Z_{i,ref}}$, were taken at the intersection between stiffness from Eq. 2.31 and 2.32 and the parameter $\mathrm{a} = 0.6$ was set to give a good agreement between the two methods. A similar response is also proposed by Hardin and Drnevich (1972), Pestana and Salvati (2006) and Oztoprak and Bolton (2013), to determine the initial subgrade modulus ($\mathrm{K_h}$) through the shear modulus at small strain in sandy soil ($\mathrm{G_{max}}$), which is directly proportional to the root of the confining stress. As discussed in Section 2.2.3.5, the initial stiffness was also investigated by other studies (Achmus et al., 2007, Ashford and Juirnarongrit, 2003, Fan and Long, 2005, Sørensen et al., 2009, Terzaghi, 1955) on the effect of pile diameter and conclusion of their findings were contradictory.

$$\mathrm{K_h} = \mathrm{K_{i,ref}}\left(\frac{\mathrm{Z}}{\mathrm{Z_{i,ref}}}\right)^{\mathrm{a}} \tag{2.32}$$

A nonlinear distribution of initial stiffness (modulus of subgrade reaction) was also suggested by Brødbæk et al. (2009) to construct the p-y curves and determine the monotonic responses on a rigid pile in sandy soil. Sørensen (2012) carried out an experiment to verify this variation and suggested a reformulated expression shown in Eq. 2.33, with the reference parameters, $\mathrm{Z_{i,ref}}$, $\mathrm{D_{ref}}$ and $\mathrm{E_{s,ref}}$ are 1 m, 1 m, 1 MPa, respectively. The constant u, b, c and d were set with values of 1000 kPa, 0.3, 0.5 and 0.8, respectively to fit the results. The soil modulus, $\mathrm{E_s}$ was defined by using Eq. 2.34, where $\mathrm{D_r}$ is relative density and σ'_3 is mean effective stress. Furthermore, Klinkvort and Hededal (2013) carried out centrifuge tests on instrumented model piles in sandy soil and linear variation of initial stiffness was observed to accurately fit p-y

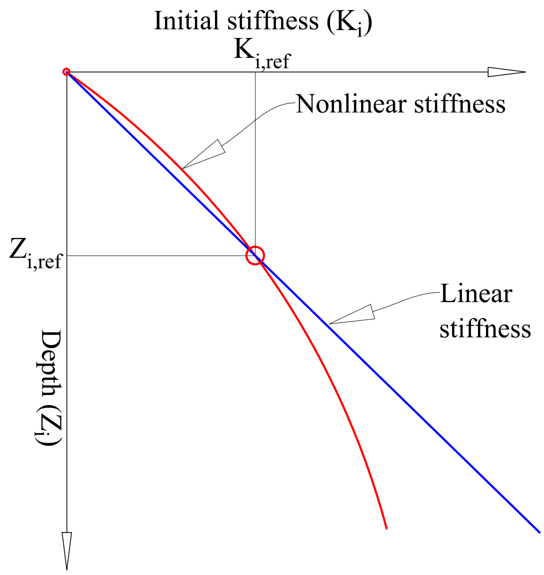

Figure 2.9: Variation of initial stiffness with depth, from Lesny and Wiemann (2006).

curves. This observation was seen to be different from early discussion on nonlinear variation. In general, most of the current studies employed a linear variation of initial stiffness modulus and have been reported to provide high values when compared to experimental results (Abdel-Rahman and Achmus, 2005, Kirkwood, 2016, Klinkvort and Hededal, 2013, Rosquoet et al., 2007, Sørensen, 2012, Sørensen et al., 2009).

$$\mathrm{K_h} = \mathrm{u}\left(\frac{\mathrm{Z}}{\mathrm{Z_{i,ref}}}\right)^{\mathrm{b}}\left(\frac{\mathrm{D}}{\mathrm{D_{ref}}}\right)^{\mathrm{c}}\left(\frac{\mathrm{E_s}}{\mathrm{E_{s,ref}}}\right)^{\mathrm{d}} \tag{2.33}$$

$$\mathrm{E_s} = (1.15\mathrm{D_r} + 20000)\left(\frac{\sigma_3'}{100}\right)^{0.58} \tag{2.34}$$

Before carrying out the cyclic loading experiments, the monotonic response is essential for determination of the displacement ($\mathrm{Y_s}$) or rotation (θ_s) and its ultimate capacity ($\mathrm{H_u}$) on the pile-head. Several studies (Abadie and Byrne, 2014, Dyson and Randolph, 2001, Garnier, 2013, Hansen et al., 2013, Klinkvort, 2013, Klinkvort and Hededal, 2014, LeBlanc, 2009) have been carried out on monopile response under static loading where ultimate capacities were estimated. For instance, Garnier (2013) carried out experimental tests for piles installed in sandy soil and the response (see Fig.2.10(a)) shows a hardening H-y behaviour without achieving the ultimate capacity of the pile ($\mathrm{H_u}$). The two straight line branches separated by a clear inflexion point from three load-displacement curves were used to estimate an ultimate capacity. A similar approach was also applied by Zhu et al. (2012) to define the yield capacity of the overall moment-rotation response (see Fig 2.10(b)). The monotonic response on pile head observed from Klinkvort and Hededal (2013) was not possible to achieve the ultimate capacity (H_u) thus a recommended rotation of the pile was used to define the yield point (see Fig 2.10(c)). In general, the maximum accumulated rotation at seabed is specified by the wind turbine suppliers

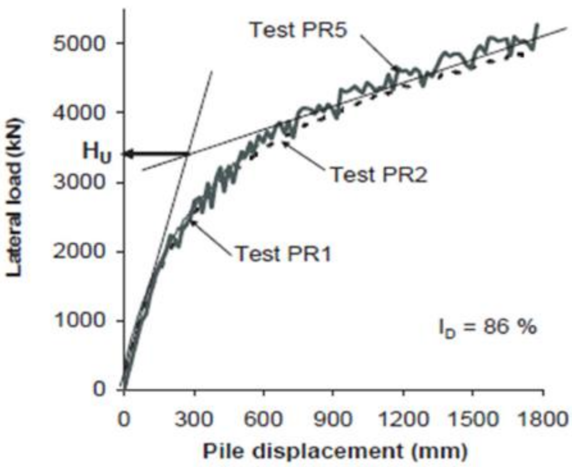

(a) H_u by tangent method, after Garnier (2013)

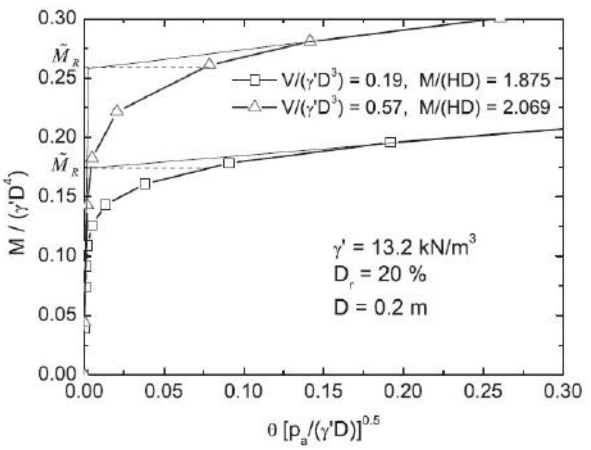

(b) M_R by tangent method, after Zhu et al. (2012)

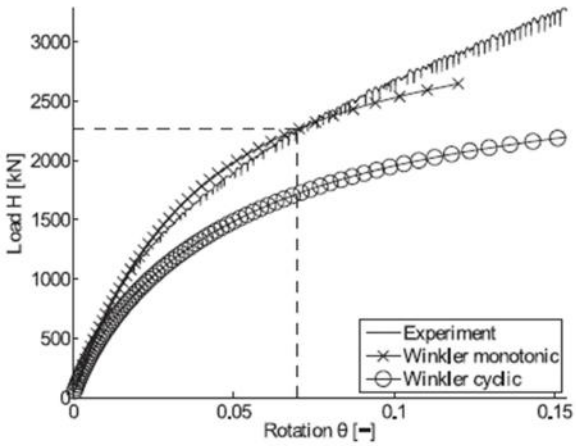

(c) H_u by rotation method, after Klinkvort et al. (2012)

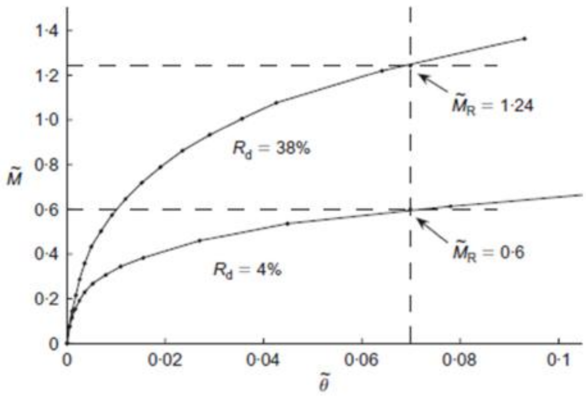

(d) M_u by rotation method, after after LeBlanc (2009)

Figure 2.10: Behaviour of monopile under monotonic loading and estimation of ultimate capacity

which is normally 0.5^o (Roesen et al., 2012a). Similarly other studies (Hansen et al., 2013, LeBlanc, 2009, Roesen et al., 2012a) used the same approach to determine the ultimate capacity of the pile. However, in Figs. 2.10(c) and 2.10(d), the responses from Klinkvort (2013) and LeBlanc (2009) did not follow the standard limits based on supplier and failure behaviour was taken at rotation of $\theta = 4^{o} = 0.0698$ rad.

From several studies, achieving the failure limit of monopiles subjected to monotonic lateral loading remains a great challenge (Abadie and Byrne, 2014). Thus, studies from (Broms, 1964, Hansen, 1961, Petrasovits and Awad, 1972, Zhang et al., 2005) suggest the estimation of ultimate capacities through either established theories or by evaluation of lateral displacement or rotation of the pile as previously discussed. However, the work from (Zhang et al., 2005), (Fan and Long, 2005), (Klinkvort and Hededal, 2013) and (Kirkwood, 2016) challenges the previous literature for a rigid pile in sandy soil, where they argue that theoretical calculation observed significantly high and tend to overestimate the pile-head displacement. Therefore, they recommended to fix the pile displacement failure limit in the range of 5-10% of the pile diameter for estimation of ultimate lateral capacity (Abadie and Byrne, 2014). Knowing the pile displacement and point where the pile rotates, the angle of pile rotation can be estimated assuming that the pile is perfectly rigid.

2.3 Behaviour of soil under cyclic loading

2.3.1 Introduction

Modelling of stress-strain response of cohesionless soil under cyclic load is an essential factor for designing and analysis of civil engineering structures. In prototype condition, the layers of soil subjected to cyclic loads are affected by cyclic stresses caused by repetition of loads (cyclic) such as vibration from machine structures, earthquakes, traffic loads, sea waves, and the wind (Basheer, 2002, Reddy, 1996, Shahnazari et al., 2010). These loads may induce a permanent soil deformation, which will significantly damage the support structure located on a specified soil layer (Shahnazari et al., 2010). Cyclic loading is a series of loads that vary within a certain regularity of both magnitude and frequency (O'Reilly and Brown, 1991). Under such loading conditions, the soil undergoes alternating cycles of compression and extension stresses and is known to exhibit a nonlinear behaviour (Basheer, 2002).

A nonlinear soil under cyclic loading undergoes recoverable and irrecoverable strains, frequently accompanied by change in density (Reddy, 1996). The recoverable strains tend to return to its position, while irrecoverable continue to increase with the number of cycles and never returns to its origin. When the soil interacts with the pile, the irrecoverable strain is likely to occur, which might lead to the failure of the foundation. In general, the rate of accumulation of irrecoverable strains in soil is a function of cyclic stress and strain levels (Reddy, 1996).

To assess the nonlinear response of the soil under cyclic lateral loading, the mathematical models are very important. Two general broad classes of soil models have been proposed, such as equivalent linear and cyclic nonlinear models. The equivalent linear soil model (Ishihara, 1996, Schnabel, 1972) is simple and widely used in one-dimensional (1D) analyses, to simulate a nonlinear soil behaviour. As noted from Stewart (2008), the advantages of this model include small computational effort and few input parameters, but it has some limitations. The main drawback is that it ignores the irrecoverable strains ($\gamma_{\mathrm{i}} \leq 10^{-3}$) and increase in pore pressure (Rascol, 2009). The cyclic nonlinear soil type models include relatively simple cyclic stress-strain relationships (Kondner, 1963, Matasović and Vucetic, 1993, Pyke, 1980, Ramberg and Osgood, 1943) to advanced constitutive models (Dafalias and Popov, 1975, Manzari and Dafalias, 1997, Mrz et al., 1978, Prevost, 1985, Roscoe, 1963), which incorporate the yield surfaces, hardening laws, and flow rules (Stewart, 2008). Advanced constitutive models are based on the framework of plasticity, capable of simulating complex 3D soil behaviour under a variety of loading conditions. The model relies on parameters determined through laboratory and field tests. Due to complexity, this type of model is limited for many practical challenges (Kramer, 1996). The nonlinear cyclic models can adequately represent the shear strength of the soil during cyclic loading by including the effect of excessive pore pressure, which cannot be accounted for in equivalent linear models (Stewart, 2008).

The important parameters used to assess the response of soil under cyclic loading are soil modulus, shear modulus or subgrade reaction modulus, damping ratio and ultimate soil resistance. These parameters are the key characteristics to construct hysteretic loops under cyclic loading (Ishihara, 1996, Oztoprak and Bolton, 2013, Shahnazari et al., 2010, Stewart, 2008). The estimation of lateral soil resistance ($\mathrm{P_u}$) and subgrade reaction modulus ($\mathrm{K_h}$) have previously been discussed in Section 2.2.2. Therefore, the main focus of this section is to assess other parameters related to soil (shear modulus and damping ratio). The soil bed used in the current thesis is from quartz sand and the previous studies related to this material might be useful. The maximum Young's modulus of soil ($E_{s,max}$) is related to the initial (maximum) shear modulus (G_{max}) and Poison's ratio (υ_s) (see Eq. 2.35). The shear modulus and damping ratio are used to represent the soil effective stiffness and dissipation of energy within the soil, respectively. The two parameters are key characteristics to construct the shear stress-strain hysteretic loops under cyclic loading (Ishihara, 1996, Oztoprak and Bolton, 2013, Shahnazari et al., 2010, Stewart, 2008), and will be discussed in the following section.

$$E_{s,max} = 2G_{max}\left(1 + \upsilon_s\right) \tag{2.35}$$

2.3.2 Shear modulus and damping ratio of soil

Several field and laboratory tests have been developed to characterise the cyclic behaviour of soil (Dobry and Vucetic, 1988, Ishihara, 1996, Shahnazari et al., 2010, Stewart, 2008), which are classified into two types: behaviour under low-strain and those at high-strain levels (see Fig. 2.11). As noted from Dobry and Vucetic (1988) and Shahnazari et al. (2010), the low-strain category is one at strain levels that are low in a way that its response behaves more elastically and is generally recoverable, approximately found at strains less than or equal to 0.001% . In this range, the shear modulus is a key parameter to model the stress-strain behaviour of soil. In Fig. 2.11, at a very small strain (Zone-1, $10^{-6} \leq \gamma_i \leq 10^{-5}$), the shear modulus has reached its maximum point known as initial or maximum shear modulus, G_{max}. For the second range (Zone-2) of shear strain (approximately below 10^{-3}), the soil behaviour is still non-degradable. In this range the strain level is still small enough to not cause any progressive change within the soil, hence, the shear modulus and damping ratio will not change with progression of cycles and behaviour will be non-degraded hysteresis type (Ishihara, 1996). For the medium range of shear strain ($10^{-3} \leq \gamma_i \leq 10^{-2}$ in Zone-3), the soil behaviour becomes elastoplastic. The shear modulus tends to decrease as the shear strain increases and energy dissipation occurs during the cyclic loading application. The damping ratio (loss coefficient) is used to present the energy absorbing capacity of soils (Shahnazari et al., 2010). For cyclic shear strain greater than 10^{-2} (Zone-4), the properties of soil changes with cycles and the behaviour is termed as degraded hysteric type. The strain in this zone is larger enough to induce a nonlinear response with both recoverable and irrecoverable elasticity. The shear modulus and damping ratio change with both the shear strain and the progression of cycles. Furthermore, the stress-strain nonlinear response of soil in this range can be achieved by employing a numerical procedure involving step-by-step integration techniques (Shahnazari et al., 2010). In this case, a cyclic nonlinear behaviour of the soil can be characterised through high-strain tests, such as cyclic triaxial and direct simple shear tests, which involve pseudo-static stress-controlled or strain-controlled cyclic loading of a vertically loaded soil specimen (Ishihara, 1996, Stewart, 2008).

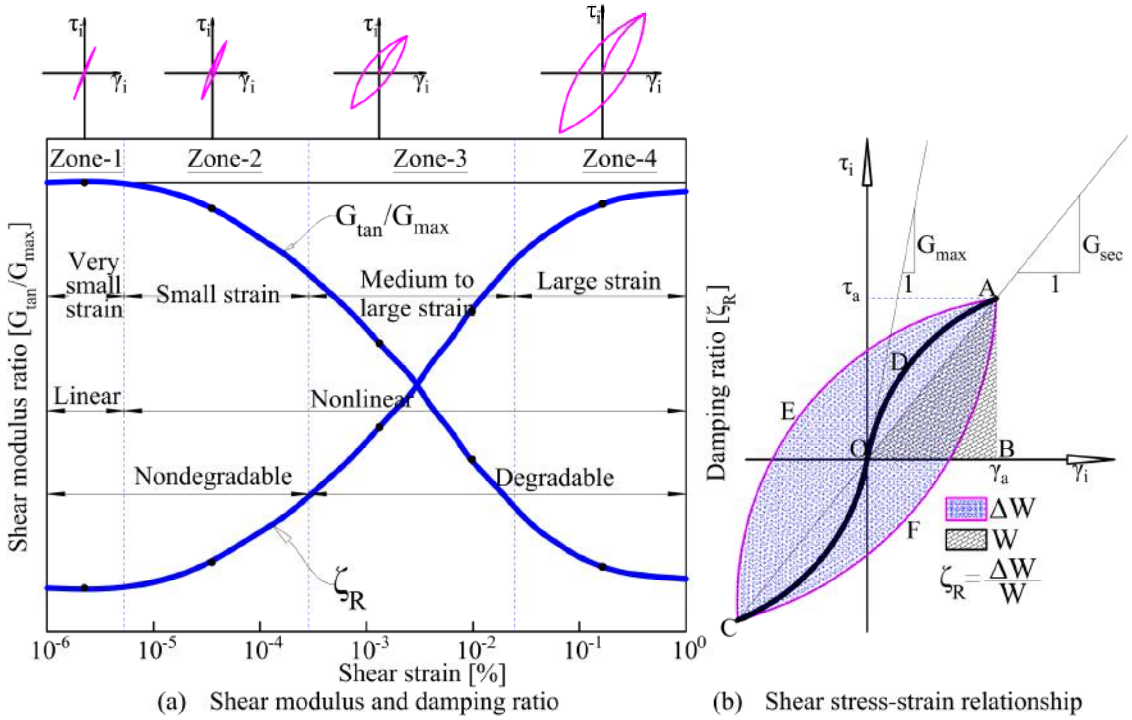

Figure 2.11: Dependence of shear modulus, damping ratio, and stress-strain relationship to shear strain amplitude, from Ishihara (1996).

As shown in Fig. 2.11, the energy dissipation per cycle (ΔW) is represented by the area enclosed within hysteresis loop CEAF. The damping ratio or loss coefficient is defined as the ratio between the energy loss per cycle (ΔW) and the maximum stored energy (W). For the nonlinear soil behaviour under cyclic loading, the energy stored is defined by assuming the area of the triangle OAB bounded by a straight line defining the secant modulus, G_{sec} (see Eq. 2.36). According to Masing (1926), the hysteresis loop is obtained from the backbone curve after multiplying by a factor of two in γ_i and τ_i directions. Therefore, the half-moon shape ACE has similar shape as the half-moon part AOD and hence the area ACE is four times the area AOD.

The energy loss per cycle is determined as shown in Eq. 2.37 and the damping ratio (ζ_R) is estimated by using Eq. 2.38.

$$W = \frac{1}{2} f(\gamma_a)\gamma_a \tag{2.36}$$

$$\Delta W = 8\left[\int_0^{\gamma_a} f(\gamma_i)d\gamma_i - W\right] \tag{2.37}$$

$$\zeta_R = \frac{\Delta W}{4\pi W} = \frac{2}{\pi}\left[\frac{\int\limits_0^{\gamma_a} f(\gamma_i)d\gamma_i}{\gamma_a f(\gamma_a)} - 1\right] \tag{2.38}$$

The shear modulus, G, is always presented as a secant modulus (G_{sec}) defined by extreme points on the hysteresis loops (Idriss and Seed, 1970, Ishihara, 1996). This property mostly depends on the magnitude of shear strain for which the hysteresis loop is defined (see Fig. 2.11). Several empirical functions have been developed to predict the maximum shear modulus, G_{max}. For cohesionless soil, G_{max} is primarily affected by two important parameters; the void ratio (e_o) and mean effective stress (P_m) (Hardin and Drnevich, 1972). Hardin and Drnevich (1972) proposed a function which relate the maximum shear modulus, G_{max}, and the two parameters (see Eq. 2.39), where $P_a = 100$ kPa is the reference pressure, *m* is exponent material constant (for sand it lies between $0.40 \leq m \leq 0.55$) (Hardin, 1978, Oztoprak and Bolton, 2013), G_b is the material constant which can be correlated with angularity of materials.

$$G_{max} = G_b P_a f(e) \left(\frac{P_m}{P_a}\right)^m \tag{2.39}$$

Pestana and Salvati (2006) and Oztoprak and Bolton (2013) used Eq. 2.39 to compare different types of sand and gravel materials. For instance, as shown in Fig. 2.12(a) three functions were used to describe the effect of void ratio on G_{max}; $f_1(e)=(1+e_o)e_o^{-1}$ (Pestana and Whittle, 1995), $f_2(e)=e_o^{-1.3}$ (Pestana and Salvati, 2006), and $f_3(e)=(2.17-e_o)^2(1+e_o)^{-1}$ (Hardin and Richart Jr, 1963). From the figure, $f_1(e)$ and $f_3(e)$ are shown with typical values of G_b while $f_2(e)$ provides a uniform sand with G_b values ranging from 400-800. The trend of the data is best fitted by the function $f_2(e)$. The values of G_b seem to be well-correlated with the angularity of the material, for instance, in Fig. 2.12(a) the sands with more angular grains tend to have higher values of G_b. The values of the void ratio functions in relation to void ratio (e_o), for all materials, are plotted in Fig. 2.12(b). The data are observed to be within the 20% error bars, hence, the G_{max} for uncemented cohesionless materials was best fitted by using Eq. 2.39. The values of G_b and m constants, angularity and C_u from the published work are summarised in Table 2.6.

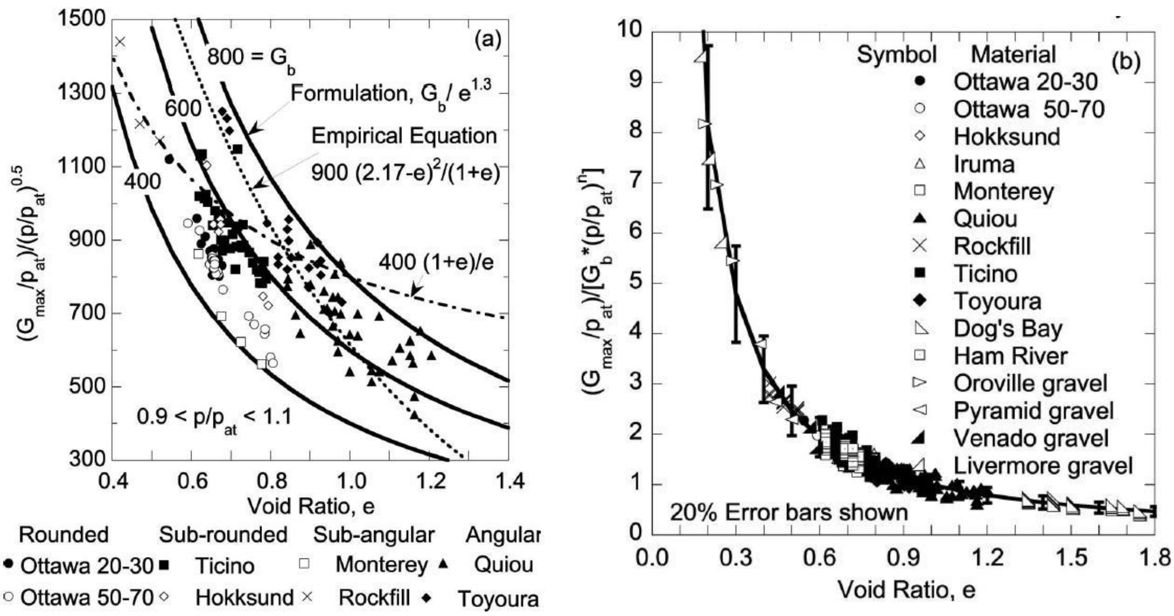

(a) Effect of angularity on G_{max} (b) Effect of void ratio

Figure 2.12: Effect of particle angularity and void ratio on G_{max}, from Pestana and Salvati (2006).

Table 2.6: Parameters for maximum shear modulus, G_{max}

Sand tested	Angularity	C_u	G_b	m	Reference
Ottawa	R	1.2	475-500	0.5	Hardin and Drnevich (1972)
Toyoura	SA	1.46	700-900	0.38	Kokusho (1980)
Dogs Bay	A	2.4	1800	0.5	Jovičić and Coop (1997)
Monterey	R	1.5	420-500	0.48	Chung et al. (1984)
Clean sand	R, SR, A	≤ 1.8	570	0.4	Iwasaki and Tatsuoka (1977)
Toyoura	SA	1.35	720	0.45	Presti et al. (1993)
Quartz	SA	1.33	724	0.45	Bellotti et al. (1996)

R=Rounded, A=Angular, SA=Sub-Angular, SR=Sub-Rounded

Seed and Idriss (1970) proposed a different approach to determine the values of G_{max} (kPa) (see Eq. 2.40). As shown in Eq. 2.40, G_{max} is based on modulus coefficient $(K_2)_{max} = 3.5(D_r)^{0.67}$ (Yan and Byrne, 1992). The parameter $(K_2)_{max}$ ranges from 30 for loose sand to 75 for dense sand. Wichtmann and Triantafyllidis (2009) recommended four different equations to estimate G_{max} (kPa) and concluded that Eq. 2.41 and 2.42, formulated in terms of void ratio, are more precise than Eq. 2.43 and 2.44, which employ the relative density to estimate G_{max} (kPa), where C_u is the coefficient of uniformity and D_r is the relative density of sand. Wichtmann and Triantafyllidis (2009) suggested that for practical purpose the empirical relations in terms of relative density are sufficient to use (Qin, 2010).

$$G_{max} = 48(K_2)_{max}\,(p')^{0.5} \tag{2.40}$$

$$G_{max} = G_b P_a \frac{(a_i - e_o)^2}{1 + e_o}\left(\frac{p'}{P_{ref}}\right)^{n_i} \tag{2.41}$$

where; $a_i = 1.94\exp(-0.066C_u)$, $G_b = 1563 + 3.13C_u^{2.98}$, $n_i = 0.4C_u^{0.18}$

$$G_{max} = 218.8G_k \frac{(a_k - e_o)^2}{1 + e_o}(p')^{0.5} \tag{2.42}$$

where; $a_k = 1.94\exp(-0.066C_u)$, $G_k = 69.9 + 0.21C_u^{2.84}$

$$G_{max} = 177000\frac{\left(1 + \frac{D_r}{100}\right)}{\left(17.3 - \frac{D_r}{100}\right)^2}(P_{ref})^{0.52}(p')^{0.48} \tag{2.43}$$

$$G_{max} = 1509720\frac{\left(1 + \frac{D_r}{100}\right)}{\left(16.1 - \frac{D_r}{100}\right)^2} \tag{2.44}$$

2.3.3 Nonlinear material models

2.3.3.1 Introduction

The mathematical models to describe the hysteresis behaviour of materials are classified into two groups: piecewise linear and curvilinear hysteresis models (Allotey and El Naggar, 2008, Bouc, 1971, Gerolymos and Gazetas, 2005b, Kagawa and Kraft, 1980, Naggar and Bentley, 2000, Pugasap, 2006, Thavaraj, 2000, Thyagarajan, 1989, Wen, 1976). Piecewise linear models are constructed by line segments, which represent a relationship between restoring force (F_y) and displacement ($y_{z(i)}$). The models within this group are elasto-plastic, bi-linear, and

multi-linear hysteresis. However, a drawback of this model is the sharp yield transitions; It is widely used in structural mechanics (Mostaghel, 1999). Therefore, they are not discussed further in this section. The curvilinear models provide a smooth transition curves and include the nonlinear models such as Bouc-Wen, Ramberg-Osgood and hyperbolic models. These types of models have been widely accepted to predict the response of soil and piles under both static and cyclic loading due to their simplicity and practical accuracy (Naggar and Bentley, 2000).
The procedures in developing the nonlinear p-y curves under monotonic or cyclic loading are similar to those applied in developing one-dimensional (1D) stress-strain response models (Allotey and El Naggar, 2008). Hence, even though the focus is on the components of p-y curves, reference is made to methods used in 1D shear stress-strain models. For instance, as noted by Ishihara (1996), the cyclic response of soil is made by constitutive models which described the soil behaviour as a relation between the shear stress, τ, and shear strain γ. The cyclic stress-strain behaviour can be determined by employing a relatively simple constitutive model (Ishihara, 1996, Kondner, 1963, Pyke, 1980, Ramberg and Osgood, 1943, Vucetic and Dobry, 1988). Therefore, by using simplified models (curvilinear type), the stress-strain (τ-γ) or p-y curve for cyclic behaviour of soil can be investigated.
Following the curvilinear type models, two different aspects can be used to determine the stress-strain relationship, namely, the path of the first loading, known as the backbone curve, and the path of unloading and reloading, which are termed as the hysteresis loops. The first aspect is when the soil is in a strain state of higher magnitude than the previous magnitude attained by the soil, while the latter is when the soil is in a strain state of lower magnitude than the previous maximum and can either decrease or increase with time (Ishihara, 1996, Stewart, 2008). The detail of the curvilinear type models is described in the following subsections.

2.3.3.2 Bouc-Wen model

Mathematical models have been developed in the past to model the hysteresis load-deformation behaviour of structural materials (Song and Der Kiureghian, 2006). One of the most popular is the Bouc-Wen class of hysteresis models, which was originally proposed by Bouc (1971) and later generalised by Wen (1976). The model was initially employed to describe inelastic cyclic force-displacement response in probabilistic structural dynamics, and later applied to soil liquefaction analysis in a simple shear, and currently used for the study of laterally loaded piles as monotonic or cyclic *p-y* curves (Baber and Wen, 1981, Badoni and Makris, 1996, Gerolymos et al., 2009, Gerolymos and Gazetas, 2005a,b, Park et al., 1986, Trochanis, 1994, Trochanis et al., 1991a,b). This model has the advantage in computation procedure, which relies on one auxiliary differential equation to compute the hysteresis behaviour of soil. Furthermore, the model is versatile in describing the characteristics of hysteretic behaviour such as stiffness and strength degradation, the pinching effect and asymmetry of the peak restoring force (Baber and Wen, 1981, Gerolymos and Gazetas, 2006, Park et al., 1986, Song and Der Kiureghian, 2006). Trochanis (1994) conducted a study on the nonlinear response of piles using a Winkler foundation model and utilised the Bouc-Wen model to describe the total load-deflection of distributed springs along the pile (Gerolymos and Gazetas, 2005b). The study focused on developing both monotonic and cyclic load-deflection, and the Bouc-Wen model shown to predict well the responses. Badoni and Makris (1996) utilised a Bouc-Wen model in conjunction with dashpots placed in parallel along the flexible piles under dynamic loading. The efficiency of the model demonstrated experimentally and analytically, was shown to predict well the response of the soil-pile systems. Moreover, the extension and modification of the model were utilised by Gerolymos and Gazetas (2005b) to model both the lateral soil reaction, pile inelasticity and computation of nonlinear response of single piles under monotonic and cyclic lateral load. The work by Gerolymos et al. (2009) simulated the piles in dry sand and subjected to cyclic lateral loading, using a cyclic nonlinear Winkler Bouc-Wen spring model and the results were in good agreement. A simple extended model utilised by Gerolymos and Gazetas (2005b) and Gerolymos et al. (2009) is of interest and is outlined in this section for demonstration.

According to Gerolymos et al. (2009), a cyclic nonlinear Winkler Bouc-Wen spring model, which describes the full range of inelastic phenomena, including separation and reattachment of the pile from and to the soil, was developed. The model was applied to tress the monotonic and cyclic response of piles, expressing the *p-y* relationship of the vertical pile embedded in dry sand. The model is made up of three mathematical functions capable of reproducing a wide range of monotonic and cyclic experimental *p-y* curves. As shown in Eq. 2.45, the mathematical relationship for lateral soil reaction, $\mathrm{P_{z(i)}}$ against pile deflection, $\mathrm{y_{z(i)}}$, is expressed as the sum of the elastic and hysteretic component, where ζ_{bw} is a dimensionless inelastic parameter expressed in Eq. 2.46, $\mathrm{P_{z(i)}}$ is the resultant soil resistance, $\mathrm{y_{z(i)}}$ is the pile deflection at the location of the spring, P_y is a characteristic value of the soil reaction related to the initiation of significant inelasticity (yielding), and y_o is a characteristic value of pile deflection related to the initiation of yielding in soil, *n* control the sharpness of the transition from the linear to the nonlinear range during the monotonic loading, α is the ratio of steady-state post yielding to the initial elastic stiffness, *b* and *g* control the unloading-reloading rule (*b*+*g*=1). To match the results of experiment *p*-*y* curves, the parameter *n* and α can be adjusted. More details of the model are described by Gerolymos et al. (2009).

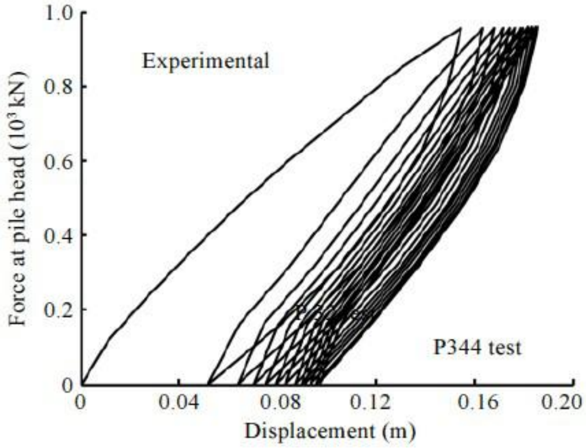

(a) One-way cyclic response (test P334)

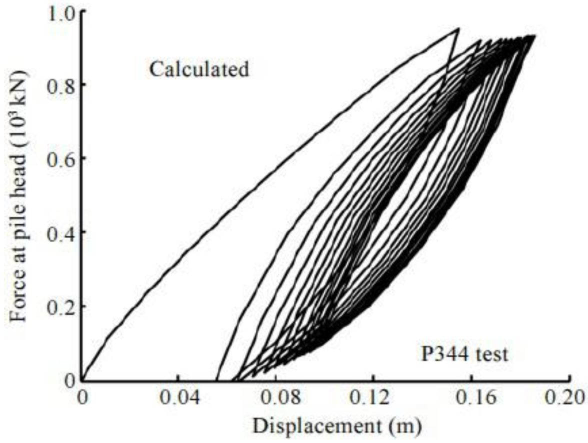

(b) One-way Bouc-Wen force-deflection

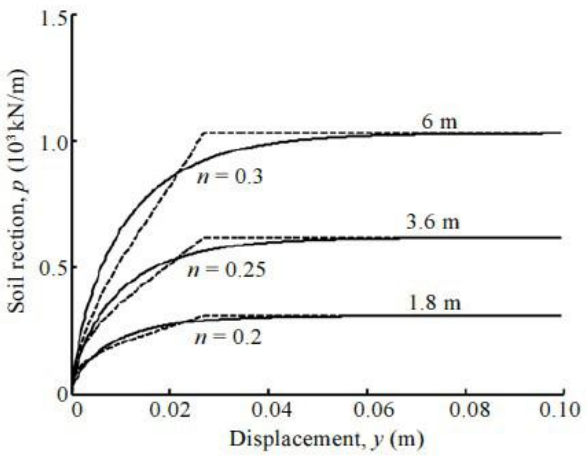

(c) Prediction of p-y curves (test P32)

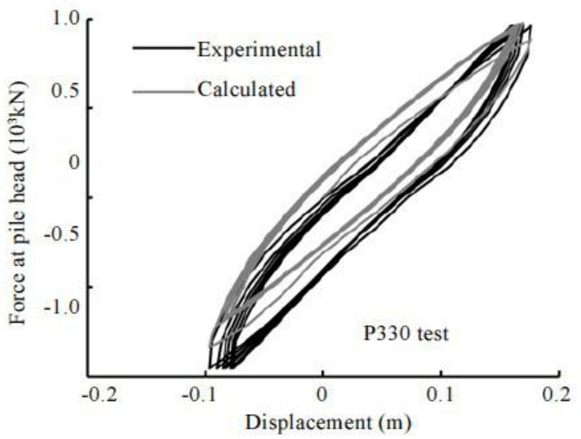

(d) Two-way cyclic H-y response (test P330)

Figure 2.13: Experimental and computed cyclic force-displacement and monotonic p-y curves (Bouc-Wen model), from Gerolymos et al. (2009)

$$P_{z(i)} = \alpha K_h y_{z(i)} + (1-\alpha) P_y \zeta \tag{2.45}$$

$$\frac{d\zeta_{bw}}{dy} = \frac{1}{y_o}\left\{1 - |\zeta_{bw}|^n\left[b + g\mathrm{sign}(dy\zeta_{bw})\right]\right\} \tag{2.46}$$

From Fig. 2.13, the validity of the model and its ability to capture several features of the pile-soil interaction is presented. The cyclic load-deflection response was achieved by comparing the results of centrifuge tests from Rosquoët et al. (2004) and prediction from the Bouc-Wen theoretical model. The test results show a positive trend with the model. It should be noted that this type of model has been used for flexible piles only, therefore, further investigation is required for the rigid piles.

2.3.3.3 The Ramberg Osgood and hyperbolic model

The Ramberg Osgood and hyperbolic models are widely used in geotechnical practice to capture the fundamental aspect of actual soil behaviour and soil-structure interaction systems, subjected to monotonic as well as cyclic loading. They usually include two parts, the initial loading stress-strain nonlinear curve, which extend into the negative domain, known as the initial or backbone curve (see Fig. 2.14(a)) and the constructed hysteresis loop described by subsequent unloading and reloading stress-strain curves (see Fig. 2.14(b)) (Chen et al., 2013, Matasović and Vucetic, 1993, Yi, 2010). The shear stress-strain or soil resistance-displacement models have been proposed in the past (Chen et al., 2013, Dobry and Vucetic, 1988, Duncan and Chang, 1970, Hardin and Drnevich, 1972, Ishihara, 1996, Kondner, 1963, Matasović and Vucetic, 1993, Nakagawa and Soga, 1995, Pestana and Salvati, 2006, Pyke, 1980), and utilised Masing rules suggested by Masing (1926), to construct the τ-γ or p-y hysteresis loops (Matasović and Vucetic, 1993). By employing the Masing Rule, the nonlinear stress-strain relationships of soils under cyclic loading can be constructed as illustrated in Fig. 2.14(b) (Ishihara, 1996, Stewart, 2008).

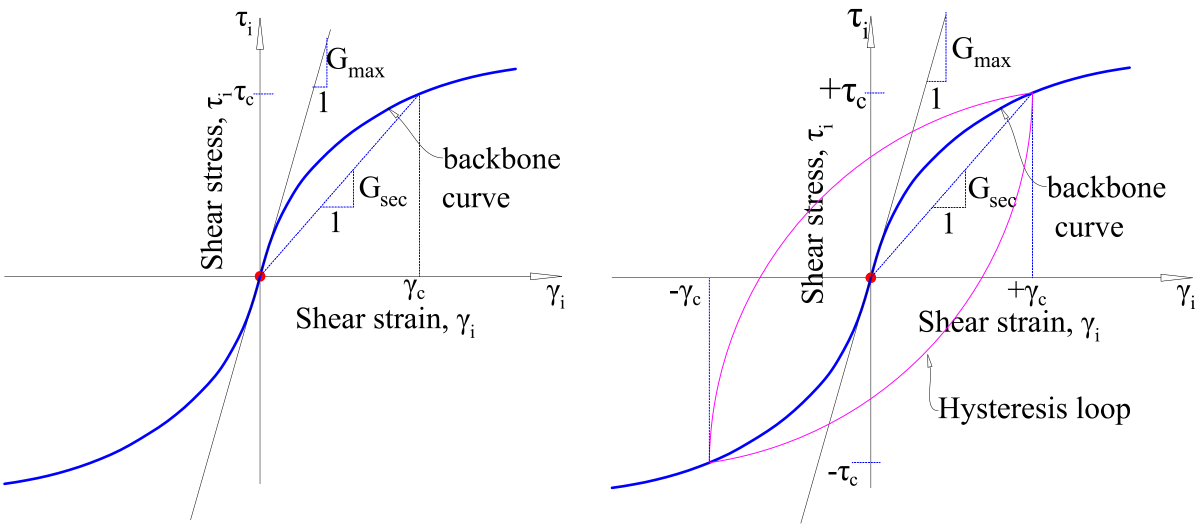

(a) Shear stress-strain backbone curve

(b) Shear stress-strain hysteresis loop based on Masing Rule

Figure 2.14: Schematic diagrams of shear stress-strain curves, from Stewart (2008) and Dobry and Vucetic (1988)

Both the Masing Rule (Masing, 1926) and the extended Masing Rule (Pyke, 1980, Vucetic and Dobry, 1988) are used with nonlinear stress-strain or p-y backbone curves to describe the hysteresis loops. In Fig. 2.15 the rules to construct the hysteresis loops are defined as follows:

1. The shear stress-strain curve follows the backbone curve for initial loading. The tangent shear modulus at each reversal of unloading and reloading branches of the loop are the same to the initial tangent shear modulus of the backbone curve.

2. The reloading curve of any cycle starts with a shape that is identical to the shape of the initial loading backbone curve enlarged by a factor of two. The same applies to the unloading curve in connection with the negative part of the initial loading backbone curve.

3. If the unloading or loading curve exceeds the maximum past strain and intersects the backbone curve, it follows the backbone curve until the next stress reversal.

4. If the unloading or loading curve crosses the unloading or loading curve from a previous cycle, the stress-strain curve follows that of the previous cycle. As reported from Pyke

(1980), the rule accounts for irregular cyclic and modified the second law, instead of enlargement by a factor of two, it was suggested to use a factor C as shown in Eq. 2.47, in which the first term is negative for unloading and positive for reloading.

$$C = \left| \pm 1 - \frac{\tau_a}{\tau_{ult}} \right| \tag{2.47}$$

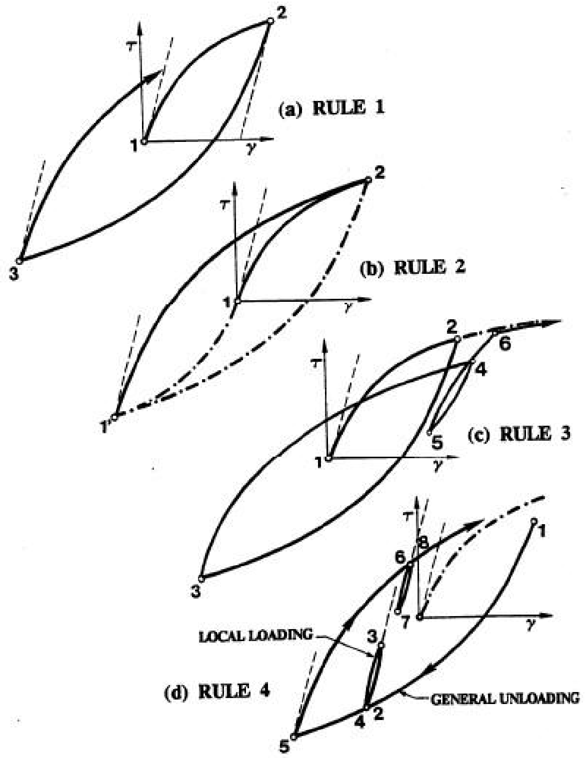

Figure 2.15: Extended Masing rule, from Vucetic and Dobry (1988).

Ramberg and Osgood (1943) developed a mathematical formulation known as Romberg Osgood (R-O), to define monotonic as well as cyclic stress-strain and p-y curves (Abendroth and Greimann, 1990, Desai and Wu, 1976, Desai and Zaman, 2013, Pugasap, 2006, Richart Jr, 1975). The model is more useful with advantage to validate observed data compared to others since it includes the commonly used hyperbolic function with addition parameters. For instance, Greimann et al. (1986) and Greimann (1987) utilised the model in the finite element method to approximate the load-displacement curves for axially and laterally loaded piles. The characteristics of soil parameters, describing the skin friction and vertical displacement (*f-z* curve), end bearing (*q-z* curve) and lateral resistance (*p-y* curve), were used in finite element models to idealise the nonlinear soil behaviour (Abendroth and Greimann, 1990). According to Abendroth and Greimann (1990), a further modification of the model expression known as

Ramberg-Osgood (R-O) was employed in the Winkler model analysis and the results were correlated with centrifuge experimental data. The results of the pile-soil system of a particular pile tests were correlated well with the measured values. Pugasap (2006) used these types of hysteresis model in FE method to determine the response of soil-pile interaction on bridge abutments. More details of this model for pile-soil interaction can be found from Desai and Zaman (2013) and Greimann et al. (1984). This expression was also employed by Richart Jr (1975) to describe the shearing stress-strain behaviour as the strain level increases. Shear stress-strain Ramberg-Osgood mathematical curves were incorporated into analytical procedures to approximate the experimental data and the results were in good agreement. In Eq. 2.48, the modified R-O model for backbone curve suggested by Greimann et al. (1984) is presented in the form of a *p-y* curve, where $\mathrm{P_{z(i)}}$ is generalised soil resistance, $\mathrm{P_u}$ is the ultimate soil resistance, $\mathrm{K_h}$ is the initial lateral stiffness, *n* is the shape parameter, and $\mathrm{y_{z(i)}}$ is generalised displacement.

$$\mathrm{P_{z(i)}} = \frac{\mathrm{K_h y_{z(i)}}}{\left[1 + \left|\dfrac{\mathrm{K_h y_{z(i)}}}{\mathrm{P_u}}\right|^{\mathrm{n}}\right]^{\frac{1}{\mathrm{n}}}} \tag{2.48}$$

As noted from Greimann et al. (1984), the R-O model for cyclic loading was used to determine the pile-soil interaction in integral abutment bridge. In abutment bridge, the occurrence of expansion and contraction might cause the pile to move back and forth, which will result in unloading and reloading behaviour. This model was created to accommodate the loading and unloading of the pile movement. The nonlinear behaviour of the pile-soil system was expressed by the concept of stress versus strain and soil resistance versus deflection. For both symmetrical and irregular cyclic loading, the R-O model in the form of p-y curves is shown in Eq. 2.49, where $\mathrm{P_c}$ is soil resistance at the last load reversal and $\mathrm{y_c}$ is soil displacement at the previous load reversal.

$$\mathrm{P_{z(i)i}} = \mathrm{P_c} + \frac{\mathrm{K_h(y_{z(i)} - y_c)}}{\left[1 + \left(\dfrac{1}{\mathrm{C}}\left|\dfrac{\mathrm{K_h(y_{z(i)} - y_c)}}{\mathrm{P_u}}\right|\right)^{\mathrm{n}}\right]^{\frac{1}{\mathrm{n}}}} \tag{2.49}$$

where;

$$\mathrm{C} = \left|\pm 1 - \frac{\mathrm{P_c}}{\mathrm{P_u}}\right| \tag{2.50}$$

From Eq. 2.50, the first term is negative for unloading and positive for reloading (Pyke, 1980). Therefore, by using Eq. 2.49, the construction of hysteresis loops is achieved by adopting rules presented by Pyke (1980). However, application of this model is widely used on flexible piles and further research is required for a rigid pile.

The hyperbolic model, originally proposed by Kondner (1963) and Duncan and Chang (1970), has been extensively used in the past to represent the relation between the shear stress (τ_{i}) and shear strain (γ_{i}) (Vucetic and Dobry, 1988). Matasović and Vucetic (1993) conducted extensive testing on different types of liquefiable sands. The results obtained from the tested sand were simulated by utilising the model suggested by Kondner (1963), named as the KZ model. However, the KZ model was incapable of describing the soil stress-strain behaviour with sufficient degree of accuracy. Accordingly, two curve fitting constants (β_{o} and s) were introduced into the KZ model to accurately fit the data. With the addition of these two constants, the modified model, abbreviated as MKZ model, was developed. The curve fitting constants were used to adjust the position of the curve along the ordinate and control the curvature. For more details of the KZ and MKZ hyperbolic models, the reader is referred to Matasović and Vucetic (1993). Yi (2010) proposed backbone (see Eq. 2.51) and hysteresis (see Eq. 2.52) models to simulate the measured data obtained from Santa Monica Beach (SMB) sand. From the two equations, $\mathrm{G_f} = \dfrac{\tau_{\mathrm{f}}}{\gamma_{\mathrm{f}}}$, $\mathrm{R_f} = \dfrac{\tau_{\mathrm{f}}}{\gamma_{\mathrm{u}}}$, $\mathrm{G_o} = \mathrm{G_{max}}$, the parameter α is similar to s, which was introduced to control the shape of backbone curve and β is the parameter related to damping ratio.

$$\tau_{\mathrm{z(i)}} = \frac{\mathrm{G_o}\gamma_{\mathrm{z(i)}}}{1 + \dfrac{\mathrm{R_f}}{1-\mathrm{R_f}}\left|\dfrac{\gamma_{\mathrm{z(i)}}}{\gamma_{\mathrm{f}}}\right|^{\alpha}} \tag{2.51}$$

$$\tau_{\mathrm{z(i)}} = \frac{\mathrm{G_o}\gamma_{\mathrm{z(i)}}}{1 + \mathrm{B}\left|\dfrac{\gamma_{\mathrm{z(i)}}}{\gamma_{\mathrm{a}}}\right|^{\beta}} \Rightarrow \mathrm{B} = \frac{\mathrm{R_f}}{1-\mathrm{R_f}}\left|\frac{\gamma_{\mathrm{a}}}{\gamma_{\mathrm{f}}}\right|^{\alpha} \tag{2.52}$$

In Fig. 2.16, Yi (2010) presented the plots of measured data and calculated $\mathrm{G_{sec}/G_{max}} = \mathrm{G/G_o}$, $\zeta_{\mathrm{R}} = \mathrm{D}$ and $\tau_{\mathrm{i}} = \tau$ against $\gamma_{\mathrm{z(i)}} = \gamma$, including the results of KZ and MKZ models. From these plots, the MKZ model is in a good agreement with experimental data than KZ model. All parameters used for the analysis are shown in these figures.

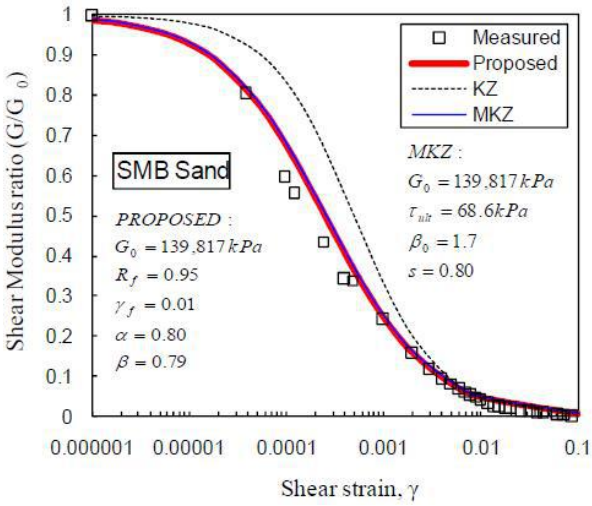

(a) Simulation of G/G_o against γ

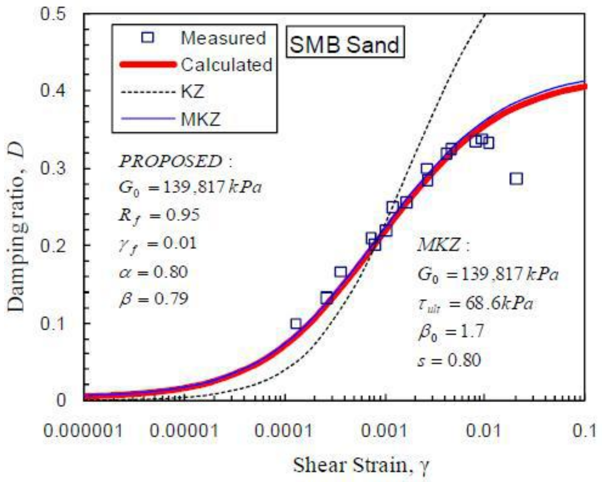

(b) Simulation of damping ratio against γ

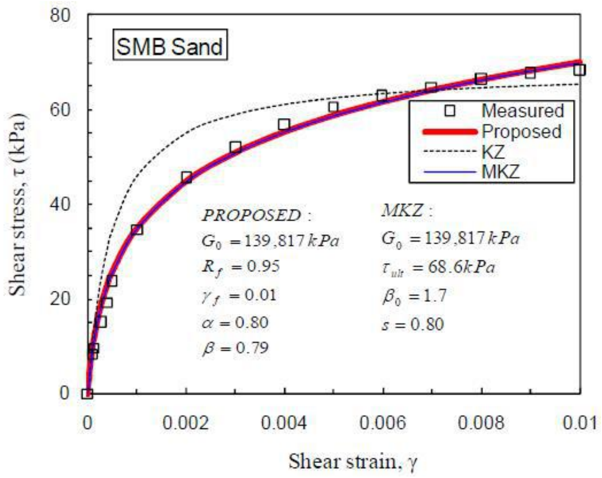

(c) Simulation of τ against γ

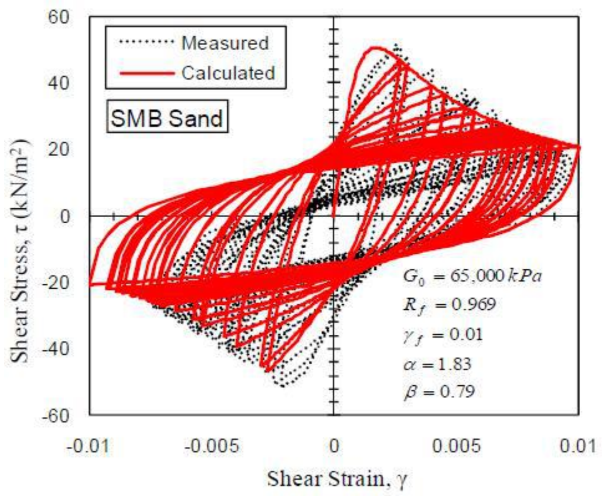

(d) Simulation of hysteresis loops

Figure 2.16: The response of SMB sand under monotonic and cyclic loading, from Yi (2010).

Furthermore, Yang et al. (2003) proposed a shear stress-shear strain relationship of backbone curves at given reference pressure by using Eq. 2.53 to 2.54, where $\tau_{\mathrm{f}} = \left(\dfrac{2\sqrt{2}\sin\phi}{3-\sin\phi}\right)\mathrm{P_{at}}$, ϕ is friction angle at peak shear strength in degrees, $\mathrm{P_{at}}$ is the reference pressure equal to 100 kPa, and γ_{r} is the reference strain attained at failure.

$$\tau_{\mathrm{z(i)}} = \frac{\mathrm{G_{max}}\gamma_{\mathrm{z(i)}}}{\left(1+\left|\dfrac{\gamma_{\mathrm{z(i)}}}{\gamma_{\mathrm{r}}}\right|^{\mathrm{b}}\right)}, \Rightarrow \gamma_{\mathrm{r}} = \frac{\tau_{\mathrm{f}}\gamma_{\mathrm{max}}}{\mathrm{G_{max}}\gamma_{\mathrm{max}} - \tau_{\mathrm{f}}} \tag{2.53}$$

$$\tau_{z(i)} = \frac{G_{max}\gamma_i}{\left(1 + \left|\left(\frac{G_{max}}{\tau_f} - \frac{1}{\gamma_{max}}\right)\gamma_{z(i)}\right|^b\right)} \tag{2.54}$$

As noted by Blaney and O'Neill (1986), Kagawa and Kraft (1980), Lin and Liao (1999) and Kumar et al. (2006), for pile in a cohesionless soil and subjected to lateral loads, 70% of its displacement concentrated in the soil mass within a two-radius distance of the pile. An increase of shear strain due to soil-pile interaction was suggested to concentrate on this zone. According to Kagawa and Kraft (1980), the average normal strain, ε, in the direction of pile movement and average shear strain around the pile was approximated as $\varepsilon = \frac{y_{z(i)}}{2.5D}$ and $\gamma_{z(i)} = \left(\frac{1+\nu_s}{2.5D}\right)y_{z(i)}$, respectively. Therefore, with the available deflection along the pile, the shear stress-shear strain backbone curve can be created using Eq. 2.55, where γ_{max} is the maximum shear strain which depends on the pile deflection, b is fitting constant to control the curvature, ν_s is Poisson's ratio, D is the diameter of the pile and G_{max} is the maximum shear modulus in kPa.

$$\tau_{z(i)} = \frac{\left(G_{max}\frac{1+\nu_s}{2.5D}\right)y_{z(i)}}{\left(1 + \left|\left(\frac{G_{max}}{\tau_f} - \frac{1}{\gamma_{max}}\right)\left(\frac{1+\nu_s}{2.5D}\right)y_{z(i)}\right|^b\right)} \tag{2.55}$$

As discussed in the previous section, the unload and reload curves can be created based on Masing rules and defined in the form similar to Romberg Osgood model (Desai and Wu, 1976, Desai and Zaman, 2013). The function used for analysis is shown in Eq. 2.56, where τ_c and γ_c are the shear stress and shear strain, respectively, at last load reversal.

$$\tau_{z(i)} = \tau_c + \frac{G_{max}(\gamma_{z(i)} - \gamma_c)}{\left(1 + \frac{1}{C}\left|\left(\frac{G_{max}}{\tau_f} - \frac{1}{\gamma_{max}}\right)(\gamma_{z(i)} - \gamma_c)\right|^b\right)} \tag{2.56}$$

For monopiles, the analysis of the previous studies have been performed based on the recommendation from DNV (2014). However, Klinkvort (2013) employed the concept of the hyperbolic KZ model from Kondner (1963) to construct the backbone *p-y* curves (see Eq. 2.57), where P_u is the ultimate soil resistance, $k_h = \frac{K_h}{Z}$ is the constant modulus of subgrade reaction of the *p-y* response in kN/m^3, k is elastic unloading at appropriate stiffness, $P_{u,drag}$ is the constant friction drag on the pile sides, A is an empirical factor defined in Eq. 2.58 (this function was modified as the parameter used from API (2007) and DNV (2014) was not suitable). The initial stiffness proposed from DNV (2014) was higher than initial stiffness proposed from the experiment *p-y* curves and the $\mathrm{k_h}$ =100 $\mathrm{K_p}\gamma$ was used instead.

$$\mathrm{P_u^{virgin}} = \frac{\mathrm{k_h Z y}}{1 + \dfrac{\mathrm{k_h Z y_{z(i)}}}{\mathrm{AP_u}}} \tag{2.57}$$

$$\mathrm{A} = 0.9 + \frac{1.1}{2}\left\{1 + \tanh\left(9 - 3\frac{\mathrm{Z}}{\mathrm{D}}\right)\right\} \tag{2.58}$$

For hysteresis loops, Eq. 2.59 and 2.60 were used to construct the *p-y* curves and displacement of pile, respectively, where the hardening parameter, α, $\mathrm{y_{bt}}$ and k are all shown in Fig. 2.18(a). The parameter k=5$\mathrm{k_h}$Z was set to provide a good agreement with measured data. To model the cyclic pile-soil interaction, four input parameters, namely elastic stiffness k, initial stiffness of the backbone curve $\mathrm{K_h}$, ultimate capacity $\mathrm{P_u}$ and drag soil resistance $\mathrm{P_u^{drag}}$ = 0.1$\mathrm{P_u}$ (assumed constant when the pile is moving in the gap), were required. The model parameters was set as D = 3 m, L = 18 m, $\mathrm{L_e}$ = 45 m. $\mathrm{D_r}$ = 0.9 (ϕ_{max} = 42$^{\mathrm{o}}$). The stiffness of the virgin curve was reduced to 60% of the initial stiffness found from monotonic test. The focus on this thesis is to provide an overview of the hysteresis loops, more details can be found from Klinkvort (2013).

$$\mathrm{P_u^{virgin}(y^*)} = \frac{2\mathrm{y}^* - \dfrac{\mathrm{P}}{\mathrm{k}} + \mathrm{y_{bt}}}{\dfrac{1}{\mathrm{k_h}} + \dfrac{2\mathrm{y}^* - \dfrac{\mathrm{P}}{\mathrm{k}} + \mathrm{y_{bt}}}{\mathrm{P_u}}} - \mathrm{P_u^{drag}} \tag{2.59}$$

$$(\mathrm{y}^*) = \mathrm{y} - \alpha = \frac{(\mathrm{y_{max}} + \mathrm{y_{p,min}})}{2} \tag{2.60}$$

As shown in Fig. 2.17(b), the total response of the model in the first few cycles is observed to follow the backbone curve with a high degree of accuracy, but when reversed it shows softer behaviour than measured due to a mechanical potentiometer. The hysteresis loops from measured are large than predicted, which indicate that the model underestimates the dumping in the soil.

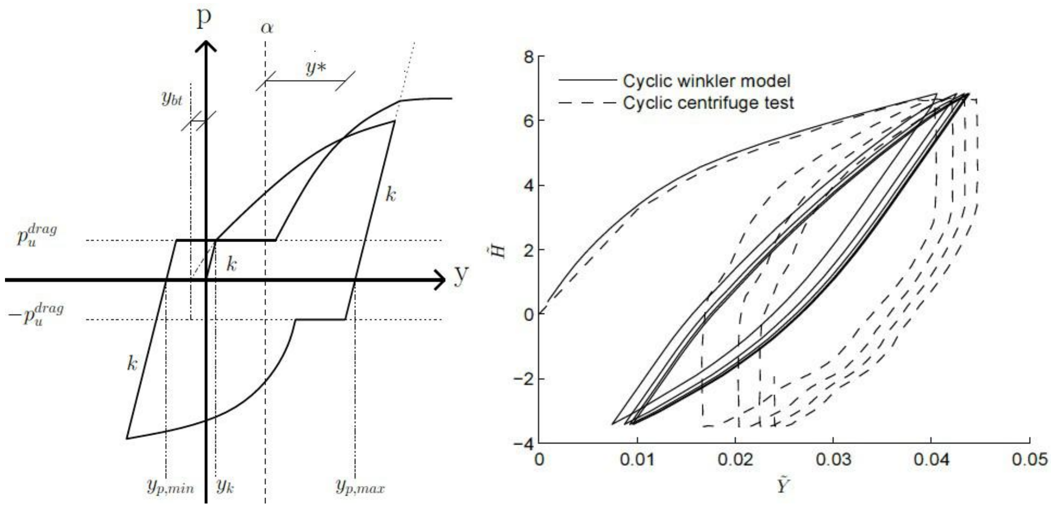

(a) Idealised spring element model (b) Global test and Winkler model responses

Figure 2.17: Model definitions and its use in total responses, from Klinkvort (2013)

Furthermore, the local pile-soil interaction curves from experiment were also modelled by the proposed spring model as shown in Fig. 2.18. For the chosen depths, a satisfactory agreement was observed but the spring element does not change with number of cycles as seen in the tests. This was due to an increase of soil capacity during the experiment as the number of cycles increases. The response was observed to be stiffer due to soil compaction with in number of cycles. The method suggested by Klinkvort (2013) has not been verified by further testing, therefore, it requires further research.

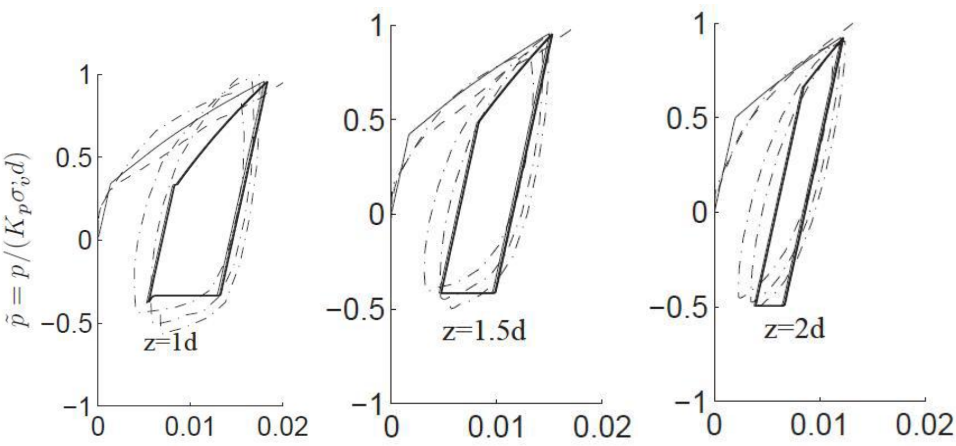

(a) *p*-*y* curves at Z=1D (b) *p*-*y* curves at Z=1.5D (c) *p*-*y* curves at Z=2D

Figure 2.18: *p*-*y* tests and spring model responses, from Klinkvort (2013)

2.4 Behaviour of piles under cyclic lateral loading

2.4.1 Introduction

This section describes the behaviour of monopiles subjected to cyclic loading caused by wind and waves. The cyclic behaviour of piles has been developed from the results of numerous laboratory and full-scale physical model tests. Several 1 g laboratory tests (Arshad and O'Kelly, 2014, 2016, Arshad and OKelly, 2016, 2017, Chen et al., 2015, Cuéllar, 2011, Foglia et al., 2012, LeBlanc, 2009, Nicolai et al., 2014, Nikitas et al., 2016, Peng et al., 2011, Roesen et al., 2012b, Zhu et al., 2012), Ng centrifuge tests (Bienen et al., 2011, Cox et al., 2014, Kirkwood, 2016, Klinkvort and Hededal, 2013, 2014, Li et al., 2010, Rosquoet et al., 2007, Rudolph et al., 2013, Zhang et al., 2010) and field experiments (Doherty et al., 2012, Hald et al., 2009, Lin and Liao, 1999, Little and Briaud, 1988, Long and Vanneste, 1994) have been carried out to investigate the behaviour of monopiles under cyclic loading. A brief detail of these studies related to 1g and Ng test models is presented in Table 2.7. Most of these studies described the behaviour of monopiles based on the following phenomena;

1. Accumulation of monopile rotation or displacement.
   The accumulation of rotation of a monopile over its design life must be accurately estimated and typically limited by serviceability constraints (Klinkvort et al., 2012, LeBlanc, 2009).

2. Change in cyclic stiffness with number of cycles.
   The monopile in the soil must be accurately designed to account for the change of pile stiffness and therefore the interaction of the pile and soil. To evaluate monopile stiffness it is important to assess natural frequencies of the structure and essential consideration for wind turbine design (Bhattacharya and Adhikari, 2011, LeBlanc, 2009). Any changes of the monopile stiffness, during and after the application of millions of load cycles, might be critical in the assessment of the fatigue life and dynamic response of the structure.

Table 2.7: Summary of physical modelling of offshore monopile foundations

Reference	**Model type**	**Load direction** ζ_c	**Model diameter** D [mm]	**Prototype diameter** D [m]	**Model Embedded** L [mm]	Prototype **Embedded** L [m]	**Load cycles** [N]
Peng et al. (2006)	1g	OW/TW	44.5	-	400	-	10000
Rosquoet et al. (2007)	N_S g	OW	18	0.72	-	-	44
Li et al. (2010)	N_S g	OW	-	5	-	25	1000
Peralta and Achmus (2010)	1g	OW/TW	60	-	0.2-0.5	-	10000
LeBlanc et al. (2010)	1g	OW/TW	-	4	-	21.5	10000
Cuéllar (2011)	1g	OW/TW	-	7.5	-	30	5000000
Bienen et al. (2011)	N_S g	OW	-	2.4	-	-	10,000
Roesen et al. (2012a)	1g	OW	100	-	0.5	-	60,000
Klinkvort and Hededal (2013)	N_S g	OW/TW	24,40	3	6D	-	500
Rudolph et al. (2013)	N_S g	OW/TW	-	5	-	-	30,000
Arshad and O'Kelly (2014)	1g	OW/TW	53	-	0.54	-	30,000
Lau (2015)	N_S g	OW/TW	38.3, 76.2	-	-	-	1,000
Zhu et al. (2015)	1 g	OW/TW	165	5	915	-	10,015
Abadie (2015)	1 g	OW/TW	51-102	4-8	360	28.8	100,000
Kirkwood (2016)	N_S g	OW/TW	38.1	3.81	200	20	4,000
Nanda et al. (2017)	1 g	OW/TW	90	4	530	21.2	1,000
Truong et al. (2018)	N_S g	OW/TW	11,40	3.92	240	21.72	1,500

OW : One-Way loading direction
TW : Two-Way loading direction

The key effects mentioned above are discussed in detail in the following subsections, however, before the discussion, the typical cyclic behaviour is described to get a general overview. Under cyclic loading, the response of the pile can be divided into either one-way or two-way as demonstrated in Fig. 2.19. In one-way loading, the load cycles from zero to the maximum applied load in one direction only, whereas with two-way loading the load direction changes to the opposite orientation.

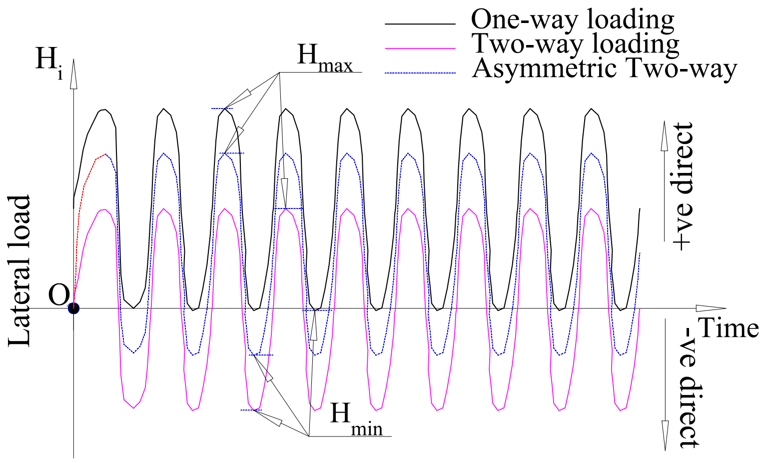

Figure 2.19: Modes of load variation against time, from Arshad and O'Kelly (2016).

Based on the typical sketch of pile loading shown in Fig. 2.19, examples of outcomes of one-way and two-way cyclic load characteristics are discussed below;

1. One-way cyclic load characteristics

   Figs 2.20(a) and 2.20(b) present typical behaviour of one-way cyclic loading from Li et al. (2010) and Rosquoet et al. (2007), respectively. It can be observed that over the virgin sand the loading response for the first cycle exhibits nonlinearity of soil. The slope of each cycle is observed to increase as the lateral displacement increases. The tangent stiffness of the first cycle contrasts with the stiffness trend of the following cycles, which becomes more linear and stiffer as the number of cycles increases. As noted from Li et al. (2010), the repetition of load under one-way cyclic loading is likely to remould the soil during the first few cycles, with larger displacements being generated than for the following cycles. This indicates that the tangent stiffness of the first cycle is lower than those observed in the following cycles due to soil compaction occurring around the pile, leading to an increased stiffness.

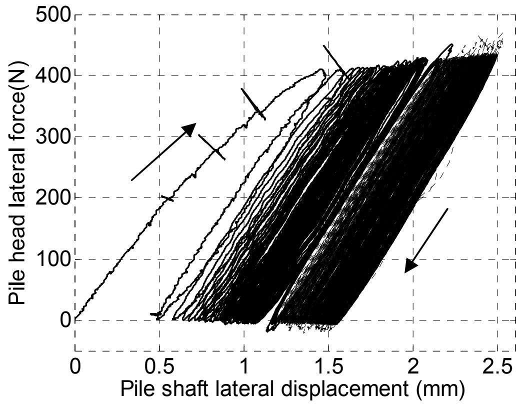

(a) The response, from Li et al. (2010)

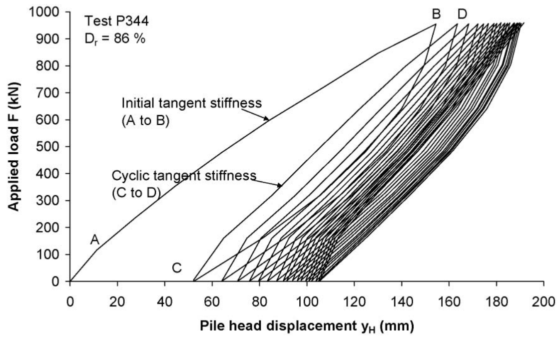

(b) The response, from Rosquoet et al. (2007)

Figure 2.20: The response of one-way cyclic lateral load in a centrifuge.

2. Two-way cyclic loading characteristics

   Under two-way cyclic loading, the behaviour of the pile can be described in four stages in one complete cycle (Long and Vanneste, 1994). In the first quarter of a cycle (see Fig. 2.19), the magnitude of the load varies from zero to a maximum load (H_{max}) in the positive direction (assume push from left to right). The deflection of the pile is resisted by soil in front of the pile while the soil to the left maintains contact by flowing with the pile. In the second quarter, the load decreases from H_{max} to zero, and the pile deflects towards the original location (towards the left). As the pile continues to the left side (negative direction), the soil resistance increases while resistance on the right side decreases with sand flowing with pile to prevent the gap formation. During this process, the cohesionless soil changes in volume and particles rearranged. In the third quarter cycle the pile continue to deflect to the left and the magnitude of load changes from zero to H_{min} (in the negative direction). The response of the fourth quarter-cycle is similar to the second quarter-cycle but in the opposite direction. In Fig. 2.21, the results reported by Klinkvort (2013) provide a typical example of the pile response under two-way cyclic loading.

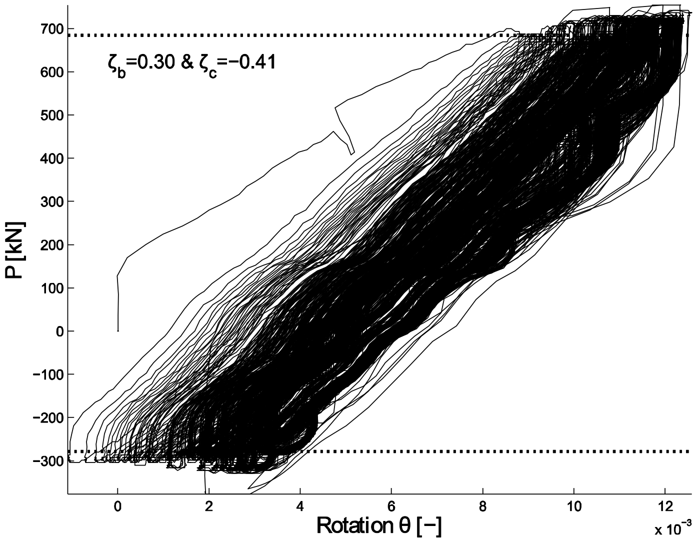

Figure 2.21: Two-way cyclic lateral load on centrifuge, from Klinkvort (2013).

2.4.2 Long term cyclic response review

Monopiles may be exposed to a small number of load cycles with large amplitudes (storms) to large numbers of cycles (10^7 load cycles) with low amplitudes, over a period of 20-25 years. The long-term cyclic loading (10^7 cycles) has a potential to induce a permanent accumulated rotation and change of the monopile stiffness. The pile rotation is important as offshore wind turbines have serviceability limit criteria of 0.25^{o} (installation) and 0.25^{o} (operational) (Byrne and Houlsby, 2003, Villalobos, 2006). According to DNV (2014), the accumulated rotation is required to be less than the value provided by wind turbine suppliers (usually 0.5^{o}). To ensure that the natural frequency of the combined structure does not coincide with excitation frequency, the change in foundation stiffness must be designed accurately (Bhattacharya et al., 2013a, Byrne and Houlsby, 2003, Kirkwood, 2016, LeBlanc, 2009, Villalobos, 2006, Zhu et al., 2012).

According to API (2007) and DNV (2014), the current design methodology has been recognised by several investigators to account for the failure of the pile. The method relies on the model created by Murchison and O'Neill (1984), upon empirical data of flexible piles from Reese et al. (1974). In contrast, the existing monopile foundations behave more rigidly with a slenderness ratio of less than 10 (typically 5 - 6) (Achmus et al., 2009). No sufficient guidance has been provided regarding the deflection of the pile under cyclic loads. Instead, it was recommended that for piles subjected to more than 50 cycles, the ultimate soil resistance should be reduced to account for cyclic loading (Murchison and O'Neill, 1984, Reese et al., 1974). Therefore, employing the current design method is still questionable.

Little and Briaud (1988) proposed a method to correlate the displacement of pile head in relation to the number of cycles, N. The method was used to generate the *p-y* curves based on the results of six cyclic pressure meter tests on flexible piles. The soil resistance was assumed to remain unchanged, but the displacement could increase with an increase of load cycles. 20 tests were carried on concrete and steel piles, and the results were used to develop a displacement power function (see Eq. 2.61) for estimation of accumulated displacement, $\mathrm{Y_N}$, where, q is an empirical factor that depends on loading and soil characteristics. The soil resistance, $\mathrm{P_N = P_1}$, was assumed unchanged as the number of cycles increases. The parameter q = 0.04-0.09, was derived experimentally for flexible piles and q=0.135 for rigid piles (Abdel-Rahman and Achmus, 2005). A clear validation of Equation 2.61 was provided by Peralta and Achmus (2010) for model piles in medium-dense quartz sand subjected to 20 load cycles.

$$\mathrm{Y_N = Y_1 N^q} \tag{2.61}$$

Long and Vanneste (1994) proposed a model to calculate the deflection of 34 full scale pile tests under cyclic loading. From these tests, it was concluded that the pile head displacements depended on soil density, cyclic load characteristics and installation method. Using a beam on elastic foundation (BEF) analysis, the accumulated displacement at the ground surface was estimated by using Eq. 2.62, with a degradable coefficient of horizontal subgrade reaction after N cycles, $\mathrm{k_{h,N}}$, estimated by Eq. 2.63, where EI is the flexural rigidity of the pile; $\mathrm{H_i}$, $\mathrm{M_i}$ are lateral load and moment, respectively; A, B are the constants; $\mathrm{k_{h,1}}$ is the coefficient of horizontal subgrade reaction for the first cycle, $\mathrm{F_L}$, $\mathrm{F_I}$, $\mathrm{F_D}$ are factors accounting for the influence of the cyclic load ratio (ζ_c), pile installation method, and soil density, respectively. The cyclic load ratio (ζ_c) is defined as the ratio of minimum and maximum lateral loads. Equation 2.64 was proposed for accumulated displacement, $\mathrm{Y_N}$, similar to Little and Briaud (1988) with typical degradation parameter, t, of the values from 0.1 to 0.4.

$$\mathrm{Y_N = \frac{AH_i}{EI^{0.4} k_{s,N}^{0.6}} + \frac{BM_i}{EI^{0.6} k_{s,N}^{0.4}}} \tag{2.62}$$

$$k_{h,N} = k_{h,1}N^{-t_r}, \Rightarrow t_r = 0.17F_LF_IF_D \tag{2.63}$$

$$Y_N = Y_1N^t \tag{2.64}$$

The finding is restricted to soil nonlinearity, stratification, unit weight and strength, which cannot be considered in the simulation. Furthermore, a greater displacement was observed for pure one-way cyclic loading ($\zeta_c = 0$) than partial unloading ($\zeta_c > 0$).

Lin and Liao (1999) applied a method developed by Stewart (1986) to model the cyclic lateral loading of piles. Stewart (1986) used the triaxial testing results to developed a model that predict the strain incurred by a sample at variable loading magnitudes. The pile head displacement was assumed to be similar to the soil strain recommended by Stewart (1986). As shown in Fig. 2.22, N_a was assumed as the number of cycles at load level, $Y_a = \varepsilon_{ia}$ and $Y_b = \varepsilon_{ib}$ are the pile-head displacement after a single load cycle of magnitude *a* and *b*, respectively. The corresponding permanent displacement (Y_{Na} and Y_{Nb}) on the pile-head after N_a and N_b load cycles are shown in Eq. 2.65 and 2.66, respectively, where t_a, t_b are degradation parameters. For load cycles with varying amplitude, the accumulated displacement after N_a cycles was obtained by Eq. 2.67, where N_b^* is the equivalent number of load cycles calculated as shown in Eq. 2.68.

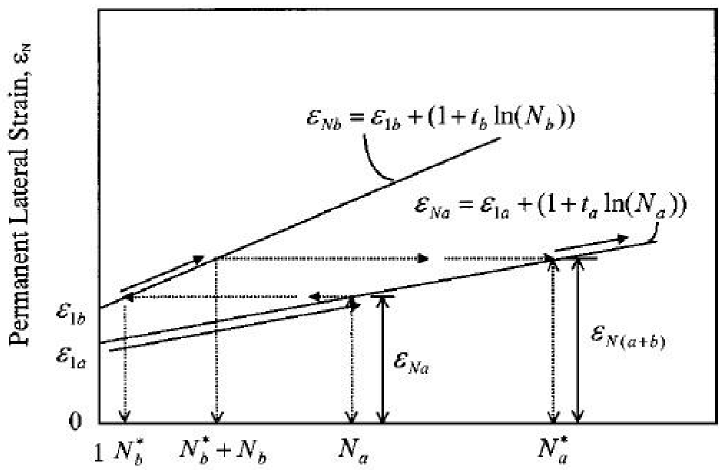

Figure 2.22: Strain accumulation, from Lin and Liao (1999), Stewart (1986).

$$Y_{Na} = Y_{N1}\left(1 + t_a\text{In}(N_a)\right) \tag{2.65}$$

$$Y_{Nb} = Y_{N1}\left(1 + t_b\text{In}(N_b)\right) \tag{2.66}$$

$$Y_{N(a+b)} = Y_{1b}\left(1 + t_b \text{In}(N_b^* + N_b)\right) \tag{2.67}$$

$$N_b^* = \exp\left(\frac{1}{t_b}\left(\frac{Y_{1a}}{Y_{1b}}(1 + t_b \text{In}(N_a) - 1\right)\right) \tag{2.68}$$

From the results of 26 full-scale cyclic load tests, Lin and Liao (1999) employed a Stewart (1986) method to develop a logarithmic trend. The method was used to capture the accumulated strain, ε_N, at the ground surface (see Eq. 2.69), where t_r is degradation factor suggested by Long and Vanneste (1994) (see Eq. 2.71), L is embedded depth, T_R is relative stiffness, k_i is a coefficient of a horizontal subgrade reaction for static loading condition, and ε_1 is the lateral strain for the first cycle. As noted from Kagawa and Kraft (1980), the lateral strain of the soil, ε, was related to the pile deflection, $Y_{z(i)}$, distributed along the depth of the pile as shown in Eq. 2.70, where D is the pile diameter. The value of t_r calibrated from 20 field tests on piles in sand (Little and Briaud, 1988) and the number of cycles was limited to 100 cycles.

$$\varepsilon_N = \varepsilon_1 \left(1 + t_r \ln(N)\right) \tag{2.69}$$

$$\varepsilon = \frac{Y_{z(i)}}{2.5D} \tag{2.70}$$

$$t_r = 0.032\frac{L}{T_R}F_L F_I F_D, \Rightarrow T_R = \left(\frac{EI}{k_h}\right)^{0.2} \tag{2.71}$$

In Fig. 2.23, a superposition method was used to predict the response of accumulated displacement due to variable loading conditions. The measured data were fitted using Eq. 2.67 and the results were in good agreement. A similar approach was employed by Leblanc et al. (2010) to determine the accumulation of pile rotation, whereby the loads of magnitudes A, B and C were applied in the ratio that would be experienced by monopiles. The plots of the measured and predicted pile rotation in response to the loading sequence A-B-C are shown in Fig. 2.24(b). Truong et al. (2018) predicted the results of centrifuge tests, conducted at different cyclic loads and magnitude ratios while varying cyclic load sequence, using a superposition approach described by Lin and Liao (1999). As shown in Fig. 2.24(a), a reasonable agreement was observed based on the fitting function shown in Eq. 2.72, where θ_1 and θ_N are the accumulated rotation after the first and N cycles, respectively. The parameter α_r is the accumulation coefficient shown in Eq. 2.73 and named as equation (9) in Fig. 2.24(a), where D_r is relative density and ζ_c is the loading ratio. Few studies have been reported on this method and further work is required to investigate the findings.

$$\theta_{\mathrm{N}} = \theta_1 \mathrm{N}^{\alpha_{\mathrm{r}}} \tag{2.72}$$

$$\alpha_{\mathrm{r}} = (0.3 \pm 0.22\mathrm{D_r})[1.2(1 - \zeta_{\mathrm{c}}^2)(1 - 0.3\zeta_{\mathrm{c}})]\mathrm{D_r} > 0.5 \tag{2.73}$$

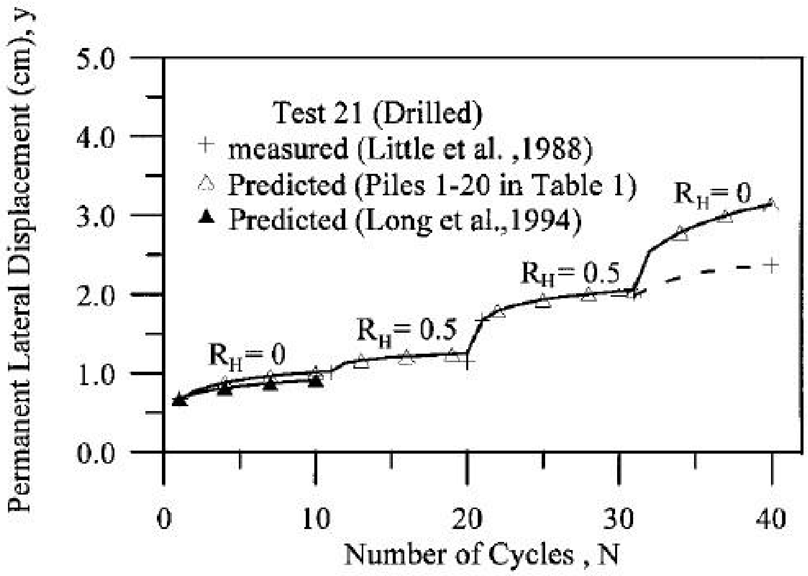

Figure 2.23: Superposition of pile head displacement, from Lin and Liao (1999).

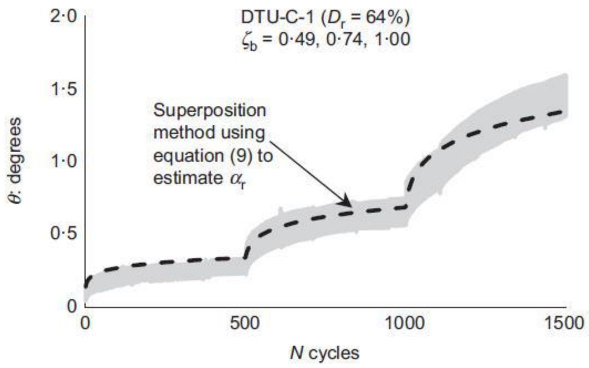

(a) Rotation from Truong et al. (2018)

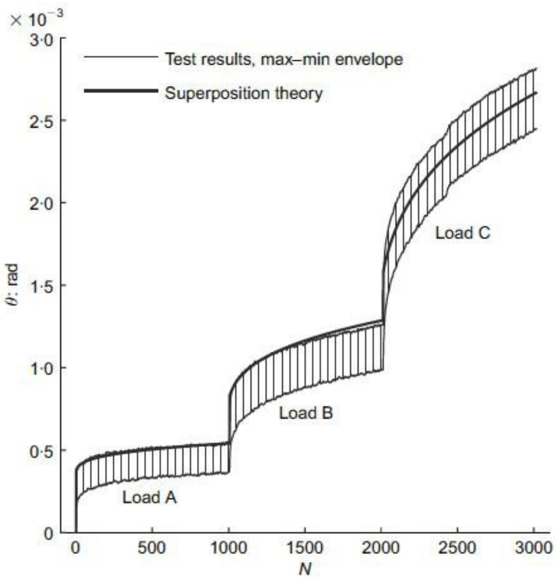

(b) Rotation from LeBlanc (2009)

Figure 2.24: Comparison of measured and predicted accumulated rotation of pile in response to variable loading.

Peng et al. (2006) developed a new loading system which applied one-way and two-way cyclic loads on monopiles. A model pile with a diameter of $\mathrm{D} = 44.5\mathrm{mm}$, embedded length $\mathrm{L} = 400\mathrm{mm}$, and relative density of $\mathrm{D_r} = 71.7\%$, was tested in a 1g laboratory equipment. Eight tests were conducted and approximately 10000 load cycles were achieved. The cyclic amplitude loading was set as $\zeta_\mathrm{b} = [0.2, 0.4, 0.6]$ and cyclic load characteristics $\zeta_\mathrm{c} = [-0.1 - (-0.6)]$. The loading frequency was varied from 0.45 to 0.95 Hz. From the findings, the increase of loading frequency was observed to increase the pile-head displacement and its accumulation was significantly greater in growing magnitude of the loading, ζ_b, which corresponded to the behaviour obtained by Lin and Liao (1999) and Long and Vanneste (1994).

Achmus et al. (2009) presented a study of monopiles in cohesionless soil subjected to long-term cyclic loading. A FE numerical model was developed based on the results of drained cyclic triaxial tests, which employed a Mohr-Coulomb constitutive model. With the use of soil stiffness degradation concept from Long and Vanneste (1994) and Long and Vanneste (1994), the degradable hyperbolic soil model was employed to define the cyclic load-deflection response. The secant stiffness degradation proposed by Huurman (1996) was also employed to achieve the accumulation of plastic strain. The simulation was performed under one-way cyclic loading ($\zeta_\mathrm{c} = 0$), and design charts were developed, which relate the ratio between static and cyclic pile deflection. The findings indicated that the pile diameter, embedded depth and relative density tend to affect the rate of strain accumulation.

Peralta and Achmus (2010) conducted 1g laboratory tests to investigate both flexible and rigid piles installed in dry sand subjected to one-way cyclic loading (ζ_c =0). Approximately 13 tests were conducted in the prepared sand of relative density ($\mathrm{D_r}$) between 40% to 60%, and achieved approximately 10000 load cycles from each test. The data were fitted with power and logarithmic functions as proposed by Long and Vanneste (1994) and Lin and Liao (1999), respectively. The research concluded that the power function $\left(\frac{\mathrm{y_N}}{\mathrm{y_1}} = \mathrm{N^m}\right)$ was best fitted the accumulated displacement of the rigid pile while the logarithmic function, $\left(\frac{\mathrm{y_N}}{\mathrm{y_1}} = 1{+}\mathrm{t_r}\ln(\mathrm{N})\right)$, best fitted to flexible pile displacement behaviour, where $\mathrm{y_N}$ is the displacement after N cycles, $\mathrm{y_1}$ is displacement after the first cycle, $\mathrm{t_r}$ and m are empirical degradation factors.

Verdure et al. (2003), Rosquoet et al. (2007) and Li et al. (2010) conducted centrifuge tests on model piles in sand. The experiment from Verdure et al. (2003) and Rosquoet et al. (2007) were carried out on flexible piles subjected to not more than 50 load cycles, while Li et al. (2010) on other hand considered a rigid monopile in sand subjected to one-way cyclic loading of about

1000 cycles. The two responses were discussed from each author to tress the accumulation of pile-head displacement and change of cyclic secant stiffness. Each author reported that the logarithmic function (see Eq. 2.74) was the best fit for the relative pile-head displacement (Y_p/Y_1). For instance, the results shown in Fig. 2.25 indicate that a relative displacement (Y_p/Y_1) of the pile head increases with an increasing number of load cycles (N) given that Y_1 is the pile lateral displacement of the first cycle. Clearly, in Fig. 2.25(a), Y_p/Y_1 increases as the function of N and the smaller the value of DF is related to the lower relative pile displacement. A similar observation is also identified in Fig. 2.25(b), in which the relative displacement is affected by the increase of load cycles.

$$\frac{Y_N}{Y_1} = 1 + C_N \mathrm{In}(N) \tag{2.74}$$

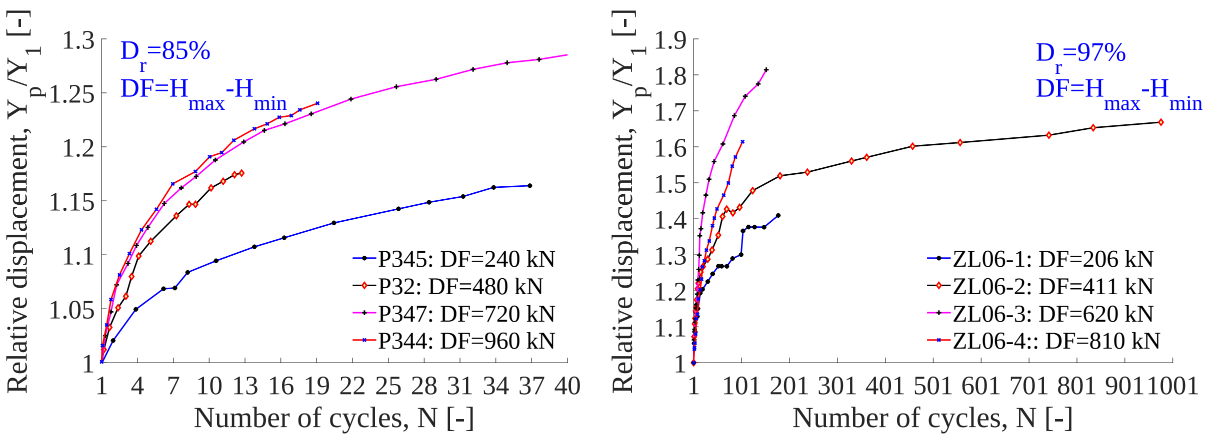

(a) Response from Rosquoet et al. (2007)

(b) Response from Li et al. (2010)

Figure 2.25: Relative displacement versus number of cycles for different tests

As noted from Li et al. (2010), the rate of lateral displacement C_N (shown in Eq. 2.74), was observed to increase with an increase of amplitude cyclic loading, ζ_b, which indicated that the increment rate had a significant impact on the accumulated displacement of the pile head. The rate of pile displacement was argued to be caused by local densification of sand around the pile shaft due to repeated lateral loads which had an impact on the shear modulus of soil, leading to a continuous increase of pile secant stiffness as the number of load cycles, N, increases. Rosquoet et al. (2007) proposed a method to estimate the parameter, C_N, using the ratio of load amplitude (DF) and maximum cyclic load (F_{max}=H_{max}) $\left(\frac{DF}{F_{max}}\right)$ (see Eq. 2.75). As shown in Fig. 2.26(a) and 2.26(b), the coefficient C_N versus $\left(\frac{DF}{F_{max}}\right)$ is estimated for F_{max} = 720 kN and F_{max} = 960 kN, respectively. It is evident that C_N values are observed to rise with the increasing number of load cycles. This is because the cyclic amplitude loads cause shearing in the sand surrounding the pile, thus inducing larger permanent pile lateral displacements in each cycle (Li et al., 2010).

$$C_N = 0.08\left(\frac{DF}{F_{max}}\right)^{0.35} \tag{2.75}$$

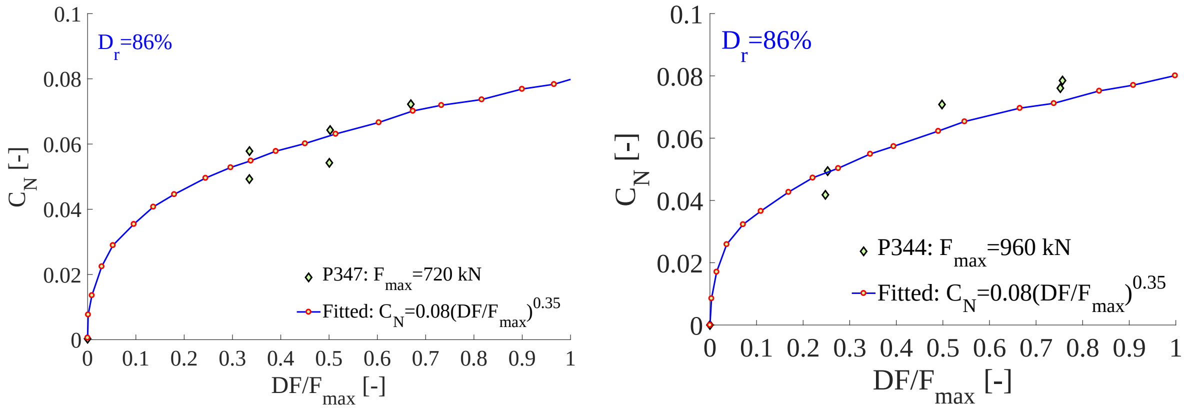

(a) $\frac{y_N}{y_1}$ versus N, F_{max} =720 kN (b) $\frac{y_N}{y_1}$ versus N, F_{max} =960 kN

Figure 2.26: C_N coefficient versus cyclic load ratio, from Rosquoet et al. (2007).

As shown in Fig. 2.27(a) and 2.27(b), Li et al. (2010) and Rosquoet et al. (2007), respectively, have shown that using similar logarithm function (see Eq. 2.76), the stiffness of pile response increases with load cycles, N, and the magnitude of the increase was high during the first cycles. After the first cycle, K_N is slightly increased with the increasing number of cycles but at a reducing rate. A cyclic secant stiffness rate (C_k) slightly reduced due to the local densification of sand around the pile, which increases the soil stiffness and the values of K_N.

$$\frac{K_N}{K_1} = 1 + C_k \mathrm{In}(N) \tag{2.76}$$

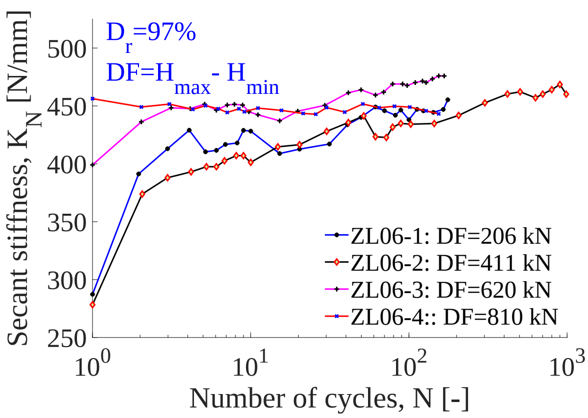

(a) Pile stiffness, from Li et al. (2010)

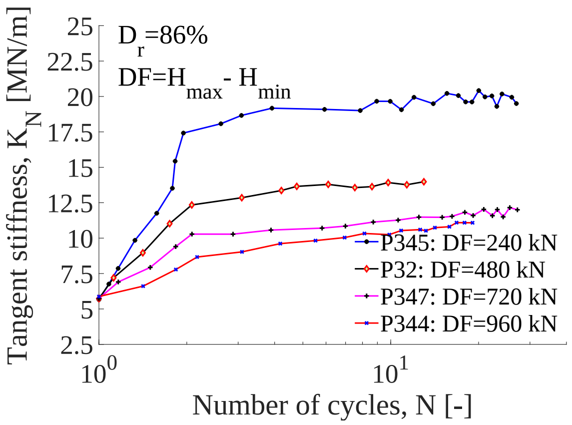

(b) Pile stiffness, from Rosquoet et al. (2007)

Figure 2.27: Cyclic secant stiffness versus load cycles for different load amplitude

These findings have proven that the existing models from Achmus et al. (2009), API (2007), DNV (2014) and Reese and Matlock (1956) were incorrect as they have recommended that the stiffness degradation of cohesionless soil has caused the accumulation of a pile-head displacement during cyclic loading. However, the cohesionless soil under cyclic loading tends to densify, leading to pile stiffness increase as the number of cycles increases.

LeBlanc et al. (2010) investigated the cyclic response of monopile foundation installed in a cohesionless soil through a small-scale 1g laboratory device. The tested model pile of 80 mm diameter and embedded depth of 360 mm was installed in loose and medium Leighton Buzzard sand, at a relative density of 4% and 38%, respectively. The data collected were used to examine the accumulation of pile rotation and change in cyclic unloading stiffness. The experiment was conducted using a series of load characteristics (ζ_b and ζ_c). The variation of parameter ζ_b and ζ_c was found to induce a significant increase of accumulated pile rotation, leading to pile-soil system stiffness increase as the number of cycles increases. It was reported that for the first 100 load cycles, a logarithmic expression (see Eq. 2.77) was accurately fitted to the pile head rotation, however, for larger numbers of cycles an exponential function (see Eq. 2.78) provided a better fit with measured data. The evolution of the accumulated rotation was estimated in terms of the dimensionless ratio defined in Eq. 2.78, where $\alpha = 0.31$ is exponential constant, T_b and T_c are dimensionless parameters, D_r is relative density of sand, ζ_b and ζ_c are the measure of cyclic load amplitude (see Eq. 2.79) and characteristic of cyclic load (see Eq. 2.80), respectively, and pile rotation (θ_s) from static load having the same magnitude as the maximum cyclic load of the first cycle (see Fig. 2.28).

$$\frac{\theta_N}{\theta_s} = 1 + C_\theta \mathrm{In}(N) \tag{2.77}$$

$$\frac{\Delta\theta(N)}{\theta_s} = T_b(\zeta_b, D_r)T_c(\zeta_c)N^\alpha \tag{2.78}$$

$$\zeta_b = \frac{M_{max}}{M_R} \tag{2.79}$$

$$\zeta_c = \frac{M_{min}}{M_{max}} \tag{2.80}$$

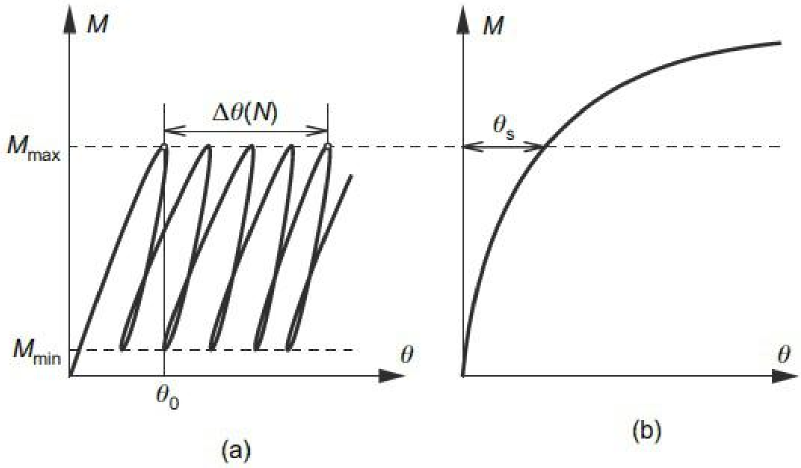

Figure 2.28: Definitions of accumulated rotation: (a) Cyclic tests (b) Static tests, from LeBlanc et al. (2010)

Abadie and Byrne (2014) has shown that the rotation of monopiles from 1g tests was well fitted by using α = 0.31, which is similar to LeBlanc et al. (2010). Different values of α were recommended from other studies, for instance Zhu et al. (2012) provided α = 0.39 for 1g test on sand while Foglia et al. (2014) and Cox et al. (2014), provided the value of α = 0.18 and 0.3, respectively. As shown in Fig. 2.29, the test results of accumulated pile rotation were modelled as increasing exponentially with N. They are plotted by varying ζ_c while keeping ζ_b constant, and the response exhibit an erratic behaviour for $\zeta_c < 0$.

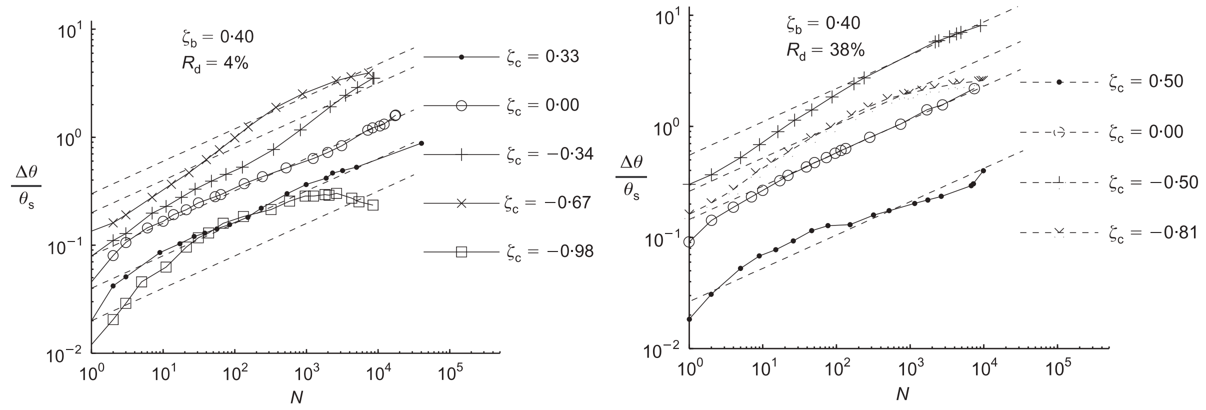

(a) Pile rotation against N, D_r =4%, ζ_b=0.4 (b) Pile rotation against N, D_r =38%, ζ_b=0.4

Figure 2.29: The response of pile rotation in relation to number of cycles, N, for varied ζ_c, from LeBlanc et al. (2010).

It should be noted that the parameters ζ_b and ζ_c are related to constants T_b, T_c and relative density D_r. Clearly, when ζ_c = 1, T_c must be zero because no accumulated rotation is expected to occur under static load and when ζ_c = -1, T_c is also expected to be zero, since the load is applied in both directions. The maximum one-way loading is obtained when ζ_c=0, which implies that the loading will cause the large accumulated rotation. As shown in Fig. 2.30(a), a nonlinear relationship between T_c and ζ_c is observed with a maximum value of T_c found at ζ_c =-0.6, which indicates that the unbalanced two-way cyclic loading provided a significantly large accumulated rotation of the pile compared to one-way loading (ζ_c >0).

Furthermore, LeBlanc et al. (2010) also investigated the variation of dimensionless pile stiffness, k_N, and the data were fitted by a logarithmic function shown in Eq. 2.81, where A_k is the dimensionless constant, k_o is the initial pile stiffness. As shown in Fig. 2.31, the cyclic pile stiffness was observed to increase with number of load cycles, however, the increase rate A_k was independent of the relative density, D_r, load magnitude, ζ_b, and the cyclic load ratio, ζ_c. The expression in Eq. 2.81 was fitted to the data in Fig. 2.31 (see the dashed lines) using the value of A_k = 8.02. The values of k_o were determined from the point of intersection of k_N axis at N=1. The parameter $k_o = K_b K_c$ relates to the dimensionless functions K_b and K_c and dependent on ζ_b, ζ_c and D_r. A typical example behaviour of K_c in relation to ζ_c, at constant ζ_b (D_r=4%, 38%), is shown in Fig. 2.30(b). From this figure, it is unclear about the effect of the two relative densities, which indicates that the values of the stiffness are independent of D_r. An increase of stiffness without an influence of relative density, D_r, was reported as questionable

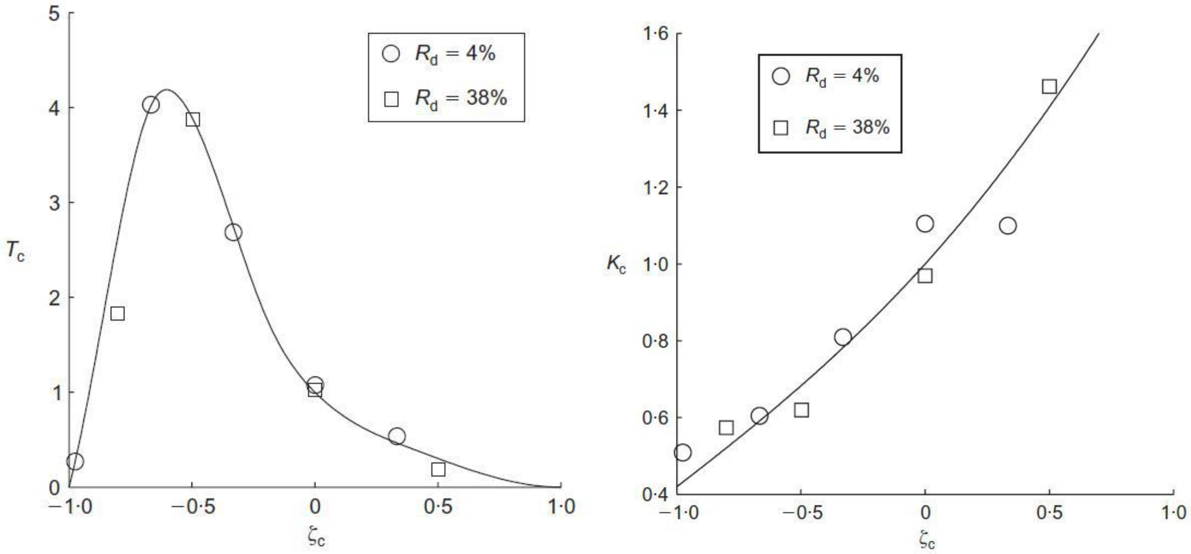

(a) Function relate T_c vs ζ_c to D_r (b) Function relate K_c vs ζ_c to D_r

Figure 2.30: Fitted plots of T_c, K_c against ζ_c for D_r=R_d, from LeBlanc et al. (2010).

and further investigation is required.

$$\tilde{k_N} = \tilde{k_o} + A_k In(N) \tag{2.81}$$

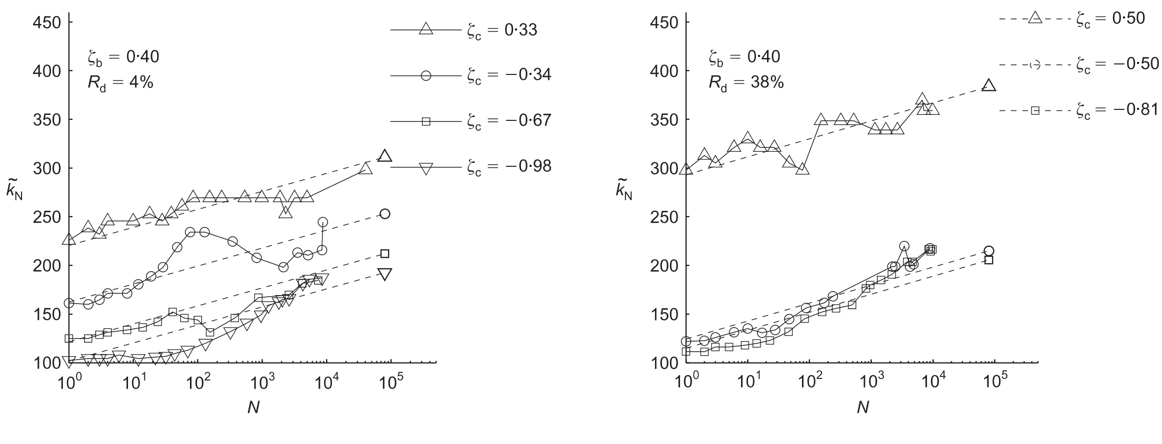

(a) Pile stiffness against N, D_r =4%, ζ_b=0.4 (b) Pile stiffness against N, D_r =38%, ζ_b=0.4

Figure 2.31: The response of pile stiffness in relation to number of load cycles, N, for varied ζ_c, from LeBlanc et al. (2010).

Bienen et al. (2011) experimented on monopiles installed in dry medium-dense sand and tested them at both 1g and 200g in a centrifuge. The prototype dimension of the tested pile was 2.4 m diameter (D) and embedded depth (L) of 9.6 m (rigid) and 30 m (flexible). The research investigated different magnitudes of one-way lateral loading and managed to achieve approximately 10000 load cycles at a constant frequency of 0.25 Hz. The pile-head accumulated deflection against the number of load cycles was approximated using Eq. 2.82, where H is the horizontal load applied to the pile head, Q_c is the rate of change in CPT cone resistance, A_s and α_s are dimensionless parameters (Dyson and Randolph, 2001) and f_N is the factor to modify the monotonic into a cyclic deflection (Cuéllar, 2011, Rosquoet et al., 2007). The function f_N was estimated using Eq. 2.83, where B_{N1} and B_{N2} were determined from the plots of the deflection against load cycles, N. The functions were found to provide a reasonable prediction of strain accumulation under cyclic loading.

$$Y_p = Df_N A_s \big(100 \frac{H}{D^2 L Q_c}\big)^{\alpha_s} \tag{2.82}$$

$$f_N = 1 + \frac{N - 1}{N} B_{N1} \big(\mathrm{In}(B_{N2} + 1)\big) \tag{2.83}$$

Klinkvort et al. (2012) conducted a series of monotonic and cyclic load tests, in a centrifuge, to investigate the effect of displacement accumulation and change of secant stiffness of the monopiles. The two effects were investigated based on relationships proposed by LeBlanc (2009). The model piles were installed in both saturated and dense dry sand and tested at different centrifuge acceleration, $N_s g$. Approximately 500 load cycles were achieved at a constant frequency and relative density. From the data collected, the empirical relationships shown in Eq. 2.84, 2.85, 2.86 and 2.87 were derived to explain the accumulation of a pile-head displacements during the cyclic loading, where $Y_{max,N}$ is the maximum displacement of the pile head, $Y_{max,1}$ is the pile-head displacement of the first cycle, ζ_b, ζ_c are defined in Eq. 2.79 and Eq. 2.80, respectively, H_{min}, H_{max} are the minimum and maximum applied load in the cyclic loading, H_{mon} is the maximum lateral load capacity found from corresponding monotonic tests, α is an empirical coefficient controlling the shape of the curve and N is the number of load cycles. Figure 2.32 shows the results of the load characteristics used to develop Eq. 2.86 and 2.87. In Fig. 2.32(a), the maximum value of Eq. 2.87 is found at $\zeta_c = -0.01$, suggested that the most damaging effect is when the monopile is loaded at an interval of $-0.4 < \zeta_c < 0$. This trend contradicts the findings of LeBlanc (2009) in which the most damaging load situation was for two-way cyclic loading ($\zeta_c = -0.61$). Klinkvort et al. (2012) does not show the same trend;

instead it was recommended that the one-way load situation ($\zeta_c = 0$) is the most damaging condition. Further description of this disagreement was due to different compaction of sand. For instance, a 1g test was conducted in a loose sand to capture the maximum angle of friction, which is different from centrifuge tests where the model stresses and relative density were considered (Klinkvort and Hededal, 2013).

$$\mathrm{Y_{max,N}} = \mathrm{Y_{max,1}}.\mathrm{N}^{\alpha} \tag{2.84}$$

$$\alpha(\zeta_b, \zeta_c) = \mathrm{T_b}(\zeta_b).\mathrm{T_c}(\zeta_c) \tag{2.85}$$

$$\mathrm{T_b}(\zeta_b) = 0.61\zeta_b - 0.03 \tag{2.86}$$

$$\mathrm{T_c}(\zeta_c) = (\zeta_c + 0.63)(\zeta_c - 1)(\zeta_c - 1.64) \tag{2.87}$$

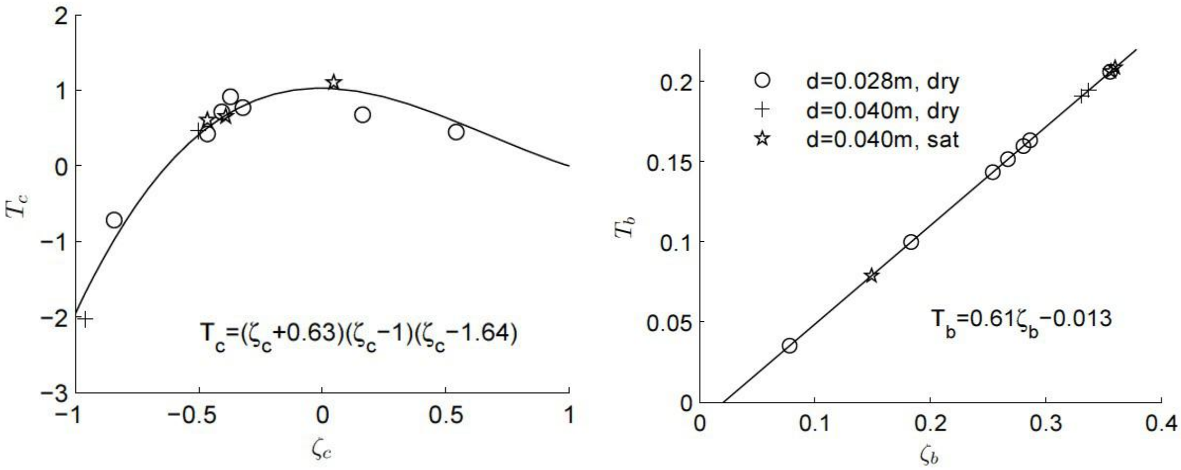

(a) Function relate $\mathrm{T_c}$ vs ζ_c

(b) Function relate $\mathrm{T_b}$ vs ζ_b

Figure 2.32: Cyclic dimensionless functions for accumulation of displacement, after Klinkvort et al. (2012).

Furthermore, Klinkvort (2013) described the changes in cyclic secant stiffness ($\mathrm{K_N}$) by using a logarithmic function shown in Eq. 2.88, where $\mathrm{K_1}$ is stiffness of the first cycle, and κ is accumulation rate of cyclic unloading stiffness. A developed linear dependency of magnitude (see Eq. 2.89) implies that an increase of cyclic load magnitude has led to an increase of κ (see Fig. 2.33(b)). After obtaining κ_b, a linear plot of κ_c (see Eq. 2.90) was derived after fitting the data (see Fig. 2.33(a)). In Fig. 2.33(a), shifting from one-way ($\zeta_c = +\mathrm{ve}$) towards two-way ($\zeta_c = -\mathrm{ve}$) loading lead to an increase of stiffness accumulation rate, κ_c. Based on this trend, it is noted that the secant stiffness is affected by the characteristics of cyclic loading.

$$\mathrm{K_N} = \mathrm{K_1}(1 + \kappa.\mathrm{In(N)}) \tag{2.88}$$

$$\kappa_{\mathrm{b}}(\zeta_{\mathrm{b}}) = 0.05\zeta_{\mathrm{b}} + 0.02 \tag{2.89}$$

$$\kappa_{\mathrm{c}}(\zeta_{\mathrm{c}}) = -6.92\zeta_{\mathrm{c}} + 1 \tag{2.90}$$

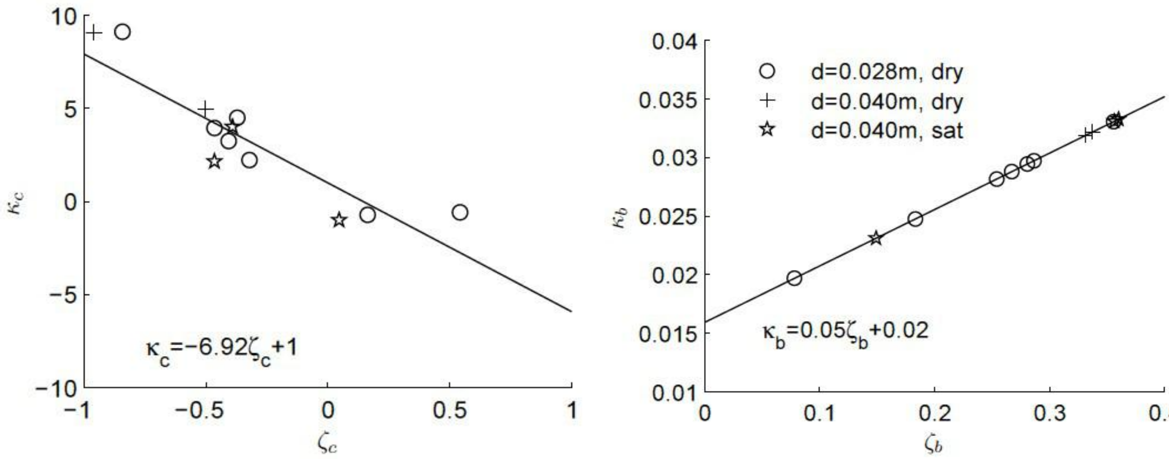

(a) Function relate κ_{c} vs ζ_{c}

(b) Function relate κ_{b} vs ζ_{b}

Figure 2.33: Cyclic dimensionless functions for change in secant stiffness, after Klinkvort et al. (2012).

Rudolph et al. (2015) conducted small scale 1g and centrifuge modelling of monopiles in dry sand, where the load direction was varied to reflect the different wind and wave loading directions. Both experiments considered medium density and dense dry sand, representing a typical 5 MW class offshore wind turbine installed in the North Sea, having 5 m pile diameter, 25 m embedded depth, and 72 m of 2 MN (12 N at model scale) load eccentricity. A small scale 1g model testing, scaled by $\mathrm{N_s}$ = 55, providing a model pile diameter of 90 mm and 450 mm embedded length. In a centrifuge, the prototype was scaled at $\mathrm{N_s}$ = 200, providing a model pile diameter of 25 mm and an embedded depth of 125 mm. In both tests, the loading directions were varied over an angle between 0^{o} and 120^{o}. The load cycles achieved from 1g tests were 10000 and 30000 cycles (at a frequency of 0.1 Hz, which corresponded to 1 day and 3 days, respectively) and centrifuge tests were approximately 3000 and 13000 cycles (at a frequency of 0.2 Hz, which corresponded to 4 and 18 hours, respectively). These frequencies were chosen to ensure a fully drained response. The results indicated that the 1g tests gave much higher accumulated pile head displacements (and hence rotations) than the centrifuge tests (for the same relative density), which further highlights the need to consider carefully scale effects in 1g experiments. The results show an increase of pile head displacement when the direction of cyclic loading varies, and larger angles resulted in larger accumulated displacement.

Kirkwood (2016) investigated a typical 3.5 MW class offshore wind turbine, supported by a monopile installed in sand, subjected to a series of lateral load tests conducted in a centrifuge. A prototype monopile (D=3.81 m, L=20 m and L_e=30 m) was scaled down by N_s = 100 to the model dimensions (D=38.1 mm, L=200 mm and L_e=300 mm). 16 centrifuge tests were conducted on relatively loose, medium and dense sand and 4000 lateral load cycles were applied in four sets of 1000 cycles. In each test, the loading magnitude of subsequent set was increased by cyclic loading ratio programmed in an automated load control system. It should be noted that during testing the centrifuge was not spun down. The effect of cyclic lateral loading on the pile as a function of the loading magnitude, cyclic loading ratio, previous loading and the relative density of the sand was investigated. From all tests, the stiffness of the pile was observed to increase as the result of cyclic lateral loading applied at constant amplitude, which has been previously reported by LeBlanc (2009) and Klinkvort (2013). Furthermore, the damaging effect of pile-head stiffness and accumulated displacement was observed for pure one-way cyclic loading (ζ_c = 0), which agrees with the findings of Klinkvort (2013) but contradicts those from LeBlanc (2009) with damaging effect observed for ζ_c <0 (-0.67). Moreover, the study reported by Nanda et al. (2017) investigated the performance of monopiles under uni-directional and multi-directional lateral cyclic loading, using the two load characteristics (ζ_c = -1 and 0 for two-way and one-way, respectively). Tests were carried out on a model rigid pile (L=500 mm, D=9 mm, D_r=77%), which includes the effect of open and closed ended pile. The observations indicated that multi-directional loading provided higher displacements and lower stiffness compared to uni-directional loading. Furthermore, an open ended-pile developed a significant lateral displacement compared to closed ended pile.

Truong et al. (2018) employed beam and drum centrifuge testing to study the response of monopiles in medium dense and dense sand, subjected to lateral cyclic loading. The tests were carried out at varying cyclic load sequence and magnitude ratios. Three packages of load cycles (500 cycles for each) were applied in different sequences to determine the effect of accumulated rotation. The tests were conducted on pile in medium dense dry Fontainebleau sand.

As shown in Fig. 2.34(a), the pile head rotations (θ_N), for one-way cycling (ζ_c=0) of three 500 cycle packages with different cyclic magnitude ratios (ζ_b=0.5, 0.75 and 1.0), are plotted against the number of load cycles, and maximum rotation of 1.25$^\mathrm{o}$, 1.65$^\mathrm{o}$ and 1.9$^\mathrm{o}$ were achieved. A similar set of measurements for another three packages (300 cycles each), at constant ζ_b=0.5 with different values of ζ_c, is shown in Fig. 2.34(b). It is evident that the loading sequence affects the final value of accumulated pile rotation when the one-way cyclic packages was applied (see Fig. 2.34(a)). When the value of ζ_c becomes more negative (two-way cyclic loading), the final value of pile rotation reduced dramatically, indicating that a more damaging effect was observed under one-way cyclic loading. This observation agrees well with findings of Klinkvort (2013) and Kirkwood (2016).

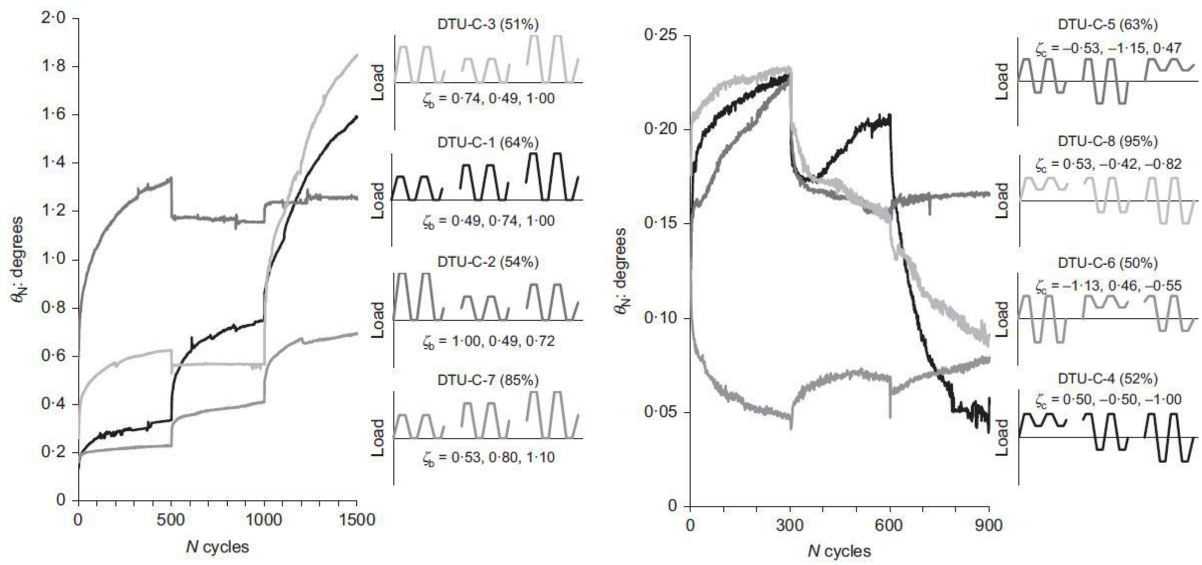

(a) Function relate κ_c vs ζ_c (b) Function relate κ_b vs ζ_b

Figure 2.34: Pile rotation at peak load versus load cycles, in three package of cyclic load sequences, from Truong et al. (2018).

2.5 Existing cyclic loading devices

Over the past decades, different loading devices have been developed for testing piles under monotonic and cyclic loading (Arshad and O'Kelly, 2014, Basack, 2005, Hansen et al., 2013, LeBlanc, 2009, Peng et al., 2006, Peralta and Achmus, 2010, Roesen et al., 2012a). In general, the standard methods of operation of these devices can be broadly classified as mechanical, electromechanical and hydraulic (Abadie, 2015, Arshad and O'Kelly, 2014, LeBlanc, 2009, Peng et al., 2006). As discussed from the studies of these devices, the loading systems have different challenges in their operations. For instance, the system operated under monotonic loading applied the gravity, gear and hydraulic drive loading systems (El Naggar and Wei, 1999, Peng et al., 2004). The statnamic and vibration device systems have been used to provide the lateral response with low to high loading frequency. This statnamic type was successfully used in the field with low frequency (0-10 Hz) but has not been proven yet in the laboratory compared with vibration type (frequency of 5-50 Hz). It was successfully used for cyclic loading tests but was found insufficient for wind turbine (Peng et al., 2006). Furthermore, a pneumatic loading device system (Chandrasekaran et al., 2010, El Naggar and Wei, 1999, Kumar and Rao, 2012, Qin, 2010) has been successfully used for lateral monotonic and one-way cyclic loading, however, due to complexities in their operations, only limited number of load cycles were achieved (less than 500 cycles). Moreover, at Oxford University, a three degree of freedom loading rig on the laboratory floor has been developed to carry out a combined loading on the model piles (Byrne and Houlsby, 2004). From this model, the load level, the number of load cycles and frequency were varied, but the consistency of load amplitude was unstable and led to a limited number of load cycles. Although the above-mentioned loading devices have been widely used to carry out model tests, the assessment described by Peng et al. (2006) showed that further improvements were required.

The most common method of operation, which has been used frequently in small-scale 1g laboratory, is an electromechanical loading device. This type of loading system employ a gearbox, power system, speed controller and other components to provide either one-way or two-way cyclic loading on the pile head. The system is capable of adjusting the frequency and load level under load or displacement control (Arshad and O'Kelly, 2014, Peng et al., 2006). The research of this type provides the results in a sinusoidal waveform due to mechanical interaction between the components (Peng et al., 2006). The only review of this type is discussed in this section, focused on the development of the current research devices. The different setups of electromechanical devices for cyclic loading on monopile foundations are shown in Fig. 2.35 and the findings are described in the following paragraphs.

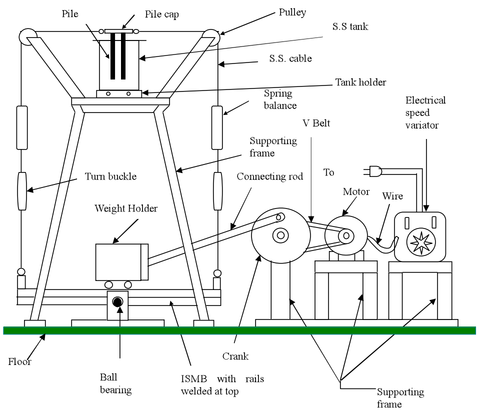

(a) Basack (2005)

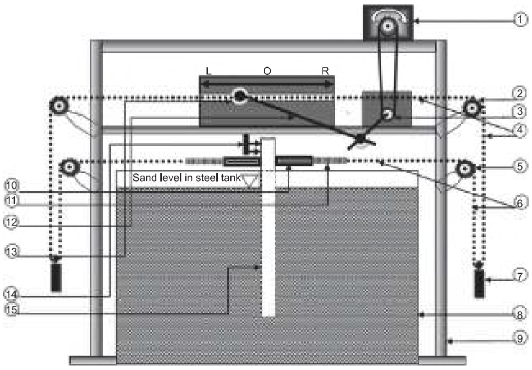

(b) Arshad and O'Kelly (2014)

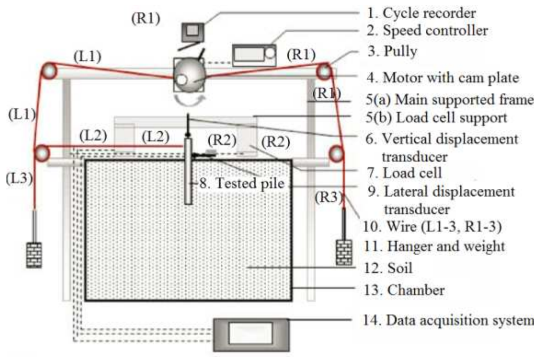

(c) Peng et al. (2006)

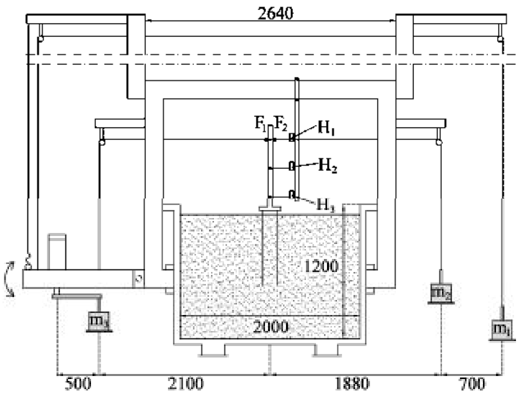

(d) Roesen et al. (2012a)

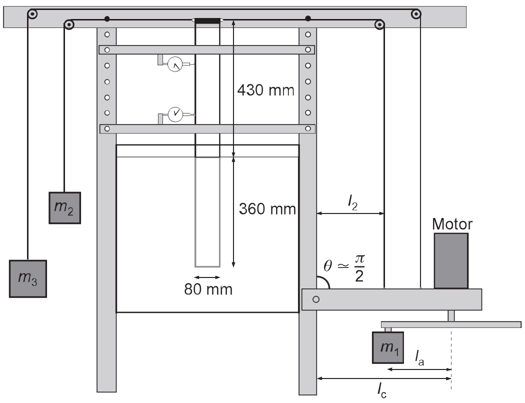

(e) LeBlanc (2009)

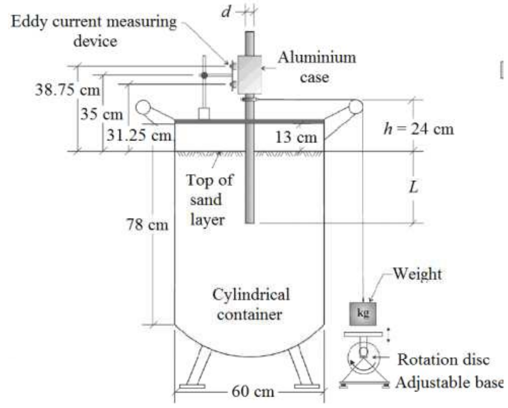

(f) Peralta and Achmus (2010)

Figure 2.35: Existing electro-mechanical loading rig for monopile investigated at 1 g.

From the studies shown in Fig. 2.35, the mechanical operation of the loading systems and its capabilities to simulate the field conditions are complex (Arshad and O'Kelly, 2014). For instance, Basack (2005) developed a loading device (see Fig. 2.35(a)) for testing pile groups under both lateral monotonic and cyclic loading. Peng et al. (2006) developed a rigged system shown in Fig. 2.35(c) to investigate a 44.5 mm diameter monopile, embedded in 400 mm dry, dense sand (Dr = 71.7%) and subjected to both one-way and two-way cyclic loading. The model piles were tested to approximately 10000 load cycles. The outcomes have shown that with the increased number of load cycles, the displacement of unbalanced cyclic two-way observed to increase than one-way balanced. Furthermore, Peralta and Achmus (2010) developed a loading device shown in Fig. 2.35(f) to investigate a 60 mm diameter flexible and rigid piles in the sand (L=200-500 mm), and subjected to one-way cyclic loading. The results were used to develop the power and logarithmic fitting functions as proposed by Long and Vanneste (1994) and Lin and Liao (1999), respectively. Moreover, the device developed by LeBlanc (2009) (see Fig. 2.35(e)), employed both one-way and two-way loading conditions. The study was carried out on the model pile in dry, dense sand (D_r= 4% and 38%) with 80 mm diameter and embedded depth of 360 mm. A total of 21 tests was carried out and approximately a maximum of 65000 load cycles was achieved. The results were in agreement with Peng et al. (2006) and Peralta and Achmus (2010). They all concluded that for an unbalanced loading condition, the pile rotation or displacement continues to deform with an increase in the number of load cycles. Roesen et al. (2012a) conducted the cyclic loading tests on 100 mm diameter model pile with a slenderness ratio of 6. The device proposed (see Fig. 2.35(d)) was managed to achieve 46000 load cycles with the load applied in a one-way direction only. Furthermore, Arshad and O'Kelly (2014) developed a novel mechanical loading system (see Fig. 2.35(b)) for the application of many thousands of lateral loading cycles, with full control provided over the direction, amplitude, frequency and waveform shape. The tests were carried out on 53 mm diameter model piles, embedded (L=360 mm) in dense sand (D_r= 70% and 74%), and subjected to both one-way and two-way cyclic loading. Approximately 6000 load cycles were achieved on the tested piles and the results revealed that under two-way loading, a greater pile rotation was observed, which supported the outcomes of LeBlanc (2009) and Peng et al. (2006). An in-depth discussion of the existing loading system is beyond the scope of this study and the reader is referred to the publication cited for more information.

Much of the research conducted for the response of piles under cyclic loading, using these types of loading devices, has some limitation based on the number of load cycles, loading direction, frequency, and prototype stresses similarity. For offshore wind turbine foundations, millions of load cycles are required for design purpose, and further study is still in demand. The current research will use the knowledge from these studies to develop a new electromechanical device for investigating monopiles in a geotechnical centrifuge.

2.6 Chapter summary

In this chapter a general review of previous research about the behaviour of a single pile in a cohesionless soil subjected to both monotonic and cyclic loading has been discussed and summarised below;

1. Monopile response under monotonic loading

    - A literature review regarding the behaviour of piles under monotonic lateral loading has been presented. The Winkler approach and the *p-y* curve formulation have been used as reference points. The formulations proposed are based on physical modelling carried out on flexible piles from offshore oil and gas industries. It is unclear if they apply to the design of monopiles. The uncertainties and limitations addressed are important for the design of monopile foundations for offshore wind turbines and required further research.
    - In offshore wind turbines, it is important to enable accurate predictions of the foundation stiffness and ultimate capacities, so that the displacement (rotation) of the pile and the natural frequencies can be accurately predicted. Therefore, the initial stiffness of the *p-y* curves needs to be determined with high accuracy. Several studies have been reported regarding the initial stiffness of the *p-y* curves on different aspects. However, Carter (1984) and Ling (1988) have found that the initial stiffness is linearly proportional to the pile diameter and both linear and a non-linear distribution of initial stiffness can be employed on the piles. Therefore, further study is in demand to accurately predict the initial stiffness of monopiles in cohesionless soil.
    - 3-D numerical solutions are a potential means of conducting soil-structure interaction analysis in a fully coupled manner without resorting to independent calculations. However, there are uncertainties regarding the type of constitutive models to be implemented and interface elements cannot be readily determined. For this

reason, the method has not been used for routine analysis of offshore wind turbine foundations. In this study, a brief review of the method was presented, but a detailed discussion is beyond the scope of this thesis. Theoretical approaches have been widely used in many studies on piles due to their simplicity. They provide an insight into critical issues regarding pile-soil interaction problems. Therefore, the current study employed these methods to develop solutions for the study of rigid monopiles.

2. Behaviour of soil under cyclic loading

   - Studies have been carried out to determine the response of monopile foundations in sandy soil to cyclic lateral loading. Empirical functions have been developed to describe the accumulation of displacement/rotation and change in unloading stiffness of the pile as a function of relative density, cyclic loading ratio, and loading magnitude. From these studies, it is unclear about the response of the soil itself, which controls the behaviour of the monopile. For this purpose, the study reviewed the cyclic response of sandy soil under cyclic loading. The outcomes are used in the current study to develop a theoretical model of the pile under monotonic and cyclic loading.

3. Monopile response under cyclic loading

   - Studies conducted to investigate the effect of cyclic lateral loading on monopile foundations in sand, including the change in cyclic stiffness, accumulated displacement and rotation of the pile, were reviewed. The review also included empirical functions developed to predict the response of monopiles under load cycles. It was revealed that the current design standards used for offshore foundation design offered limited guidance on the effect of cyclic loads. A significant amount of research has been carried out to fill the gap. Most of the studies conducted experiments, however, the effect of lateral cyclic loading on offshore wind turbine foundations is still a challenging task and many aspects remain unclear until now. No general approach has been accomplished to include the influence of cyclic loading on the current standard guide.

- Few experimental pile tests have been carried out regarding the effect of random long-term cyclic loading on the accumulation of pile rotation/ displacement and change of cyclic stiffness. For instance, Lin and Liao (1999) and Leblanc et al. (2010) found that the accumulation of pile head displacement or rotation is independent of the loading sequence, which disagrees with work by Peralta and Achmus (2010). Therefore, the influence of loading sequence still requires further research.
- Under long-term cyclic loading, accumulation of rotation of the pile has been investigated experimentally for both flexible and rigid piles. For flexible piles, several tests have been reported with the number of cycles not exceeding 100. Meanwhile, on a rigid pile, most of the research was carried out on physical modelling with a limited number of load cycles. The studies on rigid piles proposed empirical functions to predict the accumulation of pile head displacement or rotation results. However, these studies did not achieve the required number of cycles ($N=10^7$). Therefore, further research is still required.

4. Existing loading device for the model piles

    - A literature review of the existing loading systems on the behaviour of piles under cyclic loading has been presented. Different systems have been developed to simulate the field conditions and achieving many numbers of loading cycles. Many numbers of cycles can be achieved by the system developed under the 1g laboratory model, however, the model is limited to stress similarities and soil density. The stress similarity is possible when the model is conducted in a centrifuge, but the model space is very limited, and the system arrangement is complex to achieve a larger number of load cycles. Therefore, in this study, available loading devices at 1g were reviewed to develop a new loading device, capable of achieving the very high number of cycles in a centrifuge.

Chapter 3

EXPERIMENTAL METHODS

3.1 Introduction

Physical modelling techniques have been used to study how deep foundations respond during cyclic loading. In the case of monopile design, it provides an insight on pile behaviour that enables a better understanding of the three-dimensional physical problems of the pile-soil interaction and the development of theoretical and numerical models. For the study of soil-pile interaction, it is important that representative stress levels are recreated within the soil and hence centrifuge modelling is the best option.

This chapter gives details of the development of a centrifuge package that was to study the behaviour of monopile in sand. Firstly, a brief description explaining the motive of using a centrifuge to study the response of a stiff pile in sand instead of 1g laboratory modelling is presented in Section 3.2. Secondly, Section 3.3 describes the principles behind centrifuge modelling and scaling laws. It also discusses the g-field and scaling effects. Thirdly, Section 3.4 describes the beam centrifuge available at the University of Nottingham. Information about the sand and the model pile is presented in Sections 3.8 and 3.5, respectively, followed by the experimental apparatus used to perform tests. The model equipment are described in Sections 3.6 and 3.7 for monotonic and cyclic load tests, respectively. Section 3.7 includes the general model layout and loading operation principles under cyclic loading. The details of instrumentation and data acquisition systems are presented in Section 3.9. Finally, the experimental procedure and testing programme are described in Section 3.10. Processes and analysis of the data collected and the experimental results are all presented and discussed in the subsequent chapters, however, the preliminary results of test OWTP/C-T15 are discussed at the end of this chapter to describe the effect of load control factor ζ. The chapter concludes with a summary of the centrifuge tests.

3.2 Centrifuge motivation

The review in chapter two showed that the current design guidelines are insufficient to provide a necessary design methodology for large diameter offshore monopiles. Efforts to provide a new design standard for cyclic lateral loading on monopiles have been carried out by several investigators, yet the target has not been achieved. To achieve a better understanding, a full-scale testing is a preferable option. It allow an estimation of specific behaviour and provide realistic geotechnical parameters for the design purpose. However, it is not attractive from an economic perspective and only conducted when their costs are justified. When this method is not useful, other physical model techniques (unit gravity (1g) and geotechnical centrifuge (N_Sg)) are cost-effective way to understand the key aspects of a full-scale behaviour.

A laboratory 1g model enables a straightforward design of the loading equipment, and is capable of exploring the pile response to a large number of load cycles. A key advantage is that it can be used with high resolution instrumentation and capable of measuring very small displacements, which is more difficult on the centrifuge. In addition, the tests involve larger model piles and the costs for running are much less than centrifuge technique. The key challenge of this model is the stress difference between the model and full-scale. For instance, LeBlanc (2009) conducted a 1-g cyclic tests of monopiles in dry sand. As shown in Fig. 3.1, the full-scale responses were simulated at low confining stress with a low relative density of sand in a model scale. Bolton (1986) demonstrates that the angles of friction and dilation are proportional to the relative density and inversely proportional to the stress level. The use of this relationship into 1-g model means that as the stress level in the laboratory is much smaller than that in the field, the sample relative density must be accordingly smaller to reproduce the rate of dilatancy at full scale (Abadie and Byrne, 2014). The sample prepared at a very low relative density was affected by densification, which would negate the similarity between the unity gravity (1g) model and full-scale densities (Kirkwood, 2016). Several studies (Arshad and O'Kelly, 2014, Basack, 2005, Chen et al., 2015, Cuéllar et al., 2012, Foglia et al., 2012, LeBlanc, 2009, Nicolai and Ibsen, 2016, Peng et al., 2006, Roesen et al., 2012a) have been reported on this type of model. In general, the soil models tested at 1-g have a stress level significantly lower than that present in the prototype scale. Hence, with non-linear stress-strain behaviour of soil, tests carried out at 1g cannot provide quantifiable results which are directly applicable to a full-scale.

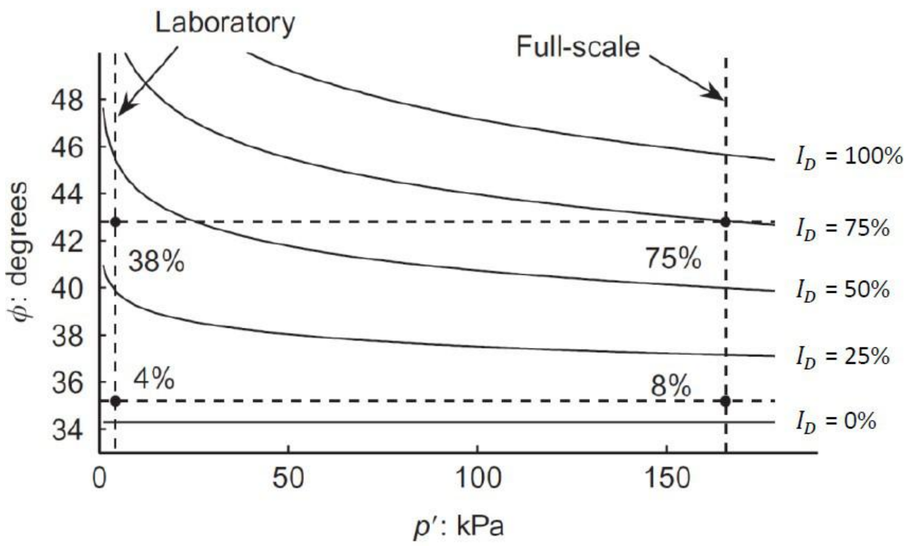

Figure 3.1: Scaling of the dilatant response of sand, from LeBlanc et al. (2010).

The key advantage of the model testing, on centrifuge, is that the soil stresses are accurately scaled so that the model stress level corresponds directly to the full-scale condition (Taylor, 1995). However, the testing equipment must be designed to work at high gravitational acceleration and in a limited space. On top of that, the centrifuge container is limited and therefore affecting the size of the model pile. The instruments attached to the model are complex and sensitive, which required to work at high resolution. Furthermore, for long-term cyclic loading, for instance on monopiles, centrifuge tests are often limited to a certain number of load cycles, requires an advanced control system and overnight operation of the centrifuge to obtain a larger number of load cycles. Technically, it is still a challenge to develop equipment that will fit onto centrifuge to provide millions of loading cycles related to offshore wind turbine foundations. Further studies are still in demand to create a model that would be able to apply millions of load cycles in a reasonable amount of time. Recently, model studies have been carried out on the centrifuge with different loading devices (Dührkop et al., 2010, Haigh et al., 2010, Kirkwood, 2016, Klinkvort and Hededal, 2013, Li et al., 2010), to investigate the cyclic loading of monopolies foundations.

In this study, loading devices were developed to conduct a series of monotonic and cyclic loading tests on model piles, which representing offshore wind turbine monopile foundations. The mechanical systems were designed at the Nottingham Centre for Geomechanics (NCG), as a load and displacement control of cyclic and monotonic responses, respectively. The load control system can apply many thousands of load cycles on the centrifuge at different frequencies. The targeted loading frequency, at centrifuge acceleration of 100g was 15 Hz, however, due to technical challenges of the model set-up, only 2.5 Hz was achieved at 30g.

3.3 Fundamental theory and scaling laws

3.3.1 Scaling laws of model testing

A geotechnical centrifuge consists of a large beam supported in its centre, with one side carry a model package and on the opposite side a counterweight was designed to ensure that the beam remains balanced. During testing, the centrifuge is spun about its axis, and the centrifugal acceleration is acting on the model package, causing it to swing-up about the pivot connected to the beam. As noted from Kim and Kim (2011) and Madabhushi (2014), the basic idea of centrifuge modelling is to accelerate a model package to an appropriate high g-level to simulate a prototype scale stress field. When the model is made in a geotechnical centrifuge, it is accelerating at N_s times earth gravity (g=9.81 m/s^2). As the centrifugal acceleration is proportional to distance from the centre of rotation, the g-level increases with depth through centrifuge model packages. In this case the stress level at any point of the model correspond to the point on the prototype. A diagrammatic representation of this variation, in a g-level across the depth of the centrifuge and the prototype, is shown in Fig. 3.2. In Fig. 3.2, a centrifuge model with radius R, rotating at an angular velocity ω, will experience a radial acceleration a equal to N_s multiples of gravitational acceleration g (see Eq. 3.1). Thus, the inertia acceleration field of N_s is provided by using Eq. 3.2.

$$a = \omega^2 R = N_s g \tag{3.1}$$

$$N_s = \frac{\omega^2 R}{g} \tag{3.2}$$

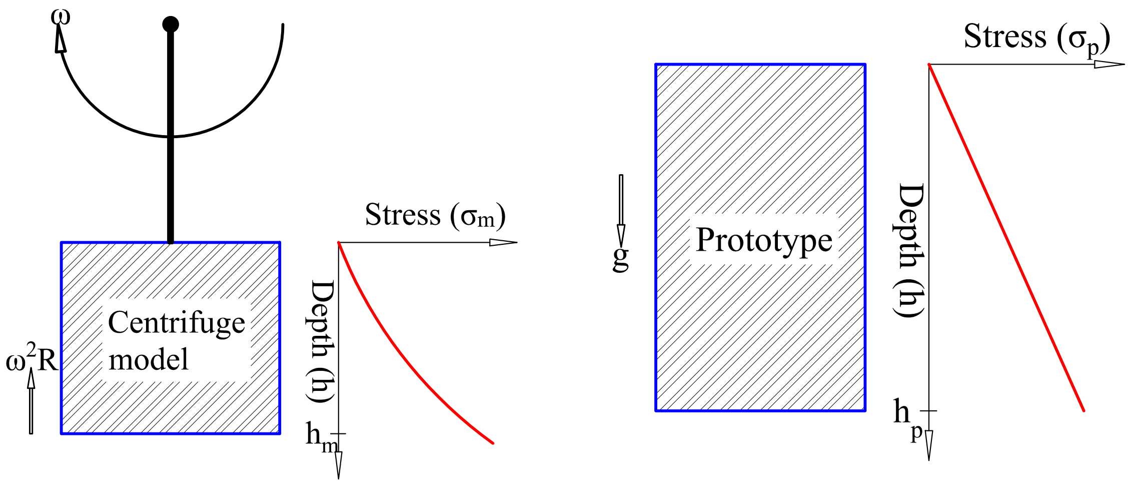

(a) Centrifuge model
(b) Full-scale mode

Figure 3.2: Schematic of the centrifuge and full-scale models, from Taylor (1995).

The monopiles in the offshore are typically installed in the saturated soil. In a centrifuge, an effective vertical stress can be achieved by using either dry or saturated sand. For saturated sand, the scaling issue is straightforward as the increase in gravitational acceleration is similar to geometric scaling factor, N_s (Klinkvort, 2013). For a model in a centrifuge, the effective vertical stress of soil (σ'_m) at depth h_m is given by relationship shown in Eq. 3.3, while the vertical effective stress (σ'_p) at depth h_p (see Eq. 3.4) represent a full-scale model. Due to stress similarity between the model and prototype ($\sigma'_m = \sigma'_p$), h_m is obtained by Eq. 3.5, where h_m is the depth dimension in the model, h_p is the depth dimension in full-scale, ρ'_{sat} is the buoyant density of saturated soil, N_{sat} is the acceleration to be imposed in a centrifuge test under saturated condition, and g is normal gravity. As noted from Klinkvort (2013), the flow of water in a centrifuge is occurring N_s times faster compared to a full-scale and is unlikely that pore pressures will build up at the current rate of loading. The scaling approach was designed so that tests under dry conditions can be related to a full-scale scenario with saturated ground. The basic assumption for using this procedure was that for quasi-static test, no excess pressure will develop. With no excess pore pressure in dry sand, the identical effective stress distribution between the model and prototype can be achieved. However, the increase in acceleration gravity and geometric scaling factor will not be identical due to difference in effective density.

$$\sigma'_{\mathrm{m}} = \gamma'_{\mathrm{sat}} \mathrm{N}_{\mathrm{sat}} \mathrm{h}_{\mathrm{m}} = \rho'_{\mathrm{sat}} (\mathrm{N}_{\mathrm{sat}} \mathrm{g}) \mathrm{h}_{\mathrm{m}} \tag{3.3}$$

$$\sigma'_{\mathrm{p}} = \rho'_{\mathrm{sat}} (\mathrm{g}) \mathrm{h}_{\mathrm{p}} \tag{3.4}$$

$$\mathrm{h}_{\mathrm{m}} = \mathrm{h}_{\mathrm{p}} \frac{1}{\mathrm{N}_{\mathrm{sat}}} \tag{3.5}$$

If the model is prepared with soil of similar density as prototype, the stress similarity in the model will be achieved at scale of 1:N_{S}. Diagrammatically, the stress similarity between the model and prototype is shown in Fig. 3.3, where L is embedded depth, L_{e} is load eccentricity, Y_{p} is pile head displacement, Y_{g} is ground displacement, D is the diameter of the pile, Z is depth below the ground surface, Z_{r} is depth of rotation below the ground surface, and Z_{o} is depth of rotation above the pile tip.

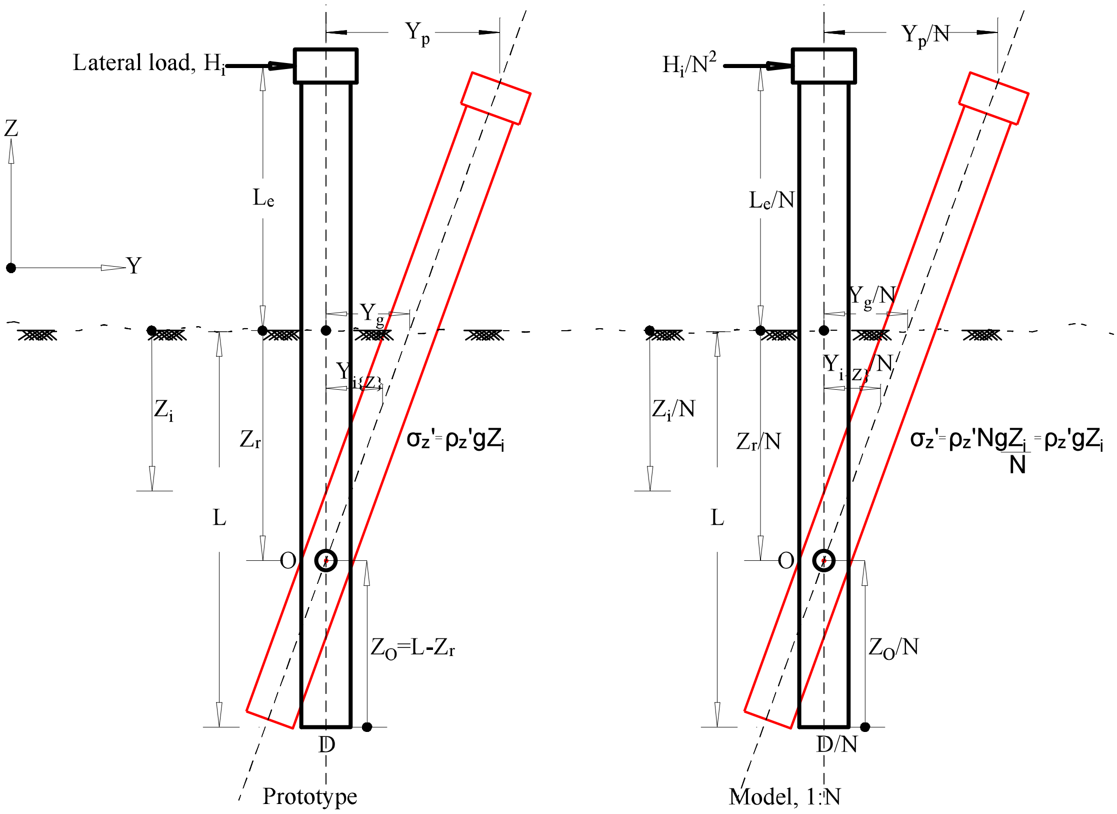

Figure 3.3: Centrifuge scaling laws.

A series of scaling factors to relate model behaviour in a centrifuge to a full-scale was first developed by Schofield (1980) and have been used frequently by many authors (Beemer, 2016, Kirkwood, 2016, Klinkvort and Hededal, 2013, Lau, 2015, Li et al., 2010, Truong et al., 2018, Wood, 2003). Scale factors relevant to common geotechnical applications of centrifuge modelling are presented in Table 3.1 (Garnier et al., 2007, Taylor, 1995).

Table 3.1: Scaling relations for basic quantities in centrifuge modelling

Parameter	**Symbol**	**Units**	**Scaling laws** (Prototype:Model)
Length/Displacement	L/Y	m	$1{:}N_s$
Area	A	m^2	$1{:}N_s^2$
Volume	V	m^3	$1{:}N_s^3$
Mass	M	Kg	$1{:}N_s^3$
Force	H_i	kg	$1{:}N_s^2$
Acceleration	a	ms^{-2}	$1{:}N_s$
Density	ρ	kg/m^3	1:1
Stress	σ	Nm^{-2}	1:1
Strain	ξ	-	1:1
Unit weight	γ	Nm^{-3}	$N_s{:}1$
Rotation	θ	^{o}	1:1
Bending moment	M_i	Nm	$1{:}N_s^4$
Time(Dynamic)	T	s	$1{:}N_s$
Frequency(Dynamic)	f	Hz	$N_s{:}1$

In order to achieve the equivalent soil conditions, vertical stress of dry sand in Eq. 3.6 should be equal to the vertical stress of saturated sand in Eq. 3.3 ($\gamma'_{sat} N_{sat} h_m = \gamma_d N_s h_m$), where γ_d is the dry unit weight of sand, ρ_d is the dry density of sand. Therefore, the value of N_{sat} in saturated sand can be obtained by Eq. 3.7. For instance, if the dry sand used in a centrifuge test has unit weight of γ_d = 16.8 kN/m^3, specific gravity of G_s = 2.63, and void ratio of $e_o = \left(\frac{G_s \gamma_w}{\gamma_d} - 1\right)$ = 0.53, then the effective saturated unit weight is estimated as $\gamma'_{sat} = \left(\frac{(G_s + e_o - \gamma_w)}{1 + e_o} - \gamma_w\right)$ = 10.43 kN/m^3. Assuming the test is conducted in dry sand at centrifuge acceleration of N_s = 30, the acceleration to be imposed in a centrifuge test, assuming that the soil is saturated, is approximately $N_{sat} = 48$. More detail of this procedure can be found from Li et al. (2010) and Klinkvort et al. (2012).

$$\sigma_d = \gamma_d N_s h_m = \rho_d (N_s g) h_m \tag{3.6}$$

$$N_{sat} = \frac{\gamma_d}{\gamma'_{sat}} N_s \tag{3.7}$$

For the purpose of this study, the excess pore water pressures were to be avoided to allow the fully drained cyclic response. It was realised that dry sand could conveniently be used to achieve the stress similarity between the model and full scale conditions.

3.3.2 Gravity field (g-field) and scaling error

There are two common challenges of geotechnical centrifuge that have to be taken into account during the centrifuge model design to ensure similarities between the model and prototype.

3.3.2.1 Variation of the acceleration field

When the model is tested in a centrifuge, the effect of the gravitational field (g-field) is chosen that the model is to be subjected to. This effect will influence not only the radial depth, but also the width of the model geometry (Park, 2013, Taylor, 1995). The gravitational acceleration field is uniform and acts vertically, however, in a centrifuge, the uniformity deviates slightly compared to the prototype (Taylor, 1995). The reason is that when the centrifuge is spinning, the inertial acceleration field a_c becomes proportional to $\omega^2 R$ ($a_c = \omega^2 R$, where ω is angular velocity, R is centrifuge radius) and there is a variation in acceleration within the model. To minimise this error, a reference level of $\frac{2}{3}$ of the model height (L) and appropriate selection of effective radius are to be considered (see Fig. 3.4).

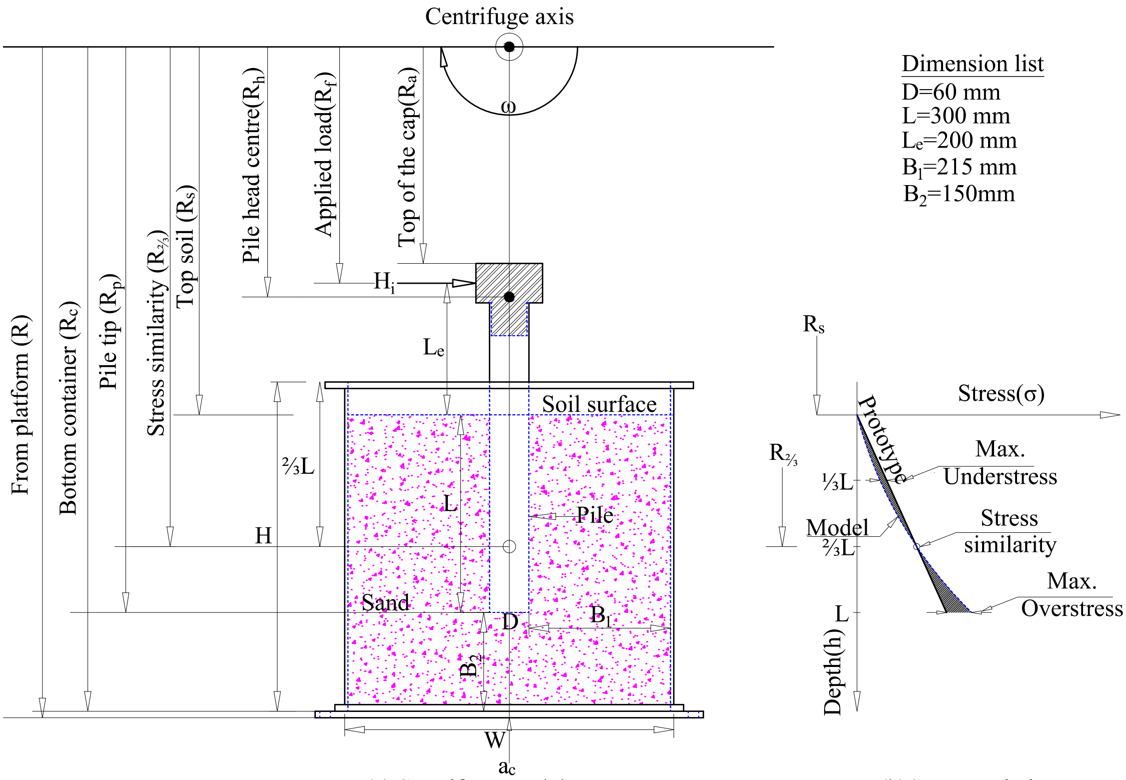

(a) Centrifuge model (b) Stress variation

Figure 3.4: Minimisation of stress distribution error in centrifuge model.

In Figure 3.4, the ratio of the model height (Z = L) to an effective centrifuge radius ($\mathrm{R_e}$) of the model determines the maximum *under-stress* and *over-stress* (Taylor, 1995). A vertical stress in a prototype, at depth $\mathrm{Z_p} = \mathrm{N_s Z}$, is given by $\sigma_\mathrm{p} = \rho \mathrm{g N_s Z}$ while the stress at depth Z in the model can be determined as $\sigma_\mathrm{i} = \rho \mathrm{w}^2 \mathrm{Z}(\mathrm{R_t} + \frac{\mathrm{Z}}{2})$, where $\mathrm{R_s}$ is the radius of the top of the soil (Li et al., 2012, Taylor, 1995). If the gravity is correct at $\mathrm{Z} = \frac{1}{3}\mathrm{L}$ then the maximum under-stress occurs. At this depth, the error on stress distributions is minimised and the effective radius $\mathrm{R_e} = \mathrm{R_s} + \frac{\mathrm{L}}{3}$ is used to calculate the ratio $\mathrm{r_u} = \frac{\mathrm{L}}{6\mathrm{R_e}}$ of the maximum *under-stress* (error in stress) to the nominal stress. At the base of the model ($\mathrm{Z} = \mathrm{L}$), the maximum *over-stress* occurs, with the ratio of stress error to the nominal stress being $\mathrm{r_o} = \frac{\mathrm{L}}{6\mathrm{R_e}}$. At depth of $\mathrm{Z} = \frac{2}{3}\mathrm{L}$, the radius where the vertical stress in the model and prototype are identical is given as $\mathrm{R_s} + \frac{2}{3}\mathrm{L}$. The distance from the centre of the centrifuge to different depths are shown in Fig. 3.4 and summarised in Table 3.2. In Fig. 3.4, a nonlinear stress distribution in the centrifuge soil sample is due to non-constant increase in gravity, which depends on the radius of the container (Klinkvort et al., 2013). The height of the centrifuge soil model introduces a parabolic non-linear increase in vertical soil stresses compared with linear increase that occurs in the prototype (Schofield, 1980). As shown in Table 3.2, suppose the prototype is scaled down at 100g (N_s=100) using a centrifuge radius, R_t = 1.7 m (an effective radius of the model and prototype stress are similar), then the angular rotation at the centrifuge can be given as shown in Eq. 3.8, where RPM is revolution per minute.

$$\omega = \sqrt{\frac{N_s g}{R_{\frac{2}{3}}}} = \sqrt{\frac{100 * 9.81}{1.7}} = 24.022 \mathrm{rad/s} \tag{3.8}$$

For 1rev/min=0.10472rad/s, $\Longrightarrow \omega$ =229.4 RPM

Table 3.2: Effective centrifuge dimensions from centrifuge axis

Parameter	**Symbol**	**Value**	**Unit**
Radius top of pile-head	R_a	1.95	m
Centre of pile-head radius	R_h	1.35	m
Top soil radius	R_s	1.53	m
Stress similarity radius at $\frac{2}{3}L$	$R_{\frac{2}{3}}$	1.7	m
Pile base radius	R_p	1.83	m
Bottom of container radius	R_c	1.98	m
Platform radius	R	1.6	m

3.3.2.2 Scaling effect on soil particle

In a centrifuge, the grain size effect is important for the interaction between the soil and structure interface. If the soil particles reduced by a factor N_s, the constitutive behaviour would likely to change and the models are usually constructed using the same soil as the full-scale (Garnier et al., 2007). Garnier et al. (2007) and Nunez et al. (1987) noted that no grain-size effect can be detected if the ratio between diameter, D, and average grain size, d_{50} is larger than 45 for laterally loaded piles $\left(\frac{D}{d_{50}} \geq 45\right)$. However, they both suggested that a monopile foundation should be considered with caution since the proposed ratio is only valid for tests carried out on slender piles. Furthermore, for a model pile in a centrifuge, loaded laterally, Remaud (1999) has recommended a $\frac{\mathrm{D}}{\mathrm{d}_{50}} \geq 60$ to ensure continuum behaviour. The contribution from Balachowski et al. (1998) and Liu (2010) suggested that the thickness of the shear bands is mainly related to the average size of grains and are likely to be an issue in a centrifuge. However, other studies (Garnier et al., 2007, Kirkwood, 2016, Klinkvort et al., 2012, Lau, 2015, Leth et al., 2008, Loukidis and Salgado, 2008) have reported that the models are usually constructed by using the same soil as the prototype. To ensure the continuing behaviour with $\frac{\mathrm{D}}{\mathrm{d}_{50}} \geq 60$, minimum size for monopile of the current study is established.

3.4 The University of Nottingham beam centrifuge

All tests presented in this study were conducted using the large beam centrifuge at the University of Nottingham (Nottingham Centre for Geomechanics (NCG)). The centrifuge is a 50 g-ton geotechnical beam centrifuge, designed and manufactured by Thomas Broadbent, UK. It consists three main parts; centrifuge beam, centrifuge chamber and Data Acquisition System (DAS). It is a medium-sized beam centrifuge with one swinging platform that can accelerate a 500 kg payload to 100g (at a nominal radius of 1.70 m) and can accommodate a model up to 0.6 m (circumferential) x 0.8 m (vertical in flight) x 0.9 m (radial in flight). The centrifuge beam, with a platform radius of 2.0 m, asymmetric twin tubular arms and counterweight is presented in Fig. 3.5 and its details are summarised in Table 3.3.

As shown in Fig. 3.5, a fixed counterweight, manually adjusted using a detachable screw jack prior to centrifuge flight, is used to balance the weight on swinging platform. The platform can support a model payload between 200 and 500 kg for primary balancing. Further, an automatic in-flight balancing system allows to correct the imbalance by the movement of oil in the centrifuge arms. For safety reasons, during spinning the centrifuge automatically shuts down when the tolerable out-of-balance load of ±30 kN is exceeded.

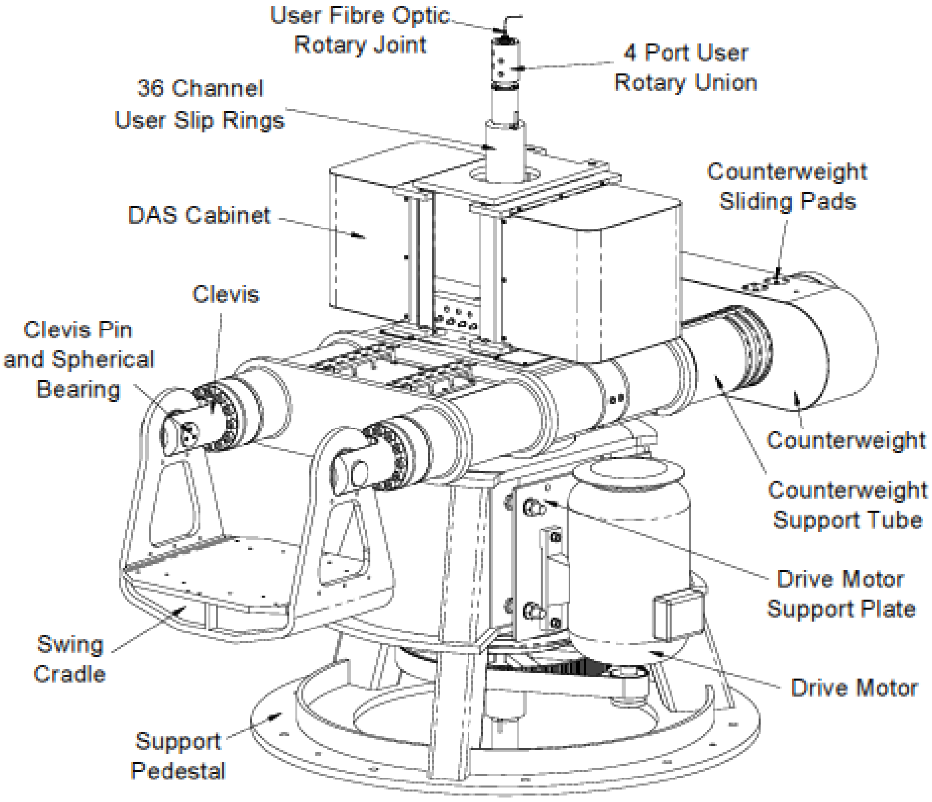

Figure 3.5: The sketch of the NCG geotechnical centrifuge, from Ellis et al. (2006).

Table 3.3: NCG geotechnical centrifuge specifications (Ellis et al., 2006, Mo, 2014)

Item	**Value**	**Units**
Rotation speed	5-281	[rpm]
Radius		
Platform	2	[m]
Nominal	1.7	[m]
Acceleration, *g*		
Maximum acceleration at 1.7 m	150g	[m/s^2]
Maximum size and weight of payload		
Maximum payload (500 kg at 1.7 m)	850 (up to 100g)	[kgm]
Width, vertical in flight	0.8	[m]
Length, circumferential in flight	0.6	[m]
Depth, radial in flight	0.9	[m]
In-flight balancing	+/-50	[kgm]
Motor	75kW 3 phase indication motor	[–]

The centrifuge is supplied with a complete control system based on an industrial programmable logic controller (PLC) (see Fig. 3.6(a)). The system comprises a Control/Drive Panel, a Local Control Panel, and Machine Instrumentation to control all safety related machine functions such as speed, automatic balancing, drive overload protection, access interlocks, and start and stop sequences. The centrifuge control system cannot control or extract data from the experimental payloads on the centrifuge. A photograph of the centrifuge and the current model is shown in Fig. 3.6(b).

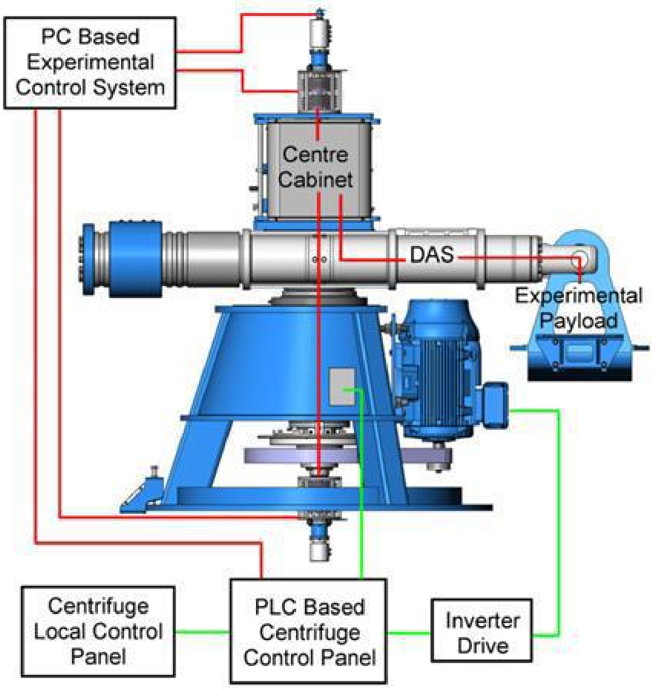

(a) Control system.

(b) Centrifuge and model.

Figure 3.6: NCG geotechnical centrifuge control system and model photograph.

3.5 Model container, pile and pile head

3.5.1 Model container

The container was specifically designed for the centrifuge tests at the University of Nottingham. It is cylindrical (see Fig. 3.7(b)), made of steel and having an outer diameter (W_o) of 500 mm, inner diameter (W_i) of 490 mm and height (H_c) of 500 mm. The detail is shown in

Fig. 3.7(a). For the laterally loaded pile, Madhusudan Reddy and Ayothiraman (2015) noted that the boundary effect, suggested by Matlock (1970), is predominant within 8-10 times the pile diameter (D) from the pile boundary. In this study, the model pile diameter is 60 mm; therefore the diameter size of the tank, W, should be between 480 - 600 mm. In Fig. 3.7(a), the space available between the horizontal (B_1) and vertical (B_2) boundaries are in order of 3.25D and 2.5D, respectively. The clearance boundaries of the pile and container wall are always considered to avoid the effect from the wall to the pile-soil interaction.

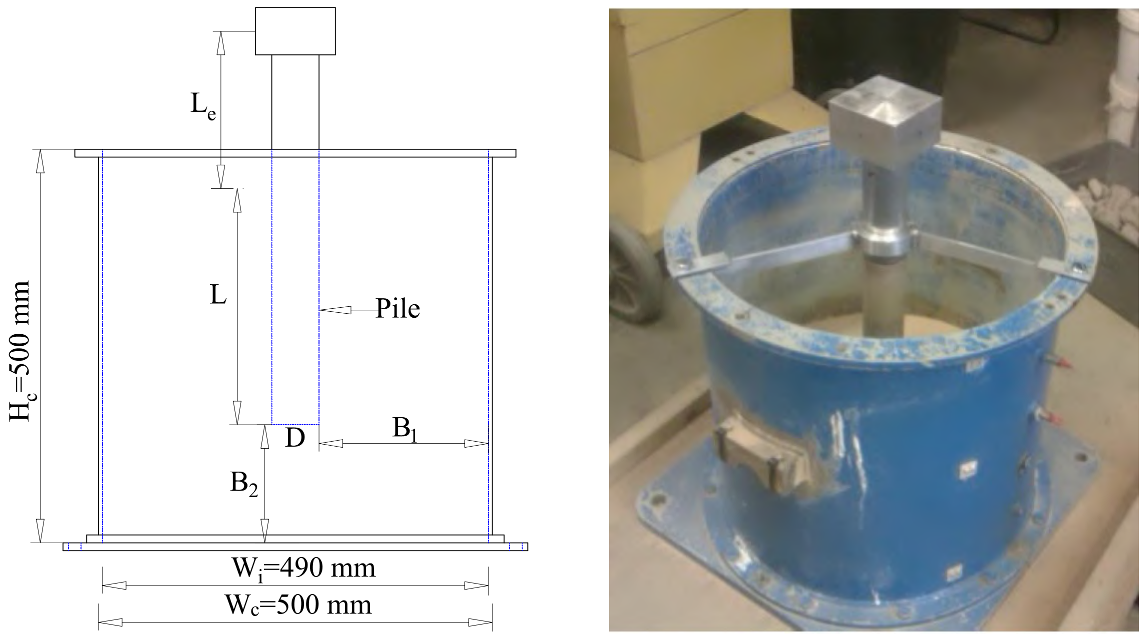

(a) Dimensions of the container

(b) A photo of steel container

Figure 3.7: The container used in soil bed preparation.

3.5.2 Model pile

The main purpose of the current study is to investigate the behaviour of laterally loaded rigid piles which represent the monopile foundation. According to Achmus et al. (2008), the typical monopiles are found at a water depth of 30 m and above and have been reported to have a diameter in the range between 6-8 metres. The model pile proposed represent a typical steel monopile that supporting a 5 MW class wind turbine. The outer diameter (D), wall thickness (t_p), embedded length (L), load eccentricity (L_e) and flexural stiffness (E_pI_p) are 6 m, 0.1 m, 30 m, 20 m and 1694 GNm^2, respectively. By using a geometric scaling factor of N_s =100, a hollow cylindrical aluminium pipe, having 60 mm external diameter, 3 mm wall thickness, 500 mm length and an embedded length of 300 mm, was designed and manufactured. The flexural rigidity of the aluminium model pile was ensured by increasing its thickness to a factor of three due to the difference of Young's modulus between aluminium and steel. The application of lateral monotonic and cyclic load was proposed at 200 mm above the soil surface, to represent a typical proportions load eccentricity ($\mathrm{L_e}$) of an offshore pile foundation.

With respect to soil characterisation, the pile may be considered as rigid or flexible (LeBlanc, 2009). The pile flexibility is given to the pile aspect ratio (embedded length (L) over diameter (D)) and relative stiffness. These two parameters are likely to be the key design and scaling variables for the model testing. As noted from Poulos and Hull (1989) and Meyerhof (1995), the flexibility of the pile is defined by the pile-soil relative stiffness, $\mathrm{K_R}$ (see Eq. 3.11) and its critical length ($\mathrm{L_c}$) (see Eq. 3.9). According to Meyerhof (1995), for the pile to behave in a rigid manner, $\mathrm{K_R}$ should be greater than 0.01, otherwise will behave in a flexible fashion. Poulos and Hull (1989) recommended that, for the pile to behave more flexibly, the embedded depth (L) should be greater or equal than the critical length ($\mathrm{L_c}$) (see Eq. 3.9) and rigid when $\mathrm{L} < \mathrm{L_c}$ (Eq. 3.10), where $\mathrm{E_p I_p}$ and $\mathrm{E_s}$ are the flexural stiffness of the pile and Youngs modulus of elasticity of soil, respectively. For a steel monopile of 6 m diameter (D), 30 m embedded length (L) and 100 mm wall thickness ($\mathrm{t_p}$), rigid behaviour is observed for $\mathrm{E_s}$ 9.6 MPa using Eq. 3.10. Flexible behaviour requires $\mathrm{E_s} > 810$ MPa for L to be less than $\mathrm{L_c}$. As noted from Kirkwood (2016), the typical range of $\mathrm{E_s}$ for dense sand is 48-81 MPa. Therefore, the monopiles lie to the condition of rigid behaviour (by using Eq. 3.10). Furthermore, this is also supported by slenderness ratio $\left(\frac{\mathrm{L}}{\mathrm{D}} = 5 < 10\right)$ (Byrne and Houlsby, 2003, Klinkvort and Hededal, 2014).

$$\mathrm{L_c} = 4.44\left[\frac{\mathrm{E_p I_p}}{\mathrm{E_s}}\right]^{0.25} \tag{3.9}$$

$$\mathrm{L_c} = 1.48\left[\frac{\mathrm{E_p I_p}}{\mathrm{E_s}}\right]^{0.25} \tag{3.10}$$

$$\mathrm{K_R} = \frac{\mathrm{E_p I_p}}{\mathrm{E_s L^4}} \tag{3.11}$$

As noted from Abadie (2015), Fig. 3.8 shows a plot of aspect ratio against pile relative stiffness, $\mathrm{K_R}$, for a range of designs relevant to UK offshore wind farms. From the figure, three sets of data are presented: wind farm monopiles in sand, wind farm monopiles in clay and piles that were used to develop the *p-y* methods recommended by Cox et al. (1974) (Reese and Van Impe, 2010). The area where the model piles should be located to capture the full-scale conditions is positioned at the top left corner. In this region, the pile of the current study is positioned based on previous published model piles frequently cited in this thesis.

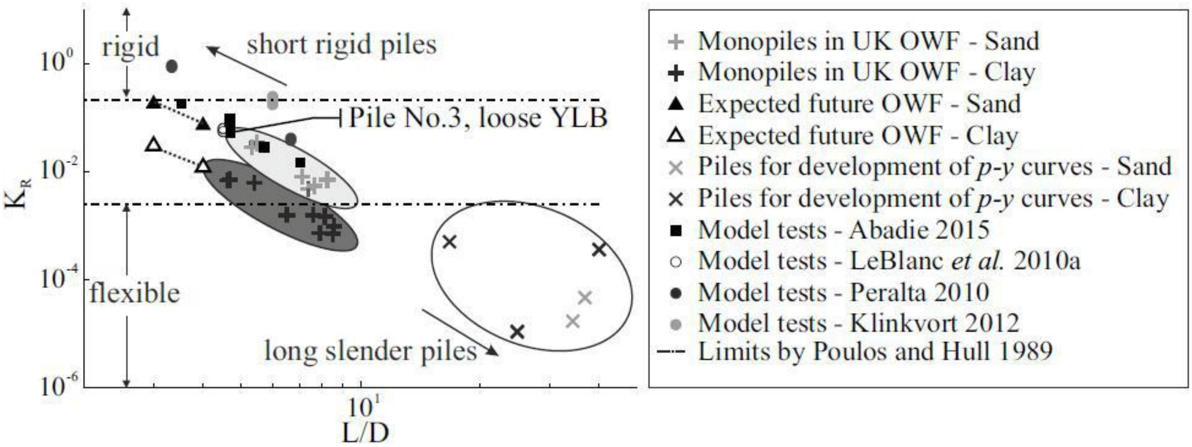

Figure 3.8: Published pile flexibility factor against L/D ratio for OWT, from Abadie (2015).

A photograph and detailed sectional view of the model pile are shown in Fig. 3.9(a) and 3.9(b), respectively, and the characteristics are summarised in Table.3.4. As shown in Fig. 3.9(a), the sand was glued to the shaft surface to understand the interface interaction between the pile and the soil (i.e purely glued). If the aluminium surface had just left without glued, then the interface interaction would not be known. It would be somewhere between smooth and rough, but you would not know where in between these extremes lies. So this decision was not motivated by a correlation to a realistic full-scale monopile, it was done to reduce uncertainty regarding the interface behaviour.

The mobilisation of shaft friction is controlled by the behaviour of a thin zone close to the pile surface, whose thickness depends on the pile surface roughness (Fioravante, 2002). The interface zone, as a result of the load applied on the pile, is subject to larger plastic straining in the way to resemble the simple shear mode. The soil in this phenomenon can exhibit a dilative or contractive behaviour depending on the pile installation and relative interface roughness (R_a). As noted from Shepley (2014), if the value of R_a exceeds 0.1 the surface is termed as rough and dilatant behaviour at the interface is expected. In contrast, if R_a is less than 0.02, then the interface surface is smooth and a low stress at the interface is expected with no dilatancy. The pile surface roughness varies between (2 to 5)D_{50} for a smooth pile up to

(10 to 15)D_{50} in the case of rough pile (Fioravante, 2002, Kishida and Uesugi, 1987), where D_{50} being the mean particle size of the sand. A smooth surface allows a slippage to occur at the interfaces with no development of shear zone while in the rough surface the failure takes place at a distance from the shaft and the interface friction angle is close or equal to the soil friction angle (Axelsson, 2000, Garnier, 1998). In centrifuge, to model the interface roughness, the normalised roughness should be similar in the model and the prototype (Garnier, 1998). For instance, Klinkvort (2013) investigated the influence of shaft friction by sandblasting the surface of one pile compared to smooth piles, in which capacity of sand glued pile (rough pile) was observed stiffer than smooth pile, however, there was no clear conclusion to whether a smooth or rough pile surface was the best to mimic the surface of a prototype monopile. It is therefore expected that the use of sand coated model pile in this thesis will provide a reasonable stiffness compared to a full-scale.

As shown in Table 3.4, the last column indicates the prototype characteristics for geometric scaling factor of N_s = 30. It can be seen that for this scale factor, the prototype dimensions are reduced compared to the model at scale of N_s = 100.

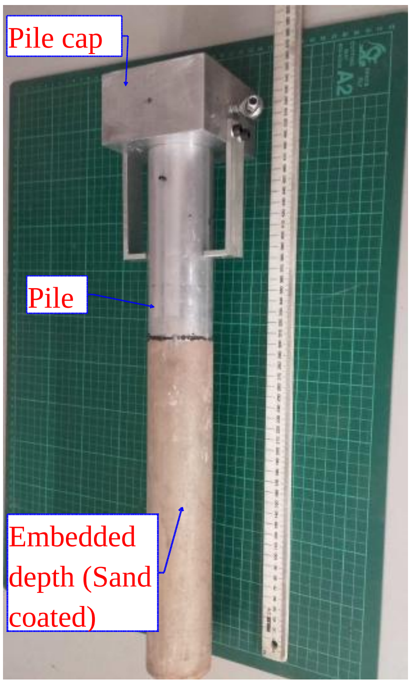

(a) Model pile with head (pile cap)

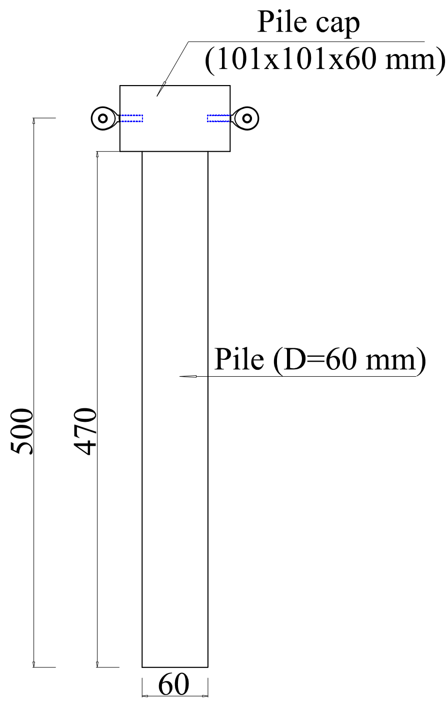

(b) Model pile section details

Figure 3.9: A photograph of full pile and section detail.

Table 3.4: Characteristic of pile in a model and prototype scale

Parameter	Symbol	Unit	Model	Prototype N_s=100	Prototype N_s=30
Diameter of pile	D	m	0.06	6	1.8
Embedded Depth	L	m	0.3	30	9
Wall thickness	t	m	0.003	0.1	0.03
Load eccentricity	L_e	m	0.2	20	6
Young's Modulus	E_p	GPa	70	210	210
Moment of Inertia	I_p	m^4	$2.188 \text{x} 10^{-7}$	8.0675	0.06535
Flexural stiffness	E_pI_p	MNm^2	0.0153	$1.6942 \text{x} 10^6$	$1.3723 \text{x} 10^4$
Vertical load	V_p	kN	0.02088	10000	289
Load frequency	f	Hz	2.5	0.025	0.083

3.5.3 Model pile head

An aluminium pile-head, rectangular of size 101x101x60 mm, is built-in with a circular solid cylinder (54 mm diameter by 50 mm height), which is attached on top of pile to simulate the static vertical load (see Fig. 3.10(a)). A typical 5 MW class wind turbine, having a vertical load (V_T=10 MN), represents the weight of the turbine, tower and transition piece. By using centrifuge acceleration and effective radius (see Fig. 3.11), the prototype vertical load was reduced to a model weight of 2 kg (see Table 3.5). As shown in Fig. 3.11, effective radius (R_h) from the centrifuge axis to the centre of the pile head was used to estimate the centrifuge acceleration, N_s (see Eq. 3.12), where ω is the angular rotation in rad/s and g is the gravitation acceleration in m/s^2. By using the value of ω = 24 rad/s, g= 9. 81 m/s^2 and R_h 1.345 m, the weight of the pile-head (W_m) at 100g was estimated to be 166.5 kg (1633 N) (see Table 3.5). At 1g unit gravity, the design weight is approximately 2 kg. This weight was taken as the vertical load on the model pile with all dimensions presented in Fig. 3.10(b). The material used for the model pile-head was aluminium with density of ρ =2700 kg/m^3. It should be noted that the angular velocity of $\omega = 24$ rad/s was considered in the pile-head design to achieve a stress similarity at $\frac{2}{3}$L (R_e=1.72 m), which corresponds with a centrifuge gravity of 100g. Therefore, for tests conducted at 30g, the angular velocity is ω=13.08 rad/s. All parameters at 100g and 30g are presented in Table 3.5.

$$N_s = \frac{\omega^2 R_h}{E_s L^4} \tag{3.12}$$

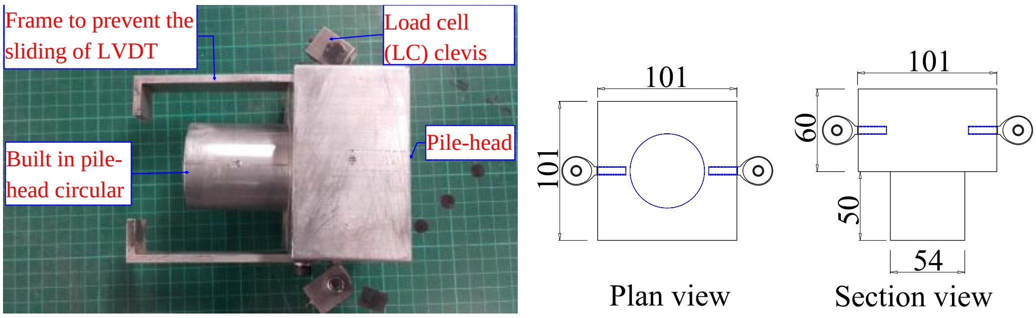

(a) Pile-head (b) Pile-head section view

Figure 3.10: A photograph of pile-head and section detail.

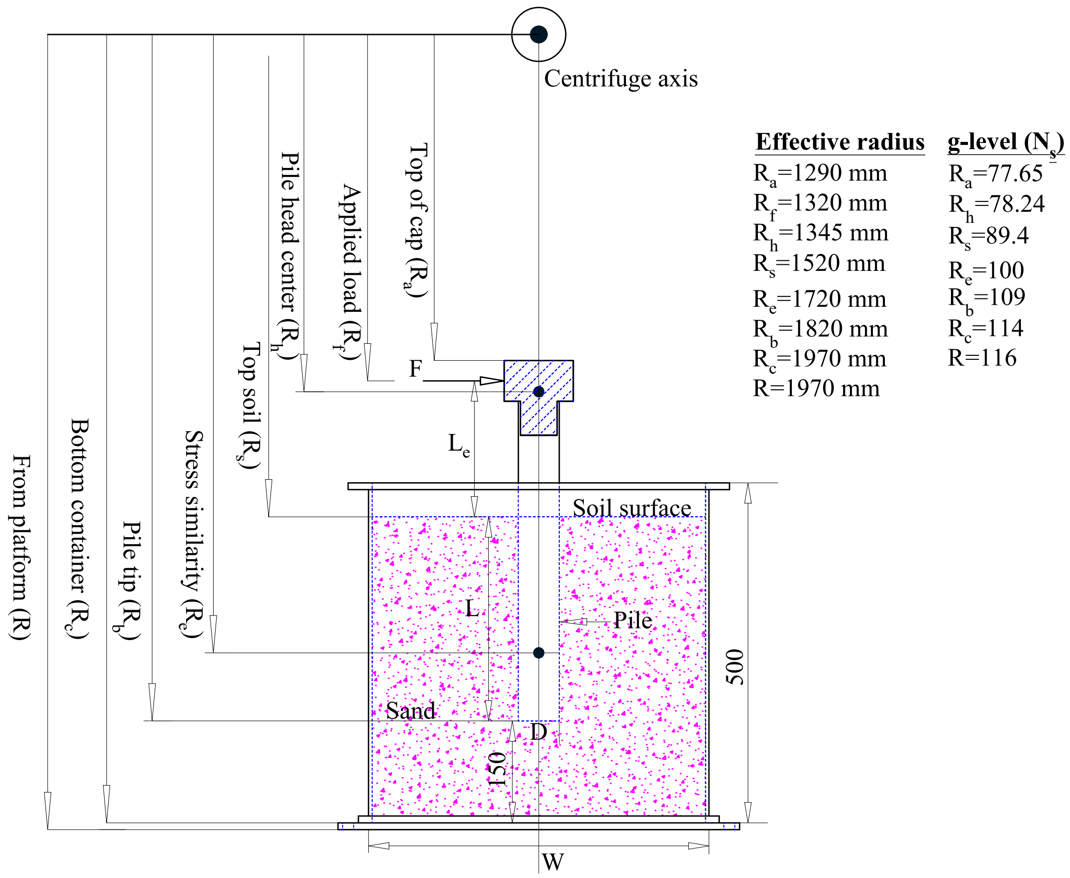

Figure 3.11: Effective radius (R) and artificial gravity from the centrifuge axis.

Table 3.5: Characteristics and design weight of the pile-head

Item	**Symbol**	**Unit**	**Value N_s=100**	**Value N_s=30**
Effective radius	R_h	m	1.345	1.345
Embedded depth	L	m	0.3	0.3
Angular velocity	ω	rad/s	24	13.08
g-level at R_h $\left(N_s = \frac{\omega^2 R_h}{g}\right)$	N_s	-	78.24	24
Prototype vertical load	V_T	kN	10000	289
N_s g weight $\left(W_m = \frac{V_p}{N_s^2}\right)$	W_m	kN	1.634	0.501
1 g weight $\left(W_{(1g)} = \frac{W_m}{N_s}\right)$	$W_{(1g)}$	N	20.88	20.88
1 g mass $\left(M_{(1g)} = \frac{M_1}{g}\right)$	$M_{(1g)}$	kg	2.12	2.12

3.6 Monotonic experimental apparatus

3.6.1 Introduction

The section describes the apparatus used to investigate the monotonic responses of the pile in dry sand and subjected to monotonic loading. The details of each component are described in the following sections. The loading device was developed to determine the capacity of the monopiles and contributes to the findings made in the cyclic tests. The loading system was designed to deliver a uniform rate of displacement at a relatively low speed. All monotonic experiments were carried out with deformation-controlled loading of the pile at a constant rate of approximately 2 mm/s for tests OWTP/S-T1/T2, OWTP/S-T3 and 0.05 mm/s for test OWTP/S-T4.

3.6.2 Experimental setup and equipment description

Figure 3.13 shows a sectional layout of the lateral loading device that is used to apply monotonic lateral loads on the head of the model pile. The pile, identified as (5) in the figure, is installed in dry sand that is contained in a circular container, having an internal diameter of 0.49 m and overall depth of 0.5 m. The driving torque to the loading system is provided by a stepper motor (1), which applies torque to a gear-head (10). The operation of the gear-head is used to drive a ball-screw (9) at a rate of 2 mm/sec. The rotating ball-screw (9) allows the gantry (11) to move towards the pile-head (6). The gantry (11) is directly connected to the rail with carriage to enable the movement of connected components, such as the vertical aluminium frame (12) and miniature load cell (2). The load cell (2), connected to spherical connector (7), was used to record the magnitude of the monotonic loads applied to the pile-head (6). The spherical connector (7), at the front of the pile-head (6), kept the applied load in a horizontal direction even when the pile is rotating. The two horizontally mounted LVDTs (3, 4) with holders on the vertical beam (13) were attached to the pile-head and along the pile to record the horizontal displacement. The aluminium base plate (8), which is fixed on the top of the container, was used to support the linear rail, stepper motor and other associated components. Figure 3.12 shows photos of the arrangement of the developed apparatus for monotonic loading experiment.

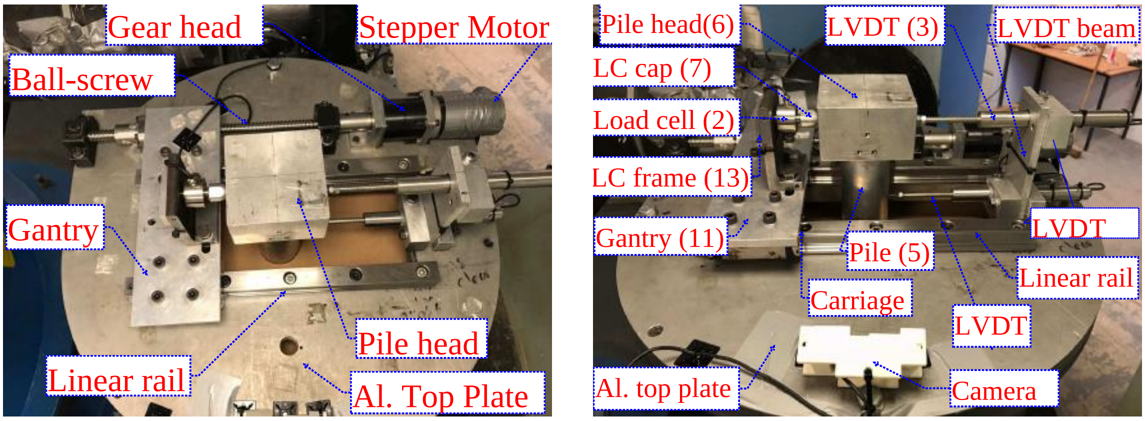

(a) Top view (b) Side view

Figure 3.12: Photos of the monotonic loading system.

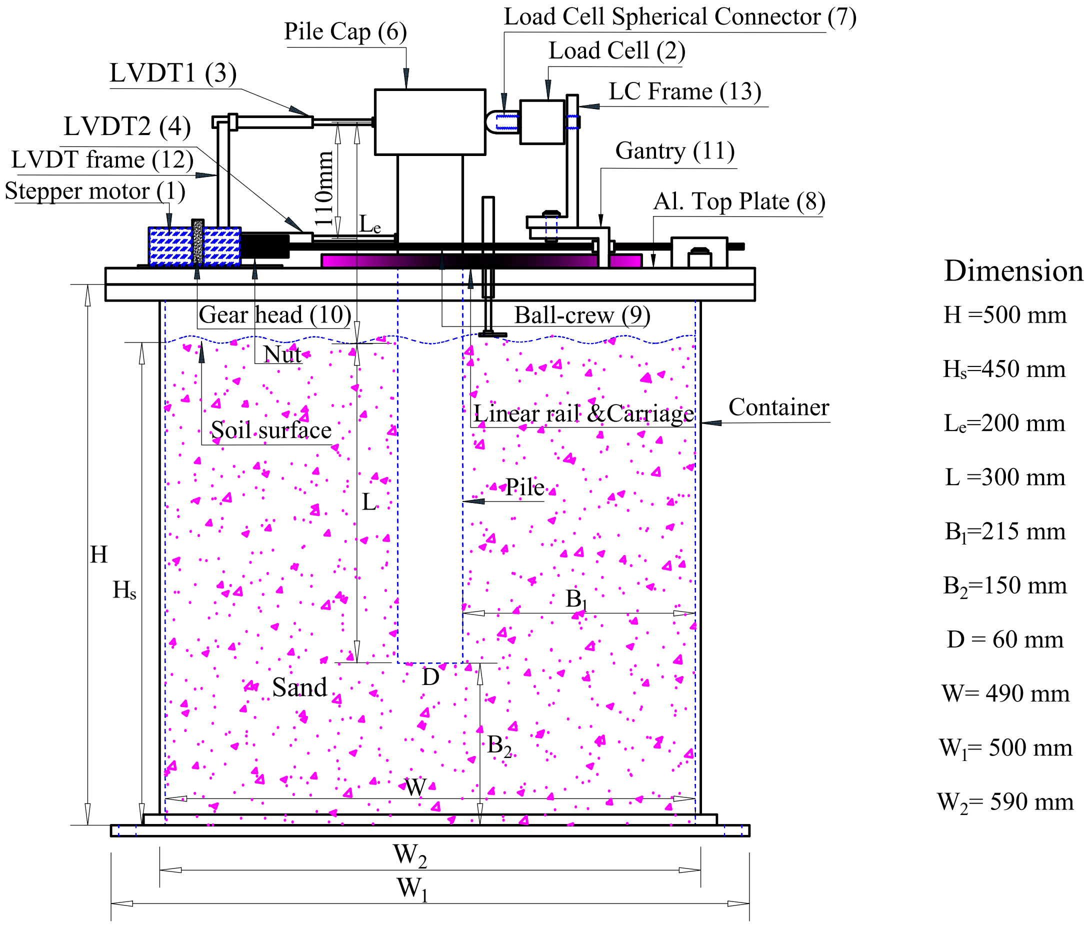

Figure 3.13: A section layout of monotonic loading device

3.7 Cyclic experimental apparatus

3.7.1 Introduction

As part of research programme, a new mechanical loading device was developed to enable the application of the lateral cyclic loads on the pile head. The device can apply either one-way or two-way cyclic loading. This section describes the cyclic loading components and how the loading device operates.

3.7.2 General layout

In this research, a mechanical loading device (see section layout in Fig. 3.14) was designed to apply cyclic lateral loads to the head of the model pile. It consists of the following major parts; aluminium base plate (1), steel container (2), reaction frame (3), applied weight device (4), dead and balance weight block (5), powerful operating system (AKM (6) and stepper (7) motor), crank disc (8,9), connecting rod (10) and Plummer block (14). The model pile shown in Fig. 3.14 was installed in a dry sand that contained in a circular container having the dimensions detailed in Fig. 3.7, Section 3.5.1. The location of the model pile and its dimensions were the same to those shown in Fig. 3.13. Figure 3.15 shows a 3-D sketch of the front and back side

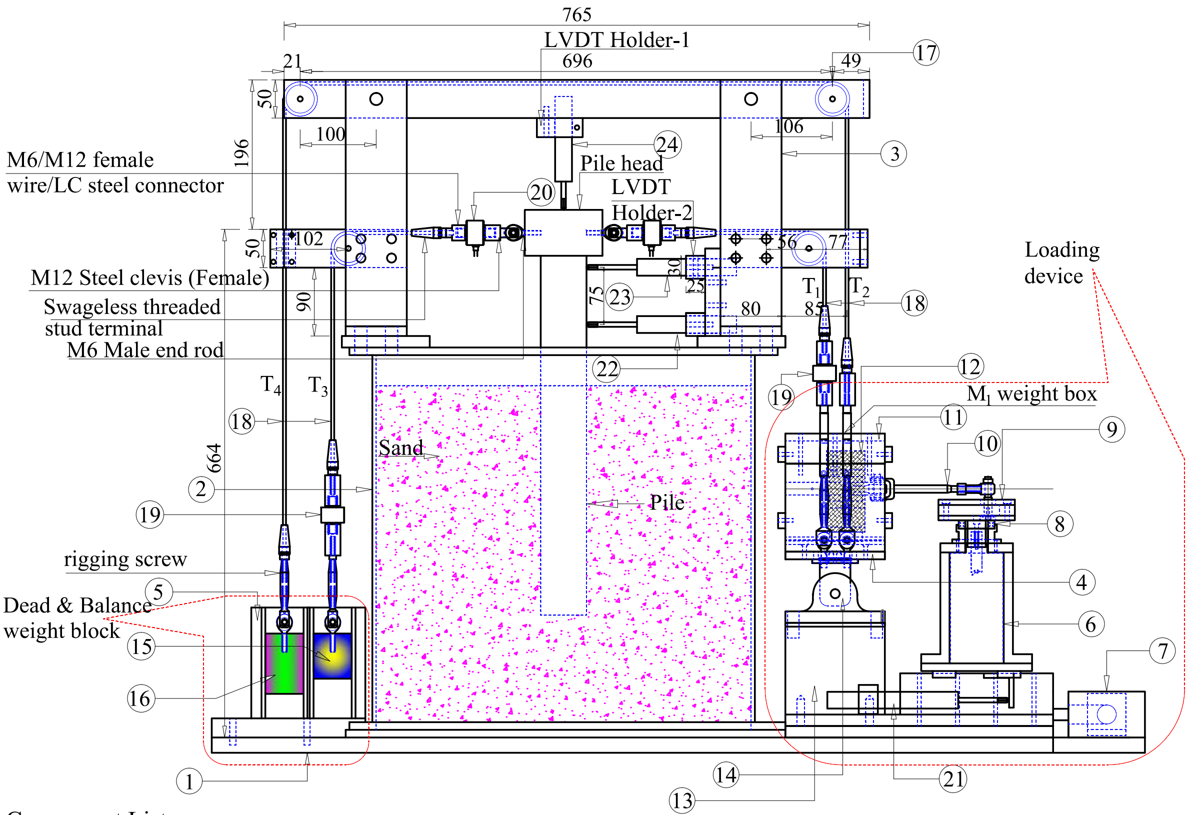

Component List

1.Al. base plate	5.M_2&M_3 block	9.AKM motor disc	13.Spacer block	17.Pulley	21.Stepper LVDT-1
2.Container	6.AKM motor	10.Connecting rod	14.Plummer block	18.Tension wires	22.Horizontal LVDT-2
3.Reaction frame	7.Stepper motor	11.M_1 cover box	15.Dead weight (M_2)	19.Stud terminal	23.Horizontal LVDT-3
4.M_1 load device	8.Spherical bearing	12.Applied weight (M_1)	16.Balance weight (M_3)	20.Load cell	24.Vertical LVDT-4

Figure 3.14: A section layout of model test setup for cyclic lateral loading.

views of the rig system. The components of the model setup are described in the following sections. Photos of the cyclic model test set up in a centrifuge can be seen in Fig. 3.16.

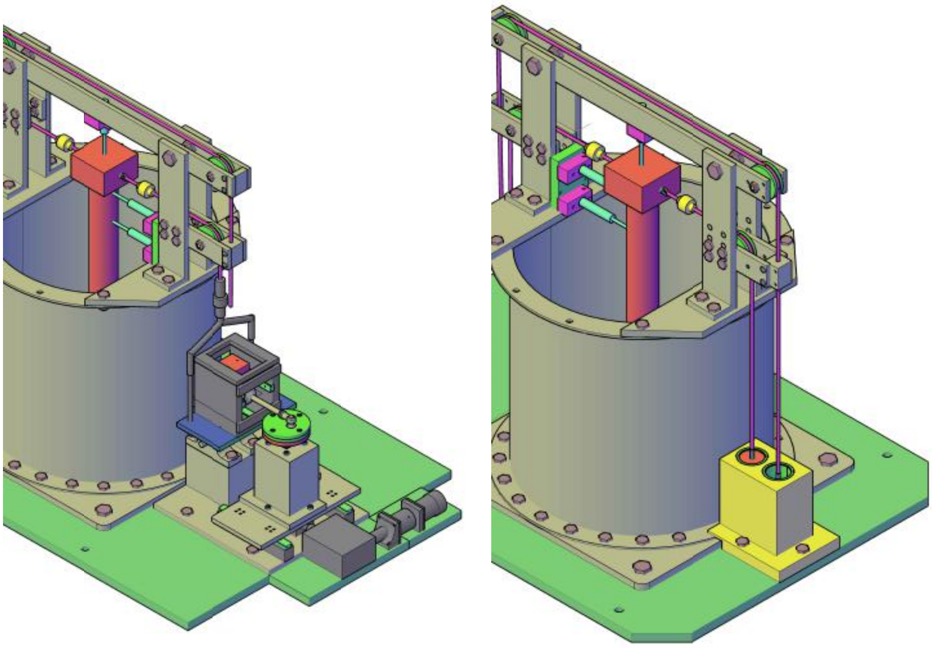

(a) Front side of the model device. (b) Back side of the model device.

Figure 3.15: A 3-D sketch of the model setup device for cyclic loading.

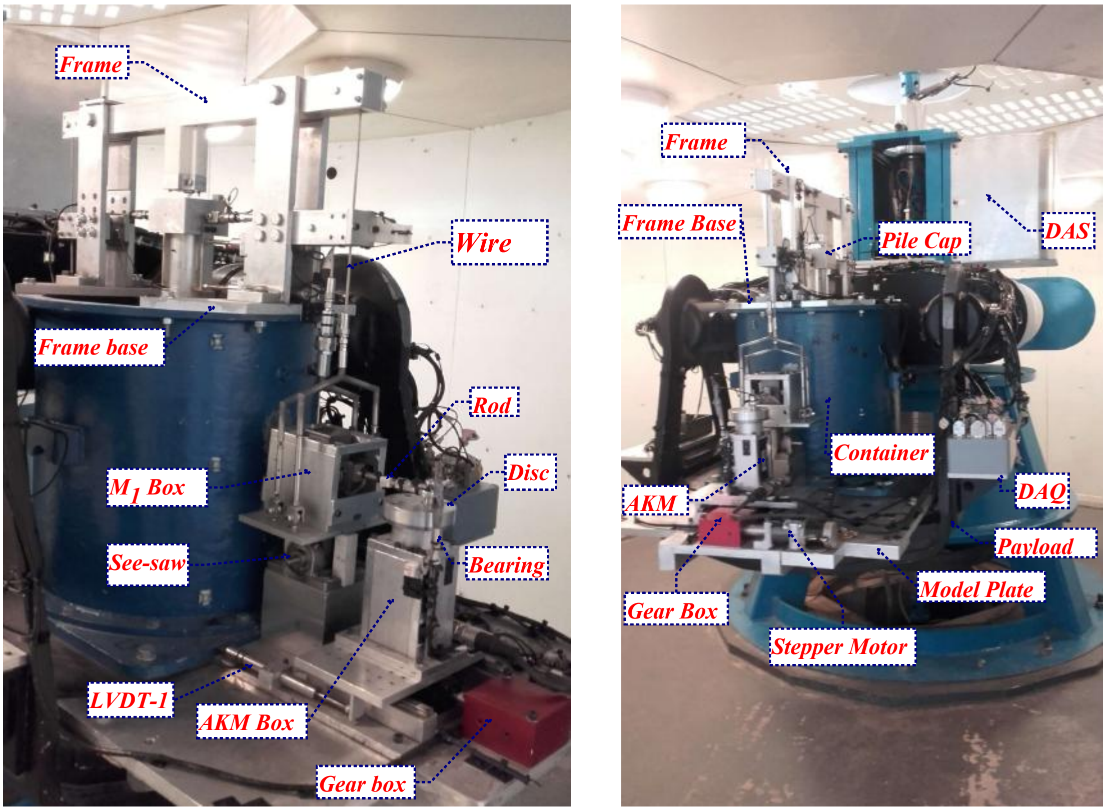

(a) LHS view (b) RHS view

Figure 3.16: Photos of the cyclic loading model setup in a centrifuge.

3.7.3 Component descriptions

1. Aluminium base plate (1).

   - A base plate with a thickness of 20 mm is a separate part, designed to connect the platform of centrifuge, container and act as cantilever support for the loading components and power system (this is addition length exceeding the centrifuge platform). Furthermore, four holes were created to allow an easy transport of the model using a fork lift. A typical sketch of the base plate and corresponding dimensions are shown in Fig. 3.17 and 3.18, respectively.
   - With a limited space on the centrifuge platform, an overhang base plate was design, capable to receive the total weight from load device, AKM and stepper motor including the associate components. A simple cantilever beam calculation for 20 mm thickness gave 0.46 mm deflection. Although the deflection was too small, which theoretically could not affect the plate, two pieces of aluminium bars were welded at the bottom to reinforce the added length (cantilever beam plate).

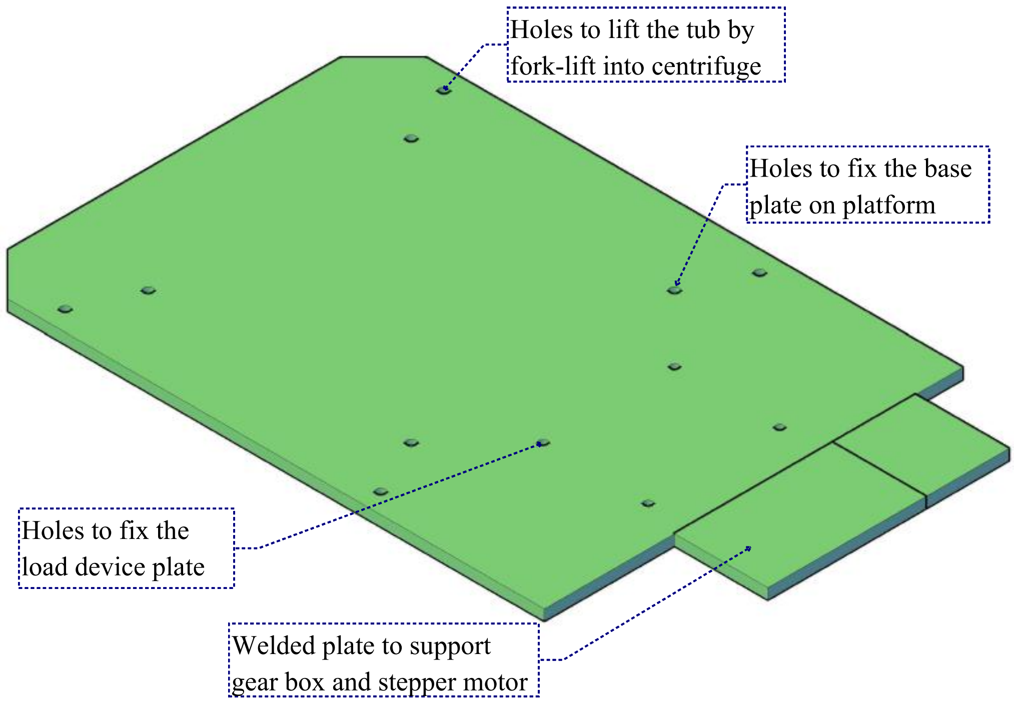

Figure 3.17: 3-D sketch aluminium base plate (not to scale)

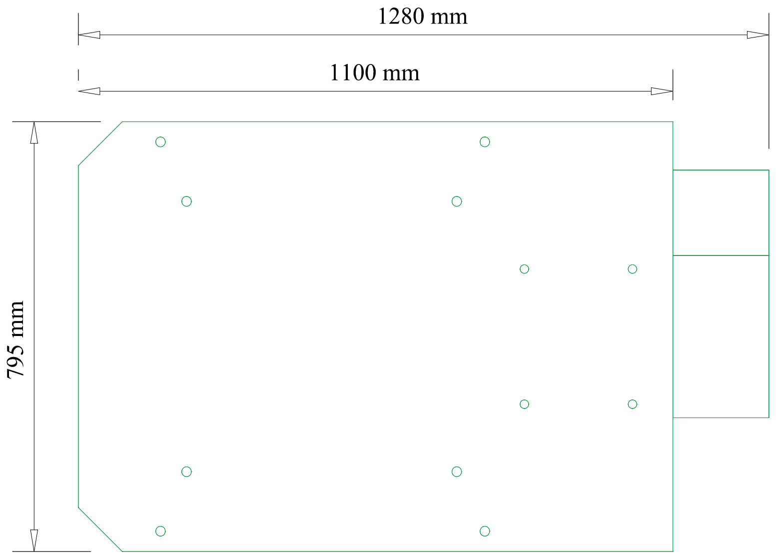

Figure 3.18: Dimensions of aluminium base plate

2. Steel container (2)

    - The tests are carried out in a circular steel container, which is welded with steel plate at the bottom and consisted of four 16 mm bolt holes, used to fix the container and a base plate. Its top is used to support the reaction frame (3). The more detail of this component was described in Section 3.5.1.

3. Loading frame (3)

    - A loading frame (3), made up of aluminium with four pulleys (17) holes, is fixed on top of the container. The wires (18), passing through the pulleys were designed to support the weight M_1, M_2 and M_3. As shown in Fig. 3.19, the loading frame consists of base plates (fixed on top of the container), four aluminium rectangular columns (main support frame) connected with overhang and top frame to support the pulleys.

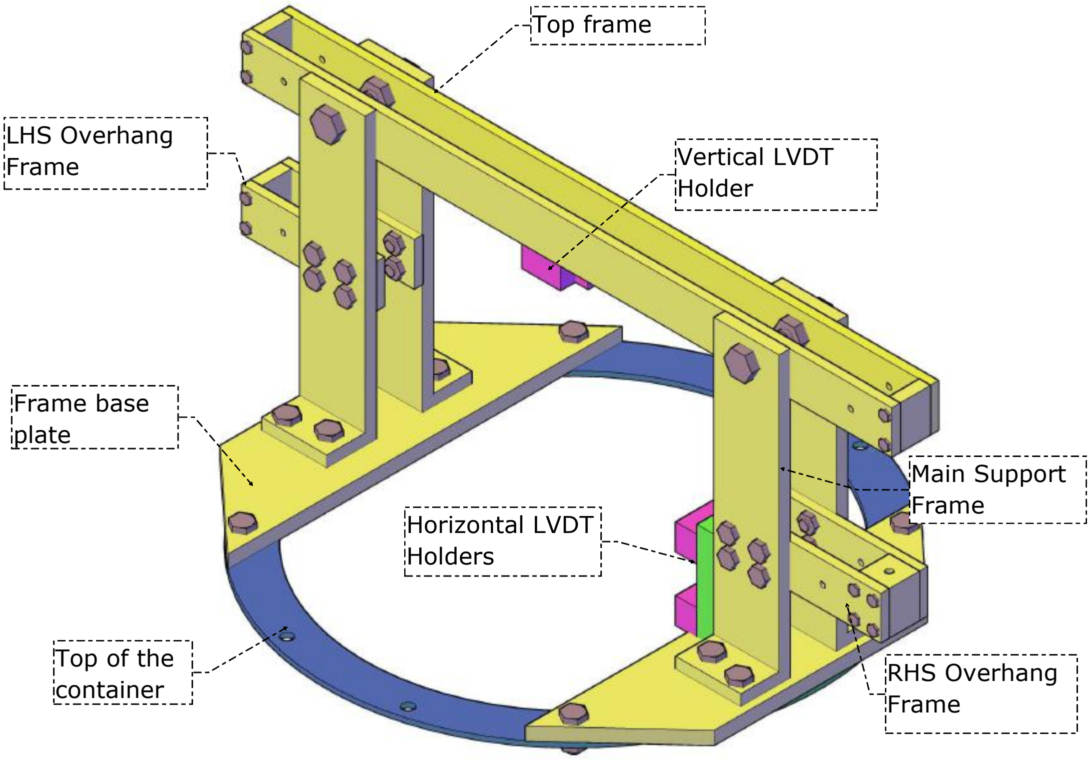

Figure 3.19: A 3-D sketch of loading frame.

A cross section layout, which shows the dimensions of the loading frame and a photo taken from the centrifuge model setup, can be seen in Fig. 3.20 and 3.21, respectively.

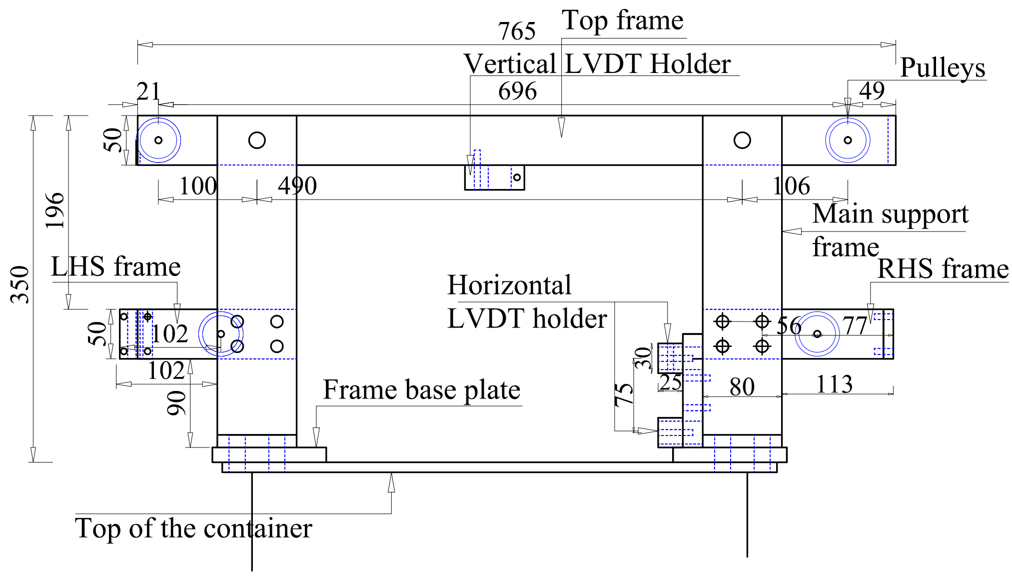

Figure 3.20: Cross section layout of the loading frame.

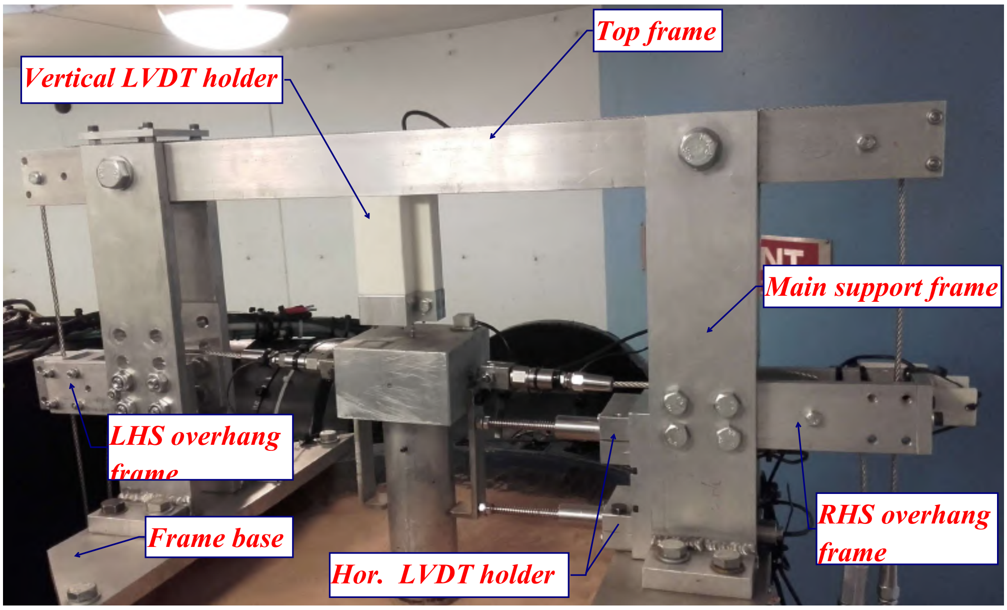

Figure 3.21: A photograph of the loading frame.

4. Pulleys and Wires (17 and 18)

    - Four pulleys (17), which are made up with brass materials and supplied by Barton Marine, have a diameter of 35 mm and breaking load capacity (WL) of 400 kg, sufficient to hold the weights M_1, M_2 and M_3. The steel pins with bearing are fixed on the frame (3) to support and allow the pulleys to rotate freely.
    - The tension wires (18), passes through the pulleys, are supplied by Techni-cable wire rope solution. They have 4 mm diameter and tensile capacity of 9.09 kN. As shown in Fig. 3.14, the wires are connected in-line with LC (load cell), passing on the pulleys directly to the pile head with its ends connected to the load device base plate (4) (on the RHS) and weights M_2, M_3 on the LHS. These wires are used to provide the tension forces generated by the action of the loading mechanism, and can be recorded through the LC sensors.

5. Loading device components

    - From Fig. 3.14, a loading device includes the following components; the power system (AKM (6) and Stepper motor (7)), the loading weight (M_1), motor disc, connecting rod and thrust bearing. A section layout and photograph taken from the centrifuge model setup can be seen in Fig. 3.22 and 3.23, respectively.

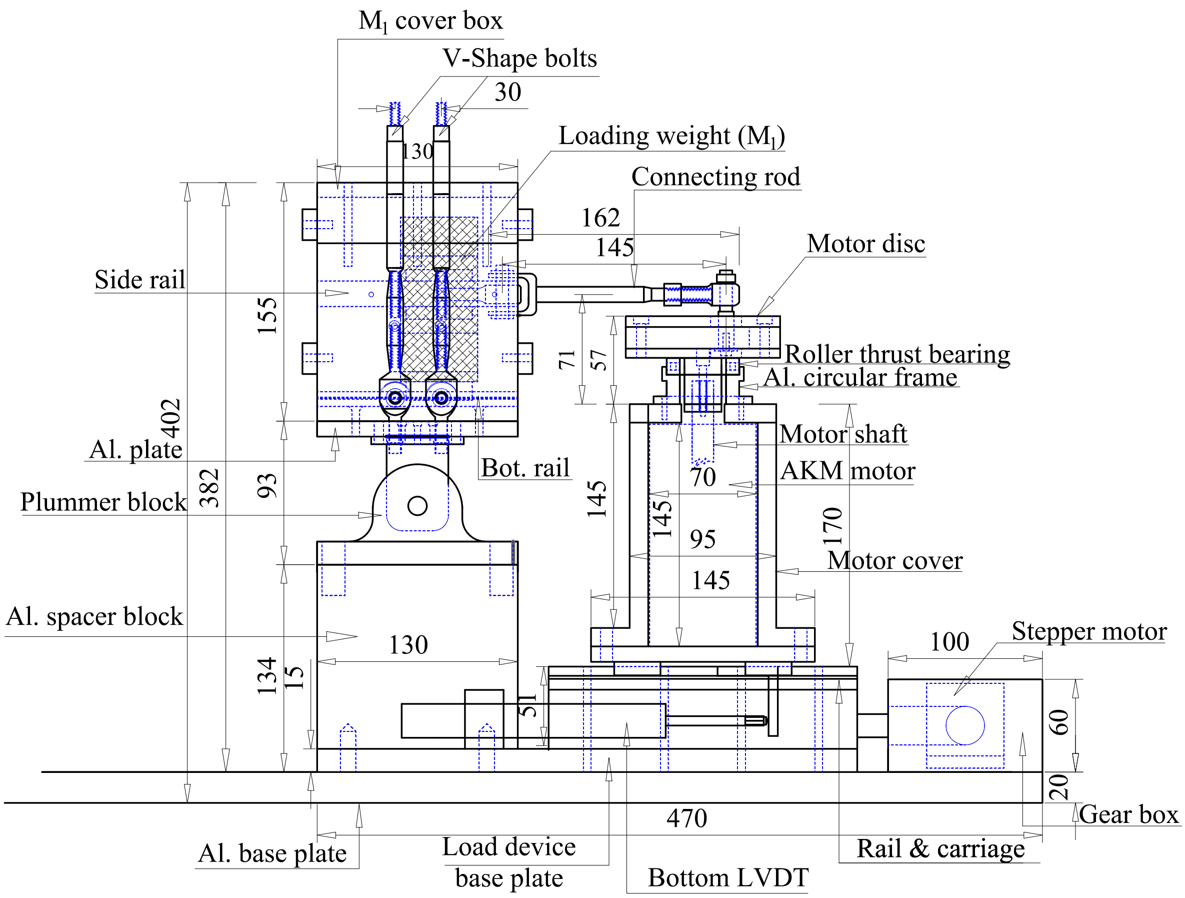

Figure 3.22: Section layout of the loading device.

- Fig. 3.22 shows the section detail of two power system; AKM servo motor (6) and stepper motor (7) (connected with gearbox). An AKM motor (6), having a frequency range between 0.3-1.5 kHz, is used to rotate the motor-crank disc (9). When the centrifuge is spinning, the thrust needle roller bearing (8) was fixed to support the weight of crank disc and connecting rod (10). An AKD speed controller (not shown in the figure) is used to manage the speed of the motor shaft with a maximum output of 8000 rpm. The motor can operate under a maximum torque of 6.72 Nm. An AKM motor detail is shown in Fig. 3.24.

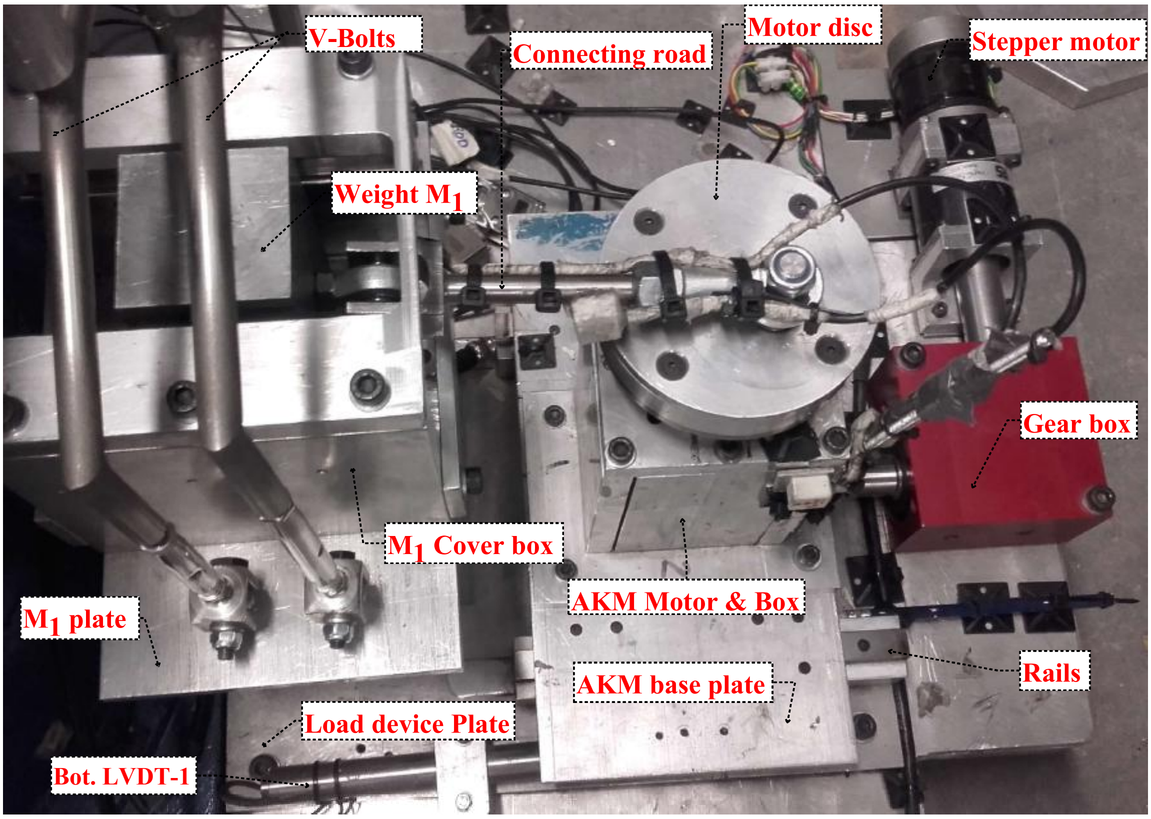

Figure 3.23: A plan view photo of the loading device.

(a) A photo of AKM motor

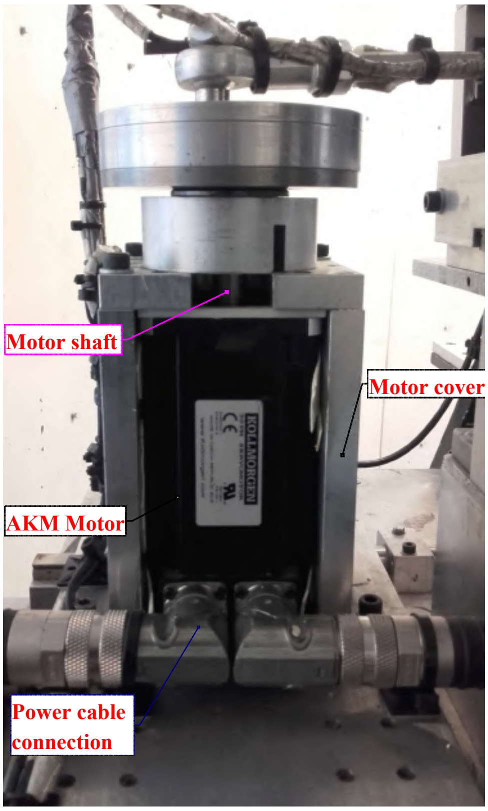

(b) AKM motor connected to crank-disc

Figure 3.24: The AKM motor detail.

- A single shaft stepper motor (7), manufactured by RS Pro Hybrid Stepper Motor, is used to control the movement of the loading system including the AKM motor. It is connected to the gearbox to change the location of the weight, M_1, and outbalance the loading system before an AKM motor start to spin. A photo of the stepper motor and square gear box is shown in Fig. 3.25.

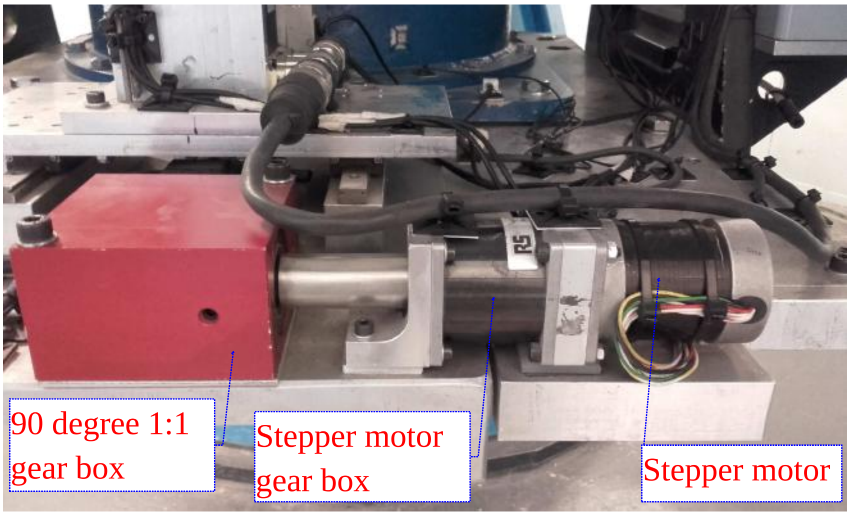

Figure 3.25: Stepper motor photo detail.

- As shown in Fig. 3.22 and 3.23, 100 mm diameter circular motor discs (9) are connected to an AKM motor shaft. From the disc plates, a threaded pin (10 mm diameter) is connected to an angular contact bearing, located 15 mm from the centre. A female rod end bearing is fixed to the pin, and then threaded to the end of steel connecting rod (10). The pin bearing is used to allow the free movement of the connected rod during the spinning. The steel rod (10 mm diameter) is linked to the weight, M_1, using a 10 mm male heavy-duty rod end. The male-rod end is used to provide both horizontal and vertical movement of the steel rod. During the spinning of the AKM motor, the weights of the crank-disc and steel rod are prevented by a cylindrical thrust roller bearing (8), which are supported by a circular aluminium frame. The roller bearings allow the motor shaft to rotate freely without being affected by weights applied on it. Photographs and sectional detail of the motor-disc, thrust bearing, and connecting rod are presented in Fig. 3.26.

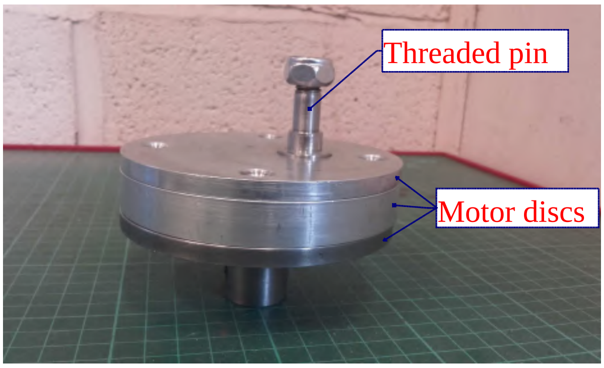

(a) Motor discs with thread pin

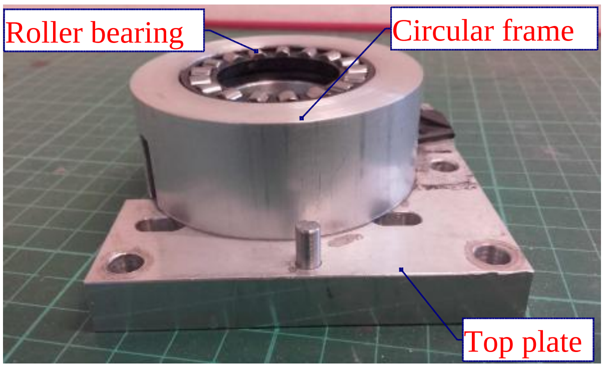

(b) Thrust bearing and circular frame

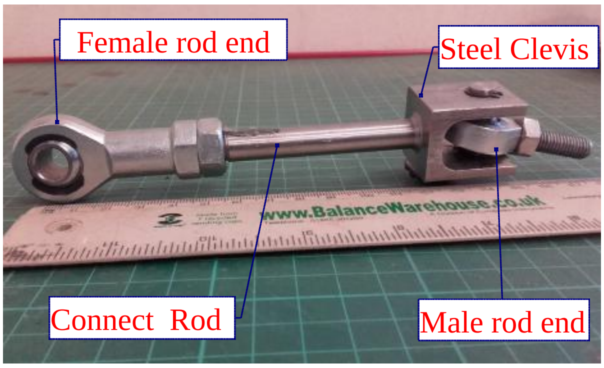

(c) Connecting rod

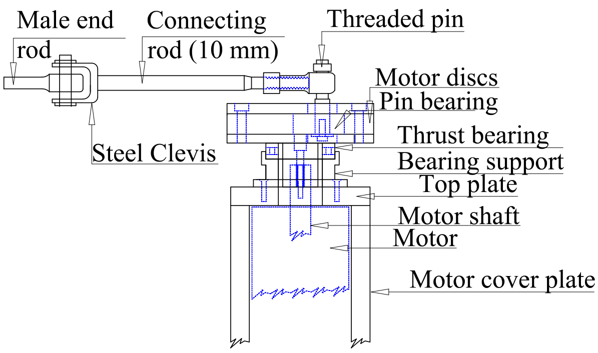

(d) Section layout of the components

Figure 3.26: Photos of the motor disc, connecting rod, thrust bearing and section detail.

6. Loading cage and calibrated weights

   - The loading system is consisted of RHS and LHS devices for the loading weight, M_1 (12), and both dead and balance weights (M_2 (15), M_3 (16)), respectively. On the LHS of the model, an aluminium cage (5), fitted with PTFE tube, was designed to protect the weights (M_2 and M_3) and allow them to move freely. The section layout and photos of the LHS components are shown in Fig. 3.27.

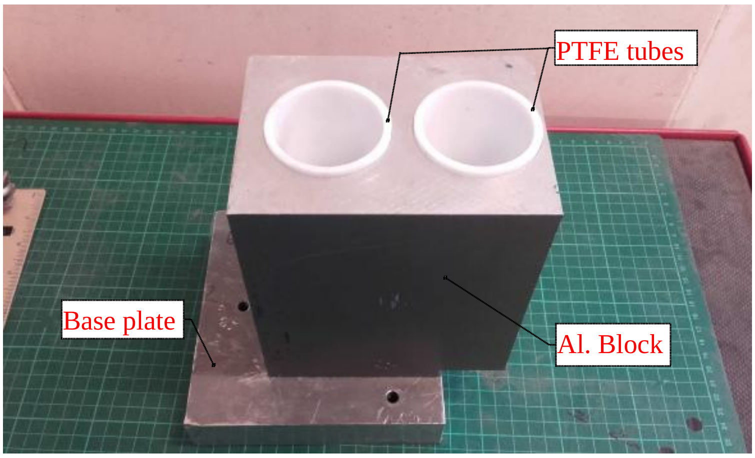

(a) M_2 and M_3 aluminium block and PTFE fitted

(b) M_2 and M_3 on cage

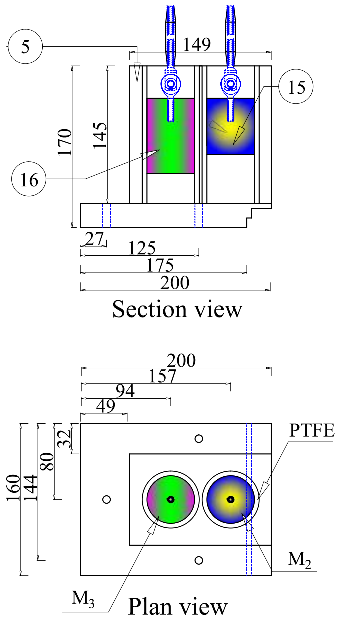

(c) Section of the cage

Figure 3.27: Photos and section layout of aluminium block.

- Likewise, the device on the RHS consists a loading box (16), which includes three rails and carriage (for free movement of weight, M_1 (12)) and Plummer block (see-saw) (14). The see-saw is connected to aluminium plate (4) to provide rotation of the system during the spinning. Photographs of loading components on the RHS of the container are portrayed in Fig. 3.28.

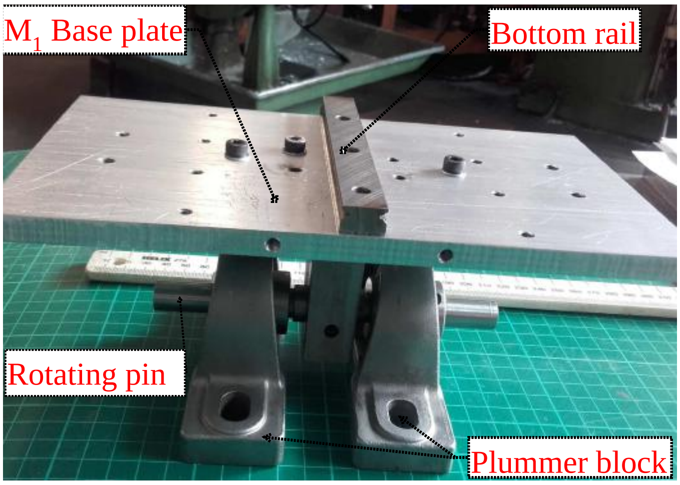

(a) Plummer block, base plate and bottom rail

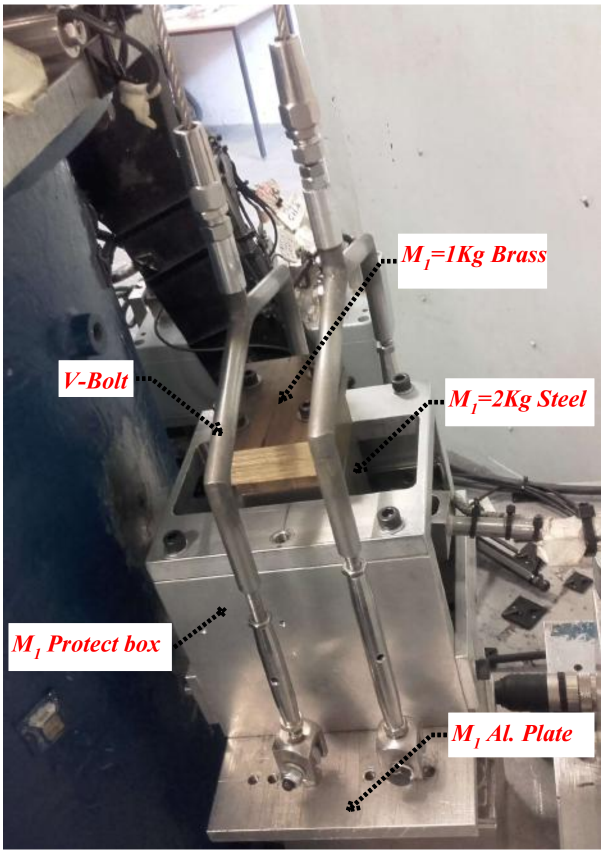

(b) Load box and M_1

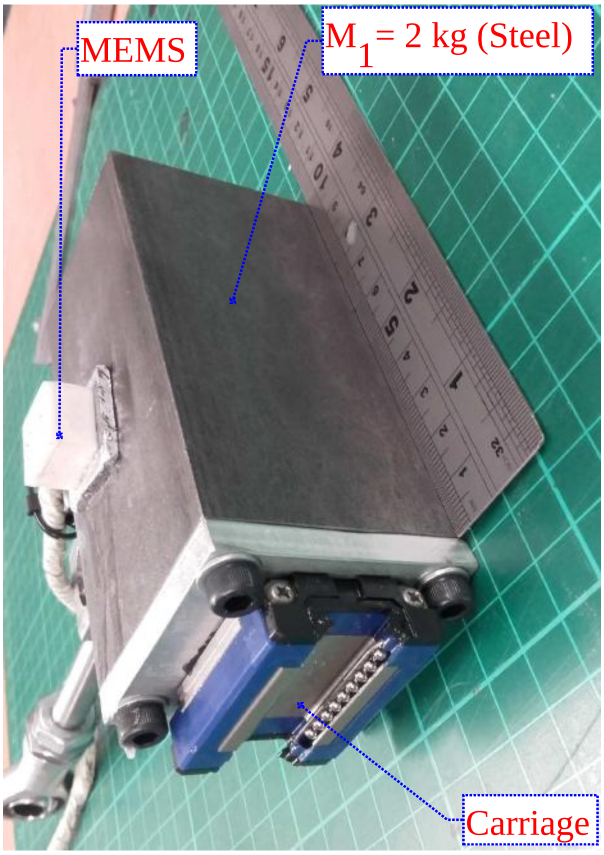

(c) Loading weight, M_1=2 kg

Figure 3.28: Photos of the loading device on the RHS of container.

3.7.4 Working mechanism of the loading system

The working mechanism of the new loading system depends on the required load scheme (M_1, M_2, and M_3) and the frequency of AKM motor. Referring from Fig. 3.14, the cyclic lateral loading behaviour of the pile head is obtained by the transfer of loads (supplied by loading weight, M_1 and dead weight, M_2) through the wires (T_1 and T_3); that is, tension forces are generated in the load cells. As shown in Fig. 3.29, the system arrangement includes; applied weight (M_1) sliding on the frictionless rail, dead weight (M_2), balance weight (M_3), sea-saw beam, pile head, tension wires (T_1, $T_2 = T_4$ and T_3), the load cells named LC (RHS) (connected on the right-hand side of the pile head), LC (LHS) (connected on the left-hand side of the pile head) and beam plate. The tension wires (T_1 and T_2) are connected directly to the loading plate, and separated by an equal distance ($l_1 = l_2$), from the centre O=B_1. It should be noted that the weight applied on the tension wire T_2 is outbalance with weight applied on the tension wire T_4.

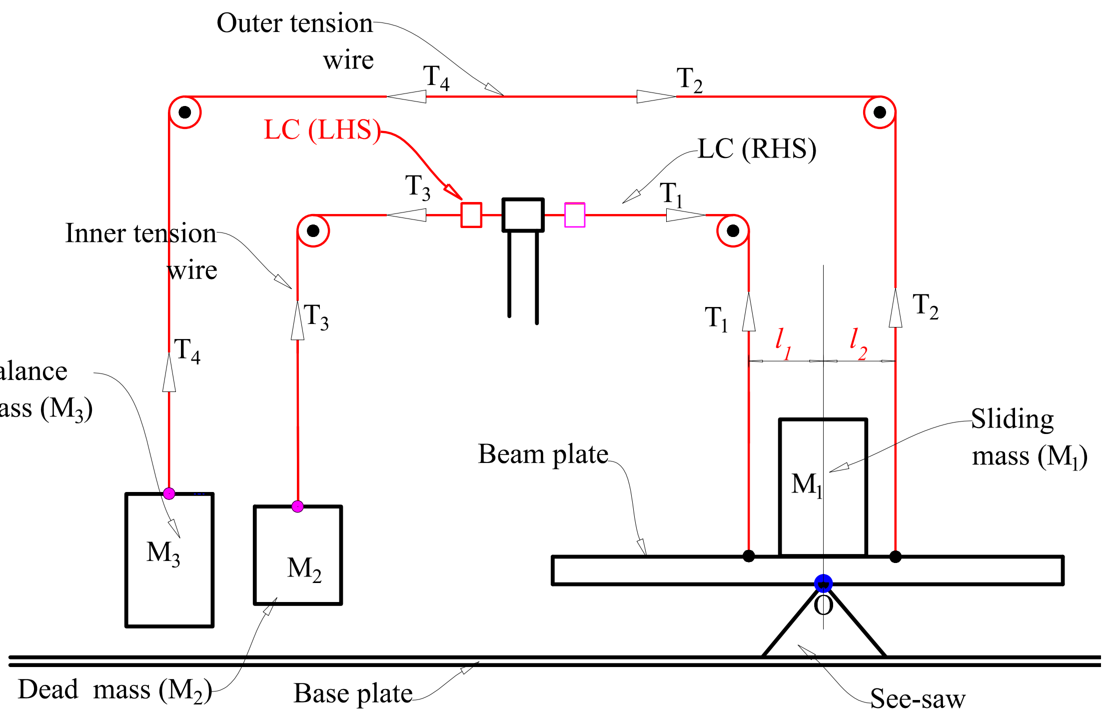

Figure 3.29: Schematic diagram of working operation on the system.

From the system arrangement, a sinusoidal waveform is generated to describe the cyclic loading behaviour of the pile head. Control over the frequency of the load and the movement of loading weight (M_1), is primarily achieved by adjusting the speed of the driving motor. For instance, when a sliding node O, of the weight M_1, is in its middle range, the tension on wires are assumed to be in a balance with zero wave amplitude. Meanwhile, the weight M_3 is chosen sufficiently to balance loads of the components connected with M_1, creating an outer system in a balance. The weights M_1 and M_2 are each attached to the pile through load cells LC(RHS) and LC(LHS), with tension wires T_1 and T_3, respectively. These weights can provide different loading scenarios as they control the cyclic load characteristics. The weight M_1 designed to control the amplitude of the loading, H_{max}, while the load M_2 is used to control the mean loading level, H_{avg}.

As shown in Fig.3.30, a schematic of weight sliding-crank mechanism is also used to describe the system operation. The weight, M_1 is assumed to slide horizontally on the rail from point B to B_1 at distance X, while the crank-disc rotates in a clockwise direction at an angle, θ_i. L_i and R_i are the length of the rod and distance from the pin to the centre (on the crank-disc), respectively. β_i is defined as the angle between the line of weight movement ($\overline{BO}$) and connecting rod $\overline{B_2A}$, θ_i is the rotation of the circular disc, h_i is the vertical height between the horizontal line and pin on the crank-disc, and $\omega_c = 2\pi f$ is the angular velocity provided by the AKM motor, *f* is the frequency. The frequency of the cyclic loading is controlled by the rotational speed of the AKM motor. Initially, the proposed frequency to run the motor was set to be 15 Hz in order to represent a prototype frequency of 0.15 Hz. However, due to technical challenges related to centrifuge acceleration (g-level), the cyclic tests were conducted to a constant rotational frequency of 2.5 Hz.

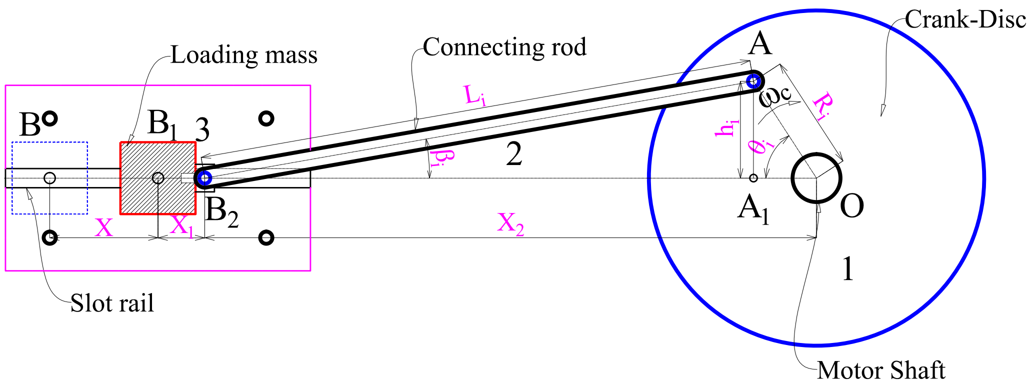

Figure 3.30: Sketch showing general arrangement of crank-motor disc.

Theoretically, the displacement, X, linear velocity, V, and acceleration, a_i of the weight (M_i), moving horizontally from point B to B_1 can be calculated as follows;

1. Displacement X when the motor disc has turned through an angle θ_i from the inner dead centre, is obtained by Eq. 3.14.

$$X = B_1B = BO - B_1O = (L_i + R_i) - (X_1 + X_2) = (L_i + R_i) - (B_2A_1 + A_1O) \quad (3.13)$$

$$\Rightarrow X = (nR_i + R_i) - (nR_i\cos\beta_i + R_i\cos\theta_i), \rightarrow n = \frac{L_i}{R_i}$$

$$\Rightarrow, \cos\beta_i = \sqrt{1 - \sin^2\beta_i} = \sqrt{1 - \frac{h_i^2}{L_i^2}} = \sqrt{1 - \frac{(R_i\sin\theta_i)^2}{L_i^2}}$$

$$\therefore X = R_i\left[(n+1) - \left(\sqrt{n^2 - \sin^2\theta_i} + \cos\theta_i\right)\right] \quad (3.14)$$

2. Velocity of the weight (M_i) from inner dead centre, V

   - The linear velocity of the weight sliding can be obtained by finding derivative of weight displacement, ∂X with respect to time, ∂t. This can be determined as shown in the following equations;

$$V = \frac{\partial X}{\partial t} = \frac{\partial X}{\partial \theta}\frac{\partial \theta}{\partial t}, \Longrightarrow \frac{\partial \theta}{\partial t} = \omega \quad (3.15)$$

$$\Rightarrow \mathrm{V} = \frac{\partial}{\partial \theta_{\mathrm{i}}} \left[\mathrm{R} \left\{ (\mathrm{n}+1) - \left(\sqrt{\mathrm{n}^2 - \sin^2\theta_{\mathrm{i}}} + \cos\theta_{\mathrm{i}} \right) \right\} \right] \omega_{\mathrm{c}}$$

$$\therefore \mathrm{V} = \mathrm{R_i}\omega_{\mathrm{c}} \left[\sin\theta_{\mathrm{i}} + \frac{\sin 2\theta_{\mathrm{i}}}{2\sqrt{\mathrm{n}^2 - \sin^2\theta_{\mathrm{i}}}} \right] \tag{3.16}$$

3. Acceleration of the weight (M_i) from inner dead centre, a_i

   - The linear acceleration of the weight (M_i) sliding can be obtained by finding derivative of weight velocity, ∂V with respect to time, ∂t. This can be determined as shown in the following equations;

$$\mathrm{a_i} = \frac{\partial \mathrm{V}}{\partial \mathrm{t}} = \frac{\partial \mathrm{V}}{\partial \theta}\frac{\partial \theta}{\partial \mathrm{t}}, \Longrightarrow \frac{\partial \theta}{\partial \mathrm{t}} = \omega \tag{3.17}$$

$$\Rightarrow \mathrm{a} = \frac{\partial}{\partial \theta_{\mathrm{i}}} \left[\mathrm{R}\omega_{\mathrm{c}} \left\{ \sin\theta_{\mathrm{i}} + \frac{\sin 2\theta_{\mathrm{i}}}{2\sqrt{\mathrm{n}^2 - \sin^2\theta_{\mathrm{i}}}} \right\} \right] \omega_{\mathrm{c}}$$

$$\therefore \mathrm{a_i} = \mathrm{R_i}\omega_{\mathrm{c}}^2 \left[\cos\theta_{\mathrm{i}} + \frac{\cos 2\theta_{\mathrm{i}}}{\mathrm{n}} \right] \tag{3.18}$$

From Fig. 3.29, the movement of the sliding weight (M_1) on the slot rail will initiate loads on the pile head. When the system is in a balance (see Fig. 3.31(a)), any movement of the weight M_1 will determine the tension force on the wires. The free body diagrams (FBD) (see Fig. 3.31), consists of oscillating components supported by the see-saw on pin joint B_1. When the loading weight, M_1 slides on the rail using the crank-motor disc mechanism (see Fig. 3.30), keeping the joint B_1 at the mean, the weight M_1 is assumed to move at distance X from B_1 (see Fig.3.31(b)). As the crank rotates, the weight M_1 creates a tensile force in wire T_1, which is transferred onto the pile-head through the load cell (LC (RHS)); however, there is another tension force, T_3, acting on the left (LC (LHS)). Theoretically, the net lateral load on the pile head may be written as $\Delta T_i = T_1 - T_3$ (see Eq. 3.19). The distance X can be rewritten in sinusoidal form as $X = X_o \sin 2\pi f$ and the net load, H_i can be calculated as shown in Eq. 3.20, where the quantity $\left(\frac{M_1 g X_o}{l_1}\right)$ is the amplitude of the applied cyclic load, X_o is the maximum value of X on the tension wire T_1, g is the gravitational force, f is the loading frequency. By altering the weight M_1, different values of cyclic load levels can be achieved.

$$H_i = \Delta T_i = \frac{M_1 g X}{l_1} \tag{3.19}$$

$$H_i = \frac{M_1 g X_o}{l_1} \sin 2\pi f \tag{3.20}$$

In the initial stage of model testing, the design of weight M_1 was based on the ultimate ca-

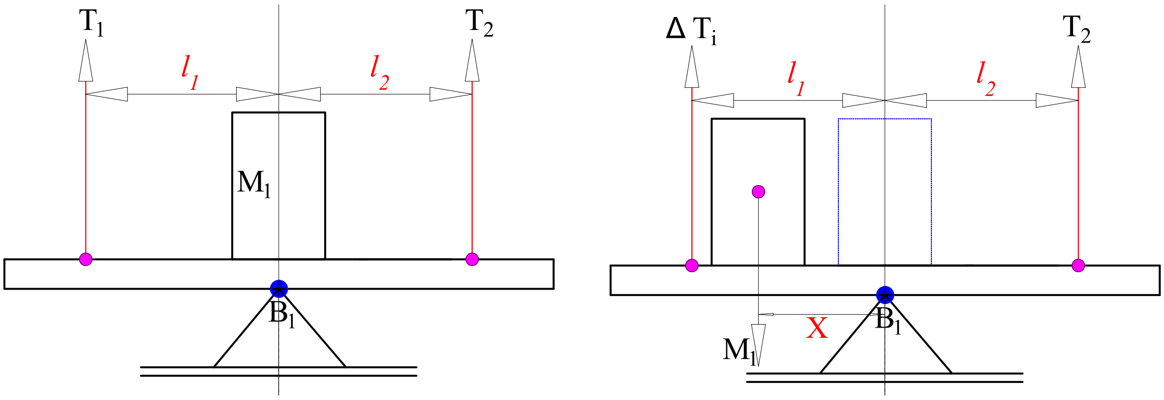

(a) Free body diagram (M_1 at B_1)   (b) Free body diagram (M_1 at distance X)

Figure 3.31: Load mechanism free body diagram of applied mass, M_1.

pacity obtained from monotonic tests conducted at 100g. From these tests, the recommended maximum force for the cyclic load was preferable as 50% of the ULS load (H_u $\approx$ 4.0 kN). The combination of design weight was chosen to achieve a maximum load of H_{cyc} = 0.5 H_u = 2 kN. This load was obtained at acceleration gravity of 100g, which corresponds to a mass of M_1 = 2 kg at 1 g $\left(\frac{200\text{kg}}{100}\right)$. In the preliminary stages of the model development, the initial set up (M_1 = 2kg, M_2=2kg and M_3 = 2kg) did not balance the loading system, therefore the adjustment was made by increasing the weight M_1 to 3 kg, reducing M_2 to 1.5 kg and M_3 was increased to 4 kg. This arrangement was seen to balance the loading system and used to run all the tests. However, with technical challenges relating to the AKM motor (torque incapable to drive the weight M_1 when the centrifuge spun at more than 30g), only the maximum centrifuge acceleration of 30g was used for all cyclic tests.

Theoretically, at centrifuge acceleration of 30g, the tension force on T_1 and T_3 are 900 N and 450 N, respectively, and the expected net force will be H_{cyc} = H_i = T_1-T_3 = 450 N. This cyclic load amplitude is approximately 26% of the ultimate capacity of the pile H_u, based on a 30g centrifuge monotonic test (D_r = 85%). A model setup of the loading system to provide a net force of H_i = 450 N was a challenging task. During the tests, the resultant load was achieved incrementally by carrying out experimental trials, while changing T_2 tension wire location (l_1) and the weight M_2 keeping M_1 and M_3 constant. A thorough investigation, which might affect the result, was carried out through the following procedure;

1. For each test trial, the location of wire (l_2) and dead weight (M_2) were changed while keeping M_1 = 3 kg and M_3 = 4 kg constant. For instance, (a) test trial 1: l_2 =25 mm, M_2 = 2 kg, (b) test trial 2: l_2 = 45 mm, M_2 = 2 kg, (c) test trial 3: l_2 =35 mm, M_2 = 1.75 kg, test trial 4: l_2 =35 mm, M_2 = 1.5 kg. More details of the test trial results are presented in Section 3.11.

2. After spinning the centrifuge to 30g, the stepper motor (7) was switched on to adjust the weight M_1. This was achieved by moving the weight M_1 on sliding rail (forward or backward) to balance the tension forces ($T_1 \approx T_3$). The initial values were recorded to observe the effect of load balance between the weight M_1 and M_2.

3. Before the AKM motor was switched on, the load control factors (ζ) of 0, 0.5, 1.0, 1.5, -0.5, -1, for each test trial, were considered to observe its effect on the net loads applied to the pile head. The load orientation factor was obtained by Eq. 3.21, with typical locations of load variation versus time shown in Fig. 3.32. From Eq. 3.21, H_{min} and H_{max} are the minimum and maximum cyclic amplitude loads, respectively, and H_{avg} is taken as the tension force from dead load, M_2, received on SLC (LHS).

$$\zeta = \frac{\left[\left(\frac{H_{max} - H_{min}}{2}\right) - H_{avg}\right]}{\left[\frac{|\ H_{max} + H_{min}\ |}{2}\right]} \tag{3.21}$$

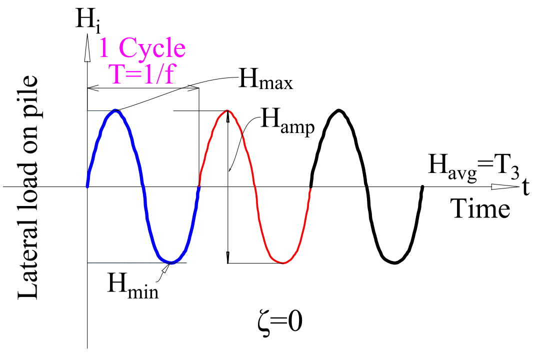

(a) Constant ratio ζ =0

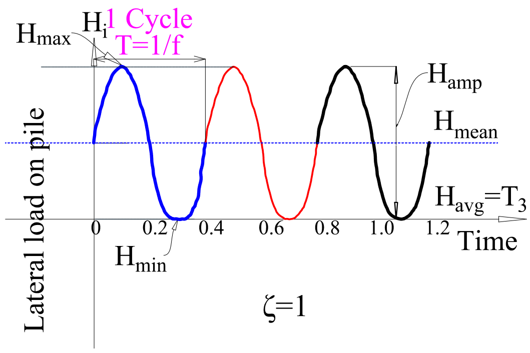

(b) Constant ratio ζ =1

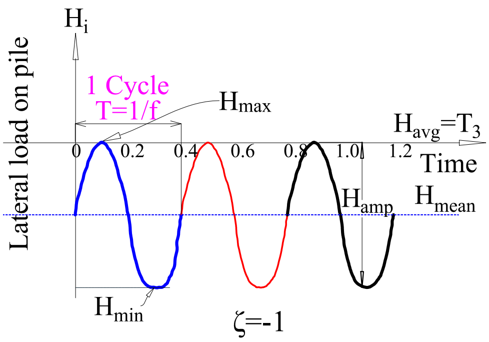

(c) Constant ratio ζ =-1

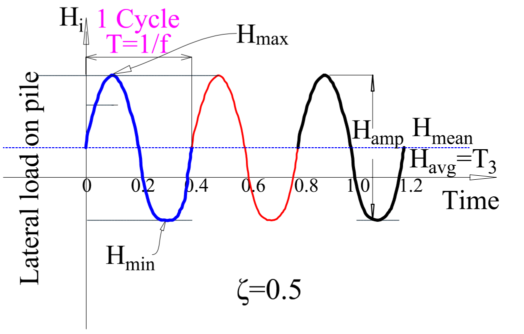

(d) Constant ratio ζ =0.5

Figure 3.32: Typical sketch indicating ζ position curves.

4. The Stepper motor (7) was turned off, and then an AKM motor was switched on to allow a sinusoidal amplitude force in the form of Eq. 3.22. The sinusoidal forces on the pile-head were achieved by appropriately choosing the weight M_1 and M_2. From Eq. 3.22, H_a is the cyclic load amplitude, ω=2f is the angular frequency, ϕ is a phase shift, H_o is the vertical shift of the curve related to the average of the curve, H_{mean}. Referring to Fig. 3.33, a typical sketch is used to demonstrate the sinusoidal amplitude force.

$$\mathrm{H(t) = H_a sin(\omega t + \Phi) + H_o, \Rightarrow H_a = \frac{M_1 g X_o}{l_1}} \tag{3.22}$$

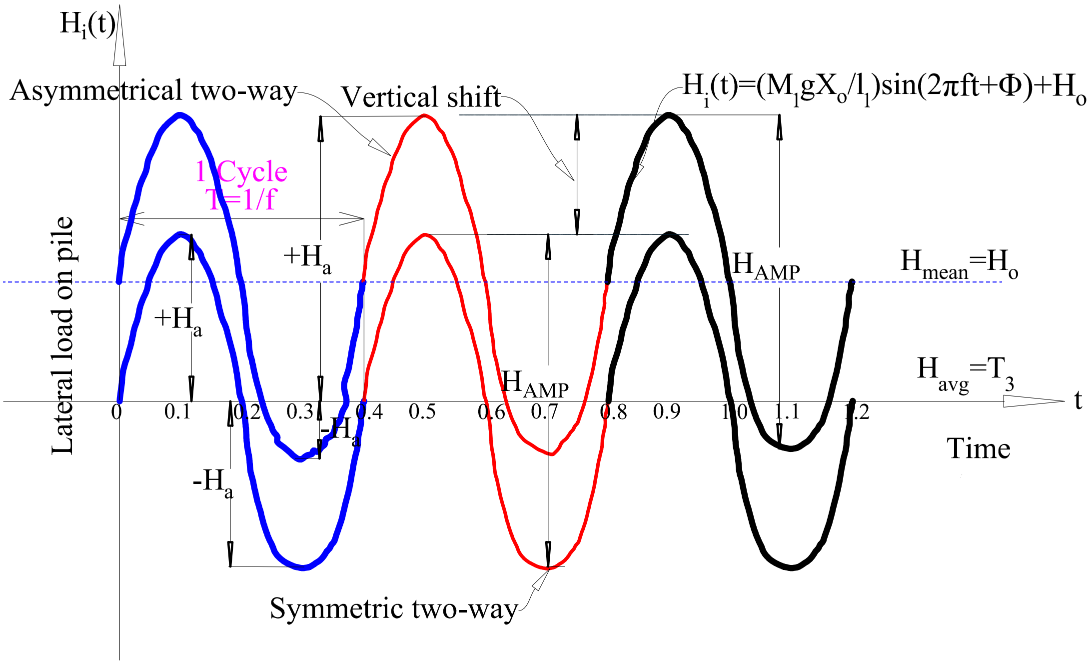

Figure 3.33: Sketch indicating sinusoidal cyclic load curves.

3.8 Laboratory soil and sample preparation

3.8.1 Material properties

Material characteristics are essential part of the research to understand on how the sand state will affect the model behaviour. A Congleton silica sand (HST95) from Bent Farm in Congleton, Cheshire, was chosen as the model sample material of this study and used throughout the centrifuge tests. HST95 sample is fine silica sand, typically consisting of 94.5% quartz (Al-Defae and Knappett, 2014). The sample was tested in the NCG laboratory to determine grain size distribution, strength parameters, maximum and minimum densities and void ratios. A scanning electron microscope (SEM) was used to examine the size and shape of grains. Samples were prepared and coated with platinum before the scanning so that the grains were electrically conductive. As shown in Fig.3.34(a), most of the particles are observed to be sub-angular and sub-rounded. Fig. 3.34(b) shows a dry sieving test result of the samples tested at

NCG, to determine the particle size distribution and the coefficient of uniformity.

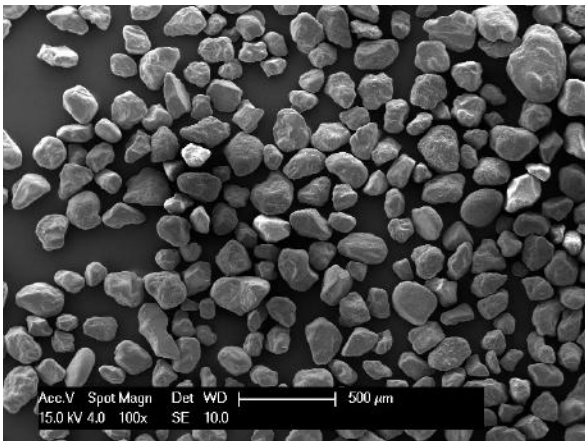

(a) SEM photo

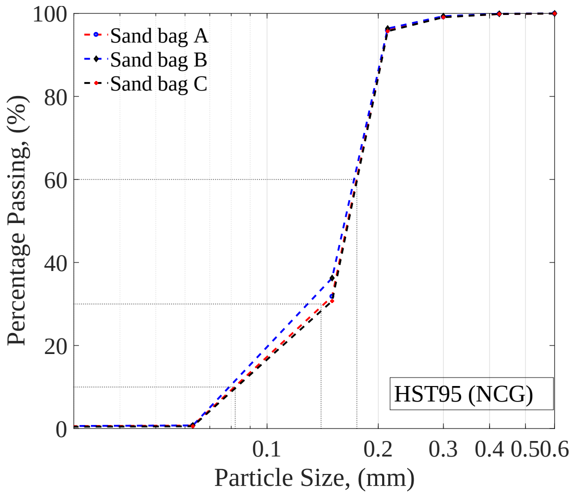

(b) Particle size distribution

Figure 3.34: (a) SEM photo and (b) particle size distribution for HST95 sand.

Direct shear and triaxial tests were carried out on dry sand to obtain the angle of internal friction. From direct shear, the tests were conducted under normal stresses of 20 kPa, 50 kPa, 100 kPa, 200 kPa and 400 kPa and samples were prepared into three different methods: spade pouring (the sand was poured directly into the shear box without tamping, giving a loose relative density of 33%), and sand pouring using a nozzle aperture size of either 3.3 mm or 8.3 mm,giving a relative density of 85% and 33%, respectively. As shown in Fig. 3.35, a Mohr-Coulomb failure envelopes are plotted from the test results at the two different relative densities (33% and 85%). The equation for the best fit line obtained from experiment results is expressed as $\tau_{\mathrm{f}} = \mathrm{c}' + \sigma_{\mathrm{n}}\tan(\phi')$, and the peak friction angle can be determined as $\phi_{\mathrm{p}} = \arctan\left(\frac{\tau_{\mathrm{f}} - \mathrm{c}'}{\sigma_{\mathrm{n}}}\right)$, where c' is cohesion of sand. While the critical friction angle is given as $\phi_{\mathrm{cr}} = \arctan\left(\frac{\tau_{\mathrm{f}}}{\sigma_{\mathrm{n}}}\right)$, where the line of best fit is forced through the y = 0 intercept. The peak and critical state including cohesion values were estimated as indicated in Fig. 3.35(a) and 3.35(b), respectively. However, only critical state value of $\phi_{\mathrm{cr}} \approx 31^{\mathrm{o}}$ is used in the analysis, hence ϕ_{max} and c' are not presented in Fig. 3.35(b).

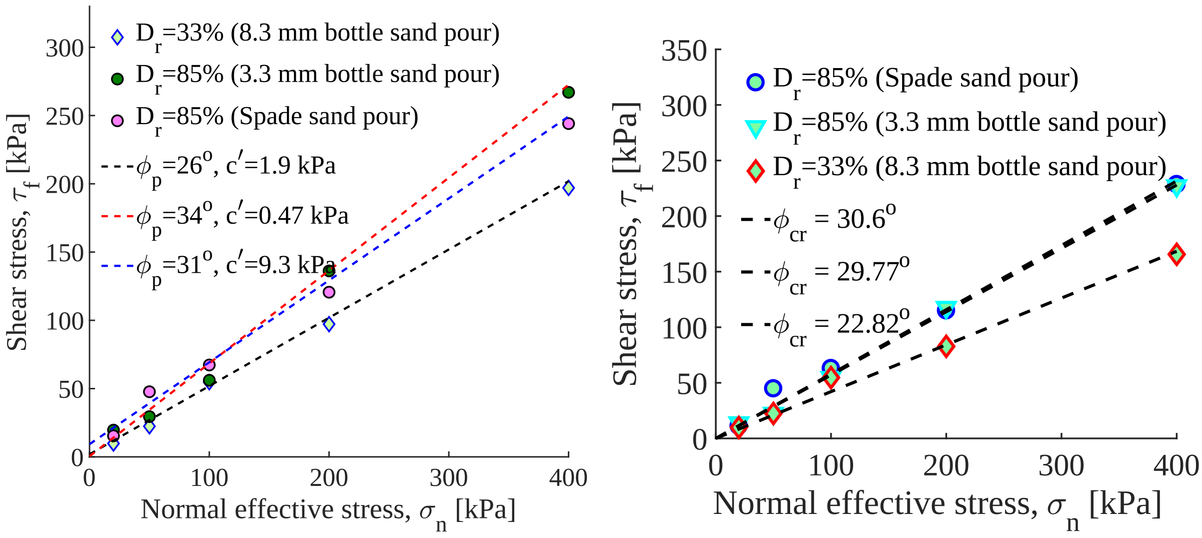

(a) Estimate of peak friction angle (ϕ_p) (b) Estimate of critical friction angle (ϕ_{cr})

Figure 3.35: Mohr-Coulomb failure envelopes drawn from the direct shear tests carried out in HST95 Congleton sand.

The triaxial tests were conducted in dry sands at confining pressures of 50 kPa, 100 kPa and 200 kPa. As shown in Fig. 3.36, the Mohr-Coulomb failure envelopes and cycles of the peak stress results are plotted. The value of peak friction angle ($\phi_p = 35^o$) is shown in the figure. As shown in Fig. 3.35(a), the maximum value of ϕ_p is 34^o. Therefore, the values ϕ_p (from triaxial test), ϕ_{cr} (from direct shear test) are listed in Table 3.6 and ϕ_{cr} = 31^o can be used throughout the thesis. The minimum and maximum density tests were carried out according to BS 1377:

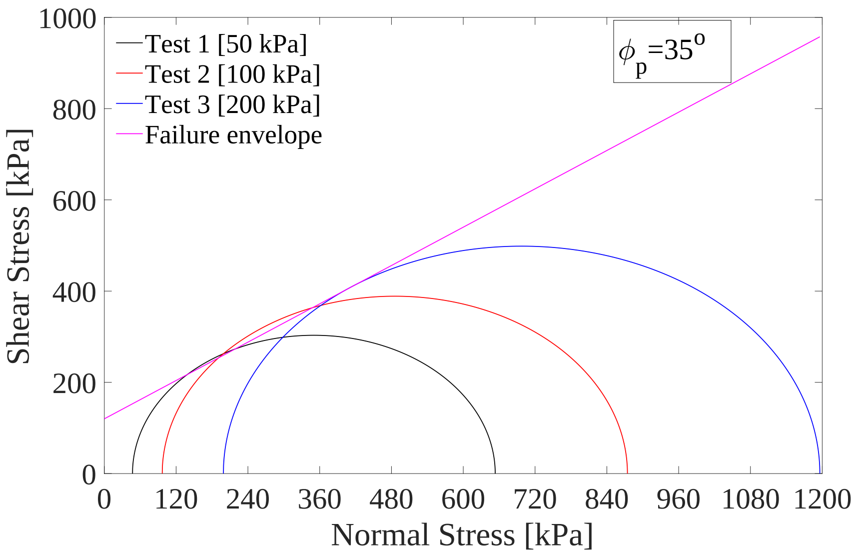

Figure 3.36: Mohrs Circle plotted with the peak stresses of each test.

part 4: 1990, Section 4. All sample tests, conducted in the laboratory, indicated a minimum and maximum densities of ρ_{min} =1450 kg/m^3, ρ_{max} = 1703 Kg/m^3, with corresponding void ratios of e_{max} = 0.776, e_{min} =0.519, respectively. The coefficient of uniformity, $C_u = \frac{D_{60}}{D_{10}}$ = 2.235, indicating that the sand is poorly graded. A summary of material properties is presented in Table 3.6.

Table 3.6: Material properties of of HST95 Congleton sand

Property	**Symbol**	**Unit**	**NCG test**
Particle size	d_{10}, d_{30}, d_{60}	mm	0.082, 0.15,0.17
Specific gravity	G_s	-	2.63
Coefficient of uniformity	C_u	-	2.235
Minimum dry unit weight	$\gamma_{dry,min}$	kN/m^3	14.22
Maximum dry unit weight	$\gamma_{dry,max}$	kN/m^3	16.8
Minimum void ratio	e_{min}	-	0.519
Maximum void ratio	e_{max}	-	0.776
Critical friction angle	ϕ_{cr}	^{o}	30
Peak friction angle	ϕ_p	^{o}	35

The HST95 sand contains about 95% of uniformly graded quartz grains, which after Bolton (1986) and Houlsby (1991), the grains tend to have a critical state angle of friction (ϕ_{cr}) of around 33^o $\pm$ 2^o. To understand the sandy soil behaviour, Bolton (1986) had clarified the relationship between the peak angle of friction (ϕ_p), the angle of dilatancy (ψ), the relative density (D_r) and the mean effective stress at failure (P_m). The angle of dilation (ψ) is mostly depend on the relative density of sand while the critical state friction angle (ϕ_{cr}) is independent. $\phi_{max} - \phi_{cr}$ has been shown as a useful measure of strength due to dilatancy occurred in dense sand and plane strain condition shown by Eq. 3.23 was considered true, where ϕ_{max} is the maximum triaxial angle of friction, ϕ_{cr} is the critical state friction angle, P_m is the mean effective stress (see Eq. 3.24), K_o = 1-sinϕ_{cr} is the earth pressure coefficient at rest, σ_v = γ_dZ is vertical stress, γ_d is the dry unit weight and Z is the depth below the ground surface. The term

$I_R = D_r(10 - \ln P') - 1)$ is known as a relative dilatancy index, which is defined by relative density and effective stress level. I_R offers a unique set of correlations for the dilatancy related behaviour of sands (Bolton, 1986). For most sands, a dilatancy index is available in the range of $0 \leq I_R \leq 4$.

Klinkvort and Hededal (2014) has used Eq. 3.23 to determine the maximum triaxial friction angle, ϕ_{max}, and reported that $\phi_{cv} = 30^o$ observed to capture well the distribution of ϕ_{max} for the tested sand in relation to mean effective stress (see Fig. 3.37(b)).

$$\phi_{max} \approx \phi_{cr} + 3\left[D_r\left(10 - \ln(P_m)\right) - 1\right] \tag{3.23}$$

$$P_m = \frac{1}{3}\left(1 + 2K_o\right)\sigma'_v \tag{3.24}$$

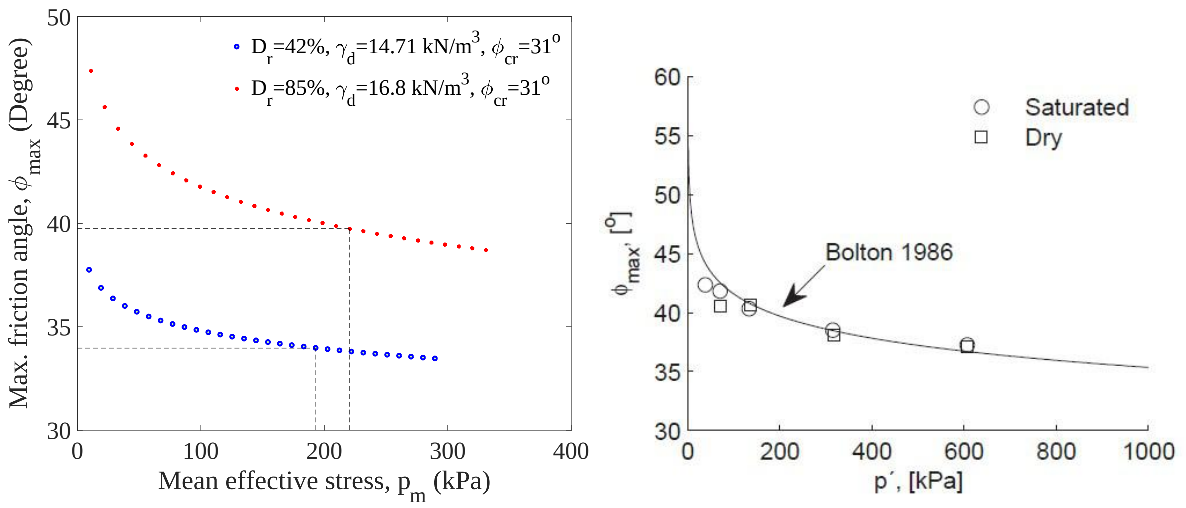

(a) ϕ_{max} from NCG ($P_m = p'$) (b) ϕ_{max} from Klinkvort and Hededal (2014)

Figure 3.37: Estimation of maximum friction angle along the depth of the model.

A dry pluviation single spot hopper was used to prepare the sample and the average relative densities were estimated. The distribution of the maximum friction angle (ϕ_{max}) was calculated using Eq. 3.23 and presented in Fig. 3.37(a), for medium dense and dense sand. The mean effective stress (P_m) was found at a soil depth of $Z = \frac{2}{3}L$, with L defined as the embedded depth of the pile. At this depth, a full similarity of stress between the prototype and model is achieved. In Fig. 3.37(a), the corresponding maximum friction angles at this depth were found to be 40^o and 35^o for dense (D_r = 85%) and medium dense (D_r = 42%) sand, respectively. The critical state friction angle was considered as $\phi_{.cr} = 31^o$.

3.8.2 Soil preparation and pile installation

In the previous studies, related to monopiles in sand, the air pluviation (sand raining) method of sample preparation has been widely used (Arshad and OKelly, 2017, Klinkvort, 2013, LeBlanc et al., 2010). To achieve granular soil models with certain uniform densities, this method was adopted to prepare soil samples for the centrifuge tests. In this study, the multiple-sieving air pluviation method (employed by Mo (2014)) was employed to achieve the relative densities of 42% and 85% for the medium dense and dense sand, respectively. A single-holed sand pour was used to prepare the sample, which include a sand hopper, plate nozzle, and multiple sieves (mesh). The hopper was moved vertically to adjust the falling height and horizontally to fit the circular perimeter of the container. The nozzle and multiple sieves are used to control the flow rate of sand pouring. For instance, the soil model with higher density is obtained with lower flow rate and larger drop height. More details are described below;

1. Before preparing the sample, the sand was glued around the embedded depth (L) and bottom of the cover attached to the pile base to ensure good coupling between the pile and soil (see Fig. 3.38). The roughness of the pile will influence the degree of interaction, which has direct effect on the dilation of the soil. A smooth surface allows the slippage to occur at the interfaces while in the rough surface the failure is expected to take place at a distance from the shaft and the interface friction angle is close to the soil friction angle (Axelsson, 2000, Garnier, 1998). A closed end pile cover was used to replace a volume of soil equal to that of the pile during the installation in order to avoid the soil plugging effect. However, in this study the pile was fixed in the container while allowing the sand to deposit around the pile.

2. The model container was lined with duxseal to a thickness of approximately 15 mm along the sides of the container and 20 mm at the base. The duxseal was used to minimise the effect of vibrations induced by the AKM motor, which could affect the response of pile during testing. A rubber mat was also placed between the base of the container and the aluminium base plate to help reduce the transmission of vibrations. A photo of duxseal and rubber mat on the model container is shown in Fig. 3.39.

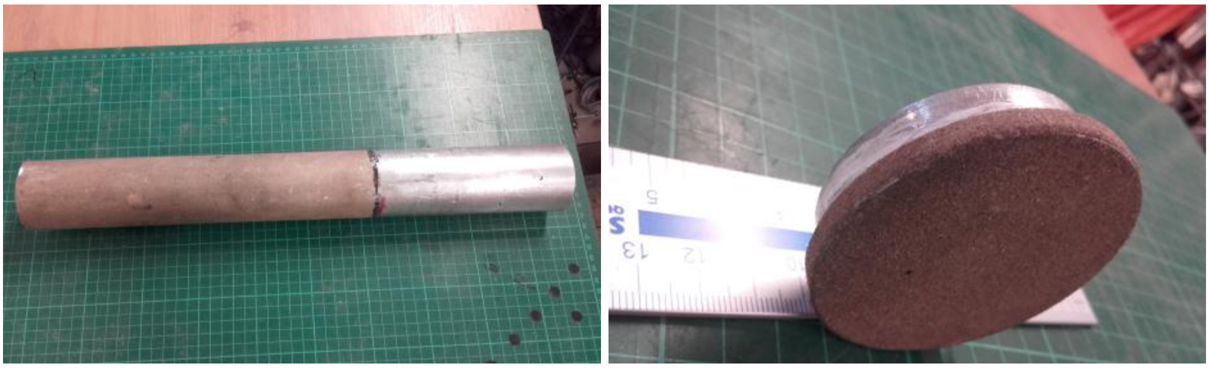

(a) Model pile with sand stuck on it (b) Sand stuck on bottom cover

Figure 3.38: Photograph of sand stuck on pile and bottom cover.

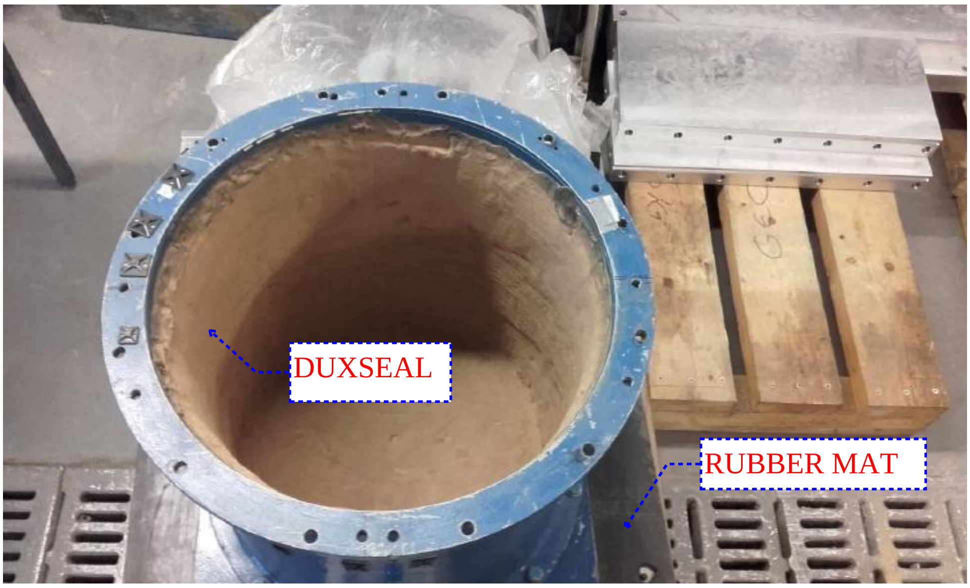

Figure 3.39: Model container lined with duxseal and rubber mat at the base.

3. A range of relative densities (D_r), from medium dense to dense sand, were calibrated by the use of small box ($0.2\text{x}0.2\text{x}0.1$ m^3 in size). The mass of empty box (m_b) was initially recorded and then the hopper, containing sand, was moved vertically to adjust the drop height, h_f, and horizontally to fill the box. From each height, the sample was recorded three times, and its average value was used to determine the relative densities. A photograph indicating this process is shown in Fig. 3.40(a). It is observed that the method of sand pouring provided a high-quality soil preparation. For instance, a medium dense sand (D_r = 42%) was prepared using a large nozzle with pouring height of h_f =

0.5 m, while dense sand (D_r = 85%) was achieved with small nozzle of h_f = 1.2 m. The corresponding void ratio (e_o) for medium dense and dense sand was estimated as 0.769 and 0.467, respectively. According to BS EN ISO 14688-2:2004, the range of relative density sand are in the range of D_r = 35-65% (medium dense sand) and D_r = 65-85% (dense sand).

4. The sand pouring progress was used in the model container, following the circular shape of the container with an adjustment of falling height, h_f. A schematic figure to illustrate the process is shown in Fig. 3.40(b).

(a) Sample calibration process

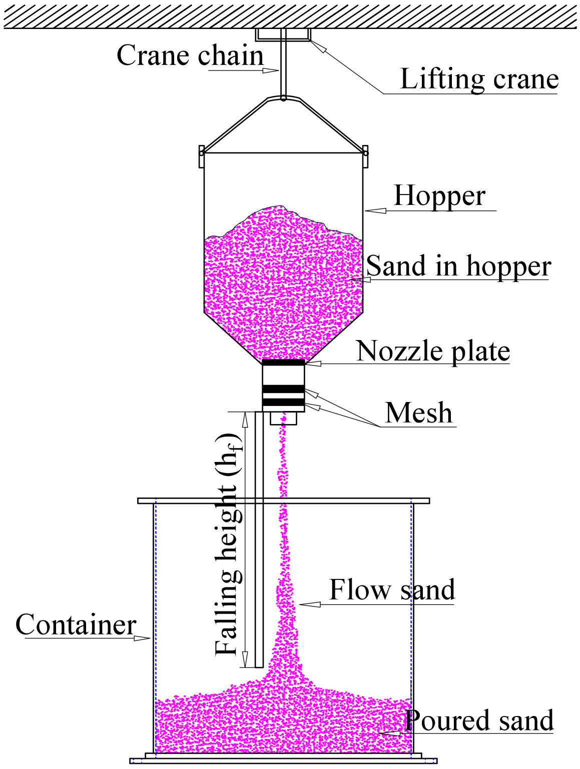

(b) Typical model preparation sketch

Figure 3.40: Sample calibration and model preparation process.

5. When the height of the first layer was reached about 150 mm from the bottom of the container, the pouring process was paused. The model pile was placed in the tub and aligned vertically at the centre (see Fig. 3.41(b)), with temporary supports holding the pile (see Fig. 3.41(a)). The installation of the pile was considered as a *wished in place* closed-ended pile. The capacity of the pile depends on the soil properties and stress state (Engin et al., 2015). The effect of pile installation can be transferred in sand grains

and the pile, leading to an altered soil state and properties. The change of stress and density as well as change of the physical properties depends on the applied installation technique. There are two types of installation techniques: displacement (driven) and non-displacement (wished in place) pile installation. The most notable difference is the stress state around the pile. In the case of displacement piles, the soil is not removed, but displaced and compacted, leading to large stress increases around the pile and the associated increases in strength and stiffness of the soil. In contrast, in a wished-in-place pile, the effect on the stress state of the soil is limited and the soil density around the pile is reasonably constant, or at least lower than would be the case for a driven pile. In this study, wished-in-place method was chosen to avoid the disturbance of the soil structure and the change of the stresses in the soil mass. With glued sand, the method produces an irregular interface between the pile and surrounding soil, which affords good skin frictional resistance under subsequent loading.

(a) Pile support bars

(b) Pile set up process

Figure 3.41: Photographs of pile set up during sand pouring.

6. The sand pouring continued while maintaining a consistent flow rate and falling height until the top of the soil surface was about 50 mm below the top rim of the container.

7. The surface of the sample was levelled to ensure a constant height across the model.

8. At the end of sand pouring, the weight of the container including the base plate, load devices and sand sample was recorded to determine the density. After that, the sample was taken to the preparation room, where the model frame and load devices were connected.

9. Finally, the prepared model was transported and loaded onto the centrifuge cradle using a forklift.

3.9 Instrumentation and data acquisition

The arrangement of the load cells (LC) and linear variable differential transducers (LVDT), for both monotonic and cyclic experiments, is presented in Figure 3.42 and 3.44, respectively. These instruments were connected to record/measure the static/cyclic loads and displacements, respectively. The connected sensors aimed to determine the load-displacement response, rotation of model pile and its settlement.

Under monotonic loading (see Fig. 3.42), the miniature load cell (with the capacity of 10 kN, provided by Richmond Industries Ltd) was used to record the magnitude of monotonic loads applied to the pile head. The lateral loads were employed by use of the loading system actuator. Along the section of the pile, above the soil surface, two horizontally mounted LVDTs (top and bottom), one located 110 mm below the other, were used to record the lateral displacement of the pile. This arrangement allows to determine the rotation (tilt) of the rigid pile from its initial vertical alignment, the depth to the point of rotation below the ground surface, and lateral displacement at the ground surface. Figure 3.43 shows a photograph of the load cells and LVDTs used for the monotonic lateral loading tests.

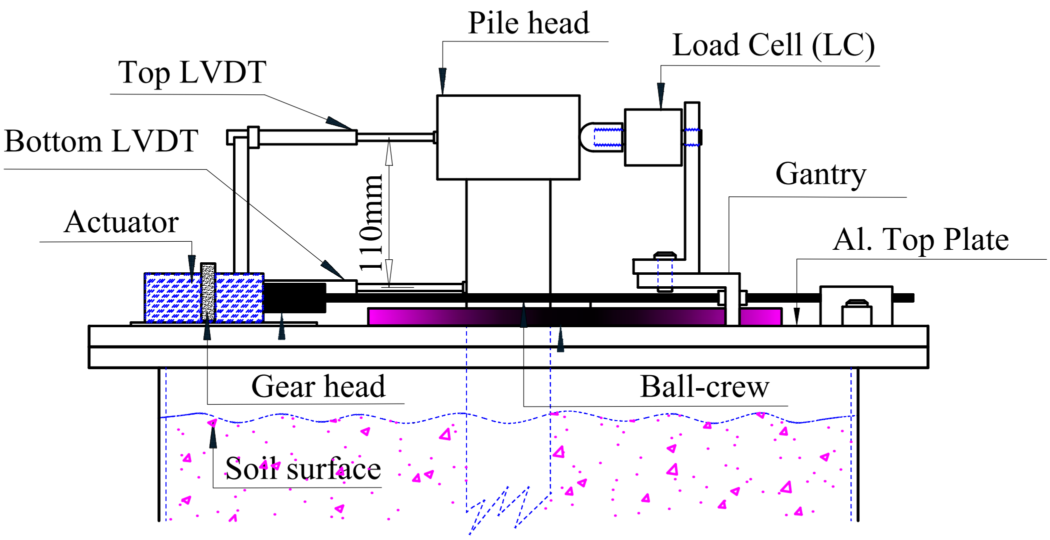

Figure 3.42: A general layout of the load cell and LVDTs arrangement used for monotonic loading tests

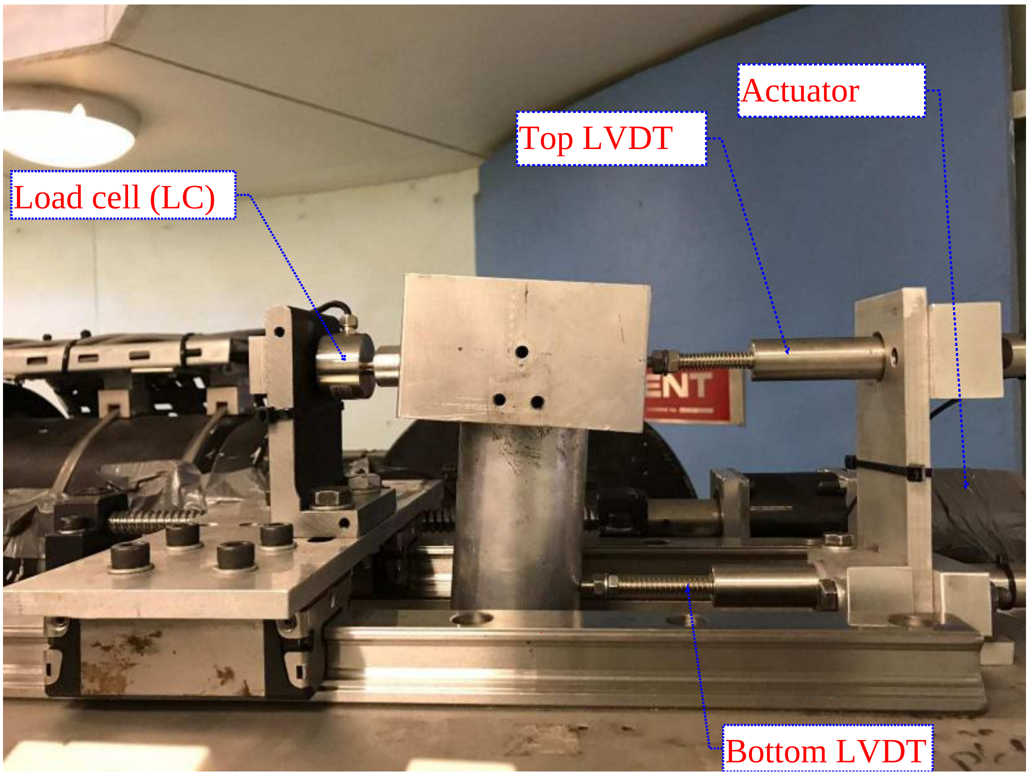

Figure 3.43: A photo of the load cells and LVDTs used for monotonic loading tests.

Under cyclic loading, a new system arrangement was made (see Fig. 3.44) with two horizontally mounted LVDT (2 and 3) located 80 mm and 155 mm above the soil surface, respectively. A fourth LVDT (4), mounted vertically on the top of pile head, was used to measure the vertical pile displacement. Another LVDT (1) was connected to the loading device and not shown in Fig. 3.44 (presented in the previous section). Two miniature in-line load cells were mounted on either side of the pile head for recording the tensile forces applied to the pile cap. Figure 3.45 shows a photograph of the load cells and LVDTs used for the cyclic lateral loading tests.

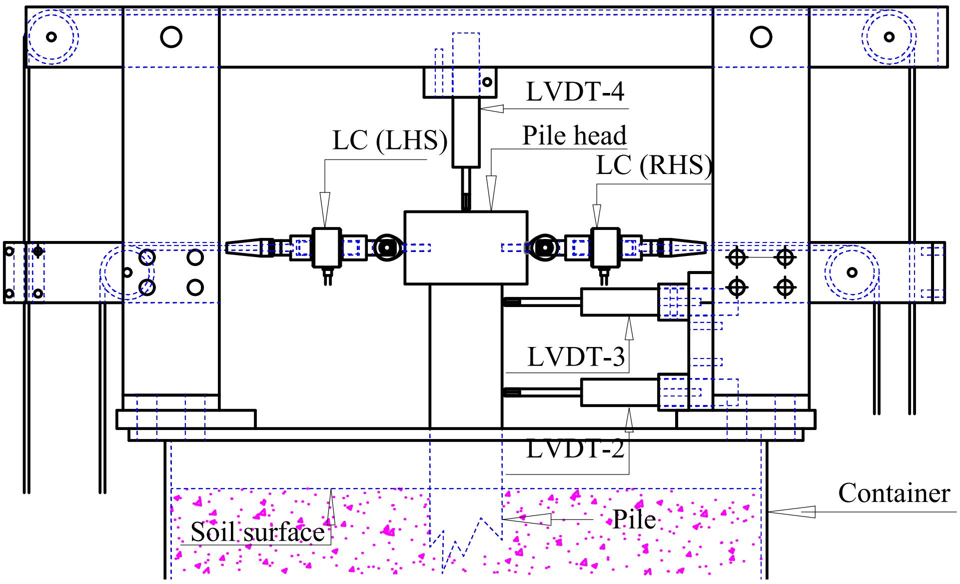

Figure 3.44: Arrangement of load cells and LVDTs on pile under cyclic test.

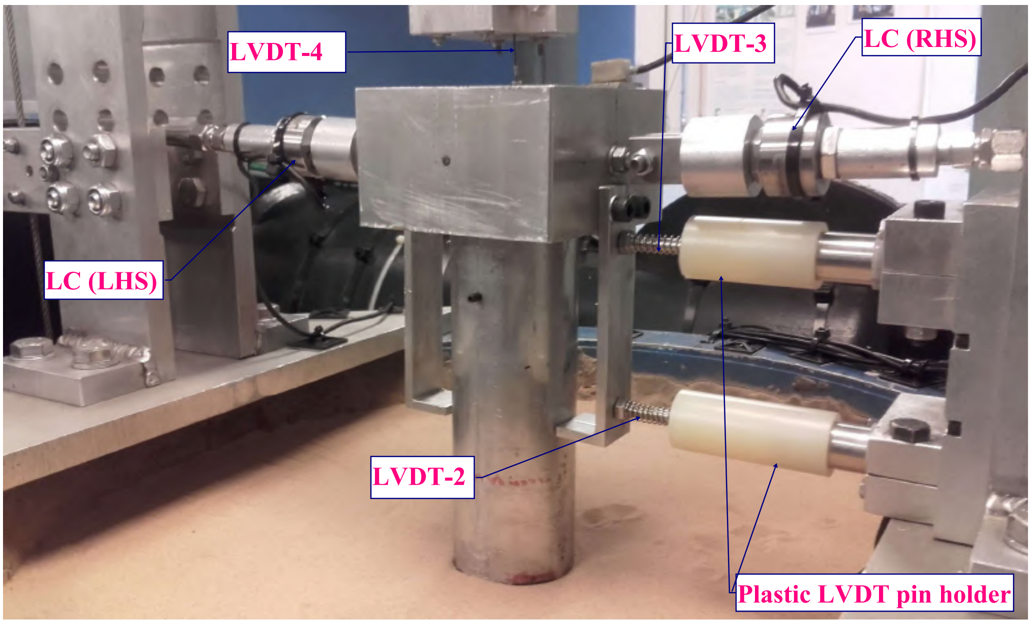

Figure 3.45: A photograph of the load cells and LVDTs used for cyclic loading tests.

The instruments utilised on both monotonic and cyclic tests are briefly described in the subsequent sections.

3.9.1 Linear Variable Differential Transducer (LVDT)

To measure the lateral and vertical displacement and settlement of the surface, Linear Variable Differential Transformers (LVDTs) were utilised. An LVDT, as shown in Figs. 3.43 and 3.45, provides an accurate indication of cumulative displacement. It converts a linear displacement from mechanical reference into electrical signal containing phase (for direction) and amplitude (for distance) information. In this study, a Solartron Metrology LVDTs were used with a maximum stroke length of 25 mm (horizontal LVDT, see Fig. 3.46(a)) and $\pm$2.5 mm (vertical LVDT, see Fig. 3.46(b)). The output voltage range is specified as 5V and sensitivity of 750 mV/mm @ 10 V dc for horizontal and vertical LVDT, respectively. These LVDTs offers an excellent accuracy of better than 0.1% and 0.5% on the lateral and vertical LVDT, respectively.

(a) LVDT1, LVDT2 and LVDT3 (b) Vertical LVDT-4

Figure 3.46: Linear variable differential transducers (LVDT).

3.9.2 Micro-Electro-Mechanical System (MEMS)

Micro-Electro-Mechanical System (MEMS) accelerometers are the small electrical device which measures acceleration by measuring the force that a mass applies to a spring. They have been used widely in geotechnical engineering for full-scale monitoring and have also been used laboratory testing. At the initial stage of the model development, the soil sample and the system were affected by the AKM motor vibration. The MEMS accelerometers, which are shown in Fig. 3.47(a), 3.47(b) and 3.47(d), were primarily utilised to monitor the the vibration of the model system. Plastic material was used to cover the MEMS which was then glued to a thin square aluminium plate with Araldite. Type ADXL78 MEMS accelerometers, manufactured from Analog Devices, measure the acceleration with a full-scale range of ±35g and ±70g. The ADXL78 MEMS type of ±35g were used to monitor the vibration induced to fixed components. The ADXL78 MEMS type ±70g were installed to monitor the acceleration due to vibration of the moving parts: loading weight, M_1, connecting rod and see-saw. These ADXL78 MEMS accelerometers have an accuracy of 0.2% of the full-scale.

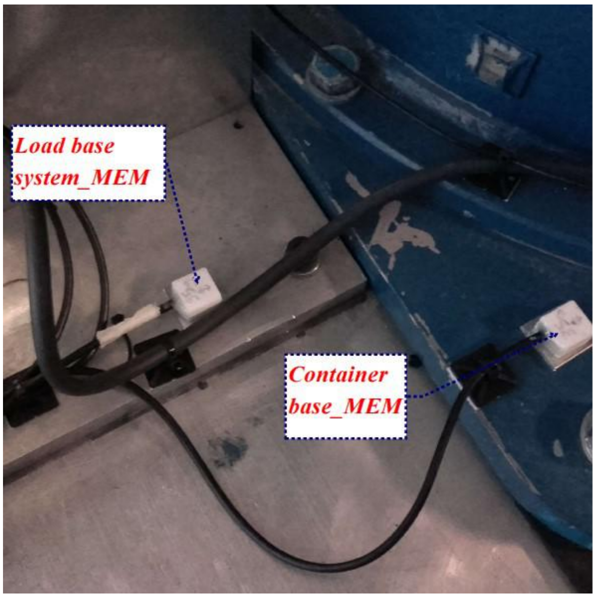

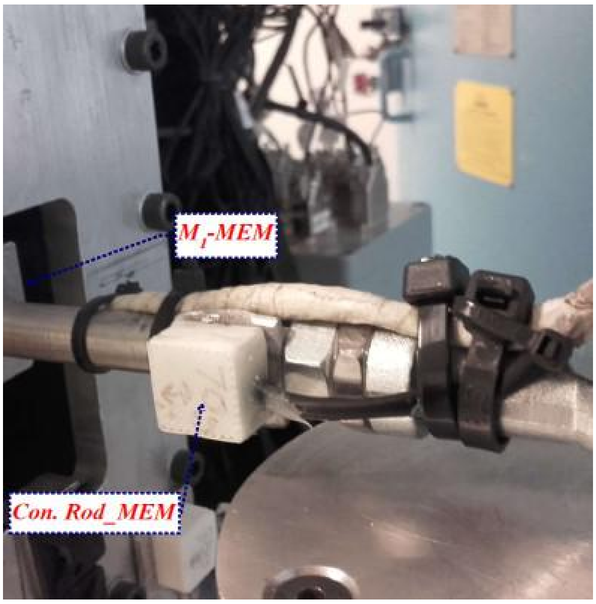

(a) MEMS on M_1 loading and container bases (b) MEMS on weight, M_1, and connecting rod

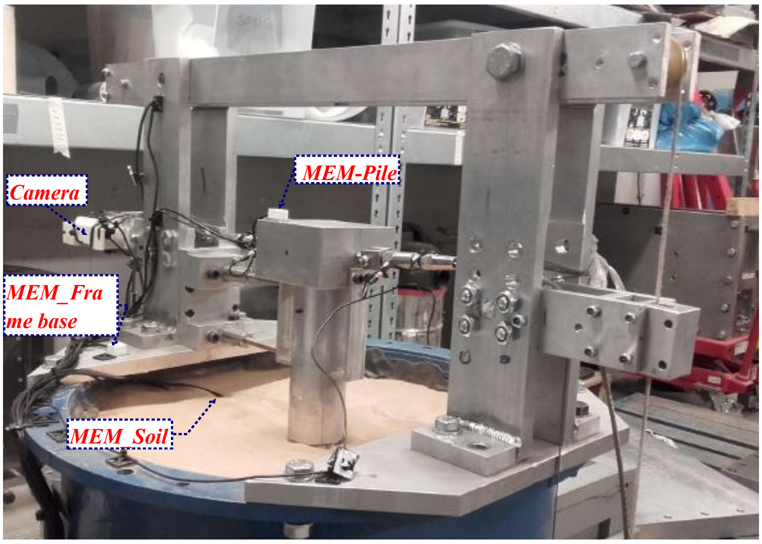

(c) Camera fixed on RHS frame (d) MEMS on pile head, soil and base frame

Figure 3.47: MEMS placed on the model and camera fixed on LHS overhang frame.

3.9.3 Web camera

As shown in Fig. 3.47(c), a web camera was installed and utilised. In the cyclic loading system, the camera was fixed on the RHS frame facing down to observe and monitor the operation of the mechanical load system, ensuring safety and avoid any damage to the centrifuge. The web camera installed in monotonic device was placed on top of the aluminium base plate facing the load cell and two LVDTs (bottom and top). This was aimed to monitor the performance of these instruments. Photos were not taken and video were not recorded during the testing.

3.9.4 Load cells

The 200 Series miniature in-line load cells (provided by Richmond Industries Ltd, UK) were mounted on pile head to measure the total load acting at the pile (see the arrangement in Figs. 3.42 and 3.44). These load cells have an accuracy of ±0.05% and a safe overload of 150%. The excitation Voltage and sensitivity of this type of load cell is 10V and 2.0 mV/V, respectively. The capacities of the load cell were 5, 10 kN and 2 kN for monotonic and cyclic load experiments, respectively. The photograph of 2 kN load cell including its dimensions are shown in Figs. 3.48.

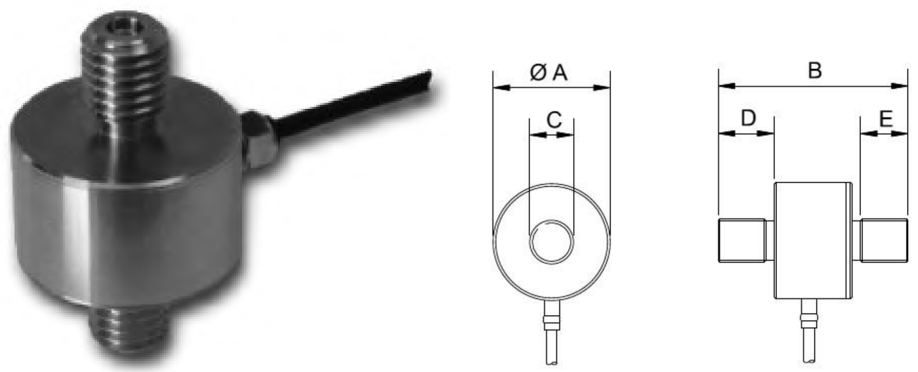

(a) Inline load cell, 2 kN (b) A=32, B=50, C=M12, D=15 mm

Figure 3.48: Typical load cell (LC) and its dimensions.

3.10 Testing programme and procedures

3.10.1 Introduction

A centrifuge model testing program was carried out to study the monotonic and cyclic lateral response of monopiles. The testing plan, as well as the general procedure used for testing model pile in dry sand, is discussed in this section. The detail of the testing plan is outlined in Section 3.10.2 and the process involved to carry out each the experiment is presented in Section 3.10.3.

3.10.2 Testing programme

The proposed cyclic load testing plan is categorised into four phases described below and summarised in Table 3.7;

1. *Phase one*; During the course of this study, 4 centrifuge monotonic tests were conducted and named as OWTP/S-T01, OWTP/S-T02, OWTP/S-T03 and OWTP/S-T04. The tests were identified as follows; OWTP-Offshore Wind Turbine Pile, S-Static and T-Test. The first three tests, OWTP/S-T01 to T03, were used to determine the pile-head load-displacement response and ultimate capacity of the pile. Test T04 was used as a reference to cyclic loading tests.

2. *Phase two*; The tests, OWTP/C-T10 to OWTP/C-T11, were used to develop the equipment and testing methodology. To ensure that the loading devices and other components of the system are operating in a centrifuge, the tests were conducted at centrifuge acceleration of 1g to 90g. The test bed was poured into the container and compacted without considering the relative density. The pile was installed following the procedure described in Section 3.8.2.
   At the initial stage, unrecorded tests were carried out at 1g to check the system part connections and performance of all sensors. During the testing trials, the load cells (dynamic and static) were connected inline with tension wires on the pile-head and ends of the loading weights (M_1, M_2), to check the friction losses. The dynamic load cells did not provide proper results, and only static load cells (SLC) were used. The centrifuge was

then spun again, however, in the midst of 40 - 50g, the AKM motor stopped to rotate the shaft due to the effect of weight, M_1. To address the challenge, the side and bottom rails were added to the weight, M_1, to prevent the effect of bending during the spinning. This option was unsuccessful, so thrust bearings were alternatively added on top of box used to protect the AKM motor. It was aimed to free the shaft from the weights of the crank-discs and connecting rod. In addition, the initial set-up of loading weight M_1 = 2 kg was reduced to 0.5 kg. The testing was then repeated and centrifuge was successfully spun up to 90g. The centrifuge was spun down to 1g. The loading weight of M_1 = 0.5 kg was replaced by the weight of 2 kg, the centrifuge package was then spun in stages, however, at more than 30g the AKM motor was unable to spin the shaft, and all tests were set at the centrifuge acceleration of 30g.

3. *Phase three*; The preliminary cyclic loading tests: OWTP/C-T12, OWTP/C-T13, OWTP/C-T14 and OWTP/C-T15. The tests were identified as; for instance, OWTP/C-T15-FO3, where OWTP is Offshore Wind Turbine Pile, C is Cyclic, T is a Test and F is Flight. The test-bed was prepared by pouring dry sand in the container and compacted. The pile was installed as described in Section 3.8.2 and all connections followed the normal procedure. The tests were carried out at 30g. From the four tests, only results of test OWTP/C-15 were recorded during the testing trials to understand the effect of cyclic load control factor, ζ, change of applied weight, M_2, and tension wires location of T_1 and T_2 on the see-saw plate. The results of test OWTP/C-T15 is presented in Section 3.11.
   Before carrying out test OWTP/C-T15, tests OWTP/C-T12 to OWTP/C-T14 were performed to balance the dead weight, M_2 and applied load, M_1, on the see-saw. For instance, in test OWTP-T12-F03, the tension wire locations (l_1 and l_2) on the see-saw plate were adjusted to increase the effect of applied weight, $M_1 = 2$ kg, in order to balance the weight $M_2 = 2$ kg. This option did not work, which resulted in the reduction of the dead weight M_2, from 2 kg to 1 kg. This set-up was successfully carried out in test OWTP/C-T12-F04 with a balance on both sides when spun at 30g (125 rpm). However, the results for test OWTP/C-T13, which take into account the influence of increasing motor frequency (f_m) was not ignored despite the fact that the system did not balance. Before carrying out test OWTP/C-T14, the mass on the dead weight side, M_2, was increased to 1.5 kg, with additional mass on M_1 from 2 to 3 kg and balanced weight, M_3

Table 3.7: Testing programme

Test ID	**Test type**	**D_r**	γ_d	ζ	**g-level**	**M_1**	**M_2**	**M_3**	**f**	**N**
	Phase-1									
OWTP/S-T1	Static	85	16.8	-	100	-	-	-	-	-
OWTP/S-T2	Static	85	16.8	-	100	-	-	-	-	-
OWTP/S-T3	Static	42	14.2	-	100	-	-	-	-	-
OWTP/S-T4	Static	85	16.8	-	30	-	-	-	-	-
	Phase-2									
OWTP/C-T10	Cyclic	-	U	-	$N^*_{g(10)}$	2	2	2	f^*_{10}	NR
OWTP/C-T11	Cyclic	-	U	-	$N^*_{g(11)}$	2	2	2	f^*_{11}	NR
	Phase-3									
OWTP/C-T12	Cyclic	-	U	0	30	2	$M^*_{2(12)}$	2	2.5	NR
OWTP/C-T13	Cyclic	-	U	0	30	2	1	4	2.5	NR
OWTP/C-T14	Cyclic	-	U	0	30	2	1.5	4	2.5	NR
OWTP/C-T15	Cyclic	-	U	ζ^*_{15}	30	3	$M^*_{2(15)}$	4	f^*_{15}	R
	Phase-4									
OWTP/C-T16	Cyclic	85	16.8	ζ^*_{16}	30	3	1.5	4	2.5	N^*_{16}
OWTP/C-T17	Cyclic	85	16.8	ζ^*_{17}	30	3	1.5	4	2.5	N^*_{17}

D_r, γ_d, U ; Relative density [%], Dry unit weight [kN/m^3], Unprepared sample
NR, R ; Not Recorded, Recorded
M_1, M_3 ;Applied weight [kg], Balance weight [kg]
$N^*_{g(10)}$, $N^*_{g(11)}$; Centrifuge acceleration gravity from 1g to 90 g
f^*_{10}, f^*_{11}, f^*_{15} ; Loading frequency, [Hz], f^*_{10}=f^*_{11}= 0.5-2.5Hz, and f^*_{15}=1, 2.5 Hz
$M^*_{2(12)}$, $M^*_{2(15)}$; Dead weight, [kg], $M^*_{2(12)}$ =1, 2 Kg and $M^*_{2(15)}$ =1, 1.75, 2 Kg
ζ^*_{15}, ζ^*_{16}, ζ^*_{17} ; load control ratio, ζ_{15} =-1.5, 0, 0.5, 0.75, 1, 1.5 ζ^*_{16} =-1, 0, 1 and ζ^*_{17} =-1, 0
N^*_{16}; Number of load cycles T16, [F02, N=8600; F03A, N=11186; F03B, N=21025; F04, N=32880; F05, N=58200]
N^*_{17} ; Number of load cycles T17, [F03, N=58800; F04, N=4000; F05, N=16395]

was set to 4 kg. Although the system under this setting was successfully balanced, there were minor setbacks caused by the stepper motor and bottom LVDT. These were checked before running the following tests.

4. *Phase four*; The main cyclic load tests: OWTP/C-T16 and OWTP/C-T17. The model sample on these tests was carefully prepared at a relative density of 85% and the model package was spun to centrifuge acceleration of 30g (equates to speed of 125 rpm). It should be noted that the similar model pile designed at a geometrical scale of N_S=100 was used for all tests. Due to technical challenges, all tests were conducted at a centrifuge acceleration of 30g and the results was aimed to demonstrate model performance and

Table 3.8: Description of the test OWTP/C-T15, OWTP/C-T16, and OWTP/C-T17

Test ID	Flight	Description
OWTP/C-T15	F01	Tested from 1-30g to stabilise the soil, long run test at 30g, problem with LVDT, data was recorded.
	F02	Malfunction of stepper and AKM motors, the data recorded to checking the capability of the two motors.
	F03	Technical challenge from weight M_1, no data was recorded.
	F04	Load control ratio, ζ, was tested to observe maximum AKM velocity and voltage, no data was recorded.
	F05	The problem with bottom LVDT, data was recorded.
	F06-10	Tests were carried at 30g to observe the effect of ζ (Varied from -1.5 to 1.0), T_2 location from l_2=25 mm to 45 mm and M_2=1.5, 1.75, 2 kg. The results are presented in Section 3.11.
OWTP/C-T16	F01	Prepared sample and tested from 1-30g to stabilise the soil, problem with weight imbalance, the data was not recorded.
	F02	Tested from 1-30g to observe the weight balance and some data were recorded for ζ=0.
	F03	The long run test carried out at 30g (ζ = 0) in the late hours of the first day and then continue the following day, data was recorded.
	F04	The long run test at 30g (ζ = 1) continued in the second day, data was recorded.
	F05	Long run test conducted at 30g (ζ = -1), data was recorded
OWTP/C-T17	F01	Prepared sample and tested from 1-30g to stabilise the soil, problem with weight imbalance, data was not recorded.
	F02	Tested from 1-30g but LVDT sensors did not respond in the LabVIEW user interface, data was not recorded
	F03	Long run test carried at 30g (ζ = 0), data was recorded
	F04	Test continued at 30g (ζ = 0) and thereafter it was changed to ζ = -1; data was recorded.

Note: Each F represents a single flight, where the centrifuge was spun to the specified g-level and a test was performed.

ability to represent the behaviour of offshore monopile foundations. Description of tests OWTP/C-T15, OWTP/C-T16 and OWTP/C-T17 is summarised in Table 3.8.

3.10.3 Testing procedure

The general centrifuge test procedure was as follows;

1. As discussed in Section 3.8.2, once the model was loaded onto the swinging platform, the data acquisition computers, the power for all instruments, amplifiers and the servo control were switched on and checked.

2. Calibration of the instruments such as load cells and LVDTs was carried out before connecting to the centrifuge model.

3. All instruments (load cells, LVDTs, MEMS and cameras), power components (AKM and stepper motor) including tension wires were connected to the specific locations. The tension wires were connected in-line with the load cells and its ends were attached to the weights and pile-head.

4. All instruments and motor cables were connected to the data acquisition panel of the centrifuge arm. Thereafter, the counterweight of the package about the mass of the model was set-up to balance the system.

5. All cameras and video monitors in the centrifuge and control rooms, respectively, were turned on to observe the model in-flight.

6. A user interface in LabVIEW was checked to ensure that the controls and indicators for all sensors connected in the DAS were responding correctly.

7. Under the cyclic loading experiment, the centrifuge package was spun incrementally until the desired 30g centrifugal acceleration was achieved. The initial readings of the vertical LVDT (LVDT-4) were recorded prior to stabilisation. Thereafter, the centrifuge package was spun down to 20g, 10g and back to 30g while recording the values of LVDT-4. The process was repeated three number of times until the settlement stabilised. After stabilisation, the speed of the centrifuge was kept constant at 30g. This process was performed only for the first series of pile loading. It should be noted that this process was only performed on the first pile loading of each test. However, for the monotonic centrifuge experiment, a similar procedure of stabilisation was used at 100g and 30g.

8. During the cyclic experiments, the load cycles were applied to the pile in different sets of cycles based on the cyclic load control ratio, ζ. Throughout the cycles in a particular test, the control ratio, ζ, was programmed using an automated load control system. For each set of the centrifuge tests conducted in a similar sandy soil, the load characteristics

programmed into the automated load control system were maintained with only cyclic load control ratio varied. Therefore, after stabilisation, the next stage was to switch on the stepper motor to allow the adjustment of the desired value of ζ. This was aimed to set the loading magnitude at zero, positive or negative direction. Furthermore, after choosing the factor ζ the location of weight M_1 was adjusted by moving the stepper motor (which controlling the position of the AKM motor and discs (refer in Fig. 3.14)) forward and backward while observing the peaks of the load cell graphics in the LabVIEW interface. During this process the AKM motor was switched on and rotated at low frequency of f = 0.5 Hz.

9. After setting the location of weight M_1, the stepper motor was switched off while the frequency of the AKM motor was increased stepwise from 0.5 to 2.5 Hz. At constant frequency of 2.5 Hz, the test was allowed to run for a specified period. It should be noted that the time and the number of load cycles achieved from each test were different. For instance, in test OWTP/C-T16, a total period of 10 hours was used to achieve approximately 60,000 load cycles.

10. At the end of each experiment, the centrifuge was spun down to 1g and the above steps were repeated for the next test.

3.11 Overview of testing programme and preliminary results

3.11.1 General overview

Tests OWTP/C-T16 and OWTP/C-T17 were carried out at 30g with model piles installed in the dry Congleton sand. The primary purpose of these tests was to demonstrate the capability of the newly developed rig compared to previous studies. During each of these tests, a series of tests (named flights) were conducted based on the cyclic load ratio as shown in Table 3.7. To determine the effect of the loading magnitude affected by ζ, three flight sets of N cycles were conducted during each test with the load control varied after each flight.

Test OWTP/C-T15 was carried out as a preliminary experiment to observe the effect of load control factor, ζ, dead weight (M_2) and location (l_2) of applied weight (M_1). The observations were made regarding the adequacy of the testing arrangement and its results are presented and discussed in the following section.

Monotonic tests were carried out at 100g (OWTP/S-T1, OWTP/S-T2, and OWTP/S-T3) for the comparison to the current formulations suggested by DNV (2014) and Ramberg and Osgood (1943). Test OWTP/S-T4 was performed at 30g as a reference for the cyclic tests and to identify a suitable backbone curve for the analysis of cyclic lateral loading.

To accurately simulate the full-scale cyclic loading condition, the monopile has to be loaded cyclically with frequency and number of load cycles representing 20-25 years of turbine lifetime. In general, the loading frequency for the design of monopile foundations falls in soft-stiff design criteria with a natural frequency between 0.3 to 0.5 Hz, for 5 MW class wind turbines. The loading frequency for the centrifuge model is N_s times that of the prototype frequency. The model size was is reduced 100 times compared to the prototype. As shown in Fig. 1.7, Chapter 2, the design natural frequency between 1P and 3P (0.3 to 0.5 Hz) would be 30 to 50 Hz in a centrifuge. The monopiles for offshore wind turbines are expected to experience 10^7 number of cycles over their design life, hence the model pile in the centrifuge should be loaded at least 10^6 cycles. This ensure the change of the model pile natural frequency is measured over most the expected cyclic loading. In this study, efforts were made to achieve the frequency of 30 Hz using the AKM motor, however due to technical limitations of the AKM motor, the cyclic loading of the monopile was not a complete representation of prototype loading conditions. The frequency range between 0.1 to 2.5 Hz was used as the loading frequency in the centrifuge. This converted to prototype frequencies that are many times below the full-scale frequencies between 1P and 3P. With a low loading frequency, including time and physical constraints, it was not possible to achieve millions of load cycles. The pile was cyclically loaded with the number of cycles shown in Table 3.7. For the last two tests OWTP/C-T16 and OWTP/C-T17, the pile was loaded with a constant frequency of 2.5 Hz and results are limited only for demonstration of the model capability.

3.11.2 Displacement and stiffness of the test OWTP/C-T15-F01

For the preliminary experiments, Congleton sand and aluminium model pile were used. The test bed was prepared by pouring sand in layers in the container and compacting it using a steel rod.

The pile was installed in similar method discussed in Section 3.8.2. A number of cyclic load tests were conducted on the model pile and observations were made regarding the amplitude of load, displacement and unload-reload stiffness. During this test, the load cycles were applied to the pile in different flights of N cycles. An automated load control system was used throughout all the flights to programme the cyclic loading factor, ζ. As discussed in Table 3.8, the long run test OWTP/C-T15-F01 was set at ζ=0 and the number of cycles achieved as shown in Fig. 3.49 was approximately 43000 cycles. Fig. 3.49 plots the maximum and minimum displacement of the pile-head during a load cycle, which occur under corresponding maximum and minimum loads at the pile head. The observed behaviour indicates that the displacement increased most during the first 500 cycles and then the increase rate reduced as number of cycles increased. The accumulated displacement of the pile is affected by the system stiffness. As shown in Fig. 3.49, the stiffness of the first 30 cycles is noisy and was not taken into account due to difficulties related to the ability of the loading system to apply consistent loads. These results provide a good indication of the model performance.

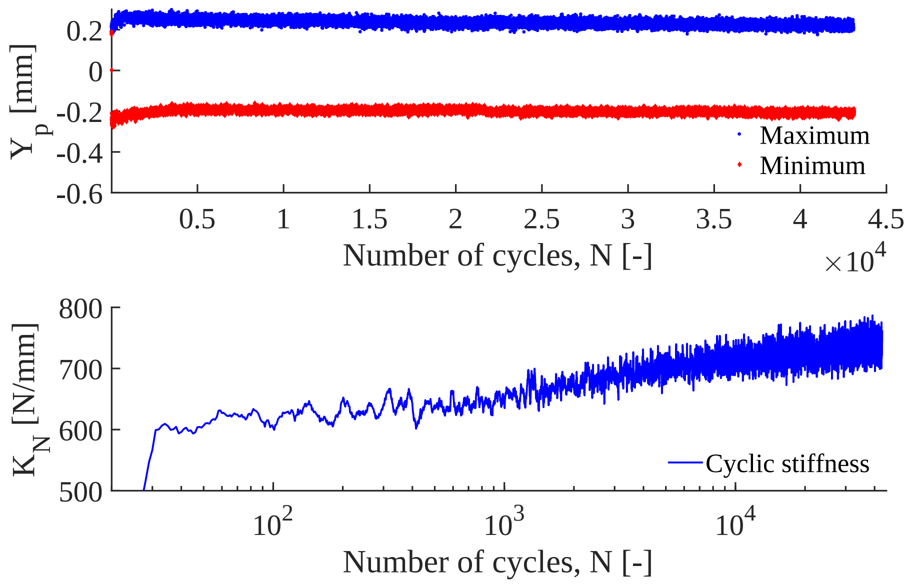

Figure 3.49: Pile-head displacement and cyclic secant stiffness versus number of load cycles, N, for test OWTP/C-T15-F01

3.11.3 Effect of load control factor, ζ

In the test OWTP/C-T15, the observations of load and displacement were made based on the effect of parameter ζ. The following are the major observations and modifications made to the loading device for further tests.

1. The observations of test OWTP/C-T15-F01 were described in Section 3.11.2. The tests T15-F02 to T15-F05 were briefly described in Table 3.8. Only tests from T15-F06 to T15-F10 are used in this section to demonstrate the effect of changing the load control, weights and their locations on the loading device system. However, test T15-F06 is similar to test T15-F07 and is not shown in the discussion.

2. The graphs in Fig. 3.50 and 3.51 shows the results of cyclic loads versus number of load cycles. From each figure, the dead weight M_2=2 kg was kept constant while varying the load control ratio, ζ. It can be seen that by changing the T_2 position from l_2=25 to l_2=45 mm, the value of cyclic loads, H_i, is increased. For instance, by using the value of ζ=0 and ζ=1, the cyclic load increased from 188 N to 398 N and 255 N to 560 N, respectively.

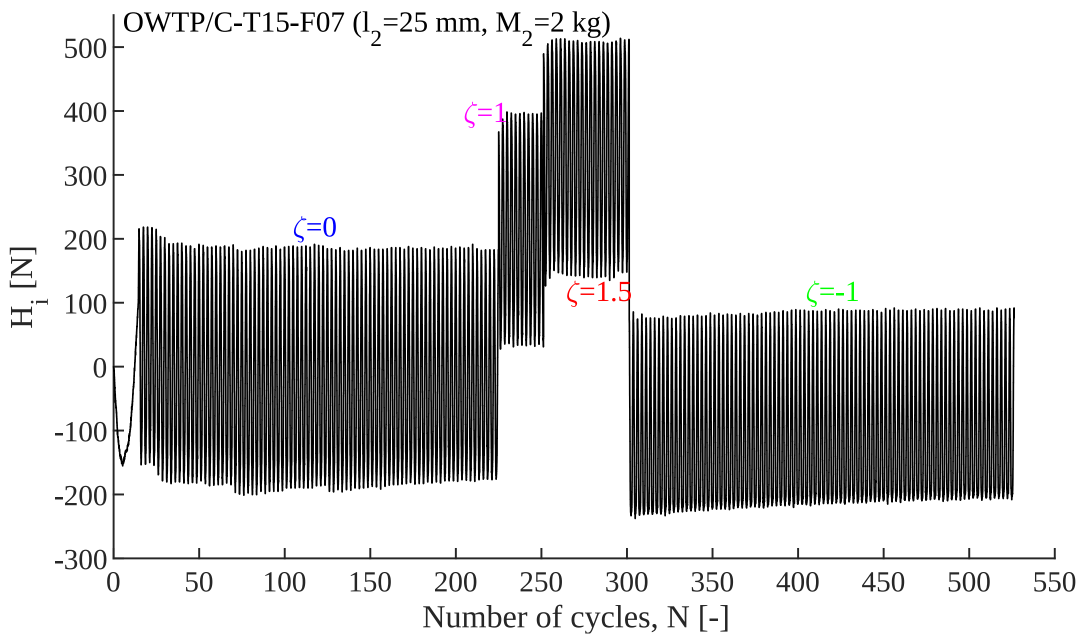

Figure 3.50: Effect of ζ, l_1=15 mm, l_2=25 mm, and M_2=2 kg.

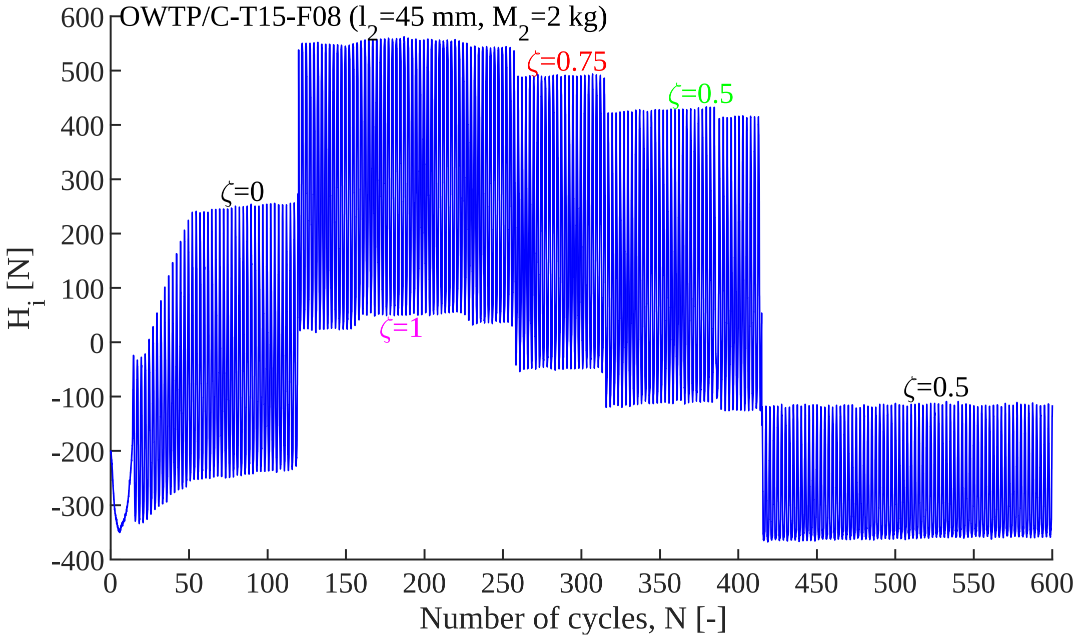

Figure 3.51: Effect of ζ, l_1=15 mm, l_2=45 mm, and M_2=2 kg.

3. The graph in Figs. 3.52 and 3.53 show the variation of load application caused by ζ against the number of load cycles. In these tests, the location of T_2 (l_2=35 mm) was kept constant while changing the weight M_2 from 1.5 kg to 1.75 kg. By taking the value of ζ equal to 0, 1. 1.5 ans -1.5, the cyclic load (H_i) observed to be lower for 1.5 kg compared to 1.75 kg. This is inline with the concept that any increase of load amplitude will induce more load on the model pile.

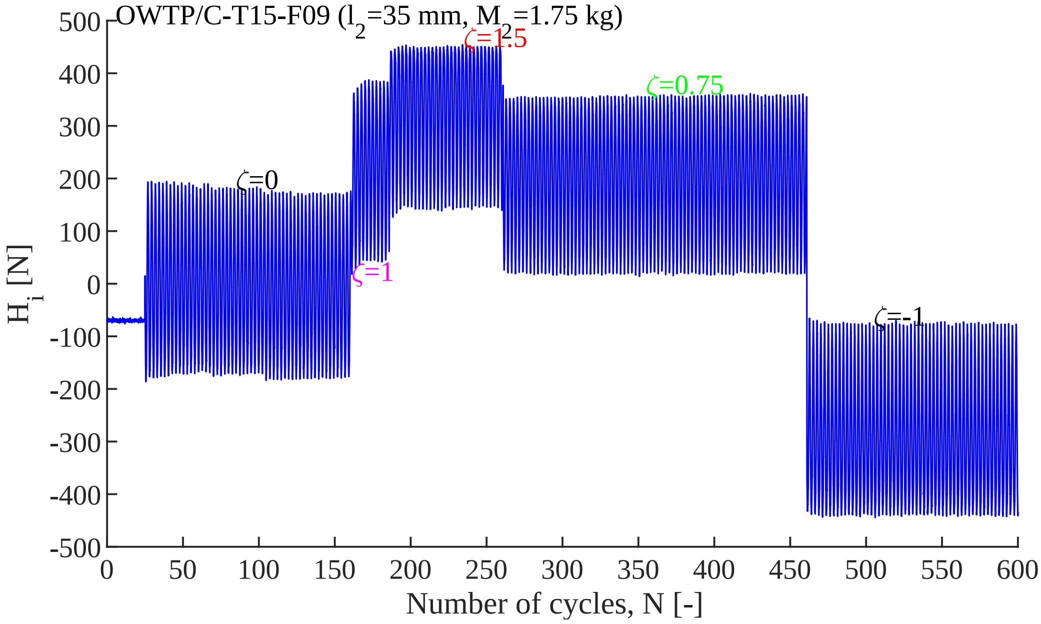

Figure 3.52: Effect of ζ, l_1=15 mm, l_2=35 mm, and M_2=1.75 kg.

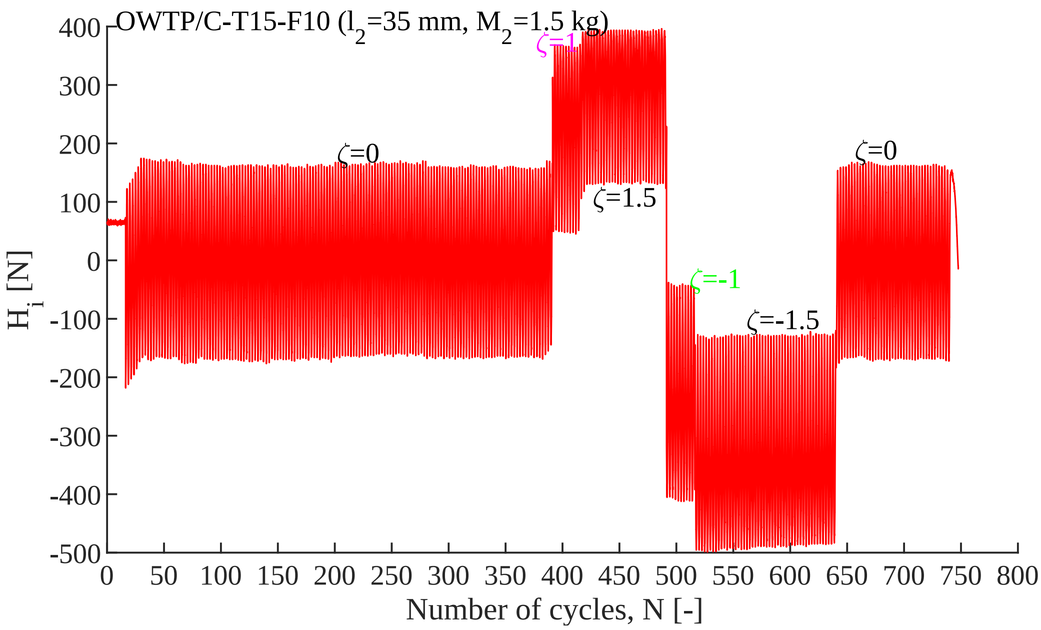

Figure 3.53: Effect of ζ, l_1=15 mm, l_2=35 mm, and M_2=1.5 kg.

4. Overall, it can be seen that the tension wire position (T_2) and change of weight M_1 have an impact on load transferred to the model pile. For instance, in Fig. 3.51, the model pile experience a large magnitude of load compared to Fig. 3.53. Therefore, to avoid any damage to the loading system and ensure that the load will be in balance during the

tests with a large number of cycles, the arrangement in Fig. 3.53 was chosen for tests OWTP/C-T16 and OWTP/C-T17.

3.12 Chapter summary

This chapter described the developed testing equipment and methodologies employed in the research programme. In Section 3.2, the chapter begins with general description of the centrifuge motivation compared to other physical model tests. It describes the advantages and disadvantages of using the physical modelling and provides the reasons why the development of the new loading device was necessary. Aspects of scaling for the design of centrifuge model tests, including the fundamental theory, were discussed in Section 3.3, followed by details about the University of Nottingham beam centrifuge. The tested model pile and sand bed properties and its preparation were described in Sections 3.5 and 3.8, respectively. All details of the testing equipment and its working operation were presented in Section 3.7, followed by comprehensive and detailed test programme provided in Section 3.10 and summarised in Table 3.7 and 3.8. This table will be frequently referred to in the following chapters of this thesis. The test run are divided into two phases: monotonic and uni-directional cyclic, and the test programme table is organised accordingly. Finally, at the end of this chapter, the general overview and preliminary results of test OWTP/C-T15 were presented in Section 3.11 to demonstrate the achievement of the model testing programme.

Chapter 4

MONOTONIC RESPONSE OF MONOPILE

4.1 Introduction

In geotechnical engineering, the cyclic loading is often considered relative to monotonic load-deflection response. A well-defined monotonic response provides a solid benchmark from which to consider the effects of long term cyclic loading. The initial slope (known as tangent stiffness), displacement and capacity of the first lateral load cycle defines the skeleton or backbone curve. Therefore, it is important to first investigate the response of monopile foundations to cyclic lateral loading by identifying the monotonic behaviour. This chapter presents centrifuge monotonic test results of OWTP-S1, OWTP-S2, OWTP-S3 and OWTP-S4 and analyses that are related to the lateral monotonic behaviour of monopile in sand. The centrifuge package used for testing purpose was described in Section 3.10, Chapter 3. The main objectives of these tests was to ensure that the response obtained using the developed experimental apparatus adequately reflected the characteristics of monopile behavior subjected to monotonic loading. The *p-y* curve formulation that is proposed in this chapter (MR-O) is used throughout the remainder of the thesis for estimating the results of the monotonic centrifuge data. The modified traditional p-y curves from DNV (2014) and published experimental data from Klinkvort (2013) and Kirkwood (2016), at the ground surface, are also compared with the MR-O model.

4.2 Analysis framework

Typical sketches, which are shown in Fig. 4.1, describe the response of a rigid pile in cohesionless soil. The overall trend of these figures shows a hardening behaviour, which is expected for a rigid pile embedded in cohesionless soil. For this pile behaviour, it is difficult to achieve an ultimate stage. The figures defined the initial (tangent) stiffness, K_t, and ultimate capacity, H_u, of the pile. Three methods have been suggested in the past for estimation of H_u; asymptotic tangent method (Fig. 4.1(a)) (Rosquoet et al., 2007), rotation criteria method (Klinkvort and Hededal, 2013, LeBlanc, 2009), and the use of 10% of pile diameter, D (Fig. 4.1(b)) (Chen et al., 2015). The value of K_t can be estimated by using Eq. 4.1, where ΔH_A, ΔM_A are the change in lateral load or moment at point A and Δy_A, $\Delta \theta_A$ are the change in lateral displacement and rotation of pile at point A, respectively. It should be noted that the rotation criteria are based on the limit of pile rotation suggested by DNV (2014) for the maximum rotation of 0.5^o at ground surface.

$$K_t = \frac{\Delta H_A}{\Delta y_A} = \frac{\Delta M_A}{\Delta y_A} \tag{4.1}$$

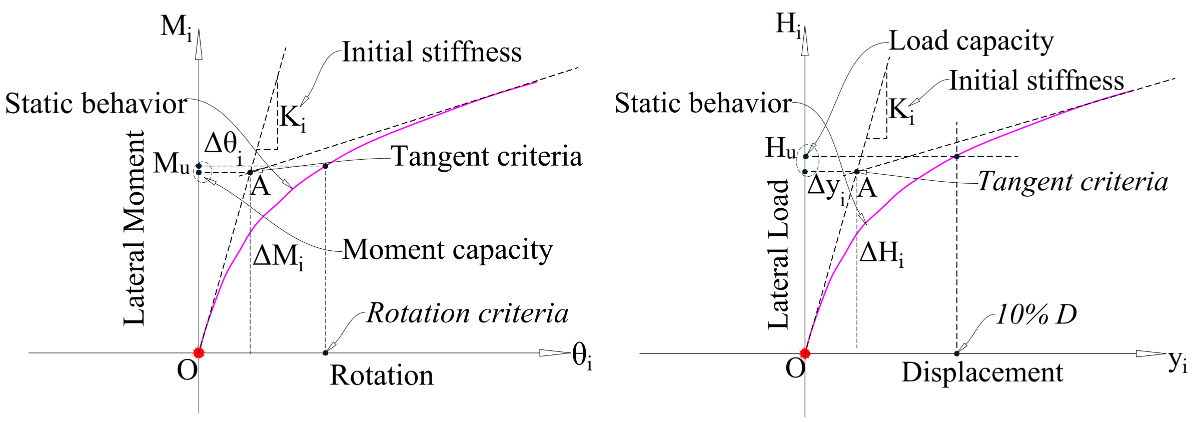

(a) Asymptotic tangent and rotation (θ) criteria (b) Asymptotic tangent and y_i=10%D criteria

Figure 4.1: Typical behaviour of rigid pile and estimation of H_u and K_t.

An ultimate lateral capacity of the pile, H_u, and tangent stiffness, K_i = K_t, from the experimental monotonic response, can also be estimated from the method proposed by Kulhawy and Chen (1995). In Fig. 4.2, a typical sketch of the hyperbolic curve is used to determine these parameters. The actual hyperbolic curve in Fig. 4.2(a) can be replotted as shown in Fig. 4.2(b) and the slope of the data can be estimated. From the Fig. 4.2(b), the reciprocal of *a* and *b* is the initial (tangent) stiffness, K_t and hyperbolic capacity, H_u, of the pile, respectively.

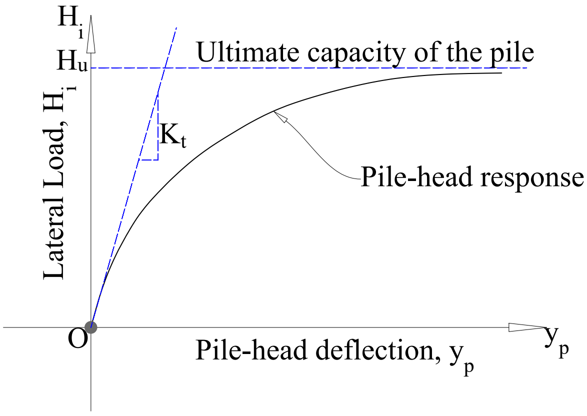

(a) Load-deflection response

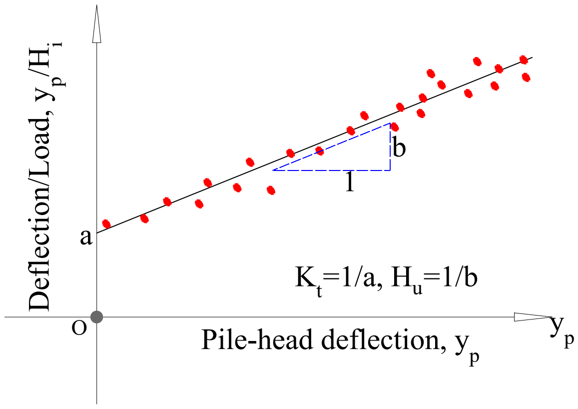

(b) Parameter estimation

Figure 4.2: Estimation of K_t and H_u, from Kulhawy and Chen (1995).

It is also important to scale the results of centrifuge tests to prototype. This is achieved by the use of non-dimensional groups suggested by Klinkvort (2013) (see Table 4.1), which permits comparisons between the results of this study with those conducted at different scales.

Table 4.1: Non-dimensional parameters

Item definition	Dimensional function
Lateral displacement	$\hat{Y} = \dfrac{Y_p}{D}$
Pile rotation	$\hat{\theta} = \theta\sqrt{\dfrac{P_a}{L\gamma'}}$
Horizontal loading	$\hat{H} = \dfrac{H_i}{\gamma' D^3}$
Moment loading	$\hat{M} = \dfrac{M_{z(i)}}{\gamma' D^4}$
Soil resistance	$\hat{P} = \dfrac{P_{z(i)}}{K_p \gamma' Z D}$

4.3 Monotonic experimental results

4.3.1 Introduction

The monotonic centrifuge experiments, three at 100g and one at 30g, were conducted. The analysis and results of tests OWTP/S-T1, OWTP/S-T2, OWTP/S-T3 and OWTP/S-T4 are presented and discussed in this section. The tests are used to determine the load-displacement response of the pile, ultimate capacity, depth about which the pile rotated, and lateral and rotational stiffness of the pile at the ground surface. The tests were carried out under displacement-controlled conditions. One test (OWTP/S-T3) was conducted at medium relative density of $\mathrm{D_r} = 42\%$ and the other three (OWTP/S-T1, OWTP/S-T2 and OWTP/S-T4) at relative density of $\mathrm{D_r} = 85\%$. All results are interpreted at model scale, unless stated otherwise. A comparison between centrifuge model scale and full-scale is also presented regarding the non-dimensional parameters shown in Table 4.1.

4.3.2 Load-displacement response and ultimate capacity of pile

Monotonic tests were conducted on the aluminium model pile and displaced laterally by imposing a horizontal force at an eccentric height of 200 mm. At this location, the load-deflection responses of the pile head were determined. In Fig. 4.3, the results from monotonic load tests can be seen. From both figures, the curves are observed to follow a nonlinear hyperbolic shape, however, a defined ultimate load was not achieved.

As expected, the pile loaded with small centrifuge acceleration of 30g has lower values of soil resistance compared with the one at high gravity (100g), with the same relative density ($\mathrm{D_r}$ = 85%). The data also provide evidence that the increase of relative density has a significant effect on the load capacity of the system.

The non-dimensional expressions described in Table 4.1 were used such that the model results can be interpreted at any scale. For this purpose, the normalised parameters should be identical between the model and prototype to avoid scaling effects. The experimental data shown in Fig. 4.3 were normalised, and the result is shown in Fig. 4.4. These plots show that, using the

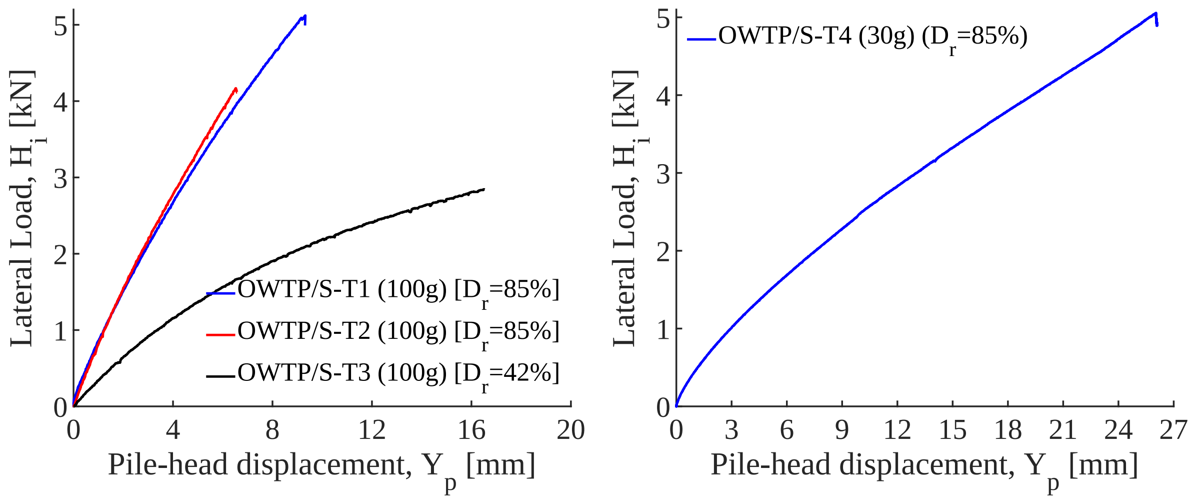

(a) Global responses at 100g (b) Global responses at 30g

Figure 4.3: Global pile-head load-displacement response.

properties of sand (γ_d), geometry of the pile (D), the load with N_s^2 and displacement with N_s, identical normalised results can be achieved.

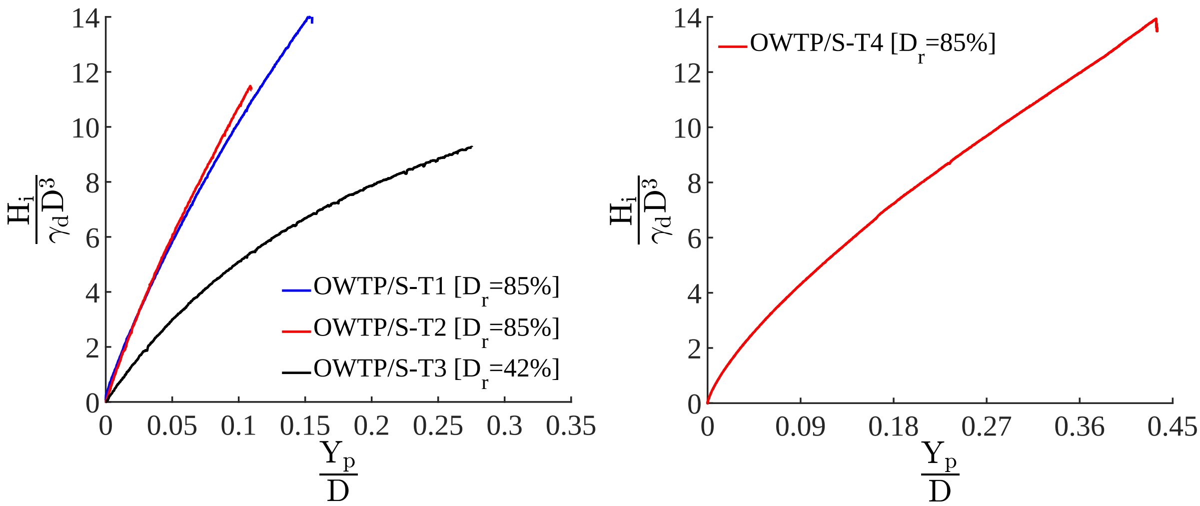

(a) Normalised responses at 100g (b) Normalised response at 30g

Figure 4.4: Normalised monotonic test results.

A laterally loaded model pile, installed in sandy soil, appeared to exhibit a hardening behaviour, which makes it difficult to determine the yield points (H_u or $\hat{H}_u$) as shown in Figs. 4.5(a) and 4.5(b), for normal and normalised tests, respectively. The ultimate capacities were taken as the load at the pile-head displacement of 10% pile diameter (D). This method was also employed by other studies (Chen et al., 2015, Cuéllar, 2011), to determine the ultimate capacities of monopiles. Therefore, the ultimate capacities shown in Fig. 4.5(a) were estimated as 3800 N (D_r = 85%, at 100g), 1560 N (D_r = 42%, at 100g) and 1690 N (D_r = 85%, 30g), from tests OWTP/S-T1/T2, OWTP/S-T3 and OWTP/S-T4, respectively. The corresponding normalised ultimate capacities are shown in Fig. 4.5(b).

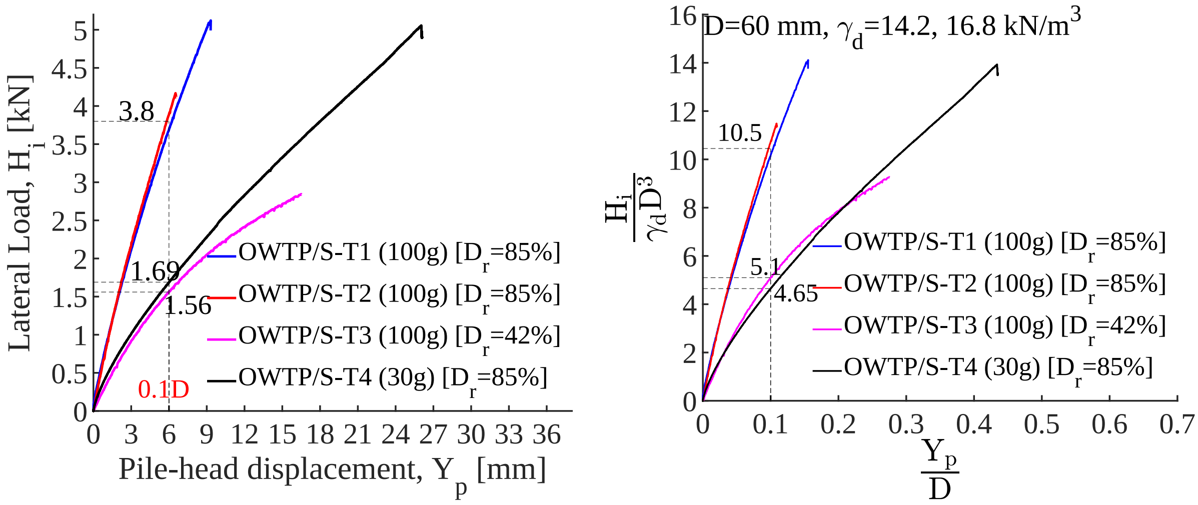

(a) Global ultimate capacities (b) Normalised ultimate capacities

Figure 4.5: Ultimate capacities of the pile-head load versus displacement.

According to DNV (2014) design guideline, four important design loads for the wind turbine are highlighted: (1) ultimate load-carrying capacity, which relates to ultimate limit state (ULS), H_u, (2) the worse expected transient load (ULS/1.35), (3) serviceability limit state (SLS), which occurs approximately 10^2 times during the lifetime of the wind turbine and (4) fatigue limit state (FLS), which occurs approximately 10^7 times during the lifetime of the wind turbine. For the current thesis, inline with recommendation from LeBlanc (2009), the SLS and FLS were estimated as 53% and 30% of ULS, respectively. By using these estimates, the design loads from the experimental work, with corresponding values in a prototype scale, are listed in Table 4.2. In Table 4.2, M_i (kNm), H_i (kN) and V_T (kN) are the moment, lateral and vertical loads applied to the pile-head, respectively, in the experiment. In prototype, the units are M_i (MNm), H_i (MN) and V_T (MN).

Table 4.2: Loads applied in experimental work, scaled to prototype at centrifuge acceleration of 100g and 30g

Load Type	Experiment				Prototype		
	M_i	H_i	V_T		M_i	H_i	V_T
		OWTP/S-T1/T2	(100g)	[D_r=85%]			
ULS [N = 1]	0.76	3.8	2		760	38	10
ULS/1.35	0.56	2.82	2		563	28	10
SLS [N = 10^2]	0.4	2	2		400	20	10
FLS [N = 10^7]	0.23	1.14	2		230	11.4	10
		OWTP/S-T3	(100g)	[D_r=42%]			
ULS [N = 1]	0.312	1.56	2		312	15.6	10
ULS/1.35	0.231	1.16	2		231	11.6	10
SLS [N = 10^2]	0.165	0.827	2		165	8.27	10
FLS [N = 10^7]	0.094	0.468	2		94	4.68	10
		OWTP/S-T4	(30g)	[D_r=85%]			
ULS [N = 1]	0.338	1.69	2		9.126	1.52	0.289
ULS/1.35	0.25	1.252	2		6.76	1.126	0.289
SLS [N = 10^2]	0.179	0.896	2		4.84	0.806	0.289
FLS [N = 10^7]	0.101	0.507	2		2.74	0.456	0.289

4.3.3 Pile rotation depth

To further investigate the failure mechanism, the point of rotation is compared for the three tests and approximate values can be deduced. With assumption that the pile does not translate and is sufficiently stiff, the relative ground displacement of the pile ($\frac{Y_g}{D}$) is related to the depth below the ground surface (see Fig. 4.6) to identify the point of the rotation Z_r. Its value can be deduced from LVDT measurements and the typical geometry sketch shown in Figure 4.6(a). The lateral displacements were measured from the lower (LVDT1) and upper (LVDT2) transducers, at a relative distance of 110 mm, to determine the pile rotation angle (θ). From the figure, once the pile rotation is obtained, the depth to the point O (Z_r) is identified geometrically by comparing the original and inclined location of the pile-head displacement.

The result is shown in Fig. 4.6(b). Initially, the depth of rotation (Z_r) was found at a depth of Z = 0.1L, it then drop quickly to a depth of 0.55L and finally stabilised at approximately depth of Z = 0.68L (Test T3). This value is less than Z_r = 0.718L, which was estimated by an empirical equation 4.2 (Prasad and Chari, 1999) (L_e = 0.2 m and L=0.3 m). Other studies (Motta, 2012, Petrasovits and Awad, 1972, Zhu et al., 2015) have reported that the depth of pile rotation should fall in a range of (0.7-0.79) L. The findings of Klinkvort and Hededal (2014) and Kirkwood (2016) on monopiles have reported that Z_r should be 0.8L and 0.7L, respectively. The parameter L represents an embedded depth of the pile. The observed rotation centres, from this study, are found between 0.6 - 0.72L. Allowing for experimental scatter, the depth of pile rotation is stipulated as 0.68L to develop a simple solution.

$$Z_r = L\left[\frac{\sqrt{7.29\left(\frac{L_e}{L}\right)^2 + 10.541\left(\frac{L_e}{L}\right) + 5.307} - \left(2.7\left(\frac{L_e}{L}\right) + 0.567\right)}{2.1996}\right] \tag{4.2}$$

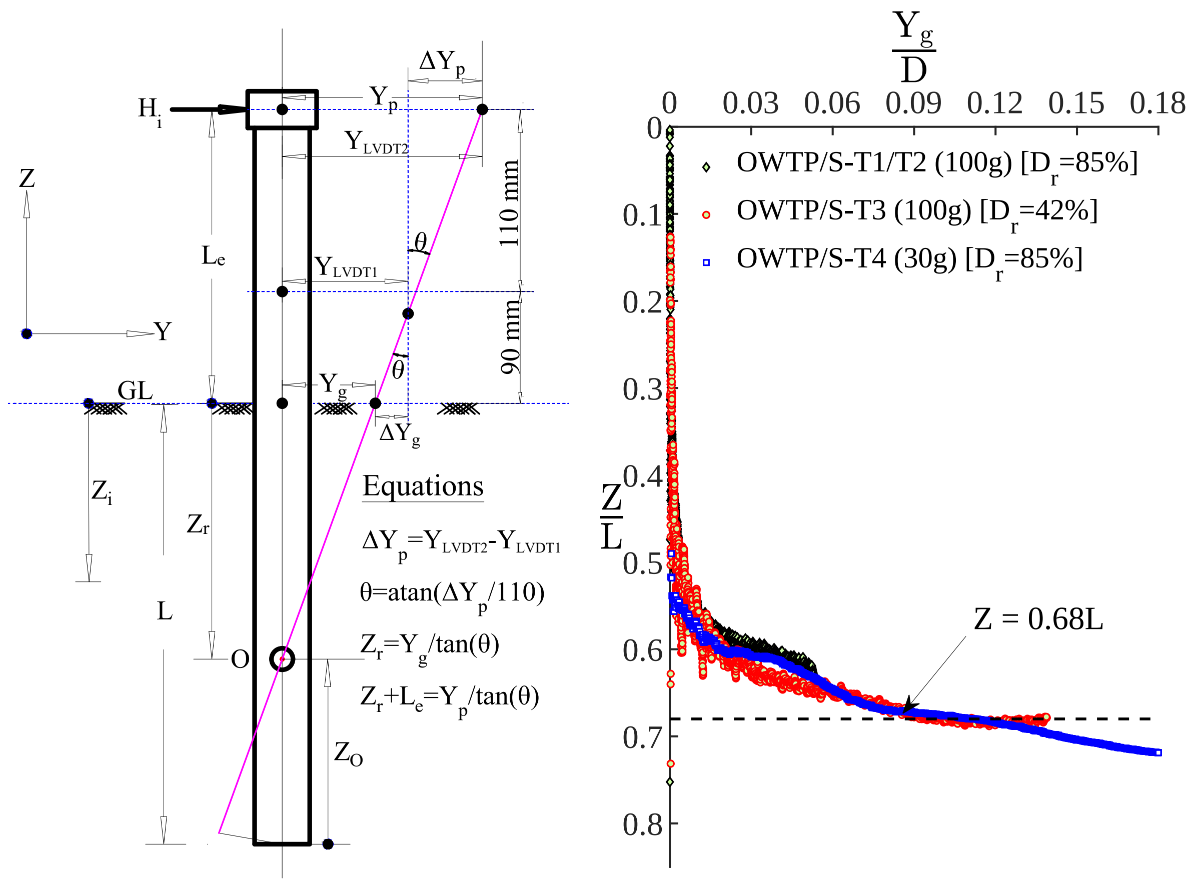

(a) Typical pile geometry definitions (b) Pile rotation depth, Z_r

Figure 4.6: Point of rotation versus normalised displacement, assuming that the pile does not translates.

4.3.4 Monotonic responses at ground level

The load and displacement measured during the monotonic tests allowed the calculation of moment ($\mathrm{M_i}$) and pile rotation (θ_i) to be made at the ground surface (see Fig. 4.7). Utilising the relationships described in Table 4.1 it was possible to normalise the results in Fig. 4.7(a), thus presenting the behaviour in terms of the load level ($\hat{\mathrm{M}}$) and rotational strain ($\hat{\theta}$). Overall, it is found that the moment-rotation behaviour is nonlinear, however; it is not possible to identify a point of failure. It is evident that the capacity at larger rotation increases with the sand relative density ($\mathrm{D_r}$) for the tests conducted at 100g ($\mathrm{T_1}$, $\mathrm{T_2}$ and $\mathrm{T_3}$). In addition, the increase of centrifuge acceleration from 30 to 100, for tests $\mathrm{T_1}$ and $\mathrm{T_4}$, is an evidence that the g-level in the centrifuge can also affect the capacity of the pile.

The model pile in this study exhibits work hardening behaviour, which makes it difficult to determine the moment capacity ($\mathrm{M_u}$). The $\mathrm{M_u}$ was determined by 10% of the pile diameter method, and the corresponding value of pile rotation θ, is 0.016 radians. Using this value, the moment capacities, $\mathrm{M_u}$, were recorded as 0.32 kNm (at 100g; $\mathrm{D_r}$=42%) and 0.35 kNm (30g; $\mathrm{D_r}$=85%), 0.78 kNm (100g; $\mathrm{D_r}$=85%) (see Fig. 4.7(a)). The corresponding normalised capacities are shown in Fig. 4.7(b).

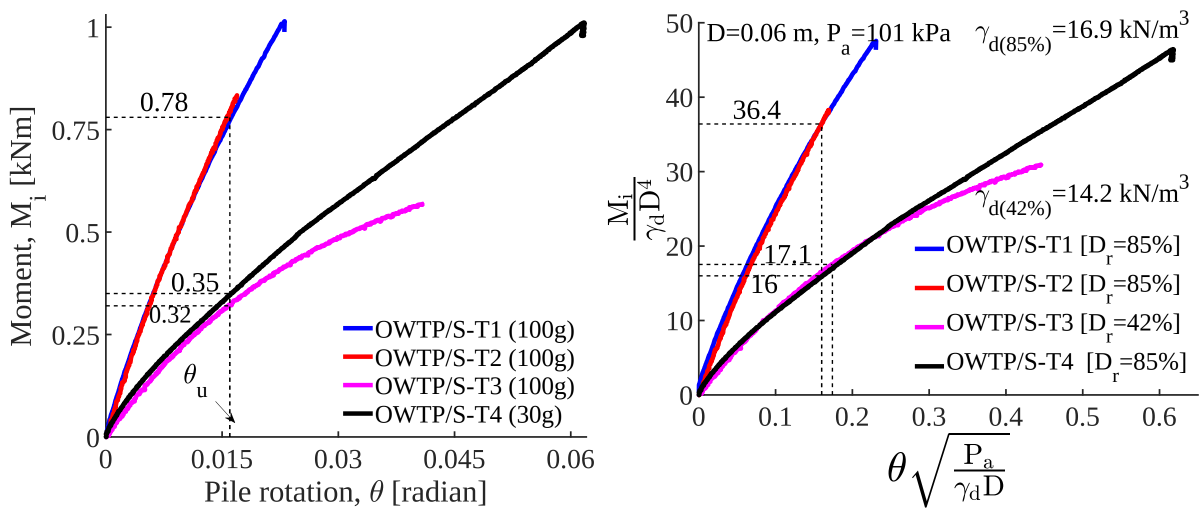

(a) Moment-rotation response and capacities (b) Normalised moment capacities

Figure 4.7: Moment-rotation response and ultimate capacities at the ground surface.

The pile-soil response at the ground surface can be used to asses the foundation stiffness. The foundation stiffness of an offshore wind turbine can be modelled by the two coupled springs, K_L (lateral stiffness) and K_R (rotational stiffness) (see Fig. 4.8). The lateral and rotational springs were estimated experimentally by monotonic tests with the results shown in Figure 4.9(a) and 4.9(b), respectively. The initial tangents of the load-displacement and moment-rotation curves at the ground surface are plotted in Fig. 4.9 to represent the values of K_L and K_R, respectively (see the values in the figures). These parameters provided a useful information on the dynamic sensitivity of the wind turbine structures (Arany et al., 2014).

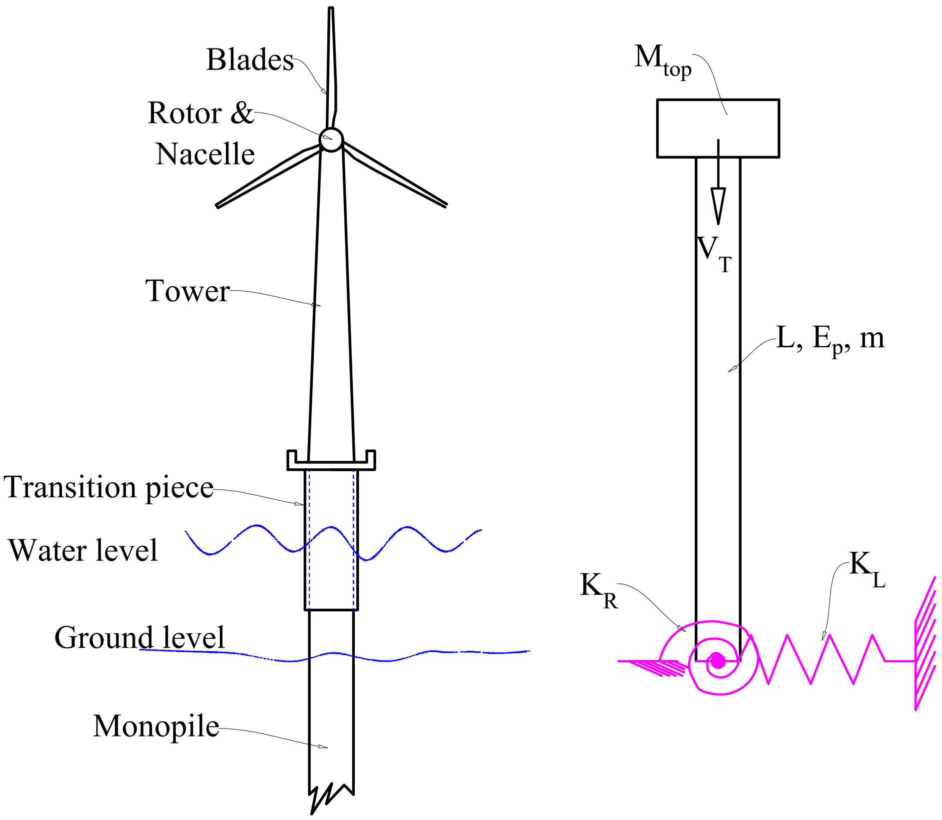

Figure 4.8: Transverse and rotational springs, from Arany et al. (2014).

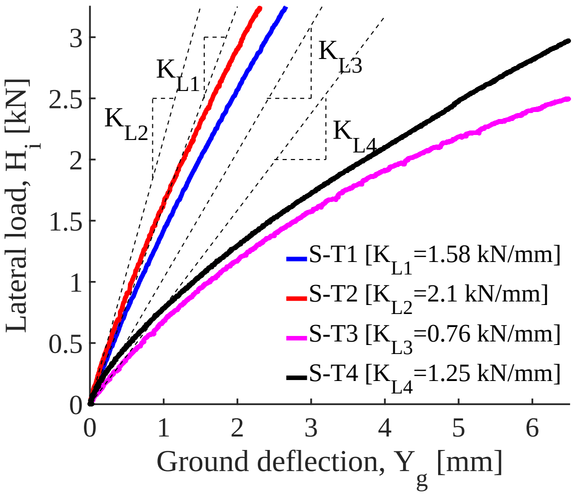

(a) Lateral stiffness at ground surface

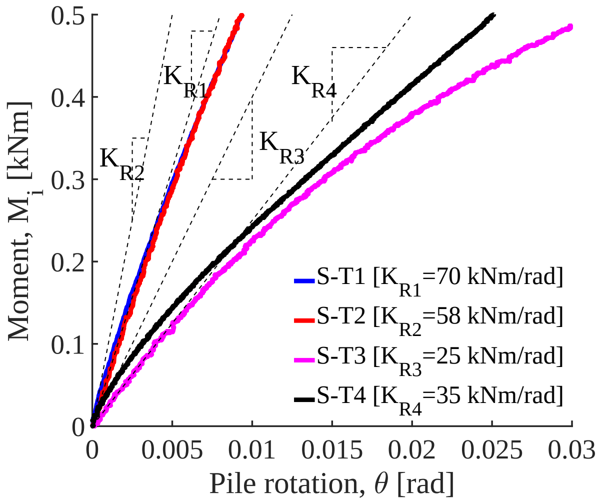

(b) Rotational stiffness at ground surface

Figure 4.9: Lateral (K_L) and rotational (K_R) stiffness of the pile at ground surface.

4.3.5 Comparison of current study and published centrifuge tests

In this section, the results of tests OWTP/S-T1 and OWTP/S-T4 (D_r = 85%, γ_d = 16.9 kN/m^3, D = 60 mm, L = 300 mm, 100g and 30g,respectively) are compared to the published centrifuge tests from Klinkvort (2013) (D_r = 90%, γ_d = 16.8 kN/m^3, D = 40 mm, L = 240 mm, 125g) and Kirkwood (2016) (D_r = 49%, γ_d = 14.41 kN/m^3, D = 38.1 mm, L = 200 mm, 100g). The variation of the applied lateral load (H_i) with displacement at the ground surface, for all tests, is plotted in Fig. 4.10. Overall, it can be seen that the load-displacement responses of all tests are nonlinear, however, the point of failure was not achieved.

The key findings revealed that the capacity and initial stiffness of the centrifuge acceleration of 30g are lower as expected, however, the initial stage of test OWTP/S-T1 (100g) shows a close response compared to other published tests, but the response starts to deviate from the ground displacement above 0.5 mm (with Kirkwood (2016) test) and 1.5 mm (with Klinkvort (2013) test). As noted from Dyson and Randolph (2001) and Klinkvort (2013), a model pile installed at 1g can lead to a softer response, however, this contradicts with the comparisons shown in Fig. 4.10 wheres the model pile from Klinkvort (2013) was installed at an elevated stress field. Further study is required to investigate the response of monopiles due to different size of pile diameter, load eccentricity, embedded depths, soil type, method of pile installation and change of centrifuge acceleration. As described from Section 4.2, a semi-empirical hyperbolic

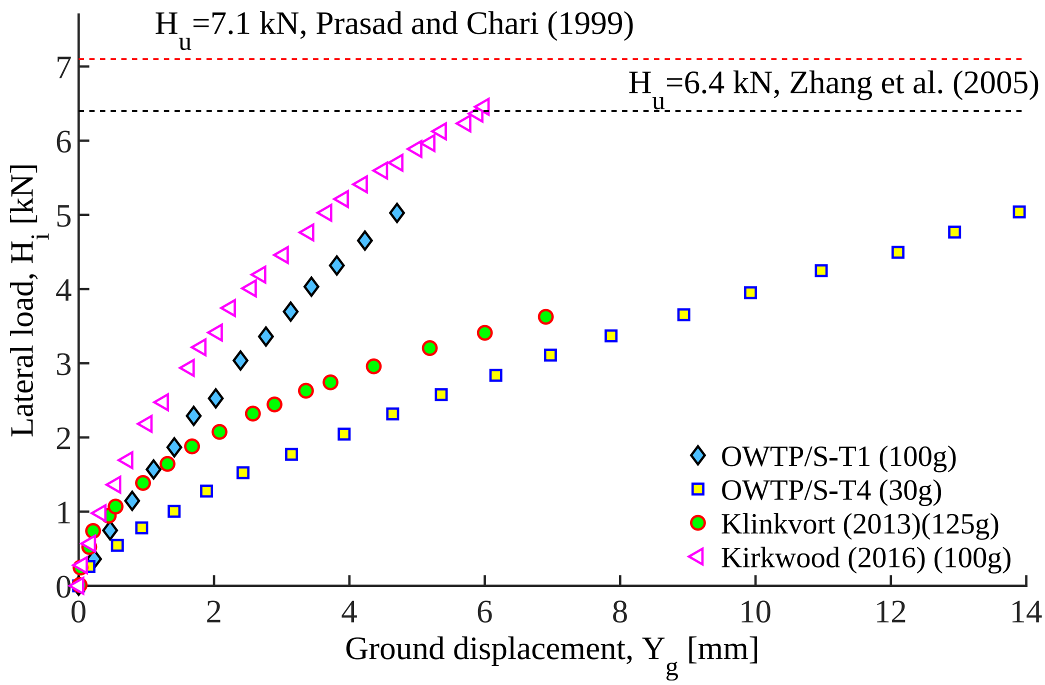

Figure 4.10: Comparisons between tests OWTP/S-T1/T4 and published centrifuge tests from Klinkvort (2013) and Kirkwood (2016).

expression (see Eq. 4.3) is used here to interpret the tangent stiffness ($\mathrm{K_t}$) and ultimate capacity ($\mathrm{H_u}$) of the global monotonic responses at the ground surface. The data was transformed by using Eq. 4.4, in relation to hyperbolic function (see Eq. 4.3), to obtain a linear fitting in the form of y=a+bx, where $\mathrm{K_t}=\frac{1}{\mathrm{a}}$ and $\mathrm{H_u}=\frac{1}{\mathrm{b}}$.

$$\mathrm{H_i} = \frac{\mathrm{K_t Y_g}}{1 + \dfrac{\mathrm{K_t}}{\mathrm{H_u}}\mathrm{Y_g}} \tag{4.3}$$

$$\frac{\mathrm{Y_g}}{\mathrm{H_i}} = \mathrm{a} + \mathrm{bx}, \Rightarrow \mathrm{a} = \frac{1}{\mathrm{K_t}}, \mathrm{b} = \frac{1}{\mathrm{H_u}} \tag{4.4}$$

This method is employed for all four tests as shown in Fig. 4.11. The parameter extracted are summarised in Table 4.3. The ultimate capacities from Prasad and Chari (1999) and Zhang et al. (2005), discussed in Chapter 2, are calculated and plotted in Fig. 4.10. In Fig. 4.10, the ultimate capacities calculated based on Kulhawy and Chen (1995) method (see Table 4.3), from tested data, are shown to be closely related to the two available ultimate state methods ($\mathrm{H_u}$=6.4 kN and 7.1 kN). In Table 4.3, the values of $\mathrm{K_t}$ for test S-T3 and S-T4 are very close, which indicates that the test conducted in dense sand at low gravity could be similar to tests in medium dense sand with high gravity. However, the ultimate capacities have a big difference, indicating that further study is required. The parameters obtained from test OWTP/S-T4 are the basis for developing the backbone curves of hysteresis loops in Chapter 6.

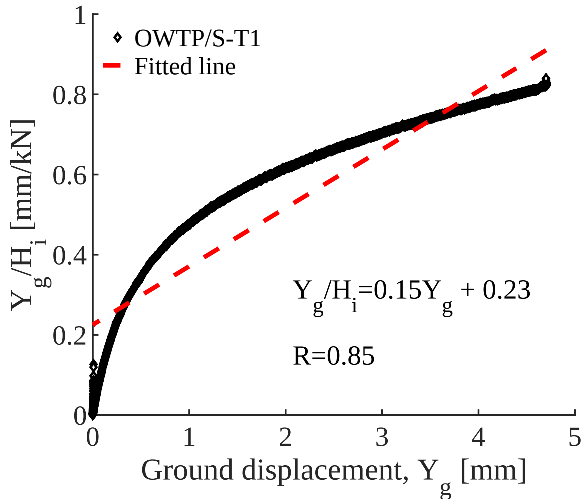

(a) Parameters for test OWTP/S-T1

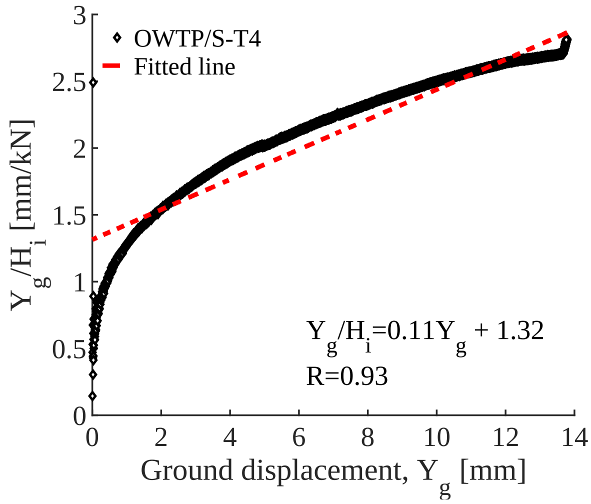

(b) Parameters for test OWTP/S-T4

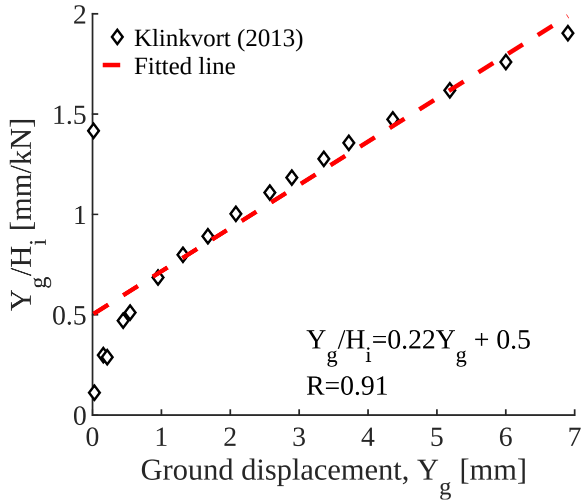

(c) Parameters from Klinkvort (2013)

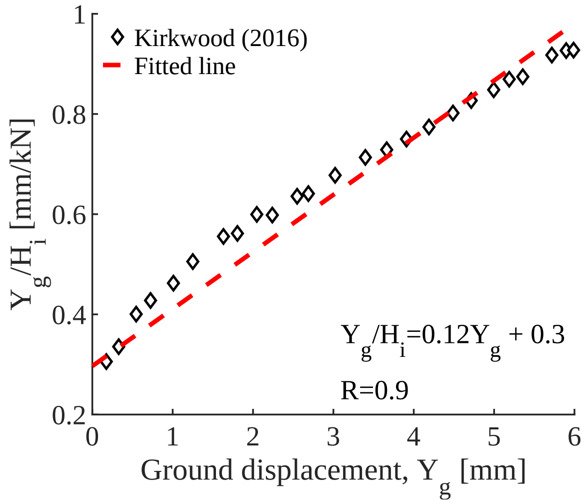

(d) Parameters from Kirkwood (2016)

Figure 4.11: Kulhawy and Chen (1995) method to extract parameters H_u and K_t.

Table 4.3: Extracted model parameters based on Kulhawy and Chen (1995) analysis

SN	Test name	**b** [1/kN]	**a** [mm/kN]	K_t [kN/mm]	H_u [kN]
1	OWTP/S-T1	0.1457	0.2253	4.44	6.9
2	OWTP/S-T3	0.204	1.269	0.79	4.9
3	OWTP/S-T4	0.1123	1.315	0.76	8.9
4	Test No. 30 (Klinkvort, 2013)	0.216	0.501	1.996	4.64
5	Test PK08 (Kirkwood, 2016)	0.114	0.297	3.37	8.77

4.4 Comparisons of prediction methods

4.4.1 Introduction

Based on the observations from centrifuge tests presented in Section 4.3, this section presents the models to calculate nonlinear *p-y* curves. Three *p-y* curve models from DNV (2014), Kondner (1963) and Ramberg and Osgood (1943), discussed in chapter 2, are used in this section to model the monotonic test results. Although these methods are simple to implement in the analysis, some of them suffer from limitations. For instance, a hyperbolic function from Kondner (1963) is limited by only two parameters (Ishihara, 1996, Vucetic and Dobry, 1988). However, a four parameter model, known as Ramberg Osgood model (R-O model) (Desai and Zaman, 2013, Ramberg and Osgood, 1943), can be adjusted to achieve a good fit to experimental data. Three main features of this model are different from the DNV (2014) model: the magnitude of ultimate resistance, the shape and slopes (tangent stiffness) of the *p-y* curves.

The Ramberg Osgood model function (see Eq. 4.5), initially proposed by Ramberg and Osgood (1943) and later identified by Desai and Zaman (2013) as a suitable formulation, is used to define the shape of the *p-y* curves. From Eq. 4.5, $P_{z(i)}$ is the soil resistance at point Z in kN/m, P_u is the ultimate soil resistance in kN/m, $y_{z(i)}$ is the pile deflection in m, K_h is the initial (tangent) stiffness in kN/m^2 at each depth Z and r is the constant to control the curvature. By setting r=1, Eq. 4.5 is referred as the hyperbolic model and known as the KZ (Kondner and

Zelasko) model (Vucetic and Dobry, 1991). Based on this similarity, the R-O model is used throughout the subsequent chapters.

$$P_{z(i)} = \frac{K_h y_{z(i)}}{\left(1 + \left|\frac{K_h y_{z(i)}}{A_i P_u}\right|^r\right)^{\frac{1}{r}}} \tag{4.5}$$

The results of the tests are compared with both original (old) and modified (new) methodologies of DNV (2014) and Ramberg and Osgood (1943) models. As shown in Eq. 4.6, the modified Ramberg Osgood (MR-O) model is created with additional parameters β_p, $K_f = aK_h$ (final tangent stiffness), a (the constant to control the final tangent), s to replace the denominator r and A_j instead of A_i. Only parameters β_p and A_j can be used to modify the original DNV (2014) model function.

$$P_{z(i)} = \frac{\beta_p (K_h - K_f) y_{z(i)}}{\left(1 + \left|\frac{\beta_p (K_h - K_f) y_{z(i)}}{A_j P_u}\right|^r\right)^{\frac{1}{s}}} + K_f y_{z(i)} \tag{4.6}$$

All three methods have been used to analyse the response of flexible piles with no guidelines regarding the shearing force at the pile tip (Abadie, 2015). In the analysis, when the pile is said to be in equilibrium, the shear forces at the pile tip are ignored, which may result in overestimating the experimental data. This is not acceptable for a rigid pile and therefore a method of analysis to include the shearing force at the pile tip is required to equate the sum of forces to zero.

This section is therefore suggesting a simple equilibrium analysis, aiming at reworking the available *p-y* curve model functions in order to match the results of the monotonic centrifuge tests, while accounting for the shear forces at the pile tip. The objective here is to find a suitable *p-y* curve approach that provides a good agreement of the backbone curve as this will be used as the basis of the work on cyclic loading. Therefore, the parameters derived from the results of this section will be used as a modelling base to predict the results of the centrifuge cyclic loading tests in Chapter 6. In Table 4.4, the function and parameters of the original (old) and modified (new) models are presented with more details in the following sections.

Table 4.4: Original (old) and modified (new) soil model functions and parameters.

Model type	**Equation**	**Model inputs**	**Fittings**
DNV (2014), old	$\mathrm{P_z = A_iP_u tanh}\left(\dfrac{\mathrm{k_hZ}}{\mathrm{A_iP_u}}\mathrm{y_z}\right)$	$\mathrm{A_i}$ (Eq. 4.8), $\mathrm{P_u}$ (Eq. 4.7)	-
		$\mathrm{k_h}$ (Eq. 4.11)	-
R-O, old	$\mathrm{P_{z(i)}}$, Eq. 4.5	$\mathrm{A_i}$, Eq. 4.8, $\mathrm{P_u}$ (Eq. 4.7)	*r*
		$\mathrm{K_h}$=$\mathrm{k_h}$Z, $\mathrm{k_h}$ (Eq. 4.11)	-
DNV (2014), new	$\mathrm{P_z = A_jP_u tanh}\left(\dfrac{\beta_\mathrm{b}\mathrm{k_hZ}}{\mathrm{A_jP_u}}\mathrm{y_z}\right)$	$\mathrm{A_j}$ (Eq. 4.10), $\mathrm{P_u}$ (Eq. 4.7)	β_b
		$\mathrm{k_h}$ (Eq. 4.11)	-
MR-O, new	$\mathrm{P_{z(i)}}$ (Eq. 4.6)	$\mathrm{A_j}$ (Eq. 4.10), $\mathrm{P_u}$ (Eq. 4.7)	β_b, r, s, a
		$\mathrm{K_h}$=$\mathrm{k_h}$ Z, $\mathrm{k_h}$ (Eq. 4.11)	-
		$\mathrm{G_{max}}$, $\mathrm{E_s}$, $\mathrm{P'_m}$, $\mathrm{P_a}$	$\mathrm{G_b}$, m

r, s and a: curve control constants for MR-O model, β_p, $\mathrm{G_b}$ and m: initial stiffness constants

$\mathrm{A_i}$, $\mathrm{A_j}$: are origin and modified depth factors, ϕ_max: is the maximum friction angle

D, Z: are the pile diameter and depth below the ground surface, respectively

The parameters $\mathrm{A_j}$ and β_p, shown in Table 4.4, were introduced to reformulate the published *p-y* curves, which can be used to fit the results of the centrifuge tests. The original ultimate soil resistance is calculated by using an empirical factor $\mathrm{A_i}$ and thereafter it is modified to a new depth factor $\mathrm{A_j}$. The factor $\mathrm{A_i}$ from DNV (2014) was not suitable for use with a rigid pile due to overestimation of the experimental results (Kirkwood, 2016, Klinkvort, 2013). A constant β_p is introduced to both *p-y* curve model functions to better fit the tangent stiffness $\mathrm{K_h}$ (or modulus of subgrade reaction) of the experimental results. The discussion of $\mathrm{P_u}$ and $\mathrm{K_h}$ is presented in the following sections prior to discussion of the equilibrium analysis.

4.4.2 Ultimate resistance

As discussed from Section 2.2.2.3 in Chapter 2, several methods are available for determining the ultimate lateral resistance of soil surrounding the pile. However, there is no rigorous closed-form solution as the soil resistance around the pile is a complex three-dimensional problem of the ultimate state of the nonlinear elastoplastic medium (Tak Kim et al., 2004). For simplicity, the simple expression (see Eq. 4.7) from DNV (2014) can be used throughout to calculate the values of $\mathrm{P_u}$. The value of depth factor, $\mathrm{A_i}$, currently available in the DNV (2014) design standard (see Eq. 4.8), is reduced from 3 at shallow depth to 0.9 at greater depth. In this study, the depth factor, $\mathrm{A_i}$, was modified to $\mathrm{A_j}$ (shown in Eq. 4.10). As can be seen in Eq. 4.9, Klinkvort (2013) has modified the DNV depth factor to fit the centrifuge test results. As discussed in Section 4.5.5, the modified depth factors were used in the MR-O soil model to best fit the *p-y* curves of test no. 30 from Klinkvort (2013). The three functions were plotted in Fig. 4.12(a), and the value of $\mathrm{A_j}$ was found to decrease from 3 to 2.5 at shallow depth. At the shallow depth, the values of $\mathrm{A_k}$ and $\mathrm{A_j}$ are lower than $\mathrm{A_i}$. $\mathrm{A_i}$ was derived from the field-scale tests conducted on flexible piles and always overestimates the results of the monopiles tests.

$$\mathrm{P_u} = \min \begin{cases} (\mathrm{C_1 Z + C_2 D})\gamma' \mathrm{Z} \\ \mathrm{C_3 Z}\gamma' \mathrm{Z} \end{cases} \tag{4.7}$$

$$\mathrm{A_i} = 3 - 0.8\frac{\mathrm{Z}}{\mathrm{D}} \geq 0.9 \tag{4.8}$$

$$\mathrm{A_k} = 0.9 + \frac{1.1}{2}\left(1 + \tanh\left(9 - 3\frac{\mathrm{Z}}{\mathrm{D}}\right)\right) \tag{4.9}$$

$$\mathrm{A_j} = 2.5 - 1.6\tanh\left(\frac{\mathrm{Z}}{\mathrm{D}}\right) \geq 0.9 \tag{4.10}$$

As shown in Fig. 4.12(b), a normalised $\mathrm{P_u}$ was first obtained by fitting the experimental *p-y* curves conducted by Klinkvort (2013) (see Section 4.5.5). This was chosen due to the following reasons: (i) the pile in the current study was not instrumented below the ground, which makes it difficult to estimate the $\mathrm{P_u}$ values (ii) the material parameters from this test are closely related to the study of Klinkvort (2013) (see Table 4.6) (iii) The test was conducted on a stiff pile (D = 5 m) in dry sand with centrifuge acceleration of 125g. The *p-y* curves were only recorded up to a depth of 3.5 D, therefore, the $\mathrm{P_u}$ from DNV (2014) and Broms (1964) were extended up to the base of the pile and used throughout as the basis for the analysis of the global load-deflection response at the ground surface.

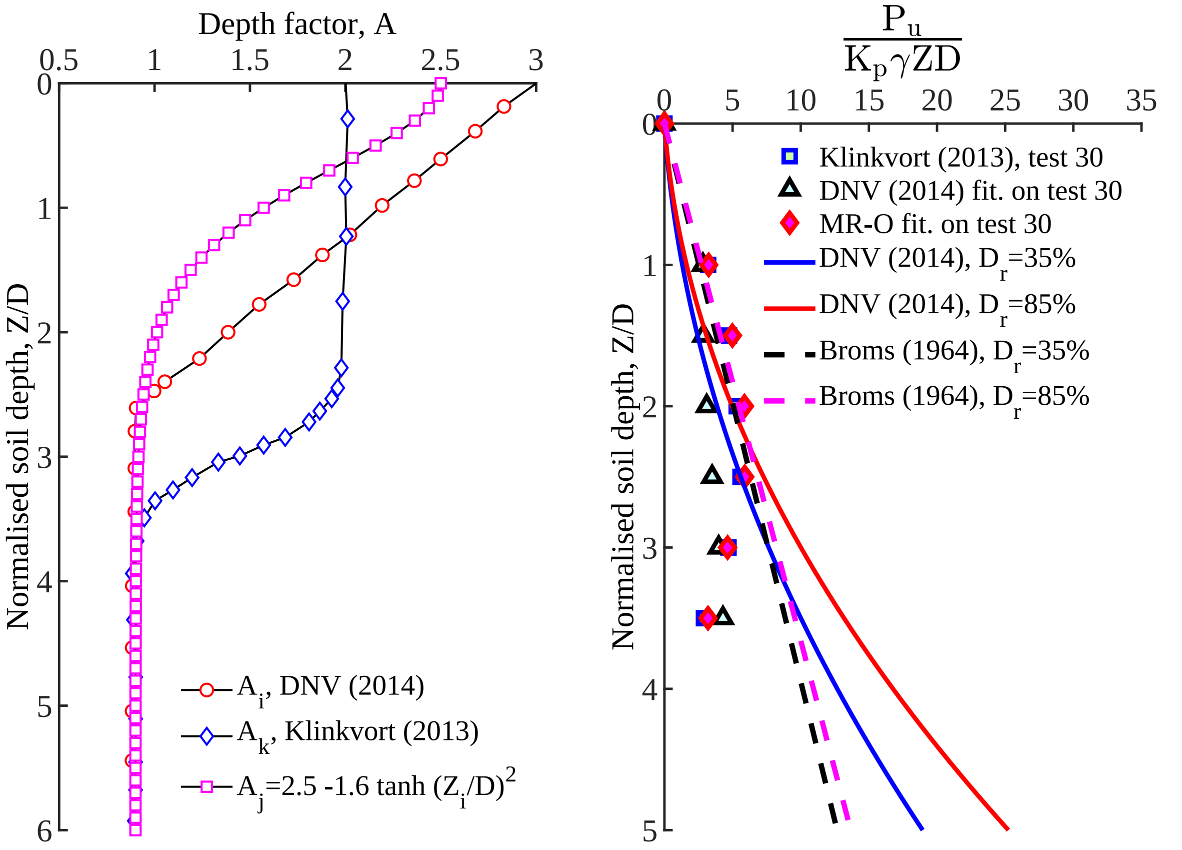

(a) Depth factors, A_i, A_k and A_j (b) Distribution of ultimate soil resistance, P_u

Figure 4.12: Comparisons of depth factor and distribution of ultimate soil resistance.

4.4.3 Initial modulus of horizontal subgrade reaction

The modulus of horizontal subgrade reaction, K_h (kN/m^2), is conventionally used to correlate the response of soil resistance per unit length ($P_{z(i)}$) in relation to the local pile deflection, $y_{z(i)}$. There has been discussion in the previous studies regarding the rate at which the initial stiffness of the *p-y* curves increases with depth. For instance, in sandy soils K_h is assumed to vary linearly with depth (Reese et al., 1974). As noted from Reese et al. (1974), API (2007) and DNV (2014), the variation of K_h can be expressed as K_h=k_hZ, where k_h is the coefficient of subgrade reaction in kN/m^3. With a known value of ϕ_{max}, $k_{h,max}$ can be estimated by using Eq. 4.11 (Reese and Van Impe, 2010) or Fig. 2.8(b) in Chapter 2. The parameter $k_{h,max}$ is considered when Z = L (at the base of the pile), where L is embedded depth of the pile.

$$k_{h,max} = (0.008085\phi_{max}^{2.55} - 26.09)10^3 \tag{4.11}$$

An empirical relationship suggested by Carter (1984) and Desai and Zaman (2013) (see Eq. 4.12) can be used to estimate the nonlinear variation of K_h along the pile. This function is related to initial modulus of soil, $E_{s,max}$ (see Eq. 4.13), where G_{max} is the maximum shear modulus in kPa; v_s is Poisson's ratio; D is the pile diameter; D_{ref} is the reference pile diameter (taken as $D_{ref} = 1$ m) and E_p I_p is the flexural rigidity of pile (kNm^2). The coefficient α_p in Eq. 4.12 can be adjusted to best fit the initial tangent of the tested *p-y* curves.

$$K_h = \alpha_p \frac{E_{s,max}}{1 - v_s^2} \frac{D}{D_{ref}} \left(\frac{E_{s,max} D^4}{E_p I_p} \right)^{1/12} \tag{4.12}$$

$$E_{s,max} = 2G_{max}(1 + v_s) \tag{4.13}$$

An empirical function (see Eq. 4.14) was suggested by Pestana and Salvati (2006) and Oztoprak and Bolton (2013) to determine the maximum shear modulus (G_{max}). The G_{max} is the function of function of void ratio (F(e)), material constants (G_b and m) and the confining stress (P_m) (see Eq. 4.15), where P_a=101 kPa is atmospheric pressure. Pestana and Salvati (2006) investigated the small-strain behaviour of granular soil and suggested that if the cohesionless material is isotropic, the void ratio function F(e) = $e_o^{-1.3}$ can be used as it provide the best match for the experimental data on various sand. As discussed in Chapter 2, the values of m = 0.5 and 0.75 were suggested for sand and gravel, respectively and the constant G_b was correlated well with the angularity of the material for homogeneous sand in the range between 400-800. It was recommended that sands with more angular grains can provide a high value of G_b, while the well-graded sand will give the low values of G_b. The material used in this study are within this recommendation and therefore this range of G_b can be used throughout for analytical purposes.

$$G_{max} = G_b P_a F(e) \left(\frac{P_m}{P_a} \right)^m \tag{4.14}$$

$$P_m = \frac{1}{3}\gamma' Z(1 + 2K_o), \Rightarrow K_o = 1 - \sin\phi' \tag{4.15}$$

The extracted values of k_h and K_h of test no. 30 from Klinkvort (2013) and the two modified models (DNV and MR-O), up to a depth of 3.5D, are presented in Fig. 4.13. A nonlinear distribution of k_h and K_h was calculated by using Eq. 4.12, where the parameters α_p=0.15, G_b=400, 600, v_s=0.3, D=6 m, ϕ_{max}=35°, 40°, e_o=0.54, 0.82, γ_d=14.2, 16.8 kN/m^3 were used

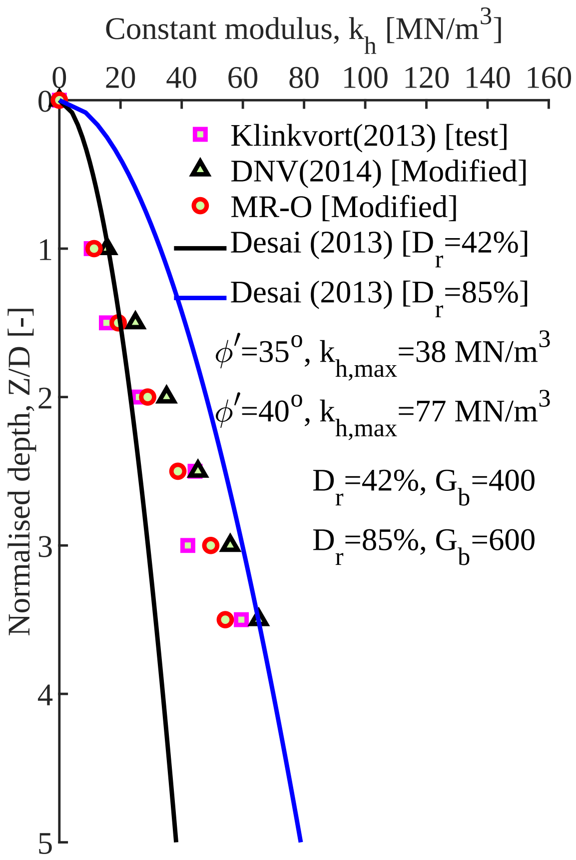

(a) The profile of coefficient k_h

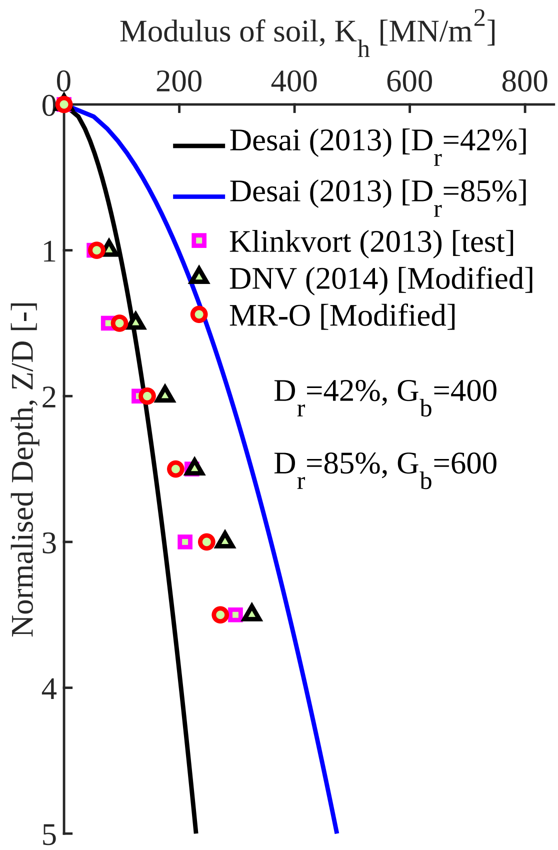

(b) The modulus of soil profile, K_h

Figure 4.13: The profile of coefficient, k_h, and modulus, K_h, of subgrade reaction.

for the analysis. The objective here was to set the basis for analysing the global load-displacement response of the current study due to the absence of the tested *p-y* curves below the ground surface. In Fig. 4.13(a), the $k_{h,max}$ for medium dense (D_r = 42%, G_b=400) and dense (D_r = 85%, G_b = 600) sands were 38 and 77 MN/m^3, respectively. From Eq. 4.11 and Fig. 2.8(b) in Chapter 2, the $k_{h,max}$ is found to be 43 and 72 MN/m^3, respectively. These values are found to be close and will be used throughout in the analysis.

4.5 Deflection prediction and comparisons

4.5.1 Introduction

An equilibrium of forces outlined in Section 4.5.2 is used in combination with MR-O *p-y* expression (see Eq. 4.5) for replication of experimental data. Since the current study included non-instrumented piles, firstly, the procedure has been benchmarked against the experimental *p-y* curves from Klinkvort (2013). In carrying out the analysis, reasonable assumptions were made in selecting the properties of initial stiffness in-terms of the modulus of subgrade reaction, K_h, and ultimate soil resistance, P_u. From the equilibrium analysis, the global load-displacement response at the ground surface is compared with the experimental data. All the model parameters were carefully employed in the analysis and the best estimates were made.
In making discussion of the comparisons between calculated and experimental results, the term 'underestimate' is used to indicate that the computed values are less than the corresponding measured values, and the term 'overestimate' will indicate that the computed values are more than experimental values.

4.5.2 Implementing the modified Ramberg-Osgood method

In this section where the pile is assummed perfectly rigid, it is possible to deduce an expression of the soil reaction curves based on the measured data and equilibrium of forces and moment. The definition sketch, shown in Fig. 4.14, is used to describe the statement of the problem. From the figure, a free head rigid pile driven in sand having a total length, L_T = L+L_e, embedded depth, L, external diameter, D, is pushed by lateral force, H_i. The load H_i is located at a distance L_e above the ground level, which creates a moment, M_i = H_i x L_e, at the ground surface, GL. A monopile foundation is a rigid pile, unrestrained and assumed to rotate at an angle, θ, about point O at a depth Z_r and Z_o from the ground and base of the pile, respectively. A one-dimensional idealised sketch for the pile and equivalent horizontal spring for soil are both shown in Fig. 4.14, which indicate the important parameters applied in the analyses.
A set of springs with the modulus of subgrade reaction, K_h and ultimate lateral soil resistance, P_u, along the embedded depth, are used to represent a pile-soil interaction response. The pile

is rigid and its deflection, $y_{z(i)}$, varies linearly with depth, Z. The soil resistance $P_{z(i)}$ is related to pile deflection, $y_{z(i)}$, by MR-O model function shown in Eq. 4.6, Section 4.4.1.

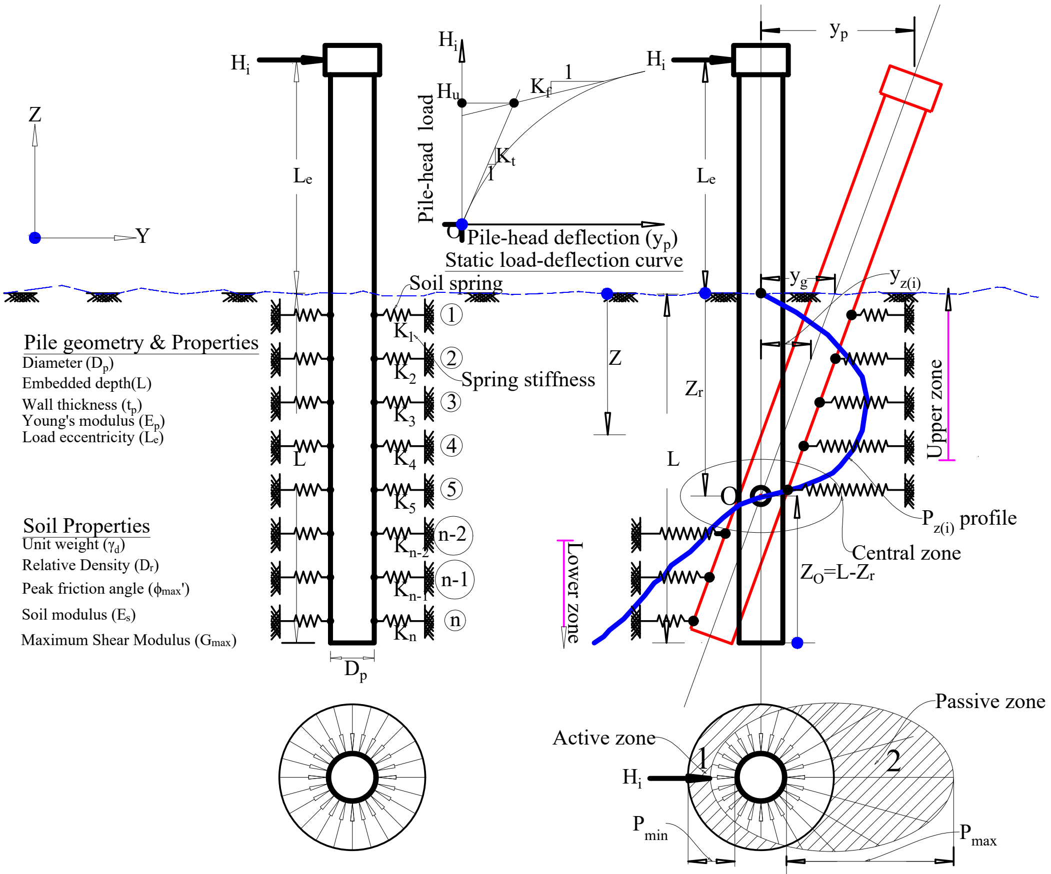

(a) Before the application of load (b) After load application

Figure 4.14: Schematic diagram for typical definition of analytical model on a rigid pile.

4.5.2.1 Basic assumptions

By using the sketch shown in Figs. 4.14 and 4.15, the basic assumptions are listed below ;

- The monopile is assumed to be rigid and its motion is pure rotation so that the deflection of the pile at the ground surface, y_g, is a result of its rotation at depth, Z_r.
- With a known depth of rotation at O (see Fig. 4.14), the soil is assumed homogeneous and can be divided into upper, central and lower zones.
- The soil resistance ($P_{z(i)}$) and the pile deflection ($y_{z(i)}$) relation is nonlinear as shown in Fig. 4.15(a). In Fig. 4.15(b), the modulus of horizontal subgrade reaction (K_h) will

decrease with increasing pile deflection ($y_{z(i)}$). As the pile displacement continues to increase to a certain level, the ultimate soil resistance will be achieved.

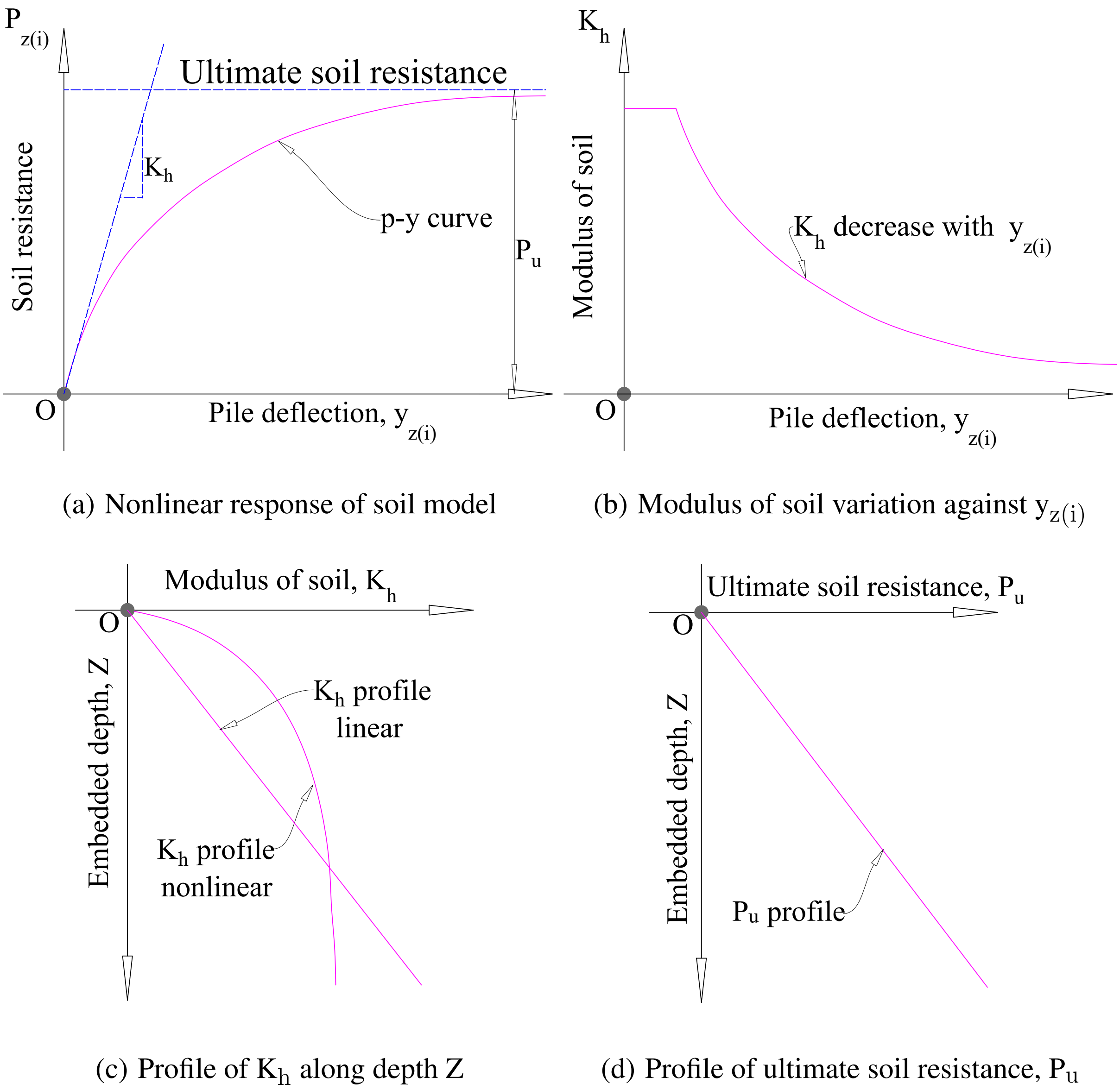

(a) Nonlinear response of soil model

(b) Modulus of soil variation against $y_{z(i)}$

(c) Profile of K_h along depth Z

(d) Profile of ultimate soil resistance, P_u

Figure 4.15: Sketches of typical parameters in the analysis of monotonic response.

- There has been discussion from the published work regarding the rate at which the initial stiffness of the *p-y* curves increases with depth. For instance, DNV (2014) assummed a linear profile while Carter (1984) and Desai and Zaman (2013) have suggested a nonlinear profile of the horizontal subgrade modulus of soil with depth, Z_n (see Fig. 4.15(c)).
- The ultimate soil resistance is assumed to vary linearly with depth (see Fig. 4.15(d)).

- The action of the vertical loads on the pile is discarded and the moment at the base is assumed to be zero.

4.5.2.2 General equilibrium solution

In this section, a developed equilibrium solution, with estimation of initial modulus, K_h, and ultimate soil reaction, P_u, is discussed. The pile is described by the depth of rotation centre from the ground surface, $Z = Z_r$, the depth, Z, the loading height, L_e, the embedded depth, L, horizontal displacement at the loading point, y_p, and ground surface, $y_g = Z_r \tan(\theta)$. The displacement along the depth of the pile, $y_{z(i)}$, can then be correlated with y_g using Equation 4.16 and 4.17 at the top and bottom of rotation point O, respectively. Eq. 4.18 can be used to determine the deflection of pile head (y_p) once the point of pile rotation (θ) is known. The rotation, θ, is constant with depth and can be valid only for small displacements of the pile ($\theta \leq 0.9^o$). This is the case for test results of this study, and is considered to be the case of monopiles in a full-scale conditions.

In Section 4.3.3, the location of Z_r was estimated as $0.68L \approx 20.4$ m in full-scale. It is therefore assumed that Z_r=20.4 m and θ is varied from 0 to 0.9^o to determine the ground deflection.

$$y_{z(i)} = \frac{(Z_r - Z)\,y_g}{Z_r}, \Rightarrow 0 \leq Z \leq Z_r \tag{4.16}$$

$$y_{z(i)} = \frac{(Z - Z_r)\,y_g}{Z_r}, \Rightarrow Z_r \leq Z \leq L \tag{4.17}$$

$$y_p = (L_e + Z_r)\tan(\theta) \tag{4.18}$$

The loads acting on the pile are the horizontal force and the distributed soil resistance along the pile. Knowing the soil resistance mobilised along the embedded depth, the total horizontal load at the pile head (similar to shear force at ground level) can be estimated. As can be seen in Fig. 4.14 and listed assumptions in section 4.5.2.1, the moment and force equilibrium are therefore estimated as follows:

1. Force equilibrium equation

$$\sum_{Z=0}^{L} \text{Force} = 0$$

$$\Longrightarrow \mathrm{H_i} + \int_{\mathrm{Z_r}}^{\mathrm{L}} \mathrm{P_{z(i)}dZ} - \int_{0}^{\mathrm{Z_r}} \mathrm{P_{z(i)}dZ} = 0$$

$$\therefore \mathrm{H_i} = \int_{0}^{\mathrm{Z_r}} \mathrm{P_{z(i)}dZ} - \int_{\mathrm{Z_r}}^{\mathrm{L}} \mathrm{P_{z(i)}dZ}$$

By using Eq. 4.6 and assumed that Δ K=$\mathrm{K_h}$-$\mathrm{K_f}$, $\Gamma = \mathrm{K_f y_i}$, the global resultant force at the ground surface can be estimated as shown in Eq. 4.19.

$$\mathrm{H_i} = \int_{0}^{\mathrm{Z_r}} \left[\frac{\Delta \mathrm{K y_i}}{\left[1 + \left|\frac{\Delta \mathrm{K y_i}}{\mathrm{P_u}}\right|^{\mathrm{r}}\right]^{\frac{1}{\mathrm{s}}}} + \Gamma \right] \mathrm{dZ} - \int_{\mathrm{Z_r}}^{\mathrm{L}} \left[\frac{\Delta \mathrm{K y_i}}{\left[1 + \left|\frac{\Delta \mathrm{K y_i}}{\mathrm{P_u}}\right|^{\mathrm{r}}\right]^{\frac{1}{\mathrm{s}}}} + \Gamma \right] \mathrm{dZ} \tag{4.19}$$

2. Moment equilibrium equation

   In Fig. 4.14, the equilibrium of bending moment about the rotation centre, O, can be derived as follows;

$$\sum_{\mathrm{Z=0}}^{\mathrm{L}} \mathrm{Moment} = 0, \Longrightarrow \mathrm{M_i} = \mathrm{H_i L_e}$$

$$\Rightarrow \mathrm{M_i} - \int_{\mathrm{Z_r}}^{\mathrm{L}} \mathrm{P_{z(i)}(Z - Z_r)dZ} - \int_{0}^{\mathrm{Z_r}} \mathrm{P_{z(i)}(Z - Z_r)dZ} = 0$$

$$\therefore \mathrm{M_i} = \mathrm{H_i(L_e + Z)} = \int_{0}^{\mathrm{Z_r}} \mathrm{P_{z(i)}(Z - Z_r)dZ} + \int_{\mathrm{Z_r}}^{\mathrm{L}} \mathrm{P_{z(i)}(Z - Z_r)dZ} \tag{4.20}$$

3. Normalised forces and moment

   The model was investigated by a series of centrifuge tests and the results can be transformed to prototype scale by means of normalised analysis to allow the comparisons. In this analysis, the normalised framework suggested by Klinkvort (2013) are employed to compare the results (see Table 4.1).

Methodology was coded in Matlab using the above expressions and the total load-displacement responses corresponding to the experimental tests were achieved.

4.5.3 Material properties

Under the given relative densities, the parameters to estimate ultimate soil resistance, modulus of subgrade reaction and MR-O soil model were first considered in the analysis as listed in Table 4.5. It includes the soil and pile properties and other constants used for adjustment and fitting.

Table 4.5: Parameters used in the analysis of monopile foundations.

SN	Parameter	Symbol	Unit	Medium dense	Dense
		Soil properties			
1	Relative density	D_r	%	42	85
2	Dry unit weight	γ_d	kN/m^3	14.2	16.9
3	Friction angle	ϕ_{max}	^{o}	35	40
4	Specific gravity	G_s	-	2.63	2.63
5	Void ratio=$\frac{\gamma_w G_s - \gamma_d}{\gamma_d}$	e_o	–	0.82	0.54
6	Poison ratio	ν_s	–	0.3	0.3
7	Material constant	G_b	–	400	600
8	Atmospheric pressure	P_a	kPa	100	100
		Pile properties			
1	Diameter	D	m	6	6
2	Embedded length	L	m	30	30
3	Load eccentricity	L_e	m	20	20
4	Flexural stiffness	E_pI_p	kNm^2	$1694x10^6$	$1694x10^6$
5	Max. rotation	θ_{max}	^{o}	0.9	0.9
		Fit parameters			
1	K_h fitting	α_p	-	0.15	0.15
2	P_i fittings	β_p, r, s, a	-	varied	varied

4.5.4 Comparison of experimental and calculated global response

The monotonic test results, obtained from this study are limited to the pile head load-deflection response. The pile was not instrumented, and therefore the *p-y* curves are compared to typically published *p-y* experimental data. Table 4.6 provides the properties of each of these stiff piles and soil they are tested in a centrifuge. The listed values from this table were used in the analysis.

Table 4.6: Parameters of the stiff model pile in sand, extracted from the the published centrifuge tests.

Reference	Model type	D	L	E_p	γ	e_o	ν_s	ϕ_{max}	N_s
	Unit	m	m	GPa	kN/m^3	-	-	o	-
Klinkvort (2013)	Model	0.04	0.24	70	16.8	0.7	0.4	42	125
	Prototype	5	30	210	16.8	0.7	0.4	42	-
Kirkwood (2016)	Model	0.0381	0.2	70	15.89	0.8	0.42	35	100
	Prototype	3.81	20	213	15.89	0.8	0.42	35	-

D = Pile diameter, L = Embedded dept, t_p = Wall thickness, E_p = Pile stiffness.

γ = Unit weight, e_o = void ratio, ν_s = Poisson ratio, N_s = centrifuge scale factor.

The ability of the method to predict the response of laterally loaded monopiles in dry sand is demonstrated by comparing the original and modified (new) *p-y* curve model functions, named as R-O and DNV original and MR-O and DNV modified (new). The original DNV and R-O models were first suggested by DNV (2014) and Ramberg and Osgood (1943), respectively, however, in order to match with experimental data, further modifications were introduced. As shown in Table 4.5, the constant parameter β_p was introduced into both models to increase or reduce the initial modulus of subgrade, K_h, however, the parameter α_p used to define the K_h suggested by Carter (1984) and Desai and Zaman (2013), was kept constant as discussed in Section 4.4.3. Each family of the *p-y* curves was estimated with the same ultimate soil resistance, which is based on a modification factor A_j. The *p-y* curves from MR-O employed the parameter *r*, *s* and *a* to give the best fit of experimental load deflection responses.

The two parameters (P_u and K_h) are first estimated as discussed in Section 4.4.2 and 4.4.3, respectively. The experimental ground load-displacement responses were verified by back calculating the rotation of the pile and corresponding displacement. The method in Section 4.5.2 utilised the calculated displacements and estimated P_u, K_h to define the soil resistance as a series of uncoupled springs. Each spring is characterised by nonlinear curves describing the relationship between the soil reaction and displacement. By using equilibrium of force and moment, the obtained p-y curves were combined, and back-calculated load-deflection behaviours were obtained.

The comparison between the experimental and calculated total lateral load-displacement behaviour at the ground surface, for the two model functions, are shown in Figs. 4.16 and 4.17, for the medium dense sand (100g) and dense sand (30g), respectively. In Fig. 4.16, the experimental response of the test OWTP/S-T3 is compared with calculated responses, in normalised form, using the original and modified (new) *p-y* models. The responses from original models significantly overestimates the lateral loads of the experimental data. The fitting parameters were introduced into these models and the responses are to some extent comparable with experimental data; however, a discrepancy still exists for the modified DNV model. It can be seen that the results of MR-O model agree well with those from the centrifuge model test OWTP/S-T3.

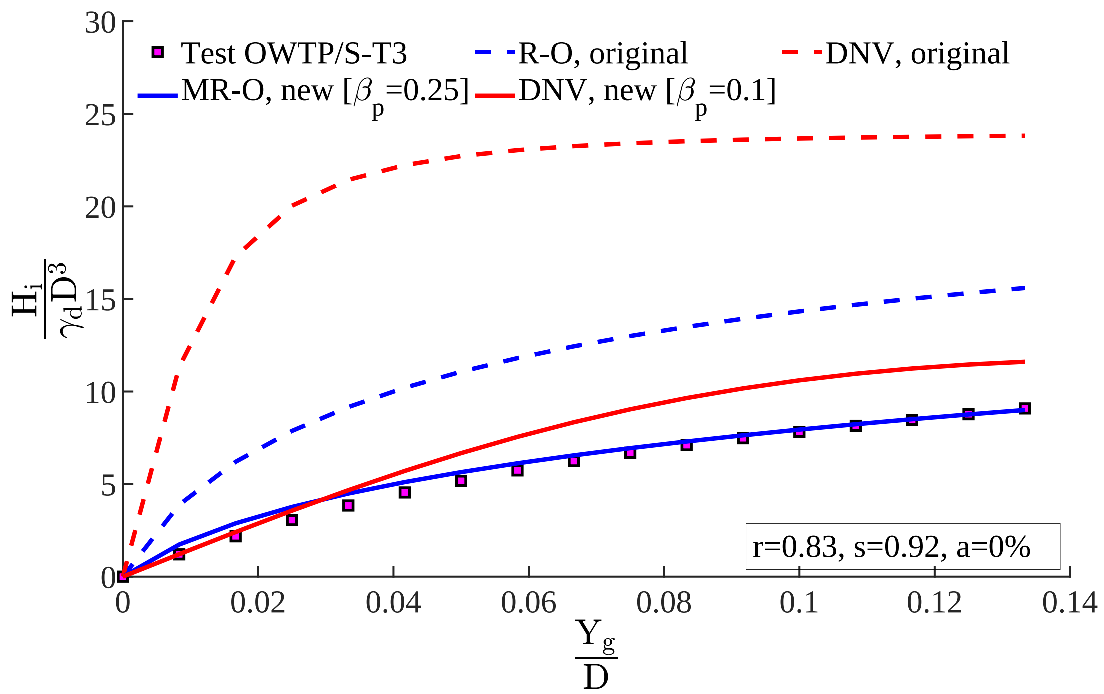

Figure 4.16: Comparisons of global load-deflection responses between experimental results (test OWTP/S-T3) and predictions from DNV (2014) and MR-O models.

A similar behaviour is also observed in Fig. 4.17 with significant difference of lateral load-displacement between the experimental and original *p-y* curve methods. From both figures, the agreement between the experimental and MR-O is excellent, while the DNV model is in poor agreement.

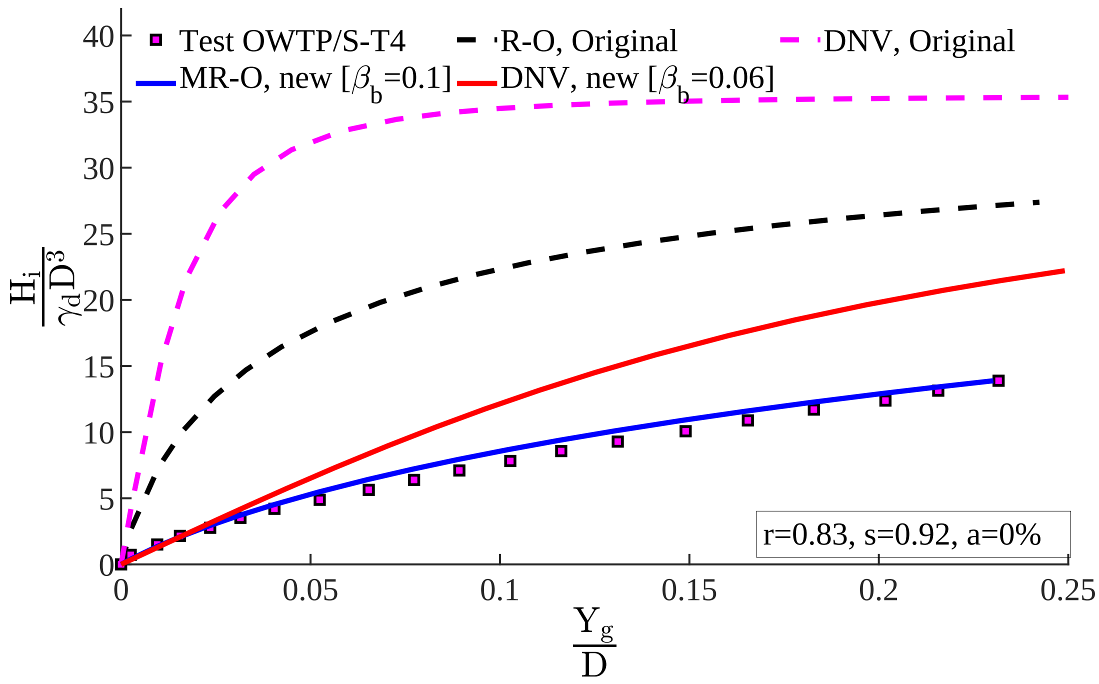

Figure 4.17: Comparisons of global load-deflection responses between experimental results (test OWTP/S-T4) and predictions from DNV (2014) and MR-O models.

The modified DNV and MR-O models were employed in the analysis to fit the global results of test OWTP/S-T1 (100g), test no. 30 (125g) (Klinkvort, 2013) and test P08 (100g). The plots of the computed and three tests are shown in Fig. 4.18. Test OWTP/S-T1 was compared with experimental results conducted by Klinkvort (2013) and Kirkwood (2016). It should be noted that the published works have been performed under different test setup compared to the current study, therefore, it is not possible to have direct comparison.

In Fig. 4.18, a comparison of the results indicate similar nonlinear responses, however, the tangent stiffness and ultimate capacities are seen to be different. A high capacity observed from Kirkwood (2016) highlights the difference of the model setup and other properties such as pile diameter, load eccentricity, embedded depth and soil state condition. From the figure, the initial stiffness of the present study is shown to be lower than the other two tests. This difference is due to increase of pile diameter from D=3.81 m (Kirkwood, 2016) to D = 6 m of the present study. The ultimate capacities observed from Kirkwood (2016) and present study were somewhat larger than the results from Klinkvort (2013). This is due to smaller point of load eccentricity (L_e) despite of identical slenderness ratio (L/D = 5) with the current study. This is also noted from Klinkvort and Hededal (2014) who concluded that the piles loaded with small L_e have higher capacities compared with one of the lower values.

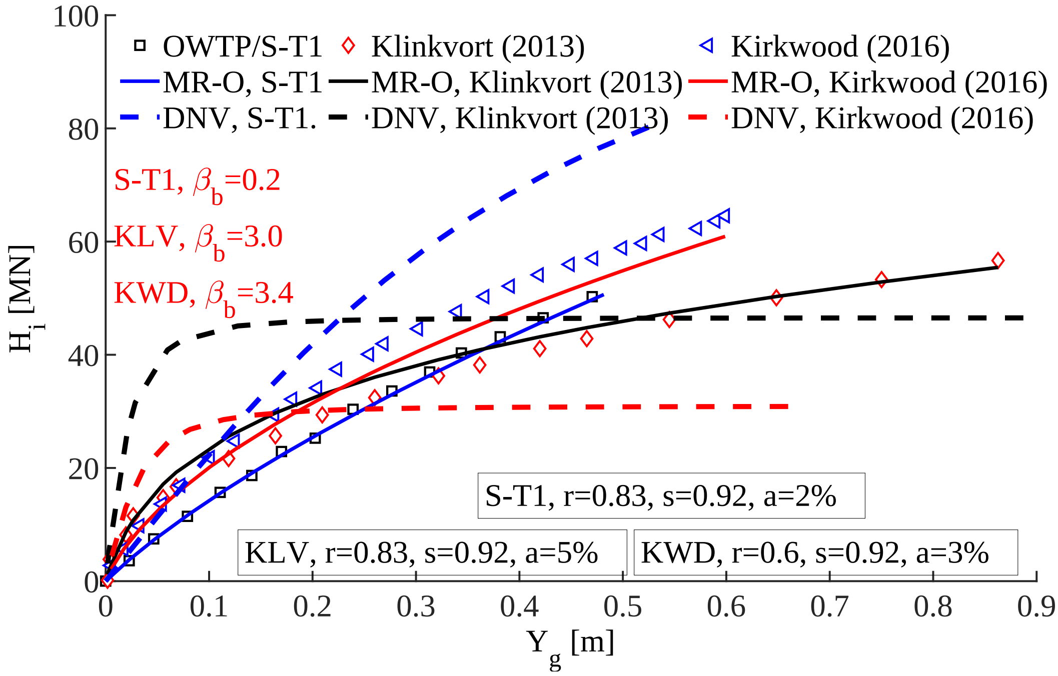

Figure 4.18: Comparisons of global load-deflection responses between experimental result (test OWTP/S-T1) and predictions from (DNV, 2014) and MR-O models, including the results from Klinkvort (2013) and Kirkwood (2016).

Furthermore, in Fig. 4.18 the plots shows that the MR-O model compared well with experimental results and the responses are in excellent agreement. For instance, in test OWTP/S-T1 the initial stiffness (K_t) of the DNV model agrees well with experiment, however, the ultimate capacity (H_u) is in poor agreement. The H_u was obtained by considering the ultimate soil resistance (P_u) from DNV (2014) with the use of modified depth factor A_j, however, it does not clearly provides the accuracy of the results. With no clear conclusion drawn from the use of this factor, further study is recommended.

Several studies have shown that the *p-y* relationship described from DNV (2014) is not suitable for estimating the response of the global monotonic load-displacement response. The slopes of load-deflection curves are greater than those determined from the experimental tests because the DNV method was derived from field tests on flexible piles, which has a significant effect on the behaviour of monopiles. The stiffness of the pile-soil interaction is a function of relative density, stiffness of sand, friction angle and pile installation, which can not be predicted accurately with the model function derived from small pile diameter. All these factors require a full-scale in-depth research to evaluate the effect of the monopile diameter on the p-y curves. In conclusion, the response obtained by DNV (2014) *p-y* curve model overestimates both initial stiffness and ultimate capacity of the pile used in this study (see Fig. 4.16, 4.17 and 4.18). The centrifuge tests by Klinkvort (2013) and Kirkwood (2016) were also compared with modified DNV models. The use of nonlinear variation in the soil stiffness resulted in an over-estimate of the tangent stiffness ($\mathrm{K_t}$), however, the ultimate capacity of the pile ($\mathrm{H_u}$) was observed to be lower than the experimental data. The MR-O soil model provides the best fit to experimental data of the current and published studies. The model allows for a change in the initial modulus of subgrade reaction, final tangent modulus and ultimate soil resistance with depth, which involves additional fitting parameters. It is also revealed that the modification proposed to increase or decrease the initial stiffness of the *p-y* curves leads to improved *p-y* formulation compared to those that employed from previous studies.

4.5.5 Comparison of *p-y* curves

As noted from the previous section, the current study is only limited to a non-instrumented pile with data only related to the global response of the load-deflection at the pile head. Therefore, a comparison is made to typically published *p-y* curve data from Klinkvort (2013) to demonstrate the capability of the model suggested in this study.

The details of the mathematical expressions, used to analysed the *p-y* responses, are given in Table 4.4, Section 4.4.1. A matlab code was written to enable comparison between the *p-y* experimental behaviour of test no. 30 (Klinkvort, 2013) and the response computed by DNV (2014) and Ramberg and Osgood (1943) models. The relationship between the soil resistance $\left(\mathrm{P_{z(i)}}\right)$ and deflection of the pile $\left(\mathrm{y_{z(i)}}\right)$, from the two soil models, are presented and compared against the experimental data. From these models, the parameter $\mathrm{K_h}$ and $\mathrm{P_u}$, described in Sections 4.4.3 and 4.4.2, respectively, were determined. Each family of the *p-y* curves as presented in Fig. 4.19 were constructed based on the $\mathrm{P_u}$ function defined by DNV (2014). However, the empirical depth factor $\mathrm{A_i}$ was modified to $\mathrm{A_j}$ in order to match the results of

Klinkvort (2013) centrifuge test (see Fig. 4.12(a), Sec. 4.4.2). As shown in Table 4.6, some properties of the material used for test no.30 are closely related to the current study, for instance, γ_d = 16.8 (16.9) kN/m^3, ϕ_{max} = 42^o (40^o) and L = 30 m in prototype condition. Therefore, the values of P_u and K_h extrapolated from the experimental *p-y* curves shown in Fig. 4.19, were used to set the boundaries of the calculated initial stiffness and ultimate soil resistance variation along the embedded pile.

In Fig. 4.19, the initial slopes of the pile-soil interaction curves were defined as described in Fig. 4.13(b), Sec. 4.4.3. This method assumed that K_h is increased nonlinearly with depth as suggested by Carter (1984) and Desai and Zaman (2013). The non-dimensional constants G_b (400 and 600 for the medium dense and dense sand, respectively) and m = 0.5 were adopted for the analysis throughout the chapter. By using the fitting constants shown in Table 4.5, the experimental *p-y* curves were set as the benchmarks and compared with modified DNV and MR-O *p-y* curve models. The coefficient β_p was introduced into these models to either increase or reduce the initial stiffness of the computed *p-y* curves. The experimental *p-y* curves at depth of 1D, 1.5D, 2D, 2.5D, 3D and 3.5D (where D is diameter of pile) are compared with original and modified models in a normalised form.

The local pile-soil interaction behaviour is thus estimated initially by the original DNV and R-O methodology and then modified by using the constants listed in Table 4.5. In Fig. 4.19, all model responses are plotted together. A comparison of the original *p-y* curves shows a significant difference in shapes, stiffness and magnitude as compared to the published experimental data and MR-O *p-y* curves. Clearly, it can be seen that the original DNV (2014) method indicates high values of initial stiffness and magnitude of soil resistance compared to modified models. The MR-O model function agree well with experimental data over a larger range. The ultimate soil resistance is overestimated in the upper soil layers of Z=1D, reasonably estimated at depth of Z = 1.5D, 3D and 3.5D, and is underestimated in the soil layers from Z = 2-2.5D. As described in the previous studies (Choo and Kim, 2015, Kirkwood, 2016, Klinkvort and Hededal, 2014) into response of monopiles, the *p-y* curves from DNV (2014) method observed to overestimate the stiffness at shallow depth and underestimate at greater depths and recommended that the method is not suitable for use with rigid piles. For instance, Klinkvort and Hededal (2014) used hyperbolic *p-y* model to fit the results and confirmed that the stiffness was underestimated below the rotation point. Similar behaviour is observed in this study, however, the additional factors considered in the MR-O was successfully used to close the gap.

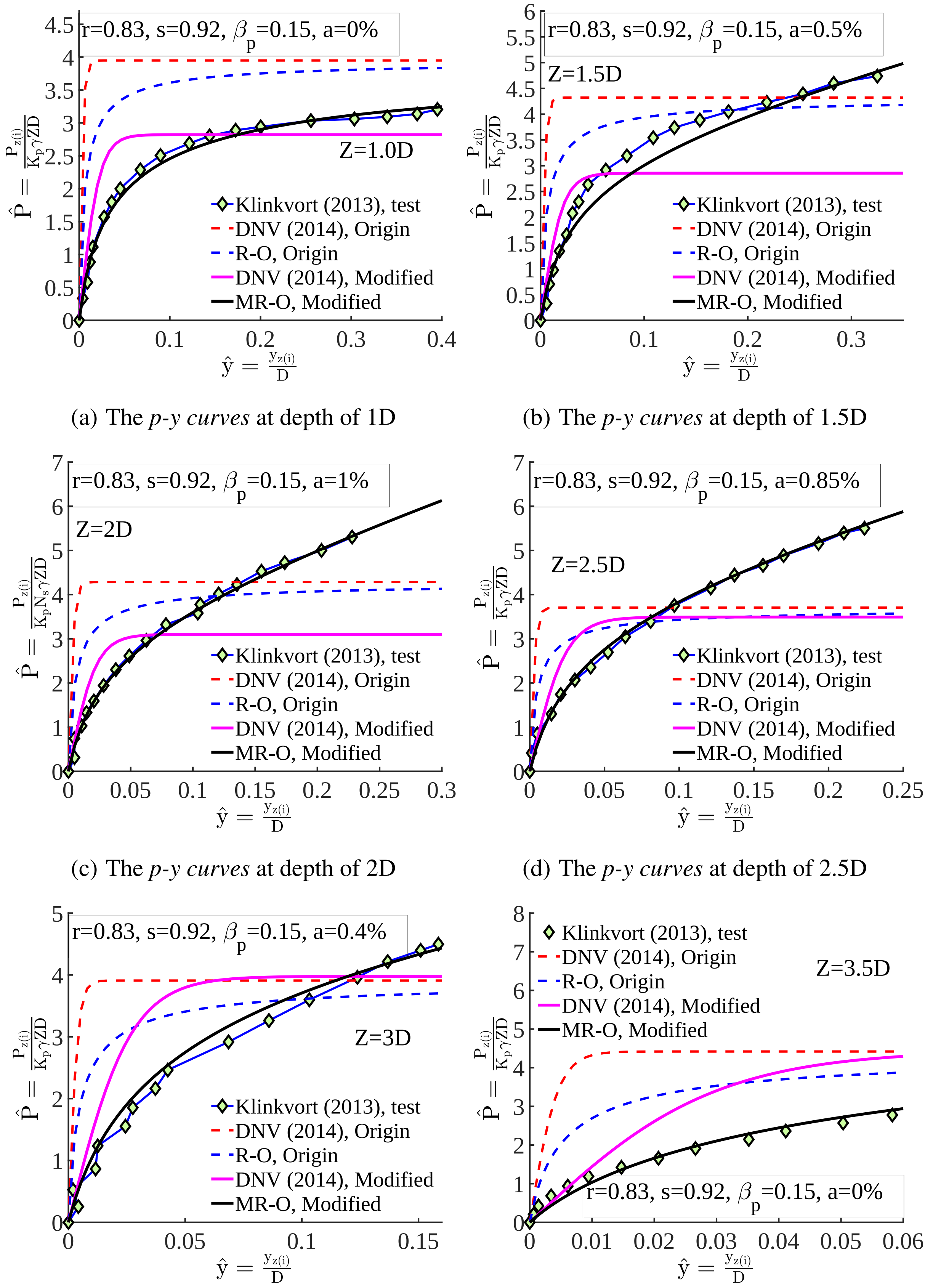

(a) The *p-y curves* at depth of 1D

(b) The *p-y curves* at depth of 1.5D

(c) The *p-y curves* at depth of 2D

(d) The *p-y curves* at depth of 2.5D

(e) The *p-y curves* at depth of 3D

(f) The *p-y curves* at depth of 3.5D

Figure 4.19: The comparisons of the Klinkvort and Hededal (2014) experimental and calculated DNV and MR-O *p-y* curves models.

In conclusion, the MR-O model function by Desai and Zaman (2013) observed to agree well with chosen published local p-y curves. The assumption of using depth factor in the calculation of ultimate soil capacity into monopile foundation is clearly lacks some accuracy as it was derived from flexible piles. The factor A_i is a site dependent to where it was originally and one should be carefully when it is applied at different locations. Therefore, no clear conclusion can be drawn from this study and further investigation is required. The empirical related factors, used in calculating the modulus of subgrade reaction and ultimate capacity for MR-O model function, are dependent on the specific test and should be used with care outside the calibration limits. However, the calibration limits of the current study were based on published local *p-y* curves, therefore, it has to be investigated further.

4.6 Soil resistance and bending moment profile

4.6.1 Soil resistance profiles

The soil reaction profiles, for the maximum pile rotation of $\theta = 0.9^{o}$ (Equivalent to 10% of pile diameter at the ground surface), were obtained as shown in Fig. 4.20. Figs. 4.20(a) and 4.20(b) show the profiles for the medium dense and dense sand, respectively. The results are presented to enable a comparison between the original and modified published *p-y* curves models in relation to global responses of the test OWTP/S-T1, OWTP/S-T3 and OWTP/S-T4. From both figures, the general shape of the two modified soil resistance (DNV and MR-O) are well estimated with very little difference from the usage of adjustment fitting constants created *p-y* curves. The MR-O model was used as a benchmark to represent the global response. Overall, the agreement between MR-O and other computed *p-y* curves is satisfactory at shallow depths in the upper zones and overestimated at depth below Z = D.

From the figures, some differences occurred between the fitted MR-O and DNV soil resistance distribution. For instance, at shallow depth ($Z \leq 1D$), all models show a close agreement with MR-O. However, in Fig. 4.20(a), at depth $0 \leq Z \leq 2.6D$ m, the modified DNV model agrees well with MR-O but slightly overestimated at depth of $2.5D \leq Z \leq 5D$ m. A similar observation is also found in the test OWTP/S-T4, in which the modified DNV model (see red line in Fig. 4.20(b)) overestimated the fitted MR-O model at depth of $1D \leq Z \leq 5D$ m. In Fig. 4.20(b), the

MR-O model fitted to test OWTP/S-T1 is underestimated by DNV at a depth between zero to 0.5D m, and over-predicted from $0.6D \leq Z \leq 5D$ m. The discrepancy alongside the depth of pile may be attributed to several factors, including (a) the approximate nature of the maximum shear modulus, G_{max} profile obtained from the literature and not experimentally, which was applied to derive the initial stiffness profile (b) the empirical constants used to develop an ultimate soil resistance, which relied on flexible piles.

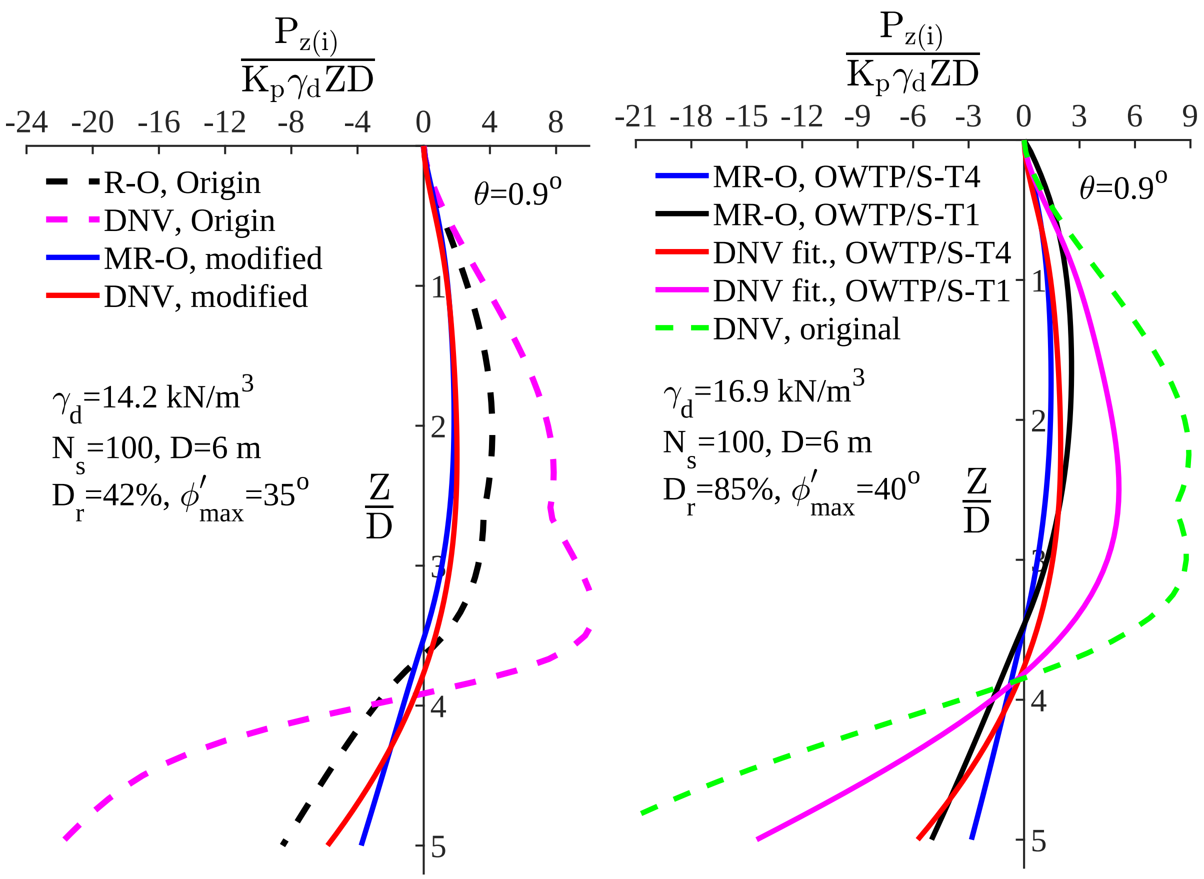

(a) Original and modified $P_{z(i)}$, test OWTP/S-T3

(b) Original and modified $P_{z(i)}$, test OWTP/S-T1/T4

Figure 4.20: Comparisons of soil resistance distribution of the DNV and MR-O models based on test OWTP/S-T1, OWTP/S-T3 and OWTP/S-T4.

In Fig. 4.21, the calculated $P_{z(i)}$ distributions of the original (DNV and R-O) and modified DNV, in the normalised form, are presented alongside the benchmark fitted MR-O model to the results of Klinkvort (2013) (test no. 30) and Kirkwood (2016) (test P08). The kinematic equilibrium solution from this study yields a good fit to the experimental global response and used to develop a soil resistance profile. However, careful consideration of the soil resistance profile shows that the modified DNV and original models accurately predict the $P_{z(i)}$ profile to depth of approximate 2D m in Fig. 4.21(a) and underestimates up to a depth of 2.5-3.7D in Fig. 4.21(b). From both figures, at a depth between 3D up to the pile base, both original and modified DNV model overestimates the soil resistance profile while the original R-O underestimates this depth. Overall, the DNV model appears to give the good agreement of lateral soil resistance at shallow depth but none of it allows an accurate prediction at the middle and lower zones.

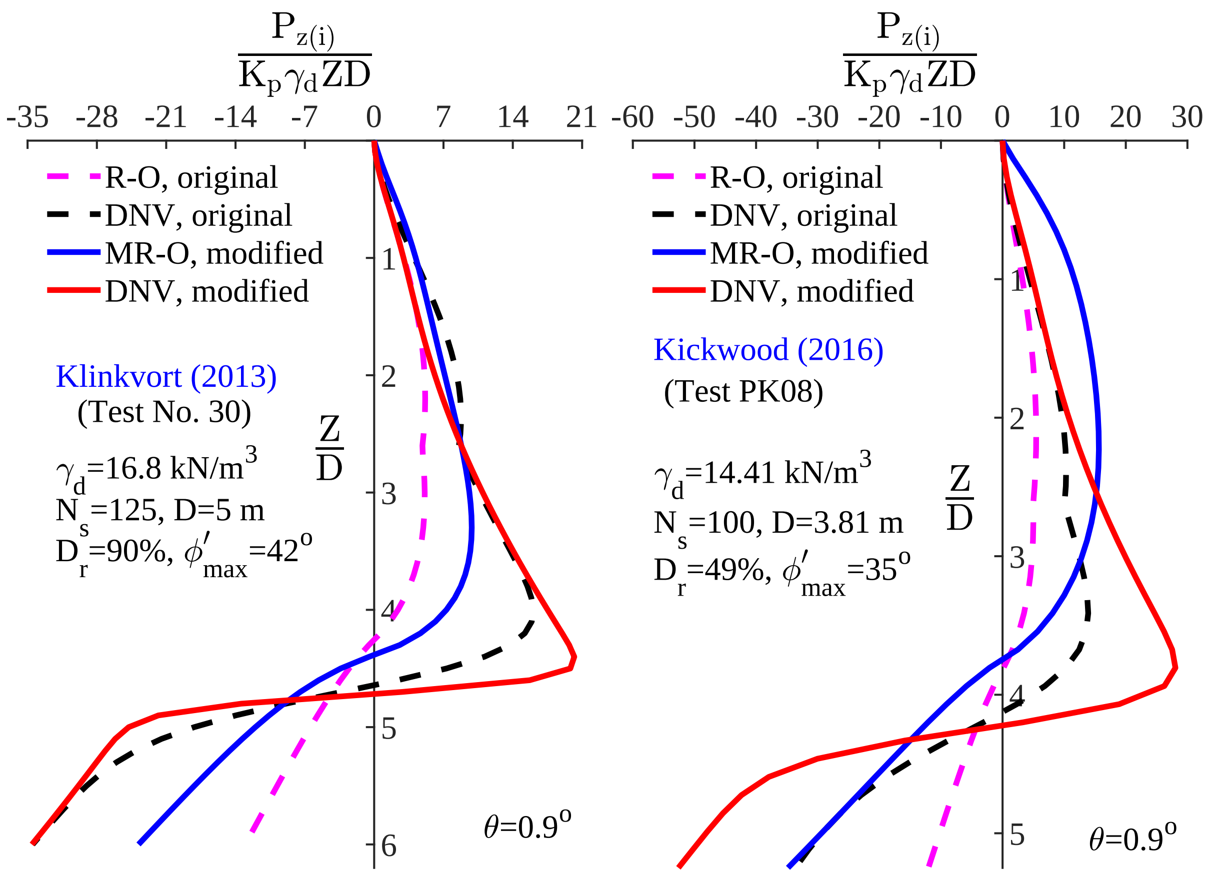

(a) Fitted $P_{z(i)}$, test No. 30 (Klinkvort, 2013) (b) Fitted $P_{z(i)}$, test PK08 (Kirkwood, 2016)

Figure 4.21: Comparisons of the fitted *p-y* distribution of the original and modified DNV and MR-O models to the published total load-deflection response at the ground surface.

4.6.2 Bending moment profiles

The basis behind the selection of P_u and K_h profiles was utilised in the analysis to describe the bending moment distribution along the pile length. Figure 4.22(a) and 4.22(b) shows the moment profiles for the medium dense and dense sand, respectively. For clarity, the curves are shown only to a maximum of 10% of the pile diameter displacement at the ground surface, which correspond to 0.9^{o} pile rotation. In Fig. 4.22(a), the original and modified bending moment distributions of Ramberg and Osgood (1943) and DNV (2014) models are presented and compared. The general shape of the bending moment, of the two modified models, are well estimated with very little difference from the usage of adjustment fitting constants created from the *p-y* curves. The bending moment variations from the original *p-y* curves overestimated the fitted models. It should be noted that in Section 4.5.4, Fig. 4.16, the computed MR-O model agrees well with the test OWTP/S-T3, hence, it is used here as the benchmark. In Fig. 4.22(b), the similar observations of tests OWTP/S-T1 and OWTP/S-T4, conducted at centrifuge acceleration of 100g and 30g, respectively, are presented. There is a significant difference between the bending moment curves of the modified DNV and MR-O models of the test OWTP/S-T1. In the test OWTP/S-T4, the modified DNV model has little difference compared to MR-O model. In Fig. 4.22(a), the difference in the maximum bending moment, between the benchmark MR-O and modified DNV, was about 10%, which shows a closer agreement but still overestimated the results. For dense sand (See Fig. 4.22(b)), the difference is approximately 40% of the test OWTP/S-T4 and 73% of the test OWTP/S-T1. The calculated DNV model overestimated the bending moment variation in this study, in spite of the fact that the original model was modified.

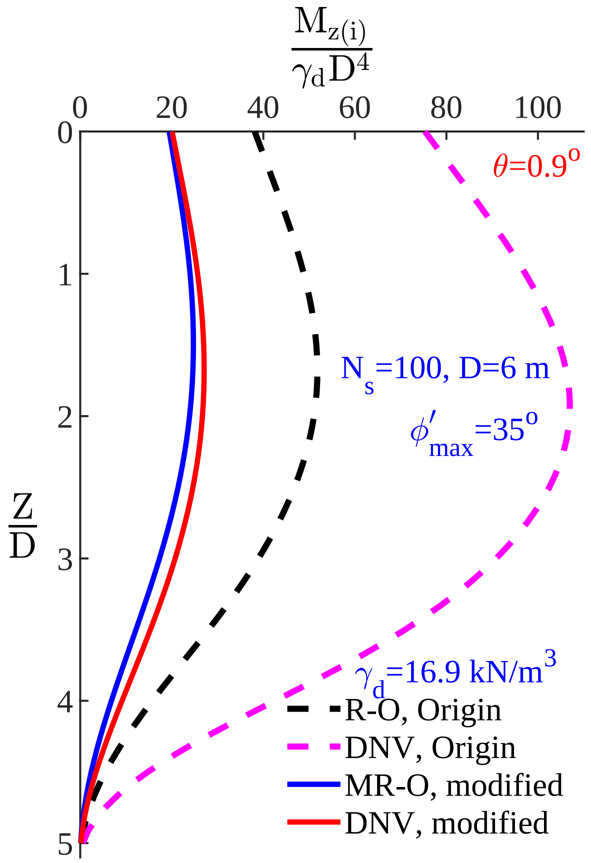

(a) Original and modified M_i, of the test OWTP/S-T3

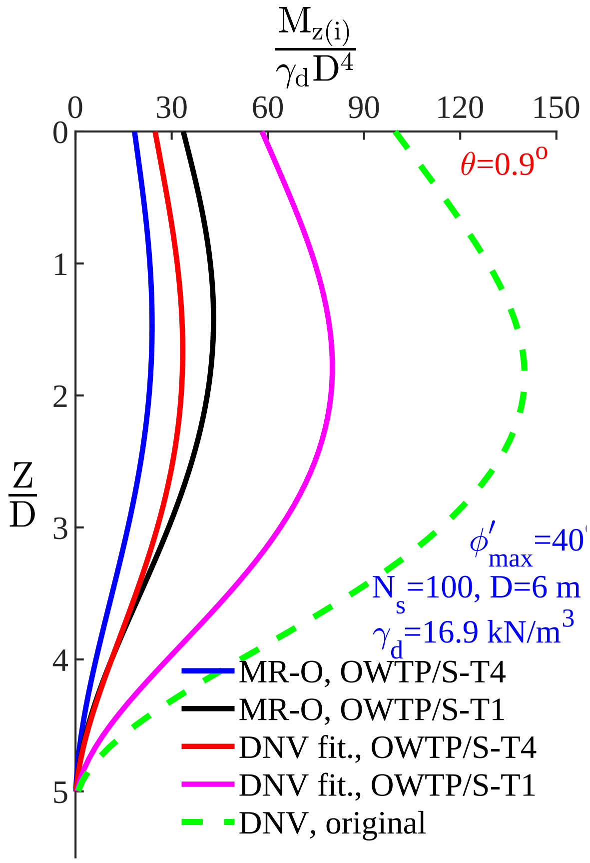

(b) Original and modified M_i, of the test OWTP/S-T1/T4

Figure 4.22: Comparisons of original and modified bending moment distribution of the DNV and MR-O models of the tests OWTP/S-T3 (medium dense sand, 100g) and OWTP/S-T1/4 (dense sand, 100g and 30g).

Figs. 4.23(a) and 4.23(b) depicts the bending moment profile of the fitted published Klinkvort (2013) and Kirkwood (2016) global response centrifuge tests, respectively. The MR-O model agreed well with experimental results and is chosen here as the benchmark of the other models. Overall, it can be seen that in Fig. 4.23(a) the moment profile of the MR-O model is underestimated by R-O and overestimated by DNV models. This is also observed in Fig. 4.23(b), however, from the depth of 2D m to the pile base, the DNV model underestimates the MR-O profile. The DNV model shows a big difference of bending moment profile, despite that the original model was modified. It is possible that this difference is due to the effect of shear force at the pile base that has not been accounted for in the flexible piles. An in-depth experimental field study is required regarding this effect on monopiles.

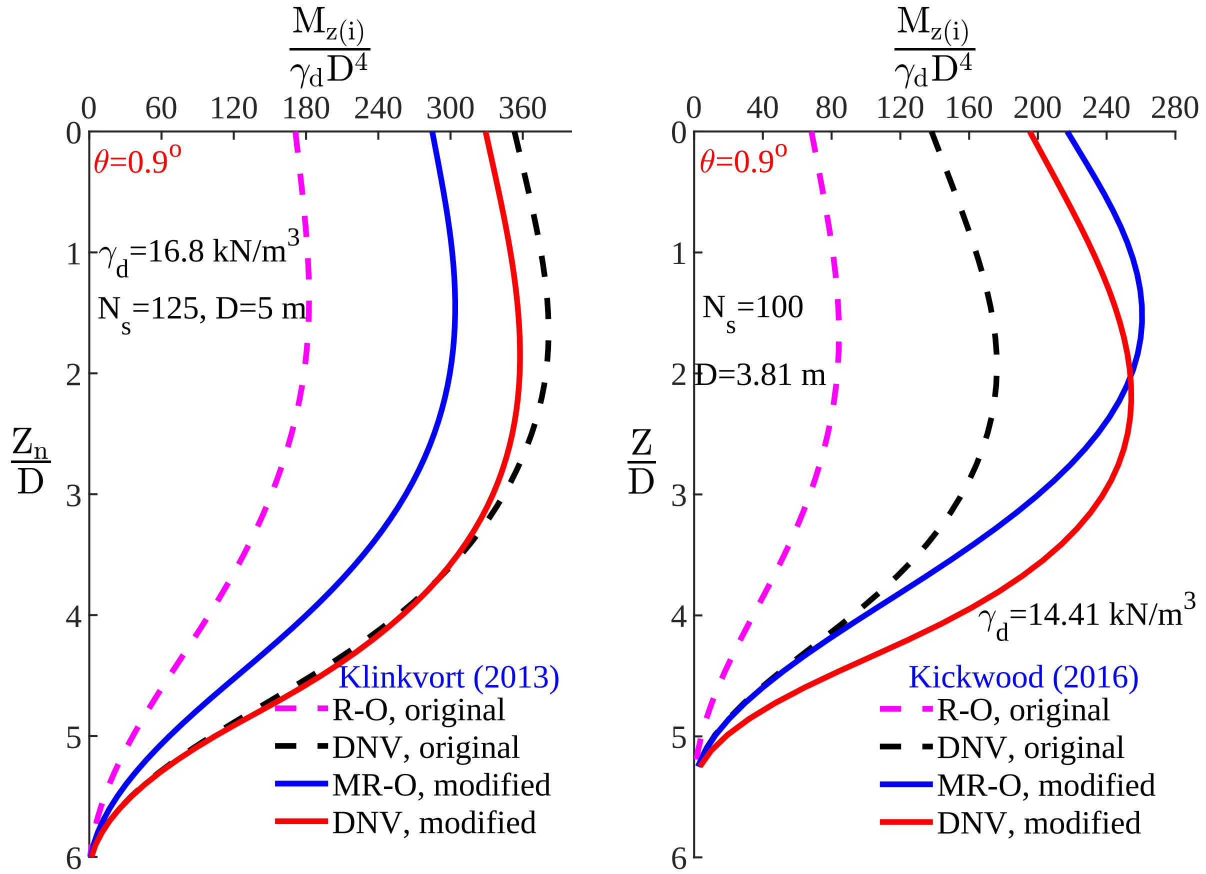

(a) Origin and modified M_i for test OWTP/S-T3

(b) Modified M_i from test OWTP/S-T1 and Klinkvort (2013)

Figure 4.23: Comparisons of origin and modified bending moment distribution of the DNV and MR-O models.

In the analysis of rigid piles, the presence of shear force at the base increases the lateral resistance, however, it does not contribute significantly to the ultimate capacity of the pile and its effect on bending moment is minimum. The monopile design to resist the bending moment is controlled by the maximum moment at shallow depth, close to the surface. A slightly increase in bending moment towards the base is of little concern and has also been discovered by Abadie (2015), Lau (2015) and Kirkwood (2016). Therefore, the results obtained in this study suggest that the effect of shear force at the base is minimum and is not considered in the design.

4.7 Chapter summary

In this chapter four monotonic tests have been conducted on a non-instrumented rigid model pile in dry sand subjected to lateral loading. Comparisons have been made between the lateral response of the model pile in the centrifuge and the response predicted based on the kinematic approach solution using p-y curves from MR-O (Desai and Zaman, 2013) and DNV (DNV, 2014) models. The primary conclusions from the work presented in this chapter are described as follows:

1. In the centrifuge tests, the lateral response of the pile is mostly affected by relative density and level of centrifuge acceleration. A non-linear behaviour is observed in the model tests, however, the ultimate loads were not achieved. The 10% of pile diameter and DNV (2014) rotation limit methods were used to determine the capacity of the pile, H_u.

2. The model pile was observed to rotate rigidly to a depth of $0.65L \leq Z_r \leq 0.68L$, which is approximate to 200 mm from the ground surface. However, this is slightly different compared to analytical solutions, with approximately Z_r from 0.7L to 0.76L.

3. The model pile in a centrifuge was non-instrumented; hence, it was difficult to predict the total force-deflection behaviour using *p-y* curve method. The similar experimental *p-y* curves, derived from Klinkvort (2013), were used as a benchmark to estimate the ultimate soil resistance, P_u and modulus of subgrade reaction K_h. The model experiment (Test No. 30) from Klinkvort (2013) was chosen due to close properties of sand and geometry of the pile. The modified depth factor, A_j, recommended by DNV (2014), was used throughout to estimate the ultimate capacity, P_u.

4. By using the *p-y* curves of test no. 30 (Klinkvort, 2013), a nonlinear variation of K_h suggested by Vesic (1961), Carter (1984) and Desai and Zaman (2013) was set and used throughout. The fitting coefficient β_p was employed into the models to adjust the initial slopes of the *p-y* curves for the purpose of matching the global responses.

5. An optimisation technique was proposed, which considered the force and moment equilibrium of the pile, rotation and deflection. By using the equilibrium of the forces and moment and minimising the difference between the calculated and experimental total

load-deflection response, the soil reaction and bending moment profile due to rotation and deflection of the pile were obtained. This method was applied to match the results of the centrifuge from the current study and the published work of Klinkvort (2013) and Kirkwood (2016).

6. The ultimate soil resistance (P_u) values were assummed as those recommended by DNV (2014) and *p*-*y* curves from Klinkvort (2013). This assumption was important because the values of P_u in this study was not identified experimentally.

7. The *p*-*y* curves from the experimental tests and MR-O models were found to exhibit a softer responses than those from DNV (2014), which were originally developed for piles with smaller diameter ($\leq$ 2 m). The significant difference in the *p*-*y* curves between the experiment and DNV (2014) may originate from the increase of pile diameter of the monopile, and therefore, further research is important to observe this effect.

8. Studies recommended that p-y curves proposed by DNV (2014) are unconservative for estimating the behaviour of rigid piles. The results provided in this study prove that the use of DNV model overestimates initial stiffness and response of soil resistance. The MR-O model, which includes more parameters, allows the change in stiffness and ultimate capacity with depth and provides best fit to experimental data. At shallow depth, the modified DNV model provide a good estimate, however, below the rotation point it underestimates the stiffness of the MR-O *p*-*y* curves. This trend has already been noted by other studies and more experimental research is required to substantiate this result.

9. A depth factor A_i (API, 2007, DNV, 2014) was modified to A_j and used to match the results of this study. The total load-displacement response showed a satisfactory agreement with MR-O model. However, the use of this factor needs a further study to be used accurately into other models.

10. Because the centrifuge tests were conducted with a non-instrumented piles, a complete proposal regarding the appropriate design methods for monopiles cannot be concluded based on the results of this study. However, the author suggests that the findings achieved in this chapter may provide a strong motivation for further research on the diameter effect, relative densities, soil types, multi-layers, load eccentricity and embedded depths.

Chapter 5

CYCLIC PILE LOADING EXPERIMENTAL RESULTS

5.1 Introduction

The description of nonlinear hysteresis behaviour of monopiles using theoretical models requires an understanding of the key parameters derived from the model pile experiment response. As described in Chapter 3, this is achievable using centrifuge model testing with experiments focused towards this objective.

This chapter presents centrifuge test results (tests OWTP/C-T16 and OWTP/C-T17) and analyses that pertain to the cyclic behaviour of the monopiles in dry sand. The centrifuge package used for testing purposes was described in Chapter 3. The main objective of these tests was to ensure that the cyclic behaviour, obtained using the developed experimental apparatus, adequately reflected the cyclic behaviour of monopile foundations. This objective was achieved and, in analysing the data, some features of pile-head load-displacement, for pile in sandy, were revealed. The results presented here serves as the basis for comparison with the theoretical model development in Chapter 6.

5.2 The analysis framework

5.2.1 General concept

The offshore wind turbine foundations are exposed continuously to the cyclic action of wind and waves, demanding reliable design procedures that would take into account the possible cyclic stiffness degradation and accumulation of plastic deformations. The term cyclic loading is used to characterise variable loads having clear, repeated patterns and degree of regularity in cyclic peak-to-peak magnitude ($\mathrm{H_{amp}}$) and return period (T) (Andersen et al., 2013). There are four main types of loads acting on monopiles; winds, waves, 1P, and 3P (see Fig. 5.1) (Nikitas et al., 2016). These loads are random and vary in their magnitude and direction over its design life. Winds and waves are termed as cyclic loads acting in different directions while 1P and 3P are acting dynamically, caused by the rotational frequency of the rotor and blade shadowing effect, respectively. More details can be found in Chapter 2.

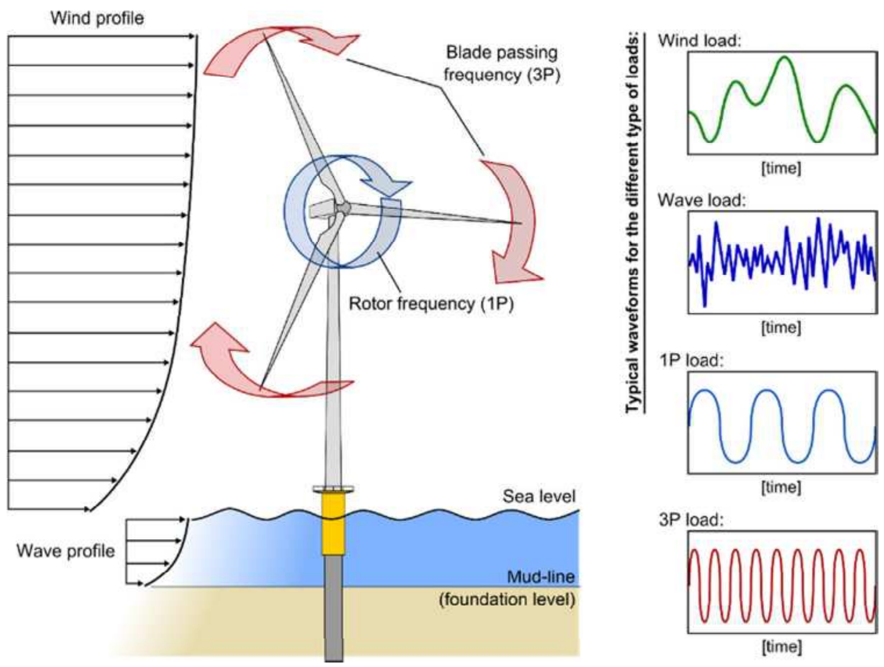

Figure 5.1: Loads on wind turbine with typical waveform, from Nikitas et al. (2016).

For experiment and design purposes, the cyclic loading effects are usually restricted to the time frame and cyclic rate that allow suitable control, precision and data capture rate (Andersen et al., 2013). Hence, the best option is to carry out a uniform cyclic pattern with a load or displacement sequence, which employs a fixed frequency and regular amplitude. In this study the loading frequency was fixed to 2.5 Hz.

5.2.2 Filter frequency for data analysis

To analyse the data, the calibrated voltage readings from all sensors were filtered with low pass filter from MATLAB (MATLAB, 2016). By employing the Butter-worth filter, using the command line and the interactive filter design, the high frequency signal components from the signal data can be removed. The MATLAB code to generate the filter coefficients is shown by $[\mathrm{b}, \mathrm{a}] = \mathrm{butter}(\mathrm{n}, \mathrm{W_n}, \mathrm{ftype})$. From this function, *b* and *a* are the transfer function coefficients, the first argument is an $\mathrm{n^{th}}$-order low-pass Butter-worth filter, the second argument is the normalised cutoff frequency $\mathrm{W_n} = \frac{\mathrm{f_c}}{0.5\mathrm{f_s}}$, where $0 \leq \mathrm{W_n} \leq 1$. The *ftype* speciffies the filter type of either *low* or *high*, $\mathrm{f_c}$ is the cut-off frequency and $\mathrm{f_s}$ is the sampling rate. The output of the filtered data were determined with expression, $\mathrm{Y} = \mathrm{filtfilt}(\mathrm{b}, \mathrm{a}, \mathrm{X})$ where X and Y are input and output data arrays, respectively. From this study, a 5^{th} low-pass Butter-worth filter, with a cut-off frequency ($\mathrm{f_c}$ = 10 Hz) and data sampled at 100Hz, was used. The chosen frequency was low enough to ensure that the readings across all sensors were not changed substantially.

5.2.3 Data analysis framework

The analysis of data is first described by considering the basic definitions of the pile geometry shown in Fig. 5.2. From this figure, the rotation of the pile (θ), pile head ($\mathrm{Y_p}$) and ground deflections ($\mathrm{Y_g}$) are derived from the two mounted LVDTs (LVDT-2 and LVDT-3). To investigate the accumulation of pile head displacement and change in secant stiffness, the cyclic load is load controlled. In each cycle of loading, the maximum and minimum value of load ($\mathrm{H_{max}}$, $\mathrm{H_{min}}$) and their corresponding displacement ($\mathrm{Y_{max}}$, $\mathrm{Y_{min}}$) can be obtained. The displacement of the monopiles is the results of the applied load and stiffness of the soil-structure system. The definitions used in this study was adopted from LeBlanc (2009) and Klinkvort (2013) to address the concerns of design engineers regarding the closeness between the natural frequency and cyclic load frequency.

As shown in Fig. 5.3, the cyclic loading is characterised by the two non-dimensional parameters ($\zeta_\mathrm{b}, \zeta_\mathrm{c}$) described by LeBlanc (2009) and Klinkvort and Hededal (2013). The ratio ζ_b is the measure of the size of the cyclic loading with respect to monotonic load capacity ($\mathrm{H_{mon}}$), follows that $0 < \zeta_\mathrm{b} < 1$ (refer Eq. 2.79, Chapter 2). The ratio ζ_c ranges from $-1 \leq \zeta_\mathrm{c} \leq 1$,

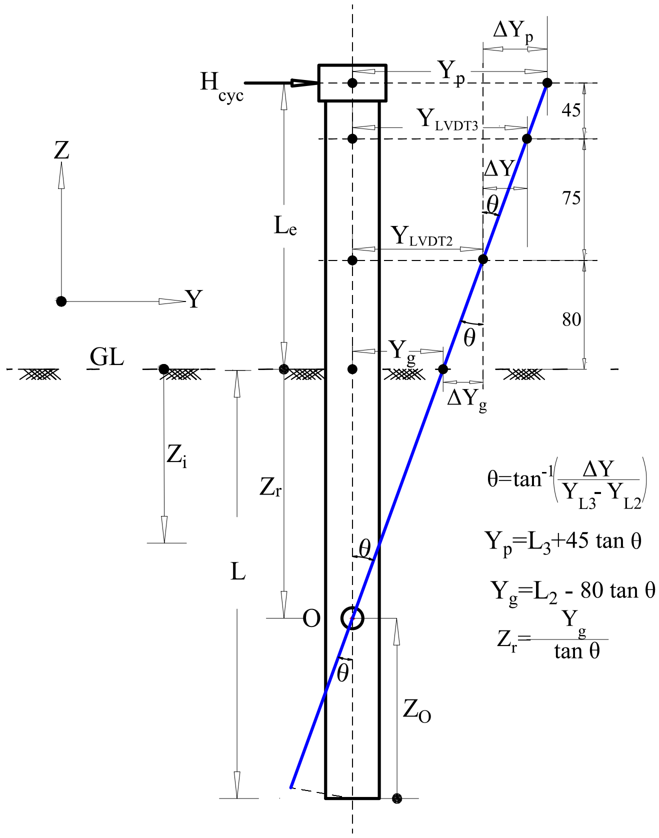

Figure 5.2: Typical model pile definitions for analysis of cyclic load responses.

quantifies the characteristic of cyclic load and takes the value of 1 for a monotonic test, 0 for one-way loading, and -1 for two-way loading (refer Eq. 2.80, Chapter 2). The parameter H_{mon} can be determined from the monotonic tests described in Chapter 4. This approach has been previously used in other studies (Klinkvort and Hededal, 2013, LeBlanc, 2009, Li et al., 2010, Lin and Liao, 1999, Long and Vanneste, 1994, Peralta and Achmus, 2010, Rosquoet et al., 2007).

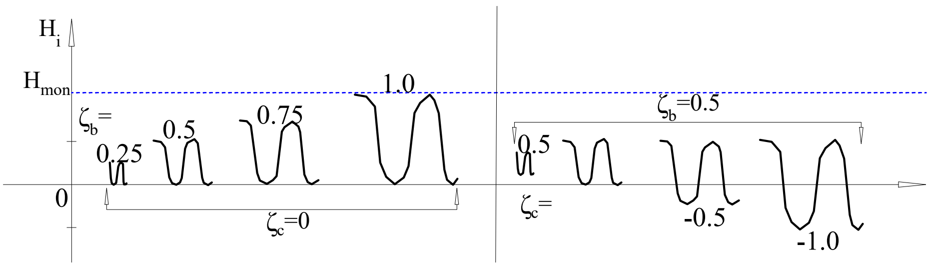

Figure 5.3: Cyclic loading characteristics defined in terms of ζ_b and ζ_c, adapted from LeBlanc (2009).

5.2.3.1 Analysis of pile displacement

The lateral displacement of the pile is the result of the applied load and the stiffness of the soil-pile system. The minimum and maximum displacement can be found as when the load on pile (H_{cyc}) is at the minimum or maximum point of each cycle. There are two ways to quantifies the accumulation of pile-head displacement, exponentially as proposed by LeBlanc et al. (2010) and logarithmically as proposed by Lin and Liao (1999). More detail of these functions can be found in Section 2.4.2, Chapter 2. Both logarithmic (see Eq. 5.1) and exponential (see Eq. 5.2) functions are used to fit the average measured total and accumulated displacement of the pile-head, respectively. The parameters Y_1, Y_N are defined as displacement for the first and N-cycles, respectively. The parameter Y_1 is always the same as Y_s, and can be determined from the monotonic test. C_N, T_N and α_n are the constants to adjust the fitting of the curve. Diagrammatically, the definitions of these parameters were adopted from LeBlanc (2009), which can be seen in Fig. 2.28, Chapter 2. Instead of utilising bending moments, as shown from this figure, a horizontal load applied onto the top of the monopile was used to define these functions.

$$Y_N = Y_1 + C_N \log(N) \tag{5.1}$$

$$\Delta Y(N) = Y_1 T_N N^{\alpha_n} \tag{5.2}$$

5.2.3.2 Analysis of cyclic stiffness

The definition for the pile stiffness was selected as the part to address the concern of the interaction between the natural frequency of the system and cyclic loading frequency. By using the pile-head load-displacement plots of the data, it is possible to calculate the unloading stiffness of the model pile throughout the experiment. The analysis is described by defining the tangent stiffness (K_t), monotonic cyclic stiffness, K_{mon}, the first cyclic secant stiffness, K_1, and N-cyclic unloading stiffness, K_N. Once the maximum and minimum loads from each cycle and the corresponding displacements are known, the unloading stiffness for each cycle is estimated as shown in Eq. 5.3.

$$K_N = \frac{\Delta H}{\Delta y} = \frac{H_{max} - H_{min}}{y_{max} - y_{min}} \tag{5.3}$$

5.2.4 Summary of the experiment programme

The section presents a brief description of the tests used to analyse the behaviour of monopile foundations. Three centrifuge tests (OWTP/C-T15, OWTP/C-T16 and OWTP/C-T17) were conducted at 30g to investigate the response of a monopile to cyclic lateral loading. Tests were conducted on relatively dense sand. The results from test OWTP/C-T15, discussed in Chapter 3, were used to describe the preliminary responses of the model pile. During testing, the cyclic load ratio (ζ) (varied from negative to positive) were programmed using an automated load control system. Each series of the test was achieved by stopping the AKM motor and setting the automated load control system to a new load control ratio, ζ. After setting the value of ζ, the process was resumed and the AKM motor was switched on, and increased slowly from a loading frequency of 0.5 to 2.5 Hz. At constant frequency of 2.5 Hz, the test was resumed to a specific number of load cycles. The raw data, for lateral loads and pile-head displacements, were obtained from load cells and LVDT sensors, respectively. From these data, the relationship between the applied cyclic loads, displacement, cyclic load-displacement, total displacement and change in cyclic stiffness against the number of load cycles were achieved. The loading set of each test was characterised in a sequence starting with F01 followed by F02, F03, F04, F05. As can be seen in Table 5.1, the first series (F01) of each test was used to stabilise the soil and data was not taken for the analysis. The data from the subsequent test series was recorded except series F02 of test OWTP/C-T17. It should be noted that during testing, the first few cycles of the first recorded test series was assumed to be affected by rapidly displacement increase of the pile before the rate of increase stabilises. Furthermore, another factor which affect the first few cycles of the subsequent test series is the setting process of an automated load control ratio. By changing ζ, the rearrangement of the loading system could affect the the behaviour and magnitude of the first few cycles before it stabilises. Thereafter, the rate of displacement and stiffness decreases with increasing number of cycles. With further increase in number of cycles, the sands have more potential to compact and resulting into local densification of sandy soil around the pile. The local densification might raise the shear modulus of sand and leading to the increase of pile secant stiffness. In the subsequent test series, the load control ratio (ζ) was seen to affect the displacement of the pile, however, the change in pile stiffness continue to increase with increasing number of cycles. It can be seen that the progressive increase in magnitude due to the change of load control factors had also an impact on the initial stiffness increase and change in the pile displacement. A summary of the test series, including number of cycles (N_S), is presented in Table 5.1. The analysis of each test is presented in the subsequent sections. All results are interpreted in a model scale, unless stated otherwise.

Table 5.1: A summary of tests OWTP/C-T16 and OWTP/C-T17

Test ID	Test series	ζ	N_S	Description
OWTP/C-T16	F01	Nil	Nil	Soil stabilisation, tested from 1-30g, data was not recorded
	F02	0	8600	Long run test set at ζ=0, data was recorded
	F03	0	32200	Long run test at ζ=0 in the late hours of the first day (F3A) and then continue the following day (F3B), data was recorded
	F04	+1	29000	New set up of ζ=1 after F3B, long run test, data was recorded
	F05	-1	58170	New set up of ζ=-1 after F04 in the following day, long run test, data was recorded
OWTP/C-T17	F01	Nil	Nil	Soil stabilisation, tested from 1-30g then 30-20-10g and back to 30g, data was not recorded
	F02	Nil	Nil	Tested but LVDT sensors did not respond in the LabVIEW user interface, data was not recorded
	F03	0	58870	Long run test at ζ=0, data was recorded
	F04	0	4060	Test continued at ζ=0 in the following day before changing ζ, data was recorded
	F05	-1	16610	New set up of ζ=-1 after F04, long run test, data was recorded

5.3 Cyclic load and displacement response

Fig. 5.4 define the notation used to identify the sinusoidal cyclic loads and displacements applied on the pile head. The uniform cyclic pattern of the resultant lateral load, H_i, can be defined by period $\left(T = \frac{1}{f}\right)$, number of cycles (N), minimum and maximum cyclic load (H_{min}, H_{max}), average load $\left(H_{avg} = \frac{H_{max} + H_{min}}{2}\right)$, and cyclic load change (H_{amp} = H_{max}-H_{min}). The pile-head lateral displacement (Y_p), that correspond to the cyclic loads, can be defined by the minimum (Y_{min}) and maximum (Y_{max}) displacements including the change of peak-to-peak displacement, Y_{amp} = Y_{max}-Y_{min}.

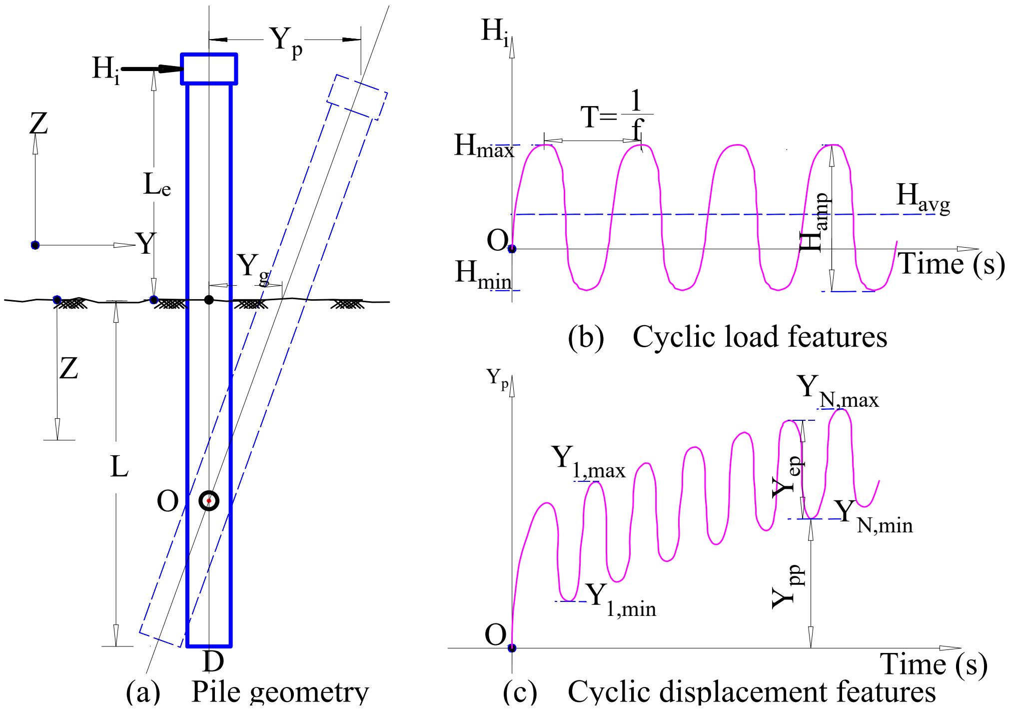

Figure 5.4: Definitions of cyclic loads and lateral displacement on the pile-head.

To have an accurate reading of the cyclic loading, two miniature load cells (LCs) were mounted horizontally on both sides of the pile cap and directly connected with tension wires, T_1 and T_3 to the weights, M_1 and M_2, respectively. The weight applied on the system to create a sinusoidal cyclic force was chosen as M_1 =3 kg (applied load (RHS)), M_2 = 1.5 kg (dead weight (LHS)) and M_3 = 4 kg (load chosen to balance the system). Before running the test, the loading system was kept in balance and initial readings were recorded. Throughout the tests, the change of load control factor (ζ) was employed and direct measurements from the two load cells (LC1 (RHS) and LC2 (LHS)) were recorded. For demonstration purpose, the results of the sinusoidal forces, extracted from 50 cycles with the values of $\zeta = -1$, $\zeta = 0$ and $\zeta = +1$, are presented in this section. Theoretically, the force recorded on the LHS (LC2) should remain constant without any sinusoidal behaviour, since there were no changes expected to the dead weight M_2. By estimating the load, H_{LC2}, it is clear that the friction between the wires and pulleys influences the system since H_{LC2} should be constant. Similarly, the friction of other components might also affect the tension force from both sides of the pile. However, the variation observed on the LHS is considered small with minimal effect on the interpretation of the resultant force, H_i. The resultant tension forces for all values of ζ were obtained as the difference between LHS, LC2 (load cell two), and RHS, LC1 (load cell one); $H_i = H_{LC2}$ - H_{LC1}. The direct measurements from the two load cells and the corresponding net forces, for ζ=0, ζ = -1 and ζ = +1, are shown in Fig. 5.5, 5.6 and 5.7, respectively.

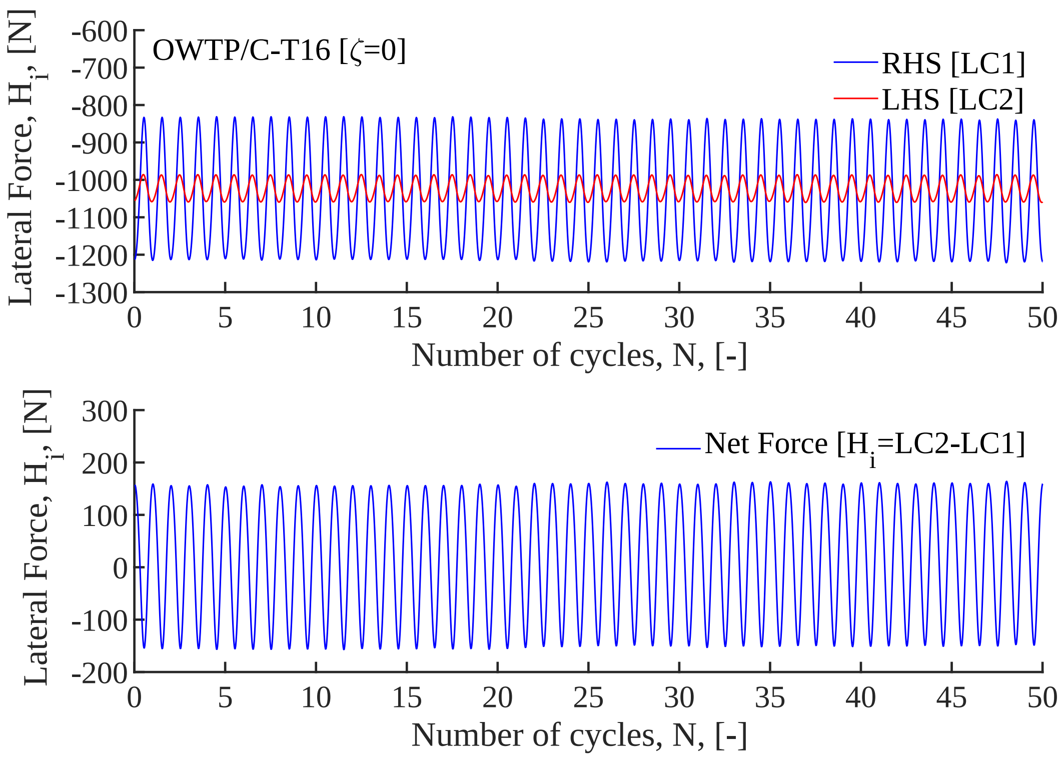

Figure 5.5: Net force from LHS and RHS load cells for test OWTP/C-T16 (ζ=0).

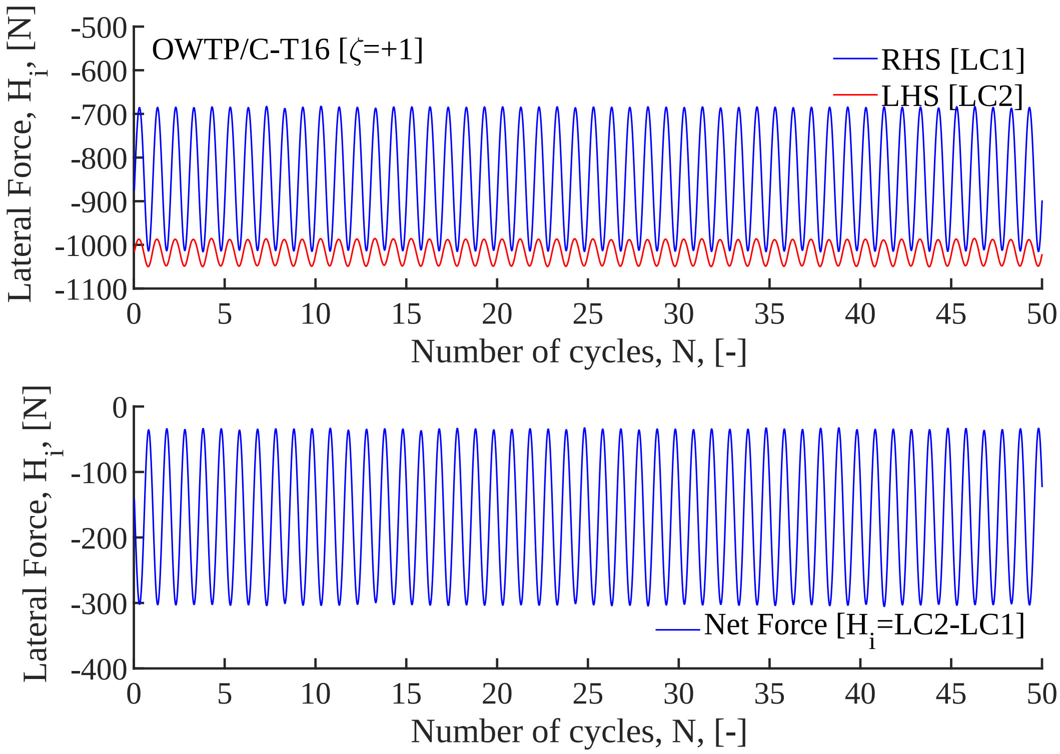

Figure 5.6: Net force from LHS and RHS load cells for test OWTP/C-T16 (ζ=+1).

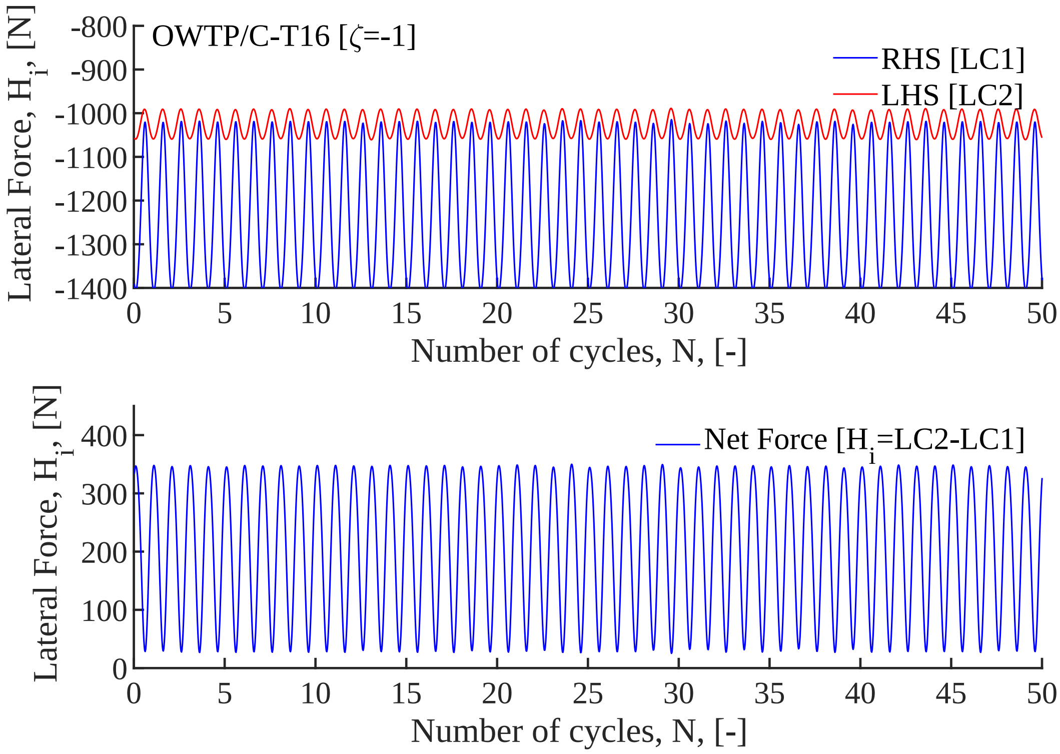

Figure 5.7: Net force from LHS and RHS load cells of test OWTP/C-T16 (ζ=-1).

The resultant lateral cyclic load (H_i), observed from tests OWTP/C-T16 and OWTP/C-T17, are shown in Fig. 5.8 and 5.9, respectively. From each test, a cyclic loading sequence is presented to show the variation of load control factor, ζ. As discussed in in Table 5.1, Section 5.2.4, the sets of loading sequence was named as F02, F03, F04 and F05 for each variation of parameter ζ. It should be noted that the series F01 was carried out to stabilise the soil and no cyclic loading was conducted on the piles. Also the test series F02 from the test OWTP/C-T17 was not recorded because the bottom LVDT sensor did not respond. A typical change of test sequence of the test OWTP/C-T17 is shown in Fig. 5.9. Throughout the entire test with approximately 79540 lateral load cycles, the load control ratio was programmed to vary using an automated load control system. For instance, as shown in Table 5.1 the first set of loading cycles (series F03) comprised 58870 cycles. This series was conducted at ζ = 0 in the

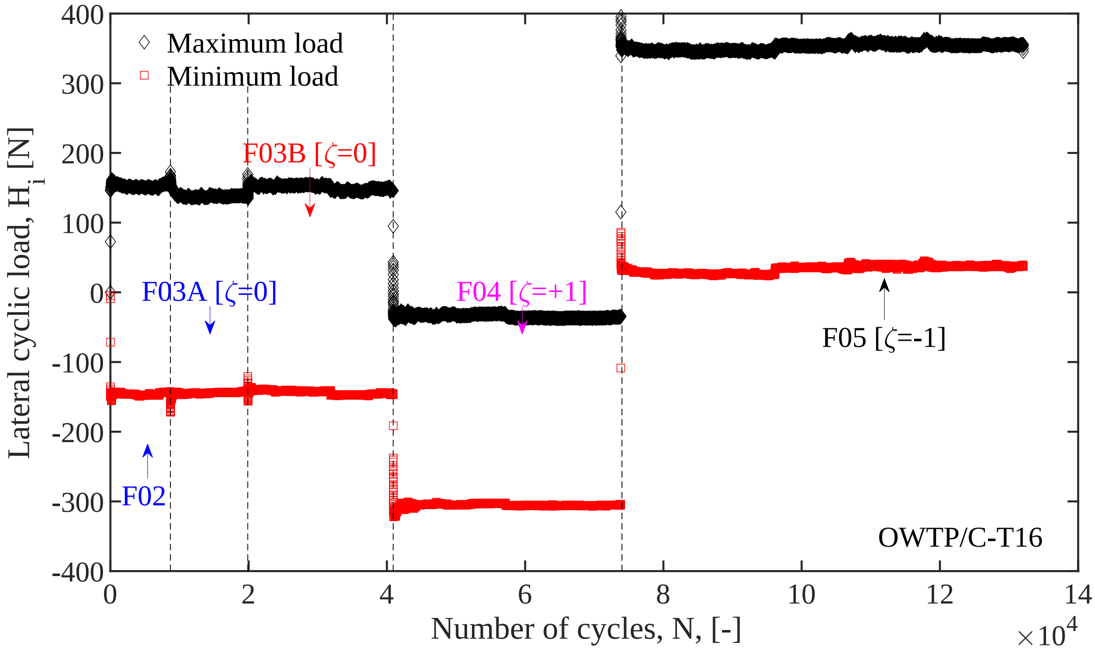

Figure 5.8: Maximum and minimum net load versus number of cycles (N) for test OWTP/C-T16.

first day and centrifuge was spun down. In the second day, the value of ζ = 0 was programmed again into the system and 4060 cycles were achieved for test series F04. For the subsequent set (series F05) the value of ζ was changed to -1 while running the test and 16610 cycles were achieved. The centrifuge package was spin down in the first day and spinning up in the second day, including the reset of ζ = 0, could be the factors which affected the results observed in the figure. Furthermore, the change of the load control factor has also contributed to the change of cyclic load magnitude. More detail is summarised in Table 5.1, Section 5.2.4. The displacement

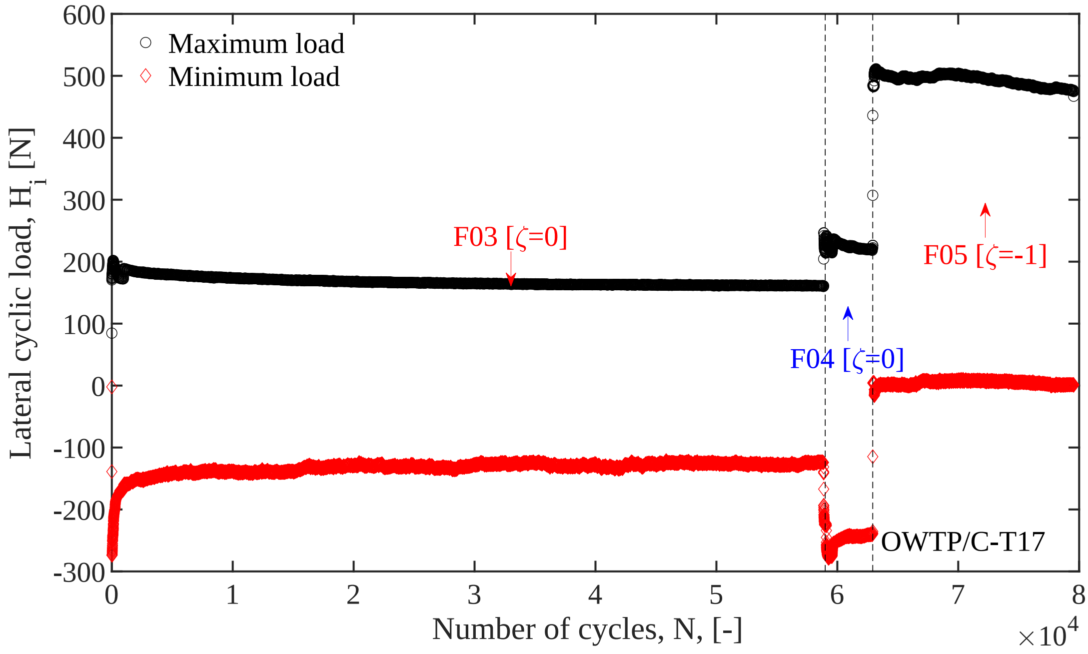

Figure 5.9: Maximum and minimum net load versus number of cycles (N) for test OWTP/C-T17.

of the pile head during the cyclic lateral loading is classified into two parts: maximum and minimum pile head deflections, which correspond to the maximum and minimum cyclic loads presented in Fig. 5.8 and 5.9. Therefore, the maximum and minimum pile-head displacement after each cycle of tests OWTP/C-T16 and OWTP/C-T17 are shown in Fig. 5.10 and 5.11, respectively. As can be seen from the figures, the displacements of the pile are both increasing with number of load cycles. This indicates that a permanent deformation of the soil develops around the pile. However, it should be noted that during the process of changing ζ from one set to another there was a disturbance of soil before the displacement of the specific set resume.

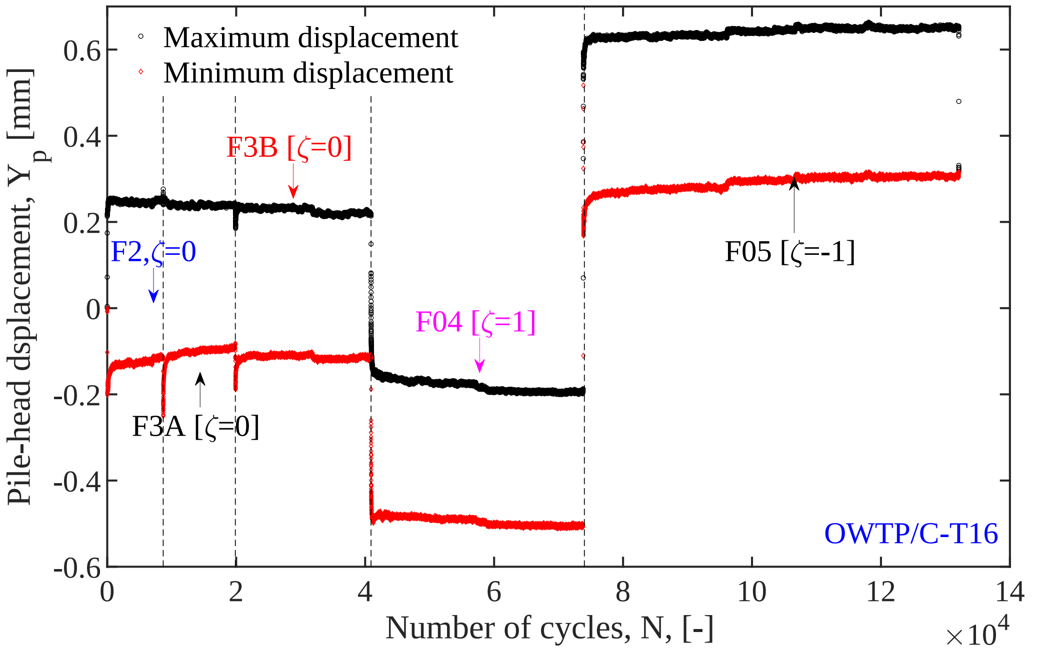

Figure 5.10: Maximum and minimum pile-head displacement versus number of cycles (N) for test OWTP/C-T16.

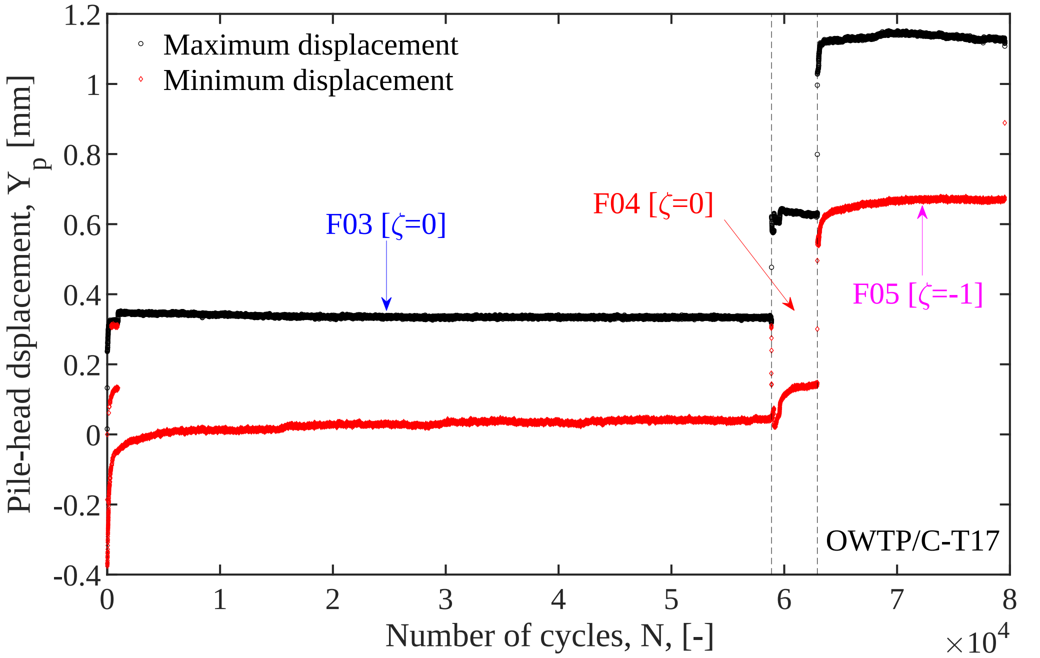

Figure 5.11: Maximum and minimum pile-head displacement versus number of cycles (N) for test OWTP/C-T17.

By utilising the maximum and minimum points recorded from each test, the evolution of cyclic pile-head displacement (Y_{amp}) and lateral load (H_{amp}) magnitude of the tests OWTP/C-T16 and OWTP/C-T17 against the number of cycles, is plotted in Fig. 5.12. From each test, the cyclic loads were applied to the pile head through a set of loading cycles. Each set was governed by the load control system, which was obtained by changing the value of ζ. For instance, the total of 79540 cycles of the test OWTP/C-T17 was achieved through the following sets: F03 (ζ = 0, from 1 to 58870 cycles), F04 (ζ = 0, from 58871 to 62930 cycles) and F05 (ζ = -1, from 62931 to 79540 cycles). It should be noted that the number of cycles from each set of the loading cycles was achieved by setting a constant frequency of 2.5 Hz from AKM motor. Moreover, after completion of one set before the subsequent sets, the frequency of AKM motor was reduced to 0.5 Hz to allow the change of ζ. After setting the value of ζ, the frequency of AKM motor was increased stepwise from 0.5 to 2.5 Hz and remain constant for the entire test. As shown in Fig. 5.12, the results of all sets were merged to observe the trend of cyclic load and displacement magnitudes. Throughout the tests, H_{amp} and Y_{amp} lost the percentage of their magnitude as the number of cycles increases. As shown in Table 5.2, $H_{amp(1)}$, $Y_{amp(1)}$ and $H_{amp(N)}$, $H_{amp(N)}$ are the magnitudes of the first and last lateral load and displacement of each set of the test sequence. There are some reasons identified for this loss. Firstly, a cyclic amplitude reduction occurs systematically due to displacement accumulation of the pile, leading to small changes due to loss of wire tightness. Secondly, the mechanical friction of the system could also have

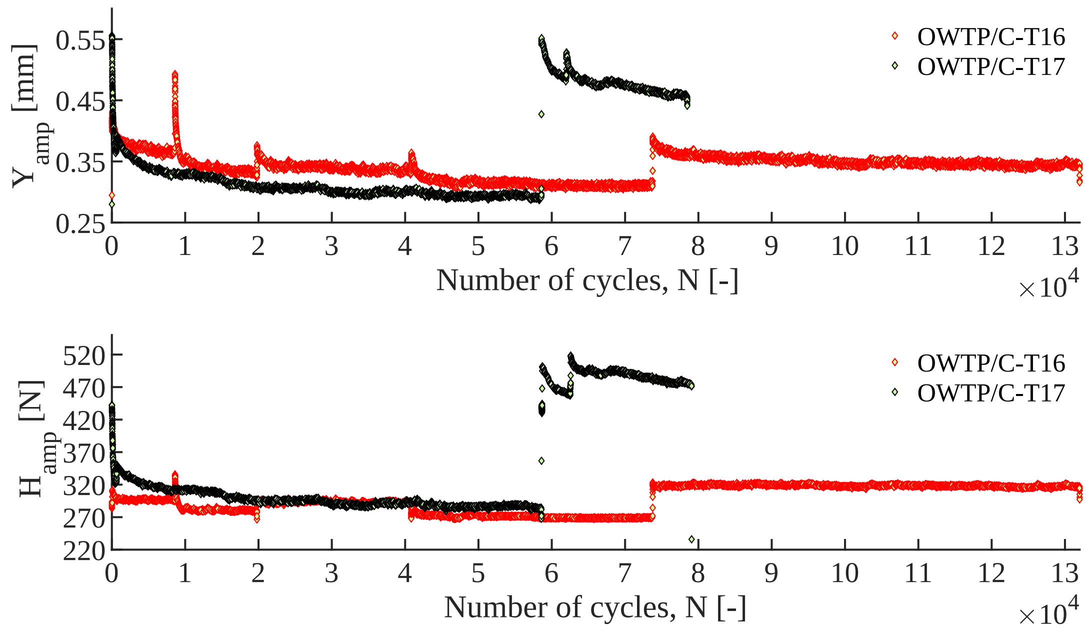

Figure 5.12: Change in cyclic displacement and load amplitudes (Y_{amp}, H_{amp}) versus number of cycles (N), for test OWTP/C-T16 and OWTP/C-T17.

some effect. However, it is not clear whether these factors equally provide this effect or if one had more influence. Further study is needed to clarify this issue.

The observation shown in Fig. 5.12 were used to determine the ratio between the change in cyclic load and pile-head displacement. The plots of cyclic load-displacement ratio $\left(\mathrm{R_a} = \frac{\mathrm{H_{amp}}}{\mathrm{Y_{amp}}}\right)$ versus number of cycles, from sets of each test, are shown in Fig. 5.13, where $\mathrm{H_{amp}}$ and $\mathrm{Y_{amp}}$ are the cyclic load and pile head displacement magnitude, respectively. Fig. 5.13 shows the development of relative cyclic magnitude from the first to the last set of test sequence. The data is presented as set of a particular number of lateral load cycles with the cycle count, N, continue from previous set. The values of $\mathrm{R_a}$ observed to increase as the experiment proceeds from one set of test series to the next. During the first few cycles of each set $\mathrm{R_a}$ increases rapidly and then becomes constant. Thereafter the rate of cyclic amplitude, $\mathrm{R_a}$, for each set, is observed to decreases with increasing number of cycles. At early stages of each test the pile experiences a low relative stiffness response compared to subsequent test series. It can be seen that the progressive increase of cyclic magnitude, due to the change of load control factor (ζ), had an impact on the relative cyclic amplitude. Furthermore, with this change of load control ratio the sands have more potential to compact and leading to local densification of soil around the pile. The local densification attributed to cyclic might raise the shear modulus of sand and lead to the increase of the relative stiffness of the pile with increasing number of cycles.

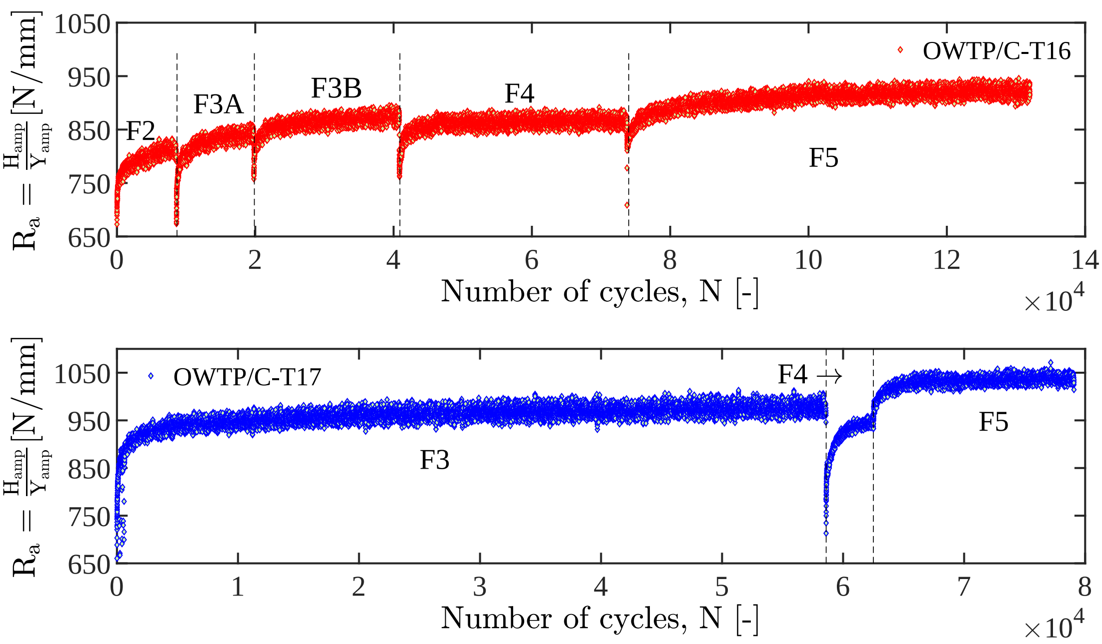

Figure 5.13: $\mathrm{R_a}$ versus cycles (N) for test OWTP/C-T16 and OWTP/C-T17.

The result of the cyclic lateral load (H_i) versus pile-head displacement (Y_p), for the tests OWTP/C-T16 and OWTP/C-T17, is shown in Figure 5.14 and 5.15, respectively. To improve the visibility the plots are divided into intervals of cycles 1-25, cycles 250-260, cycles 2500-2510, cycles 5000-5010, cycles 10500-10510. However, the response of the cyclic load against the number of cycles, from all cycles of test OWTP/C-T17, was plotted in Fig. 5.17(a) to show the sequence of the test series. For each group of cycle intervals, only five cycles were taken for demonstration, except the first 25 cycles. The figures indicate that the lateral pile displacement

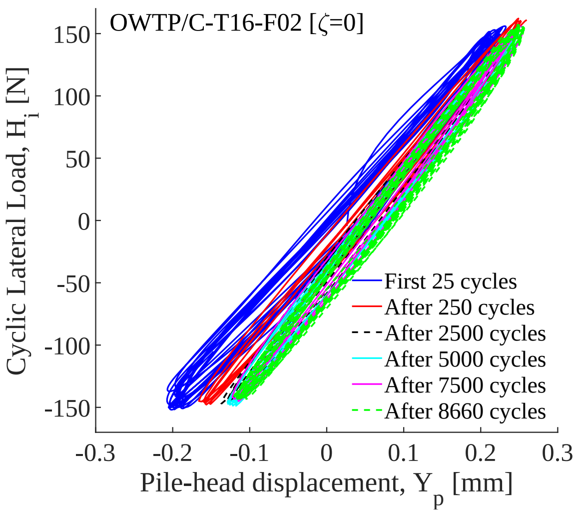

(a) OWTP-T16-F02 ($\zeta = 0$)

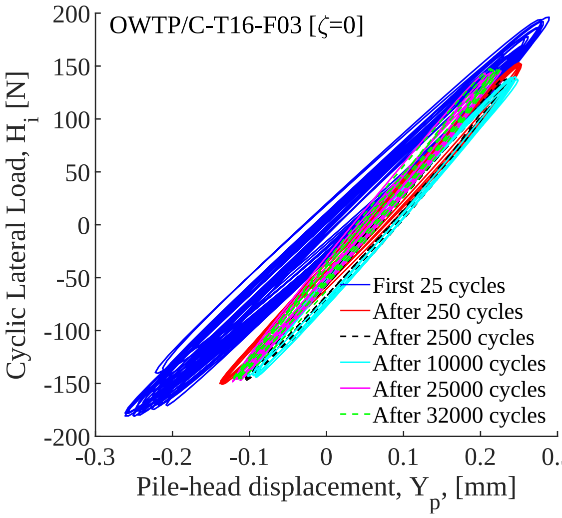

(b) OWTP-T16-F03 ($\zeta = 0$)

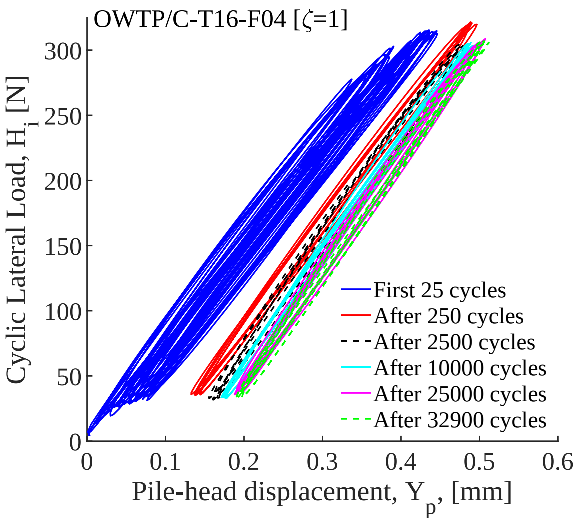

(c) OWTP-T16-F04 ($\zeta = 1$)

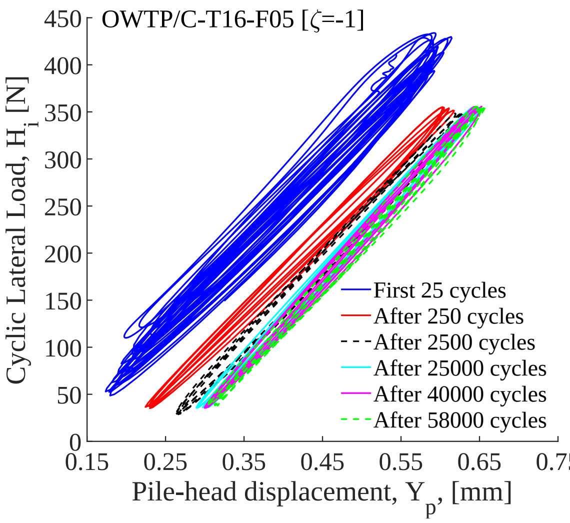

(d) OWTP-T16-F05 ($\zeta = -1$)

Figure 5.14: Cyclic load-displacement responses for test OWTP/C-T16.

increases with increasing of loading cycles. From all tests, the curves of the first 25 cycles exhibit a non-linearity of the soil, with the evolution of secant stiffness as the displacement continues to increase. Furthermore, as the number of cycles continues to increase the load-displacement responses becomes relatively linear and stiffer than the previous N-1 load cycle. This implies that the cyclic secant stiffness rises with load cycles tending towards a maximum value of each cycle.

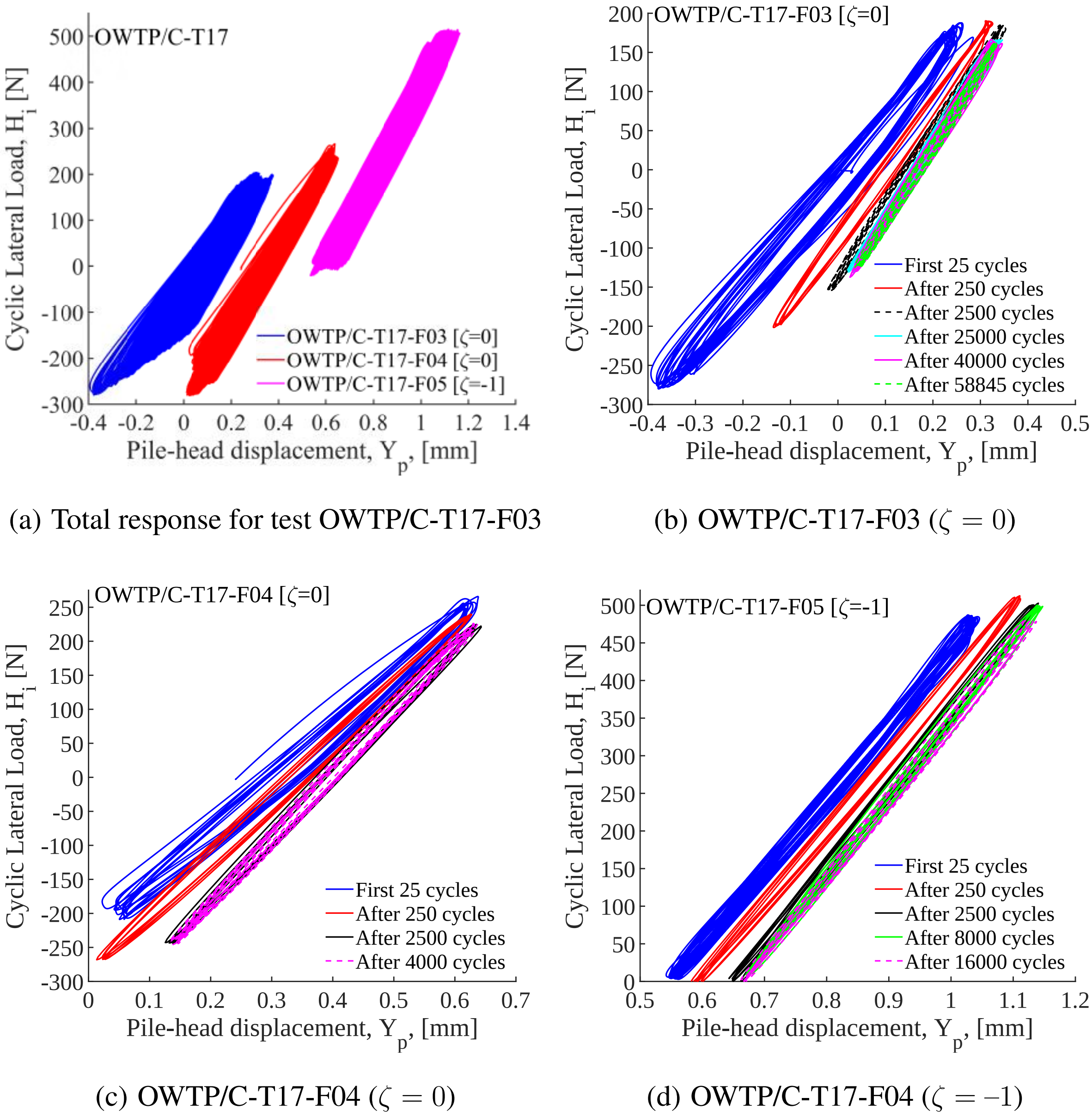

(a) Total response for test OWTP/C-T17-F03

(b) OWTP/C-T17-F03 ($\zeta = 0$)

(c) OWTP/C-T17-F04 ($\zeta = 0$)

(d) OWTP/C-T17-F04 ($\zeta = -1$)

Figure 5.15: Cyclic load-displacement responses for test OWTP/C-T17.

The cyclic load characteristics (ζ_c) between the maximum and minimum cyclic loads of the tests

OWTP/C-T16 and OWTP/C-T17 are plotted in Fig. 5.16 against the number of cycles, and the values are listed in Table 5.2. From the table, the tests OWTP/C-T16-F04 ($\zeta = 1$), OWTP/C-T16-F05 ($\zeta = -1$) and OWTP/C-T17-F04 ($\zeta = -1$) are under one-way loading direction while tests OWTP/C-T16-F03 ($\zeta = 0$), OWTP/C-T16-F04 ($\zeta = 0$), OWTP/C-T17-F03 ($\zeta = 0$) and OWTP/C-T17-F04 ($\zeta = 0$) are found to be under two-way cyclic loading condition. The pile-

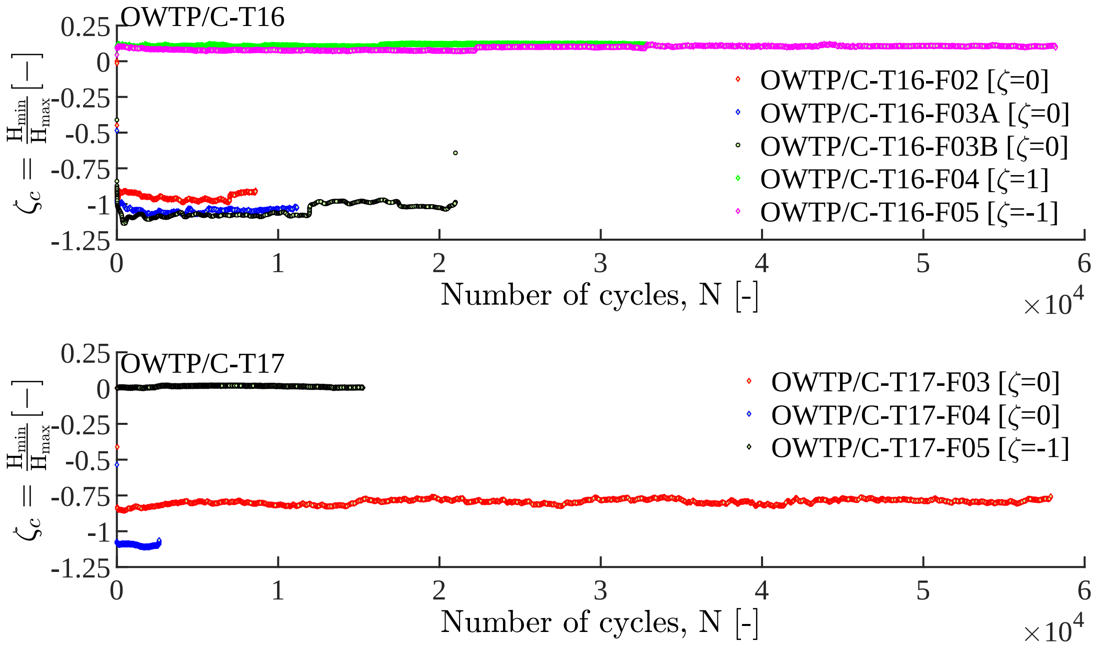

Figure 5.16: Cyclic load characteristics, ζ_c, versus number of cycles, N.

head load displacement responses from tests OWTP/C-T16/T17-F03 (under cyclic loading) and test OWTP/S-T4 (under monotonic loading) are presented in Fig. 5.17. The response of Test OWTP/S-T4 is included in the plot for comparison purpose and estimation of the initial displacement, Y_s, and tangent stiffness of the monotonic backbone curve, K_t. From these figures, the parameter Y_s was identified as 0.26 and 0.35 mm of the tests OWTP/C-T16 and OWTP/C-T17, respectively, and K_t is approximately 840 N/mm. These parameters are basis for the analysis in the subsequent chapters and hysteresis loops in Chapter 6. The values of the parameters extracted from experimental data, such as maximum and minimum cyclic loads (H_{max}, H_{min}), load magnitude ($H_{amp} = H_{max}$-H_{min}), cyclic load characteristic (ζ_c) and cyclic load ratio (ζ_b), are provided in Table 5.2. In test OWTP/S-T4, the ultimate capacity (H_u) of the pile was estimated by two methods, such as 10%D of pile head displacement and 0.5^o of the maximum tolerated pile tilt due to installation and operational condition (Abadie, 2015). From

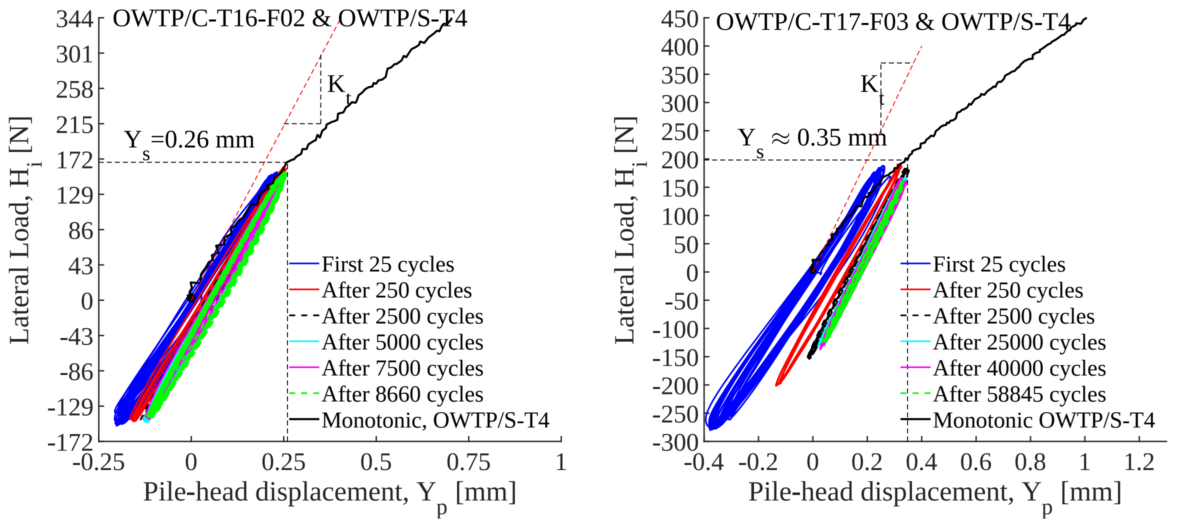

(a) Test OWTP/C-T16-F03 and OWTP/S-T4 (b) Test OWTP/C-T17-F03 and OWTP/S-T4

Figure 5.17: Load-displacement curves determined from monotonic and cyclic tests.

these methods, the ultimate capacities were 1690 N and 1130 N, respectively. Therefore, the values of $\zeta_{\mathrm{b}} = \dfrac{\mathrm{H}_{\mathrm{max}}}{\mathrm{H}_{\mathrm{u}}}$ were estimated as shown in Table 5.2.

Table 5.2: Characteristics of cyclic load tests OWTP/C-T16 and OWTP/C-T17

Test ID	ζ	$\mathrm{H}_{\mathrm{min}}$	$\mathrm{H}_{\mathrm{max}}$	ζ_{c}	$\mathrm{H}_{\mathrm{amp1}}$	$\mathrm{H}_{\mathrm{ampN}}$	$\mathrm{Y}_{\mathrm{amp1}}$	$\mathrm{Y}_{\mathrm{ampN}}$	ζ_{b} 0.1D	ζ_{b} 0.5^{o}
T16-F02	0	-155	160	-0.97	315	295	0.43	0.36	0.1	0.14
T16-F03A	0	-166	170	-0.95	336	278	0.49	0.33	0.12	0.15
T16-F03B	0	-140	158	-0.88	298	291	0.38	0.33	0.1	0.14
T16-F04	1	23	309	0.03	286	269	0.37	0.31	0.18	0.27
T16-F05	-1	25	350	0.1	323	317	0.39	0.34	0.21	0.31
T17-F03	0	-218	225	-0.97	443	285	0.56	0.29	0.13	0.2
T17-F04	0	-245	260	-0.94	505	452	0.55	0.3	0.15	0.23
T17-F05	0	5	520	0.01	515	474	0.53	0.45	0.3	0.45

5.4 Effect of cyclic lateral displacement on the pile-head

5.4.1 Introduction

From the geometry of the model pile setup (see Fig. 5.2), the lateral displacement response can be determined from the LVDT readings. The results of the tests OWTP/C-T16 and OWTP/C-T17 are investigated in this section by plotting the lateral pile-head displacement against the number of load cycles. The pile-head displacement is divided into two parts, namely the maximum (forward) and minimum (backwards) displacements, which correspond to the maximum and minimum cyclic loads, respectively. The extremes found from the results plotted in Figs. 5.14 and 5.15 are used to determine the maximum and minimum deflection of each cycle. Therefore, this section considers the average displacement at the instant when the cyclic load is applied to the pile head.

The results of each set of the test sequence, starting from the first series when the value of ζ was set-up at a constant frequency of f = 2.5 Hz, are plotted separately to demonstrate the response of the average displacement. From test OWTP/C-T16, a total of 128970 loading cycles was achieved with the first set of test series, F02, start from 1 - 8600 cycles followed by F03 (from 8601 - 40800 cycles), F04 (from 40801 - 69800 cycles) and F05 (from 69801 - 128970 cycles) while in test OWTP/C-T17 a total of 79540 cycles was achieved with first set, F03, start from 1 - 58870 cycles followed by F04 (from 58871 - 62930 cycles) and F05 (from 62931 - 79540 cycles). It should be noted that the total displacements of the test sequence, is discontinuous due to the change of load control ratio, ζ, which was programmed after each set. During testing, the change ζ observed to affect the total displacement. For instance, the change of load control ratio from F04 (ζ = 1) to F05 (ζ = -1) has shown a big different due to mechanism of automated load control system from negative to positive value through zero. Meanwhile, the response of the first few cycles of the subsequent test series were observed to be affected before the rate of increase stabilises.

As noted from Leblanc et al. (2010) and Arshad and OKelly (2016), two techniques were used to represent the evolution of the pile head displacement (rotation) against the number of cycles: total displacement ($\mathrm{Y_N}$) and accumulated displacement (ΔY) of the pile head. Each technique provides useful information for understanding the response of the monopiles. However, in this section, the total displacement method will be used to interpret the results of tests OWTP/C-T16 and OWTP/C-T17 and the information derived from each test.

5.4.2 Total displacement

For each loading condition, the total pile-head displacement of the monopile (Y_N) was assessed in this section. This was achieved by considering the average displacement between the maximum and minimum displacement observed during a single loading cycle. As shown in Figs. 5.18 and 5.19, the resulting displacement for tests OWTP/C-T16 and OWTP/C-T17, respectively, are plotted against the number of cycles. From the two figures, it can be seen that the response of the pile-head displacement increases with an increasing number of load cycles. The variation of the total displacement is significantly influenced by the load control factor, ζ. Comparing the data plots for the loading test series, the displacement is significantly lower for the value of ζ = 0 (see T16-F02/F03A/F03B and T17-F03), in contrast to ζ = 1 and ζ = -1, where the displacements were notably higher. In Fig. 5.18, the initial part of the pile displacement response experiences anomalous behaviour up to 200 cycles. If we look at the trends over several cycles, we can see that the pile head displacement increased dramatically in this zone. The displacement increased to approximately 0.19 mm, 0.32 mm and 0.42 mm for the test series T16-F02/3A/3B, T16-F4 and T16-F5, respectively. Beyond 200 cycles, the displacement response continues to rise gradually but at reduced rates until the end of each test series.

The plots from the figures show a similar trend, but the displacement differs, for instance, at the load cycle of 2000 the displacement at $\zeta = 1$ (T16-F04) rose by 0.33 mm, while at $\zeta = -1$ (T16-F05) was found to be 0.45 mm compared to 0.21 mm at $\zeta = 0$ (T16-F02/3A/3B). The discontinuous nature of total displacement, from first to the subsequent set of test series, was due to the load control ratio programmed in an automated load control system.

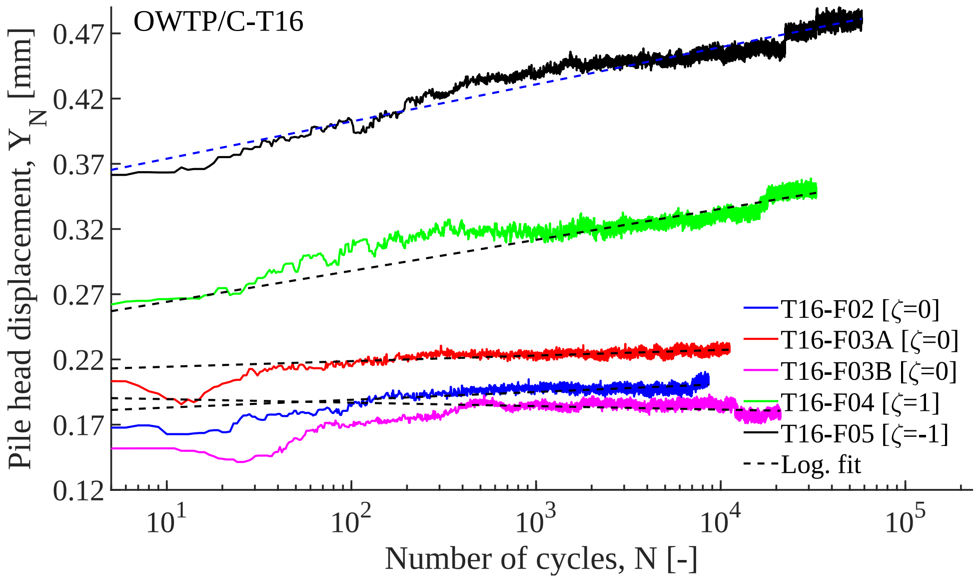

Figure 5.18: Lateral displacement against the number of cycles, test OWTP/C-T16.

The response in Fig. 5.19 followed a similar trend. Between 1 and 200 cycles, the displacement increased dramatically for the test series T17-F04/05 and then slowing growth of the test T17-F03. After 200 cycles up to the end of each test series, the displacement continued to grow slowly, but at reduced rates. By looking at the difference between the test series, it can be seen that the biggest change was influenced by the load control factor (ζ) of 1 and -1. At 3000 load cycles, the displacement of the pile shows a big difference of 0.165 mm and 0.67 mm, observed from tests T17-F04 and T17-F05, respectively. In the test T17-F04, this is more than 0.75 times the displacement of T17-F03 and around three times from T17-F05.

In conclusion, the behaviour of the first cycles of the first test series of each test was seen to be affected by soil mobilisation during the tests. However, for the subsequent test series, the behaviour was affected by the change of load control factor ζ. Furthermore, after 200 cycles the reducing rate of the pile displacement led to the more severe cyclic shearing of sand around the shaft and hence generate the permanent displacement of the pile. It is clear that asymmetric loading ($\zeta \neq 0$) had the most significant on the load-displacement response, for instance, the highest displacement was observed for the value of ζ = -1.

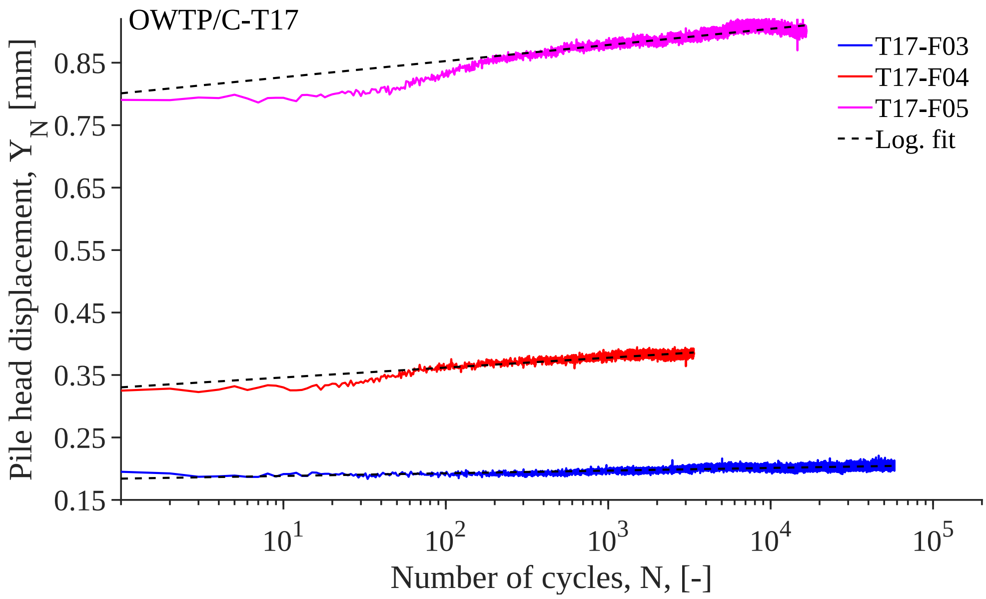

Figure 5.19: Lateral displacement against the number of cycles, test OWTP/C-T17.

As discussed in Section 5.2.3.1, the relationships to describe the total displacement of the pile, against the number of load cycles, can either be in a logarithmic or power functions. From the literature, the total displacement of monopiles in the sand was fitted by using a logarithmic function. Therefore, a logarithmic function, shown in Eq. 5.4, was chosen and employed in this study to fit the experimental data, where $\mathrm{Y_N}$ is the displacement after N cycles, $\mathrm{Y_1}$ is the displacement of the first cycle, $\mathrm{C_N}$ is the growth rate of displacement. As shown in Eq. 5.5, the displacement growth rate, $\mathrm{C_N}$, can be estimated as recommended by Rosquoet et al. (2007). It should be noted that Eq. 5.5 is derived from the tests conducted on the model pile in dense sand ($\mathrm{D_r}$ = 85%). Therefore, the pile head displacement against the number of load cycles can be fitted using Eq. 5.6, where *b* is kept constant while ζ_b and *a* are varied with test series.

$$\mathrm{Y_N} = \mathrm{Y_1}\Big(1 + \mathrm{C_N}\ln(\mathrm{N})\Big) \tag{5.4}$$

$$\mathrm{C_N} = \mathrm{b}\left(\frac{\mathrm{H_{max}}}{\mathrm{H_u}}\right)^{\mathrm{a}} \tag{5.5}$$

$$\mathrm{Y_N} = \mathrm{Y_1}\left(1 + \mathrm{b}\left(\frac{\mathrm{H_{amp}}}{\mathrm{H_u}}\right)^{\mathrm{a}}\ln(\mathrm{N})\right) \tag{5.6}$$

In Fig. 5.18 and 5.19, the fitted curves are displayed using the dashed lines, which demonstrate that Eq. 5.6 accurately captures the increase in pile-head displacement, at least after 100-300 (T16-F02/3A/3A and T17-F03), 1000-2000 (T16-F04/5) and 70-200 (T17-F04/5) load cycles.

However, less than these limits, the experiment data depart from the predictions. For instance, in Fig. 5.18, Eq. 5.6 overestimates the pile displacement prior to 100 cycles (T16-F02/3A) and 400 cycles (T16-F03B) while in series T16-F04/5 underestimation occurred between 30 to 1000 cycles (T16-F04) and 200 to 2000 cycles (T16-F05). Therefore, this equation is a conservative approach for predicting pile displacement to less than the aforementioned limits. Similar to Fig. 5.19, over-prediction occurred in less than 70 and 200 cycles for test series T17-F04 and T17-F05, respectively.

Equation 5.5 was fitted to the data to empirically determine the values listed in Table 5.3. The values of $\mathrm{C_N}$ and $\mathrm{Y_1}$, in Table 5.3, are plotted as shown in Figs. 5.20(a) and 5.20(b) as a function of ζ_b, respectively. The dependency of the load magnitude (ζ_b) can be seen on these plots. The data points are observed to be scattered and not fitted well. Table 5.3 provides the values of calculated uncertainty *a* assuming that the trend in Fig. 5.20(a) follows a power law shown in Eq. 5.7, where $\mathrm{a_1}$ = 0.19 and $\mathrm{b_1}$ = 1.565. The accuracy of the power law fitted curve is approximately R^2 = 0.81 (shown in the figure) compared to linear fit with R^2 = 0.745 (not shown). The scatter points observed from this figure were derived by the use of the function shown in Eq. 5.5, however, the proposed function (see Eq. 5.7) can also be used in Eq. 5.4.

$$\mathrm{C_N} = \mathrm{a_1}\zeta_\mathrm{b}^{\mathrm{b}1} \tag{5.7}$$

Thus, for the tests conducted in dense sand ($\mathrm{D_r}$=85%), the measured pile head displacements ($\mathrm{Y_N}$) after N cycles can be estimated by using Eq. 5.8. The trend observed here is not directly related to the previous observations of other studies. This is because, the factor ζ was set-up to control the loading magnitude of the test series. As can be seen in the figure, it is clear that the rate of displacement $\mathrm{C_N}$ is affected by loading magnitude ζ_b, which is directly influenced by ζ. Therefore, increasing the magnitude of loading is likely to affect the total displacement of the pile, however further research is needed to investigate this trend. Furthermore, this solution exclusively deduced from a centrifuge test of the model pile in dense sand, and therefore more research is required before it can be applied for estimation of the full scale pile head displacements under cyclic loading. However, the derived function can be a useful tool to improve the knowledge of monopile displacement behaviour.

$$\mathrm{Y_N} = \mathrm{Y_1}\left(1 + \left(\mathrm{a_1}\zeta_\mathrm{b}^{\mathrm{b_1}}\right)\ln(\mathrm{N})\right) \tag{5.8}$$

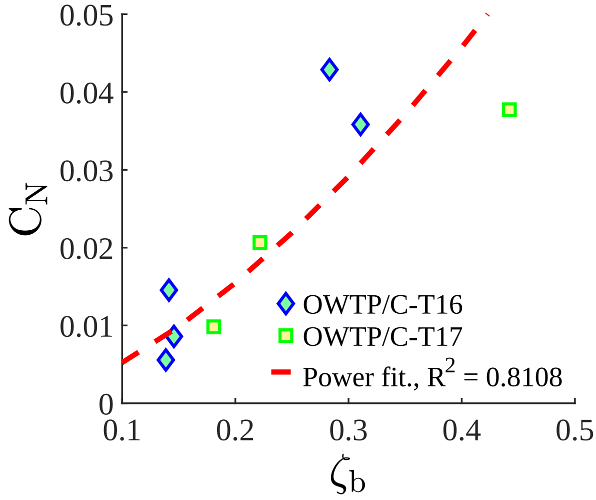

(a) Effect of ζ_b on constant rate, C_N

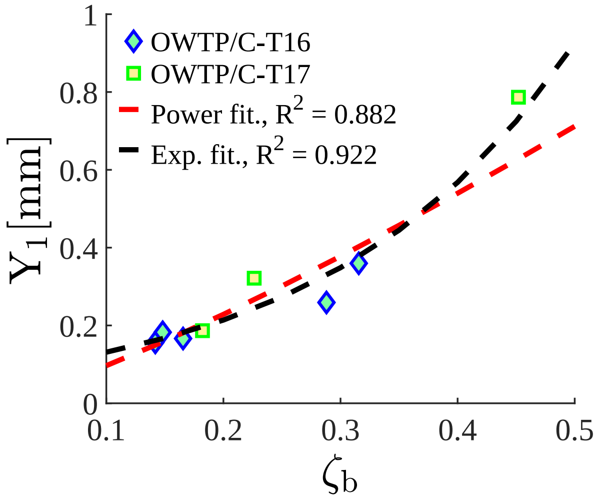

(b) Effect of ζ_b on Y_1

Figure 5.20: The effect of ζ_b on the constant rate (C_N) and initial displacement (Y_1).

In Fig. 5.20(b), the initial displacement (Y_1) values are observed to grow exponentially with load amplitude ζ_b. Both exponential and power functions (see Eq. 5.9 and 5.10, respectively) were derived from the scatter point of the test series, where a_2 = 0.0806, b_2 = 4.8804, a_3 = 1.6814, and b_3 = 1.24 are the fitting constants. Although the power law is also sufficient to fit the scattered points, the current study employed the exponential growth function to closely match the data points, with its goodness of fitting (R^2 = 0.922). The trend is observed to be in line with the experimental setup due to large displacement values of the maximum load (H_{max}). It should be noted that this approach is always used to determine the effect of the relative density in relation to the maximum load applied to the pile head. However, the current study was only limited to dense sand, therefore, further research is required.

$$Y_1 = a_2 e^{\left(b_2 \zeta_b\right)} \tag{5.9}$$

$$Y_1 = a_3 \zeta_b^{b_3} \tag{5.10}$$

Table 5.3: Characteristics of the total displacement of the pile

Test ID	ζ	H_{min} [N]	H_{max} [N]	ζ_c	$\zeta_b[0.5^o]$	a	C_N	Y_1
T16-F02	0	-155	160	-0.97	0.14	1.99	0.015	0.16
T16-F03A	0	-166	170	-0.95	0.15	2.29	0.009	0.18
T16-F03B	0	-140	158	-0.88	0.14	2.19	0.006	0.26
T16-F04	1	23	309	0.03	20.27	2.24	0.043	0.36
T16-F05	-1	25	350	0.1	0.31	2.57	0.036	0.17
T17-F03	0	-218	225	-0.97	0.2	2.5	0.01	0.19
T17-F04	0	-245	260	-0.94	0.23	2.38	0.021	0.32
T17-F05	0	5	520	0.01	0.45	3.72	0.036	0.79

5.5 Effect of cyclic secant stiffness

Several studies have been carried out for the pile under cyclic loading regarding the strength and stiffness reduction (Achmus et al., 2009, DNV, 2014, Little and Briaud, 1988, Long and Vanneste, 1994), but recent studies (Arshad and OKelly, 2016, Chen et al., 2015, Klinkvort and Hededal, 2013, LeBlanc, 2009, Li et al., 2010, y Puertos, 2011) have reported that the stiffness of the foundation are always increasing with increasing number cycles. As noted from Bhattacharya and Adhikari (2011), the cyclic stiffness is more important for the natural frequency (f_n) of the soil-monopile system of the offshore wind turbine. In this study, the first few cycles of the first recorded test series was assumed to be affected by rapidly displacement increase of the pile before the rate of increase stabilises. As the rate of displacement decreases with increasing number of cycles, the sands have more potential to compact, resulting into local densification of sandy soil around the pile, which might raise the shear modulus of sand and leading to the increase of pile secant stiffness.

Cyclic unloading stiffness (N/mm) of the monopile foundations was assessed as previously described in Section 5.2.3.2. The unloading stiffness in every cycle is normally described by either a power law (Little and Briaud, 1988, Long and Vanneste, 1994) or logarithmic (Klinkvort and Hededal, 2013, LeBlanc, 2009, Lin and Liao, 1999) functions. However, recent studies (Arshad and OKelly, 2017, Chen et al., 2015, Cox et al., 2014, Kirkwood and Haigh, 2014, Klinkvort and Hededal, 2013, LeBlanc, 2009, Li et al., 2010, Zhu et al., 2012) have reported that a logarithmic function (see Equation 5.11) was the best to predict the unloading stiffness of the monopile, where the parameter C_c is the stiffness constant, which can be varied for each test, K_N is unloading stiffness after N cycles and K_5 is the unloading stiffness after 5 cycles of loading. As a result of anomalous behaviour in unloading stiffness during the first 5 cycles, the value of K_5 can be simplified and approximated as K_1. The constant reducing rate $A_n = K_5C_c$ is obtained by best fit of the unloading stiffness of the measured data. Furthermore, by utilising this concept, a non-dimensional change in cyclic unloading stiffness can then be determined by using Eq. 5.12.

$$K_N = K_5(1 + C_c \log(N - 5)), \Rightarrow A_n = K_5C_c, N > 5 \tag{5.11}$$

$$\frac{\Delta K_s(N)}{K_5} = \frac{K_N - K_5}{K_5} = C_\alpha + C_c \mathrm{In}(N) \tag{5.12}$$

Test OWTP/C-T16 and OWTP/C-T17 were used to analyse and demonstrate the unloading stiffness of the model pile. The values of initial unloading stiffness and fitting constants, for each loading control factor (ζ), are determined. The resulting data for tests OWTP/C-T16 and OWTP/C-T17 are plotted in Fig. 5.21 and 5.22, respectively. To demonstrate the effect of load control ratio on the secant unloading stiffness, the series of each test are not plotted in a sequence. It should be noted that the behaviour of the first cycles of the first test series of each test was seen to be affected by soil mobilisation during testing. However, for the subsequent test series, the behaviour was affected by the change of load control factor ζ. The progressive increase of cyclic magnitude, due to the change of load control factor, had an impact on the relative cyclic amplitude. With this change, the sands have more potential to compact and leading to local densification of soil around the pile. The local densification of soil might raise the shear modulus of the sand around the pile and leading to an increase of the pile unloading secant stiffness with the increasing number of load cycles.

In Fig. 5.21, the unloading stiffness for each load control factor (ζ) (test series F02 - F05) is plotted against the number of loading cycles in a horizontal X-log scale. An inconsistent trend of stiffness behaviour was observed for the first 100 cycles of all test series, however, only the first five cycles were omitted and not taken into account in all analyses. It should be noted that during each of the test series, the change of loading frequency (from 0.5 to 2.5 Hz) and load control factor (ζ) at the initial stage led to some of the plots skipping during the test run, which provided some difficulties of ensuring the consistency of the applied loads. It is evident in Fig. 5.21 that the evolution of stiffness with increasing cycle numbers is quite erratic at the beginning. Similar behaviour is reported to occur from other studies, for instance, the unloading stiffness responses from LeBlanc et al. (2010) and Li et al. (2010).

Following the trend observed from other studies (Abadie, 2015, Arshad and OKelly, 2017, Chen et al., 2015, Klinkvort and Hededal, 2013, LeBlanc, 2009, Li et al., 2010) on the stiffness of the model pile-system, a logarithmic expression (see Eq. 5.11) was fitted to the data sets despite the irregularity of stiffness evolution of the first few cycles. This was achieved by using constants A_n and C_c shown in Eq. 5.11 and listed in Table 5.4 at the end of this section. From Table 5.4, the initial stiffness (K_1 = K_5) observed to be fairly consistent between test series, but it mainly depends on the loading control factor, ζ, which appeared to affect the resulting behaviour. For instance, taking into consideration a maximum value of ζ = -1 (951 N/mm) in test series T17-F05, K_1 is observed to be higher than other test series by approximately 33%, 31%, 20% and 19% for F02 (ζ = 0), F03A (ζ = 0), F03A (ζ = 0) and F04 (ζ = 1), respectively. This was expected as all tests were carried out with a similar relative density of sand in which the first test series (F02 (ζ = 0)) shows a higher percentage change than the others. It should be noted that during testing, the first few cycles of the first recorded test series was assumed to be affected by rapidly displacement increase of the pile before the rate of increase stabilises. Furthermore, during testing the setup of the automated load control programme observed to affect secant stiffness of the first few cycles of the subsequent series before the rate of increase stabilises. Thereafter, the rate of stiffness increase would have been affected due to densification of soil around the pile. However, the effect of soil densification is higher for the subsequent test series compared to the first series. Ideally each series of tests would have been done independently. However, the current study was limited due to technical challenges and time frame. Therefore, a further study is recommended.

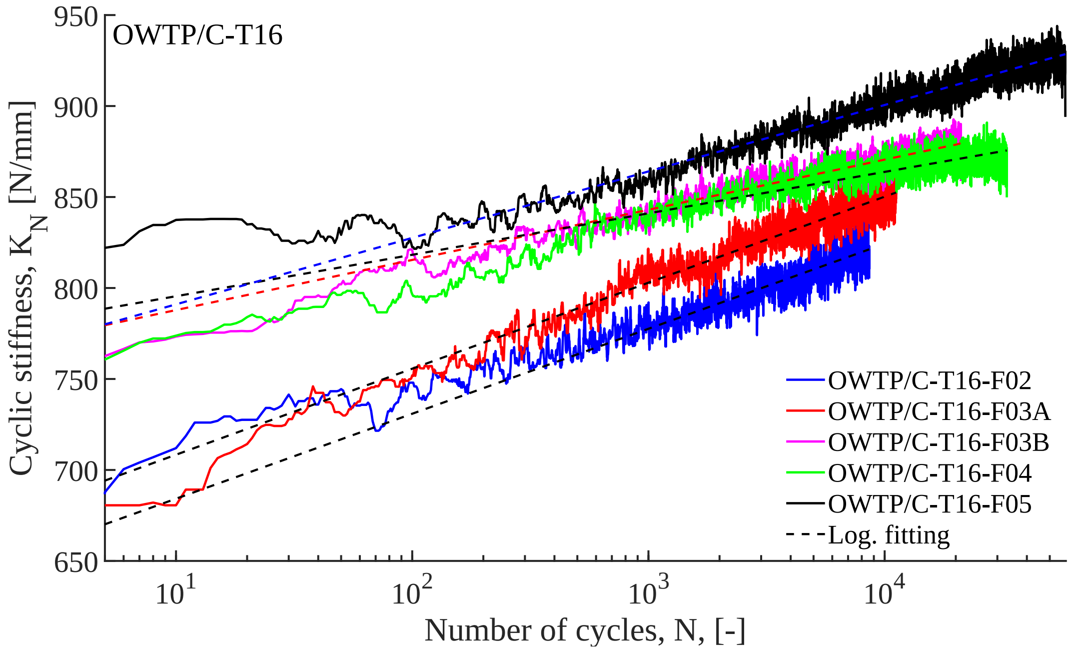

Figure 5.21: The unloading stiffness, K_N plotted against the number of cycle, N for the test OWTP/C-T16.

In Fig. 5.22, the graph shows the relationship between the unloading stiffness of test OWTP/C-T17 (test phase F03 (ζ = 0), F04 (ζ = 0) and F05 (ζ = -1)) against the number of cycles in X-log scale. For the first 200 load cycles, a similar behaviour described in the previous test was observed. The cyclic unloading stiffness was seen to increase gradually with the number of cycles. As an overall trend, it is clear that between 5-200 cycles, the unloading stiffness of all series increased gradually. For instance, at 200 cycles the stiffness was 902 N/mm and 990 N/mm for tests T17-F03/4 and T17-F05, respectively. After 200 cycles the stiffness continue to increase dramatically up to the end of the test run. In conclusion, the plots show that the unloading stiffness was increased insignificantly after 200 load cycles with decreased unloading stiffness rate. The decreasing rate, of each test series, was due to local densification of the sand surrounding the pile shaft. It should be noted that the first few cycles of each test series were affected by the automated load control setup.

In Fig. 5.22, Eq. 5.11 was fitted to all data sets of these tests to adequately predict the long-term cyclic unloading stiffness. The results show that Eq. 5.11 closely matches the test results from the cycle number greater than 200 of the test series F03 and F04 and more than 600 cycles in series F05. However, for the number of load cycles less than 100-200 cycles (test series F03 and F04), then unloading stiffness departs from the predicted trend and exhibits a steeper

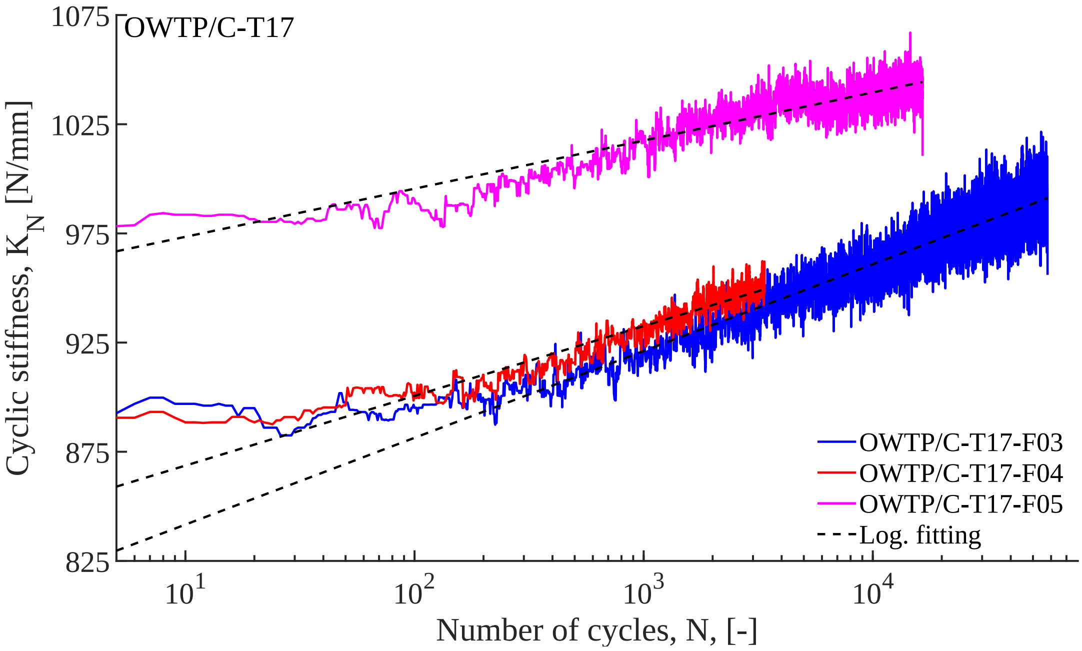

Figure 5.22: The unloading stiffness, K_s plotted against the number of cycle, N, for test OWTP/C-T17.

gradient. For the test series T17-F05, Eq. 5.11 underestimates the unloading stiffness between 30 and 800 cycles. The unloading stiffness rate, derived from both figures (A_n = 9.6 - 20.5, see Table 5.4), is observed to be different from A_n = 8.02 suggested by LeBlanc (2009) and noted to be higher by 19% of the minimum value of the listed values in Table 5.4.

In this research, the change (percentage increase) in the cyclic unloading stiffness of monopile was defined in Eq. 5.12. From this equation, the percentage increase value of zero means no reduction in the stiffness of monopile was achieved, whereas a value of 100% means no further stiffness of monopile occurred. Figures 5.23 and 5.24 show the change (percentage increase) in the cyclic stiffness of the soil-monopile system. From the two figures, the relationship between the relative stiffness and the number of cycles, for different load control factor, ζ, are plotted. It is clear that for the first 100 cycles the percentage change of unloading stiffness increased slightly and then continues to grow dramatically while maintaining a stable growth at small reducing rates. As discussed previously, the unstable growth observed in the first few cycles was due to rearrangement of soil particles for the first test series (T16-F02 and T16-F03) and change of load control factors (ζ) for the remaining series. Around 500 to 600 cycles, a permanent change of soil particles took place and led to the local densification of soil surrounding the pile shaft. The densification of the soil rose the shear modulus of sand and caused the cyclic stiffness to increase.

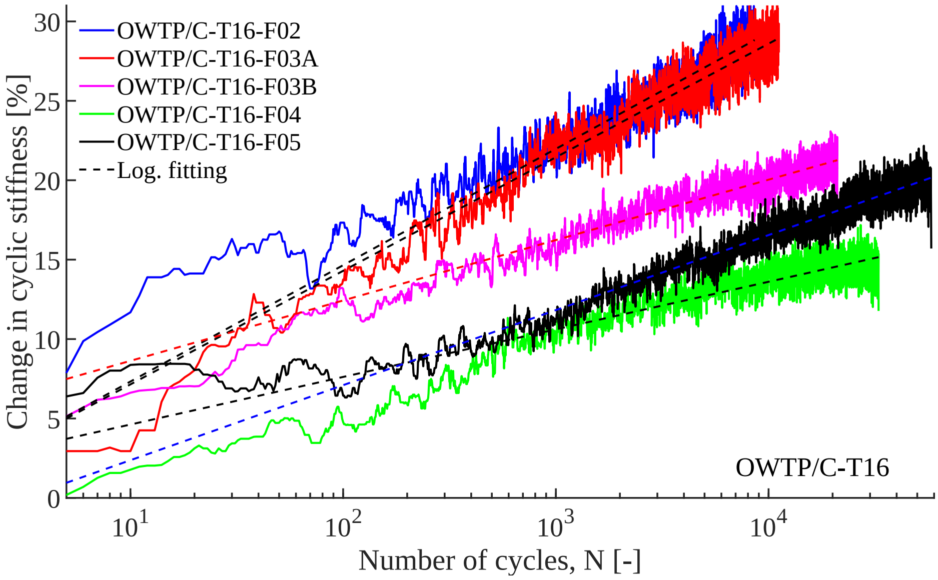

Figure 5.23: Change in cyclic stiffness against the number cycle for test OWTP/C-T16.

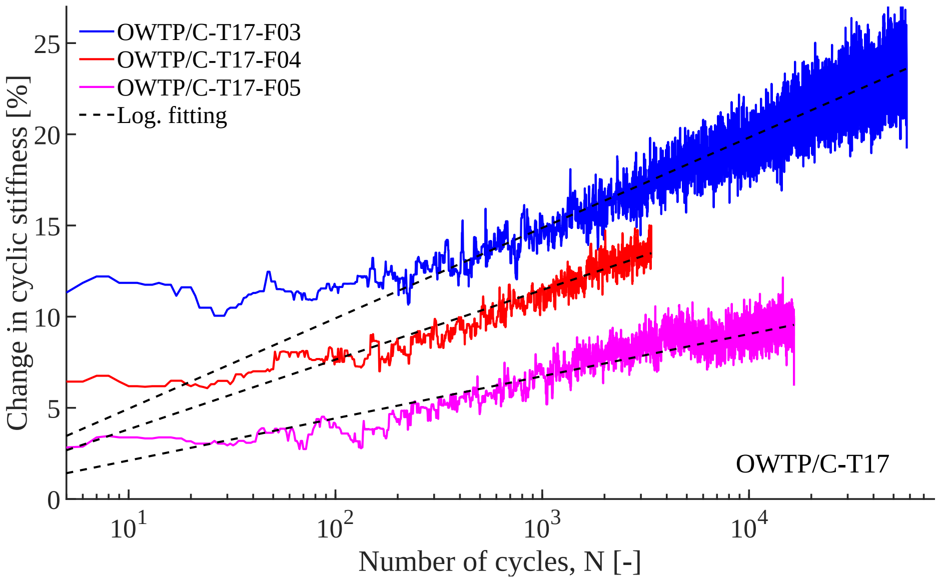

Figure 5.24: Change in cyclic stiffness against the number cycle for test OWTP/C-T17.

From figures, the following observations can be made;

1. The load control factor (ζ) affects directly the change in stiffness. For instance, with ζ = -1, the change in stiffness was 8-13% (N = 2000) lower compared with other test series (notably higher for $\zeta = 0$, 17-25%). This is expected due to the densification of the sandy soil of the subsequent test series with increased number of load cycles.

2. The trend observed contradicts the existing pile design philosophy under the frame of the *p-y* curve method from API (2007) and DNV (2014), which recommend a reduction of the pile-soil stiffness to account for cyclic effects, irrespective of the loading characteristics. Furthermore, the current design standard has no concept of cyclic stiffness compared to realistic condition of the prototype soil-monopile system interaction.

3. The monopile cyclic unloading stiffness are observed to increase with number of load cycles. This directly affects the performance of the offshore wind turbine through the natural frequency of vibration. To avoid greater rotation of the monopile, the phenomenon of resonance (the natural frequency coincides with forcing frequency) occurrence should also be avoided. Therefore, the foundation stiffness is an important parameter as this may lead to rapid deterioration of on-board machinery and ultimately structural failure (Arshad and OKelly, 2017, Bhattacharya et al., 2013a).

Two centrifuge tests were carried out in dry sand, which prepared at a relative density of 85%. Each of these tests was similar in all respects due to application of the cyclic load control factor, ζ. The effect of load control factor, in different cyclic load ratios, is described by plotting the empirical determined values of $\mathrm{A_k}$ and ζ_c as a function of ζ_b. It should be noted that the value of $\mathrm{A_k}$ is not constant and varied for each test series. As can be seen in Fig. 5.25, the measured data are scattered and making it difficulty to employ a fitting curve. In Fig. 5.25(a), the values of the unloading stiffness rate ($\mathrm{A_k}$) are observed to decrease in relation to ζ_b. This occurred as the load amplitude increases due to change of load control factor (ζ). The change of load control factor influences larger magnitude of load ($\mathrm{H_{max}}$) as the number of cycles increases. Therefore, the increase in the load magnitude resulted in a small reducing rate of unloading stiffness. Furthermore, the unloading stiffness of the first test series of each test is lower than subsequent test series. It should be noted that the subsequent test series (F03, F04 and F05) were conducted in similar prepared sand. Hence, the increase of the unloading stiffness of the subsequent series was due to the local densification of sandy soil around the pile shaft as the number of cycles increased. Therefore, with progressive increase of load cycles from each test, the sands have more potential to compact and hence increase the initial stiffness of each subsequent test series. It can be interpreted that the increased magnitude due to the change of load control factors had also an impact on the initial stiffness increase. However, the densification of soil around the pile shaft, due to many numbers of load cycles, was also a major factor of this trend.

In Fig. 5.25(b), the trend of the data indicates that for all values of $\zeta_{\mathrm{c}} < 0$, the loading direction is under two-way loading condition and bounded between $0.1 < \zeta_{\mathrm{b}} \leq 0.25$. For the values of $\zeta_{\mathrm{c}} > 0$, the direction of loading is one-way and can be found between $0.28 \leq \zeta_{\mathrm{b}} \leq 0.5$. This implies that for the model setup and load control factor suggested in this study, the rate of increase in stiffness is lower when the model pile was loaded under one-way loading direction ($\zeta_{\mathrm{c}} > 0$). This suggests that by changing the load control factor (ζ), in the negative or positive direction in the system, the damaging load condition is expected under one-way loading. This contradicts with findings from 1g experiments conducted from LeBlanc et al. (2010) and Abadie (2015), wheres the most damaging load situation found under two-way loading. However, the findings from Klinkvort et al. (2012), carried out under $\mathrm{N_s g}$, indicated that the damaging load is under one-way, which is similar to the current study. The number of tests presented here is small and not sufficient to reach a definitive conclusion about these effects in the lateral unloading stiffness. Future work is needed to consider the evolution of stiffness with regards to the variation of load magnitude and amplitude characteristics.

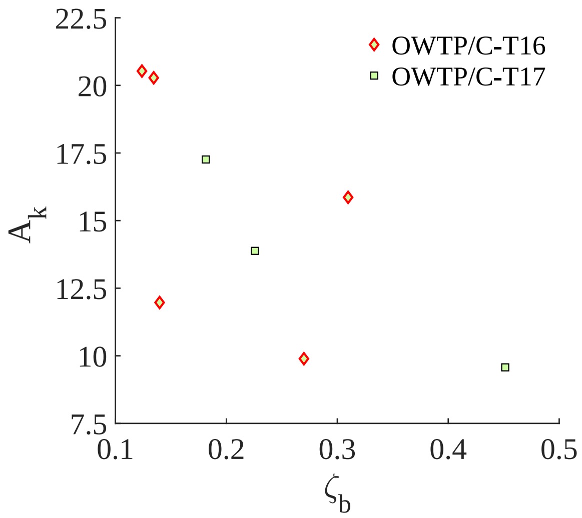

(a) Effect of ζ_b on stiffness rate, A_n

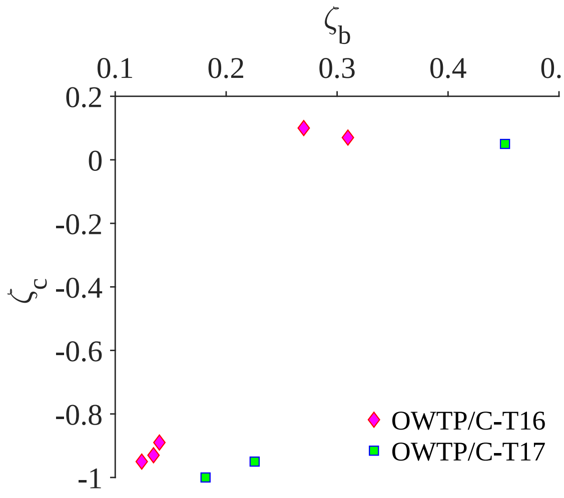

(b) Effect of ζ_b on ζ_c

Figure 5.25: The effect of ζ_b and ζ_c in the lateral unloading stiffness rate.

Table 5.4: Characteristics of the fitted curves on cyclic unloading stiffness

Test ID	ζ	ζ_c	K_1 [N/mm]	A_k	C_c
OWTP/C-T16-T02	0	-0.87	637.5	20.28	0.032
OWTP/C-T16-T03A	0	-0.95	661	20.53	0.031
OWTP/C-T16-T03B	0	-0.89	760	12	0.016
OWTP/C-T16-T04	1	0.1	773	9.89	0.013
OWTP/C-T16-T05	-1	0.07	755	15.86	0.021
OWTP/C-T17-T03	0	-1.0	802	17.26	0.022
OWTP/C-T17-T04	0	-0.96	837	13.88	0.017
OWTP/C-T17-T05	-1	0.01	951	9.573	0.01

5.6 Chapter summary

The results presented in this chapter confirmed some early observations reported in the literature, which provided insight into the aspects of cyclic pile behaviour. The fatigue limit state is governed by 10^7 load cycles, which are expected to be applied on the wind turbine over its design lifetime (normally 25 years). In this study, approximately 60,000 load cycles were achieved due to technical challenges and time-frame. Despite the limitations, concluding remarks of the research achievement are presented below.

1. From the cyclic experimental programme, three sets of testing series were investigated on small scale model pile subjected to a maximum of 60000 load cycles. A typical 5 MW monopile foundation was adopted and used to quantify the model pile dimensions using scaling laws. For all test series conducted, similar geometry of the model pile was considered. Neither the installation method nor the relative density of the sand bed was changed.

2. Two important parameters were investigated, the total displacement of the pile head and change of unloading secant stiffness. Despite the fact that tests were conducted in series, which had an effect on the soil state within each subsequent test, it was observed that the two parameters were affected by the load control factor of the system, and led to one-way or two-way loading conditions.

3. The displacement curves of the piles under cyclic loading exhibit a distinct behaviour. Initially, for the first few cycles, the displacement was seen to increase slowly followed by a second stage, where there is a dramatic increase in displacement with an increase in the number of load cycles. In this range of load cycles, the pile head displacement continues to increase but at a reducing rate until the end of each test series. The total displacement of the pile was largely affected by the load control factor, ζ. For instance, the rate of displacement was higher for ζ = -1 compared to ζ = 0. The setting of the automated load control system affected the cyclic loads, which observed to induce a significant accumulation of pile head displacement with time. The use of empirical functions recommended by LeBlanc et al. (2010) or empirical methods suggested in this study provided a first approximation of the pile head displacement.

4. Apart from anomalous stiffness behaviour of the first few cycles, the unloading stiffness was seen to increase slightly as the number of cycles continues to increase but at a reducing rate. As reported from Li et al. (2010), the reducing rate was possibly due to local densification of sand around the pile, which increases the soil stiffness and thereafter the unloading stiffness of the monopiles.

5. The increase of stiffness was approximated by a logarithmic function, which was affected by the load control factor, ζ. The data showed that changing ζ values from zero to -1 increased the initial stiffness while ζ = +1 did not affect the results significantly. The increase rate of stiffness (A_n), during the long-term cyclic loading, was higher compared to the previous value reported by LeBlanc (2009). The trend of unloading stiffness was seen to be different compared to the current methodology, which degrading the static *p-y* curves to account for cyclic loading.

6. The results presented in this chapter are aimed to offer an insight of further study to modify the developed model equipment and use it to optimise the real prototype design of monopile foundations subjected to cyclic lateral loads. Furthermore, the key parameters outlined from this chapter are referred to when identifying the mechanism for development of the theoretical model framework discussed in the next chapter.

Chapter 6

CYCLIC ANALYTICAL MODEL

6.1 Introduction

In this chapter, the centrifuge experimental data presented in Chapter five are used to develop an element model spring for cyclic local pile-soil interaction and global pile-head load-displacement responses. The centrifuge tests were conducted to establish the cyclic response on pile head. The observations from the centrifuge experiments may be used by researchers to draw conclusions of different effects observed on monopiles, as well as for design engineers to anticipated levels of displacement and corresponding change of monopile stiffness. However, in order for load-deflection responses to be efficiently used by design engineers, they must be able to replicate the anticipated shape of load-deflection cycles. A mathematical model, which is capable of reproducing the most important features of the load-deflection response by using available cyclic nonlinear Winkler spring *p*-*y* models, would be a useful tool for engineers.

As discussed in Section 4.4, the three parameter model, known as Ramberg Osgood model (R-O model), was used in the previous studies to achieve a good fit to experimental data. The R-O model was initially proposed by Ramberg and Osgood (1943) and later identified by Desai and Zaman (2013) as the modified Ramberg Osgood (MR-O) *p*-*y* spring model. The MR-O model is a mathematical expression which describes a full range of inelastic behaviour. The original MR-O model consists of four parameters, which are capable to capture a variety of non-linear backbone and cyclic *p*-*y* responses. It was used in algorithm based on descriptive kinematic equilibrium framework. The soil was modelled as a system of uncoupled nonlinear cyclic springs where the pile was considered as a elastic beam. This model was derived from flexible piles and used in the analysis of small piles and soil. The monopiles are currently designed according to semi-empirical *p*-*y* curves specified in the current design codes (API, 2007, DNV, 2014). The method has been used over decades, however its accuracy is still questionable especially on the prediction of experimental cyclic loading. The limitations of DNV model can be found in Chapter 2.

In this chapter, the MR-O model was further modified by introducing additional parameters compared to the original model, which can be adjusted to achieve a good fit to experimental data. In the following sections, the definitions of the key model parameters are explained graphically and related to experimental test responses. The nonlinear cyclic response includes two parts; firstly the load-deflection curve, known as the backbone curve, and secondly the constructed hysteresis loops described by the first unloading, first reloading, and subsequent unloading/reloading *p*-*y* (H-Y_p) curves. The backbone curves are constructed by two parameters (tangent stiffness and ultimate capacity) determined from the first cycle of the experimental cyclic responses, whereas the response of the hysteresis loops can then be investigated once the backbone curves are known.

The major objectives of this chapter includes: (i) to introduce the key features and demonstrate the capabilities of the MR-O model (ii) to use the model to understand the nonlinear behaviour of the cyclic centrifuge experiments on the model pile (iii) to apply the method to other published physical modelling tests.

6.2 An overview of cyclic model response

In the previous studies (Abendroth and Greimann, 1990, Allotey and El Naggar, 2008, Boulanger et al., 1999, Gerolymos et al., 2009, Heidari et al., 2014, Klinkvort, 2013), different types of cyclic pile-soil interaction relationships have been proposed. For instance, Boulanger et al. (1999) suggested an elasto-plastic model handled by active and passive springs, representing the backbone and unload-reload properties, respectively. The idea was further developed by Taciroglu et al. (2006) with three elements; leading face, a rear face and drag element. Furthermore, El Naggar and Novak (1995) developed a model to evaluate the response of piles based on Winkler hypothesis, using hyperbolic stress-strain relationships and accounting for slippage and gaps at the soil-pile interface. The model was later improved by Naggar and Bentley (2000), which employed the dynamic *p*-*y* curves equivalent to two springs representing the near field and far field. Allotey and El Naggar (2008), Gerolymos et al. (2009) and Heidari et al. (2014) developed Beam on Nonlinear Winkler Foundation (BNWF) models with different rules for loading, reloading and unloading, capable of accounting for cyclic degradation/hardening, separation of pile from the soil, radiation damping and loss of strength. From these models, the first loading (backbone) curve was fitted based on the concept of API (2007) static *p-y* curve and Strain Wedge Method (SWM) at each depth. The hyperbolic and Bouc-Wen *p-y* curves models were used to construct the unload and reload curves with the use of stiffness and degradation factors.

Most of the above-mentioned *p-y* curve methods have been used to analyse flexible pile-soil interactions, however, Klinkvort (2013) employed the hyperbolic type model proposed by Kondner (1963) to model the behaviour of monopiles in centrifuge experiments. For monopiles, a limited number of cyclic pile-soil interaction curves were found in the literature. Therefore, further research on this area is of importance.

In the establishment of a general model that can handle both monotonic and cyclic loading responses, it could be relevant to use the MR-O *p-y* model discussed in Chapter 4. This is the Winkler type model representing a cyclic spring element, which is capable of handling cyclic loading and accounting for degradation or hardening of stiffness and strength. As discussed in Chapter 2, Section 2.3.3.3, the old MR-O model from Desai and Zaman (2013) has got important three parameters (K_h, P_u and n) to predict the response of the experiment data, which is difficulty to adjust to achieve a good fit. In this study, the MR-O model was further modified to include more parameters: K_h, P_u and s, r, β_p and ξ_N. The parameter s and r (instead of n) can be used to adjust the non-linear hysteresis loops, while β_p is introduced to adjust the tangent stiffness of each loop. The constant function ξ_N was introduced to account for accumulated displacement during simulation, which is not available in the old model. Moreover, the effect of stiffness degradation or hardening was accounted into the tangent stiffness, K_N, by addition constant t. Furthermore, the old model did not consider the variation of load amplitude, in which the new model introduce the parameter χ to account for this effect. More detail of the comparison of these parameters is discussed in Section 6.5.3.4.

As noted from Klinkvort (2013), it is assumed that a gap will develop for fine-grain soils, while for the course-grains, the soil will cave in and close the gap. From the centrifuge tests of this study, the mechanism shows that the sand falls back and no gap was formed. Therefore, the cyclic model will not involve the drag contribution, and only buildup of soil resistance on the pile surface will be considered.

From the results of centrifuge tests, the observations of the cyclic pile head load-deflection were observed. As described in Chapter 4, the model pile of this study was non-instrumented, therefore, the cyclic experimental *p-y* curves from Klinkvort (2013) are used to demonstrate the local cyclic pile-soil interaction model. The global cyclic load-displacement response subjected to two-way loading (ζ_c = -0.7) and cyclic local pile-soil interaction are shown in Fig. 6.1(a) (test OWTP/C-T15-F07) and 6.1(b) (test no. 30), respectively. Three types of lines are drawn on top of these figures to show the various elements of the model.

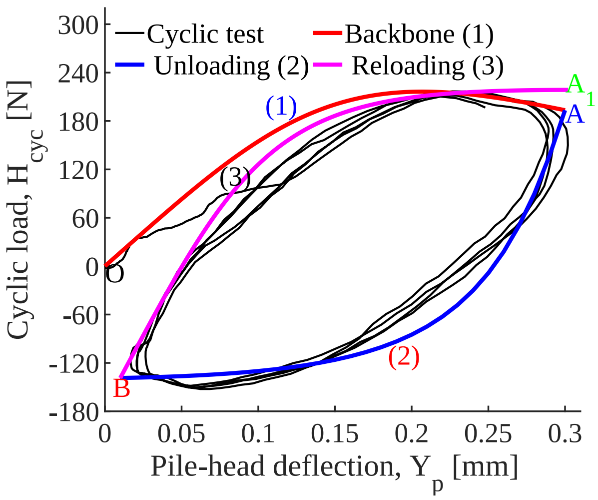

(a) Global load-deflection response

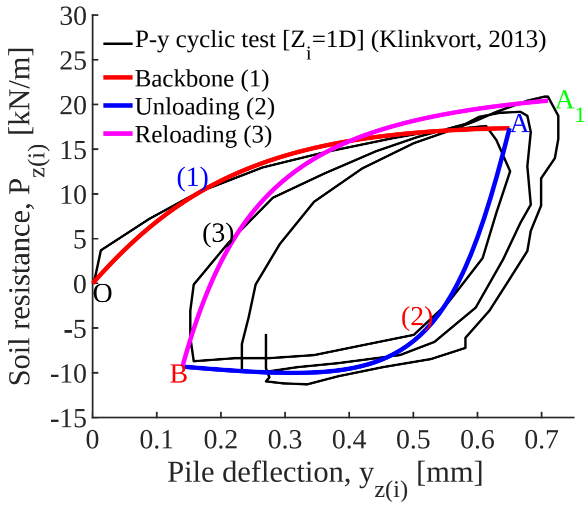

(b) Local *p-y* response, from Klinkvort (2013)

Figure 6.1: Cyclic model curve element and definitions.

As shown in Fig. 6.1, the model is created by three parts: (1) backbone phase (path O-A), (2) unloading phase (path A-B), (3) reloading phase (path B-A_1). Firstly, the backbone phase is observed when the resistance is built up after the application of load on the pile. The backbone curve is used as a benchmark for creating the subsequent unloading-reloading curves. The important parameters from the backbone curve are the initial modulus of subgrade (K_h) and ultimate soil resistance (P_u) or global tangent stiffness (K_t) and pile capacity (H_u) for the pile-soil interaction and global load-deflection response, respectively. Secondly, the unloading phase is when the pile starts to move backward with unloading force decreasing from A to B. The initial modulus or tangent of this curve is controlled by K_h or K_t of the backbone curve as suggested by Masing (1926) and Pyke (1980). Finally, a reloading phase occurs when the pile is moving towards the initial position in the gap created in stage (1). However, it is assumed that the sand totally fills the gap.

To handle the observation seen in the centrifuge cyclic tests, the MR-O function discussed in Chapter 4 is here modified. The modified model is basically identical to the model presented in

Abdel-Rahman and Achmus (2005) and Desai and Zaman (2013), but there are some changes to include the stiffness hardening and displacement accumulation. This was chosen to accurately represent the results seen in the centrifuge tests. More detail of addition parameters can be found in the subsequent sections.

6.3 Stiffness and strength parameters

In this section, the expression shown in Eq. 6.2 was used to determine the initial stiffness for small strain amplitude (Desai and Zaman, 2013), where K_h represents the initial subgrade modulus with a unit of stiffness (kN/m^2), E_s is the Young modulus of soil (kN/m^2), v_s is the Poisson's ratio, D is the diameter of the pile in m, E_pI_p is the flexural stiffness of the pile (kN/m^2), α_p = 0.15 and j = 0.108 are dimensionless constants suggested by Vesic (1961). To evaluate the initial Young's modulus of the soil, $E_s = (1 + v_s)\, G_{max}$, the Pestana and Salvati (2006) soil maximum shear modulus (G_{max}) function (see Eq. 6.1), in kN/m^2, at low amplitude strains, was applied, where the dimensionless shear modulus stiffness coefficient (G_b) was set as 600 for clean sand, P_a is the atmospheric pressure in kN/m^2, e_o is the initial void ratio, $\sigma_v = \frac{1}{3}\gamma' Z(1 + 2K_o)$ is the effective stress in kN/m^2, γ' is an effective unit weight in kN/m^3 and Z is the depth below the ground surface in m, K_o = 1-sin ϕ is the coefficient of earth pressure at rest, and ϕ is the friction angle of soil.

For $e_o \approx$ 0.54 and assuming ϕ = 40^o and G_b = 600, the maximum shear modulus G_{max} at P_a=100 kPa, Z = 30 m below the ground surface, is approximately equal to 203 MPa. It should be noted that Eqs. 6.2 and 6.1 are only used for initial stiffness of the backbone curve. For cyclic loading, the power law degradation function (see Eq. 6.3) can be applied, where $K_h = K_1$ is the initial subgrade modulus at small strain amplitude from the backbone curve, κ_1 is the degradation constant, and K_N is modulus of subgrade reaction after N cycles.

$$G_{max} = G_b P_a e_o^{-1.3} \left(\frac{\sigma'_v}{P_a}\right)^m \tag{6.1}$$

$$K_h = \alpha_p \left(\frac{E_s}{1 - v_s}\right)\left(\frac{D}{D_{ref}}\right)\left[\frac{E_s D^4}{E_p I_p}\right]^j \tag{6.2}$$

$$K_{h(N)} = K_h N^{\kappa_1} \tag{6.3}$$

In this study, the pile was embedded in dry sand where the ultimate soil resistance (P_u), for backbone curve, can be calculated through the analytical expression proposed by Broms (1964) (see Eq. 6.4), where $\sigma_v = \gamma' Z$ is the vertical stress and ϕ is the friction angle of the soil. Eq. 6.4 is preferred in practice due to its simplicity and sufficient engineering accuracy (Gerolymos et al., 2009). It can be used as a reference for unloading and reloading ultimate soil resistance.

$$P_u = 3\sigma_v \tan^2\left(45 + \frac{\phi}{2}\right) D \tag{6.4}$$

As noted by Carter (1984) and Mosikeeran and Larkin (1990), the unloading ultimate soil resistance, $P_{u(U)}$, or pile capacity, $H_{u(U)}$, for the first and subsequent unloading cycles can be estimated by using Eq. 6.5 or 6.6, which relates the ultimate unloading control parameter, *t*, and maximum resistance, P_A (H_A), emerging from the backbone curve. In Fig. 6.2, the ultimate capacity of reloading cycles can be estimated as $H_{u\{R\}}$ = H_u-H_B, where H_u is the ultimate capacity of the backbone curve.

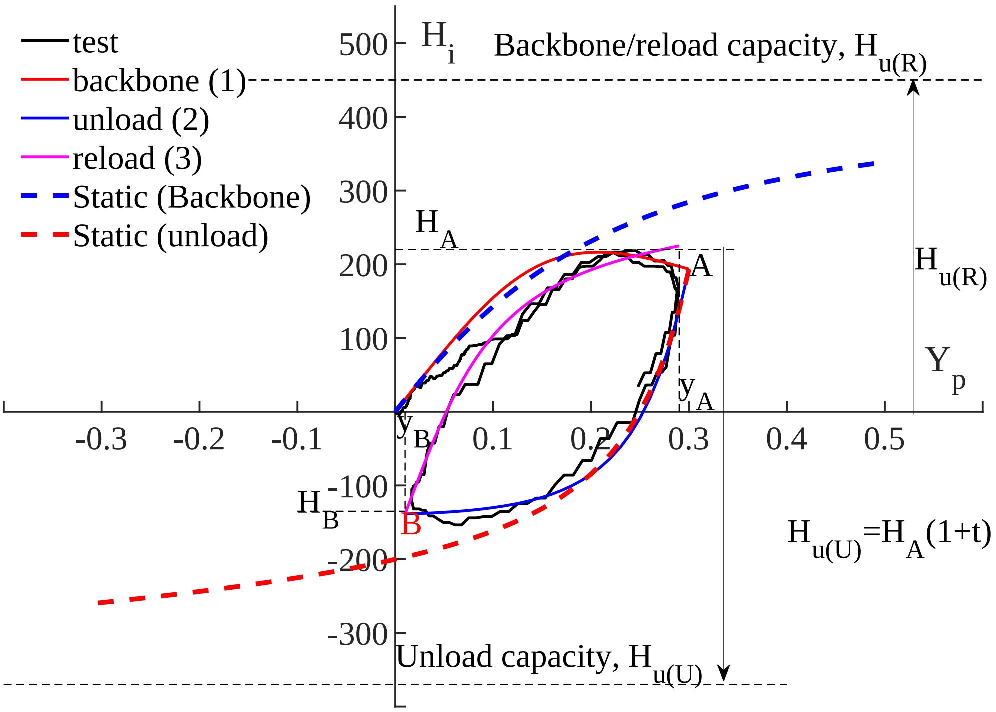

Figure 6.2: Sketch to illustrate the unloading ultimate load capacity, $P_{u\{U\}}$.

$$P_{u\{U\}} = P_A + tP_A = (1+t)P_A \tag{6.5}$$

$$H_{u\{U\}} = H_A + tH_A = (1+t)H_A \tag{6.6}$$

6.4 Theoretical model: Equations and parameters

The cyclic spring model used in this study was developed in the form of the modified Ramberg-Osgood expressions to approximate the nonlinear soil resistance and displacement behaviour of monopile response. A one-dimensional kinematic action-reaction approach is capable of reproducing a variety of stress-strain or force-displacement relationships, for both monotonic and cyclic loading. The approach is being applied to model the backbone and hysteresis loops, expressing the *p-y* relationships or the global load-deflection responses (H-y_g). A simple version of the MR-O model is outlined in the following sections.

6.4.1 Backbone curve

The backbone curve is represented as a nonlinear or multi-linear curve incorporated in different models, which are fitted to a specified nonlinear monotonic load-displacement response such as those specified in API (2007) and DNV (2014). In this study, the nonlinear backbone are *p-y* curves derived based on the modified MR-O model created at each depth. In this way, the developed kinematic hardening approach is capable of accounting for a global response (H_i-Y_g) and ultimate capacity (H_u) at the ground surface.

For a pile of diameter D installed in cohesionless soil, the soil resistance per unit length ($P_{z(i)}$) against deflection of the pile ($y_{z(i)}$) at a point along the embedded length L, is expressed as shown through Eq. 6.7 to 6.8, where K_h is the modulus of subgrade reaction (spring stiffness) in kN/m^2, y_o, P_o are displacement and soil reaction at the origin, and P_u is the ultimate soil resistance in kN/m. To better fit the test data, the parameter r, s and β_p are introduced in Eq. 6.8. r and s are used to control the shape of the backbone curves (referred as shape parameter of nonlinearity).

$$P_{z(i)} = P_o + f(y_{z(i)}) \tag{6.7}$$

$$\Rightarrow \mathrm{f}(\mathrm{y}_{\mathrm{z(i)}}) = \frac{\beta_{\mathrm{p}}\mathrm{K}_{\mathrm{h}}\left(\mathrm{y}_{\mathrm{z(i)}} - \mathrm{y}_{\mathrm{o}}\right)}{\left(1 + \left|\frac{\beta_{\mathrm{p}}\mathrm{K}_{\mathrm{h}}\left(\mathrm{y}_{\mathrm{z(i)}} - \mathrm{y}_{\mathrm{o}}\right)}{\mathrm{P}_{\mathrm{u}}}\right|^{\mathrm{s}}\right)^{\frac{1}{\mathrm{r}}}} + \mathrm{K}_{\mathrm{f}}\left(\mathrm{y}_{\mathrm{z(i)}} - \mathrm{y}_{\mathrm{o}}\right)$$

$$\therefore \mathrm{P}_{\mathrm{z(i)}} = \mathrm{P}_{\mathrm{o}} + \frac{\beta_{\mathrm{p}}\mathrm{K}_{\mathrm{h}}\left(\mathrm{y}_{\mathrm{z(i)}} - \mathrm{y}_{\mathrm{o}}\right)}{\left(1 + \left|\frac{\beta_{\mathrm{p}}\mathrm{K}_{\mathrm{h}}\left(\mathrm{y}_{\mathrm{z(i)}} - \mathrm{y}_{\mathrm{o}}\right)}{\mathrm{P}_{\mathrm{u}}}\right|^{\mathrm{s}}\right)^{\frac{1}{\mathrm{r}}}} + \mathrm{K}_{\mathrm{f}}\left(\mathrm{y}_{\mathrm{z(i)}} - \mathrm{y}_{\mathrm{o}}\right) \tag{6.8}$$

In Fig. 6.3, the typical definitions of the local and global backbone curves of test no. 30 from Klinkvort (2013) and test OWTP/S-T4, respectively are presented. Mathematically, to construct the backbone curves, Eq. 6.8 is used, with initial parameter, $\mathrm{K_h}$ ($\mathrm{K_t}$) and $\mathrm{P_u}$ ($\mathrm{H_u}$), directly related to the monotonic response. For the global response, the tangent stiffness ($\mathrm{K_t}$) and ultimate pile capacity ($\mathrm{H_u}$) are accepted as appropriate parameters to be used to construct the backbone curves of the overall load-deflection response (see Fig. 6.3(b)). However, the approach is different when used to construct the *p*-*y* curves along the depth of the pile. Usually, the solution is obtained by varying linearly or non-linearly the modulus of subgrade reaction, $\mathrm{K_h}$, and ultimate soil resistance, $\mathrm{P_u}$, considering both deflection and depth below the ground surface, Z. In Fig. 6.3(a), a typical local response at depth of Z = 1D m is fitted with the old (original) and new (modified) Ramberg and Osgood (1943) models. All mentioned parameters

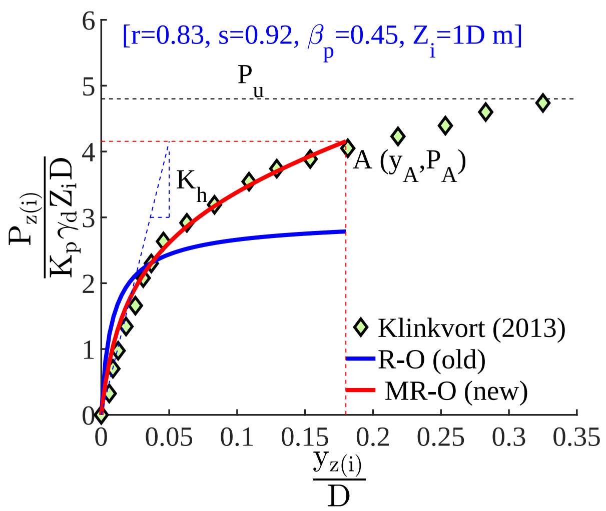

(a) Local $\mathrm{P_{z(i)}}$-$\mathrm{y_{z(i)}}$ curve

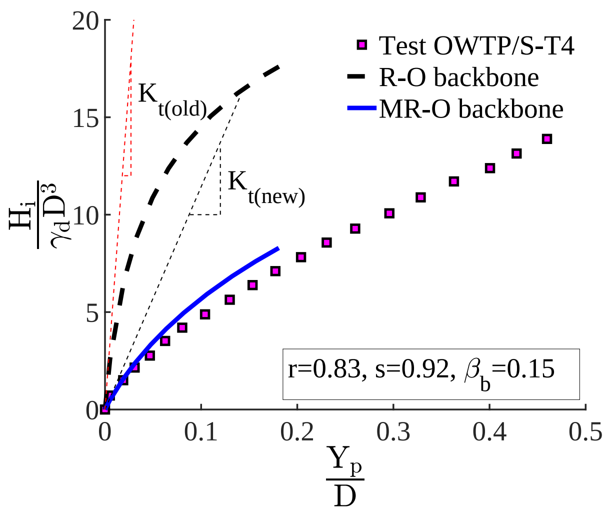

(b) Global $\mathrm{H_i}$-$\mathrm{Y_g}$ curve

Figure 6.3: Backbone parameter definitions of the local spring and global response of tests no. 30 (Klinkvort, 2013) OWTP/S-T4, respectively.

are presented in Figs. 6.3(a) and 6.3(b). As can be seen in Fig. 6.3(a), it is interesting to note that the *p-y* backbone curve from Klinkvort (2013) is underestimated with original R-O model, while in Fig. 6.3(b) the total response of test OWTP/S-T4 is overestimated. The modified R-O model agrees well with experimental test results. This concludes that the use of original model is insufficient to model the test results from the experiment.

6.4.2 Unload-reload curves

The unload-reload interaction spring element can be defined based on the backbone curve discussed in Section 6.4.1. The extra input parameters compared to backbone calculation are unloading stiffness ($K_{h(U)}$), maximum unloading load (P_A), displacement (Y_A) and the unloading ultimate resistance ($P_{u(U)}$). A schematic drawing of spring element is shown in Fig. 6.4, with two critical points A (y_A, P_A) and B (y_B, P_B), whereby coordinate A is defined as initial point of cyclic unloading curve captured along the path O-A of the backbone *p-y* curve or global response while point B indicates the maximum unloading point, at which the unloading

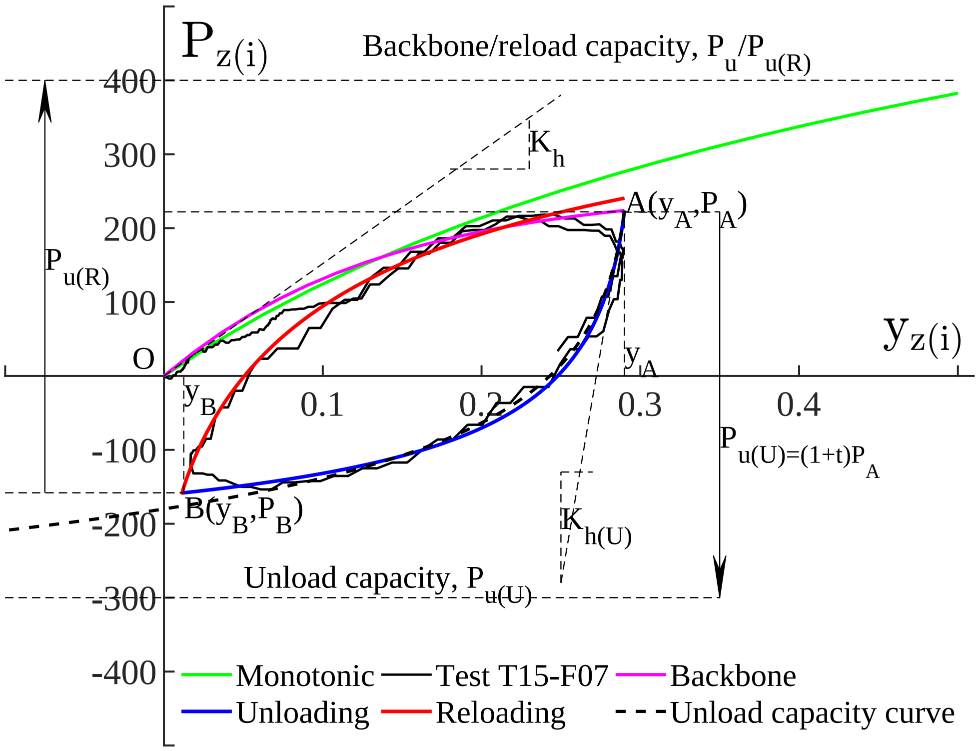

Figure 6.4: Conceptual sketch describing the parameters of the unload and reload spring elements.

soil resistance, P_B, is reached at deflection, y_B. The reload and unload curves are similar to the backbone curve, and can be derived based on the factor C (see Eq. 6.9) described in the literature, in Chapter 2 (Pyke, 1980). From Eq. 6.9, P_A is the current resistance at the onset of unloading or reloading, and Pu is the ultimate resistance. The plus (+) and minus (-) signs denote unloading and reloading, respectively.

$$C = 1 \pm \frac{P_A}{P_{uU}} \tag{6.9}$$

From Fig. 6.4, the unloading curve (path A-B) is expressed by the function shown in Eq. 6.10, where y_A, P_A are the maximum values of the coordinate A, which are assumed to be the initial values of the unloading curve. If the loading reversal occurs at point A, then the unloading resistance, P_A (H_A), is reduced from A, and the unloading curve is created by using Eq. 6.11 (MR-O model) until it reaches point B, where the minimum load at B, P_B=χP_A is related to maximum load at A, P_A, using an amplitude load ratio, χ. The parameter, χ is used to control the unloading soil resistance on path A-B. The parameter β_p was introduced to affect the unloading-reloading initial stiffness. $P_{u(U)}$ = (1+t) H_A is the ultimate unloading resistance discussed in Section 6.3.

$$f\left(\frac{P_{i(U)} - P_A}{C}\right) = f\left(\frac{y_{z(i)} - y_A}{C}\right) \tag{6.10}$$

$$\therefore P_{i(U)} = P_A + \frac{\beta_p K_h (y_{z(i)} - y_A)}{\left(1 + \frac{\beta_p}{C}\left|\frac{K_h (y_{z(i)} - y_A)}{P_{u(U)}}\right|^s\right)^{\frac{1}{r}}} + K_f (y_{i(u)} - y_A) \tag{6.11}$$

The final unloading deflection, y_B is obtained by considering the control parameters *t* and χ, maximum cyclic load, P_A and modulus of subgrade reaction, K_h. The derivation to obtain y_B (see Eq. 6.14) is shown through Eq. 6.12 to 6.14, where the model parameter *t* controls the unloading hyperbolic curve (path A-B) and deflection y_B, and χ controls the unloading force (known as cyclic load ratio).

$$\Rightarrow \Delta y_{AB} = \frac{\Delta P_{u(U)}}{K_{hU}} \tag{6.12}$$

$$y_A - y_B = \frac{P_{u(U)} - (-\chi P_{u(U)})}{tK_h + -\chi K_{h(U)}} \tag{6.13}$$

$$y_B = y_A + \frac{(1+\chi)P_A(1+t)}{(t-\chi)K_{h(U)}} \tag{6.14}$$

For the reloading curve, the soil resistance ($P_{i(R)}$) is estimated by Eq. 6.15, increasing from P_B to the maximum load, $P_{i(R)} = P_{A1}$. Coordinate $A_1(y_{A1}, P_{A1})$ is created with displacement, y_{A1} and resistance values of the next unloading cycle. The change in displacement, y_{AA1}=y_{A1}-y_A, is used to account for accumulation of subsequent cycles. From Eq. 6.15, $K_{h(R)}$ is the reloading stiffness modulus in kN/m^2, $P_{u(R)}$=$P_u - P_B$ is the reloading ultimate soil resistance in kN/m, $y_{i(R)}$ is the reloading displacement variation, y_B is the constant displacement value at B, and β_p is the dimensionless constant.

$$\therefore P_{i(R)} = P_B + \frac{\beta_p K_{h(R)}(y_{i(R)} - y_B)}{\left(1 + \frac{\beta_p}{C}\left|\frac{K_{hR}(y_{i(R)} - y_B)}{P_{u(R)}}\right|^s\right)^{\frac{1}{r}}} + K_{f(R)}(y_{i(R)} - y_B) \tag{6.15}$$

6.4.3 Cyclic displacement accumulation function ξ_N

The cyclic displacement accumulation mechanism can affect the behaviour of soils and piles subjected to cyclic loading. Soil degradation is mainly related to stiffness or strength parameters. As noted from (Allotey and El Naggar, 2008, Little and Briaud, 1988, Long and Vanneste, 1994), the stiffness or strength modification approach was used to degrade or harden the backbone and hysteretic curves. With the knowledge described from these studies, the degrading factor ξ is introduced in the MR-O model to affect the displacement of the hysteretic loops. The following assumptions and procedures were used to develop the function ξ:

1. Accumulation factor for the first cycle

   - Consider the reloading and unloading functions shown in Eq. 6.15 and 6.11, respectively. By assuming that $r = 1$, β_p = 1, C = 1 Eq. 6.16 and 6.17 were created to calculate the amplitude values at A_1 and B_1, respectively.

$$P_{A1} = P_B + \frac{K_h\,(y_{A1} - y_B)}{\left(1 + \left|\frac{K_h\,(y_{A1} - y_B)}{(P_u - P_B)}\right|\right)} \tag{6.16}$$

$$P_{B1} = P_{A1} + \frac{K_h\,(y_{A1} - y_{B1})}{\left(1 + \left|\frac{K_h\,(y_{A1} - y_{B1})}{(1+t)\,P_A}\xi\right|\right)} \tag{6.17}$$

- The model experiment was carried out under load control; therefore, assumption here made to consider the coordinate at A_1 and B_1, where the amplitude loads are $P_{A1} = P_A$ and $P_{B1} = P_B$, respectively. From this assumption, Eq. 6.17 is substituted into Eq. 6.16 and parameter ξ of the first cycle is then derived through Eq. 6.18 to Eq. 6.20.

$$\Rightarrow \frac{K_h\,(y_{A1} - y_B)}{\left(1 + \left|\frac{K_h\,(y_{A1} - y_B)}{(P_u - P_B)}\right|\right)} = \frac{K_h\,(y_{A1} - y_{B1})}{\left(1 + \left|\frac{K_h\,(y_{A1} - y_{B1})}{(1+t)\,P_A}\xi\right|\right)} \tag{6.18}$$

$\Downarrow$

$$\Delta y_{A1B1} + \frac{K_i \Delta y_{A1B1}\,(y_{A1} - y_B)}{P_u - P_B} = (y_{A1} - y_B) + \frac{K_h\,(y_{A1} - y_B)\,\Delta y_{A1B1}}{(1+t)\,P_A}\xi \tag{6.19}$$

But; $\Delta y_{A1B1} = y_{A1} - y_{B1}$

$$\therefore \xi = \frac{P_A\,(1+t)}{P_u - P_B} - \frac{(y_{B1} - y_B)\,P_A\,(1+t)}{K_h\,(y_{A1} - y_{B1})\,(y_{A1} - y_B)} \tag{6.20}$$

2. Accumulation factor for the subsequent cycles, N

- The displacement function, $y_N = y_1 N^{\kappa 2}$, was previously proposed by Long and Vanneste (1994). It is employed here to determine the accumulation factor ξ_N for the subsequent cycles.

- The change of unloading displacement between the two points (B and B_1) can be expressed as $\Delta y_{BB1} = y_{B1} - y_B$. The change of displacements between the consecutive points of each cycle, Δy_{BBN}, can be estimated by considering the displacement function shown in Eq. 6.21. Therefore, Eq. 6.21 can be used to determine the accumulation factor, ξ_N, where κ_2 is accumulation constant.

$$\Delta y_{BBN} = \Delta y_{BB1} N^{\kappa 2} = (y_{B1} - y_B)\,N^{\kappa 2} \tag{6.21}$$

- From Eq. 6.20, the change of unloading displacement for the first cycle is $y_{B1} - y_B = \Delta y_{BB1}$. Hence, for the subsequent cycles, Δy_{BB1} is replaced by Δy_{BBN}, which is shown in Eq. 6.21. Finally, the accumulation function for unloading curve after N cycles (ξ_N) can be estimated by the function shown in Eq. 6.22.

$$\therefore \xi_N = \frac{P_A\,(1+t)}{P_u - P_B} - \left[\frac{(N^{\kappa_2}\,(y_{B1} - y_B))\,P_A\,(1+t)}{(K_h\,(y_{A1} - y_{B1}))\,(y_{A1} - y_B)}\right] \tag{6.22}$$

- For subsequent unloading or reloading curves, the creation of hysteresis loops is the same as described in previous section. Therefore, the accumulation displacement control factor, ξ_N, is accounted in the model as shown in Eq. 6.23.

$$P_{i(N)} = P_{i(A)} + \frac{\beta_p K_{h(N)}\left(y_{i(N)} - y_A\right)}{\left(1 + \frac{\beta_p}{C}\left|\left(\frac{K_{h(N)}\left(y_{i(N)} - y_A\right)}{\left(P_{u(U)}\right)}\right)\xi_N\right|^s\right)^{\frac{1}{r}}} + K_{f(U)}\left(y_{i(N)} - y_A\right) \tag{6.23}$$

6.5 Key parameters and capability of the model

6.5.1 Introduction

For a better understanding of the constitutive relations used in modelling pile-soil interaction to lateral loading, a brief outline is presented herein of the key parameters. The primary purpose is to examine the response of the MR-O model by assessing the impact of varying the recommended parameters.

The MR-O model parameters, which characterise the non-linear backbone and cyclic p-y curves or force-deflection response, are classified in three categories. The first group involves the curvature control constants (s and r) and initial stiffness adjustment constant (β_p) that describe the backbone curve. Any change of these parameters might affect the initial stiffness (K_h or K_t) and ultimate capacity (P_u or H_u). The second group describes the constants used to influence the characteristics of cyclic loading such as χ and *t*. They are useful in matching the results of the experiment model tests. The third group involves the accumulation and stiffness degradation control factors (κ_1 and κ_2). The following sections describe how the model parameters would affect the backbone and hysteresis loops.

6.5.2 Parameter for backbone curve

The ability of the model to reproduce the ground surface response of the backbone curve is illustrated by considering typical local *p-y* curves, created based on fitting of the monotonic test results. A *p-y* curve at depth Z = 1D was chosen to describe the influence of the backbone shape parameters r and s which control the shape of the curves during the monotonic loading. The values of r and s can range between 0 and 3. Both the original and modified Ramberg and Osgood (1943) models were employed in this analysis to describe the parameter variation for the typical local *p-y* backbone curves, in a normalised form. For instance, in Fig. 6.5(a) the parameter r was equated to s to describe the response of the original MR-O *p-y* model, where a larger number of r is seen to approximately model a bilinear backbone curve. Thus, decreasing the values of r leads to smoother transitions where the nonlinear behaviour occurs even at low loading levels. Fig. 6.5(b) and 6.5(c) illustrate the role of r and s of the modified MR-O backbone *p-y* curves. In Fig. 6.5(b), the parameter r (while keeping β_p = 0.4 and s = 0.92 constant) is varied from 0.5 to 2.5 to observe the shape of nonlinearity. It observed that when r $<$ 1.25 a work-hardening *p-y* curve is produced, while at values of r $>$ 1.25, a work-softening *p-y* curve is created. In Fig. 6.5(c), when the value of r = 0.83 and β_p = 0.4 are kept constant the value of s is allowed to vary. It is revealing that the larger the value of s, the larger the component of lateral soil reaction resulting from constrained soil dilatancy.

Parameter β_p controls the initial stiffness (initial elastic modulus) of each *p-y* curve. The backbone curves for different values of β_p, while keeping constant values of r and s, are shown in Fig. 6.5(d). The larger the value of β_p, the larger the component of the soil resistance and tangent stiffness. When these parameters r, s and β_p are properly calibrated, the most *p-y* curves of the model pile developed from full-scale and centrifuge experimental test can be approximately matched.

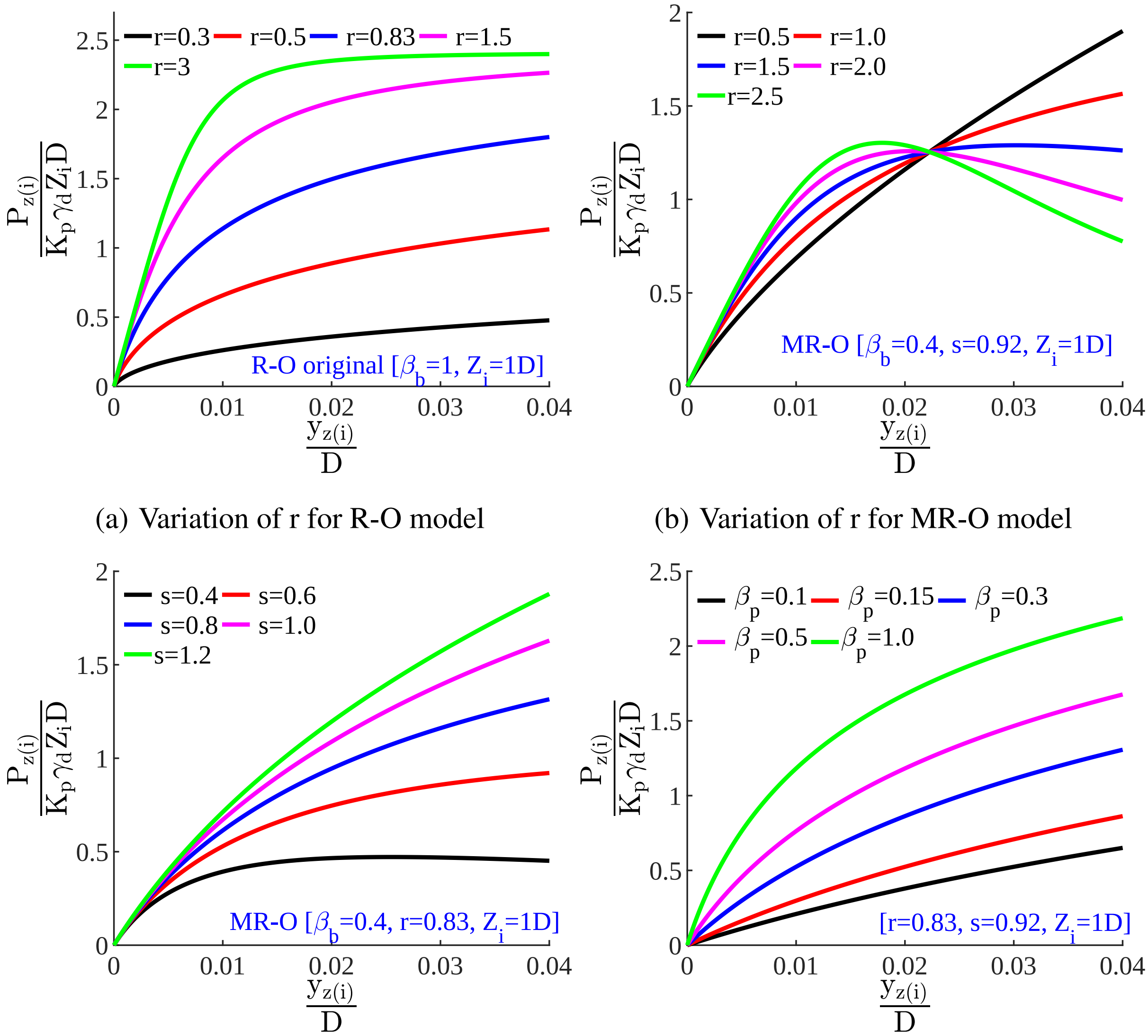

(a) Variation of r for R-O model

(b) Variation of r for MR-O model

(c) Variation of s for MR-O model

(d) Variation of β_p for MR-O model

Figure 6.5: Normalised soil reaction-pile deflection for selected values of r, s and β_p.

6.5.3 Parameters for unload-reload curves

The global cyclic nonlinear model has five important parameters, including the initial (tangent) stiffness (K_t), maximum capacity (H_u), shape of nonlinearity parameters (β_p, r, s). The initial stiffness and maximum capacity of the backbone curve were both estimated from the method suggested by Kulhawy and Chen (1995), using an equilibrium of analysis described in Chapter 4. The load-displacement backbone curves, from the original and modified Ramberg and

Osgood (1943) model functions, are given in Fig. 6.6 along with centrifuge test OWTP/S-T4. Fig. 6.6 illustrates the reduction of calculated backbone curve using modified function, where the stiffness reduction factor β_p reduced from 1 to 0.12 and s increased from 0.83 to 0.92. The modified backbone curve shows a positive agreement with the test results compared to the original model. This indicates that the modified MR-O model can be used throughout as the basis to construct the unload-reload hysteresis loops. The parametric study of global unload-reload curves can then be established with parameters listed in Table 6.1. In addition, the shape parameters of nonlinearity and estimation of K_t, H_u are shown in Fig. 6.6(a) and 6.6(b), respectively.

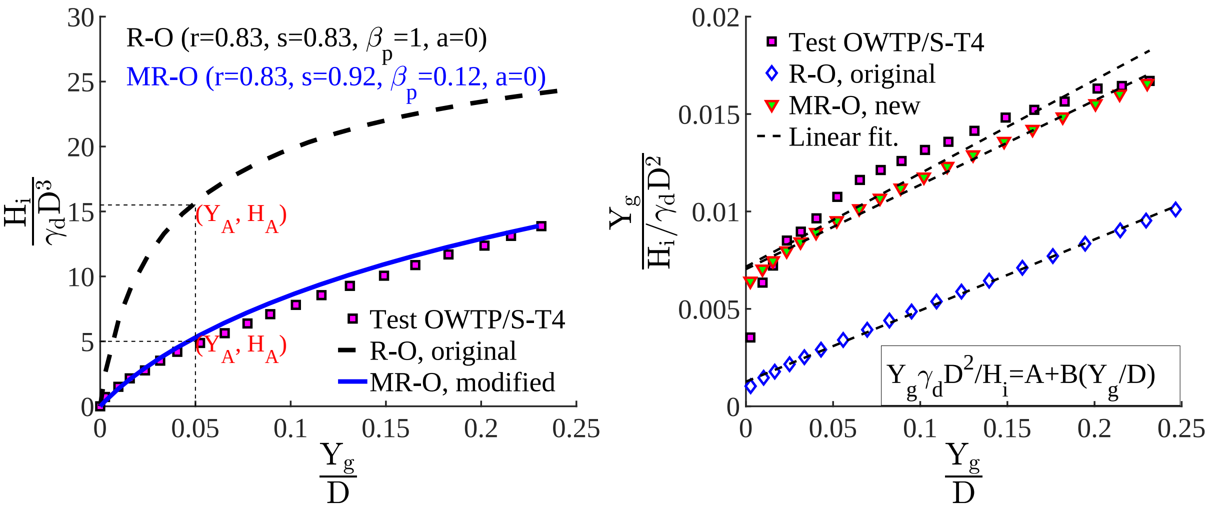

(a) H-y_g global backbone curves

(b) Input parameters K_t and H_u

Figure 6.6: (a) Comparison of the centrifuge test OWTP/S-T4 response with calculated backbone curve using the original and modified Ramberg and Osgood (1943) curves, in a normalised form. (b) Estimation of K_t and H_u

Table 6.1: Dimensionless parameters extracted from backbone curves.

SN	Parameter	Symbol	Experiment	R-O	MR-O
1	Constant A	A	0.0072	0.0013	0.007
2	Constant B	B	0.048	0.0365	0.043
3	Tangent stiffness	$\hat{\mathrm{K}_t} = \frac{\mathrm{H_i}}{\mathrm{Y_g}\gamma_\mathrm{d}\mathrm{D}^2}$	139	769	143
4	Ultimate capacity	$\hat{\mathrm{H}_u} = \frac{\mathrm{H_u}}{\gamma_\mathrm{d}\mathrm{D}^3}$	21	27	23
5	Unload deflection	$\hat{\mathrm{Y}_A} = \frac{\mathrm{Y_A}}{\mathrm{D}}$	0.05	0.05	0.05
6	Unload force	$\hat{\mathrm{H}_A} = \frac{\mathrm{H_A}}{\gamma_\mathrm{d}\mathrm{D}^3}$	5	15	5

6.5.3.1 Effect of parameter χ and t

The factor χ is introduced in the model to determine the cyclic loading amplitude ratio. The ratio is similar to $\chi = \zeta_\mathrm{b} = \frac{\mathrm{H_{min}}}{\mathrm{H_{max}}} = \frac{\mathrm{H_B}}{\mathrm{H_A}}$, which was previously suggested by Lin and Liao (1999) and Long and Vanneste (1994). According Lin and Liao (1999), the cyclic load ratio, ζ_b, is in the range between -1 and +1 ($-1 \leqslant \zeta_\mathrm{b} \leqslant 1$). $\zeta_\mathrm{b} = 1$ is used to define the pure backbone curves, $0 \leqslant \zeta_\mathrm{b} \leqslant 1$ define one-way cyclic loading, and $-1 \leqslant \zeta_\mathrm{b} < 0$ define the two-way cyclic load responses.

To capture the behaviour of cyclic tests under one-way or two-way cyclic loading, the control factor χ in combination with unloading ultimate constant *t* are introduced in the MR-O model. The constant t as related to χ is used to control the unloading curve from A to B and displacement at coordinate B. The factor χ is used to quantify the characteristic of the cyclic load as shown in Equation 6.24, where $\mathrm{H_{min}}$ and $\mathrm{H_{max}}$ are the minimum and maximum amplitudes of hysteresis loops, respectively. However, it should be noted that the parameter t and χ are based on the experimental test results.

$$\chi = \frac{\mathrm{H_{min}}}{\mathrm{H_{max}}} \tag{6.24}$$

To demonstrate the variability of χ, four basic shapes of hysteresis loops are generated based on the relationship between t and χ. As shown in Figs.6.7(a), 6.7(b) and Figs.6.7(c), when r and s are kept constant, the values of χ tend to vary from 0 to 0.5 and set to -1 for one-way and two-way loading direction, respectively. For instance, when χ=1, the hysteresis loop degenerates to the monotonic (backbone) loading curve. Therefore, the parameter χ shows the capability of the model to capture both one-way and two-way cyclic responses. Meanwhile, the constant t is introduced to control the loops through the unloading ultimate capacity. For instance, a small value of t while keeping χ constant, approximately enlarges the hysteretic bounding loops, which will lead to an increase of unloading ultimate capacity ($H_{u(U)}$). On the other hand, increasing the value of t tends to squeeze the bounding hysteresis loops while increasing in secant stiffness. Thus, this parameter will affect both shape and secant stiffness of the loops. Fig. 6.7(d) illustrates the variation of t with values of 1, 5 and 10.

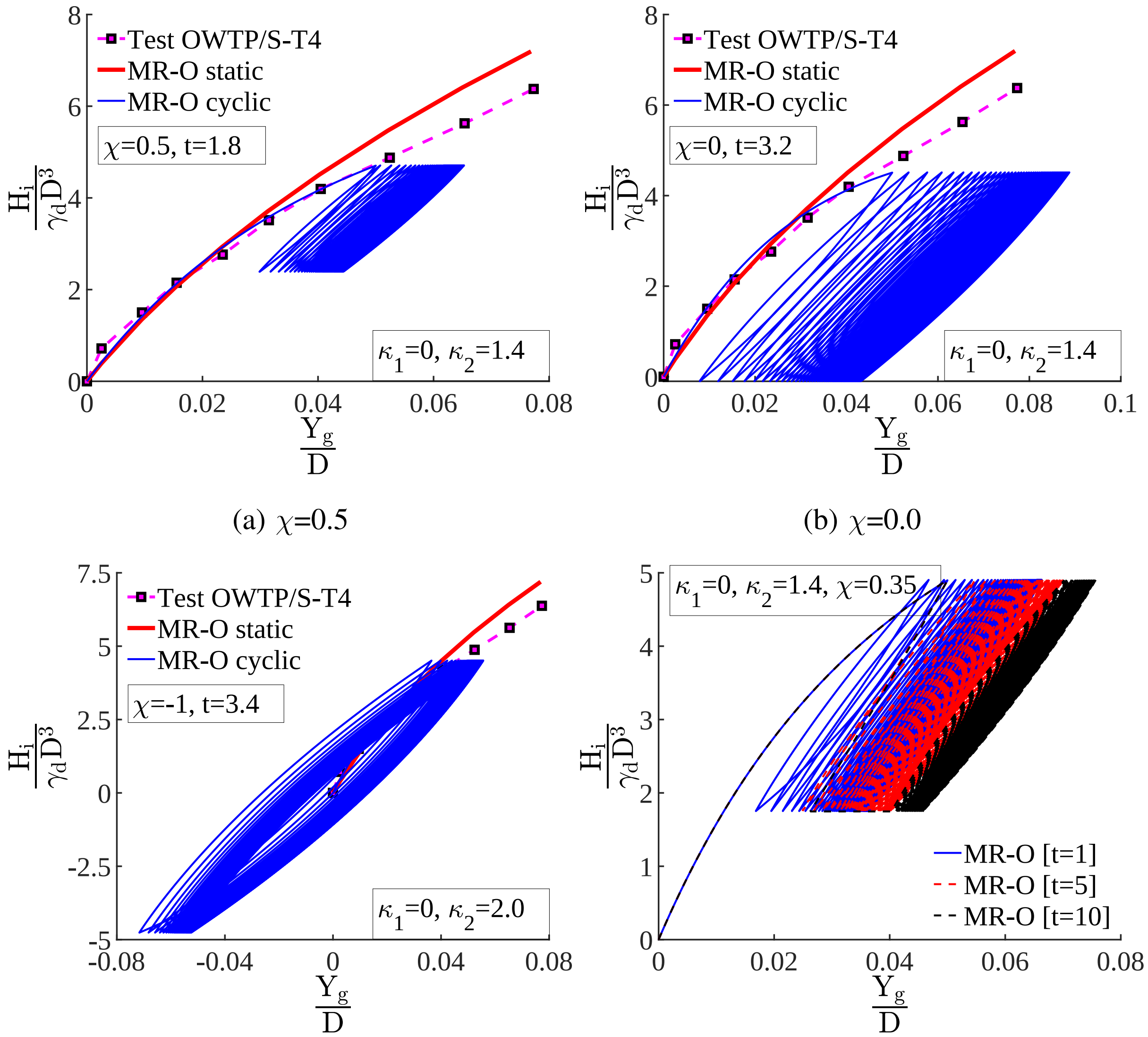

(a) χ=0.5 (b) χ=0.0

(c) χ=-1.0 (d) The influence of parameter t, for χ=0.35

Figure 6.7: The influence of cyclic load ratio, χ, and constant t on the typical overall load-displacement curve of this study.

6.5.3.2 The influence κ_2 and cyclic degradation factor ξ_N

This section presents a typical *p-y* hysteresis loop to highlight the model ability to simulate the spring soil reaction at specific depths. The *p-y* curves are typically derived by employing the modified MR-O model into the analysis, where a *p-y* curve at depth Z = 1D was selected to describe the influence of parameter κ_2. A summary of the properties and parameters used in the model is listed in Table 6.1 and 6.2.

Table 6.2: Properties and parameters used for a typical *p-y* curve

Item	D	L	N_s	ϕ_{max}	γ_d	χ	t	κ_1	κ_2	β_p, r, s, a
Unit	m	m	-	^{o}	kN/m^3	-	-	-	-	-
Values	0.6	0.3	30	40	16.8	-0.3	2.1	0.1	1.1-1.4	1.5, 0.83, 0.75, 0

Fig. 6.8(a) shows three typical hysteresis loops of spring elements positioned at depth Z = 1D. Each loop represents the effect of constant κ_2, which controls the variation of the subsequent hysteresis loops from the backbone curve. During the analysis, a smaller value of κ_2 approximately enlarge the bounding loops, while increasing values of κ_2 resulted in squeezing the loops towards the largest backbone displacement. The use of κ_2 on the resulting displacement of hysteresis bounding loops is described in Fig. 6.8(c). The increase of κ_2 was observed to affect the displacement response, in which smaller the value of κ_2, the higher is the displacement and vice verse. Furthermore, in Fig. 6.8(b), the cyclic degradation function ξ_N is plotted against the number of cycles N. It can be seen that the values of ξ_N increases with a number of cycles until it becomes constant. Despite the fact that the curves are very close, the values of ξ_N are observed to increase with increasing κ_2. Moreover, the degradation constant κ_1 was set to 0.1 to see the effect of cyclic secant stiffness and κ_2 in relation to a number of cycles, N. As shown in Fig. 6.8(d), the pile secant stiffness increases with the increasing number of load cycles. This trend of stiffness increase represents the effect of local densification of soil occurring around the pile due to lateral cycling loading.

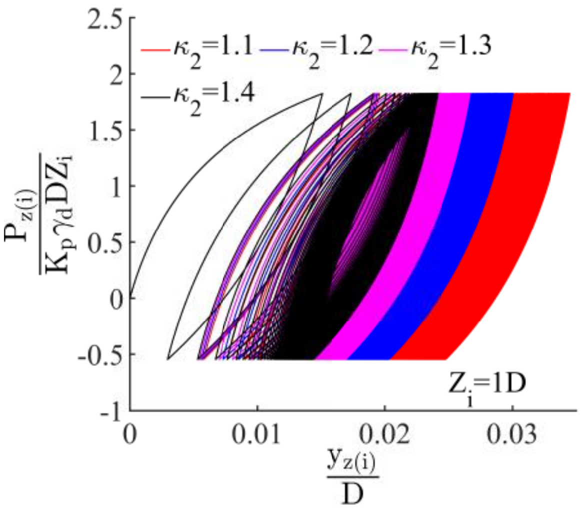

(a) Effect of κ_2 on hysteresis loops

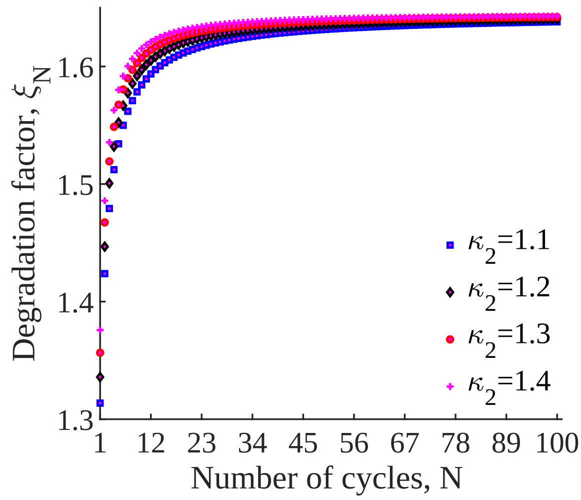

(b) Degradation factor ξ_N for each κ_2

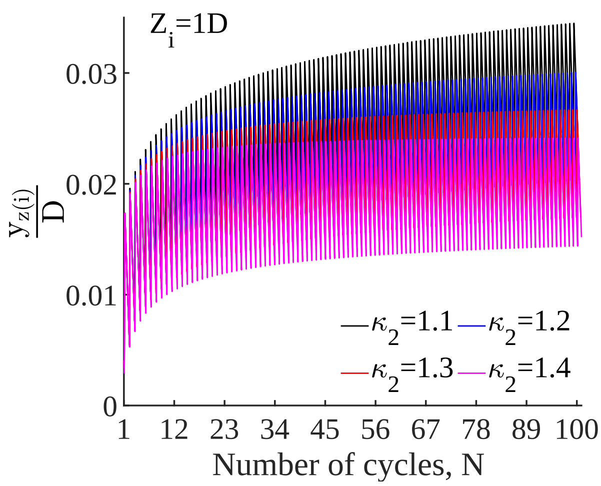

(c) Effect of κ_2 on displacement

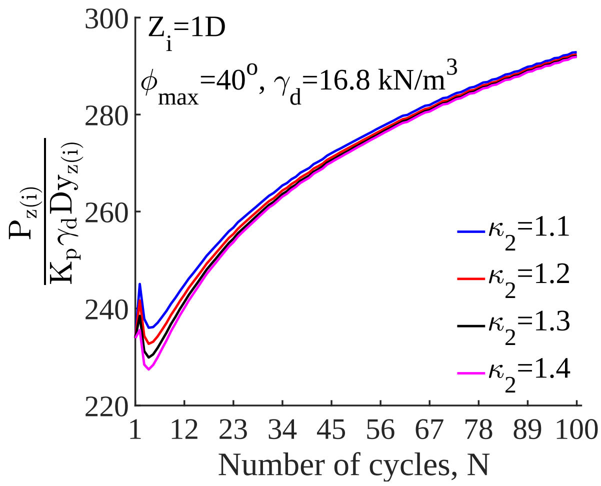

(d) Effect of κ_2 on secant stiffness

Figure 6.8: The effect of κ_2 on hysteresis loops, displacement, stiffness and degradation factor ξ_N.

6.5.3.3 Effect of parameter κ_1 on stiffness hardening

The model is also capable of reproducing stiffness degradation behaviour. The stiffness degradation-hardening (hereafter degradation generally refers to both degradation and hardening) is directly accounted in the MR-O model and controlled by the parameter κ_1 to influence the changes of the subsequent hysteresis bounding loop stiffness. The significance of parameter κ_1 is described on a typical *p-y* curve at depth Z = 1D, where D is 60 mm model pile diameter. The calculation of the backbone *p-y* curves, at depth Z, is based on the best fitting of the total response of test OWTP/S-T4. At each depth, the parameters K_h and P_u were derived from the created backbone curves and used to construct the hysteresis *p-y* loops. According to Fig. 6.9(a), there are three basic hysteretic shapes which represent the effect of parameter κ_1 for approximately 100 bounding loops. While keeping t, χ, r and s constant, the increment of κ_1 from 0.1 to 0.4 is observed to affect the secant stiffness of the subsequent hysteretic loops as number of cycles increases. It is evident that κ_1 affects both tangent and secant stiffness of each hysteretic loop. Furthermore, in Fig. 6.9(b) the cyclic secant stiffness, for each κ_1, is shown to increase with increasing number of cycles. From this figure, it can be seen that a large values of κ_1 affects the loops by increasing the secant stiffness. This is expected because in the model test the local densification of soil due to lateral cycling might raise the shear modulus of the sand around the pile and lead the pile secant stiffness to increase with the increasing number of load cycles.

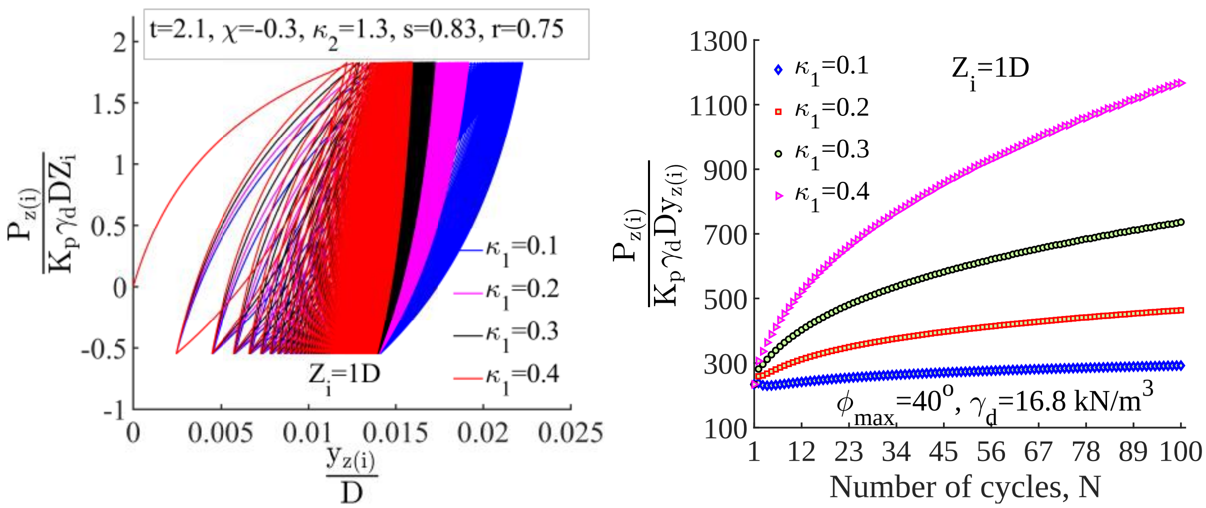

(a) Effect of κ_1 on the hysteresis loops.

(b) Effect κ_1 on secant stiffness

Figure 6.9: The influence of κ_1 on the cyclic secant stiffness of each hysteresis loop.

In conclusion, the parameter variation presented and discussed in Section 6.5.3.1 and 6.5.3.3 indicates that the model can reproduce the effect of cyclic loading direction, displacement increase/decrease and change in bounding loop stiffness. The parameters *t* and χ are dependant on the results from the experiment; however, it may require some adjustment to fit the model. With an increase of the number of cycles, N, the parameter κ_1 control the cyclic secant stiffness while the change in displacement from each cycle is affected by κ_2. It can therefore be articulated that the combination of all parameters is highly considered to influence the behaviour of any hysteretic loops.

6.5.3.4 A comparison in parameter between the old and new MR-O model

Table 6.3 summarises the parameters of the original and modified MR-O model shown in Eq. 6.25 and 6.26, respectively. In Table 6.3, the similarity and difference of parameters, from the two models, is shown with mark ✓ and ×, respectively. It can be seen that other parameters were added in the model to include the effects of load characteristics, displacement accumulation and stiffness degradation. For instance, the function ξ_N (see Eq. 6.22) employed parameter κ_1 to affect the change in displacement, the function K_{hN} (see Eq. 6.3) employed κ_2 to change the secant stiffness, the unloading displacement y_B (see Eq. 6.14) used χ and t to capture the amplitude and characteristic of load (ζ_b, ζ_c) while r, s and β_p were used to adjust the nonlinear curves. Therefore, the additional parameters shown in Eq. 6.26 and summarised in Table 6.3 indicate a further modification of the original MR-O model suggested by Desai and Zaman (2013).

Table 6.3: A summary of parameters between the original and modified R-O model

Parameters	K_h	P_u	C	r	s	a	β_p	ξ_N	χ	t	κ_1	κ_2
R-O model	✓	✓	✓	✓	×	×	×	×	×	×	×	×
MR-O model	✓	✓	✓	✓	✓	✓	✓	✓	✓	✓	✓	✓

$$P_{z(i)} = P_B + \frac{K_h y_{z(i)}}{\left(1 + \frac{1}{C}\left|\frac{K_h y_{z(i)}}{P_u}\right|^s\right)^{\frac{1}{s}}} \tag{6.25}$$

$$P_{z(i)} = P_B + \frac{\beta_p K_h (y_{z(i)} - y_B)}{\left(1 + \frac{\beta_p}{C}\left|\frac{K_h (y_{z(i)} - y_B)}{P_u}\xi_N\right|^s\right)^{\frac{1}{r}}} + K_f (y_{i(u)} - y_B) \tag{6.26}$$

6.6 Verification and demonstration of the model

6.6.1 Introduction

The previous sections introduced the modified Ramberg Osgood model that is capable of capturing the primary features of the experimental test results. In this section, the nonlinear model described in Section 6.4 is applied to describe the results from current and published experimental studies. The aim is to calibrate the model in such a way that it reproduces the experimental test pile responses as closely as possible.

In this study, centrifuge tests were carried with a non-instrumented pile with only global pile-head loading against its displacement. Therefore, to demonstrate the local pile-soil resistance of spring element against the pile movement, below the ground surface, the published results of centrifuge tests from Klinkvort (2013) were used. The local soil reaction curves were determined from the calibration study of the prototype monopile, in which the experimental tests are normalised in the form described in Chapter 4. The initial modulus and ultimate soil resistance of the *p*-*y* curves were estimated using the function suggested by Desai and Zaman (2013), Vesic (1961) and Broms (1964), DNV (2014), respectively. The adjustment was made during the analysis to follow the backbone curves observed in the centrifuge tests. The model function does not include the gap formation and sandy soil assumed to flow into the gap. During the unloading and reloading process, the maximum resistance is also assumed to remain constant. The local *p*-*y* curves of test No. 71 (Klinkvort, 2013) are first compared with the model. Afterwards, the model is employed to demonstrate its capability for the pile total response of the current research.

To have appropriate hysteresis loops for specific tests, firstly, the initial stiffness ($\mathrm{K_h}$) and ultimate capacities ($\mathrm{P_u}$) are properly estimated. Secondly, the modifications discussed in Section 6.4 were introduced in the original model and then used throughout. Thirdly, the method suggested by Kulhawy and Chen (1995) is used to estimate the values of $\mathrm{K_t}$ and $\mathrm{H_u}$ from the total load-displacement backbone curve. Finally, the simulation using the MR-O model will adopt the parameters listed in Tables 6.4 and 6.5 for the current and published studies, respectively.

Table 6.4: Model parameters for current study validation

SN	Parameter	Symbol	T15-F07	T16-F03	T17-F04	T17-F05
1	Initial unload deflection	$\hat{y_A}$	0.0035	0.0045	0.009	0.015
2	Initial unload force	$\hat{H_A}$	1.8	1.9	2.44	4.45
3	Tangent	$\hat{K_t}$	808	800	1050	1050
4	Ultimate capacity	$\hat{H_u}$	4.07	4.15	4.15	4.15
5	Cyclic load ratio	χ	-0.76	-0.78	-0.79	0.1
6	Asymptotic constant	t	1.3	1.4	2.5	1.2
7	Stiffness deg. constant	κ_1	0.03	0.026	0.026	0.026
8	Displacement deg. constant	κ_2	1.12	1.3	1.35	1.1
9	Curve control constant	r	0.83	0.83	0.63	0.83
		s	0.53	0.55	0.73	0.43

6.6.2 Local response from Klinkvort (2013)

In this section, the measured data presented by Klinkvort (2013) is evaluated and reduced in an attempt to demonstrate the use of the MR-O model to predict the cyclic experimental *p-y* curves. The response of the hysteretic MR-O spring model is compared with the results of the local *p-y* curves of test no. 71. The initial stiffness of the local backbone *p-y* curves is calculated based on the method described in Chapter 4, which is estimated as $K_h^{model} = b_k K_h^{test}$, where b_k is a reduction factor to match the model and cyclic tests backbone curves at each depth. The values of K_h^{test} at depth of 1D, 1.5D and 2D are 54.4, 67.4 and 186, respectively. Therefore, the K_h^{model} is reduced by the values of b_k equal to 0.9, 0.92 and 0.85, respectively. As shown in Fig. 6.10, the backbone curves of the model closely match with the backbone of the cyclic test *p-y* curves. The unloading initial stiffness of the first loop follows the principle suggested by Masing (1926) and Pyke (1980), however, the *p-y* test stiffness was seen to be approximately 1.5 times stiffer and therefore it is was taken as $K_h^{unload} = 1.5\ K_h^{model}$. The unloading loops also seem to predict the test results with degree of accuracy at each depth.

In general, the model represents the key observations resulted from the local pile-soil interactions of the centrifuge test of three soil layers as shown in Fig. 6.10(a). However, some discrepancies in stiffness change and shape of nonlinearity are due to compacted sand, which can not be supported in the model simulation and hysteresis loops observed to maintain an area that is approximately constant.

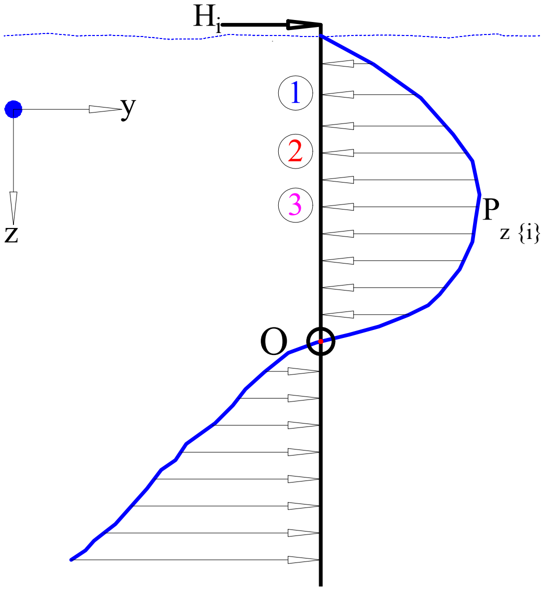

(a) Sketch of *p*-*y* curve profile

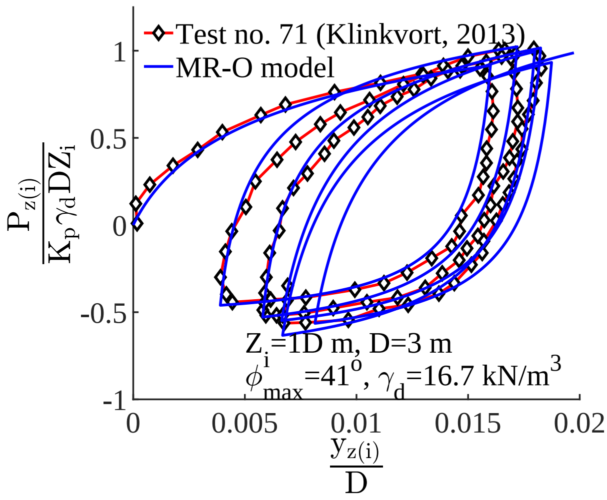

(b) *p*-*y* curves at Z_i=1.0D

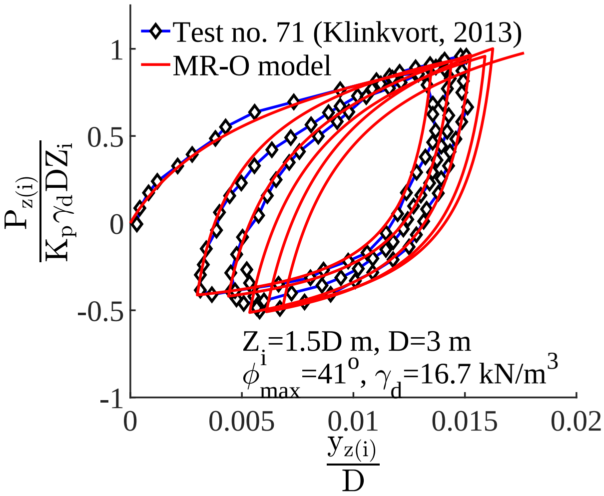

(c) *p*-*y* curves at Z_i=1.5D

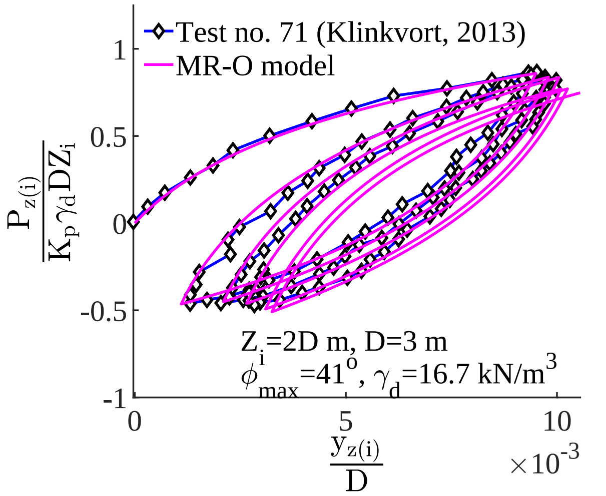

(d) *p*-*y* curves at Z_i=2.0D

Figure 6.10: Simulated local *p*-*y* curves, test no. 70 (Klinkvort, 2013), using the MR-O model at (1) Z_i=1D, (2) Z_i=1.5D and (3) Z_i=2D, where D=40 mm (model), 3 m (prototype).

6.6.3 Global response from the current study

The ability of the model to predict the response of pile is expressed through a comparison between the computed and experimental data from the centrifuge tests as presented in Chapter 5. Five centrifuge test series including test OWTP/C-T15-F07, OWTP/C-T16-F03, OWTP/C-T17-F03, OWTP/C-T16-F04 and OWTP/C-T17-F05 were chosen for model simulation, where the model is initially calibrated with cyclic loading responses of the test OWTP/C-T15, and subsequently applied to predict the experimental data of the other two tests (OWTP/C-T16 and OWTP/C-T17).

6.6.3.1 Centrifuge model test OWTP/C-T15-F07

By using the parameters listed in Table 6.4 and the equilibrium analysis described in Chapter 4, the total load-displacement backbone curve at the ground surface (in a normalised form) is given in Fig. 6.11(a) along with test OWTP/C-T15-F07. The soil reactions (not shown) are integrated along the depth using MR-O model, so that an accurate representation of the total backbone curve can be obtained. As shown in Fig. 6.11(b), the parameters K_t and H_u are extracted to simulate the hysteresis loops. By using the input parameters listed in Table 6.4, the hysteresis curves are created to compare with the experimental test. From the total response of the first couple of cycles shown in Fig. 6.11(c) it is clear that the model follows the experimental response with some degree of accuracy. The agreement between the experimental and calculated responses can be concluded to be satisfactory, hence confirming the ability of the proposed model to reasonably capture the observed cyclic stiffness hardening.

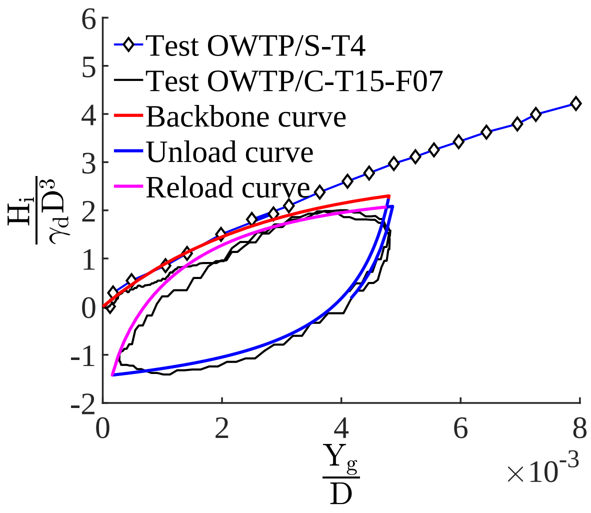

(a) Static and backbone curves

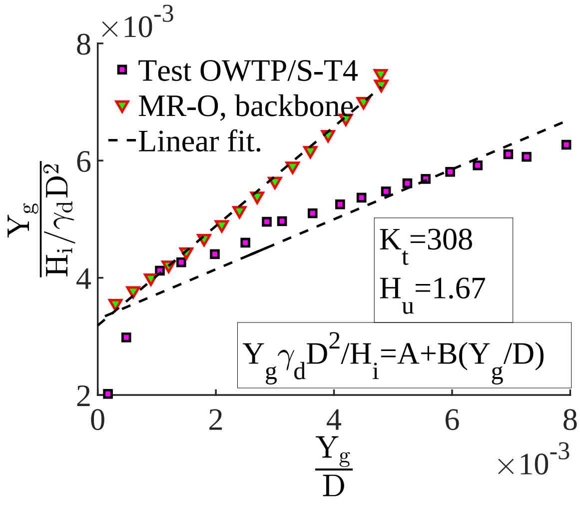

(b) The input parameters, K_t and H_u

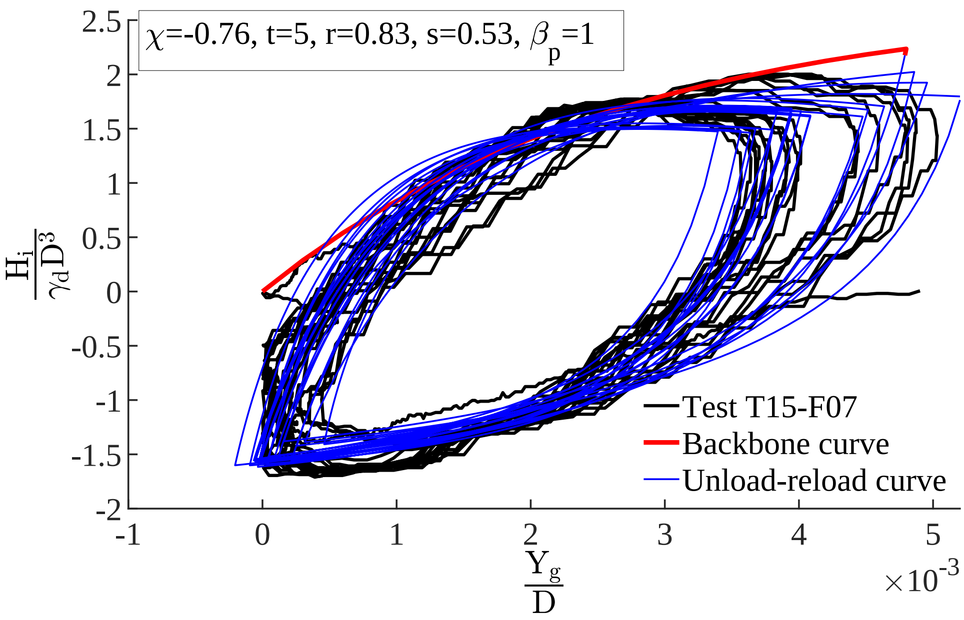

(c) Cyclic load-deflection response

Figure 6.11: Comparison between the results obtained from the centrifuge test OWTP-T15-F07 and MR-O model, for the overall response

6.6.3.2 Centrifuge model test OWTP/C-T16-F03

The ability of the model to predict the cyclic responses of a laterally loaded monopile is illustrated by comparing its predictions with centrifuge test OWTP/C-T16-F03. The model has two input parameters, K_t and H_u, which relate directly to the backbone curve. By using the parameters listed in Table 6.4 and the equilibrium analysis described in Chapter 4, the total load-displacement backbone curve at the ground surface is given as in Fig. 6.12(a) along with the backbone, first unload and reload curves of test OWTP/C-T16-F03. As shown in Fig. 6.12(b), the parameters K_t and H_u are extracted to simulate the hysteresis loops and are listed in Table 6.4. In Fig. 6.12(a), it can be seen that the model response does not exactly follows the cyclic backbone curve, however, the initial stiffness at small displacement agrees well with monotonic test OWTP/S-T4 while at larger displacement, the model shows a softer response than what is seen in test OWTP/S-T4. Furthermore, from these results the MR-O capacity of the backbone curve was reduced by 30% of the monotonic test and is adopted here as 4.15 in a normalised form. According to the Kulhawy and Chen (1995) method (see Fig. 6.12(b)), the modulus of subgrade (initial stiffness) (K_h) was approximately 1050 (in non dimensional form) and adopted throughout. The hysteresis loops can then be established with input parameters from monotonic calculation. The tangent unloading stiffness was seen to be approximately 1.5 times stiffer than backbone curve, therefore it is assigned as $K_t^{model} = 1.5K_t^{test}$ in this case. The analysis was carried out to demonstrate the response of the model, and the findings are compared with the centrifuge results of test OWTP/C-T16-F03. Approximately 40 load control hysteresis loops, corresponding to 40 cycles of the cyclic centrifuge test, were calculated. The normalised load-displacement response of the calculated and centrifuge test is shown in Fig. 6.12(c). It can be seen that the model follows the test results with a high degree of accuracy, which confirms the ability of the model to capture the results of the test.

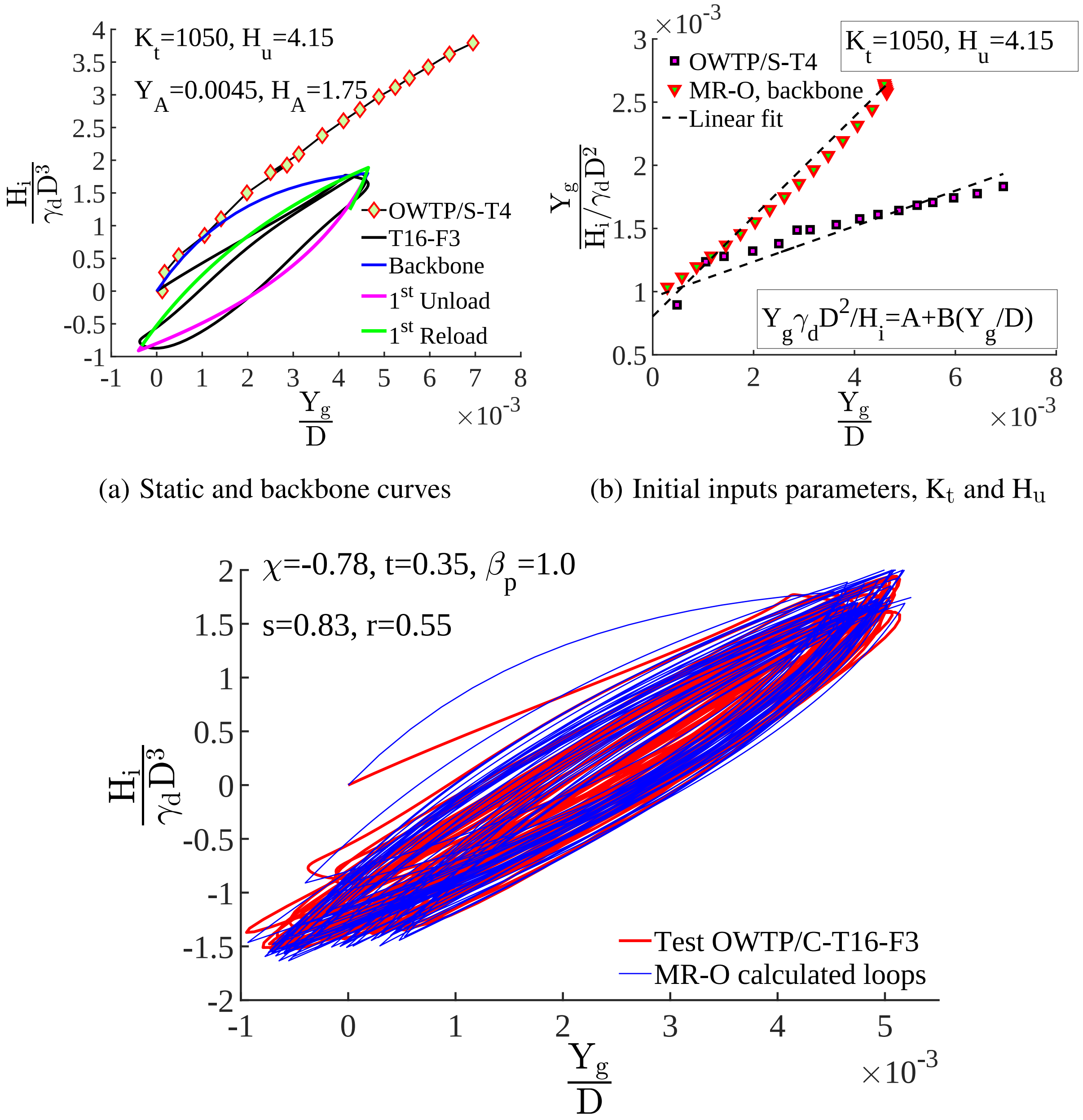

(a) Static and backbone curves

(b) Initial inputs parameters, K_t and H_u

(c) Cyclic test curves and hysteresis loops

Figure 6.12: Comparison between the results from the centrifuge test (OWTP/C-T16-F03) and the computed MR-O model, for overall response.

As shown in Fig. 6.12(c), the analysis was performed to predict the response of 40 cycles from test OWTP/C-T16-F03. Two parameters (K_t and H_u) of the computed hysteresis loops were adjusted to match the results of the test. From measured and computed curves, the maximum and minimum loads from each cycle (hysteresis loop) and their corresponding displacements, were extracted. In Fig. 6.13(a), the accumulated displacement in the first 10 cycles is high, followed by a slight decrease between 10 to 20 cycles and then it starts to increase again. This indicates that the rearrangement of soil particles took place in the first few cycles and thereafter the soil started to hardens. Following the method described in Section 5.2.3.2, Eq. 5.3, Chapter 5, the trend of the unloading secant stiffness of the computed and measured curves is plotted as shown in Fig. 6.13(b). From the figure, the anomalous behaviour of the unloading stiffness of the first 10 cycles is observed, followed by a slight increase from 10 to 40 cycles. The change in secant stiffness was not modelled accurately for the first few cycles, however, as the number of cycles increases the correlation between the measured and computed values tend to be generally satisfactory.

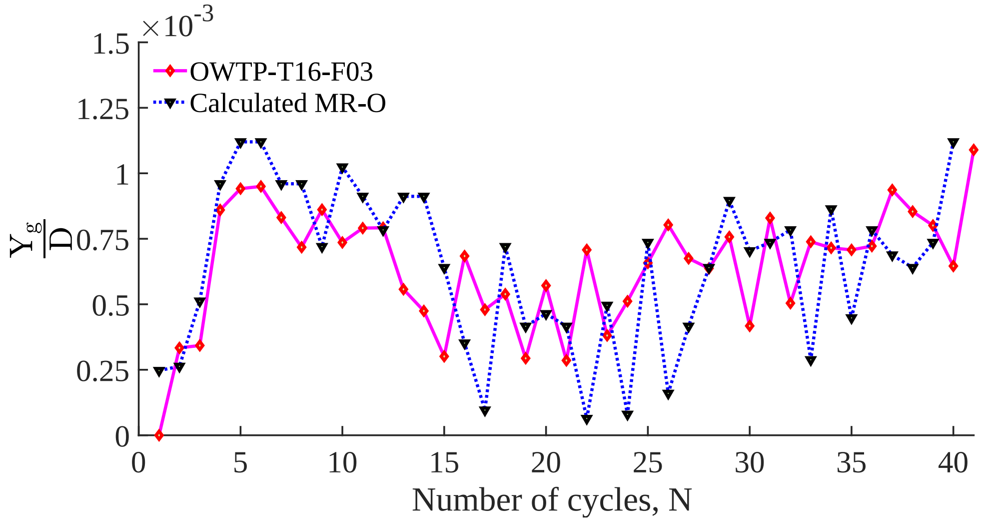

(a) Accumulated displacement

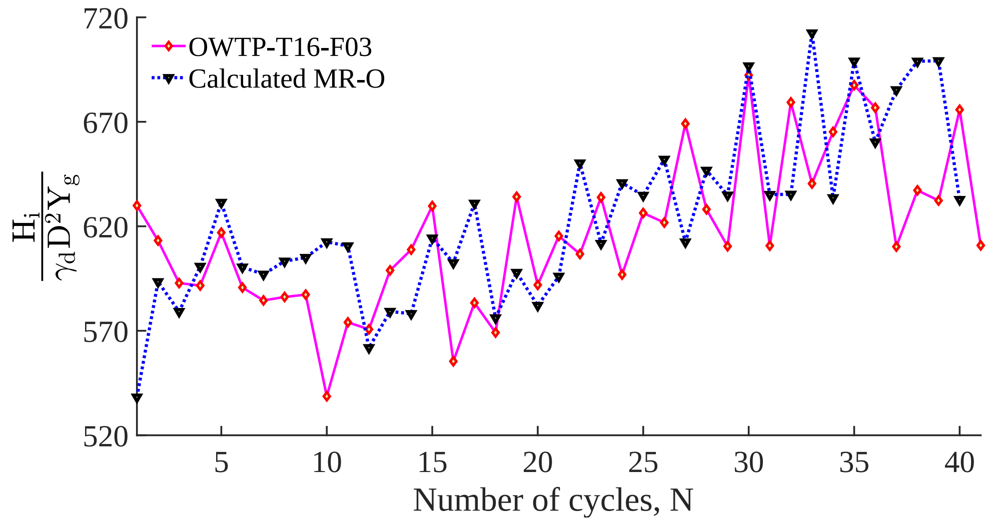

(b) Change in cyclic stiffness

Figure 6.13: Calculated accumulated displacement and change of secant stiffness compared to the centrifuge test results (OWTP/C-T16-F03).

In conclusion, Figure 6.13 shows that with adjustment of hysteresis loops, the displacement and unloading stiffness are reasonably matched with experimental results of the first 40 cycles. It should be noted that during the analysis the parameters K_t and H_u were computed and adjusted to reasonably matches the measured data. The computed trend is presented in to demonstrate the capability of the model, however, a further study with larger number of load cycles is required.

6.6.3.3 Centrifuge model test OWTP/C-T17

The calculated ground level total load-displacement response (in normalised form), for test OWTP/C-T17, is given in Fig. 6.15 and 6.14, using the MR-O function with a choice of parameters listed in Table 6.4. Fig. 6.14(a) and 6.14(b) compared the calculated and measured load-displacement responses of the backbone, first unloading and first reloading of tests OWTP/C-T17-F03 (ζ = 0) and OWTP/C-T17-F04 (ζ = 0), respectively. A positive match is observed between the result of monotonic test (OWTP/S-T4) compared to MR-O backbone curves.

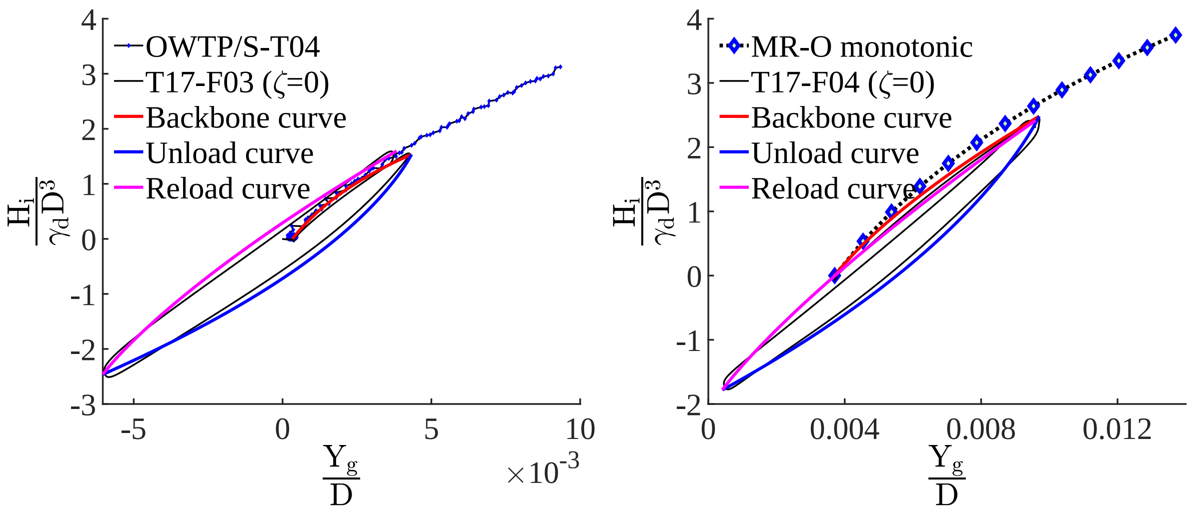

(a) Monotonic test and backbone curves of T17-F03

(b) MR-O monotonic and backbone curves of T17-F04

Figure 6.14: Comparison between the results from the centrifuge test (OWTP/C-T17) and the computed MR-O model, for monotonic, backbone, first unloading and reloading curves.

The analysis of MR-O model whose findings are compared with the centrifuge results of test OWTP/C-T17, was carried out to demonstrate the response of the model. Approximately 15 load control hysteresis loops, corresponding to 15 cycles of the cyclic centrifuge test series T17-F03 (zeta = 0), T17-F04 (ζ=0), T17-F03 (ζ = -1), were calculated. The normalised load-displacement response of the calculated and centrifuge test is shown in Fig. 6.15. The calibration shows close agreement with experimental results, which confirms the ability of the model to capture the results of the tests with different amplitude of loads.

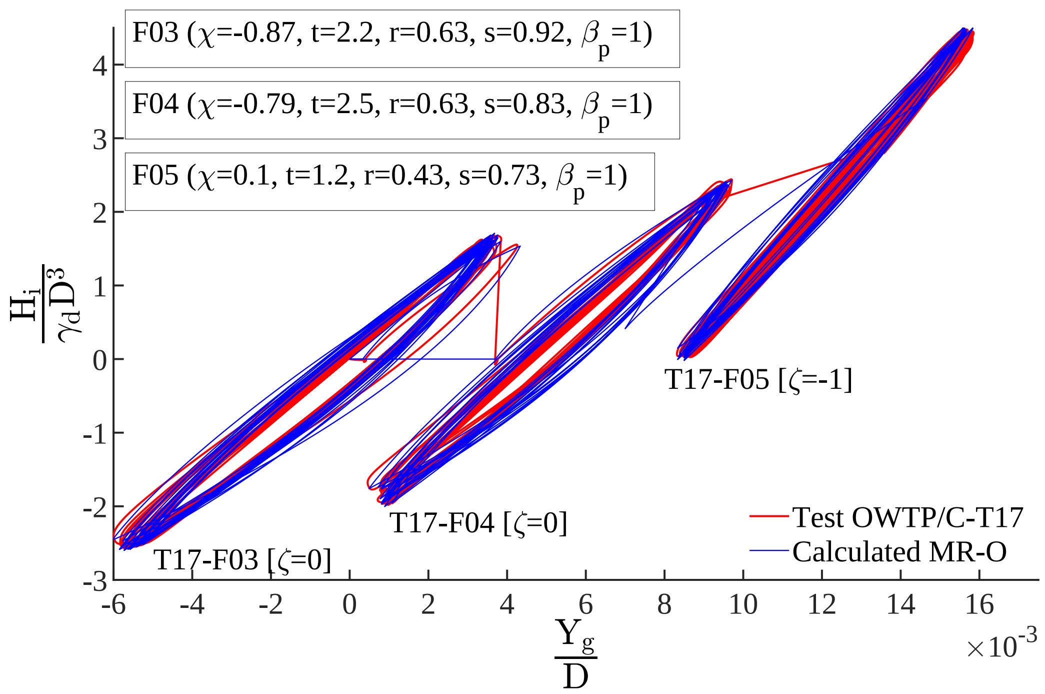

Figure 6.15: Comparison between the results from the centrifuge test (OWTP/C-T17) and the computed MR-O model, for overall response..

This section has been able to introduce the key equations that allow the MR-O model to predict the specific aspects of experimental behaviour of the current study. It also revealed the achievement of the model in capturing a change in hysteresis loop area shape due to increase in displacement and change in stiffness of each loop with a decrease in loop area. The chapter also demonstrates the ability of the model to capture the series of of load of variable amplitude identified experimentally for the response of laterally loaded piles. Furthermore, although the results are closely related, there are some discrepancies, which may have been the result of several factors involved in the analysis. Therefore, the results of the calculated model capture the experimental trends with good accuracy and demonstrate the appropriateness of the MR-O methodology for applications to offshore wind foundations.

6.6.4 Global response from the published studies

The case studies are presented herein to demonstrate the application of the MR-O model to the analysis of a pile subjected to cyclic lateral loading. These studies highlight the ability of the model to reasonably represent the main nonlinear hysteresis features of the monopile in sand.

6.6.4.1 Case study 1: Chen et al. (2015)

A series of 1-g laboratory cyclic loading tests were conducted on a vertical single stiff pile subjected to cyclic lateral loading. The model pile, 1/30 in scale, is a steel hollow cylinder placed in Qiantang river silt with relative densities (D_r) of 70% and 88%. A typical prototype monopile diameter (D) of 5 m was used to manufacture a steel model pile, having 0.165 m in diameter, 0.003 m in wall thickness, 2 m in length, and 0.915 m in embedded depth, respectively. From monotonic response, ultimate capacities were estimated as 778 N (D_r = 88%) and 463 N (D_r = 70%)), respectively. The backbone curves are generated using the analytical method described in Chapter 4. Fig. 6.16(a) shows the comparisons of the calculated and measured load-displacement at the pile-head for monotonic loading test. The agreement between the two responses is in general quite satisfactory, which confirms the ability of the model to reasonably capture the nonlinear backbone curve. Furthermore, a Kulhawy and Chen (1995) method was employed to interpret the tangent stiffness (K_t) and ultimate capacity (H_u) of the backbone curve and the results are shown in Fig. 6.16(b) and listed in Table 6.5.

The parameters K_t and H_u are used as a basis to construct the hysteresis loops of the model. Fig. 6.17(a) compares the calculated and measured load-displacement curve at the pile head for one-way cyclic loading test. The agreement between the two responses is in general satisfactory, however, some points did not agree exactly due to limitation of the model. Furthermore, for demonstration purpose, the model simulation was further extended to account for more number of cycles with the same applied parameters (see Figure 6.17(b)).

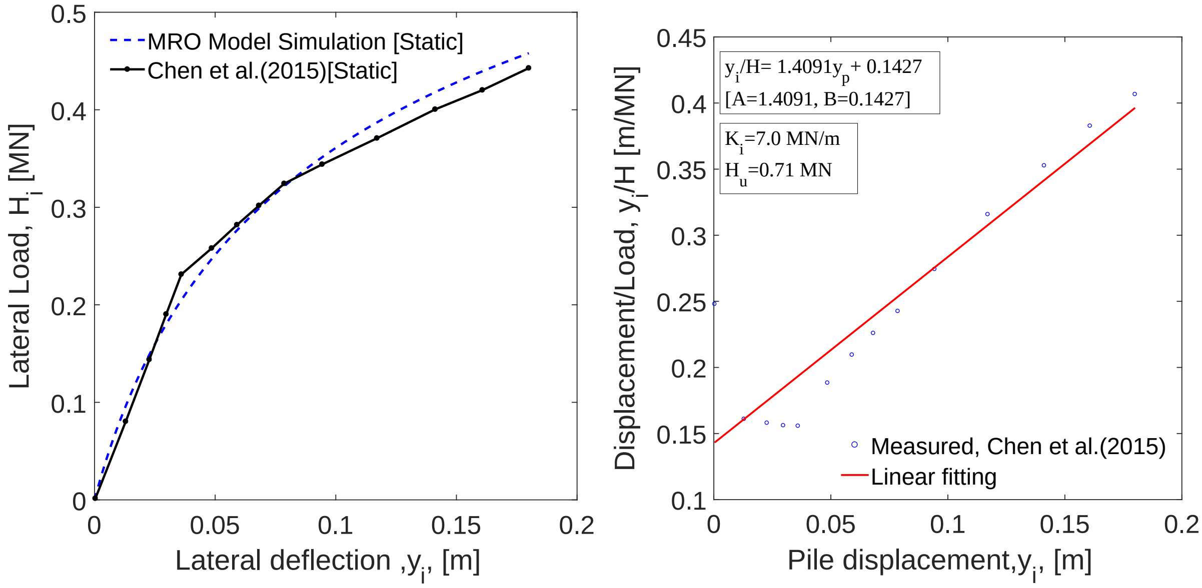

(a) Fitted H-y monotonic (backbone) response

(b) Input parameters, K_t and H_u

Figure 6.16: Comparison of model simulation and results from Chen et al. (2015) (backbone curve and initial parameters).

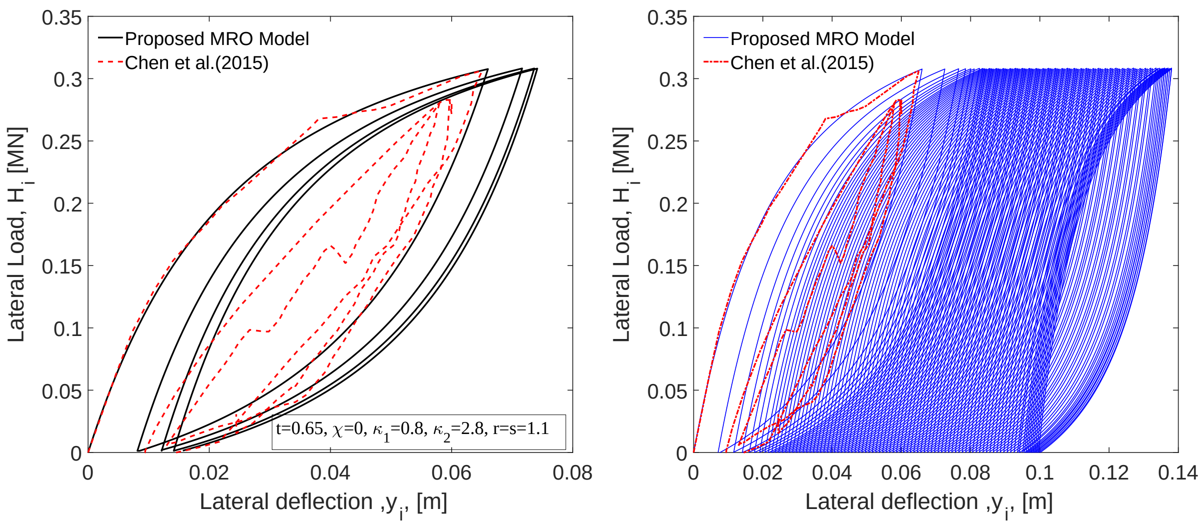

(a) Simulation of load-deflection

(b) Extended MR-O load-deflection simulation

Figure 6.17: Comparison of the model simulation and results from Chen et al. (2015).

6.6.4.2 Case study 2: Rosquoet et al. (2007)

A number of centrifuge tests were carried out on model piles subjected to cyclic lateral loading. The model tests were prepared at relative densities of 53% and 86% in dry Fontainebleau sand (density of 1540 Kg/m^3 and 1630 kg/m^3, respectively). The model pile, 1/40 in scale, has diameter of 18 mm, wall thickness 1.5 mm, embedded depth 38 mm. The mean values of peak and critical of sand specimens are ϕ_p=41.8^o and ϕ_{cr}=33^o, respectively.

As shown in Fig. 6.18(a) and 6.18(b) a similar approach used in previous section was employed to determine the response of backbone curve and extracting the parameters K_t and H_u. These parameters are listed in Table 6.5. The backbone parameters, shape of nonlinearity and degradation constants were introduced into the model to generate the hysteresis loops. For the first few cycles, Fig. 6.19 shows that the agreement between the calculated and measured responses is in general satisfactory, which confirms the ability of the developed model to capture the observed cyclic response of the pile.

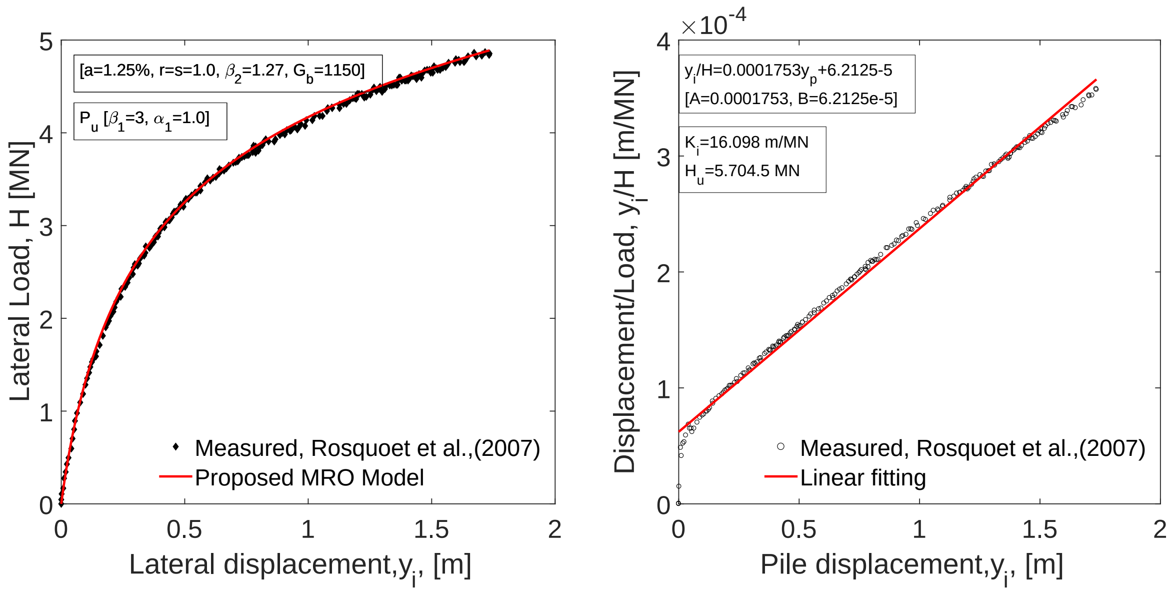

(a) Fitted H-y monotonic (backbone) response

(b) Input parameters, K_t and H_u

Figure 6.18: Backbone curve and initial parameters, from Rosquoet et al. (2007).

In conclusion, Fig. 6.17 and 6.19 show the excellent agreement between the computed and experimental data. The results indicate that the proposed model accurately describes the use of the MR-O model, considering the effect of accumulation and degradation parameter involved in the simulation. The success of this model to validate other work from the literature is also an indication of its capability.

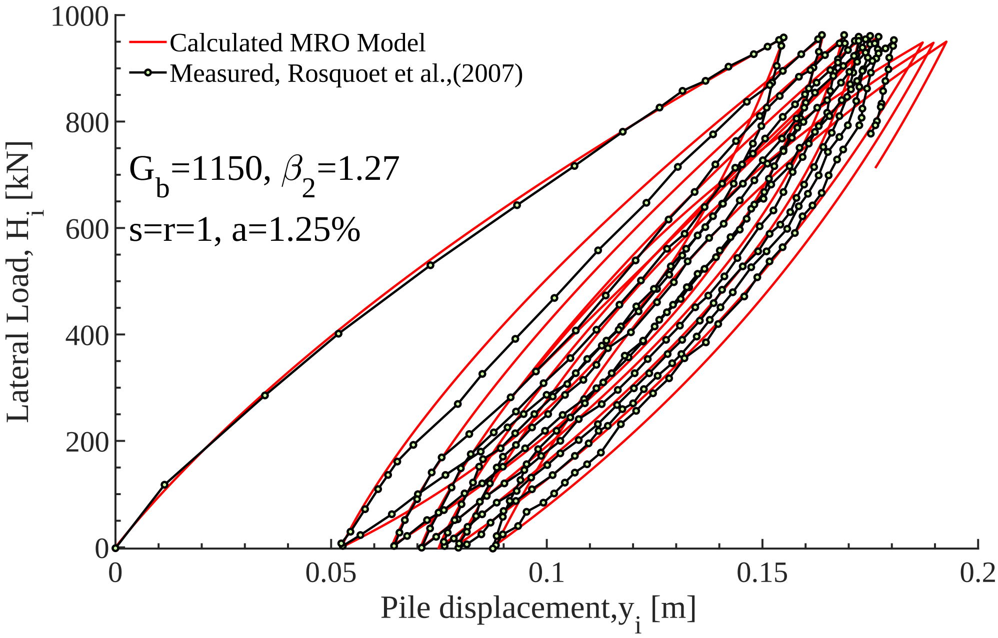

Figure 6.19: Comparison between the results from Rosquoet et al. (2007) and the computed MR-O model, for overall response..

Table 6.5: Model parameters from published research

SN	Parameter	Symbol	Chen et al. (2015)	Rosquoet et al. (2007)
1	1st unload deflection (m)	y_A	0.067	0.14
2	1st unload force (MN)	H_A	0.32	0.9
3	Initial stiffness (MN/m)	K_t	7	16.1
4	Ultimate capacity (MN)	H_u	0.71	5.7
5	Cyclic load ratio	χ	0	0
6	Asymptotic constant	t	0.65	0.75
7	Stiffness degr. constant	κ_1	0.85	0.9
8	Deflection acc. constant	κ_2	2.8	2.65
9	Curve control constants	r	0.83	0.85
		s	0.92	0.95

6.7 Limitations of the model

The MR-O model presented in this chapter captures the key aspects observed for the behaviour of stiff monopile in centrifuge subjected to cyclic lateral loading. However, before the model is applied to prototype conditions, some aspects need to be addressed.

Firstly, more work is needed to refine the trends observed from the experimental results, for instance, the evolution of displacement accumulation and change in cyclic stiffness. A more rigorous procedure for determining the accumulation or degradation constants would be useful for future design. Secondly, the actual response of the monopile is likely to have additional features that have not been investigated as described in this chapter. For instance, the MR-O model does not describe the formation of a gap between the soil and the pile, which could also be used for cohesive soil. This factor would need to be investigated in detail before developing the theoretical framework and include it in the model. Therefore, further study is needed to consider this effect

Finally, the experimental study was carried out on a non-instrumented pile, hence only the global behaviour of the monopiles was measured. However, the global response of the monopile does reflects the distribution of the soil-pile interaction below the ground surface. The local *p-y* curves of test results from Klinkvort (2013) were used in this study to describe the hysteretic *p-y* curves of the model. However, further study is recommended to investigate how the MR-O model will fit within the current DNV model. A careful study will be required, from full-scale and small-scale tests, to accurately describe the backbone curves.

6.8 Chapter summary

The entire chapter 6 presented the hysteretic MR-O model to study the experimental test responses of monopiles subjected to cyclic lateral loading. The outcomes of the model were compared with the experimental test results of the current and previous studies. The following conclusions can be drawn from calibration and the performance of the model as listed below:

1. The monotonic analysis was initially considered to model accurately the backbone response. The model considers two essential parameters, the ultimate capacity (H_u) and

initial stiffness (K_i). Both original and modified Ramberg and Osgood (1943) model functions were employed. To obtain a good match between the model and measured results, the MR-O model was used throughout as a basis to construct the hysteresis loops.

2. With the use of recommended principles from previous studies (Kondner, 1963, Masing, 1926, Matasović and Vucetic, 1993, Pyke, 1980), a procedure for estimating the hysteresis loops to validate the results of cyclic experimental tests for monopile has been suggested. The modification factors were introduced and sensitivity of the model was examined by carrying out a simple parametric study, based on the results of monotonic experimental tests carried out at 30g. The variation of these parameters show that the model successfully controls the backbone curves and hysteresis loops. For instance, (i) the change parameter of $-1 \leqslant \chi \leqslant 1$ controls the load characteristics observed from the experiment (ii) the change of parameter t control the unloading ultimate capacity (iii) the parameters κ_1 and κ_2 were varied to show the capability of the model to capture the stiffness degradation and displacement accumulation observed from the experimental tests.

3. The model is calibrated to the experimental results of the current and published studies. The results of the prediction capture the experimental trends with good accuracy and demonstrate the ability of the MR-O methodology for applications to the offshore monopiles.

4. The model is simple and limited to the cyclic response of pile-head and not the soil itself. Although the model was employed for published local pile-soil interaction test results, a further modification related to the current study is required. However, the pile should be instrumented, using strain gauges, to justify the p-y curves theoretical results.

Chapter 7

CONCLUSION AND RECOMMENDATIONS

7.1 Introduction

Offshore wind farms development is projected to increase rapidly in the coming decades. These turbines will be constructed on monopiles for which the serviceability limit are imposed on pile-head rotation. In the offshore condition, monopiles are subject to long term cyclic loading from action of wind, waves and movement of turbine blades. Minimising damage to the OWT structures during this loading is a priority for civil engineers working in this area. Although the engineers can design the structures to limit the impact of dynamic loading, through the natural frequency, such method is complex to design due to cyclic loading frequencies. It is important that natural frequency is not close to cyclic frequencies. Through better understanding the behaviour of monopiles, the amount of loading transmitted to the structure can be reduced.

The research presented in the current thesis has been conducted to understand the behaviour of monopile foundations in sand under monotonic and cyclic lateral loading. Centrifuge testing has been conducted on a newly developed tool to ensure that the behaviour of the monopiles, with large number of cycles, is correctly captured. The key findings allowed the overall load-displacement, moment-rotation, accumulated displacement and change of foundation stiffness to be examined, subsequently leading to the development of the theoretical model that accurately captures the pile behaviour. The conclusions made in this thesis and recommendations for further study are summarised in the following sections.

7.2 Monotonic loading

7.2.1 Experimental response under monotonic loading

Offshore monopiles are typically installed in saturated soil condition, however, most of the experiments have been conducted in dry sand. In a centrifuge, a given effective stress can be achieved using either dry or saturated sand, however, the scaling issues and gravitational acceleration are the prerequisite (Klinkvort and Hededal, 2014, Li et al., 2010). For instance, the scaling issues for saturated sand are straightforward as the increase in gravitational acceleration is identical to geometrical scaling factor (Klinkvort and Hededal, 2014), which implies that the effective vertical stress are similar. For dry sand, the increase in gravitational acceleration and the geometrical scaling factor are not identical, and effective stress in the field, similar to saturated sand, can be achieved with the procedure described by Li et al. (2010) and Klinkvort et al. (2012); the method works by essentially matching effective stress between a dry sand centrifuge test and a saturated full-scale scenario. Under saturated condition, the flow of water in a centrifuge is occurring N_s times faster compared to the prototype and is unlikely that pore pressures will build up at the current rate of loading within the centrifuge model. For this purpose, fully drained cyclic response was required and dry sand was used to simplify the testing procedure.

The method used to prepare the sample on a model container resulted in homogeneous sand deposits. The prepared sand had medium dense and dense relative density (D_r) of 42% and 85%, respectively. Three tests (OWTP/S-T1, OWTP/S-T2, OWTP/S-T3) and one test (OWTP/S-T4) were conducted in a centrifuge at acceleration of 100g (T1, T2, T3) and 30g (T4). The sensors attached to the model pile functioned adequately and assisted a reasonably accurate measurement of the lateral loads and displacements. The data were collected to determine the load-deflection, moment-rotation, pile rotation, ultimate capacity and tangent (initial) stiffness. Furthermore, the results of the experiment showed a significant effect of the relative density on the model pile, thus concluding that, high relative density provided a high resistance on the prepared soil sample. Although all responses were observed to follow a nonlinear behaviour with varying magnitude, the ultimate capacity of the pile was not achieved, thus a 10% of pile diameter method was used to determine the ultimate capacity of the pile. Furthermore, when the derived ultimate capacity, H_u, was used as a reference to estimate the load amplitude ratio, its magnitude was seen to be affected by centrifuge acceleration when the pile in sand (D_r=85%) was tested at 100g and 30g. The results indicated that increased g-level on the centrifuge can affect the capacity of the pile. Furthermore, from the comparison made between the depth of pile rotation measured experimentally and empirical expression derived from the literature, the estimated values from the literature were slightly different but very close to the measured data. The initial (tangent) stiffness of the global test results were derived experimentally and compared with stiffness calculated based on the method suggested by Kulhawy and Chen (1995). This will enable the calculation of K_h along the pile with a recommended subgrade modulus function, which is more valid for dry sand.

7.2.2 Theoretical response under monotonic loading

This section presents the findings observed when two families of the *p-y* curves from the original and modified DNV (2014) (DNV model) and Ramberg and Osgood (1943) (R-O and MR-O model were used to predict the monotonic response of 5 MW class offshore wind turbine monopiles. These models were compared to the experimental response of monotonic tests conducted in a centrifuge. The *p-y* curves recommended by DNV (2014) provided a significantly high global pile head load-deflection response compared to experimental results, leading to high stiffness. The results were highly supported by Sørensen (2012), Klinkvort (2013), LeBlanc (2009) and Kirkwood (2016). The original R-O *p-y* curve model, empirically developed by Ramberg and Osgood (1943), was observed to overestimate the stiffness of the pile-head load-displacement response, and modified model (known as MR-O *p-y* curve) was suggested with parameters introduced after fitting the experimental results. Furthermore, the empirical method from DNV (2014) was selected to estimate the ultimate soil resistance (P_u) along the depth of pile. From this method, the ultimate capacity obtained at shallow depth was controlled by a depth factor A_i, which plays a significant role in determining the failure mechanism (API, 2007, DNV, 2014). The factor A_i was derived from flexible piles and reported to overestimate the ultimate capacity. Therefore, it was adjusted to A_j and used in this study to calculate ultimate capacity. The initial slopes of the *p-y* curves (modulus of subgrade reaction, K_h) were considered to vary nonlinearly with depth, which depends on the maximum shear modulus of soil (G_{max}). The linearly distribution of K_h recommended by DNV (2014) was employed with the DNV hyperbolic *p*-*y* curve model, however, the parameter α_p was introduced to fit the measured data. As a result, the revised DNV (2014) model showed a satisfactory agreement with experimental data.

Since the current study was limited to a non-instrumented pile with no data related to *p*-*y* curves along the embedded depth, the capability of both DNV and MR-O models to the pile-soil interaction was assessed by comparing them with the published *p*-*y* curve results from Klinkvort (2013). The findings indicated that the DNV (2014) method overestimated the initial stiffness of the *p*-*y* curves at shallow depth and underestimated it at the greater depth. With additional parameters into R-O model (MR-O model), a satisfactory agreement with experimental *p*-*y* curves was achieved along the depth. Therefore, the use of DNV (2014) method is still seems unreliable for rigid piles. It should be noted that this calibration was based on the published *p*-*y* curves, thus further investigation is required.

When the computed behaviour of the MR-O model, used as a benchmark in developing the soil resistance and bending moment distribution along the depth of the pile, was compared with other models, the results showed a correspondence at shallow depth but at greater depths the modified DNV model overestimated the MR-O model.

It should therefore be noted that with a limited number of tests carried out in this study using a non-instrumented pile, the results of which were compared to the previously published experimental data obtained from instrumented piles. The MR-O model, which includes more parameters, was chosen to estimate the *p*-*y* curves of the measured data, because the model was found to give an accurate prediction of the monotonic response of stiff piles in sand. However, the families of the *p*-*y* curves derived from the MR-O model apply only to rigid piles and should not be used to predict the response of flexible piles as recommended by DNV (2014).

7.3 Experimental cyclic loading

In this thesis, a comprehensive study was conducted to investigate the effect of cyclic loading of monopiles in sand on the pile-head displacement and change in secant stiffness of the pile using two tests (OWTP/C-T16 and OWTP/C-T17). From the analysis it showed that a one-way loading direction, for accumulation of displacement, gave the more damaging load condition than two-way loading. The unloading stiffness was found to increase with the increase of load cycles but at a reducing rate. This is more critical for the calculation of the natural frequency variation of the turbine thus manufacturers should consider this factor when designing monopiles for offshore wind turbines. Based on cyclic experimental results of this study, the following conclusion can be drawn:

7.3.1 Cyclic lateral loading

The experimental results for the cyclic lateral loading fall within the observations cited in the literature despite the technical challenges which were limited to a centrifuge acceleration of 30g. Depending on the load control factor (ζ), the change of cyclic loads ($\mathrm{H_{amp}}$=$\mathrm{H_{max}}$-$\mathrm{H_{min}}$) were found to vary from 270 to 525 N. From the two tests, the maximum cyclic loads were successfully achieved at ζ=-1. For instance, the $\mathrm{H_{max}}$ from tests OWTP/C-T16 and OWTP/C-T17 was approximately 425 N and 500 N, respectively. LeBlanc et al. (2010) provided the primary interest of maximum cyclic loads on monopiles, which is governed by the ULS with maximum amplitude load ratio (ζ_b) between 30% and 50%. Theoretically, when ζ_b = 30% of the ultimate capacities, the maximum cyclic loads were supposed to be 510 N and 1200 N, assuming that the cyclic tests were carried out at 30g and 100g, respectively. Although this thesis was not able to conduct the the cyclic loading tests at 100g, the results of the tests at 30g, with system control set-up at ζ=-1, are consistent with this theory. Therefore, this is confirming that the model framework in this study is in the similar agreement with work reported from the previous studies.

7.3.2 Pile-head displacement

A framework to predict the total displacements of test OWTP/C-T16 and OWTP/C-T17 has been proposed and discussed in Chapter 5. From these tests, the variation of pile-head displacements was significantly influenced by load control ratio, ζ. It is clear that the asymmetric loading (when $\zeta \neq 0$) had the most significant effect on the lateral displacement, for instant, when ζ was set-up to -1 the displacement was observed high. A logarithmic function ($\mathrm{Y_N = Y_1(1 + C_N In(N))}$) employed to the measured data was able to accurately predict the total displacement, at least from 100 to 300 load cycles, however, below this range, the data departs from the predictions. The total displacement rate (C_N) was seen to be affected by ζ_b, which was directly influenced by ζ. This confirmed that increasing of load magnitude is likely to affect the displacement of the pile.

7.3.3 Cyclic secant stiffness

The cyclic secant stiffness of the monopile was found to increase when subjected to cyclic loading under fully drained conditions. This increase was approximated by a logarithmic function, which was seen to be affected by the load control ratio (ζ). The trend of increasing in stiffness during long-term cyclic loading in line with previous studies (Abadie, 2015, Kirkwood, 2016, Klinkvort, 2013, LeBlanc et al., 2010, Li et al., 2010, Peralta and Achmus, 2010).

The outcomes of this study indicate that the rate of increase in cyclic secant stiffness was affected by the model set up and load control factor. It was found that the rate of increase in stiffness is lower when the model pile was loaded under one-way loading direction ($\zeta_c > 0$). This indicates that critical damaging scenario occurs when the load control factor was changed to $\zeta = +1$ or $\zeta = -1$. This contradicts with findings from Abadie (2015) and LeBlanc et al. (2010) where the most damaging effect was found under two-way loading but agrees with results from Klinkvort (2013).

Furthermore, the cyclic stiffness was observed to increase with magnitude of load amplitude (ζ_b). This was likely to happen for the first few cycles of the first series of each test ($\zeta = 0$) because the accumulated displacement was due to sand particle rearrangement. However, when the value of ζ changed to $\zeta = +1$ or $\zeta = -1$ in the subsequent series the pile was already in the situation where the densification of sand is occurring. In this condition the lateral stiffness continue to increase but at reducing rate. Therefore, the change of ζ in the subsequent test series was observed to increase the load amplitudes, which had also an impact on the stiffness of the monopile foundations.

7.4 Analytical cyclic loading

The literature revealed that various nonlinear *p-y* models developed based on experiments carried out on flexible piles (D$\leq$ 2 m) (DNV, 2014), however, in rigid piles few models have been reported (Abdel-Rahman and Achmus, 2005, Achmus et al., 2009, Beuckelaers, 2017, Klinkvort et al., 2012). Most of the *p-y* models are limited and does not accurately predict the response of monopiles due to cyclic loading hence calling for further investigation. In this case therefore, this study modified a R-O non-linear model, derived from flexible piles, to trace the response of monopiles from cyclic experimental results. From the study, the following conclusion about the modelling of the cyclic behaviour of the pile is drawn.

1. The MR-O model was employed in the analysis to generate the *p-y* curves along the embedded depth. The the backbone response at the ground surface was first created to derive the primary parameters K_t and H_u, which were used as inputs to create the global hysteresis loops. The accumulated displacement and change of cyclic stiffness were useful in the MR-O model, however, it needs further experimental study to justify them.

2. The sensitivity of the model was examined based on the results of tests OWTP/S-T4 and OWTP/C-T15. By varying each parameter (while keeping others constant) the response of the model was examined to understand its range and limitation.

3. The model was calibrated to both local and global responses of the centrifuge tests from the current study and literature. The agreement between the calculated predictions and measured data shows how the the model can be used to replicate the response of the laterally loaded piles under cyclic loading. However, use of the method requires further justifications. For instance, the spring model requires some improvement to accurately handle the soil damping, accumulation of pile deflection and change in secant stiffness, as observed in the centrifuge.

7.5 Implications for design

The previous sections have outlined the key aspects of pile response subjected to monotonic and cyclic lateral loading that have a direct implication for the design of the offshore wind turbine foundations. This section interprets some of the conclusions with regards to the current code of practice in the offshore wind turbine industry. One of the observed limitations of the current design code (API, 2007, DNV, 2014) is that it does not indicate the accumulation of pile head displacement and change of cyclic stiffness during prolonged cyclic loading. The outcomes from this study will allow an estimate of these factors to be made for monopiles of typical 5 MW class wind turbines. Therefore, since the current design code the current design codes seem insufficient to meet the serviceability requirements of the monopile foundations, this study will enable the review for improvement of the design to provide for this inadequacy. Secondly, the accumulation of pile head displacements in relation to number of load cycles are based on the frameworks such as that suggested by LeBlanc et al. (2010) and Klinkvort (2013). In this study, these frameworks were found reasonable to provide an approach for predicting the pile response, which might be useful in early stages of monopile design process. However, it does not provide any information on the evolution of soil damping, which is important in the fatigue analysis and therefore applying the number of load cycles on monopiles will reduce the resonance loads (when the waves and wind are misaligned and aerodynamic damping is small) (Abadie, 2015, Beuckelaers, 2017, Klinkvort, 2013). This provides a stepping stone for the future research keen to undertake a study on the analysis of fatigue on monopiles.

Furthermore, calibration of analytical models provide an insight into capability and limitations. It has been shown that the DNV (2014) model tends to overestimate or underestimate the stiffness of monopile foundations in cohesionless soil, which is likely to affect the design of monopile foundations. The computed MR-O model was observed to agree well with experimental results because it predicts the response seen in experimental results, but does not accurately model the accumulated displacement and change in secant stiffness. It is recommended here that an improvement of this model (MR-O) can lead to its implementation in the DNV (2014) code for fatigue analysis.

7.6 Recommendation

This study provided a better understanding of the response of monopiles subjected to both monotonic and cyclic loading in dry Congleton sand. The *p-y* theoretical models have been proposed to predict the response of rigid piles from the experimental results. However, there are still many areas of research which could be investigated further to improve understanding of the response of offshore wind turbine foundations. The major areas suggested for further research are summarised below.

1. The theoretical models and analysis method suggested in Chapter 4 to construct the *p-y* curves can be applied to other geotechnical problems but with caution since additional checks have not been made. To verify this method on a rigid pile under monotonic loading, the effect of different parameters such as pile geometry, soil conditions, and application of lateral loads will have to be clarified. The impact of these parameters can only be achieved with more testing, analytical and numerical simulations.

2. The current study was carried out using a non-instrumented pile through an embedded depth. Understanding the behaviour of soil below the ground surface is fundamental in geotechnical structures. For instance, using strain gauges on piles can help to provide the accurate information, which might be useful to measure the moment distribution along the pile. The moment distribution can be used to derive the soil reaction in relation to pile deflection, which is important for the development of analytical *p-y* curves.

3. The present study was carried out using Congleton silica dry sand. In the offshore environment, the soil is saturated and uniform or made of strata with different types of soil. It is therefore recommended to use saturated and dry cohesive and non-cohesive soil to investigate the influence of different parameters such as soil stratification, different foundation size and its flexibility, structural stiffness, ultimate capacities, soil densities and loading frequency. Not only this will allow the understanding the behaviour of monopiles, but also it will provide more data against which a proposed analytical and numerical models can be calibrated and validated.

4. The results presented in this study consider the vertical loads from the pile head, which was used to connect the loading system components. Several studies, related to offshore monopiles, have been conducted without considering the vertical load on stiff pile subjected to lateral monotonic and cyclic loading. It is therefore recommended that the loading system are improved to consider the model piles without or with pile head of varying magnitudes, to quantify the influence of vertical loads on the monopile responses.

5. In the current study, both monotonic and cyclic lateral loads were carried on the same load eccentricity. The lateral loads should have been applied at different location on the pile above the ground surface to represent the levels of environment loads on the sea at different depth of water. This would be a major improvement for assessment of load eccentricity effect on the response of monopile foundations.

6. Due to technical challenges of the developed equipment, it was not physically possible to load the model piles at the frequency related to prototype condition (model frequency of 15 Hz at centrifuge acceleration of 100g). The loading system in a centrifuge was limited to a frequency of 2.5 Hz at centrifuge gravity of 30g. Considering this limitation, a loading system should be improved so that the experiment can be repeated with loading frequency related to prototype condition. This would also enable to obtain a large number of load cycles to be applied onto the monopiles in a short period of time. Since the monopile was loaded to a maximum of 60,000 load cycles, it is of interest to have experiments with millions of load cycles to verify the validity of the findings.

7. The newly developed device was capable of applying a unidirectional loading. It would be of interest to improve the current device capable of multi-directional loading that can load the monopiles under different angles, which represents the loading frequency similar to the finding of Rudolph et al. (2013). From this finding, it is reported that a multi-directional loading condition had high impact on both accumulated displacement and change in cyclic secant stiffness compared to uni-directional loading. Therefore, further modification of the current loading system would be able to quantify and verify the monopile response under multi-directional loading.

8. The MR-O model should be expanded to soil behaviour that includes the effect of gapping. This extension has the potential of capturing the behaviour of monopiles in cohesive soils subjected to cyclic loading. The extension could be calibrated to the results of centrifuge tests on instrumented piles in both sand and clay.

9. The current study developed a simple theoretical model that captures the key findings outlined experimentally as described in Chapter 4 and 5. Based on monotonic response, it has recently been reported that the current *p*-*y* curves method suggested by API (2007) and DNV (2014) does not represent some components of monopile-soil interaction responses. Previous studies (Abadie, 2015, Beuckelaers, 2017, Klinkvort, 2013) have mentioned the method does not consider the case of shear base, distribution of moment along the pile length, vertical shear stress on the pile as well as base moment. It is therefore recommended a further study to account these reaction components into centrifuge tests and numerical software package. Furthermore, the current design standard does not account the effect of accumulated displacement and change in cyclic secant stiffness. Introducing the accumulation or hardening model could be potentially consider these factor into DNV (2014) standard *p*-*y* curves method with greater number of load cycles. This is the major issue which will require a further improvement for the model to be integrated within the current design standard of the monopiles.

10. Numerical modelling calibration against centrifuge test results would enable the development of models that could accurately estimate the accumulated displacement and change in cyclic secant stiffness. If this can be performed in finite element or finite difference software packages, more information will be provided to better explain the response of monopile foundations.

Bibliography

Abadie, C. and Byrne, B. (2014). Cyclic loading response of monopile foundations in cohesionless soils. In *Physical Modelling in Geotechnics-Proceedings of the 8th International Conference on Physical Modelling in Geotechnics 2014, ICPMG 2014*, volume 2, pages 779–784.

Abadie, C. N. (2015). *Cyclic lateral loading of monopile foundations in cohesionless soils*. PhD thesis.

Abdel-Rahman, K. and Achmus, M. (2005). Finite element modelling of horizontally loaded monopile foundations for offshore wind energy converters in germany. In *Proceedings of the international symposium on frontiers in offshore geotechnics. Taylor and Francis, Perth*, pages 391–396.

Abendroth, R. E. and Greimann, L. F. (1990). Pile behavior established from model tests. *Journal of geotechnical engineering*, 116(4):571–587.

Achmus, M., Abdel-Rahman, K., et al. (2012). Design of piles for offshore wind energy foundations with respect to horizontal loading. *ISOPE-2012, The*, 22:17–22.

Achmus, M., Abdel-Rahman, K., and Kuo, Y. (2007). Behavior of large diameter monopiles under cyclic horizontal loading. In *ICSGE, Twelfth International Colloquium on Structural and Geotechnical Engineering, Cairo, Egypt, GTE039*.

Achmus, M., Abdel-Rahman, K., and Kuo, Y.-S. (2008). Design of monopile foundations for offshore wind energy converters. In *Geotechnics in Maritime Engineering. 11th Baltic Sea Geotechnical Conference*, pages 463–470.

Achmus, M., Albiker, J., Peralta, P., and Tom Wörden, F. (2011). Scale effects in the design of large diameter monopiles. *Scientific proceedings of the European wind energy association, Brussels*, pages 326–328.

Achmus, M., Kuo, Y.-S., and Abdel-Rahman, K. (2009). Behavior of monopile foundations under cyclic lateral load. *Computers and Geotechnics*, 36(5):725–735.

Ahmed, S. S. and Hawlader, B. (2016). Numerical analysis of large-diameter monopiles in dense sand supporting offshore wind turbines. *International Journal of Geomechanics*, 16(5):04016018.

Al-Defae, A. and Knappett, J. (2014). Centrifuge modeling of the seismic performance of pile-reinforced slopes. *Journal of Geotechnical and Geoenvironmental Engineering*, 140(6):04014014.

Allotey, N. and El Naggar, M. H. (2008). Generalized dynamic winkler model for nonlinear soil–structure interaction analysis. *Canadian Geotechnical Journal*, 45(4):560–573.

Andersen, K., Puech, A., and Jardine, R. (2013). Cyclic resistant geotechnical design and parameter selection for offshore engineering and other applications. In *Proceedings of the TC-209 Workshop, Design for Cyclic Loading: Piles and Other Foundations, Paris. Presses des Ponts*, pages 9–44.

API (1993). Recommended practices for planning, designing and constructing fixed offshore platforms–load and resistance factor design.

API, R. (2007). 2a-wsd,(2000). recommended practice for planning, designing and constructing fixed offshore platform-working stress design. *America Petroleum Institute, Washington, DC, USA*.

Arany, L., Bhattacharya, S., Hogan, S., and Macdonald, J. (2014). Dynamic soil-structure interaction issues of offshore wind turbines. In *Proceedings of the 9th international conference on structural dynamics, EURODYN*, pages 3611–3618.

Arany, L., Bhattacharya, S., Macdonald, J., and Hogan, S. (2017). Design of monopiles for offshore wind turbines in 10 steps. *Soil Dynamics and Earthquake Engineering*, 92:126–152.

Arshad, M. and O'Kelly, B. C. (2014). Development of a rig to study model pile behaviour under repeating lateral loads. *International Journal of Physical Modelling in Geotechnics*, 14(3):54–66.

Arshad, M. and O'Kelly, B. C. (2016). Analysis and design of monopile foundations for offshore wind-turbine structures. *Marine Georesources & Geotechnology*, 34(6):503–525.

Arshad, M. and OKelly, B. C. (2013). Offshore wind-turbine structures: a review. *Proceedings of the Institution of Civil Engineers-Energy*, 166(4):139–152.

Arshad, M. and OKelly, B. C. (2016). Model studies on monopile behavior under long-term repeated lateral loading. *International Journal of Geomechanics*, 17(1):04016040.

Arshad, M. and OKelly, B. C. (2017). Reducing monopile rotation under lateral loading in sandy soils. *Geomechanics and Geoengineering*, 12(1):14–27.

Ashford, S. A. and Juirnarongrit, T. (2003). Evaluation of pile diameter effect on initial modulus of subgrade reaction. *Journal of Geotechnical and Geoenvironmental Engineering*, 129(3):234–242.

Augustesen, A. H., Brødbæk, K., Møller, M., Sørensen, S. P. H., Ibsen, L. B., Pedersen, T. S., and Andersen, L. (2009). Numerical modelling of large-diameter steel piles at horns rev. In *The International Conference on Civil, Structural and Environmental Engineering Computing*.

Axelsson, G. (2000). *Long-term set-up of driven piles in sand.* PhD thesis, Institutionen för anläggning och miljö.

Baber, T. T. and Wen, Y.-K. (1981). Random vibration hysteretic, degrading systems. *Journal of the Engineering Mechanics Division*, 107(6):1069–1087.

Badoni, D. and Makris, N. (1996). Nonlinear response of single piles under lateral inertial and seismic loads. *Soil Dynamics and Earthquake Engineering*, 15(1):29–43.

Baguelin, F., Frank, R., and Said, Y. (1977). Theoretical study of lateral reaction mechanism of piles. *Geotechnique*, 27(3):405–434.

Balachowski, L., Foray, P., and Rault, G. (1998). Scale effect in shaft friction due to the localisation of deformations. pages 211–216.

Banerjee, P. and Davies, T. (1978). The behaviour of axially and laterally loaded single piles embedded in nonhomogeneous soils. *Geotechnique*, 28(3):309–326.

Barton, Y. (1982). *Laterally loaded model piles in sand: Centrifuge tests and finite element analyses*. PhD thesis, University of Cambridge.

Barton, Y., Finn, W., Parry, R., Towhata, I., et al. (1983). Lateral pile response and py curves from centrifuge tests. In *Offshore Technology Conference*. Offshore Technology Conference.

Basack, S. (2005). Development of an apparatus for imparting lateral cyclic load on model pile foundation. In *Intl. Conference on Mechanical Engineering, BUET, Dhaka, Bangladesh*.

Basheer, I. (2002). Stress-strain behavior of geomaterials in loading reversal simulated by time-delay neural networks. *Journal of Materials in Civil Engineering*, 14(3):270–273.

Beemer, R. D. (2016). *Experimental Studies of Squat Gravity Caissons and Monopiles for Offshore Applications*. PhD thesis.

Bellotti, R., Jamiolkowski, M., Lo Presti, D., and O'neill, D. (1996). Anisotropy of small strain stiffness in ticino sand. *Geotechnique*, 46(1):115–132.

Beuckelaers, W. (2017). *Numerical modelling of laterally loaded piles for offshore wind turbines*. PhD thesis, University of Oxford.

Bhattacharya, S. and Adhikari, S. (2011). Experimental validation of soil-structure interaction of offshore wind turbines. *Soil Dynamics and Earthquake Engineering*, 31(5):805–816.

Bhattacharya, S., Cox, J., and Lombardi, D. (2013a). Dynamics of offshore wind turbines on two types of foundations. *Proceedings of the Institution of Civil Engineers: Geotechnical Engineering*.

Bhattacharya, S., Nikitas, N., Garnsey, J., Alexander, N., Cox, J., Lombardi, D., Muir Wood, D., and Nash, D. (2013b). Observed dynamic soil-structure interaction in scale testing of offshore wind turbine foundations. *Soil Dynamics and Earthquake Engineering*, 54:47–60.

Bienen, B., Dührkop, J., Grabe, J., Randolph, M. F., and White, D. J. (2011). Response of piles with wings to monotonic and cyclic lateral loading in sand. *Journal of Geotechnical and Geoenvironmental Engineering*, 138(3):364–375.

Biot, M. (1937). Bending of an infinite beam on an elastic foundation. *Journal of Applied Mathematics and Mechanics (ZAMM)*, 2(3):165–184.

Blaney, G. W. and O'Neill, M. W. (1986). Measured lateral response of mass on single pile in clay. *Journal of geotechnical engineering*, 112(4):443–457.

Bogard, D. and Matlock, H. (1980). Simplified calculation of py curves for laterally loaded piles in sand. *unpublished report), The Earth Technology Corporation, Inc., Houston, TX.*

Bolton, M. (1986). The strength and dilatancy of sands. *Geotechnique*, 36(2):65–78.

Bontempi, F., Gkoumas, K., Manenti, S., and Petrini, F. (2009). Basis of design for offshore wind turbines. In *Proceedings of the OWEMES 2009 Conference, Brindisi, Italy*, pages 21–23.

Bouc, R. (1971). Modele mathematique d'hysteresis. *Acustica*, 21:16–25.

Boulanger, R. W., Curras, C. J., Kutter, B. L., Wilson, D. W., and Abghari, A. (1999). Seismic soil-pile-structure interaction experiments and analyses. *Journal of Geotechnical and Geoenvironmental Engineering*, 125(9):750–759.

Bourgeois, E., Rakotonindriana, M., Le Kouby, A., Mestat, P., and Serratrice, J. F. (2010). Three-dimensional numerical modelling of the behaviour of a pile subjected to cyclic lateral loading. *Computers and Geotechnics*, 37(7):999–1007.

Bowles, l. et al. (1996). *Foundation analysis and design*. McGraw-hill.

Briaud, J. L., Smith, T., Meyer, B., et al. (1983). Using the pressuremeter curve to design laterally loaded piles. In *Offshore Technology Conference*. Offshore Technology Conference.

Brødbæk, K., Møller, M., Sørensen, S., and Augustesen, A. H. (2009). Review of py relationships in cohesionless soil.

Broms, B. B. (1964). Lateral resistance of piles in cohesionless soils. *Journal of the Soil Mechanics and Foundations Division*, 90(3):123–158.

Brown, D. A. and Shie, C.-F. (1991). Some numerical experiments with a three dimensional finite element model of a laterally loaded pile. *Computers and Geotechnics*, 12(2):149–162.

Budhu, M. and Davies, T. G. (1987). Nonlinear analysis of laterality loaded piles in cohesionless soils. *Canadian Geotechnical Journal*, 24(2):289–296.

Budhu, M. and Davies, T. G. (1988). Analysis of laterally loaded piles in soft clays. *Journal of geotechnical engineering*, 114(1):21–39.

Byrne, B. and Houlsby, G. (2003). Foundations for offshore wind turbines. *Philosophical Transactions of the Royal Society of London. Series A: Mathematical, Physical and Engineering Sciences*, 361(1813):2909–2930.

Byrne, B. and Houlsby, G. (2006). Assessing novel foundation options for offshore wind turbines. In *World Maritime Technology Conference*, pages 1–10. London, UK.

Byrne, B. and Houlsby, G. (2015). Helical piles: an innovative foundation design option for offshore wind turbines. *Phil. Trans. R. Soc. A*, 373(2035):20140081.

Byrne, B. W. and Houlsby, G. T. (2004). Experimental investigations of the response of suction caissons to transient combined loading. *Journal of geotechnical and geoenvironmental engineering*, 130(3):240–253.

Carter, D. P. (1984). *A non-linear soil model for predicting lateral pile response*. PhD thesis, ResearchSpace@ Auckland.

Carter, J. P. and Kulhawy, F. H. (1992). Analysis of laterally loaded shafts in rock. *Journal of Geotechnical Engineering*, 118(6):839–855.

Chandrasekaran, S., Boominathan, A., and Dodagoudar, G. (2010). Experimental investigations on the behaviour of pile groups in clay under lateral cyclic loading. *Geotechnical and Geological Engineering*, 28(5):603–617.

Chen, G., Pan, H., Long, H., and Li, X. (2013). Dynamic constitutive model for soils considering asymmetry of skeleton curve. *Journal of Rock Mechanics and Geotechnical Engineering*, 5(5):400–405.

Chen, R.-p., Sun, Y.-x., Zhu, B., and Guo, W. D. (2015). Lateral cyclic pile–soil interaction studies on a rigid model monopile. *Proceedings of the ICE-Geotechnical Engineering*, 168(2):120–130.

Choo, Y. W. and Kim, D. (2015). Experimental development of the p-y relationship for large-diameter offshore monopiles in sands: Centrifuge tests. *Journal of Geotechnical and Geoenvironmental Engineering*, 142(1):04015058.

Choo, Y. W., Kim, D., Park, J.-H., Kwak, K., Kim, J.-H., and Kim, D.-S. (2013). Lateral response of large-diameter monopiles for offshore wind turbines from centrifuge model tests.

Chung, R. M., Yokel, F. Y., and Drnevich, V. (1984). Evaluation of dynamic properties of sands by resonant column testing. *Geotechnical Testing Journal*, 7(2):60–69.

Commission, E. (2010). *Europe 2020: A strategy for smart, sustainable and inclusive growth: Communication from the commission*. Publications Office of the European Union.

Cox, J. A., O'Loughlin, C. D., Cassidy, M., Bhattacharya, S., Gaudin, C., and Bienen, B. (2014). Centrifuge study on the cyclic performance of caissons in sand. *International Journal of Physical Modelling in Geotechnics*, 14(4):99–115.

Cox, W. R., Reese, L. C., Grubbs, B. R., et al. (1974). Field testing of laterally loaded piles in sand. In *Offshore Technology Conference*. Offshore Technology Conference.

Cuéllar, P. (2011). *Pile foundations for offshore wind turbines: Numerical and experimental investigations on the behaviour under short-term and long-term cyclic loading*. PhD thesis, Ph. D. thesis, Technical University of Berlin, Germany.

Cuéllar, P., Georgi, S., Baeßler, M., and Rücker, W. (2012). On the quasi-static granular convective flow and sand densification around pile foundations under cyclic lateral loading. *Granular Matter*, 14(1):11–25.

Dafalias, Y. and Popov, E. (1975). A model of nonlinearly hardening materials for complex loading. *Acta mechanica*, 21(3):173–192.

Desai, C., Sharma, K., Wathugala, G., and Rigby, D. (1991). Implementation of hierarchical single surface $\delta 0$ and $\delta 1$ models in finite element procedure. *International journal for numerical and analytical methods in geomechanics*, 15(9):649–680.

Desai, C. and Wu, T. (1976). A general function for stress-strain curves. *Numerical methods in geomechanics*.

Desai, C. S. and Zaman, M. (2013). *Advanced geotechnical engineering: soil-structure interaction using computer and material models*. CRC Press.

DNV (2014). Design of offshore wind turbine structures. *Offshore Standard DNV-OS-J101*, 6.

Dobry, R., Vicente, E., O'Rourke, M., and Roesset, M. (1982). Horizontal stiffness and damping of single piles. *Journal of Geotechnical and Geoenvironmental Engineering*, 108(GT3).

Dobry, R. and Vucetic, M. (1988). *Dynamic properties and seismic response of soft clay deposits*. Department of Civil Engineering, Rensselaer Polytechnic Institute.

Dodds, A. M. and Martin, G. R. (2006). Modeling pile behavior in large pile groups under lateral loading.

Doherty, P. and Gavin, K. (2012). Laterally loaded monopile design for offshore wind farms.

Doherty, P., Li, W., Gavin, K., Casey, B., et al. (2012). Field lateral load test on monopile in dense sand. In *Offshore Site Investigation and Geotechnics: Integrated Technologies-Present and Future*. Society of Underwater Technology.

Dührkop, J., Grabe, J., Bienen, B., White, D., and Randolph, M. (2010). Centrifuge experiments on laterally loaded piles with wings. In *Vol. 2, Proceedings of International Conference on Physical Modelling in Geotechnics (ICPMG)*, pages 919–924.

Duncan, J. M. and Chang, C.-Y. (1970). Nonlinear analysis of stress and strain in soils. *Journal of Soil Mechanics & Foundations Div*.

Dyson, G. and Randolph, M. (2001). Monotonic lateral loading of piles in calcareous sand. *Journal of Geotechnical and Geoenvironmental Engineering*, 127(4):346–352.

El Naggar, M. and Novak, M. (1995). Nonlinear lateral interaction in pile dynamics. *Soil Dynamics and Earthquake Engineering*, 14(2):141–157.

El Naggar, M. H. and Wei, J. Q. (1999). Response of tapered piles subjected to lateral loading. *Canadian Geotechnical Journal*, 36(1):52–71.

Ellis, E., Cox, C., Yu, H., Ainsworth, A., and Baker, N. (2006). A new geotechnical centrifuge at the university of nottingham, uk. In *6th International Conference of Physical Modelling in Geotechnics: ICPMG*, volume 6, pages 129–33.

Engin, H. K., Brinkgreve, R. B., and van Tol, A. F. (2015). Approximation of pile installation effects: a practical tool. *Proceedings of the Institution of Civil Engineers-Geotechnical Engineering*, 168(4):319–334.

Europe, W. (2018). Offshore wind in europe–key trends and statistics 2017.

EWEA (2013). The european offshore wind industry–key trends and statistics 2013. *EWEA Annual Report*, 2013.

Fan, C.-C. and Long, J. H. (2005). Assessment of existing methods for predicting soil response of laterally loaded piles in sand. *Computers and Geotechnics*, 32(4):274–289.

Fioravante, V. (2002). On the shaft friction modelling of non-displacement piles in sand. *Soils and foundations*, 42(2):23–33.

Fleming, W., Weltman, A., Randolph, M., and Elson, W. (1992). Piling engineering, 2nd. *Edition. Blackie, Glasgow & London*.

Foglia, A., Ibsen, L. B., Andersen, L. V., Roesen, H. R., et al. (2012). Physical modelling of bucket foundation under long-term cyclic lateral loading. In *The Twenty-second International Offshore and Polar Engineering Conference*. International Society of Offshore and Polar Engineers.

Foglia, A., Ibsen, L. B., Nicolai, G., and Andersen, L. V. (2014). Observations on bucket foundations under cyclic loading in dense saturated sand. In *The International Conference of Physical Modelling in Geotechnics*, pages 667–673. CRC Press LLC.

Garnier, J. (1998). Scale effects in piles and nails loading tests in sand. *Centrifuge'98*, pages 205–210.

Garnier, J. (2013). Advances in lateral cyclic pile design: Contribution of the solcyp project. In *Proceedings of TC 209 Workshop -18th ICSMGE (4th September, Paris)*, pages 59–68.

Garnier, J., Gaudin, C., Springman, S., Culligan, P., Goodings, D., Konig, D., Kutter, B., Phillips, R., Randolph, M., and Thorel, L. (2007). Catalogue of scaling laws and similitude questions in geotechnical centrifuge modelling. *International Journal of Physical Modelling in Geotechnics*, 7(3):1.

Georgiadis, M., Anagnostopoulos, C., and Saflekou, S. (1992). Centrifugal testing of laterally loaded piles in sand. *Canadian Geotechnical Journal*, 29(2):208–216.

Gerolymos, N., Escoffier, S., Gazetas, G., and Garnier, J. (2009). Numerical modeling of centrifuge cyclic lateral pile load experiments. *Earthquake Engineering and Engineering Vibration*, 8(1):61–76.

Gerolymos, N. and Gazetas, G. (2005a). Constitutive model for 1-d cyclic soil behaviour applied to seismic analysis of layered deposits. *Soils and Foundations*, 45(3):147–159.

Gerolymos, N. and Gazetas, G. (2005b). Phenomenological model applied to inelastic response of soil-pile interaction systems. *Soils and foundations*, 45(4):119–132.

Gerolymos, N. and Gazetas, G. (2006). Development of winkler model for static and dynamic response of caisson foundations with soil and interface nonlinearities. *Soil Dynamics and Earthquake Engineering*, 26(5):363–376.

Ghee, E. and Guo, W. (2011). Flac 3d analysis on soil moving through piles. In *Proceedings of the International Symposium on Frontiers in Offshore Geotechnics*, pages 507–512. AA Balkema Publishing.

GL, W. (2007). Rules and guidelines, iv industrial services. *Guideline for the Certification of CM Systems for Wind Turbines, Edition*.

Gleser, S. M. (1953). Lateral load tests on vertical fixed-head and free-head piles. In *Symposium on lateral load tests on piles*, pages 75–93.

Glick, G. (1948). Influence of soft ground on the design of long piles. In *2nd ICSMFE*, volume 4.

Greimann, L. (1987). Pile design and tests for integral abutment bridges. Technical report.

Greimann, L., Yang, P., Edmunds, S., and Wolde-Tinsae, A. (1984). Design of piles for integral abutment bridges. Technical report.

Greimann, L. F., Yang, P.-S., and Wolde-Tinsae, A. M. (1986). Nonlinear analysis of integral abutment bridges. *Journal of Structural Engineering*, 112(10):2263–2280.

Guo, W. (2001). Subgrade modulus for laterally loaded piles. In *Proceedings of 8th International Conference on Civil and Structural Engineering Computing*, pages 273–274. Civil-Comp Press.

Guo, W. D. (2008). Laterally loaded rigid piles in cohesionless soil. *Canadian Geotechnical Journal*, 45(5):676–697.

Guo, W. D. (2014). Nonlinear response of laterally loaded rigid piles in sliding soil. *Canadian Geotechnical Journal*, 52(7):903–925.

Guo, W. D. and Ghee, E. H. (2006). Behavior of axially loaded pile groups subjected to lateral soil movement. *Geotechnical Special Publication*, 153:174.

Haiderali, A., Lau, B., Haigh, S., and Madabhushi, S. (2014). Lateral response of monopiles using centrifuge testing and finite element analysis. *Physical Modelling in Geotechnics*, pages 744–749.

Haigh, S. (2013). Foundations for offshore wind turbines. *ICPMG2014? Physical Modelling in Geotechnics*, pages 153–159.

Haigh, S. (2014). Foundations for offshore wind turbines. In *Physical Modelling in Geotechnics-Proceedings of the 8th International Conference on Physical Modelling in Geotechnics 2014, ICPMG 2014*, volume 1, pages 153–159.

Haigh, S., Houghton, N., Lam, S., Li, Z., and Wallbridge, P. (2010). Development of a 2d servo-actuator for novel centrifuge modelling. In *Proceedings of the 7th International Conference on Physical Modelling in Geotechnics*, pages 239–244.

Hald, T., Mørch, C., Jensen, L., Bakmar, C., and Ahle, K. (2009). Revisiting monopile design using py curves. results from full scale measurements on horns rev. In *Proceedings of European Offshore Wind 2009 Conference*.

Hamre, L., Feizi Khankandi, S., Strom, P., and Athanasiu, C. (2011). Lateral behaviour of large diameter monopiles at sheringham shoal wind farm. *Frontiers in offshore geotechnics II. Taylor & Francis Group, London*, pages 575–80.

Han, F., Salgado, R., and Prezzi, M. (2015). Nonlinear analyses of laterally loaded piles–a semi-analytical approach. *Computers and Geotechnics*, 70:116–129.

Hansen, J. B. (1961). The ultimate resistance of rigid piles against transversal forces. *Geoteknisk Instit., Bull.*

Hansen, M., Wolf, T. K., Rasmussen, K. L., Roesen, H. R., and Ibsen, L. B. (2013). Physical modelling of cyclic laterally loaded pile in cohesionless soil. Technical report, Department of Civil Engineering, Aalborg University.

Hardin, B. O. (1978). The nature of stress-strain behaviour for soils. In *From Volume I of Earthquake Engineering and Soil Dynamics–Proceedings of the ASCE Geotechnical Engineering Division Specialty Conference, June 19-21, 1978, Pasadena, California. Sponsored by Geotechnical Engineering Division of ASCE in cooperation with:*, number Proceeding.

Hardin, B. O. and Drnevich, V. P. (1972). Shear modulus and damping in soils: measurement and parameter effects. *Journal of Soil Mechanics & Foundations Div*, 98(sm6).

Hardin, B. O. and Richart Jr, F. (1963). Elastic wave velocities in granular soils. *Journal of Soil Mechanics & Foundations Div*, 89(Proc. Paper 3407).

Heidari, M., El Naggar, H., Jahanandish, M., and Ghahramani, A. (2014). Generalized cyclic p-y curve modeling for analysis of laterally loaded piles. *Soil Dynamics and Earthquake Engineering*, 63:138–149.

Hetényi, M. (1946). *Beams on elastic foundation: theory with applications in the fields of civil and mechanical engineering*. University of Michigan.

Houlsby, G. (1991). *How the dilatancy of soils affects their behaviour*. University of Oxford, Department of Engineering Science Oxford.

Houlsby, G. T. and Byrne, B. W. (2000). Suction caisson foundations for offshore wind turbines and anemometer masts. *Wind Engineering*, 24(4):249–255.

Huurman, M. (1996). Development of traffic induced permanent strain in concrete block pavements. *HERON, 41 (1), 1996*.

Idriss, I. and Seed, H. (1970). Soil moduli and damping factors for dynamic response analysis. *Report EERC*, 70(10).

Ishihara, K. (1996). *Soil behaviour in earthquake geotechnics*. Clarendon Press.

ISO (2007). Petroleum and natural gas industries–fixed steel offshore structures. *English version EN ISO*, 19902:182–202.

Iwasaki, T. and Tatsuoka, F. (1977). Effects of grain size and grading on dynamic shear moduli of sands. *Soils and foundations*, 17(3):19–35.

Jovičić, V. and Coop, M. (1997). Stiffness of coarse-grained soils at small strains. *Géotechnique*, 47(3):545–561.

Kagawa, T. and Kraft, L. M. (1980). Lateral load-deflection relationships of piles subjected to dynamic loadings. *Japanese Society of Soil Mechanics and Foundation Engineering*, 20(4):19–36.

Kaiser, M. J. and Snyder, B. F. (2012). Offshore wind energy system components. In *Offshore Wind Energy Cost Modeling*, pages 13–30. Springer.

Kallehave, D., Byrne, B. W., Thilsted, C. L., and Mikkelsen, K. K. (2015). Optimization of monopiles for offshore wind turbines. *Phil. Trans. R. Soc. A*, 373(2035):20140100.

Kampitsis, A. E., Giannakos, S., Gerolymos, N., and Sapountzakis, E. J. (2015). Soil–pile interaction considering structural yielding: Numerical modeling and experimental validation. *Engineering Structures*, 99:319–333.

Kellezi, L. and Hansen, P. (2003). Static and dynamic analysis of an offshore mono-pile windmill foundation. In *Proceedings of the BGA international conference on foundations: innovations, observations, design and practice, Dundee*, pages 401–410.

Kim, N.-R. and Kim, D.-S. (2011). The role of physical modeling in the design of geotechnical systems. In *Proceedings of the 1st International Workshop on Design in Civil and Environmental Engineering*, pages 11–18. Mary Kathryn Thompson.

Kirkwood, P. and Haigh, S. (2014). Centrifuge testing of monopiles subject to cyclic lateral loading. *Proceedings of physical modelling in geotechnics. Taylor and Francis, London*, pages 827–831.

Kirkwood, P. B. (2016). *Cyclic lateral loading of monopile foundations in sand*. PhD thesis, University of Cambridge.

Kishida, H. and Uesugi, M. (1987). Tests of the interface between sand and steel in the simple shear apparatus. *Géotechnique*, 37(1):45–52.

Klinkvort, R. T. (2013). *Centrifuge modelling of drained lateral pile-soil response*. PhD thesis, Technical University of Denmark.

Klinkvort, R. T. and Hededal, O. (2013). Lateral response of monopile supporting an offshore wind turbine. *Proceedings of the Institution of Civil Engineers-Geotechnical Engineering*, 166(2):147–158.

Klinkvort, R. T. and Hededal, O. (2014). Effect of load eccentricity and stress level on monopile support for offshore wind turbines. *Canadian Geotechnical Journal*, 51(9):966–974.

Klinkvort, R. T., Hededal, O., and Springman, S. M. (2013). Scaling issues in centrifuge modelling of monopiles. *International Journal of Physical Modelling in Geotechnics*, 13(2):38–49.

Klinkvort, R. T., Leth, C. T., and Hededal, O. (2012). Centrifuge modelling of monopiles in dense sand at the technical university of denmark. In *2nd European conference on Physical Modelling in Geotechnics (EUROFUGE 2012)*.

Kokusho, T. (1980). Cyclic triaxial test of dynamic soil properties for wide strain range. *Soils and foundations*, 20(2):45–60.

Kondner, R. L. (1963). Hyperbolic stress-strain response: cohesive soils. *Journal of the soil mechanics and foundations division, ASCE*, 89(1):115–143.

Kramer, S. L. (1996). Geotechnical earthquake engineering. in prentice–hall international series in civil engineering and engineering mechanics. *Prentice-Hall, New Jersey*.

Kuhlemeyer, R. L. (1979). Static and dynamic laterally loaded floating piles. *Journal of Geotechnical and Geoenvironmental Engineering*, 105(ASCE 14394).

Kulhawy, F. and Chen, Y. (1995). A thirty year perspective of broms' lateral loading models, as applied to drilled shafts. In *Proceedings, Bengt B. Broms Symposium in Geotechnical Engineering*, pages 13–15.

Kumar, N. D. and Rao, S. N. (2012). Lateral load: deflection response of an embedded caisson in marine clay. *Marine Georesources & Geotechnology*, 30(1):1–31.

Kumar, S., Lalvani, L., and Omar, M. (2006). Nonlinear response of single piles in sand subjected to lateral loads using k hmax approach. *Geotechnical and Geological Engineering*, 24(1):163–181.

Kuo, Y.-S., Achmus, M., and Abdel-Rahman, K. (2011). Minimum embedded length of cyclic horizontally loaded monopiles. *Journal of Geotechnical and Geoenvironmental Engineering*, 138(3):357–363.

Lau, B. H. (2015). *Cyclic behaviour of monopile foundations for offshore wind turbines in clay*. PhD thesis, University of Cambridge.

LeBlanc, C. (2009). *Design of offshore wind turbine support structures*. PhD thesis, Ph. D. thesis, Aalborg University, Aalborg, Denmark.

Leblanc, C., Byrne, B., and Houlsby, G. (2010). Response of stiff piles to random two-way lateral loading. *Géotechnique*, 60(9):715–721.

LeBlanc, C., Houlsby, G., and Byrne, B. (2010). Response of stiff piles in sand to long-term cyclic lateral loading. *Geotechnique*, 60(2):79–90.

Lesny, K. and Wiemann, J. (2005). Design aspects of monopiles in german offshore wind farms. In *Proceedings of the International Symposium on Frontiers in Offshore Geotechnics*, pages 383–389. AA Balkema Publishing.

Lesny, K. and Wiemann, J. (2006). Finite-element-modelling of large diameter monopiles for offshore wind energy converters. In *GeoCongress 2006: Geotechnical Engineering in the Information Technology Age*, pages 1–6.

Leth, C. T., Krogsbøll, A. S., and Hededal, O. (2008). Centrifuge facilities at technical university of denmark. *Proceedings Nordisk Geoteknikermøte nr*, 15:335–342.

Li, Z., Bolton, M. D., and Haigh, S. K. (2012). Cyclic axial behaviour of piles and pile groups in sand. *Canadian Geotechnical Journal*, 49(9):1074–1087.

Li, Z., Haigh, S., and Bolton, M. (2010). Centrifuge modelling of mono-pile under cyclic lateral loads. *Physical Modelling in Geotechnics*, pages 965–970.

Lin, S.-S. and Liao, J.-C. (1999). Permanent strains of piles in sand due to cyclic lateral loads. *Journal of Geotechnical and Geoenvironmental Engineering*, 125(9):798–802.

Ling, L. F. (1988). Back analysis of lateral load test on piles. Technical report, Faculty of Engineering, University of Auckland, New Zealand.

Little, R. L. and Briaud, J.-L. (1988). Full scale cyclic lateral load tests on six single piles in sand. Technical report, DTIC Document.

Liu, W. (2010). *Axisymmetric centrifuge modelling of deep penetration in sand*. PhD thesis, University of Nottingham.

Lombardi, D., Bhattacharya, S., and Wood, D. M. (2013). Dynamic soil–structure interaction of monopile supported wind turbines in cohesive soil. *Soil Dynamics and Earthquake Engineering*, 49:165–180.

Long, J. and Vanneste, G. (1994). Effects of cyclic lateral loads on piles in sand. *Journal of Geotechnical Engineering*, 120(1):225–244.

Loukidis, D. and Salgado, R. (2008). Analysis of the shaft resistance of nondisplacement piles in sand. *Géotechnique*.

Madabhushi, G. (2014). *Centrifuge Modelling for Civil Engineers*. CRC Press.

Madhusudan Reddy, K. and Ayothiraman, R. (2015). Experimental studies on behavior of single pile under combined uplift and lateral loading. *Journal of Geotechnical and Geoenvironmental Engineering*, 141(7):04015030.

Malhotra, S. (2007). Design and construction considerations for offshore wind turbine foundations. In *ASME 2007 26th International Conference on Offshore Mechanics and Arctic Engineering*, pages 635–647. American Society of Mechanical Engineers.

Malhotra, S. (2010). Design and construction considerations for offshore wind turbine foundations in north america. In *GeoFlorida 2010: Advances in Analysis, Modeling & Design*, pages 1533–1542.

Malhotra, S. et al. (2009). Design considerations for offshore wind turbine foundations in the united states. In *The Nineteenth International Offshore and Polar Engineering Conference*. International Society of Offshore and Polar Engineers.

Manzari, M. T. and Dafalias, Y. F. (1997). A critical state two-surface plasticity model for sands. *Geotechnique*, 47(2):255–272.

Mardfekri, M., Gardoni, P., and Roesset, J. M. (2013). Modeling laterally loaded single piles accounting for nonlinear soil-pile interactions. *Journal of Engineering*, 2013.

Masing, G. (1926). Eigenspannungen und verfestigung beim messing [fundamental stresses and strengthening with brass]: Inter-national congress of applied mechanics, 2d. *Zirich, 1926, Proceedings*.

Matasović, N. and Vucetic, M. (1993). Cyclic characterization of liquefiable sands. *Journal of Geotechnical Engineering*, 119(11):1805–1822.

MATLAB (2016). The language of technical computing, version 2016a.

Matlock, H. (1970). Correlations for design of laterally loaded piles in soft clay. *Offshore Technology in Civil Engineerings Hall of Fame Papers from the Early Years*, pages 77–94.

Matlock, H. and Reese, L. C. (1960). Generalized solutions for laterally loaded piles. *Journal of the Soil Mechanics and Foundations Division, ASCE*, 86(5):63–91.

McClelland, B. and Focht, J. A. (1958). Soil modulus for laterally loaded piles. *Transactions of the American Society of Civil Engineers*, 123(1):1049–1063.

Meyer, B. J. and Reese, L. C. (1979). Analysis of single piles under lateral loading. Technical report, Center for Highway Research, University of Texas at Austin TX.

Meyerhof, G. (1995). Behaviour of pile foundations under special loading conditions: 1994 rm hardy keynote address. *Canadian Geotechnical Journal*, 32(2):204–222.

Meyerhof, G., Mathur, S., and Valsangkar, A. (1981). Lateral resistance and deflection of rigid walls and piles in layered soils. *Canadian Geotechnical Journal*, 18(2):159–170.

Mindlin, R. D. (1936). Force at a point in the interior of a semi-infinite solid. *Physics*, 7(5):195–202.

Mo, P.-Q. (2014). *Centrifuge modelling and analytical solutions for the cone penetration test in layered soils*. PhD thesis, University of Nottingham.

Mosikeeran, T. and Larkin, T. J. (1990). *Cyclic lateral load behaviour of piles*. Department of Civil Engineering, University of Auckland.

Mostaghel, N. (1999). Analytical description of pinching, degrading hysteretic systems. *Journal of Engineering Mechanics*, 125(2):216–224.

Motta, E. (2012). Lateral deflection of horizontally loaded rigid piles in elastoplastic medium. *Journal of Geotechnical and Geoenvironmental Engineering*, 139(3):501–506.

Mrz, Z., Norris, V., and Zienkiewicz, O. (1978). An anisotropic hardening model for soils and its application to cyclic loading. *International Journal for Numerical and Analytical Methods in Geomechanics*, 2(3):203–221.

Murchison, J. M. and O'Neill, M. W. (1984). Evaluation of py relationships in cohesionless soils. In *Analysis and design of pile foundations*, pages 174–191. ASCE.

Naggar, M. H. E. and Bentley, K. J. (2000). Dynamic analysis for laterally loaded piles and dynamic p-y curves. *Canadian Geotechnical Journal*, 37(6):1166–1183.

Nakagawa, K. and Soga, K. (1995). Nonlinear cyclic stress-strain relations of soils.

Nanda, S., Arthur, I., Sivakumar, V., Donohue, S., Bradshaw, A., Keltai, R., Gavin, K., Mackinnon, P., Rankin, B., and Glynn, D. (2017). Monopiles subjected to uni-and multi-lateral cyclic loading. *Proceedings of the Institution of Civil Engineers-Geotechnical Engineering*, 170(3):246–258.

Nicolai, G. and Ibsen, L. B. (2016). Variation in stiffness of monopiles in dense sand under cyclic lateral loads. *Journal of Ocean and Wind Energy*, 3:31–36.

Nicolai, G., Ibsen, L. B., et al. (2014). Small-scale testing of cyclic laterally loaded monopiles in dense saturated sand. In *The Twenty-fourth International Ocean and Polar Engineering Conference*. International Society of Offshore and Polar Engineers.

Nikitas, G., Vimalan, N. J., and Bhattacharya, S. (2016). An innovative cyclic loading device to study long term performance of offshore wind turbines. *Soil Dynamics and Earthquake Engineering*, 82:154–160.

Novello, E. (1999). From static to cyclic py data in calcareous sediments. In *Proc. 2nd Int. Conf. on Engineering for Calcareous Sediments*, pages 17–27.

Nunez, I., Hoadley, P., Randolph, M., and Hulett, J. (1987). Driving and tension loading of piles in sand on a centrifuge. pages 353–362.

O'Reilly, M. P. and Brown, S. F. (1991). *Cyclic loading of soils: from theory to design*. Blackie Glasgow, UK.

Oztoprak, S. and Bolton, M. (2013). Stiffness of sands through a laboratory test database. *Géotechnique*, 63(1):54.

Park, D. (2013). The effect of radial g-field on the centrifuge modelling. *Hospitality and Tourism: Synergizing Creativity and Innovation in Research*, page 385.

Park, Y., Wen, Y., and Ang, A. H.-S. (1986). Random vibration of hysteretic systems under bi-directional ground motions. *Earthquake engineering & structural dynamics*, 14(4):543–557.

Pender, M. (1993). Aseismic pile foundation design analysis. *Bulletin of the New Zealand National Society for Earthquake Engrg*, 26(1):49–160.

Peng, J., Clarke, B., and Rouainia, M. (2011). Increasing the resistance of piles subject to cyclic lateral loading. *Journal of Geotechnical and Geoenvironmental Engineering*, 137(10):977–982.

Peng, J., Rouainia, M., Clarke, B., Allan, P., and Irvine, J. (2004). Lateral resistance of finned piles established from model tests. In *Proceedings of the International Conference on Geotechnical Engineering-Beirut, CFMS, Lebanon*, pages 565–571.

Peng, J.-R., Clarke, B. G., and Rouainia, M. (2006). A device to cyclic lateral loaded model piles. *Geotechnical Testing Journal*, 29(4):1–7.

Peng, J.-R., Rouainia, M., and Clarke, B. (2010). Finite element analysis of laterally loaded fin piles. *Computers & structures*, 88(21):1239–1247.

Peralta, P. and Achmus, M. (2010). An experimental investigation of piles in sand subjected to lateral cyclic loads. In *W: Proceedings of 7th International Conference on Physical Modeling in Geotechnics, Zurich, Switzerland*.

Pérez Foguet, A. (2000). *Numerical modelling of complex geomechanical problems*. Universitat Politècnica de Catalunya.

Pestana, J. M. and Salvati, L. A. (2006). Small-strain behavior of granular soils. i: Model for cemented and uncemented sands and gravels. *Journal of geotechnical and geoenvironmental engineering*, 132(8):1071–1081.

Pestana, J. M. and Whittle, A. (1995). Compression model for cohesionless soils. *Géotechnique*, 45(4):611–631.

Petrasovits, G. and Awad, A. (1972). Ultimate lateral resistance of a rigid pile in cohesionless soil. In *Fifth Eur Conf On Soil Proc/Sp/*, number Conf Paper.

Petrini, F., Li, H., and Bontempi, F. (2010). Basis of design and numerical modeling of offshore wind turbines. *Structural engineering & mechanics*, 36(5):599.

Poulos, H. G. (1971). Behavior of laterally loaded piles i. single piles. *Journal of Soil Mechanics & Foundations Div*.

Poulos, H. G. (1988). *Marine geotechnics*. Routledge.

Poulos, H. G. and Davis, E. H. (1980). *Pile foundation analysis and design*. Number Monograph.

Poulos, H. G. and Hull, T. S. (1989). The role of analytical geomechanics in foundation engineering. In *Foundation engineering: Current principles and practices*, pages 1578–1606. ASCE.

Prasad, Y. V. and Chari, T. (1999). Lateral capacity of model rigid piles in cohesionless soils. *Soils and Foundations*, 39(2):21–29.

Presti, D. L., Pallara, O., Lancellotta, R., Armandi, M., and Maniscalco, R. (1993). Monotonic and cyclic loading behavior of two sands at small strains. *Geotechnical Testing Journal*, 16(4):409–424.

Prevost, J. H. (1985). A simple plasticity theory for frictional cohesionless soils. *International Journal of Soil Dynamics and Earthquake Engineering*, 4(1):9–17.

Pugasap, K. (2006). *Hysteresis model based prediction of integral abutment bridge behaviour*. PhD thesis, The Pennsylvania State University.

Pyke, R. M. (1980). Nonlinear soil models for irregular cyclic loadings. *Journal of Geotechnical and Geoenvironmental Engineering*, 106(ASCE 15829).

Qin, H. (2010). *Response of pile foundations due to lateral force and soil movements*. PhD thesis, Griffith University.

Ramberg, W. and Osgood, W. R. (1943). *Description of stress-strain curves by three parameters*. Technical Note No. 902. Washington, DC: National Advisory Committee for Aeronautics;.

Randolph, M. F. (1981). The response of flexible piles to lateral loading. *Geotechnique*, 31(2):247–259.

Rascol, E. (2009). *Cyclic properties of sand: dynamic behaviour for seismic applications*. PhD thesis, PhDthesis, ÉcolePolytechniqueFé déralede Lausanne EPFL.

Reddy, E. S. B. (1996). *An investigation into the response of piles in sand under vertical cyclic tensile loads*. PhD thesis, The University of Nottingham.

Reese, L. C., Cox, W. R., and Koop, F. D. (1974). Analysis of laterally loaded piles in sand. *Offshore Technology in Civil Engineering Hall of Fame Papers from the Early Years*, pages 95–105.

Reese, L. C. and Matlock, H. (1956). *Non-dimensional solutions for laterally-loaded piles with soil modulus assumed proportional to depth*. Association of Drilled Shaft Contractors.

Reese, L. C. and Van Impe, W. F. (2010). *Single piles and pile groups under lateral loading*. CRC Press.

Remaud, D. (1999). Pieux sous charges latérales: étude expérimentale de l'effet de groupe. *THESE DE DOCTORAT, DISCIPLINE: SCIENCES DE L'INGENIEUR, SPECIALITE: GENIE CIVIL*.

Richart Jr, F. E. (1975). Some effects of dynamic soil properties on soil-structure interaction. *Journal of Geotechnical and Geoenvironmental Engineering*, 101(ASCE# 11764 Proceeding).

Roesen, H. R., Andersen, L. V., Ibsen, L. B., Foglia, A., et al. (2012a). Experimental setup for cyclic lateral loading of monopiles in sand. In *The Twenty-second International Offshore and Polar Engineering Conference*. International Society of Offshore and Polar Engineers.

Roesen, H. R., Ibsen, L. B., and Andersen, L. V. (2012b). Small-scale testing rig for long-term cyclically loaded monopiles in cohesionless soil. *Ngm 2012 Proceedings*.

Roscoe, K. (1963). Mechanical behaviour of an idealized'wet'clay. In *Proc. 3rd Eur. Conf. Soil Mech. Wiesbaden, 1963*, volume 1, pages 47–54.

Rosquoët, F., Garnier, J., Thorel, L., and Canepa, Y. (2004). Horizontal cyclic loading of piles installed in sand: study of the pile head displacement and maximum bending moment. In *Proceedings of the International Conference on Cyclic Behavior of Soils and Liquefaction Phenomena*, pages 363–368. Taylor & Francis.

Rosquoet, F., Thorel, L., Garnier, J., and Canepa, Y. (2007). Lateral cyclic loading of sand-installed piles. *Soils and foundations*, 47(5):821–832.

Rudolph, C., Grabe, J., and Bienen, B. (2013). Response of monopiles under cyclic lateral loading with a varying loading direction. In *ICPMG2014–Physical Modelling in Geotechnics: Proceedings of the 8th International Conference on Physical Modelling in Geotechnics 2014 (ICPMG2014), Perth, Australia, 14-17 January 2014*, page 453. CRC Press.

Rudolph, C., Grabe, J., and Bienen, B. (2015). Response of monopiles under cyclic lateral loading with a varying loading direction. *Electromagnetic Boundary Problems*, page 453.

Saue, M., Langford, T., and Mortensen, N. (2011). Design of monopile foundations in sand for offshore windfarms. In *International Symposium: Frontiers in Offshore Geotechnics, Perth, Australia*.

Schnabel, P. B. (1972). Shake: A computer program for earthquake response analysis of horizontally layered sites. *EERC Report 72-12, University of California, Berkeley.*

Schofield, A. N. (1980). Cambridge geotechnical centrifuge operations. *Geotechnique*, 30(3):227–268.

Scott, R. F. (1980). Analysis of centrifuge pile tests; simulation of pile-driving.

Seed, H. B. and Idriss, I. M. (1970). Soil moduli and damping factors for dynamic response analyses. Technical report.

Shahnazari, H., Dehnavi, Y., and Alavi, A. H. (2010). Numerical modeling of stress–strain behavior of sand under cyclic loading. *Engineering Geology*, 116(1):53–72.

Shepley, P. (2014). *Water injection to assist pile jacking*. PhD thesis, University of Cambridge.

Song, J. and Der Kiureghian, A. (2006). Generalized bouc–wen model for highly asymmetric hysteresis. *Journal of engineering mechanics*, 132(6):610–618.

Sørensen, S. P. H. (2012). *Soil-Structure Interaction for Non-Slender, Large-Diameter Offshore Monopiles: Vol*. PhD thesis, Ph. D. thesis, Department of Civil Engineering, Aalborg University.

Sørensen, S. P. H., Brodbaek, K., Moller, M., Augustesen, A. H., and Ibsen, L. B. (2009). Evaluation of the load-displacement relationships for large-diameter piles in sand. In *The International Conference on Civil, Structural and Environmental Engineering Computing*. Civil-Comp Press.

Stewart, H. E. (1986). Permanent strains from cyclic variable-amplitude loadings. *Journal of Geotechnical Engineering*, 112(6):646–660.

Stewart, J. P. (2008). *Benchmarking of nonlinear geotechnical ground response analysis procedures*. Pacific Earthquake Engineering Research Center.

Sun, K. (1994). Laterally loaded piles in elastic media. *Journal of geotechnical engineering*, 120(8):1324–1344.

Taciroglu, E., Rha, C., and Wallace, J. W. (2006). A robust macroelement model for soil–pile interaction under cyclic loads. *Journal of geotechnical and geoenvironmental engineering*, 132(10):1304–1314.

Tak Kim, B., Kim, N.-K., Jin Lee, W., and Su Kim, Y. (2004). Experimental load–transfer curves of laterally loaded piles in nak-dong river sand. *Journal of Geotechnical and Geoenvironmental Engineering*, 130(4):416–425.

Taylor, R. (1995). Centrifuges in modelling: principles and scale effects. *Geotechnical centrifuge technology*, pages 19–33.

Terzaghi, K. (1955). Evaluation of coefficient of subgrade reaction. *Geotechnique*, 5(4):41–50.

Thavaraj, T. (2000). *Seismic analysis of pile foundations for bridges*. PhD thesis, University of British Columbia.

Thyagarajan, R. S. (1989). Modeling and analysis of hysteretic structural behavior.

Trochanis, A. (1994). Simplified model for analysis of one or two piles. *J. Engrg. Mech., ASCE*, 120:308–329.

Trochanis, A. M., Bielak, J., and Christiano, P. (1991a). Simplified model for analysis of one or two piles. *Journal of Geotechnical Engineering*, 117(3):448–466.

Trochanis, A. M., Bielak, J., and Christiano, P. (1991b). Three-dimensional nonlinear study of piles. *Journal of Geotechnical Engineering*, 117(3):429–447.

Truong, P., Lehane, B., Zania, V., and Klinkvort, R. T. (2018). Empirical approach based on centrifuge testing for cyclic deformations of laterally loaded piles in sand. *Géotechnique*, pages 1–13.

Verdure, L., Garnier, J., and Levacher, D. (2003). Lateral cyclic loading of single piles in sand. *International journal of physical modelling in geotechnics*, 3(3):17–28.

Vesic, A. (1961). Beams on elastic subgrade and the winklers hypothesis. In *Proceedings, 5th International Conference on Soil Mechanics and Foundation Engineering*, volume 1, pages 845–850.

Villalobos, F. (2006). *Model testing of foundations for offshore wind turbines*. PhD thesis, Ph. D. thesis, Univ. of Oxford, Oxford, UK.

Vucetic, M. and Dobry, R. (1988). Degradation of marine clays under cyclic loading. *Journal of Geotechnical Engineering*, 114(2):133–149.

Vucetic, M. and Dobry, R. (1991). Effect of soil plasticity on cyclic response. *Journal of geotechnical engineering*, 117(1):89–107.

Welch, R. C. and Reese, L. C. (1972). Lateral load behavior of drilled shafts. Technical report, University of Texas at Austin.

Wen, Y.-K. (1976). Method for random vibration of hysteretic systems. *Journal of the engineering mechanics division*, 102(2):249–263.

Wesselink, B., Murff, J., Randolph, M., Nunez, I., and Hyden, A. (1988). Analysis of centrifuge model test data from laterally loaded piles in calcareous sand. *Engineering for calcareous sediments*, 1:261–270.

Westgate, Z. J. and DeJong, J. T. (2005). Geotechnical considerations for offshore wind turbines. *Amherst, MA: U. of Massachusetts and the Massachusetts Technology Collaborative*.

Wichtmann, T. and Triantafyllidis, T. (2009). Influence of the grain-size distribution curve of quartz sand on the small strain shear modulus g max. *Journal of geotechnical and geoenvironmental engineering*, 135(10):1404–1418.

Winkler, E. (1867). *The doctrine of elasticity and strength: with particular regard to their application in engineering for polytechnic schools, building academies, engineers, mechanical engineers, architects, etc*, volume 1.

Wood, D. M. (2003). *Geotechnical modelling*, volume 1. CRC Press.

Xue, J., Gavin, K., Murphy, G., Doherty, P., and Igoe, D. (2016). Optimization technique to determine the py curves of laterally loaded stiff piles in dense sand. *Geotechnical Testing Journal*, 39(5):842–854.

y Puertos, C. (2011). *Pile foundations for offshore wind turbines: numerical and experimental investigations on the behaviour under short-term and long-term cyclic loading*. PhD thesis, Ph. D. thesis, Technical University of Berlin, Berlin, Germany.

Yan, L. and Byrne, P. M. (1992). Lateral pile response to monotonie pile head loading. *Canadian Geotechnical Journal*, 29(6):955–970.

Yang, Z., Elgamal, A., and Parra, E. (2003). Computational model for cyclic mobility and associated shear deformation. *Journal of Geotechnical and Geoenvironmental Engineering*, 129(12):1119–1127.

Yi, F. (2010). Nonlinear cyclic characteristics of soils. In *GeoFlorida 2010: Advances in Analysis, Modeling & Design*, pages 2601–2610.

Zhang, C., White, D., and Randolph, M. (2010). Centrifuge modeling of the cyclic lateral response of a rigid pile in soft clay. *Journal of Geotechnical and Geoenvironmental Engineering*, 137(7):717–729.

Zhang, L. (2009). Nonlinear analysis of laterally loaded rigid piles in cohesionless soil. *Computers and Geotechnics*, 36(5):718–724.

Zhang, L., Silva, F., and Grismala, R. (2005). Ultimate lateral resistance to piles in cohesionless soils. *Journal of Geotechnical and Geoenvironmental Engineering*, 131(1):78–83.

Zhu, B., Byrne, B., and Houlsby, G. (2012). Long-term lateral cyclic response of suction caisson foundations in sand. *Journal of Geotechnical and Geoenvironmental Engineering*, 139(1):73–83.

Zhu, B., Sun, Y., Chen, R., Guo, W., and Yang, Y. (2015). Experimental and analytical models of laterally loaded rigid monopiles with hardening p-y curves. *Journal of Waterway, Port, Coastal, and Ocean Engineering*, 141(6):04015007.